Civil Engineering Study
Structural Series 89-30

INELASTIC SEISMIC RESPONSE OF REINFORCED-CONCRETE LOW-RISE SHEAR WALLS AND BUILDING STRUCTURES

by Franklin Y. Cheng
Curators' Professor

Gregory E. Mertz
Graduate Assistant

Department of Civil Engineering
University of Missouri-Rolla
Rolla, MO 65401-0249

Report Series
Prepared for the National Science Foundation under Grant
NSF ECE 8513852

ABSTRACT

Low-rise structures composed of shear walls are commonly used in the United States. The seismic response behavior of these structures however, is not adequately understood. This is mainly because 1) the low-rise walls have significant coupling effect on deformations due to bending and shear; the bending and shear deformations must be separated through experimental and analytical studies, 2) for strong ground motions, the response of the structure is highly nonlinear; for nonlinear analysis, the hysteresis loops of a typical wall must be established on the basis of separated bending and shear deformations, and 3) the configurations of low-rise buildings are usually unsymmetric, for which the effect of interacting ground motion is significant and the multicomponent seismic input must be considered in the response behavior studies. The aforementioned items were not investigated previously and are studied in this research project.

A technique of calculating inelastic deformation of low-rise shear walls is presented with consideration of coupling effect for bending and shear deformations, axial deformation, and the deformation due to base rotation. An interaction surface of moment-shear-bending curvature-shear strain is developed from which the load-deformation behavior can be determined for a given moment to shear ratio.

The hysteresis loops are established on the basis of experimental data and analytical results for bending, shear and axial forces. Eleven hysteresis rules are comprehensively formulated for bending and shear cyclic and earthquake-type load-deformation relationships, with all possible combinations of large and small amplitude loops. The accuracy of the hysteresis rules for the monotonic and cyclic response is assured by comparisons with experimental data.

Response studies of low-rise symmetric and unsymmetric buildings with isolated shear walls are performed. The peak base shear, displacement, ductility, and excursion ratio are investigated for their sensitivity to the structural configurations and the interacting earthquake motions. Various earthquakes such as 1940 El Centro, 1952 Taft, and 1985 Mexico are used to study the elastic and inelastic response behavior of these structures.

The sensitivity of the code response parameters R and C_d for these two buildings is also studied. The response modification factor, R, is found to be dependent on the building configuration, earthquake ground motion, orientation of ground motion, number of components of the earthquake ground motion, and the damage level in the building. For the two buildings studied, the R value of 4.5 recommended in NEHRP is consistent with the calculated values for the 1940 El Centro and 1952 Taft ground motions. The calculated R value for the 1985 Mexico earthquake is much lower. The deflection amplitude factor, C_d, increases with damage index. The C_d value of 4 recommended in NEHRP is slightly larger than the calculated values.

The response of box-type structures is shown to be different from the response of buildings with isolated shear walls because of the influence of the shear wall's axial stiffness. The influence of the wall's axial hysteresis loops on the lateral hysteresis loops of a box-type structure is studied. The comparison of calculated and experimental response from shaking table tests for a R/C box structure is good.

ACKNOWLEDGMENTS

This is one of a series of reports on response analysis and optimum design of building systems with multicomponent seismic input and code provisions studied at UMR. This report is based on a joint research project undertaken by a team at NCKU (National Cheng-Kung University, Taiwan) and UMR. NCKU performed experimental work and UMR carried out analytical studies. UMR work was supported by the National Science Foundation under the grant NSF ECE 8513852. The authors gratefully acknowledge the NSF support and the experimental data provided by NCKU team, particularly Dr. S.C. Liu of NSF, Drs. M.S. Sheu, W.M. Liao, and Y.T. Kuo of NCKU. Dr. Sheu is the principal investigator of the NCKU team.

The authors also received some experimental data from the Los Alamos National Laboratory and deeply appreciated the cooperation of Drs. C.A. Anderson, J.G. Bennett, R.C. Dove, E.G. Endebrock, and C.R. Farrar for their cooperation.

Special thanks are due to the staff of the University of Missouri-Rolla Computer Center, the National Center for Supercomputing Applications at the University of Illinois at Urbana-Champaign, and the Center for Theory and Simulation in Science and Engineering at Cornell University, for their excellent service support.

TABLE OF CONTENTS

LIST OF ILLUSTRATIONS

LIST OF TABLES

NOMENCLATURE

[A]	transformation matrix
A	acceleration
BLC	base line correction
[C]	rotational transformation matrix; damping matrix
C_d	displacement modification factor
D	displacement
Dc	cracking displacement
DE	damping energy
DI	damage index
DIR	direction of current loading
DM	maximum past displacement
D2	displacement at common point
dof	degree of freedom
E_i	input energy
ESE	elastic strain energy
F	force
f'_c	ultimate concrete compression stress
f'_{cr}	ultimate concrete tensile stress
[G]	geometric stiffness matrix
GCS	global coordinate system
Gdof	global degree of freedom
h	height
JCS	joint coordinate system
K	stiffness
K_a	axial stiffness

K_b	bending stiffness
K_s	shear stiffness
KE	kinetic energy
M	mass; moment
N	axial load for geometric stiffness
P	load
PM	maximum past load
Pc	cracking load
PSD	power spectral density
PSE	plastic strain energy
P2	load at common point
R	response modification factor; reaction
SI	elastic stiffness
SE	strain energy
SL	reloading stiffness after unloading from the same direction in the bending hysteresis model
SR	reloading stiffness after unloading from the opposite direction in the bending and shear hysteresis models; reloading stiffness inside small amplitude loops in the bending hysteresis model
SRL, SX1, SX2	reloading stiffness inside small amplitude loops in the shear hysteresis model
SR1, SR2	reloading stiffness after unloading from the opposite direction in the shear hysteresis model
S1, S2, S3	unloading stiffness in bending and shear hysteresis models
S′	reloading stiffness after unloading from the opposite direction in the bending hysteresis model
$[T_{ms}]$	constraint transformation matrix

t	time
U	unbalanced force; bond stress
u	axial displacement
V	shear; velocity
v	shear displacement
w	width
α	mass proportional damping coefficient; height of shear wall element's upper rigid body
β	stiffness proportional damping coefficient; height of shear wall element's lower rigid body; hysteretic energy coefficient for the damage index; angle of principal concrete stress and strain
γ	shear strain
Δt	time step
δ	displacement
$\dot{\delta}$	velocity
$\ddot{\delta}$	acceleration
δb	bending displacement
δs	shear displacement
ε	strain; excursion ratio
ε_o	concrete strain at f'_c
θ	bending rotation
λ	shear softening term for concrete stress-strain model
μ	ductility
σ	stress
τ	shear stress
ϕ	bending curvature
ψ	shear bending influence angle

I. INTRODUCTION

A. OBJECTIVE

Structures composed of shear walls have large translational stiffness of which the overall lateral deformation can be attributed more to shear deformation than bending. The calculated period of such a structure is usually below the point at which the calculated response spectrum is in nearly constant acceleration that may be changed to a constant velocity. A common index value, which is used to determine the design force level in a given structure, is the fundamental period. For reinforced concrete structures the calculation of these periods is typically made for the uncracked state of the structure. Some experiments on slender walls showed that effective stiffness is much less than uncracked stiffness (42, 44, 46, 49, 53). The change in structural period can significantly influence system responses which in turn will affect floor responses. Thus a series of experimental and analytical studies of stocky walls with small height to width ratios must be conducted to formulate mathematical models for analyzing shear wall structural systems.

For earthquake excitations, the shear wall cracks and the reinforcing bars in the wall yield. As the structure vibrates, the cracks open and close, the concrete is loaded and unloaded and the reinforcing bars are subject to large and small amplitude stress reversals. Thus the behavior of the shear wall subject to a strong earthquake is highly nonlinear. A slender shear wall with boundary columns and a large height to width ratio is normally idealized (49, 61, 74, 75) as 1) an equivalent column for which uncoupled flexural and shear deformation is taken into account, 2) a braced frame in which shear deformation is represented by deformation of diagonal elements, and flexural deformation is represented by deformation of vertical elements, 3) short line segments along the height with each short segment being composed of hysteretic

segments, and 4) three vertical line elements in which the two outside line elements represent the axial stiffness (variable) of the columns and the central line element signifies the axial, shear, and rotational springs of the wall. Among other researchers, Cheng and his associates have developed computer codes and then studied structural response behavior of various structural configurations (15, 16, 21, 52). However analytical information on low-rise wall systems is scarce.

For short stocky shear walls with small height to width ratios and without boundary columns, the dominant deformation may be due to shear. The hysteretic loops resulting from shear, because of pinching effect, are much narrower than those for the hysteretic loops resulting from bending. Use of the slender wall models for stocky walls would provide inaccurate and unsafe predictions of the response.

Buildings and earthquake motions are three-dimensional in nature. Earthquake motions, in fact, have six components. Cheng, among others, studied the effect of one horizontal component coupled with a vertical seismic motion on plane structural response (24, 25, 26). He and his associates later studied the interaction of ground motion of two horizontal components and one vertical component on three-dimensional buildings and frameworks (19, 20, 21, 27), and further studied the effect of six-component seismic input on structural responses (17, 18). Low-rise buildings are normally not symmetric and are sensitive to interactive ground motions.

Low-rise buildings actually constitute a large percentage of total building construction. Many of these buildings are braced by shear walls without boundary columns. Thus the research is urgently needed and the results have significant impact on structural design for improving both the safety of these buildings as well as reducing their damage cost.

Industrial buildings, such as the auxiliary buildings at a nuclear power plant facilities, are low-rise box-shaped shear wall systems, primarily constructed of reinforced concrete, possibly including steel beams and columns to support floor slabs. Structural failure could lead to loss of function of the components housed in the building. Again, the research is urgently needed and the results may have a significant impact on the structural design of industrial buildings, on the equipment and piping design, and on their margins of of safety.

A joint research project was developed with the experimental work preformed at the National Cheng-Kung University (NCKU), Taiwan, and the analytical studies conducted at the University of Missouri-Rolla (UMR). The analytical studies include the development of a nonlinear stiffness model that has elements representing deformations due to bending, shear, and bond slip at the base of the wall. The stiffness model is used to calculate the monotonic load-deformation behavior. The dynamic response is based on the hysteresis loops and the stiffness model. The hysteresis loops are modelled from experimental and analytical work for cyclic and earthquake-type load-deformation relationships. The accuracy of the calculated behavior is assured by comparisons with experimental test data. Also included are response studies of low-rise buildings with isolated shear walls for investigating response behavior influenced by the following parameters: 1) the amount of structural damage, 2) the configuration of the building system, 3) the different records of earthquake ground motion, and 4) the number of components of the earthquake ground motion.

The response of box-type structures is also studied. The response differs from the response of buildings with isolated shear walls because of the influence of the shear wall's axial stiffness. The influence of the wall's axial stiffness on the response of a box-type structure is investigated. The analytical results are compared favorably with the experimental data from the shaking table tests.

B. OVERVIEW

A brief description of the contents is given below. In Chapter II the static experimental studies performed by Sheu, et al (72) are studied. A method is developed to separate the bending and shear deformations of isolated shear walls. The ratios of bending to total deformation of various walls are observed. Failure ductilities and excursion ratios are investigated. The ratios of vertical to horizontal expansions of the walls are obtained. Furthermore, the results of dynamic experiments performed by Bennett, Anderson, Endebrock, et al (3, 30, 31, 33, 34, 35) are compared with the analytical results. The experimental accelerations are integrated for velocities and displacements of which the spectra of the accelerations are analyzed. Correction methods to remove experimental errors from the acceleration test data are also included.

In Chapter III a method is presented to calculate the monotonic load-deformations of shear walls that considers the coupling behavior of shear and bending deformations. Comparisons between calculated and experimental load-deformation responses for 27 shear walls are made. The 27 shear walls represent various reinforcement ratios, boundary elements, and height to width ratios.

In Chapter IV bending and shear hysteresis models for low-rise shear walls are developed. These semi-empirical hysteresis models are based on the experimental results of five NCKU shear walls and the analytical monotonic load-deformation relationships. The calculated and experimental responses for the five NCKU shear walls are compared.

Chapter V presents the matrix formulation which is used to analyze three dimensional structural systems subject to both static and dynamic loadings. A shear wall stiffness element is developed that utilizes the bending and shear backbone curves

developed in Chapter III and the hysteresis models developed in Chapter IV. Additionally the energies in the structure, the damage indices, the ductilities, and the excursion ratios are calculated.

In Chapter VI the response of low-rise buildings with isolated shear walls are studied. These studies consist of two buildings (symmetric and nonsymmetric) subject to various earthquake ground motions (1940 El Centro, 1952 Taft, and 1985 Mexico) using both one and two horizontal components of ground motion. The responses of elastic (undamaged) and nonlinear (damaged) buildings are examined. The nonlinear response is calculated at three different intensities of ground motion to determine the response at various damage levels. The response parameters examined are the base shear, displacement, ductility, excursion ratio, and the damage index. Additionally the sensitivity of two building code parameters R and C_d are studied.

In Chapter VII the calculated response of two box-type structures is compared with the experimental response. One of the structures is subject to static cyclic loading, the other is subject to seismic loading. The effects of the axial stiffness on the systems stiffness are discussed.

In Chapter VIII the work is reviewed and the conclusions based on the results are outlined.

Appendix A contains the derivation of the Fourier transform. The power spectrum density and the frequency response function are also derived.

Appendix B contains the parabolic base line correction used for correcting acceleration test data.

C. LITERATURE REVIEW

The early experimental investigations on low-rise shear walls were to determine their strength to resist blast loadings from atomic weapons. These experimental investigations of R/C shear walls were performed by Galletly (39), Benjamin and Williams (9). The studies focused on the behavior of low-rise shear walls with boundary columns subject to static monotonic loadings. Parameters studied were the panel dimensions, reinforcements, and boundary element proportions. A method to calculate the approximate load-deformation relationships was proposed. Antebi, et al (6) experimentally studied the behavior of low-rise shear walls with boundary elements subject to dynamic blast loadings for which an analytical method was proposed to calculate the dynamic strength of the walls. The studies by Galletly, Benjamin, Williams, and Antebi led to the development of design criteria for R/C shear walls subject to blast loadings (4). According to Cardenas, "Their proposed design equations had limited practical use due to restrictions in their applicability." (13).

For high-rise shear walls, Oesterle, et al (37, 57, 59) studied the behavior of walls with rectangular, barbell, and flanged cross sections under static monotonic and static cyclic loadings. For these high-rise walls, "it was found that shear distortions within the hinging region are coupled to the flexural rotations." (59). Oesterle recognized the web crushing failure mechanism (60) and reported damping ratios for walls from free vibration test (58). Additional tests on repaired walls were performed by Fiorato, et al (38).

Wang (83), Vallenas (80) and Iliya (48), with Bertero and Popov, studied the behavior of high-rise shear walls with boundary columns. Vallenas observed that "Excellent behavior [to static cyclic earthquake loadings] was obtained in well designed R/C structural walls." (80). The shear deformation in several of the walls was from 43% to 87% of the bending deformation (80). This indicates a significant amount of

shear deformation. Analytical models were developed to calculate the monotonic behavior of high-rise shear walls. Additional cyclic models were investigated.

The work by Cardenas, et al (12, 13) on high-rise walls indicates that, "Results indicate that the flexural strength of rectangular shear walls can be calculated using the same assumptions as for reinforced concrete beams. Also, the strength of high-rise shear walls containing minimum horizontal shear reinforcement is generally controlled by flexure." (12). This research combined with the work of Galletly, Benjamin, Williams and Antebi led to the development of Section 11.16, Special Provisions for Walls, of the 1971 ACI Building Code (13), which is equivalent to Section 11.16, Special Provisions for Walls of the 1983 ACI Building Code (1).

From the above observations, one may conclude that the research for high-rise walls includes walls with and with out boundary elements and that the effect of shear on the total deformation for some walls is significant. For low-rise walls, the effect of shear deformations apparently should increase.

For the low-rise shear walls, Cardenas, et al (13, 14) studied the walls with a height to width ratio of 1. In the study, boundary columns were not included, and the amount and distribution of reinforcement were the major variables studied. "Results indicate that low-rise rectangular walls can develop shear stresses on the order of $10\sqrt{f'_c}$ psi. " (14).

Barda, et al (7, 8) tested low-rise shear walls with flanged boundary elements subject to both static monotonic and static cyclic loadings. The static cyclic loadings were intended to represent the demands placed on the shear wall during a severe earthquake. The behavior of these walls was dominated by shear. "The results indicate that current design procedures [ACI 318-71] underestimate the strength of low-rise

shear walls, even when the walls are subjected to reversed load." (7) Barda also proposed a modified strength design criteria.

Paulay, et al (67) tested low-rise walls subject to static cyclic loadings with and without boundary columns, having a height to width ratio of 0.54. One objective of the study was to determine methods to control sliding shear deformation. "It is postulated that with suitably arranged diagonal wall reinforcement a predominantly flexural response mode with good energy dissipating characteristics can be achieved in squat [low-rise] shear walls." (67). Paulay also proposed that the wall be designed such that the wall's shear capacity is greater than the flexural strength, thus forcing the wall to fail in flexure rather than shear.

Umemura, et al (78, 79) have performed tests on shear walls and box-type structures. The purpose of these tests was "to investigate the behavior of box and cylinder type shear walls under cyclic loading simulating earthquake forces on walls of atomic reactors and other structures." (78). The experimental investigations include: 1) test of flanged shear walls with and without web openings, having a height to width ratio of about 1, 2) test of different reinforcement schemes around web openings, and 3) test of box-type structures with and with out openings, having height to width ratios of about 1. Loading schemes consisted of both static monotonic and static cyclic loadings. Uncoupled bending and shear models were used with limited success to calculate the monotonic load-deformation behavior.

Bennett, Anderson, Endelbrock, et al (3, 30, 31, 33, 34, 35) of the Los Alamos National Laboratory (LANL), lately tested a series of small scale shear walls and box-type structures subject to both static and earthquake loadings. The purpose of these tests was to demonstrate that the nonlinear behavior of a box-type R/C structure caused the natural frequency to shift into the frequency range for which the earthquake's energy content is significant. This may result in increased amplification

in the floor response spectra at lower frequencies and will have significant impact on the equipment and piping design response spectra and their margins of safety.

From the above literature review, one may observe that a great deal of research work has been developed for low-rise shear walls. Most of the work, however, has emphasized walls with boundary elements, with the specific goals of determining the ultimate capacity of the walls, and studying the behavior under cyclic loading. The aforementioned work, among others, carried out in the U.S. and abroad cannot provide adequate information to develop hysteresis rules for isolated low-rise walls because, 1) most of the walls subjected to cyclic loading had boundary elements, 2) the shear and bending deformations were not separated on many of the walls without boundary columns, and 3) the cyclic loading patterns used in the test did not provide sufficient information to develop large and small amplitude loops for earthquake response studies. Consequently, a joint research project was established between the National Cheng-Kung University (NCKU) and the University of Missouri-Rolla (UMR).

Sheu (72) at NCKU tested a series of isolated low-rise shear walls subjected to various static monotonic, cyclic, and earthquake-type loadings as part of a cooperative research program. These tests demonstrated that lightly reinforced, isolated low-rise shear walls are capable of resisting earthquake loadings at large levels of damage. UMR has incorporated experimental data from NCKU and some from LANL in the research presented herein.

II. ANALYSIS OF STATIC AND DYNAMIC EXPERIMENTAL RESULTS

A. ANALYSIS OF STATIC RESULTS

The analysis of isolated low-rise shear walls tested by Sheu (72) at the National Cheng Kung University is discussed in this section. These walls are rectangular in cross section, have a width of 100 cm and a thickness of 10 cm as shown in Figure 1. The height varies from 50 cm to 75 cm, which gives height to width ratios from 0.50 to 0.75. The horizontal and vertical reinforcements consist of evenly spaced D10 through D19 bars[1] as shown in Table I. The steel stress-strain curves are shown in Figure 2. Concrete strengths vary from 210 kg/cm^2 to 330 kg/cm^2.

A 30 cm x 30 cm cap element is cast at the top of the wall as shown in Figure 1. Loads are applied at the center line of this element. A 30 cm x 55 cm rigid base is cast at the base of the wall. This base is bolted to the test bed. Both the cap element and the rigid base are heavily reinforced.

Four different loading patterns are used. Walls SW1a and SW4a are subject to a one sided cyclic loading as shown in Figure 3. Walls SW3 and SW6 are subject to an earthquake loading as shown in Figure 4. Walls SW5 and SW11 are subject to a two sided cyclic loading. The loading pattern for wall SW5 is shown in Figure 5. Walls SW4, SW10, SW12, SW13, SW14, SW15, SW16, SW19 and SW20 are subjected to a monotonically increasing load. A typical monotonic loading pattern for wall SW4 is also shown in Figure 5.

---

[1] D10 ≅ #3 reinforcing bar. D13 ≅ #4 reinforcing bar.
D16 ≅ #5 reinforcing bar. D19 ≅ #6 reinforcing bar.

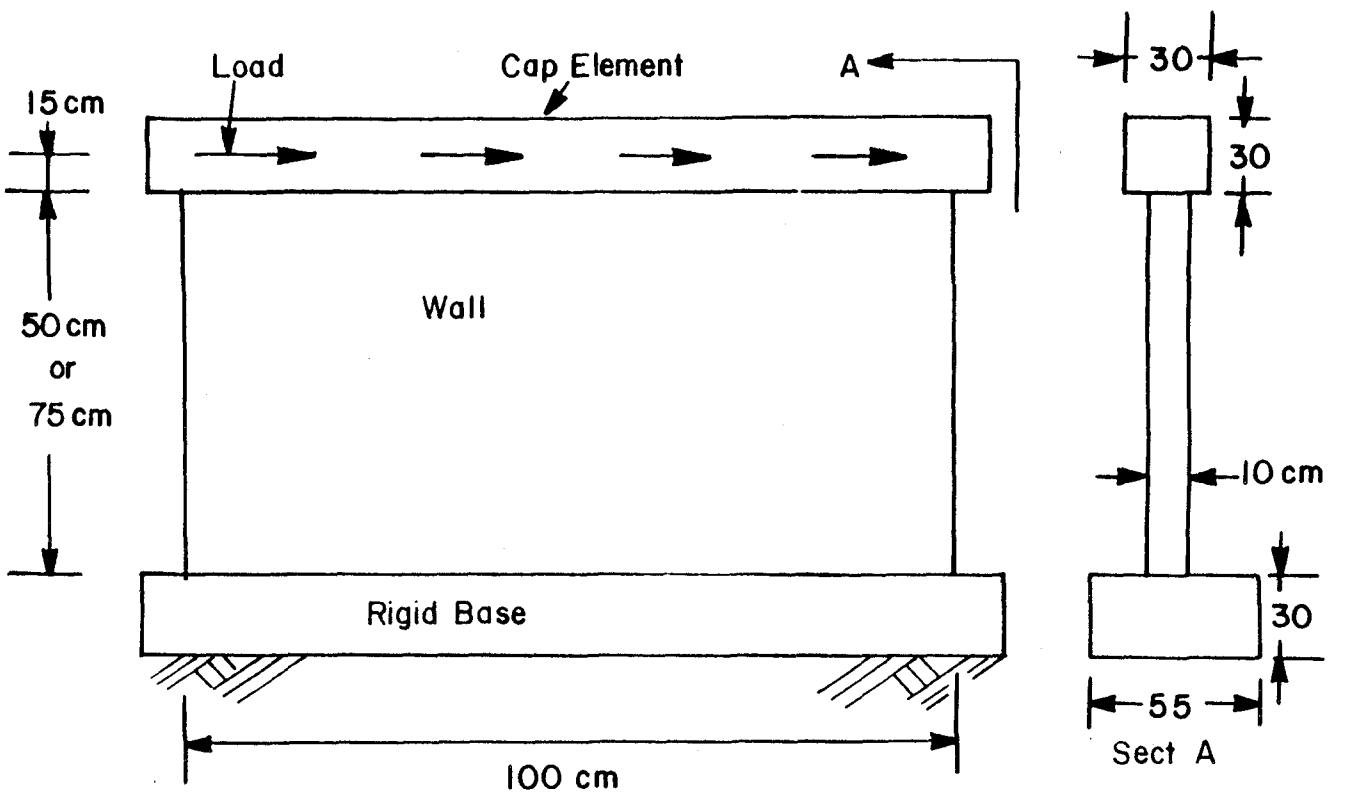

Figure 1. NCKU Shear Walls

Table I. NCKU SHEAR WALLS

Wall	W × H × T	f'_c	f'_{cr}	Vertical Bars	Vertical ρ %	Horizontal Bars	Horizontal ρ %	f_y	$\frac{H}{W}$	Loading
SW1a	100x50x10	275	40.5	6 D10	0.43	4 D10	0.57	4930	0.50	cyclic (2)
SW3	100x50x10	278	43.6	6 D10	0.43	4 D10	0.57	4930	0.50	cyclic (3)
SW4	100x50x10	270	38.9	6 D13	0.77	4 D13	1.03	4900	0.50	monotonic
SW4a	100x50x10	272	40.5	6 D13	0.77	4 D13	1.03	4900	0.50	cyclic (2)
SW5	100x50x10	278	38.9	6 D13	0.77	4 D13	1.03	4900	0.50	cyclic (4)
SW6	100x50x10	288	43.6	6 D13	0.77	4 D13	1.03	4900	0.50	cyclic (3)
SW10	100x50x10	275	30.5	6 D13	0.76	4 D10	0.57	4770	0.50	monotonic
SW11	100x50x10	265	25.3	2 D19 3 D10	0.79	4 D10	0.57	4770	0.50	cyclic (5)
SW12	100x50x10	270	28.2	2 D16 3 D13	0.78	4 D10	0.57	4770	0.50	monotonic
SW13	100x50x10	330	40.2	6 D13	0.76	none	0.00	4770	0.50	monotonic
SW14	100x50x10	320	38.4	6 D13	0.76	8 D10	1.14	4770	0.50	monotonic
SW15	100x75x10	265	26.0	2 D19 3 D10	0.79	6 D10	0.57	4770	0.75	monotonic
SW16	100x75x10	270	29.6	6 D13	0.76	6 D10	0.57	4770	0.75	monotonic
SW19	100x75x10	250	24.6	6 D13	0.76	none	0.00	4770	0.75	monotonic
SW20	100x75x10	210	22.4	6 D13	0.76	6 D10	0.57	4770	0.75	monotonic

Notes:

(1) All units are kg, cm.

(2) One sided cyclic loading as shown in Figure 3.

(3) Earthquake loading as shown in Figure 4.

(4) Two sided cyclic loading as shown in Figure 5.

(5) Two sided cyclic loading, with each cycle at a larger load level than the previous cycle.

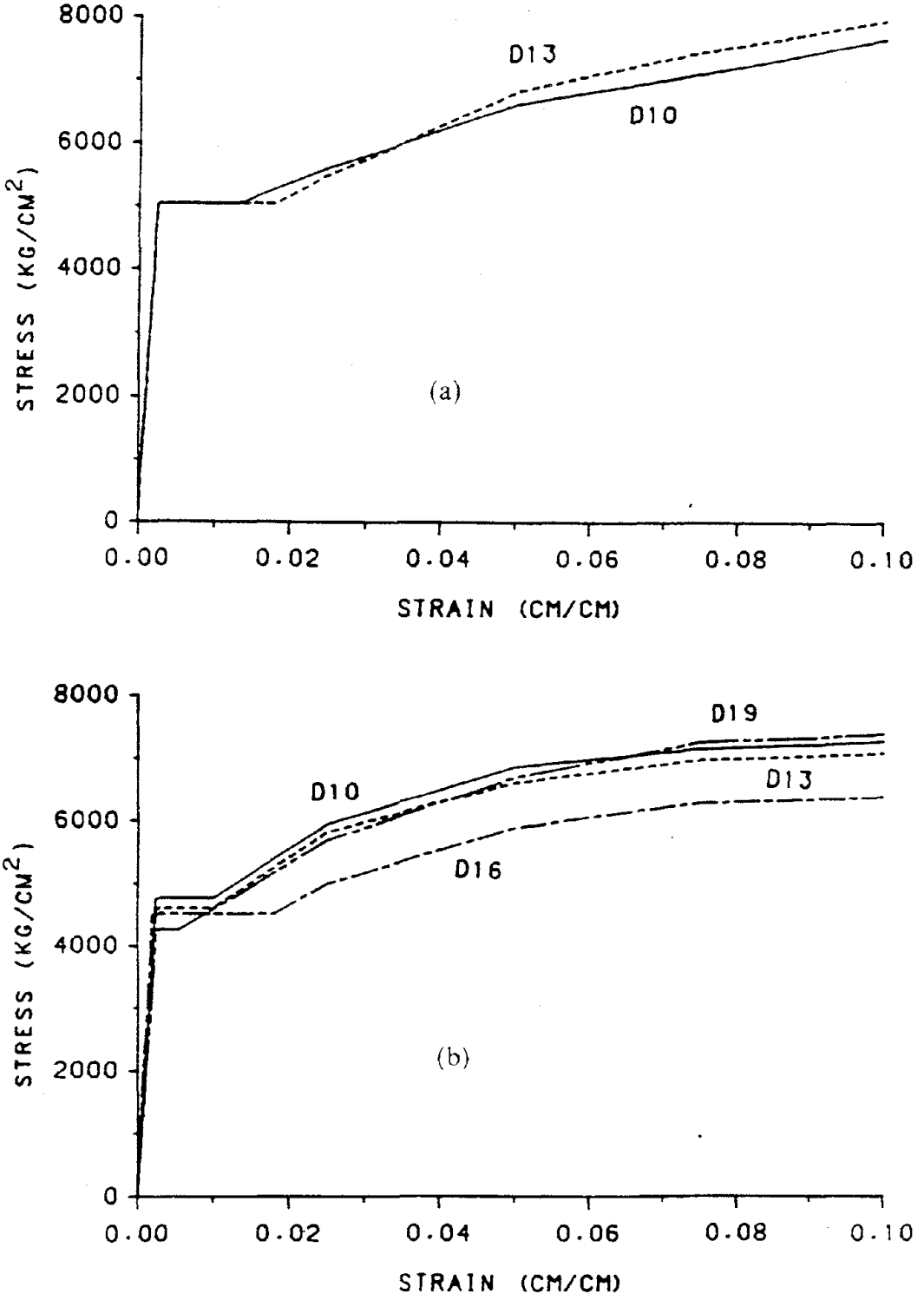

Figure 2. Steel Stress-Strain Curves for NCKU Shear Walls: (a) Walls SW1a through SW6, (b) Walls SW10 through SW20

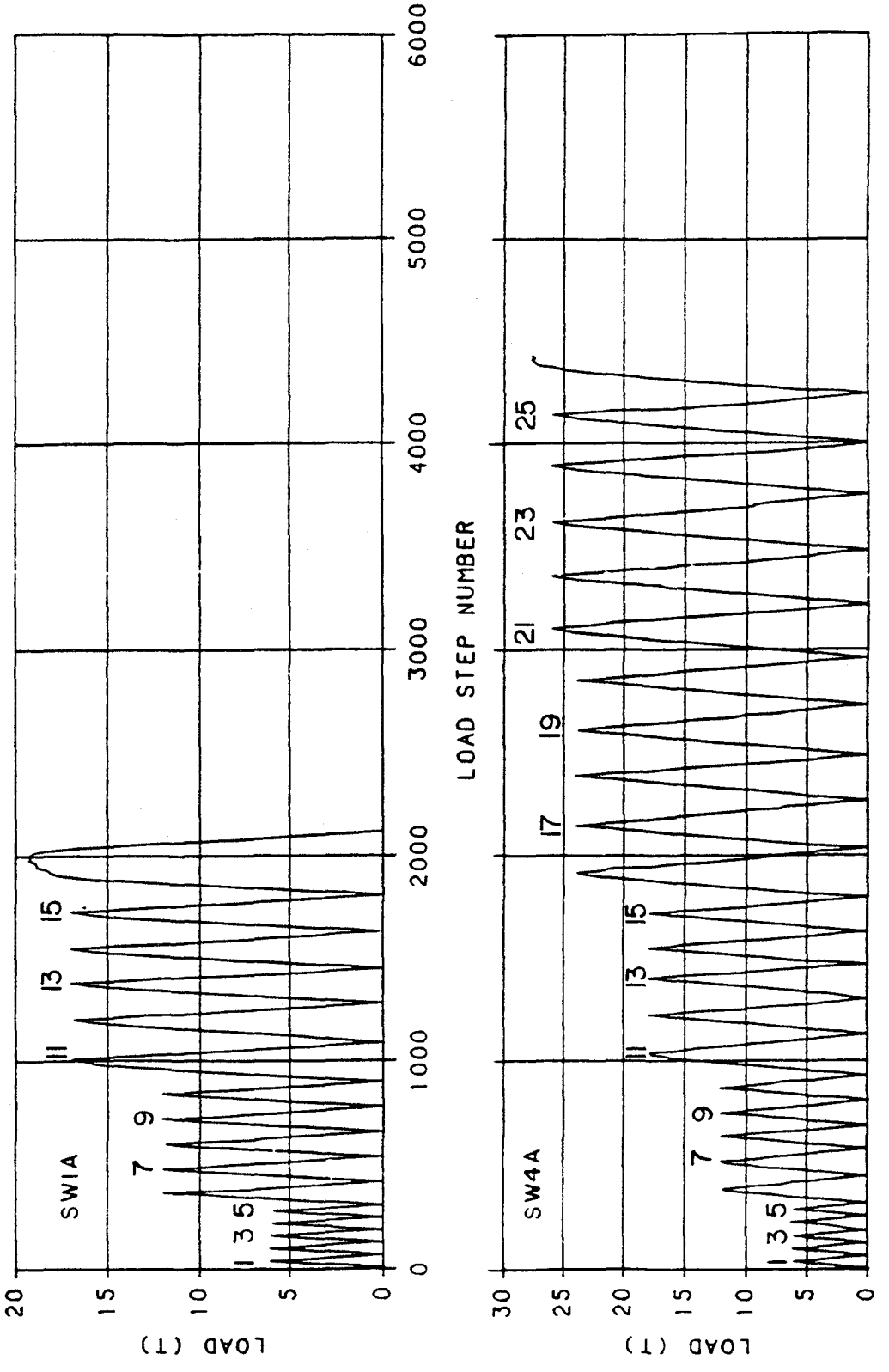

Figure 3. Loading History for NCKU Walls SW1a and SW4a

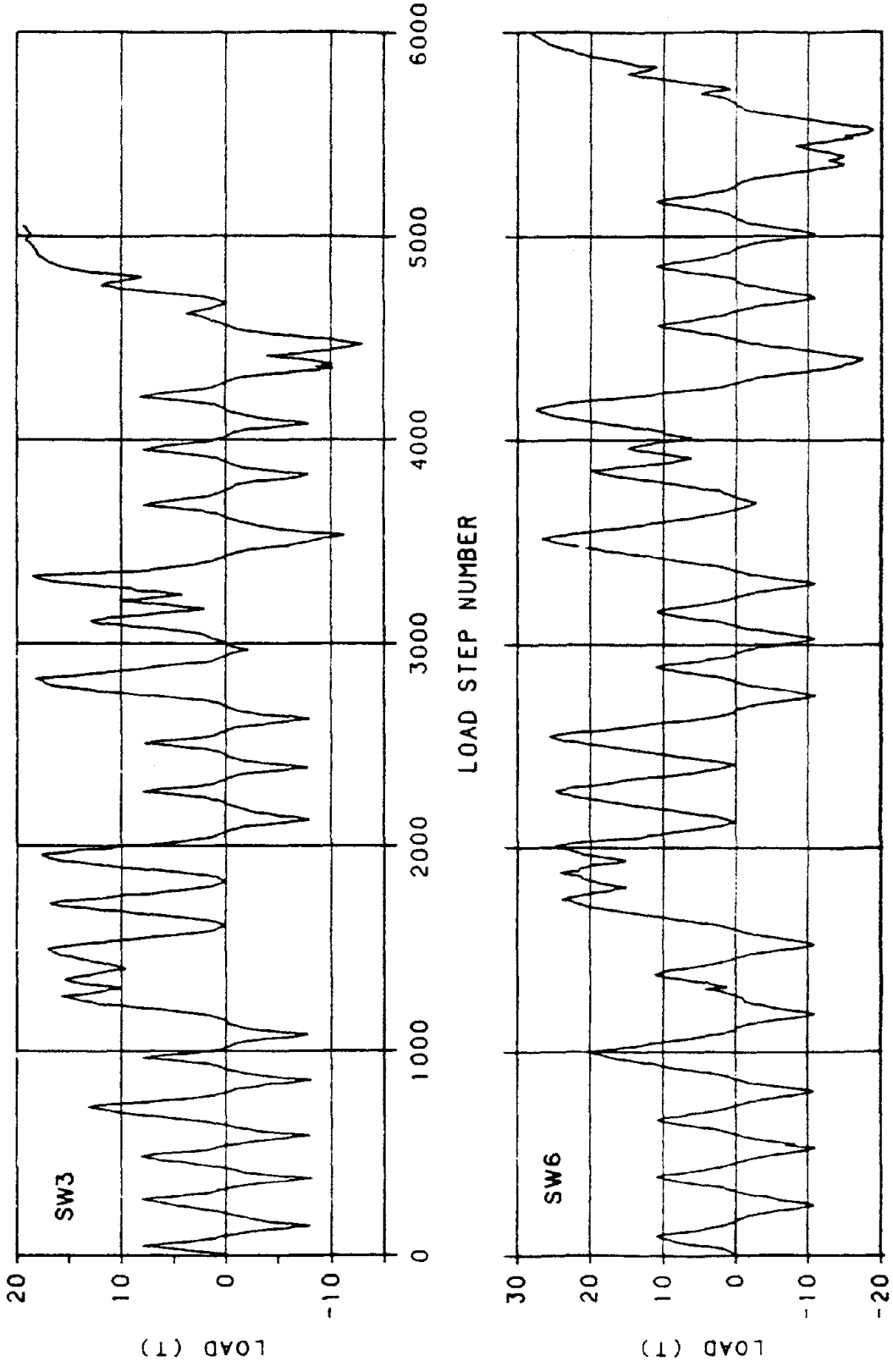

Figure 4. Loading History for NCKU Walls SW3 and SW6

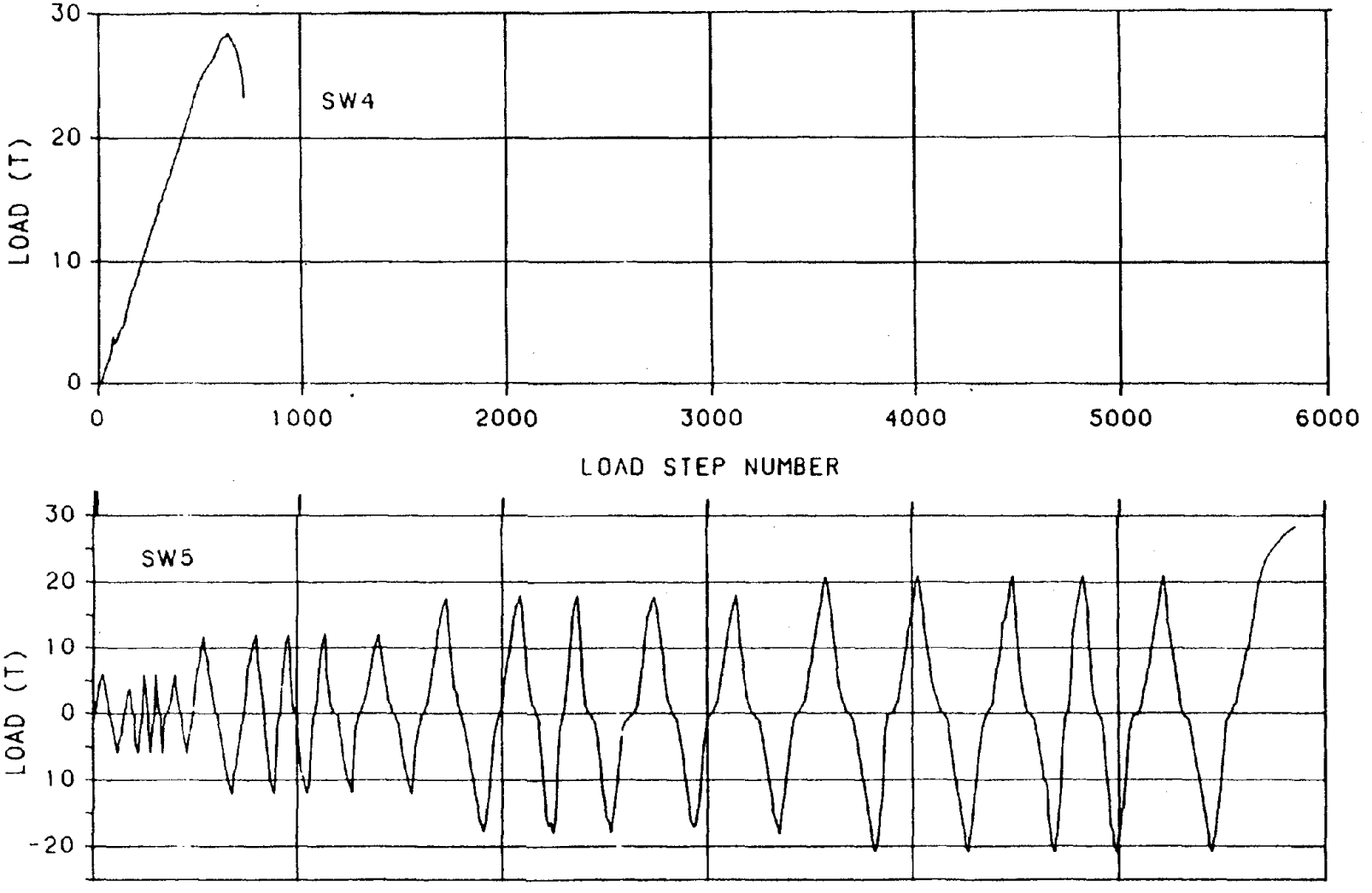

Figure 5. Loading History for NCKU Walls SW4 and SW5

The experimental displacements of the 50 cm high walls are measured with the gauges shown in Figure 6. Gages 2, 3, 4, 5, 6, 7, 16 and 20 are used to measure vertical deformations 5 cm from the edge of the wall. Gauges 8 and 9 are used to measure the change in diagonal distance across the width of the wall. Gauges 10, 11, 12, 13, 14, and 15 are used to measure the horizontal deformation of the wall. The experimental displacements of the 75 cm walls are measured with similar gauges.

1. Separation of Bending and Shear Deformation in Shear Walls. To analyze the shear wall test data, one important issue is to determine what portion of the deformation is due to shear and what portion of the deformation is due to bending. Theoretically, the bending deformation is due to the difference in longitudinal strains on different sides of the wall. Thus the bending deformation can be determined from the longitudinal displacement gauges. Shear deformation is due to the accumulation of shear strains over the height of the wall. Thus the shear deformation can be calculated from the diagonal strain gauges. The total deformation can be measured directly from the displacement gauges at edge of the wall. If the bending and shear displacements were determined correctly, the total will equal the bending plus shear displacements.

a. Theoretical Curvature Distribution. Curvature, ϕ, in a shear wall, is the change in slope ($d\theta$) over the change in length (dz), or

$$\phi = \frac{d\theta}{dz} \tag{2.1}$$

where z is the longitudinal axis of the wall. The units of curvature are radians/length. For a given wall cross section, there exists a unique moment-curvature relationship. The moment-curvature relationship is typically nonlinear, consisting of an elastic

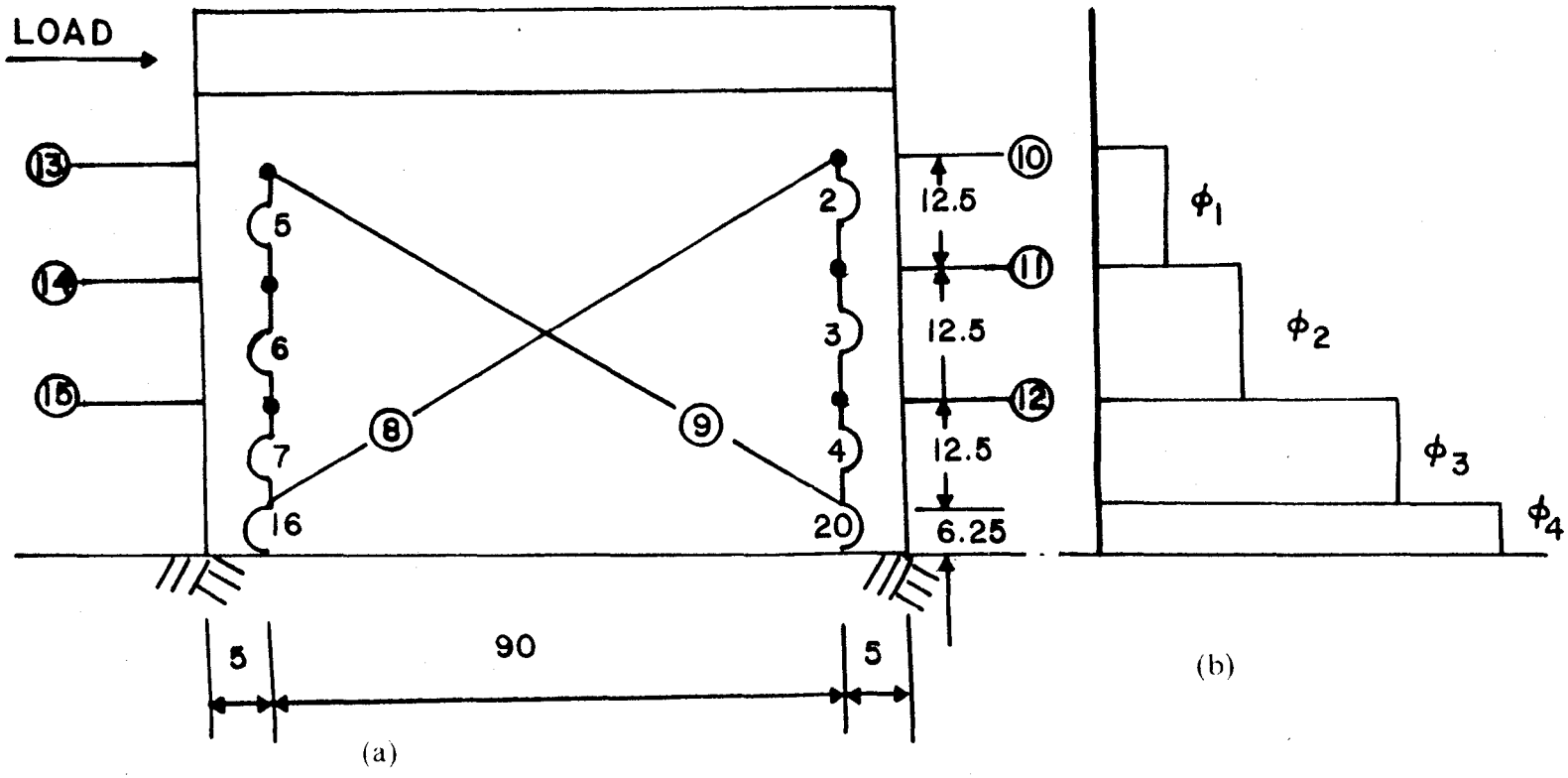

Figure 6. Displacement Gauges for 50 cm High NCKU Wall and Curvature Diagram: (a) Displacement Gauges, (b) Curvature

range, a gradual yielding, and a plastic plateau. An analytical method to calculate the moment-curvature relationship is presented in Chapter III.

Examine the typical shear wall in Figure 7 subject to a lateral load. The bending moment in the wall varies linearly with the height of the wall as shown in the accompanying figure. For a given point on the wall's longitudinal axis, the moment is known. For that moment the curvature is determined from the moment-curvature relationship. Plotting the curvatures for different points on the wall's height yields the theoretical curvature distribution as sketched in Figure 7. Note that the theoretical curvature is small at the top of the wall and is very large at the base of the wall.

The bending deformation of the shear wall is determined by

$$\delta b = \int_0^h z\,\phi(z)\,dz \tag{2.2}$$

where $\phi(z)$ is the variation of curvature along the wall's height. Thus if the curvature in Figure 7 is known, the bending deformation may be determined.

The curvature in Equation 2.1 may be approximated by

$$\phi = \frac{d\theta}{dz} \cong \frac{\Delta\theta}{\Delta z} \tag{2.3}$$

where $\Delta\theta$ is the change in rotation over the length Δz. Rotation is determined by taking the difference between longitudinal deformations at opposite sides of the wall and dividing by the width. For the 50 cm high NCKU walls, the longitudinal deformation at gauges 2 and 5 in Figure 6 is $\delta 2$ and $\delta 5$, and the distance between these gauges is 90 cm. Thus the angle of rotation in the wall under these two gauges is

$$\theta 1 = \frac{\delta 5 - \delta 2}{90} \tag{2.4}$$

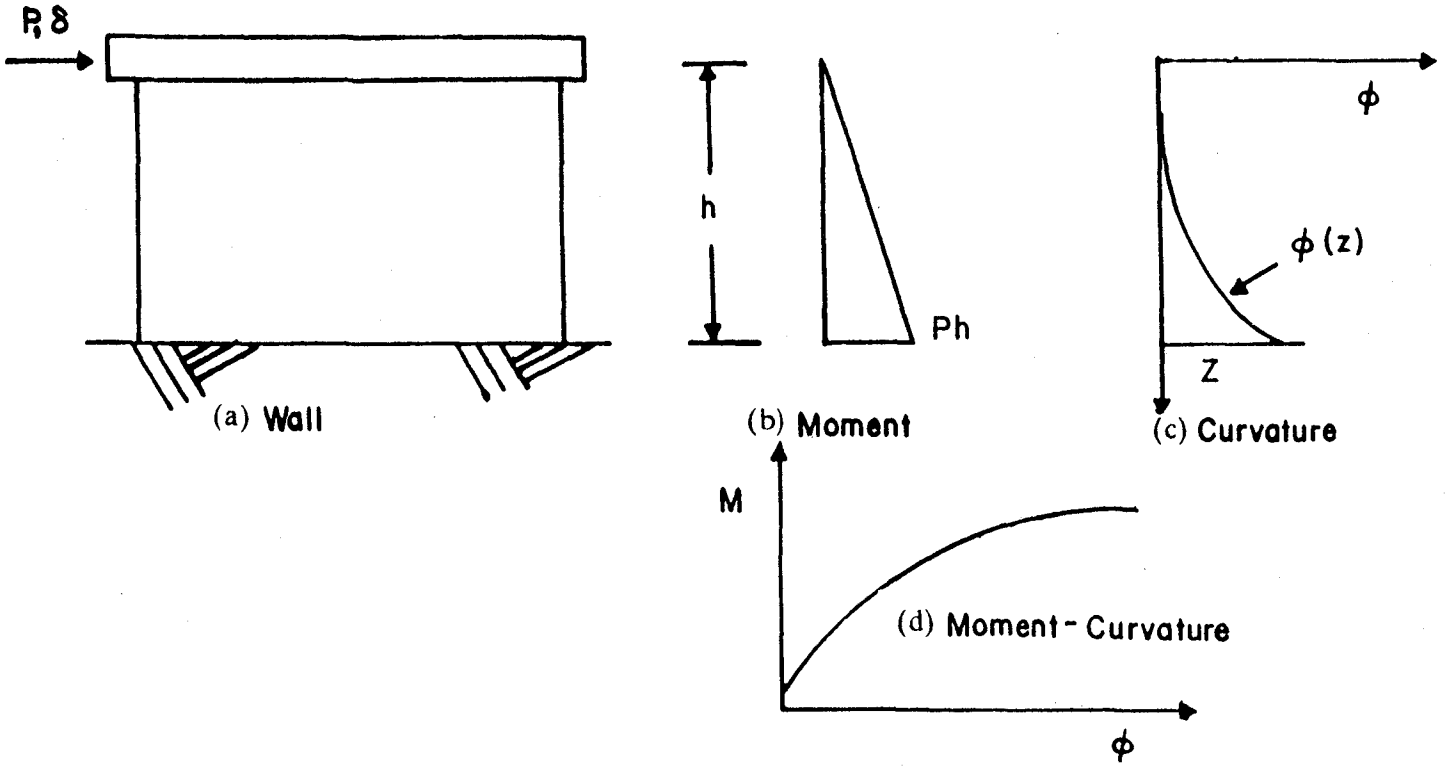

Figure 7. Theoretical Curvature for Shear Walls: (a) Wall, (b) Moment Diagram, (c) Moment Curvature Diagram, (d) Curvature Diagram

Elongation of the gauges is positive deformation. Gauges 2, 3, 4, 5, 6 and 7 are 12.5 cm long, while gauges 16 and 20 are 6.25 cm long. Dividing the rotation by the gauge length yields the average curvature under the gauge.

$$\phi 1 = \frac{\theta 1}{12.5} = \frac{\delta 5 - \delta 2}{90 \times 12.5} \text{ rad/cm} \tag{2.5}$$

Similarly the rotations and curvatures under the other gauges are calculated. Consequently let $\theta 2$ and $\phi 2$ represent the rotation and curvature under gauges 3 and 6; $\theta 3$ and $\phi 3$ represent the rotation and curvature under gauges 4 and 7; and $\theta 4$ and $\phi 4$ represent the rotation and curvature under gauges 16 and 20.

The total deformation is determined at a point 43.75 cm from the base of the 50 cm tall wall. This corresponds to the location of the lateral deformation at gauges 10 and 13. Thus the bending displacement is also calculated at this same point.

The bending displacement of this wall may be determined by Equation 2.2 However, since the average curvature distribution, rather than the exact curvature distribution is known, an approximation of the bending displacement is obtained. Thus the bending displacement at a point 43.75 cm from the base of the wall, is given by

$$\delta b = \int_0^h z\,\phi(z)\,dz = 6.25 \times \phi 1 \times 12.5 + 18.75 \times \phi 2 \times 12.5 + 31.25 \times \phi 3 \times 12.5 + 40.625 \times \phi 4 \times 6.25 \tag{2.6}$$

b. Observed Curvature Distribution of NCKU Shear Walls. The experimentally measured curvature distributions for NCKU walls SW1a, SW3, SW4, SW4a, SW5 and SW6 are presented in Figure 8. These curvature distributions correspond to a point near the ultimate load. Recall that the theoretical curvature distribution had its maximum curvature at the base of the wall, and the curvature decreased as the height

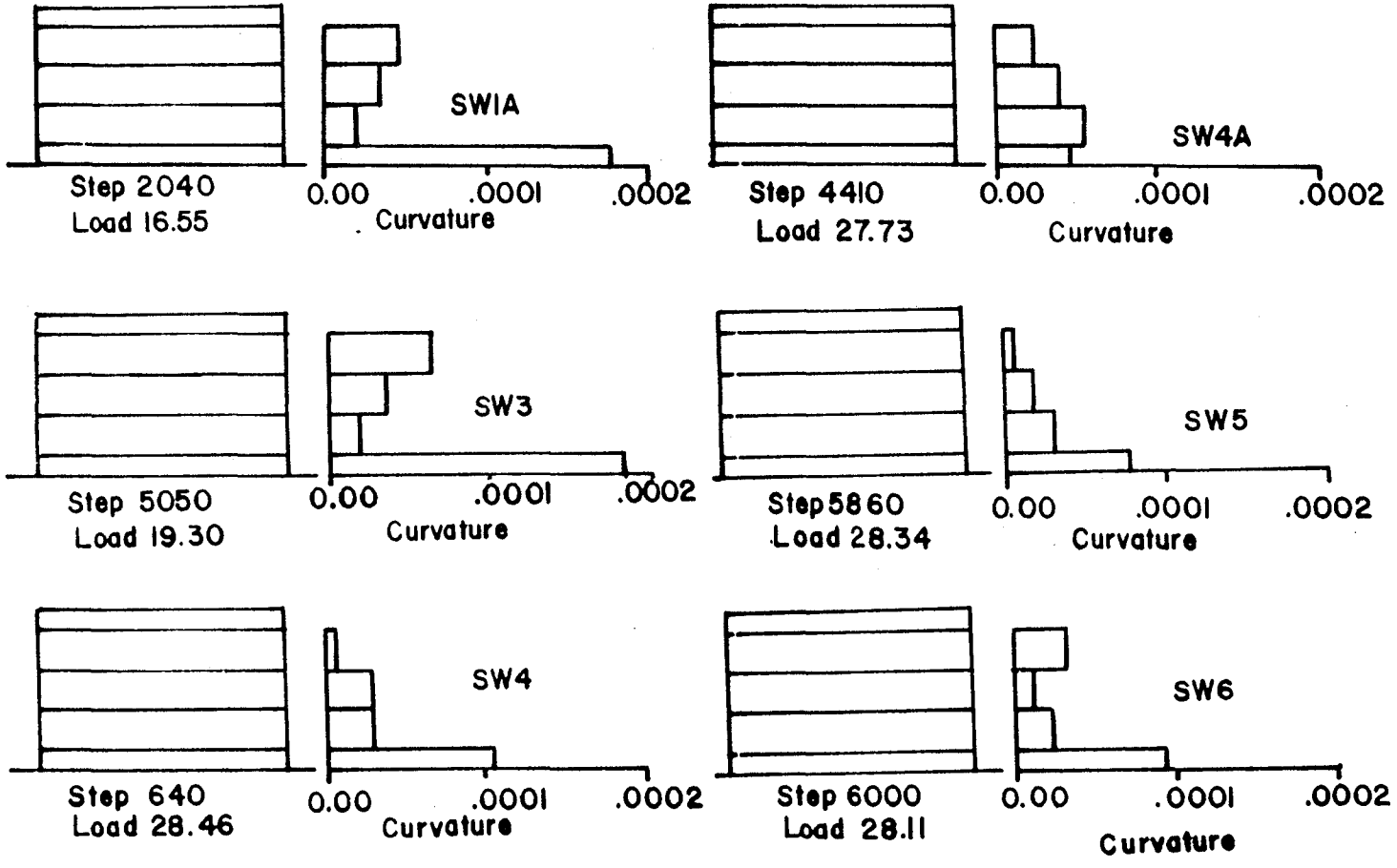

Figure 8. Experimental Curvature Distribution for NCKU Walls

increased. Note that the curvature distribution for wall SW1a also has the maximum at the base of the wall, $\phi 4$. However, the curvature distribution for the upper sections is reversed, $\phi 3$ is less than $\phi 2$ and $\phi 2$ is less than $\phi 1$.

Wall SW3 also has a similar inverted curvature distribution. For wall SW4 the curvatures $\phi 2$ and $\phi 3$ are approximately equal, when $\phi 3$ should be greater than $\phi 2$. For wall SW4a the curvature of the bottom segment, $\phi 4$, is less than the curvature in the segment above it, $\phi 3$. For wall SW6, $\phi 1$ is greater than both $\phi 2$ and $\phi 3$. Only wall SW5 has a curvature distribution similar to the expected curvature distribution.

The experimentally observed crack patterns on the face of NCKU walls SW1a and SW4a are shown in Figure 9. These crack patterns correspond to a point near the walls ultimate load. The load and cycle that the crack was first observed is represented in the figure by 'Load (Cycle #)', where the load is in tons, and the cycle numbers are on the loading diagram, Figure 3. As the wall is loaded, a flexural crack opens up at the base of the wall, and is labeled 'A' in Figure 9. For wall SW1a, this crack is formed during cycle 6, at a load near 12 tons. The crack formed in wall SW4a at a load near 8 tons during cycle 6. Near the same load, a diagonal shear crack forms and is labeled 'B' in the accompanying figure. For wall SW1a, this crack formed at a load near 12 tons. This crack formed in wall SW4a at a load near 10 tons. A flexural crack also formed in wall SW1a at 12 tons during cycle 6 as shown by curve 'C' in the figure. As the loading progresses, additional flexural, shear, and flexural-shear cracks form. Cardenas, et al (14) observed similar crack patterns in low rise shear walls without boundary elements.

Both walls SW1a and SW4a have diagonal shear cracks under gauge 5. As these cracks form, they have a vertical component of deformation. Thus gauge 5 has a deformation due to shear. The deformation of gauge 5 is used to calculate the curvature $\phi 1$. Therefore, the experimentally measured curvature $\phi 1$ is influenced by

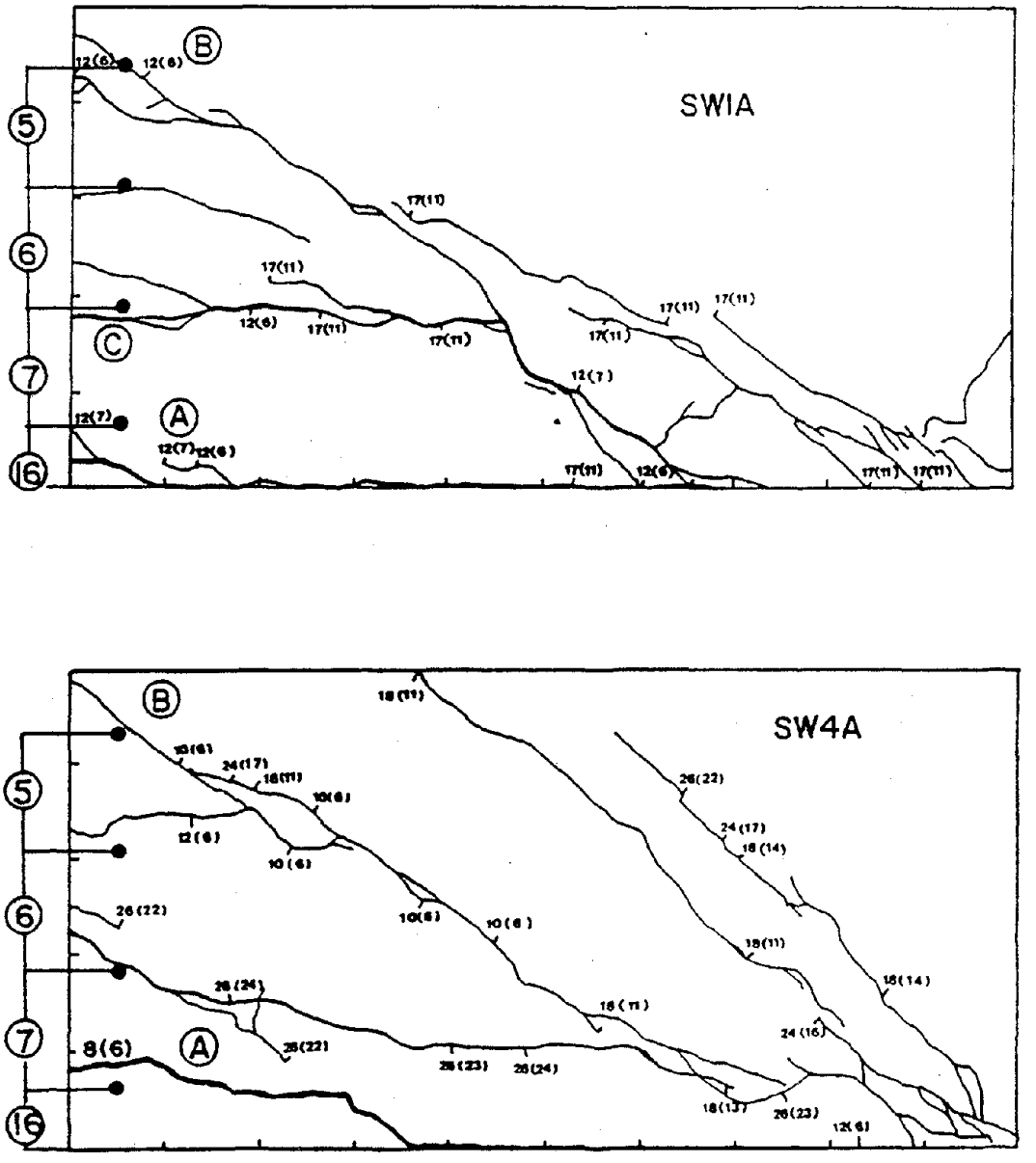

Figure 9. Surface Cracks for NCKU Walls SW1a and SW4a (Ref. 72)

shear deformation. Hence bending and shear deformations are coupled. Deformation across the diagonal shear cracks are responsible for the inverted curvature distributions.

The curvature distribution is also very sensitive to the crack location. Examine the curvature of the bottom segment, $\phi 4$. In wall SW1a, the flexural cracks at the base of the wall occur under gauge 16, and $\phi 4$ is relatively large. In wall SW4a, the flexural cracks occur above gauge 16, and the curvature $\phi 4$ is relatively small. Had the crack in wall SW4a been a few centimeters lower, it would have occurred under gauge 16 and $\phi 4$ would be larger.

Recall the bending deformation in Equation 2.6. Substituting the gauge deformations for the curvatures yields

$$\delta b = \frac{6.25(\delta 5 - \delta 2) + 18.75(\delta 6 - \delta 3) + 31.25(\delta 7 - \delta 4) + 40.625(\delta 16 - \delta 20)}{90} \qquad (2.7)$$

Assume a crack is 0.25 cm wide, and occurs under gauge 16, the bending deformation due to the crack is 0.1128 cm. Assume the same crack is a little higher in the wall, under gauge 7, the bending deformation due to the crack is 0.0868 cm. The bending displacements differ by 30%, due to a small difference in crack location.

c. Equivalent Moment Diagram for the Hinging Region of Shear Walls. Since 1) the moment and shear are strongly coupled, 2) the curvature is influenced by the diagonal shear cracks, and 3) the curvature is very sensitive to the crack location, then an average curvature over the hinging region is used to calculate the bending deformations, as shown in Figure 10. Thus the average curvature in the 50 cm NCKU walls is

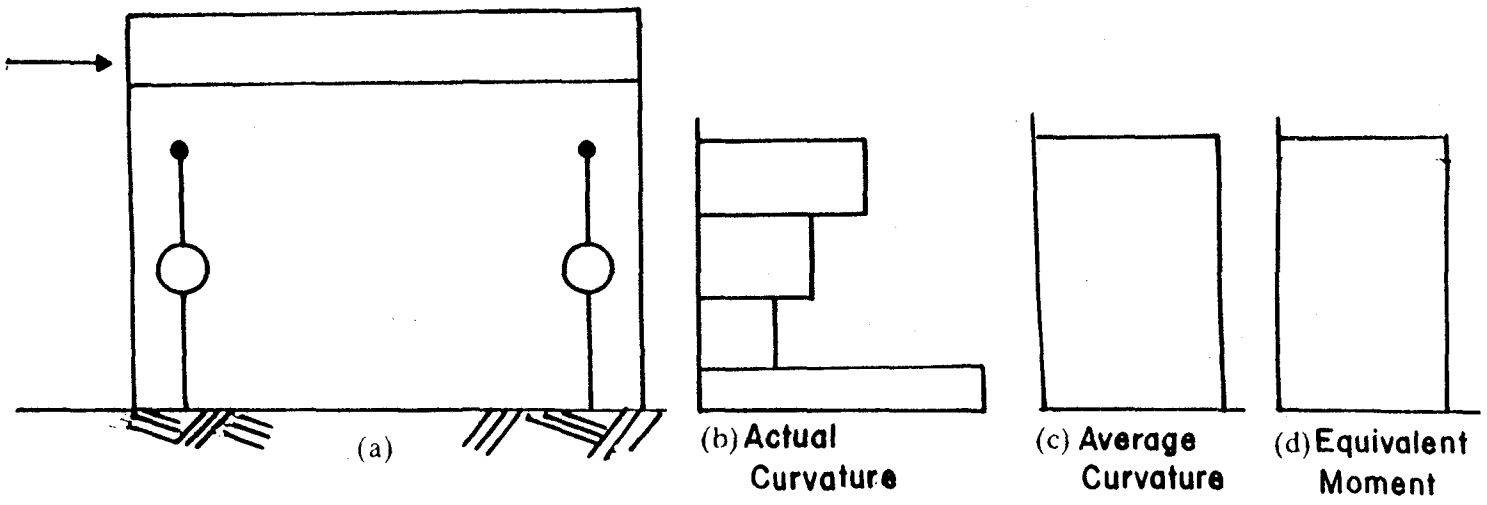

Figure 10. Average Curvature and Equivalent Moment Diagrams: (a) Wall, (b) Actual Curvature, (c) Average Curvature, (d) Equivalent Moment

$$\phi_{ave} = \frac{\delta 5 + \delta 6 + \delta 7 + \delta 16 - \delta 2 - \delta 3 - \delta 4 - \delta 20}{90} \tag{2.8}$$

and the bending deformation is

$$\delta b = \frac{43.75^2}{2} \phi_{ave} \tag{2.9}$$

The hinging region is the region of the wall where shear and bending deformations are strongly coupled. Assuming the diagonal shear cracks are from 30° to 60° above the horizontal, the height of the hinging region is between 0.6w (w tan 30°) and 1.75w (w tan 60°).

Since an average curvature over the hinging region is used, an equivalent moment diagram over the hinging region is also used as shown in Figure 10. Thus the curvatures are directly related to the moments. The analytical model developed in Chapter III and Chapter V uses the equivalent moment diagram to generate an equivalent curvature over the hinging region.

d. Determining Shear Deformation. For pure shear, the shear deformation can be related to the diagonal gauges 8 and 9. Assume the right side of the wall has a shear displacement of δsr, also assume that the deformation of gauges 2 through 7, 16 and 20 is zero. From Figure 11, the shear deformation of the right side is

$$\frac{\delta 8}{\delta sr} = \cos\gamma = \frac{b}{c}, \qquad \delta sr = \frac{c}{b}\delta 8 \tag{2.10}$$

where $c = \sqrt{a^2 + b^2}$ and the variables a and b are shown in Figure 11. Elongation of gauges 8 and 9 is positive deformation. The shear deformation on the left side, δsl is

$$\frac{-\delta 9}{\delta sl} = \cos\gamma = \frac{b}{c}, \qquad \delta sl = -\frac{c}{b}\delta 9 \tag{2.11}$$

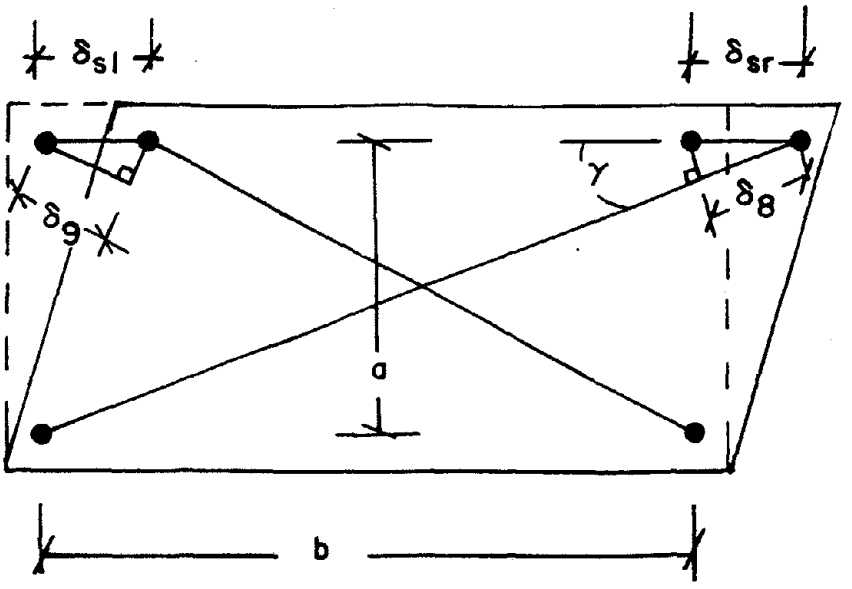

Figure 11. Pure Shear Displacement by Diagonal Distance Measurement

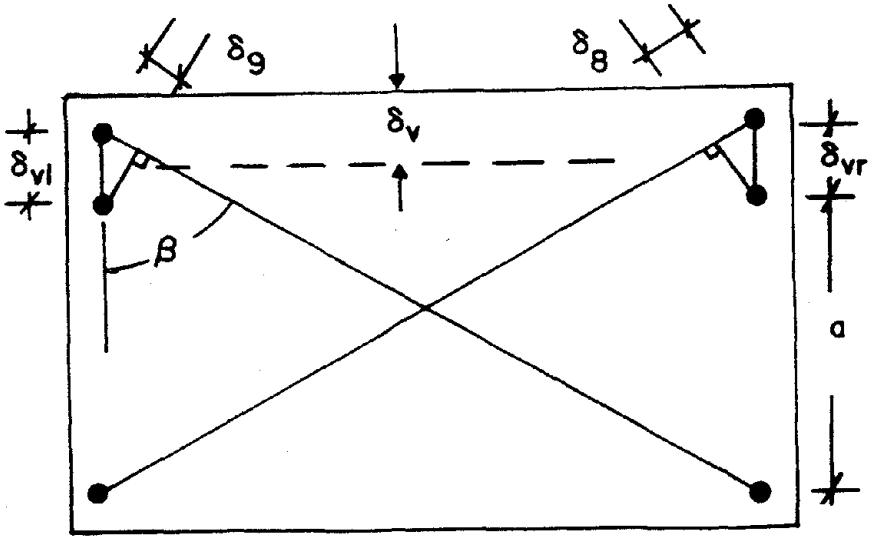

Figure 12. Effect of Vertical Deformation on Diagonal Gauges

Averaging the shear deformation at both sides yields

$$\delta s = \frac{c(\delta 8 - \delta 9)}{2b} \tag{2.12}$$

Consider the effects of vertical deformation on the diagonal gauges as shown in Figure 12. For gauge 8 and vertical deformation of the right side of the wall

$$\frac{\delta 8}{\delta vr} = \cos\beta = \frac{a}{c}, \qquad \delta 8 = \frac{a}{c}\delta vr \tag{2.13}$$

where $\delta vr = \delta 2 + \delta 3 + \delta 4$. For gauge 9 and vertical deformation of the left side of the wall

$$\frac{\delta 9}{\delta vl} = \cos\beta = \frac{a}{c}, \qquad \delta 9 = \frac{a}{c}\delta vl \tag{2.14}$$

where $\delta vl = \delta 5 + \delta 6 + \delta 7$.

The accuracy of the shear deformation can be explored by considering several theoretical deformations. Consider the case of vertical deformation, $\delta v = \delta vl = \delta vr$. The deformations of the diagonal gauges 8 and 9 are equal. Thus the calculated shear deformation in Equation 2.12 is zero in the presence of pure vertical deformation. Consider the case of pure bending as shown in Figure 13, where $\delta vl = -\delta vr$. The deformations of gauges 8 and 9 are

$$\delta 8 = -\frac{a}{c}\delta vr = \frac{a}{c}\delta vl, \qquad \delta 9 = \frac{a}{c}\delta vl \tag{2.15}$$

and the shear deformation in Equation 2.12 is

$$\delta s = \frac{c(\frac{a}{c}\delta vl - \frac{a}{c}\delta vl)}{2b} = 0 \tag{2.16}$$

Thus the calculated shear deformation is zero in the presence of pure bending.

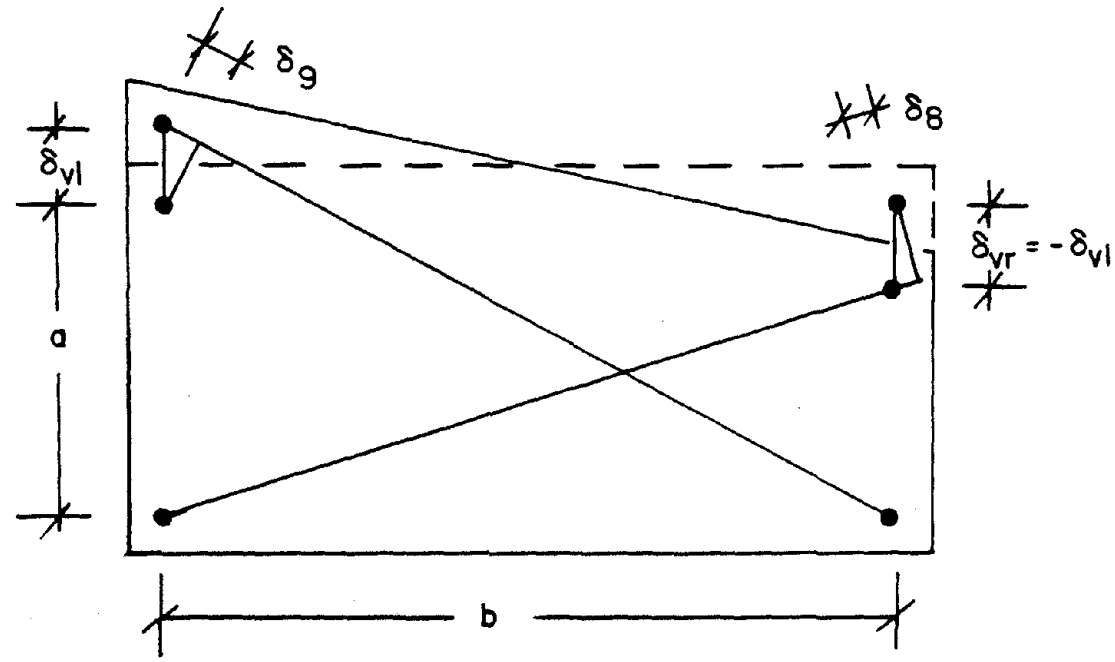

Figure 13. Effect of Pure Bending Deformation on Diagonal Gauges

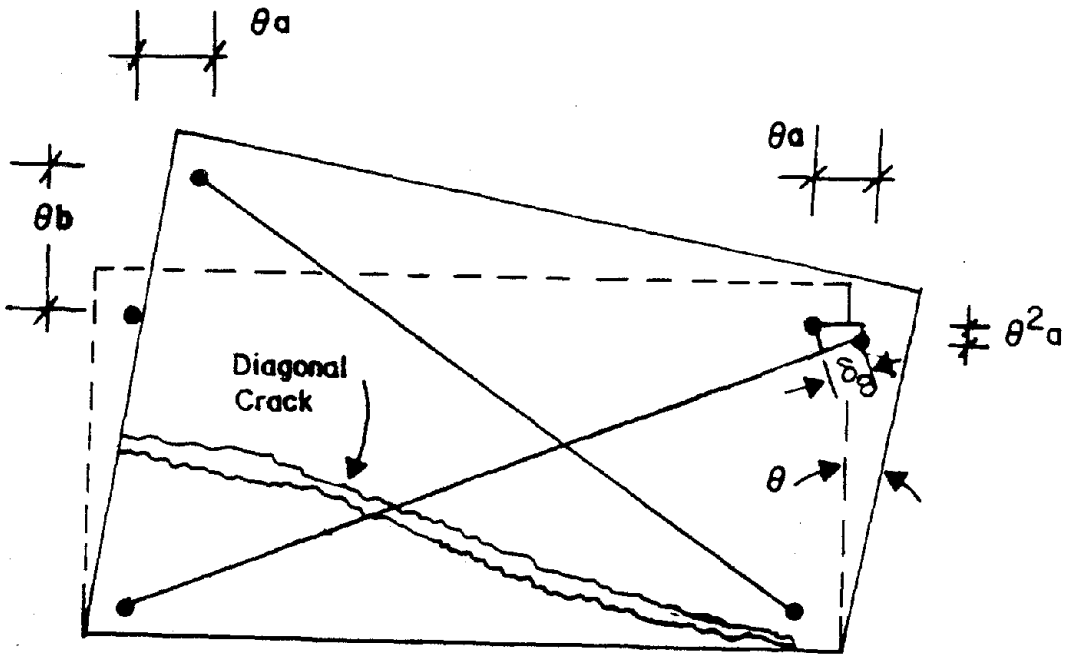

Figure 14. Effect of Bending Deformation with Diagonal Cracks on Diagonal Gauges

Consider the case of pure bending with a diagonal crack, where the wall rotates through an angle θ, as shown in Figure 14. The bending deformation in the wall is θa. Diagonal gauge 8 has a horizontal displacement of θa. The center of rotation of the wall is at the base of the diagonal crack, which is directly under point A in the figure. Thus the vertical deformation of gauge 8 is $-\theta(\theta a)$ or $-a\theta^2$. For small rotations $\theta < \frac{1}{50}$, $\theta^2 << \theta$. Thus the vertical deformation of gauge 8 is negligible. Therefore elongation of gauge 8 is

$$\delta 8 = \frac{b}{c}\theta a \tag{2.17}$$

Diagonal gauge 9 has a horizontal displacement of θa, a vertical displacement of θb and is elongated by

$$\delta 9 = -\frac{b}{c}\theta a + \frac{a}{c}\theta b = 0 \tag{2.18}$$

Thus the shear displacement from Equation 2.12 is

$$\delta s = \frac{c(\delta 8 - \delta 9)}{2b} = \frac{c\left(\frac{b}{c}\theta a - 0\right)}{2b} = \frac{\theta a}{2} \neq 0 \tag{2.19}$$

The diagonal distance gauges are misinterpreting a portion of the bending deformation and labeling it as shear deformation. This was recognized by Ma, et al (54) who used diagonal gauges to measure shear distortion in R/C T beams.

Since the shear deformation as calculated by the diagonal gauges is prone to error, in the presence of diagonal cracking, the shear deformation is determined by subtracting the bending deformation from the total deformation. Thus

$$\delta s = \delta t - \delta b \tag{2.20}$$

where $\delta t = \frac{\delta 13 - \delta 10}{2}$ and δb is calculated by Equation 2.9. This definition of shear deformation is used in this study.

e. Deformations of NCKU Shear Walls. The bending deformations for the 50 cm NCKU walls are calculated by Equation 2.9. The average curvature and bending deformation in the 75 cm tall walls is similarly calculated. The shear deformation is calculated by Equation 2.20. The bending, shear and total deformations for the NCKU walls are presented in Chapters III and IV for comparison with analytical methods.

The monotonic load deformation curves, or an envelope of cyclic load deformation curves for both the bending and shear deformations, are highly nonlinear and are presented in Section C of Chapter III. These curves are characterized by a high initial stiffness, which decreases with the formation of cracks in the wall. Yielding in these shear walls is a gradual process. After yielding, the walls exhibited a ductile behavior, and failed at relatively large deformations.

The cyclic load deformation curves for shear and bending deformations are presented in Section B of Chapter IV. Bending deformations form large stable hysteresis loops. The hysteresis loops for shear deformations are pinched. Both bending and shear have nonlinear unloading curves. When the loadings are cycled at a load level near the maximum past load, the deformations increase for each load cycle. Whereas if the loadings are cycled at lower load levels, the deformations for each cycle are similar. The shear and bending behavior under cyclic loading is discussed in Chapter IV.

2. Observed Ratio of Bending to Total Deformation in NCKU Shear Walls. Bending deformation (at load P) as a percentage of total deformation (bending + shear deformation at load P) is plotted for points on the backbone curve, against the total deformation (bending + shear deformation at load P) as a percentage of the ultimate deformation (bending + shear deformation at failure), in Figure 15 for the 50 cm high walls, and in Figure 16 for the 75 cm high walls. The initial shear deformation of walls

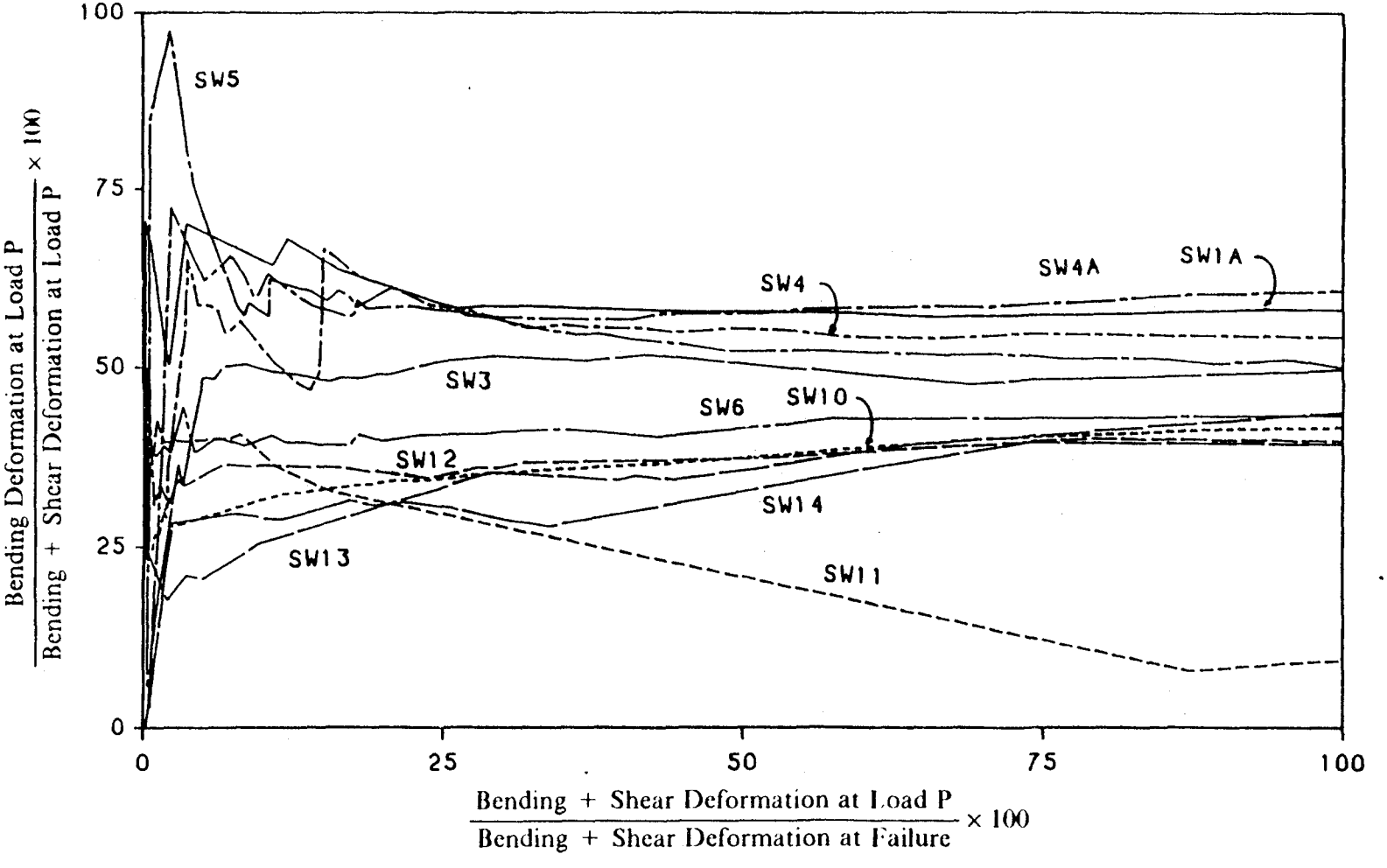

Figure 15. Ratio of Bending Deformation to Total Deformation for 50 cm High NCKU Walls

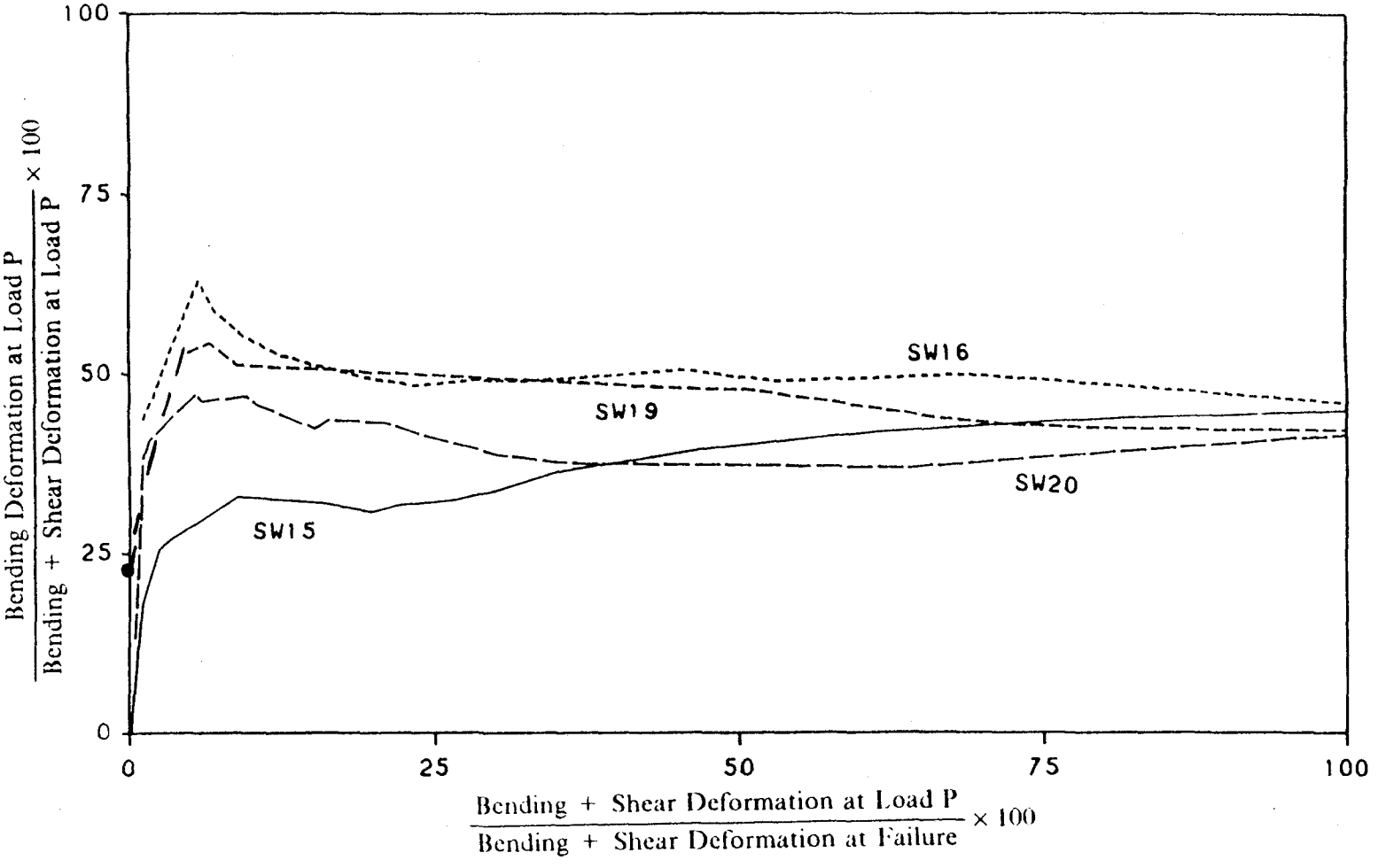

Figure 16. Ratio of Bending Deformation to Total Deformation for 75 cm High NCKU Walls

SW5, SW4a and SW1 is very erratic which may be observed in Section B of Chapter IV. Thus the ratio of bending deformation to total deformation in these walls at low deformations is also erratic, as can be seen in Figure 15. After deformations of 10% or 20% of the ultimate deformation, the bending deformation ranges between 40% to 60% of the total deformation for most walls.

Wall SW11 has very large shear deformations in the last three load cycles before failure. Prior to these three load cycles, bending deformation accounted for 30% to 40% of the total deformation. After these three load cycles, bending deformation only accounts for 10% of the total deformation. Thus the percentage of bending deformation in wall SW11 is atypical at larger deformations.

Bending deformation in the 75 cm walls is the same percentage of total deformation as in the 50 cm walls. This is because the hinging region of both walls extends over the entire wall's height.

There is not a significant difference in the percentage bending deformation for walls with different vertical or horizontal reinforcement ratios. This is because the reinforcing steel contributes to both the bending and shear stiffness. Hence, increasing the reinforcing steel for walls in this height to width range increases the bending and shear stiffnesses by similar amounts.

It is interesting to note that the transverse reinforcing steel is omitted in walls SW13 and SW19. If the traditional concept that transverse reinforcing steel resists shear and longitudinal reinforcing steel only resists bending were true, then the shear deformation for these two walls would be larger than walls with transverse reinforcing steel. However the percentage bending deformation in walls SW13 and SW19 is similar to the other walls. The roles of longitudinal and transverse reinforcing steel is discussed in Section C.3 of Chapter III.

There is not a significant difference in percentage bending deformation for walls with different loading patterns.

3. Observed Failure Ductility and Excursion Ratio in NCKU Shear Walls. The displacement definition of ductility and excursion ratio for six of the NCKU shear walls at ultimate loadings is calculated below. The bending ductility is given by

$$\mu_b = \frac{|\delta b_{ult}|}{\delta b_y} \tag{2.21}$$

where δb_{ult} is the bending deformation at the ultimate load, and δb_y is the bending deformation at the yield load. The yield load corresponds to an average strain of $\varepsilon_y = 0.0024$ in the longitudinal steel reinforcing bar, where the longitudinal strain is the larger of $\frac{\delta 2 + \delta 3 + \delta 4 + \delta 20}{43.75}$ or $\frac{\delta 5 + \delta 6 + \delta 7 + \delta 16}{43.75}$ for the 50 cm shear walls. For each bending ductility ratio, a corresponding excursion ratio exists. The excursion ratio is given by

$$\varepsilon_b = \sum(\mu_b - 1) \tag{2.22}$$

where the summation is carried out for each half load cycle.

Similar to the bending ductility and excursion ratios, the shear ductility and excursion ratio is

$$\mu_s = \frac{|\delta s_{ult}|}{\delta s_y} \tag{2.23}$$

and

$$\varepsilon_s = \sum(\mu_s - 1) \tag{2.24}$$

where δs_{ult} is the shear deformation at the ultimate load, δs_y is the shear deformation at the yield load and the summation is carried out for each half load cycle. The load, bending displacement, and shear displacement corresponding to the yield and ultimate point are given in Table II for NCKU walls SW1a, SW3, SW4, SW4a, SW5 and SW6.

Table II. YIELD AND FAILURE DATA FOR NCKU SHEAR WALLS

	Yield				Ultimate			
Wall	Step	Load	δb	δs	Step	Load	δb	δs
SW1a	370	12.01	0.485	0.270	1980	19.30	4.063	2.951
SW3	710	10.90	0.325	0.347	5050	19.30	5.709	5.777
SW4	330	15.90	0.362	0.394	640	28.46	3.237	2.751
SW4a	510	11.68	0.330	0.189	4410	27.73	3.885	2.519
SW5	1710	15.91	0.411	0.261	5870	29.23	2.647	2.660
SW6	980	17.90	0.320	0.491	5990	28.11	2.962	3.883

Notes:
(1) All units are ton, mm.
(2) The load steps are shown in Figures 3, 4 and 5

The bending failure ductilities are given in Table III. Values range from 6.44 for wall SW5 to 17.57 for wall SW3. The average bending failure ductility is 10.39. The shear failure ductilities are also given in Table III. Values range from 6.98 for wall SW4 to 16.65 for wall SW3. The average shear failure ductility is 11.00. There is not a significant pattern of failure ductility for any given loading history or wall reinforcement ratio. Thus a ductility of 10 is set as the failure limit for both bending and shear ductilities.

The bending and shear failure excursion ratios are given in Table III. Bending failure excursion ratios range from 7.37 for Wall SW1a to 50.34 to wall SW3, with an average value of 19.25. Shear failure excursion ratios range from 5.98 for wall SW4 to 55.71 to wall SW3, with an average value of 25. The walls with an earthquake loading,

Table III. FAILURE DUCTILITIES AND EXCURSION RATIOS FOR NCKU WALLS

Wall	Bending		Shear	
	Ductility	Excursion Ratio	Ductility	Excursion Ratio
SW1a	8.38	7.37	10.93	9.96
SW3	17.57	50.34	16.65	55.71
SW4	8.94	7.94	6.98	5.98
SW4a	11.77	12.93	13.33	15.38
SW5	6.44	8.74	10.19	30.67
SW6	9.26	28.20	7.91	32.32
Average	10.39	19.25	11.00	25.00

walls SW3 and SW6, have failure excursion ratios that are significantly larger than the other walls.

4. Observed Ratios of Horizontal to Vertical Expansion in NCKU Shear Walls. The average vertical strain of the 50 cm high NCKU walls is determined by

$$\varepsilon v = \frac{\delta 2 + \delta 3 + \delta 4 + \delta 20 + \delta 5 + \delta 6 + \delta 7 + \delta 16}{2 \times 43.75} \tag{2.25}$$

and the average horizontal strain is given by

$$\varepsilon h = \frac{-(\delta 10 + \delta 11 + \delta 12 + \delta 13 + \delta 14 + \delta 15)}{3 \times 100} \tag{2.26}$$

where positive strain indicates expansion. Recall that elongation is positive gauge deformation, and that gauges 10 through 15 are mounted on the wall such that expansion of the wall yields a negative gauge deformation as shown in Figure 6. Thus Equation 2.26 has a negative sign to yield positive strains for expansion. The horizontal strain is plotted against the vertical strain in Figure 17 for NCKU walls SW1a, SW3, SW4, SW4a, SW5 and SW6. The vertical strain is typically 2 to 8 times

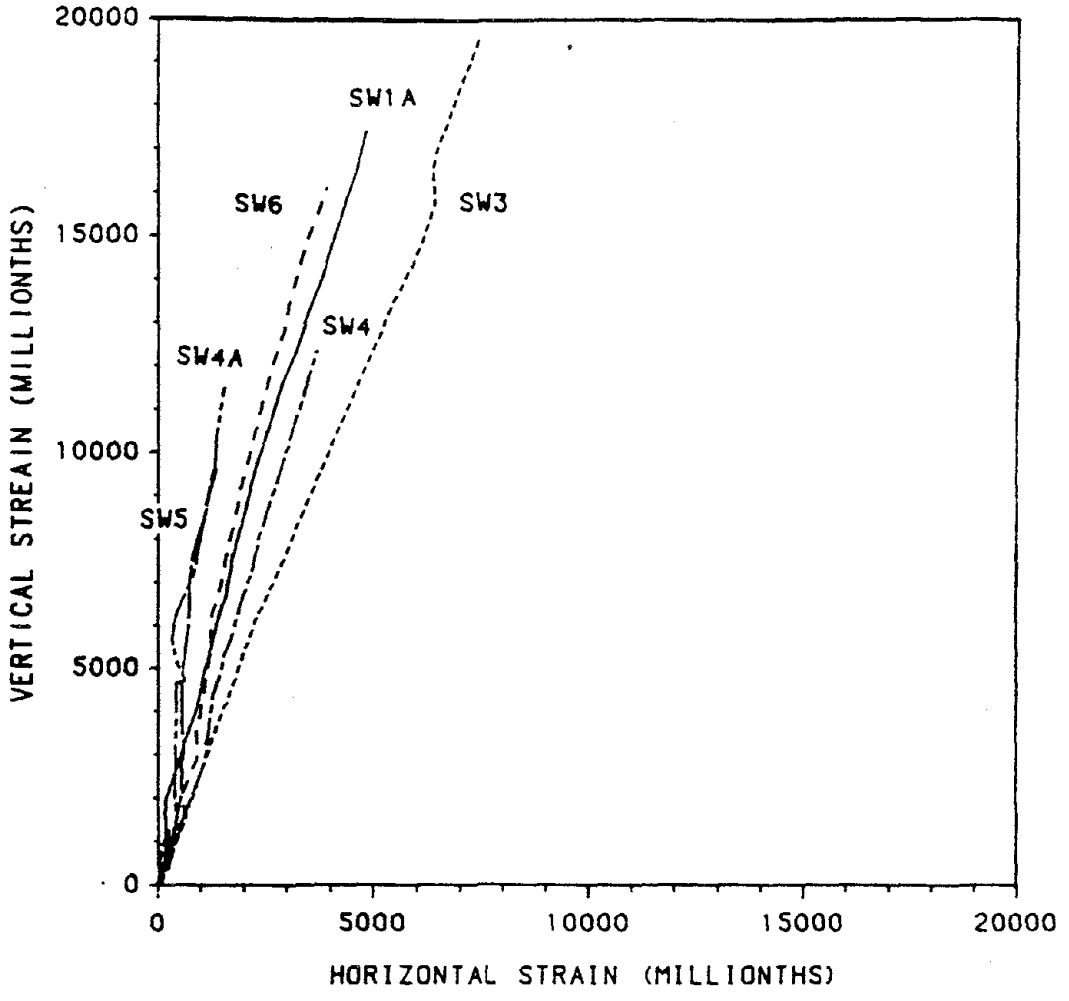

Figure 17. Vertical vs Horizontal Expansion of NCKU Shear Walls

larger than the horizontal strain. Note that the vertical strain includes the strain caused by base rotation.

The vertical expansion is not restrained, except by the weight of the wall. The horizontal expansion is restrained by the heavily reinforced horizontal elements at the top and bottom of the wall and by the reinforcing steel. This restraint and its contribution to the strength and stiffness is discussed in Sections A.1, A.5 and C.3 of Chapter III.

B. ANALYSIS OF DYNAMIC RESULTS

The two story model box structure, 3D11, was dynamically tested on a shaking table by Bennett, Anderson, Endelbrock, et al (3, 30, 31, 33, 34, 35) of the Los Alamos National Laboratory and is shown in Figure 18. The box structure is 18″ wide, 10″ deep, has two 7.75″ high stories, and 1″ thick walls. The box structure is made of micro concrete, with an ultimate stress of 2.89 ksi at $\varepsilon_0 = 0.0033$, an initial modulus of 2750 ksi, and a tensile strength of 0.42 ksi. Two layers of 0.5″ hail screen are used for the reinforcement. The reinforcement ratio is $\rho = 0.554\%$. The hail screen consists of 0.042″ϕ wires 0.5″ on center, each way, with a yield point of 42.7 ksi at $\varepsilon = 0.001668$, and an ultimate stress of 53.1 ksi at $\varepsilon = 0.04$.

The box structure is attached to a uniaxial shaking table. The direction of motion coincides with the structure's weak axis, as shown in Figure 18. Accelerations are measured at the ground, second floor, and roof with Endevco Model 2221 M24 accelerometers. These accelerometers have a frequency range from 2 hz to 8000 hz. Acceleration data were recorded for 2048 points with a time step of 0.0001 seconds. Additional weights of 0.23 k were added to both the roof and second floor.

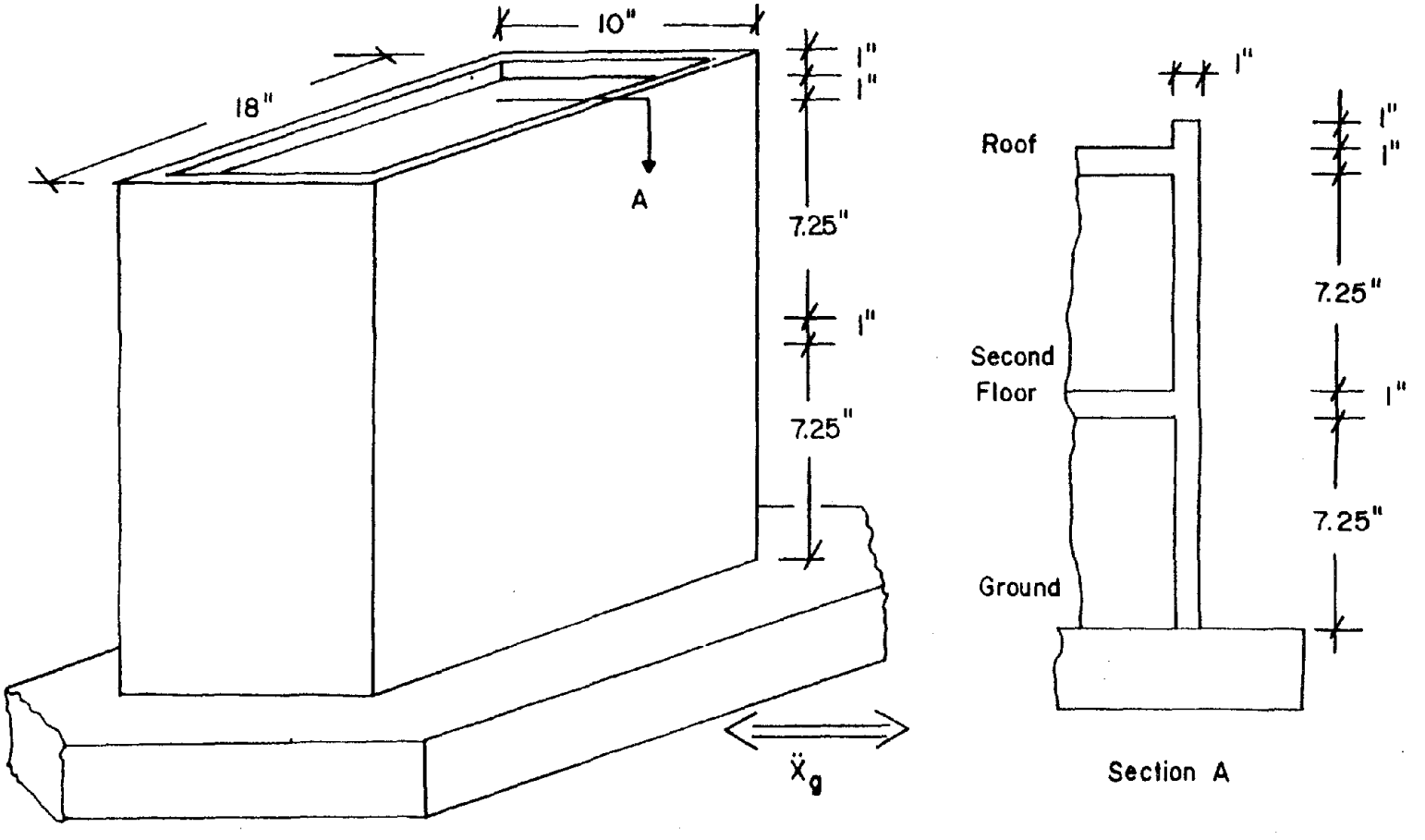

Figure 18. LANL Box Section 3D11

1. Integration of Experimental Accelerations. The experimentally measured acceleration record A(t) consisted of N data points, with a time step of Δt. Assume that the acceleration is linear between data points at times t_0 to t_1, yielding

$$A(t) = A(t_0) + \left(\frac{A(t_1) - A(t_0)}{\Delta t}\right)t \tag{2.27}$$

Integrating the acceleration yields the velocity

$$V(t) = \int A(t)dt = V(t_0) + A(t_0)t + \left(\frac{A(t_1) - A(t_0)}{2\Delta t}\right)t^2 \tag{2.28}$$

And integrating the velocity yields the displacement

$$D(t) = \int V(t)dt = D(t_0) + V(t_0)t + \left(\frac{A(t_0)}{2}\right)t^2 + \left(\frac{A(t_1) - A(t_0)}{6\Delta t}\right)t^3 \tag{2.29}$$

Evaluating the integrals at time $t = \Delta t$ yields the velocity and displacement

$$V(t) = V(t_0) + \left(A(t_1) + A(t_0)\right)\frac{\Delta t}{2} \tag{2.30}$$

$$D(t) = D(t_0) + V(t_0)\Delta t + \left(2A(t_0) + A(t_1)\right)\frac{\Delta t^2}{6} \tag{2.31}$$

Equations 2.30 and 2.31 are used to determine the velocity and displacements at the base of the structure. To determine the relative displacement between floors, one may substitute the relative acceleration $A_f(t) - A_g(t)$ into Equations 2.30 and 2.31 for the acceleration, where $A_f(t)$ is the absolute acceleration of the floor, and $A_g(t)$ is the absolute acceleration of the base of the structure or ground.

2. Error Corrections for Experimental Accelerations. The relative acceleration and acceleration power spectral density[2] for the roof of LANL box 3D11 are shown in Figure 19. The acceleration is integrated with Equations 2.30 and 2.31 to obtain the velocity and displacement as shown in Figure 20. Note that both the velocity and displacement increase with time. The velocity for a structure should fluctuate around zero, and should approach zero at large values of time. Thus there are errors in the experimental acceleration.

Recall that the accelerometers used for this test have an allowable frequency range from 2 hz to 8000 hz. Examine the acceleration PSD in Figure 19 and note that the low frequency signal content is very strong. This low frequency signal is below the threshold for which the accelerometers are accurate. Thus the accelerometers have introduced low frequency noise into the acceleration record. Other common sources of error may be the digitizing equipment, cable noise, cross axis sensitivity, etc.

Assume the acceleration has the form

$$A(t) = \cos \omega t \tag{2.32}$$

Integrating twice yields the displacement

$$D(t) = \frac{-1}{\omega^2} \cos \omega t \tag{2.33}$$

Note that the displacement is inversely proportional to the square of the frequency. Thus displacements are extremely sensitive to low frequency noise. Several schemes to remove the low frequency noise from the acceleration test data are discussed below.

---

2 The power spectral density (PSD) is a measure of a signal's frequency content, and is calculated by Equation A.18 of Appendix A.

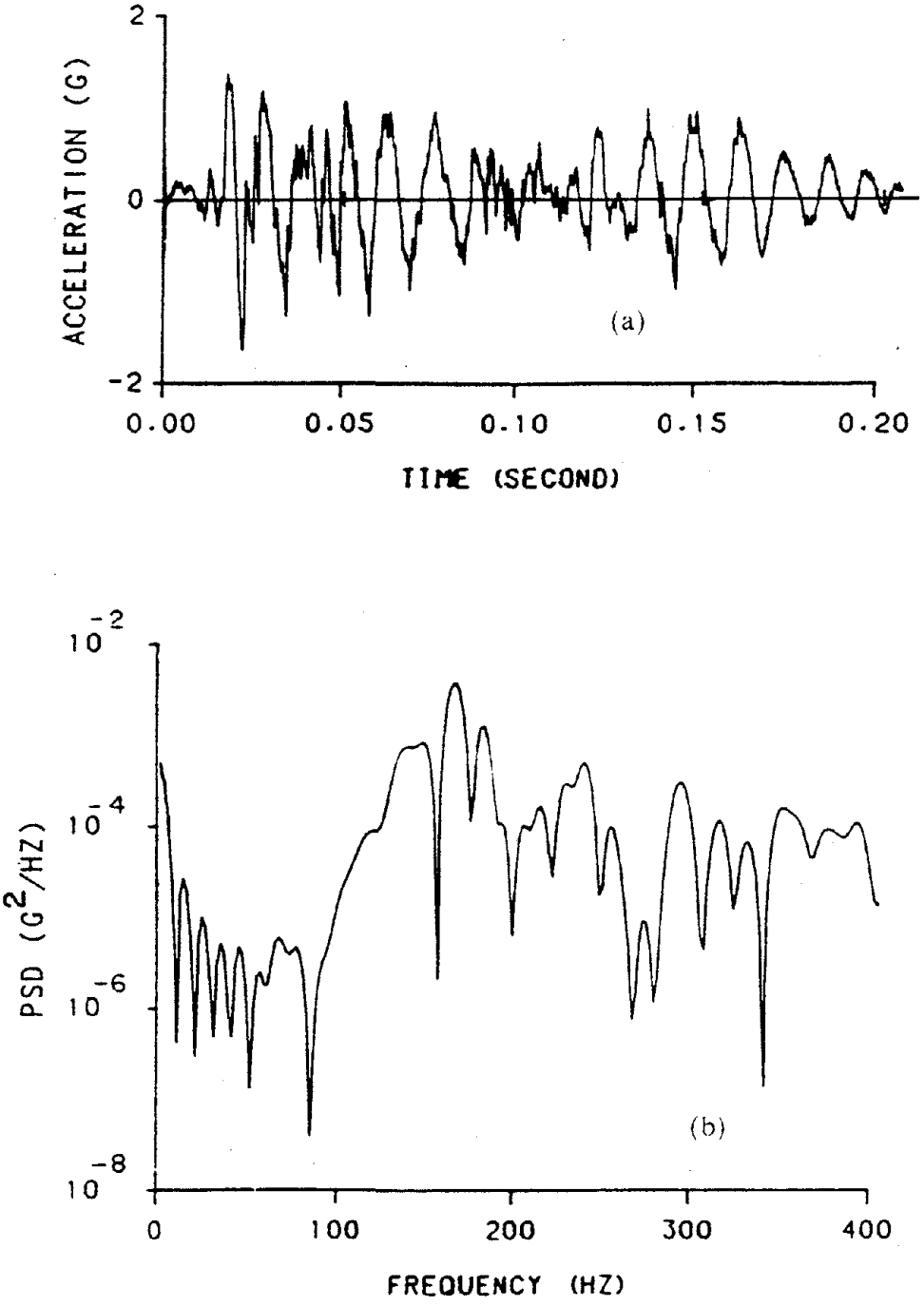

Figure 19. LANL Box 3D11 Roof Acceleration and PSD: (a) Acceleration, (b) Acceleration PSD

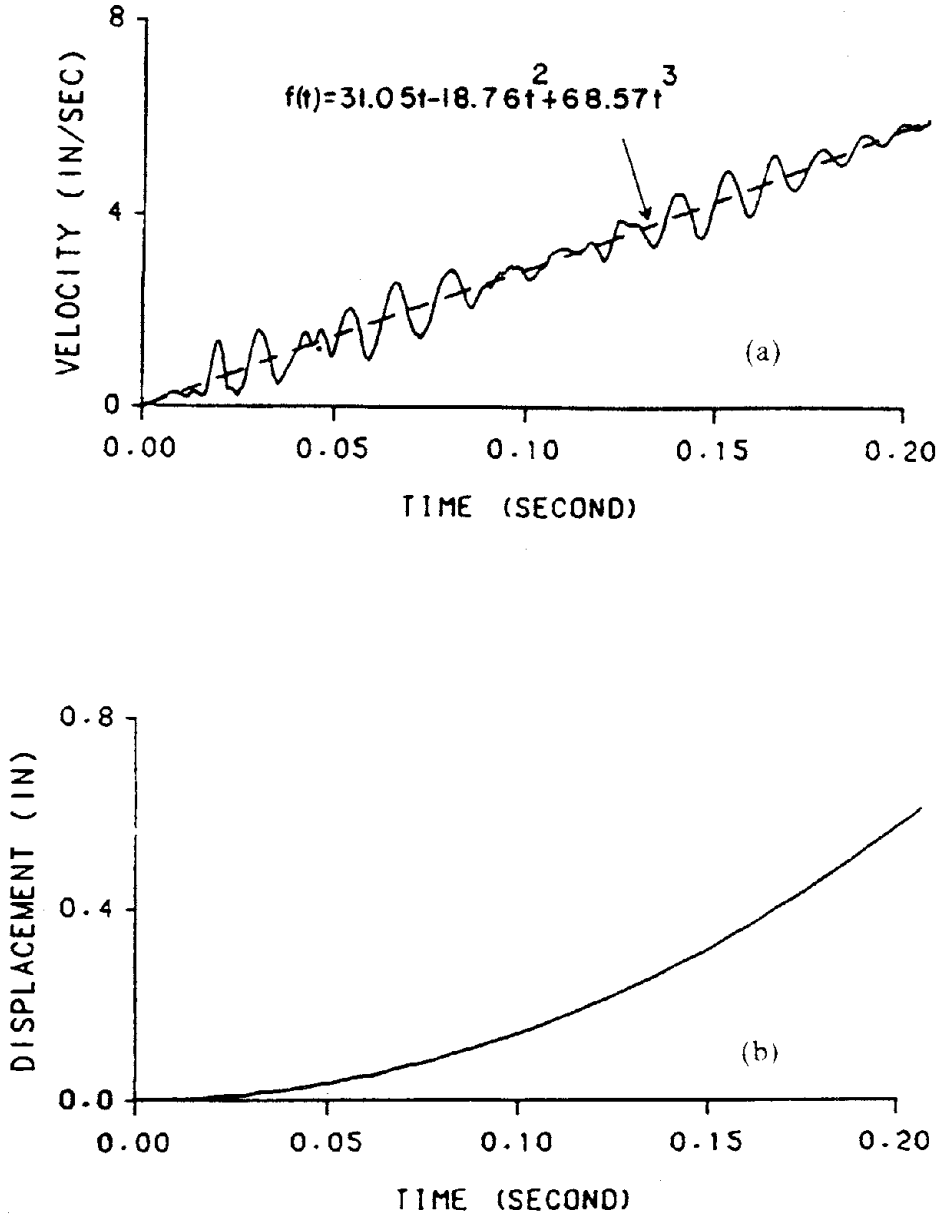

Figure 20. LANL Box 3D11 Roof Velocity and Displacement: (a) Velocity, (b) Displacement

a. Minimum Velocity Correction for Acceleration Test Data. Earthquake ground accelerations are recorded by strong motion accelerographs. One difficulty in integrating the earthquake ground acceleration is that the base line of the accelerogram is not known. Berg and Housner (10) developed a parabolic base line correction (BLC) that minimizes the kinetic energy of the ground motion. This parabolic base line correction is given by Equation B.12 of Appendix B.

The relative acceleration between the ground and the roof of LANL box 3D11 is base line corrected. The new base line is sketched on the velocity in Figure 20. The corrected acceleration and acceleration PSD are shown in Figure 21, while the velocity and displacement are shown in Figure 22, and the maximum values are given in Table IV. The acceleration PSD before the BLC was applied is also shown in Figure 21. Note that the BLC reduced the frequency content of the acceleration below 30 hz. The resulting velocities and displacements are well centered about the origin.

Table IV. MAXIMUM RESPONSE OF LANL BOX 3D11 AFTER BLC

	Maximum	@ Time	Minimum	@ Time
Acceleration	1.28044	.0172	-1.75686	.0211
Velocity	0.80933	.0194	-0.75967	.0586
Displacement	0.00179	.0328	-0.00167	.0756

Note: All units are inch, kip, second and g.

The frequency range that is modified by the base line correction is a function of the length of the record. There is no guarantee that the BLC will remove all of the noise, or that the BLC will only remove noise from the acceleration. For box 3D11's acceleration records, the BLC reduced the frequency content below 30 hz. If the structure responds to frequencies below 30 hz, the BLC removes the structure's response in addition to the noise.

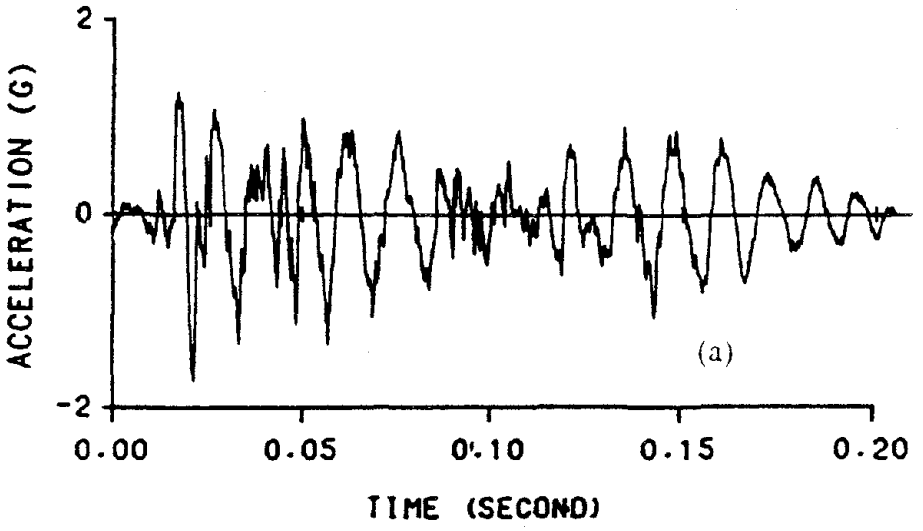

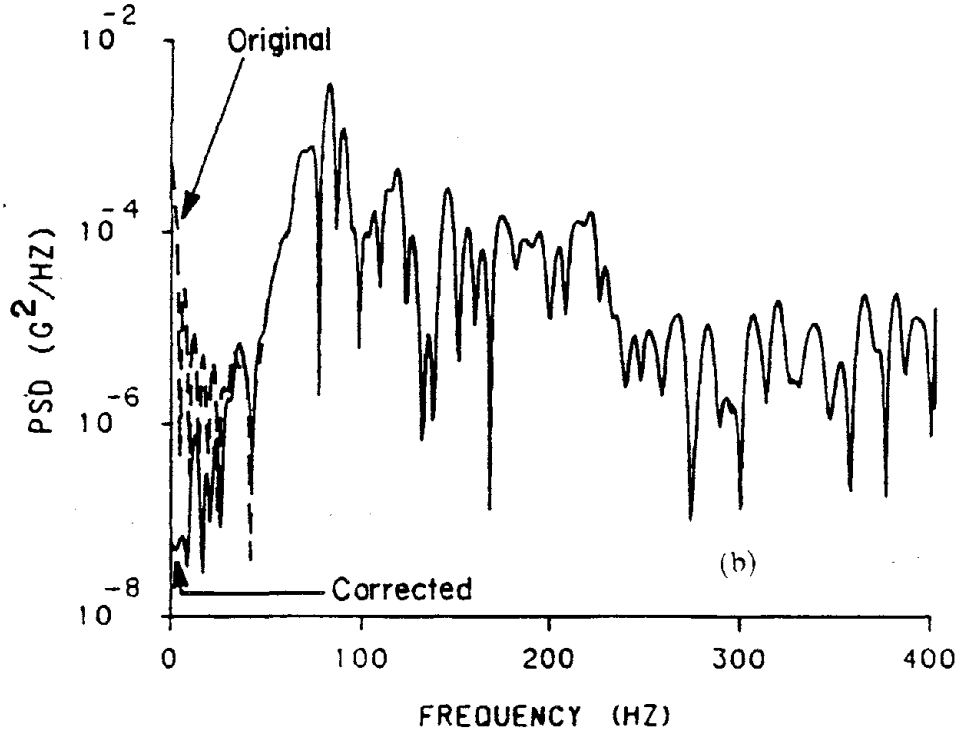

Figure 21. LANL Box 3D11 Acceleration and PSD After Base Line Correction: (a) Acceleration, (b) Acceleration PSD

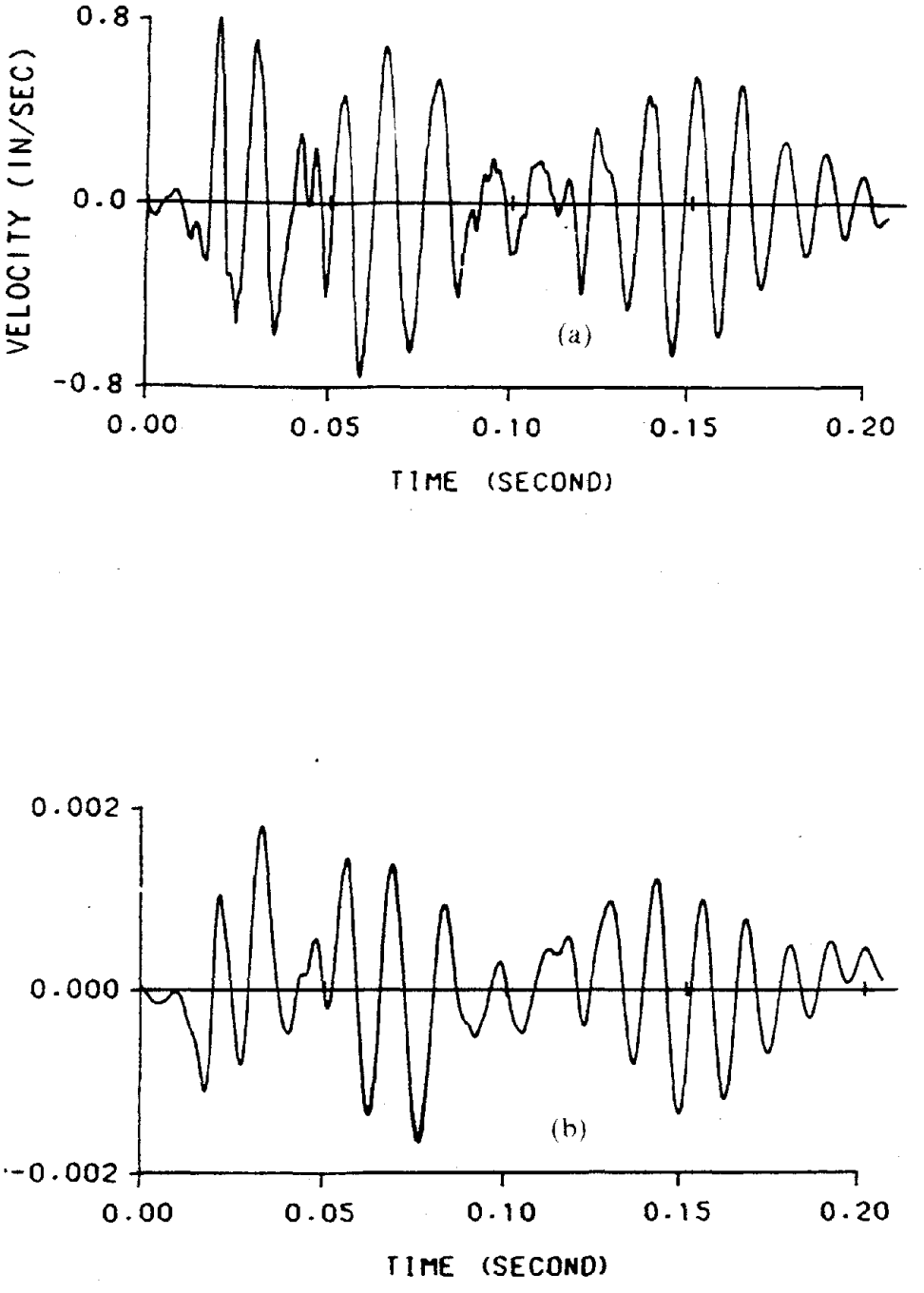

Figure 22. LANL Box 3D11 Velocity and Displacement After Base Line Correction: (a) Velocity, (b) Displacement

b. Filtering Correction for Acceleration Test Data. Another method to remove low frequency noise is by digital filters. A 28 hz high-pass filter is used to remove the errors from the relative roof acceleration of LANL box 3D11. The filtered acceleration and acceleration PSD are shown in Figure 23, while the velocity and displacement are shown in Figure 24, and the maximum values are given in Table V. The acceleration PSD before filtering is also shown in Figure 23. Note that the low frequency noise below 28 hz has been removed. The velocity appears to be well centered. However the displacement in Figure 23 has a positive permanent set for t>0.10 second. Thus while the high-pass filter removes the noise from a specific frequency content it does not guarantee that the resulting displacements will be well centered.

Table V. MAXIMUM RESPONSE OF LANL BOX 3D11 AFTER 28 HZ HIGH-PASS FILTER

	Maximum	@ Time	Minimum	@ Time
Acceleration	1.26388	.0172	-1.76708	.0211
Velocity	0.76648	.0194	-0.74841	.0586
Displacement	0.00152	.0685	-0.00141	.0755

Note: All units are inch, kip, second and g.

c. Combined Corrections for Acceleration Test Data. As discussed in the previous section, the base line correction removes low frequency noise, but the frequency content of the noise removed is a function of the length of the record. The filter can remove noise in a specific range, but it does not guarantee that the resulting displacements will be well centered. Similar problems are addressed when correcting the earthquake ground accelerations. The current trend in correcting earthquake ground accelerations is to use a combination of linear base line corrections and

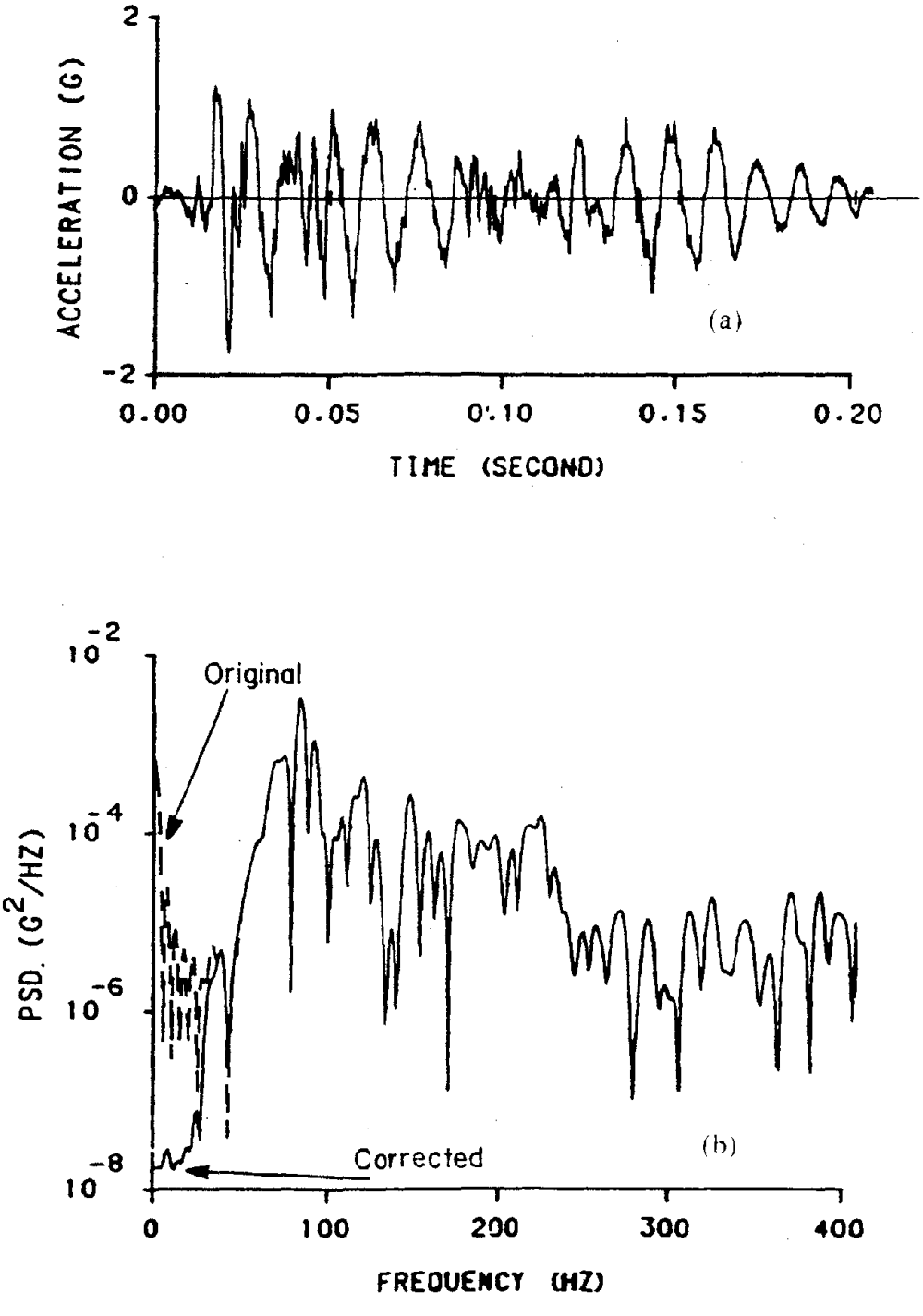

Figure 23. LANL Box 3D11 Acceleration and PSD After Filtering Correction: (a) Acceleration, (b) Acceleration PSD

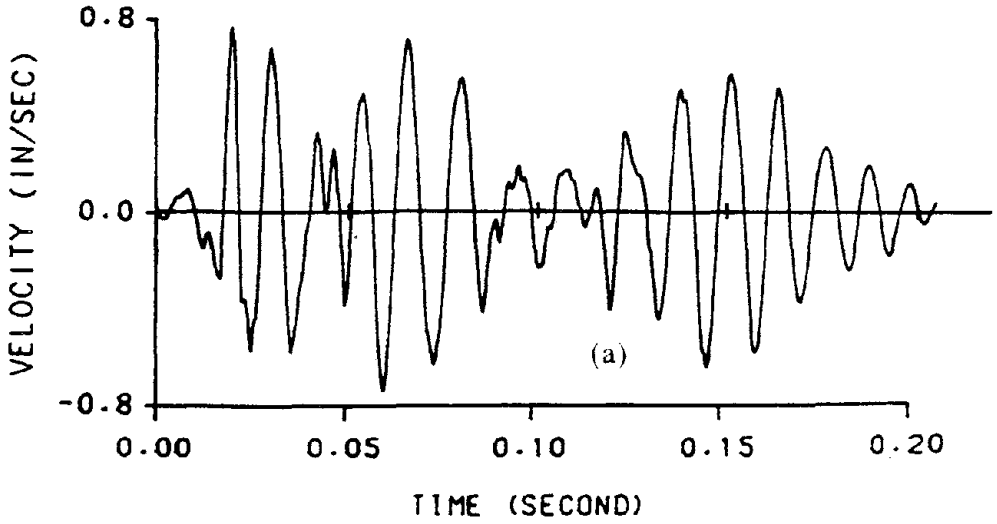

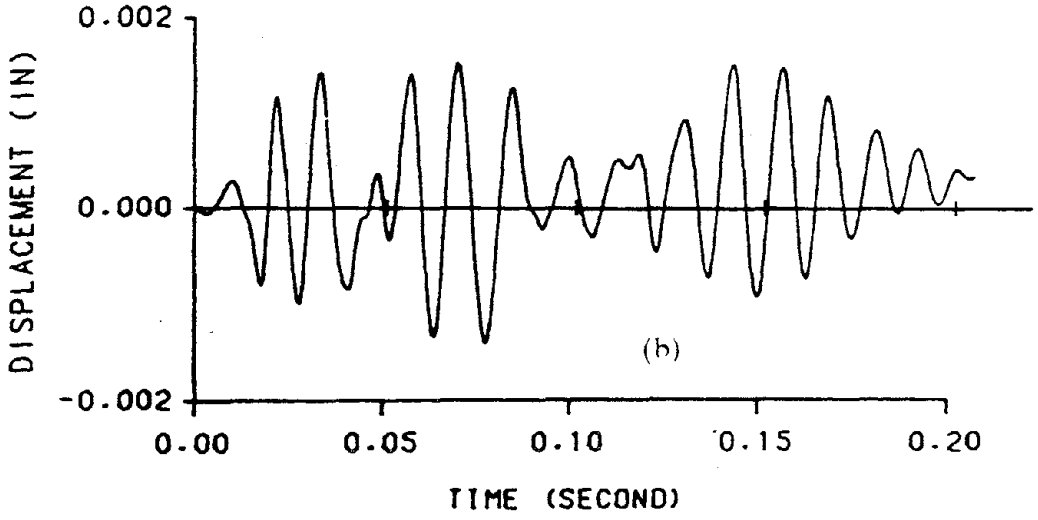

Figure 24. LANL Box 3D11 Velocity and Displacement After Filtering Correction: (a) Velocity, (b) Displacement

high-pass filters (28). Thus the base line corrections and the high-pass filters used in the previous sections are combined. Define the relative acceleration between floors as

$$A'_{relative} = \left[(A_{floor} \rightarrow BLC = A'_{floor}) - (A_{ground} \rightarrow BLC = A'_{ground}) \right] \qquad (2.34)$$

where BLC denotes that the signal is base line corrected. The relative acceleration is corrected by

$$A'_{relative} \rightarrow (28 \text{ hz High-Pass Filter}) \rightarrow BLC = A''_{relative} \qquad (2.35)$$

The corrected relative acceleration $A''_{relative}$ is integrated with Equations 2.30 and 2.31 to yield the velocity and displacement. The corrected acceleration and acceleration PSD for the roof of LANL box 3D11, are shown in Figure 25, while the velocity and displacement are shown in Figure 26 and the maximum values are given in Table VI. By comparing the acceleration PSD before and after corrections, it can be seen that the low frequency noise has been removed. Note that the velocities and displacements are well centered about the origin.

Table VI. MAXIMUM RESPONSE OF LANL BOX 3D11 AFTER COMBINED FILTER CORRECTION AND BLC

	Maximum	@ Time	Minimum	@ Time
Acceleration	1.26382	.0172	-1.76695	.0211
Velocity	0.76585	.0194	-0.75081	.0586
Displacement	0.00144	.0685	-0.00152	.0755

Note: All units are inch, kip, second and g.

d. Theoretical Accuracy of Corrections for Acceleration Test Data. Before accepting the corrected acceleration, one must know if the correction method removes only the low frequency noise and yields the actual acceleration, or does the correction

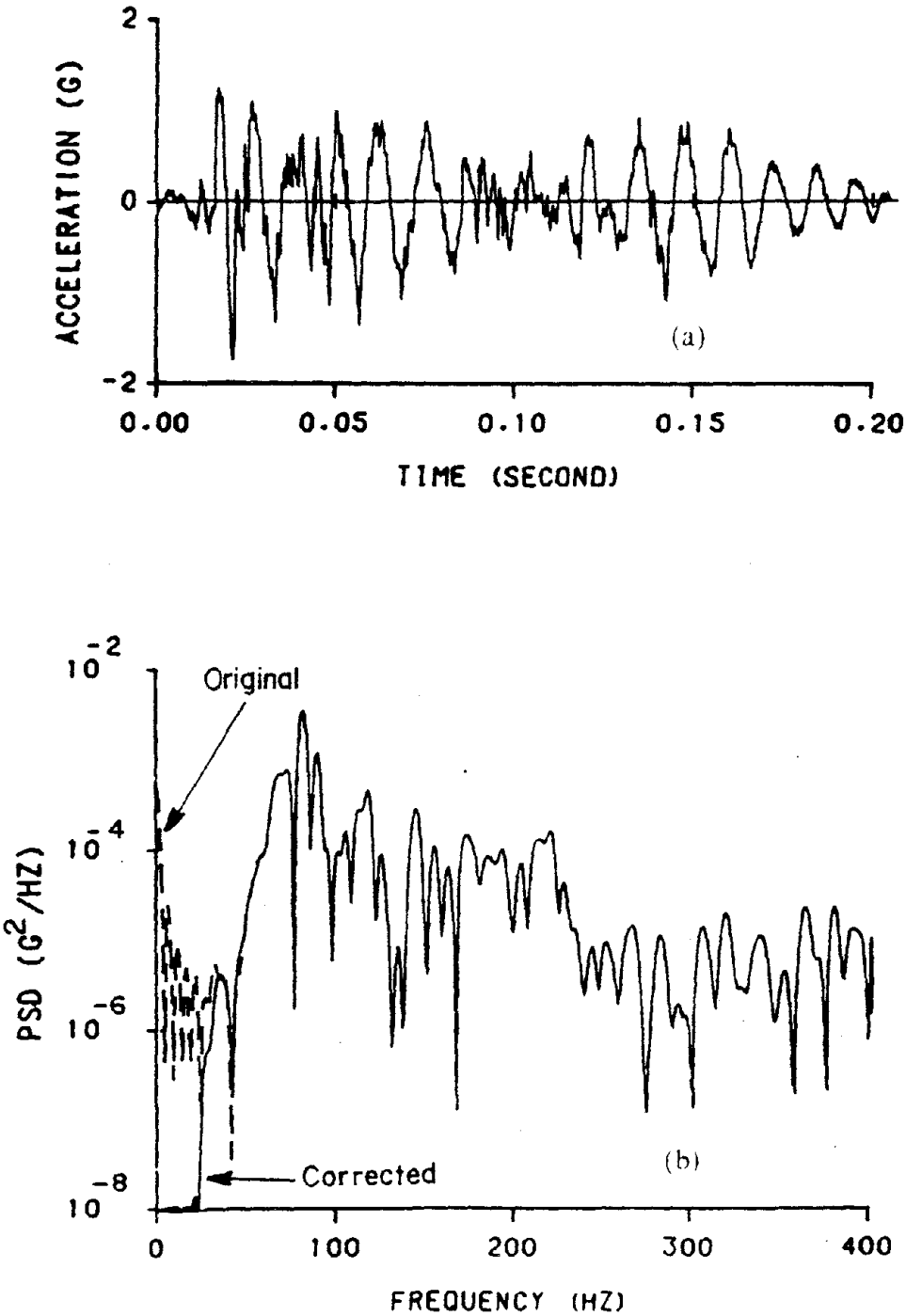

Figure 25. LANL Box 3D11 Acceleration and PSD After Combined BLC and Filter Corrections: (a) Acceleration, (b) Acceleration PSD

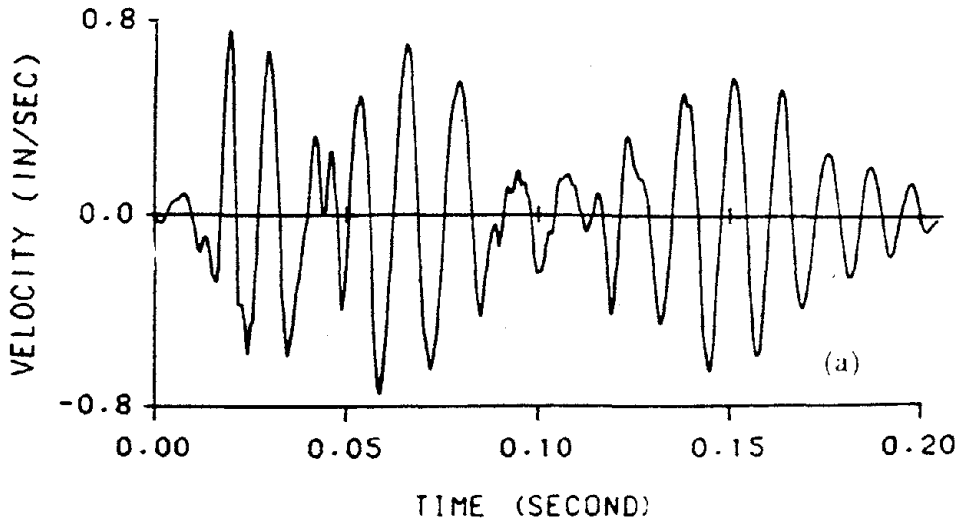

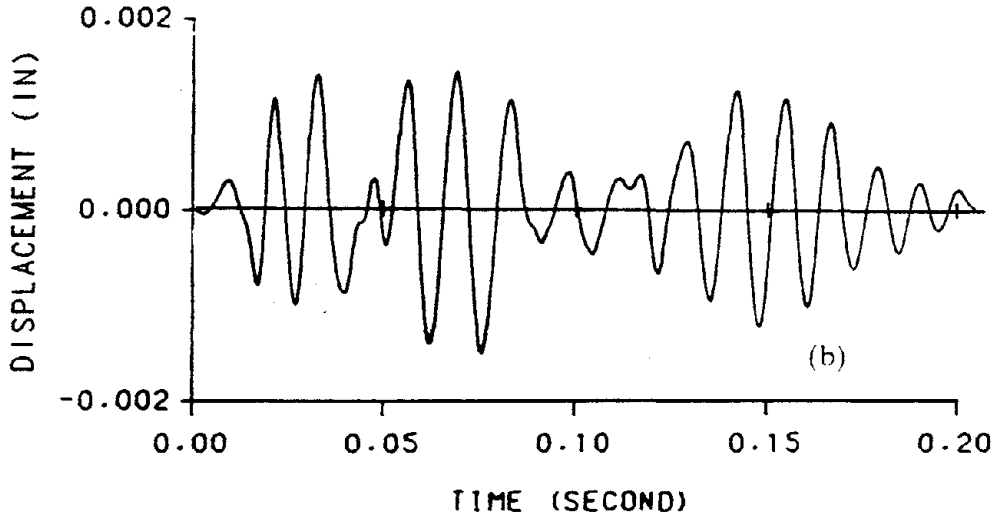

Figure 26. LANL Box 3D11 Velocity and Displacement After Combined BLC and Filter Corrections: (a) Velocity, (b) Displacement

method yield a modified acceleration? To answer this question, an elastic and a nonlinear two-degrees-of-freedom models are analyzed. The calculated response from each model was contaminated by adding low frequency noise. The noisy acceleration was then corrected, and compared to the original calculated response.

• Elastic Structure. The two-degrees-of-freedom structure is shown in Figure 27. The elastic natural frequencies are 77.5 hz and 200 hz. The elastic structure is analyzed with the experimental base acceleration from LANL box 3D11, which is also shown in Figure 27. The calculated acceleration PSD for the roof and the roof's displacements are shown in Figure 28. A low frequency noise signal of

$$A_{noise}(t) = 0.01 \sin(6\pi t) \tag{2.36}$$

is added to the roof relative acceleration. The acceleration PSD and the displacement of the roof's response with noise are also shown in Figure 28. As previously discussed, the displacements are very sensitive to low frequency noise.

The corrections in Equation 2.35 are applied to the noisy signal. The corrected acceleration PSD and the displacements are compared with the calculated values in Figure 29 and in Table VII. Note that the corrected displacements compare very favorably with the calculated displacements. From the PSD it can be seen that the corrected acceleration has less of a low frequency content than the calculated value. But since the calculated response had a very small low frequency content to begin with, this has a small effect on the displacements.

• Nonlinear Structure. The same two-degrees-of-freedom structure shown in Figure 27 is used for the nonlinear structure with the bilinear hysteresis model. The nonlinear structure is subjected to the same base excitation as the elastic structure. The calculated roof acceleration PSD and displacement are shown in Figure 30.

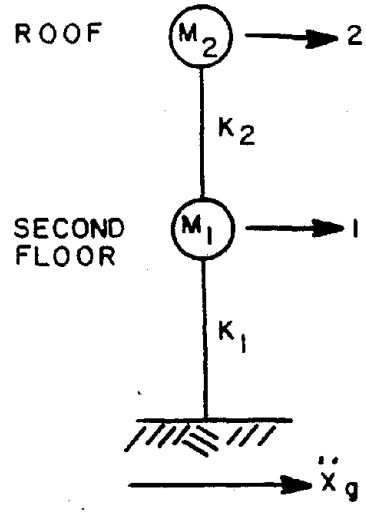

(a) Two DOF Structure

$M_1 = 7.074 \times 10^{-4}\ K\,\sec^2/IN$

$M_2 = 6.763 \times 10^{-4}\ K\,\sec^2/IN$

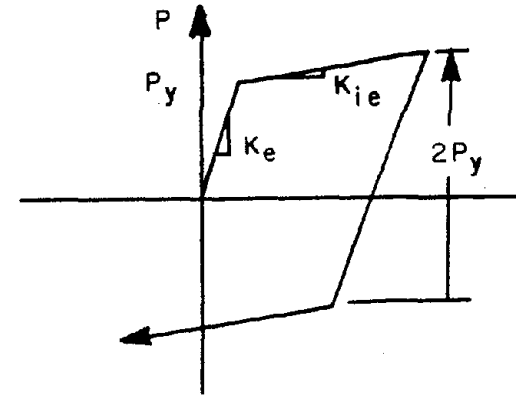

(b) Bilinear Member Hysteresis Model

$K_E = 425\ K/IN$

$P_Y = 0.25\ K$

$K_{IE} = 87.36\ K/IN$

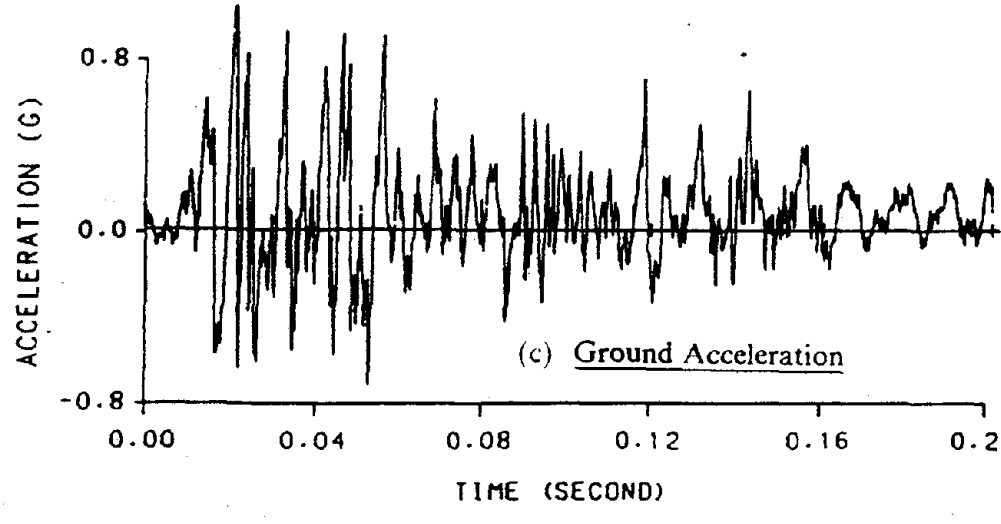

(c) Ground Acceleration

Figure 27. Two-Degrees-of-Freedom Test Structure Used to Study the Accuracy of Acceleration Corrections: (a) Two-Degrees-of-Freedom Test Structure, (b) Bilinear Hysteresis Model, (c) Ground Acceleration

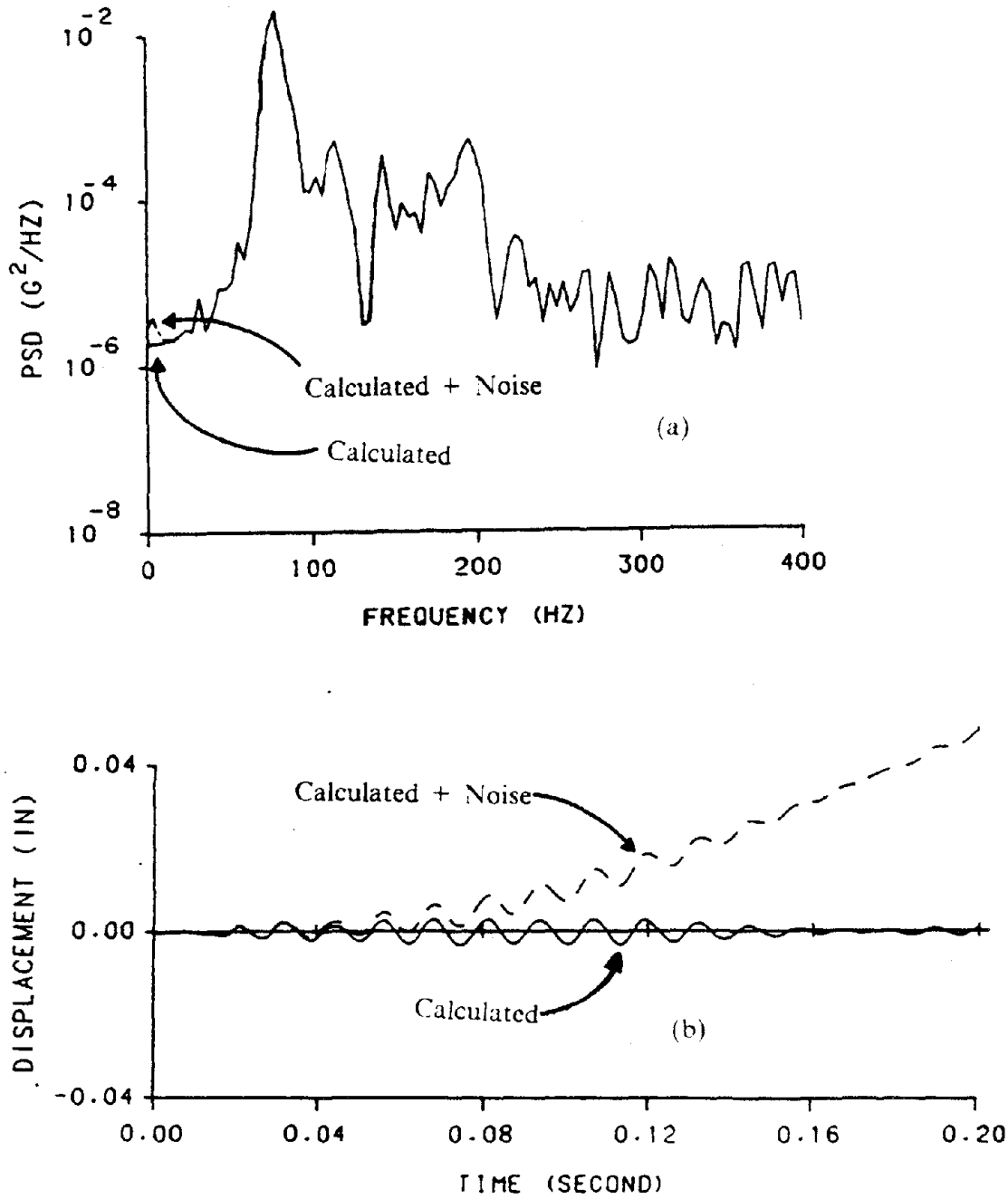

Figure 28. Elastic Response of Test Structure With Noise: (a) Acceleration PSD, (b) Displacement

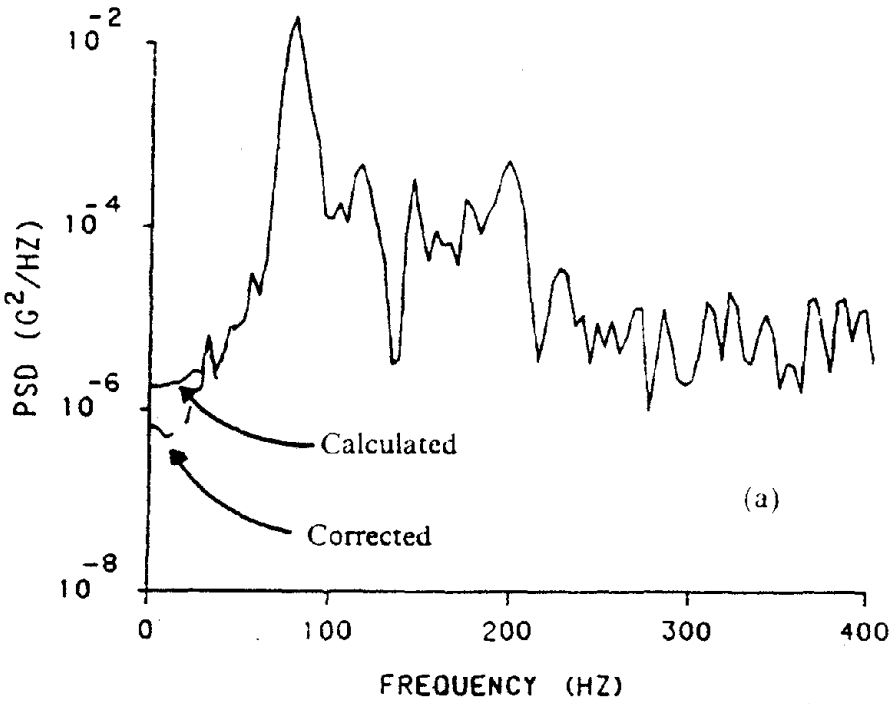

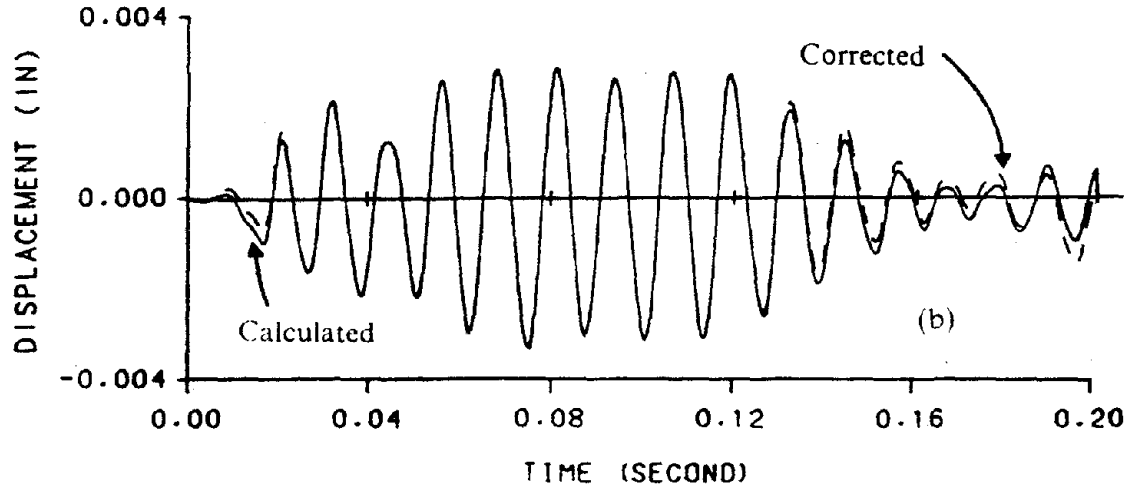

Figure 29. Elastic Response of Test Structure After Corrections: (a) Acceleration PSD, (b) Displacement

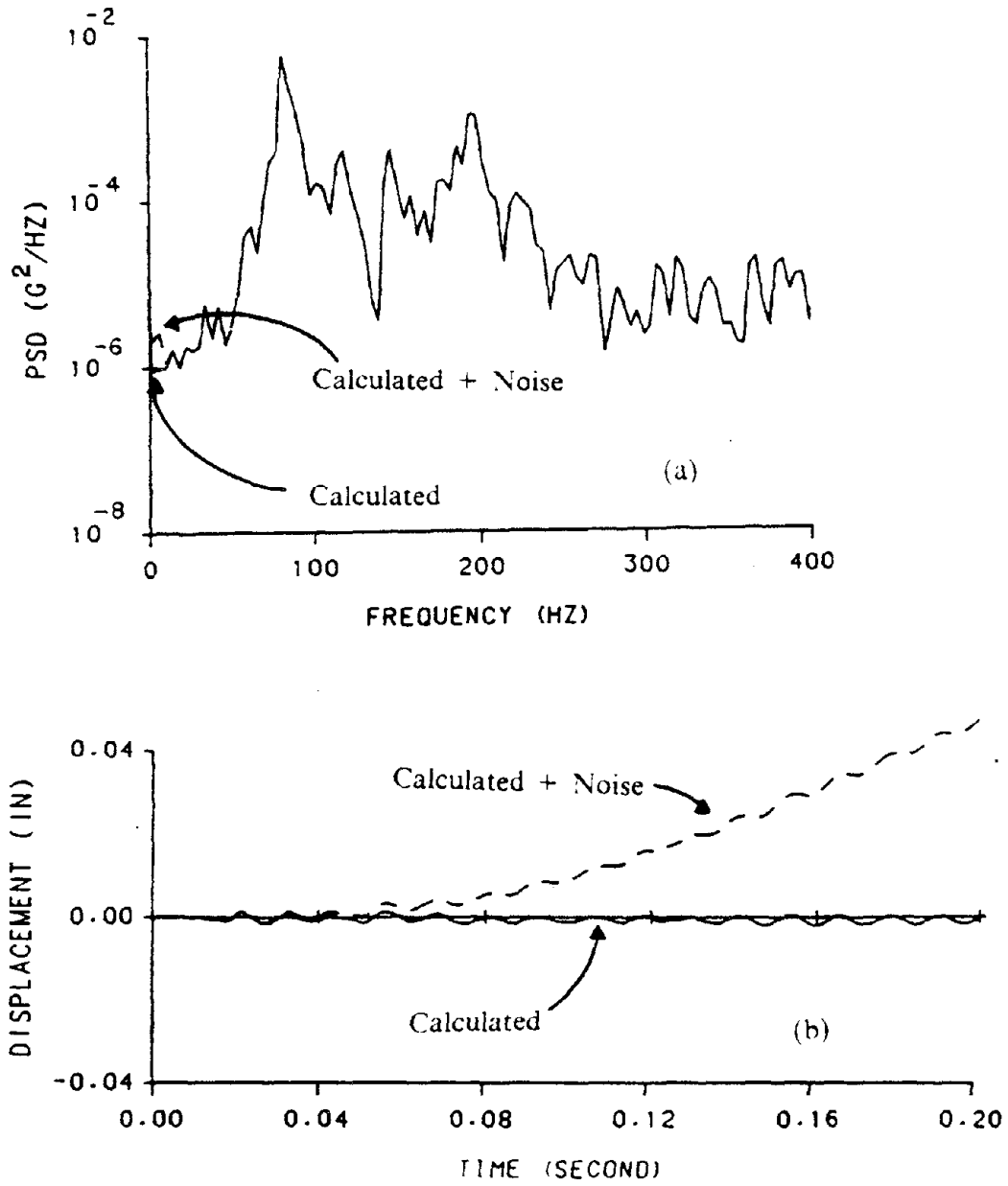

Figure 30. Nonlinear Response of Test Structure With Noise: (a) Acceleration PSD, (b) Displacement

Table VII. COMPARISON OF CALCULATED, NOISY AND CORRECTED RESPONSE FOR AN ELASTIC STRUCTURE

	Calculated Response	Noise + Calculated Response	Corrected Response
Peak Acceleration	-2.4947	-2.4859	-2.4971
@ time	0.0566	0.0566	0.0566
Peak Velocity	-1.5917	1.8741	-1.5978
@ time	0.0844	0.1164	0.0844
Peak Displacement	-0.00333	0.04901	-0.00339
@ time	0.0749	0.2044	0.0749

Note: All units are inch, kip, second and g.

Similar to the elastic case the low frequency noise in Equation 2.36 is added to the calculated relative acceleration of the roof. The resulting noisy acceleration PSD and displacements are shown in Figure 30 for comparison. The noisy signal is corrected with Equation 2.35 and compared to the calculated response in Figure 31, and Table VIII. The comparison between corrected and calculated response is poor. The corrected acceleration has less low frequency content than the calculated acceleration. While the calculated displacement was dominated by permanent set, the corrected displacement has none.

From the above observations, it becomes apparent that for the elastic response, where the natural frequency of the structure is well above the region that has noise, the corrections presented in this chapter do not significantly alter the structures response. For nonlinear response which are characterized by low frequency response (permanent set) the corrections outlined in this chapter will alter the structures response. The corrected displacements will not be similar to the true displacements.

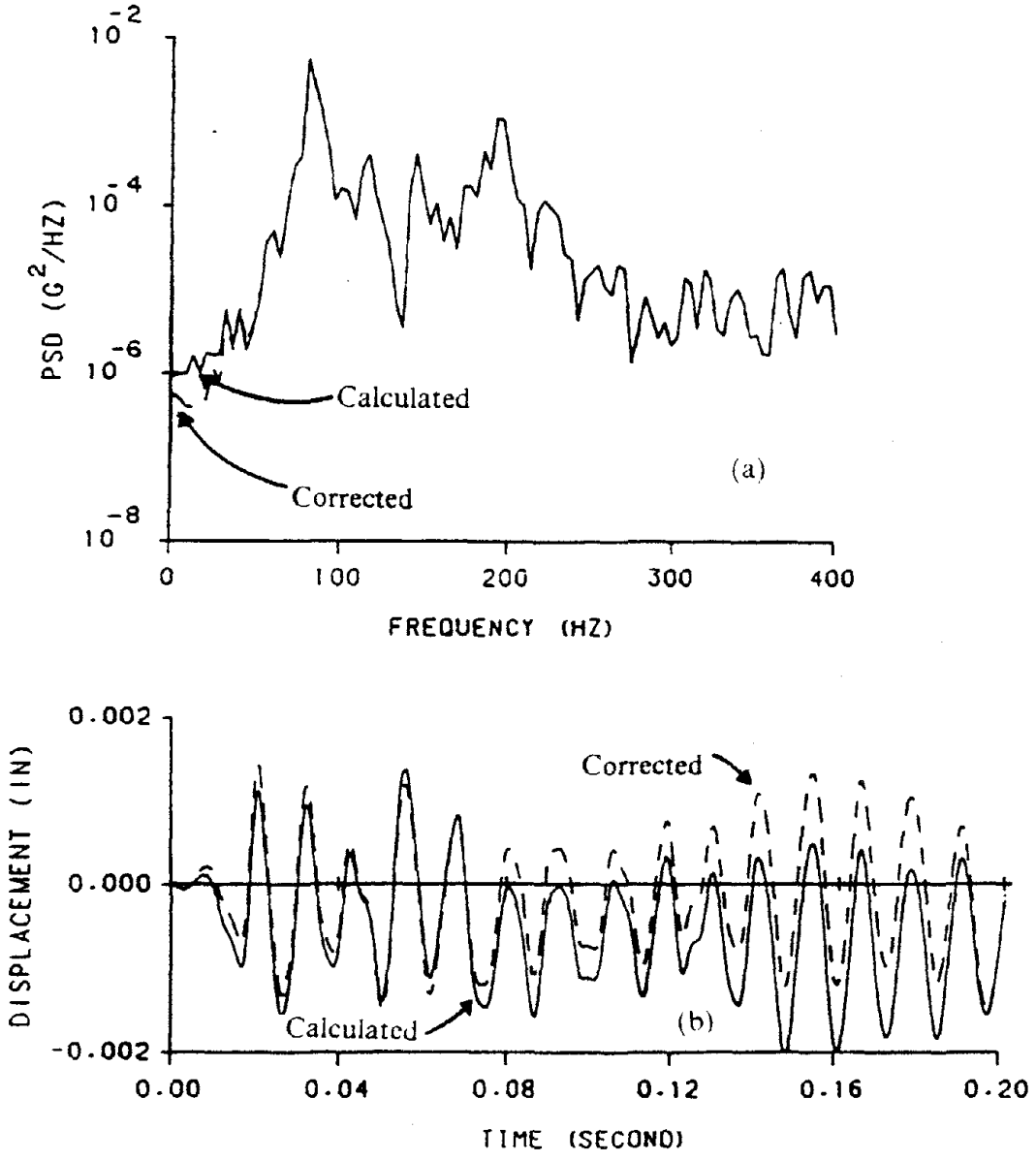

Figure 31. Nonlinear Response of Test Structure After Corrections: (a) Acceleration PSD, (b) Displacement

Table VIII. COMPARISON OF CALCULATED, NOISY AND CORRECTED RESPONSE FOR A NONLINEAR STRUCTURE

	Calculated Response	Noise + Calculated Response	Corrected Response
Peak Acceleration	-2.0326	-2.0287	-2.0402
@ time	0.0212	0.0212	0.0212
Peak Velocity	-0.8056	1.0069	-0.8047
@ time	0.0195	0.1494	0.0195
Peak Displacement	-0.00204	0.04886	-0.00149
@ time	0.1471	0.2047	0.1960

Note: All units are inch, kip, second and g.

III. MONOTONIC RESPONSE BEHAVIOR OF ISOLATED SHEAR WALLS

An analytical model for calculating the monotonic response of isolated reinforced concrete shear walls is presented in this chapter with comparisons of analytical and experimental results. The monotonic response is of interest because it contains 1) the cracking, yield and ultimate loads, and 2) the stiffness at each of these load levels. The monotonic response is also used as the basis for the cyclic loading hysteresis models in Chapter IV.

Many investigators have tested and calculated the ultimate strength of shear walls. These investigations have led to the ultimate loads in the ACI code (1). Gosh (40) calculated the bending displacements of slender walls with various cross sections by using a linear strain distribution, realistic material stress-strain models, and equilibrium. Hsu, Mo and Mau (46, 47), developed an analytical model for low-rise walls with pure shear deformation, based on the Vecchio-Collins (81, 82) shear softened stress-strain concrete model. Vallenas (80) calculated the monotonic response of high-rise walls by combining bending and shear deformations which are calculated independently, without the coupling effect. His bending model consists of a finite element solution with plane stress concrete elements that utilize the endochronic theory. A multilinear model is used to calculate shear deformations.

The proposed analytical model has coupled bending and shear deformations, that are presented as a series of interaction surfaces. For a given wall geometry, the relationship between bending and shear can be determined. Thus separate bending and shear backbone curves are extracted from the interaction surfaces. Together, they define the monotonic load deformation response.

A. MOMENT-SHEAR INTERACTION SURFACE

Both the longitudinal strain and shear strain influence the principal strains at a point in a shear wall. Principal stresses at this point are related to the principal strains through a stress-strain model. Principal stresses are rotated to longitudinal and shear stresses on the wall's cross section. Thus the magnitude of the longitudinal stress, at a point, is dependant on both the longitudinal strain and the shear strain. Since the bending moment is a function of the longitudinal stress distribution, bending moment is dependant on both the longitudinal strain and the shear strain. Similarly, the shear is dependant on both the shear strain and the longitudinal strain. Conversely, the longitudinal strain distribution is a function of both the moment and shear. Shear strain is also a function of both the moment and shear. In this section, the longitudinal strain distribution and the shear strain as a function of moment and shear are calculated. Also, the base rotation due to bond slip as a function of moment and shear is calculated. These relationships are represented as a series of interaction surfaces.

1. Assumed Strain Distribution. In Chapter II, the concept of an equivalent moment in the hinging region of the wall is developed. The low-rise wall in Figure 32 has a hinging region that extends over the walls height. Thus the equivalent moment and shear on this wall are given and do not vary over the walls height. Also, the moment to shear ratio is known for this wall.

Assume that the longitudinal strain distribution is linear across the width of the wall as shown in Figure 32a. The longitudinal strain distribution is described by specifying the extreme fiber compressive strain, ε_2, at coordinate x_2 and by specifying the tensile strain, ε_1, at coordinate x_1 as shown in Figure 32b. The origin of the x coordinate system, $x = 0$, is chosen at the centroid of the wall. The bending curvature is the slope of the longitudinal strain distribution, and is given by

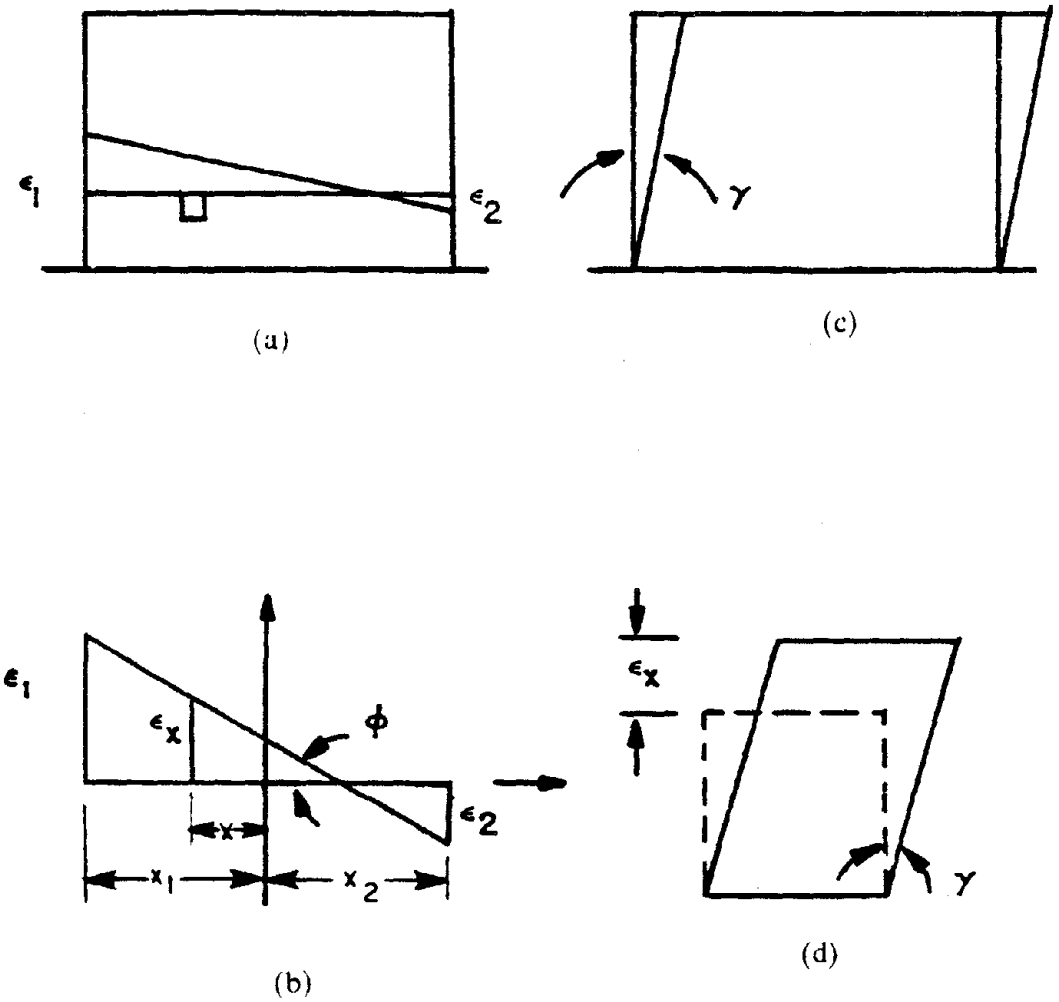

Figure 32. Assumed Strain Distribution in a Shear Wall: (a) Bending Strain Distribution, (b) Longitudinal Bending Strain, (c) Shear Strain Distribution, (d) Longitudinal Bending Strain and Shear Strain Superimposed on an Element

$$\phi = \frac{\varepsilon_1 - \varepsilon_2}{x_2 - x_1} \tag{3.1}$$

The longitudinal strain at point x, is given by

$$\varepsilon_x = \varepsilon_2 + \phi(x_2 - x) \tag{3.2}$$

The shear strain is designated γ, and is shown in Figure 32c.

The horizontal expansion of the wall is restrained by the elements at the top and bottom of the wall, and the horizontal reinforcing steel. Actual values of the horizontal and vertical expansion for NCKU shear walls are compared in Figure 17. While the horizontal expansion is not zero, it is much less than the vertical expansion. Thus the horizontal expansion of the wall is neglected.

The strains acting on a differential element are shown in Figure 32d. These strains consist of a longitudinal strain ε_x, and the shear strain γ. The principal strains acting on this element are determined by Mohr's circle, Figure 33a. The radius of Mohr's circle is given by

$$R = \frac{\sqrt{\gamma^2 + \varepsilon_x^2}}{2} = \frac{\gamma_{max}}{2} \tag{3.3}$$

The principal tensile strain, ε_{pt}, is

$$\varepsilon_{pt} = \frac{\varepsilon_x}{2} + R \tag{3.4}$$

the principal compressive strain, ε_{pc}, is

$$\varepsilon_{pc} = \frac{\varepsilon_x}{2} - R \tag{3.5}$$

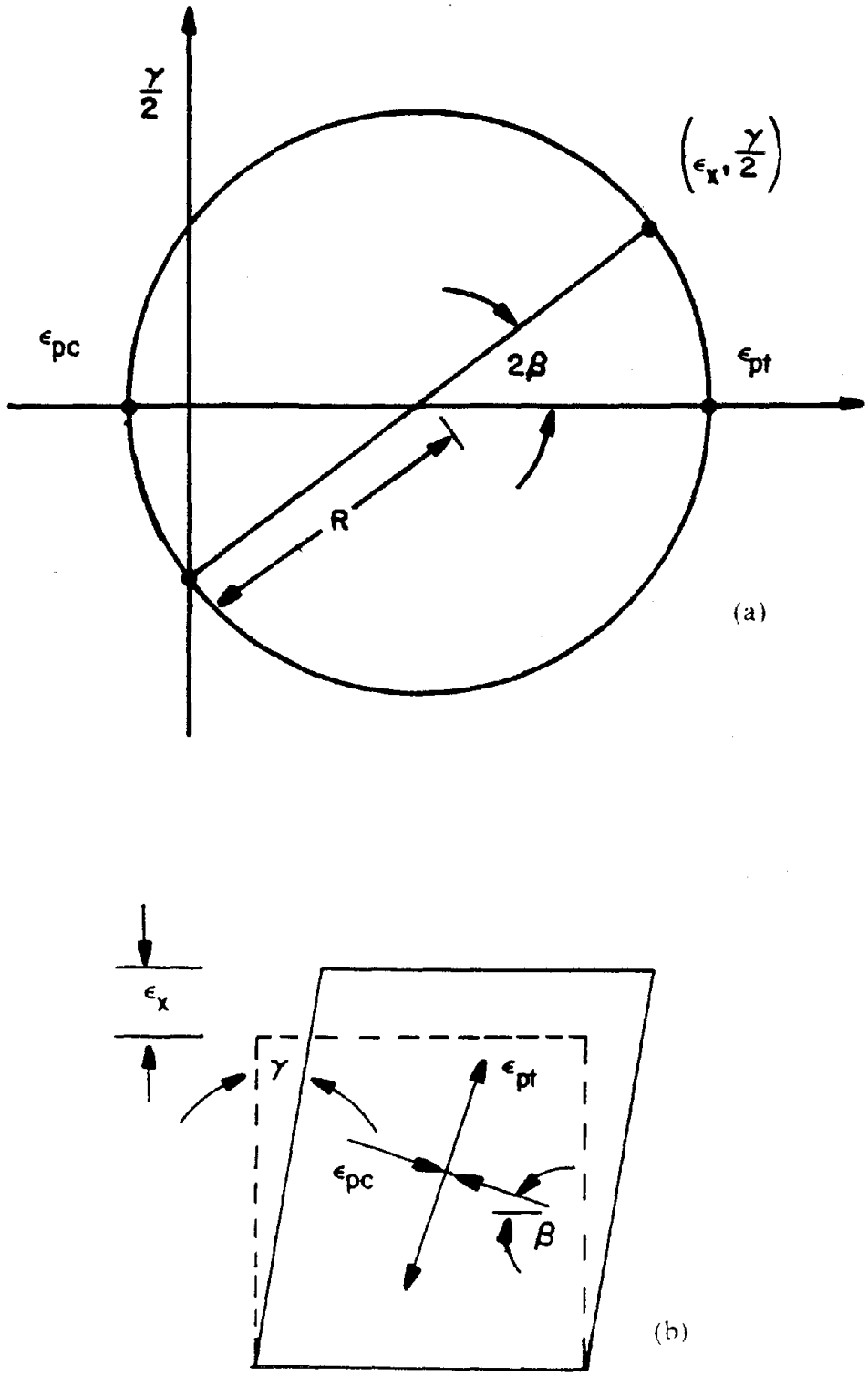

Figure 33. Mohr's Circle for Concrete Strain: (a) Mohr's Circle For Concrete Strain (b) Principal Strains on an Element

and the orientation of the principal compressive strain, β, is given by

$$\beta = \frac{1}{2}\text{atan}\left(\frac{\gamma}{\varepsilon_x}\right) \tag{3.6}$$

These principal strains and their orientation on a differential element are shown in Figure 33b. Cracks will form on the wall, perpendicular to the principal tensile strain, at angle β with the base of the wall. For a typical low-rise shear wall, β will be between $\beta = 30°$ to $\beta = 60°$. This is consistent with experimentally observed crack distributions in Chapter II.

2. Concrete Principal Stress-Strain Model. The Hognestad stress-strain model is shown in Figure 34. This model was developed for members subject to uniaxial compression. Since a biaxial state of stress exist in a shear wall, Hognestad's stress-strain model cannot be used without modification (46).

Vecchio and Collins tested a series of 30 R/C panels (81, 82). From the biaxial stresses and strains that exist in the panels, principal stresses and strains were determined. A shear softened concrete principal stress-strain model was developed.

Similar to the Hognestad model, the Vecchio-Collins model shown in Figure 34 has a parabolic loading branch. Both the ultimate compressive stress, f'_c , and the strain, ε_o, are softened by the term $\frac{1}{\lambda}$ to account for the biaxial state of strain in the panels. Thus the parabolic loading branch goes from the origin to $\left(\frac{\varepsilon_o}{\lambda}, \frac{f'_c}{\lambda}\right)$, and is given by

$$\sigma_{pc} = f'_c \left[2\frac{|\varepsilon_{pc}|}{\varepsilon_o} - \lambda\frac{\varepsilon_{pc}^2}{\varepsilon_o^2}\right] \quad \text{for } |\varepsilon_{pc}| \le \frac{\varepsilon_o}{\lambda} \tag{3.7}$$

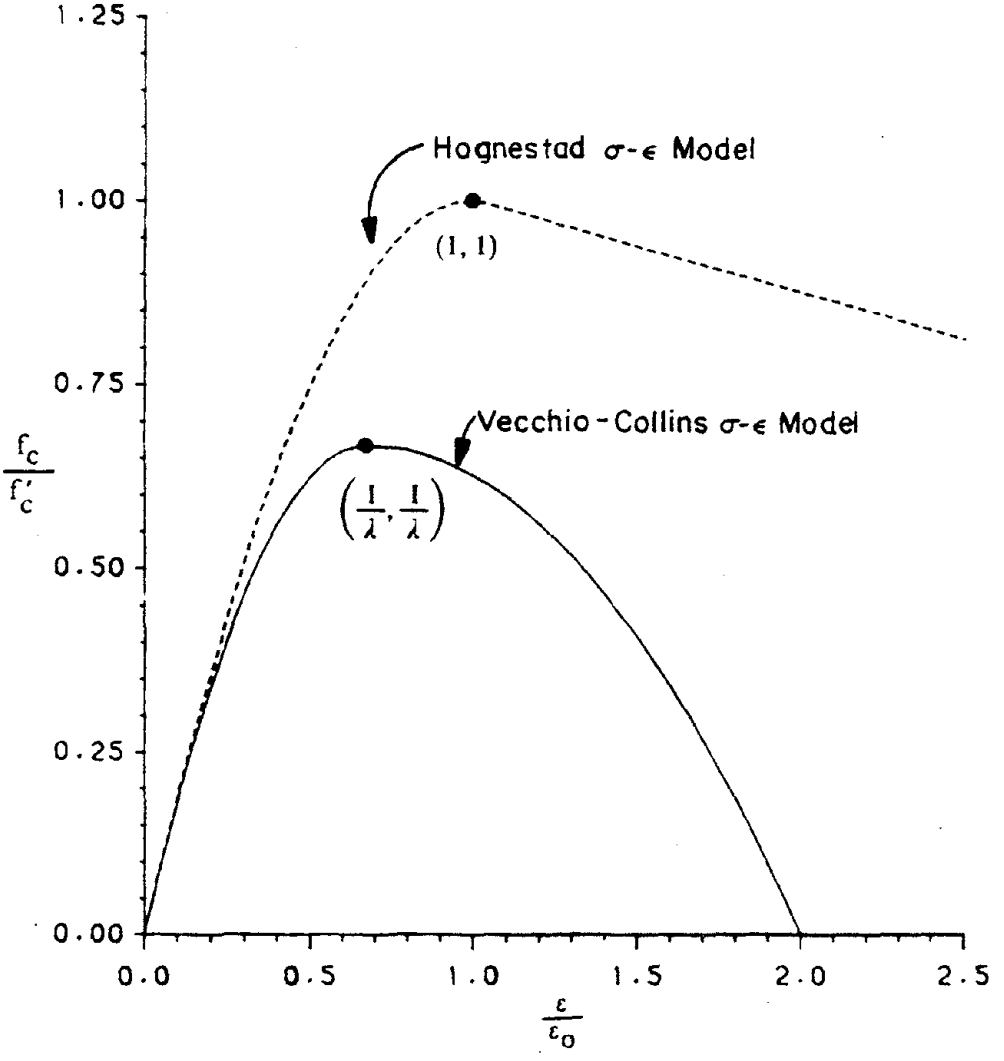

Figure 34. Concrete Principal Compressive Stress-Strain Model

Vecchio and Collins' loading branch is in very good agreement with their experimental data. For the uniaxial case, $\lambda = 1$, the loading branch and the Hognestad stress-strain model are identical.

Vecchio and Collins also used a parabolic curve for the unloading branch of their stress-strain model. This branch begins at the terminus of the loading branch, continues to $(2\varepsilon_0,0)$, and is given by

$$\sigma_{pc} = \frac{f'_c}{\lambda}\left[1 - \frac{(\lambda|\varepsilon_{pc}| - \varepsilon_o)^2}{(2\lambda - 1)^2 \varepsilon_o^2}\right] \quad \text{for } 2\varepsilon_o \geq |\varepsilon_{pc}| \geq \frac{\varepsilon_o}{\lambda} \tag{3.8}$$

At strains larger than $2\varepsilon_0$, the compressive stress is zero. Few experimental strains were observed between ε_0 and $2\varepsilon_0$. Thus the unloading branch is not strongly supported by test data. For uniaxial compression, $\gamma = 1$, the unloading branch underestimates the compressive stress, as can be seen by comparing it to the Hognestad model.

Most of the panels used by Vecchio and Collins to develop the shear softening term γ were loaded in pure shear. The bending in a shear wall subjects an element to combined shear and longitudinal stresses. Thus a modified shear softening term is used in this study.

$$\lambda = .85 + .653\left|\frac{\varepsilon_{pt}}{\varepsilon_{pc}}\right| \geq 1.0 \tag{3.9}$$

For uniaxial compression, $\lambda = 1$. The shear softening term implies a Poisson's ratio of $\mu = \frac{\varepsilon_{pt}}{\varepsilon_{pc}} = 0.23$. This is a reasonable value for concrete.

Several different concrete tensile stress-strain models have been proposed, (41) as shown in Figure 35. The stepped stress-strain model and the discontinuous model were proposed to model the tensile stress in R/C slabs, subject to bending. Vecchio and Collins used the gradual unloading model, to model the tensile stress-strain behavior in their shear panels. Each of theses models has at least one discontinuity when the concrete cracks. A discontinuous tensile stress-strain model will cause the shear and bending backbone curves to be discontinuous. Whereas, the cracking in a shear wall is observed to be a more gradual process.

The graded tensile stress-strain model is proposed in this study to provide a smooth transition between cracked and uncracked concrete. This stress-strain model is based on the following assumptions: 1) 25% of the concrete cracks at a strain of $0.25\varepsilon_{cr}$, 2) 25% of the concrete cracks at a strain of $0.50\varepsilon_{cr}$, 3) 25% of the concrete cracks at a strain of $0.75\varepsilon_{cr}$ and, 4) 25% of the concrete cracks at a strain of ε_{cr}. Each portion of the concrete behaves linearly before and after cracking. Before cracking the loading curve has a slope of E_c, where $E_c = \frac{2f'_c}{\varepsilon_o}$ is the modulus of elasticity for concrete. After cracking, each portion unloads to a strain of $25\varepsilon_{cr}$. The graded tensile model is defined as

$$
\begin{aligned}
&\text{If } \eta \le 0.25 && \text{then } \sigma_{pt} = E_c\,\varepsilon_{pt} \\
&\text{If } 0.25 \le \eta \le 0.50 && \text{then } \sigma_{pt} = f'_{cr}\ (0.0631 + .7476\eta) \\
&\text{If } 0.50 \le \eta \le 0.75 && \text{then } \sigma_{pt} = f'_{cr}\ (0.1907 + .4924\eta) \\
&\text{If } 0.75 \le \eta \le 1.00 && \text{then } \sigma_{pt} = f'_{cr}\ (0.3845 + .2340\eta) \\
&\text{If } 1.00 \le \eta \le 25 && \text{then } \sigma_{pt} = f'_{cr}\ (0.6443 - .0258\eta) \\
&\text{If } 25 \le \eta && \text{then } \sigma_{pt} = 0
\end{aligned}
\qquad (3.10)
$$

where $\varepsilon_{cr} = \frac{f'_{cr}}{E_c}$ and $\eta = \frac{\varepsilon_{pt}}{\varepsilon_{cr}}$.

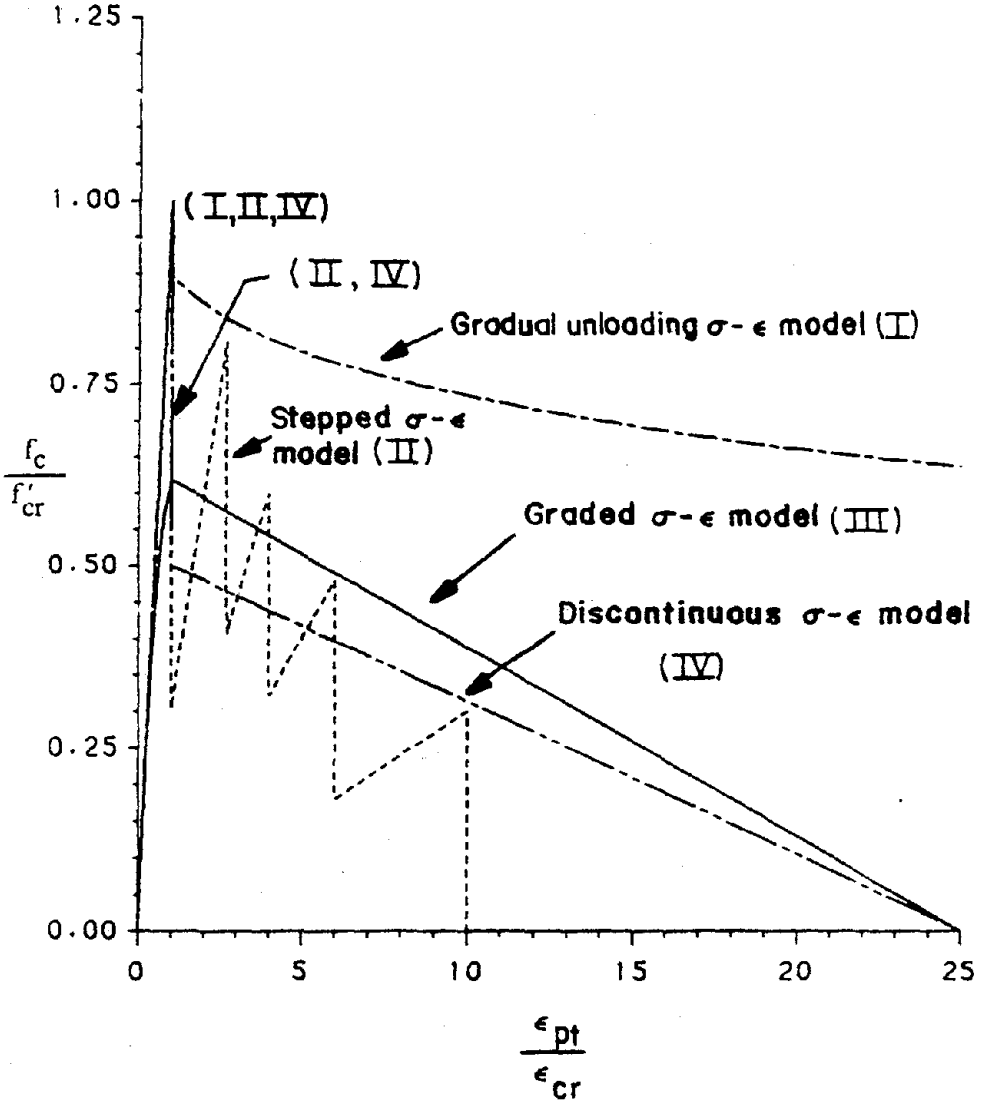

Figure 35. Concrete Principal Tensile Stress-Strain Model

Once the principal concrete stresses are determined, they are rotated by Mohr's circle for stresses to longitudinal and shear stress as shown in Figure 36. The radius of Mohr's circle for stress is

$$R = \frac{\sigma_{pt} - \sigma_{pc}}{2} = \tau_{max} \tag{3.11}$$

where τ_{max} is the maximum shear stress. The longitudinal stress, σ_x, on the wall is given by

$$\sigma_x = \frac{\sigma_{pt} + \sigma_{pc}}{2} + R\cos(2\beta) \tag{3.12}$$

Shear stress τ_x, acting on the wall's cross section, perpendicular to the longitudinal stress, is given by

$$\tau_x = R\sin(2\beta) \tag{3.13}$$

Thus the concrete longitudinal and shear stresses at point x are determined.

3. Steel Stress-Strain Model. For a longitudinal steel reinforcing bar at x, the bar's longitudinal strain, ε_x, is determined from Equation 3.2. Several different steel stress-strain models, ranging from a simple elasto-plastic model, to the more complicated, Ramberg-Osgood model, can be used to determine the stress. However, for lightly reinforced shear walls, the shape of the backbone curve is very sensitive to the shape of the steel-stress strain model. Thus if available, the actual stress-strain curve for a given steel bar is used. The experimentally measured steel stress-strain curve for the D13 steel bar used in NCKU wall SW6 is shown in Figure 37. Between data points, the longitudinal steel stress, f_{sx}, is interpolated by

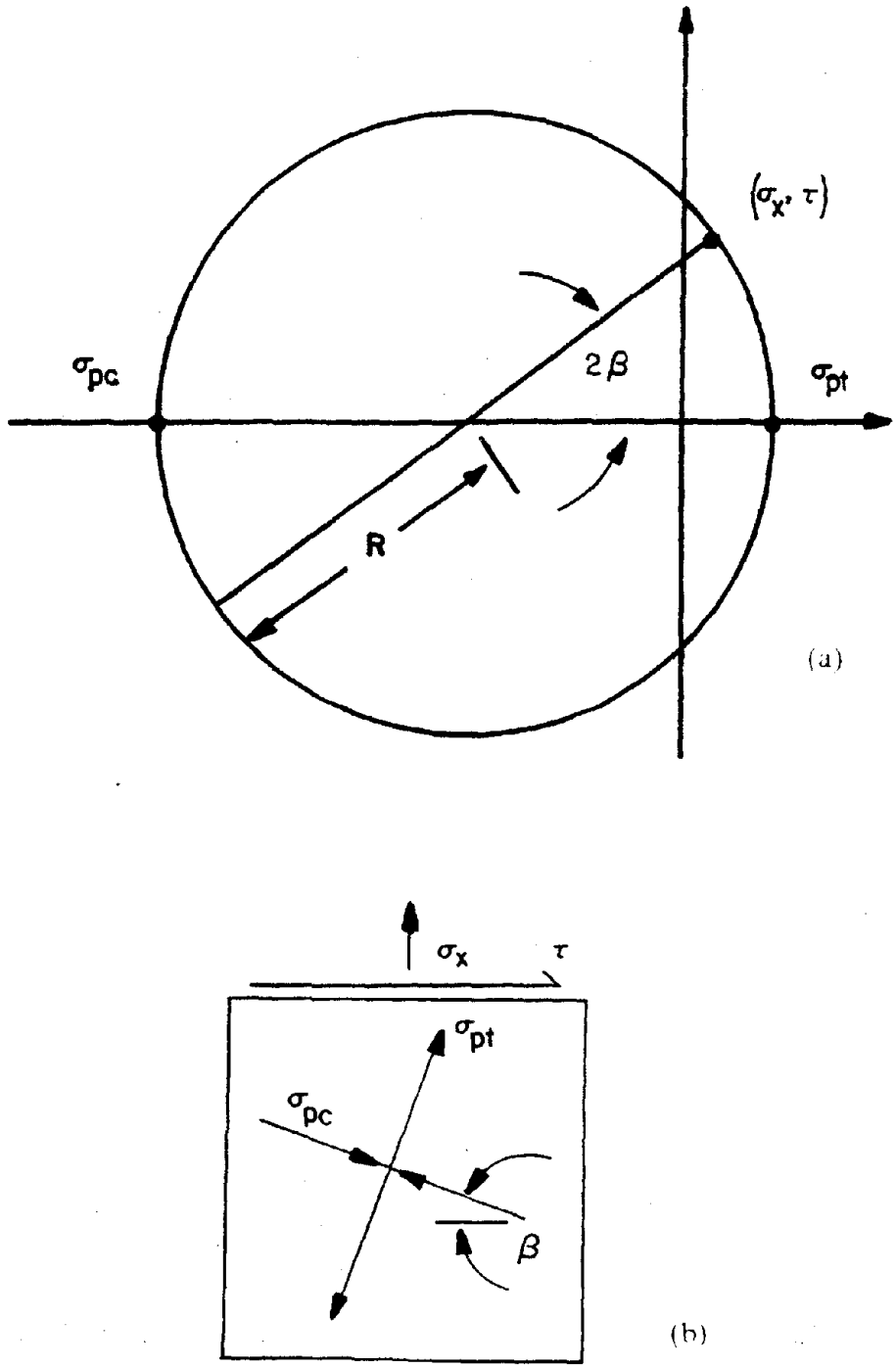

Figure 36. Mohr's Circle for Concrete Stress: (a) Mohr's Circle For Concrete Stress (b) Principal Stresses on an Element

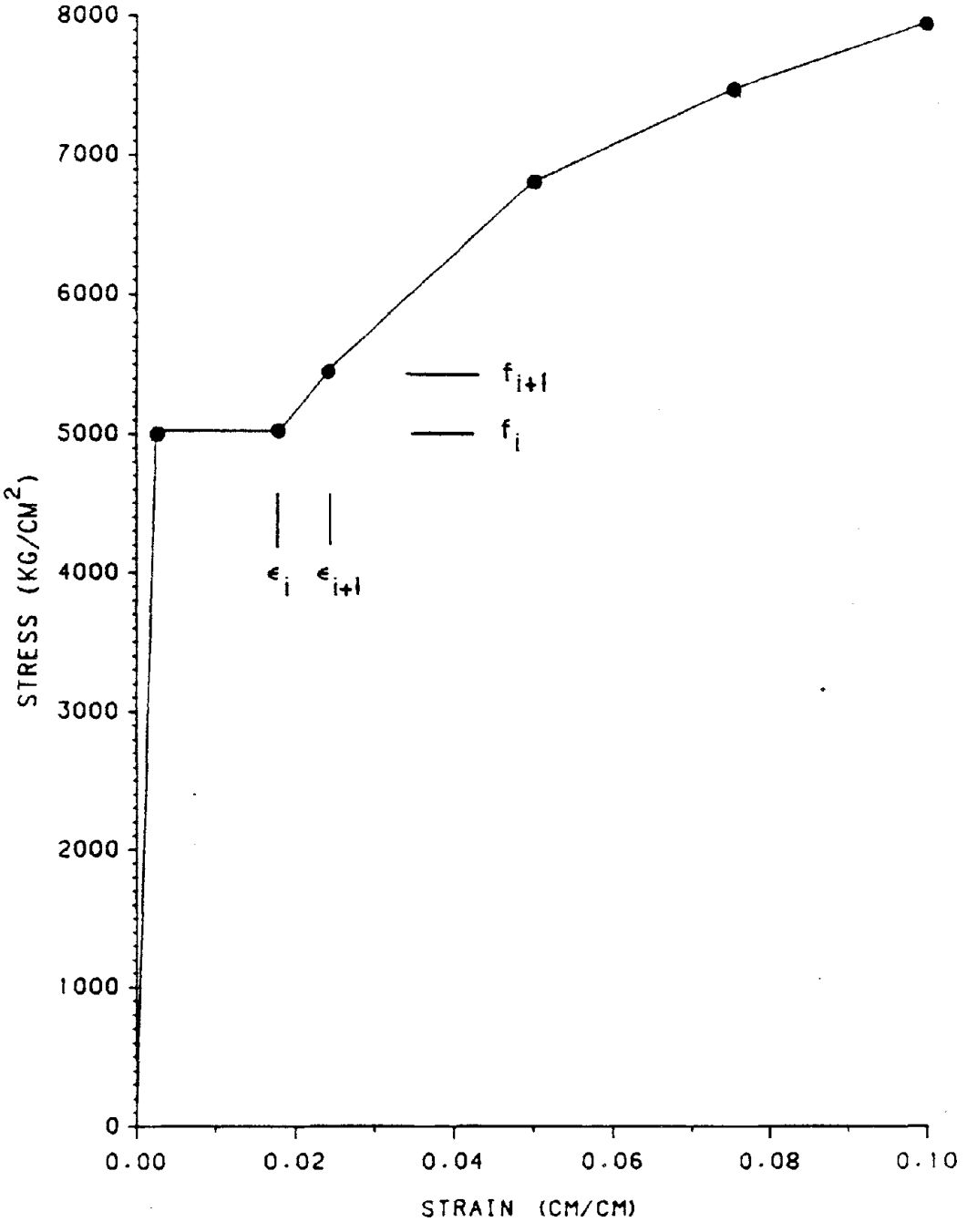

Figure 37. Incrementally Linear Steel Stress-Strain Model

$$f_{sx} = \left[f_i + (|\varepsilon_x| - \varepsilon_i)\frac{f_{i+1} - f_i}{\varepsilon_{i+1} - \varepsilon_i} \right] \mathrm{sgn}(\varepsilon_x) \tag{3.14}$$

where i is chosen such that $\varepsilon_i \le |\varepsilon_x| \le \varepsilon_{i+1}$. The term $|\varepsilon_x|$ is used to address the case when ε_x is negative and $\mathrm{sgn}(\varepsilon_x)$, yields a steel stress with the same sign as ε_x.

4. Stress Distribution on a Wall Cross Section. The strain distribution for NCKU wall SW6 is shown in Figure 38, for the case $\varepsilon_1 = .007921$ cm/cm, $\varepsilon_2 = -.001299$ cm/cm, and $\gamma = .0014$ radians. The properties for wall SW6 are given previously in Chapter II. At the extreme compression fiber, (x = 50) the principal concrete compressive strain is $\varepsilon_{pc} = -.001604$ cm/cm, the principal concrete tensile strain is $\varepsilon_{pt} = .000305$ cm/cm, and the angle of principal strain is $\beta = 66.43°$. The principal compression strain is close to the ultimate strain, $\varepsilon_o = .0020$ cm/cm. Thus this strain distribution corresponds to a point near the ultimate load. The shear softening term, for the strains at this point is $\lambda = 1.00$. The principal compressive stress is $\sigma_{pc} = 276.7$ kg/cm^2 and the principal tensile stress is $\sigma_{pt} = 11.8$ kg/cm^2. Rotating the principal strains through angle β, yields longitudinal and shear stresses of $\sigma_x = 230.6$ kg/cm^2 and $\tau_x = 105.8$ kg/cm^2, respectively.

As the coordinate x decreases, the longitudinal strain decreases, principal compressive strain decreases[3], principal tensile strain increases, the angle of principal stress decreases, and the shear softening term increases. Initially, the angle of principal

[3] Compressive strain has a negative sign. Thus the absolute value of the compressive strain is decreasing, while the numerical value of the strain is increasing.

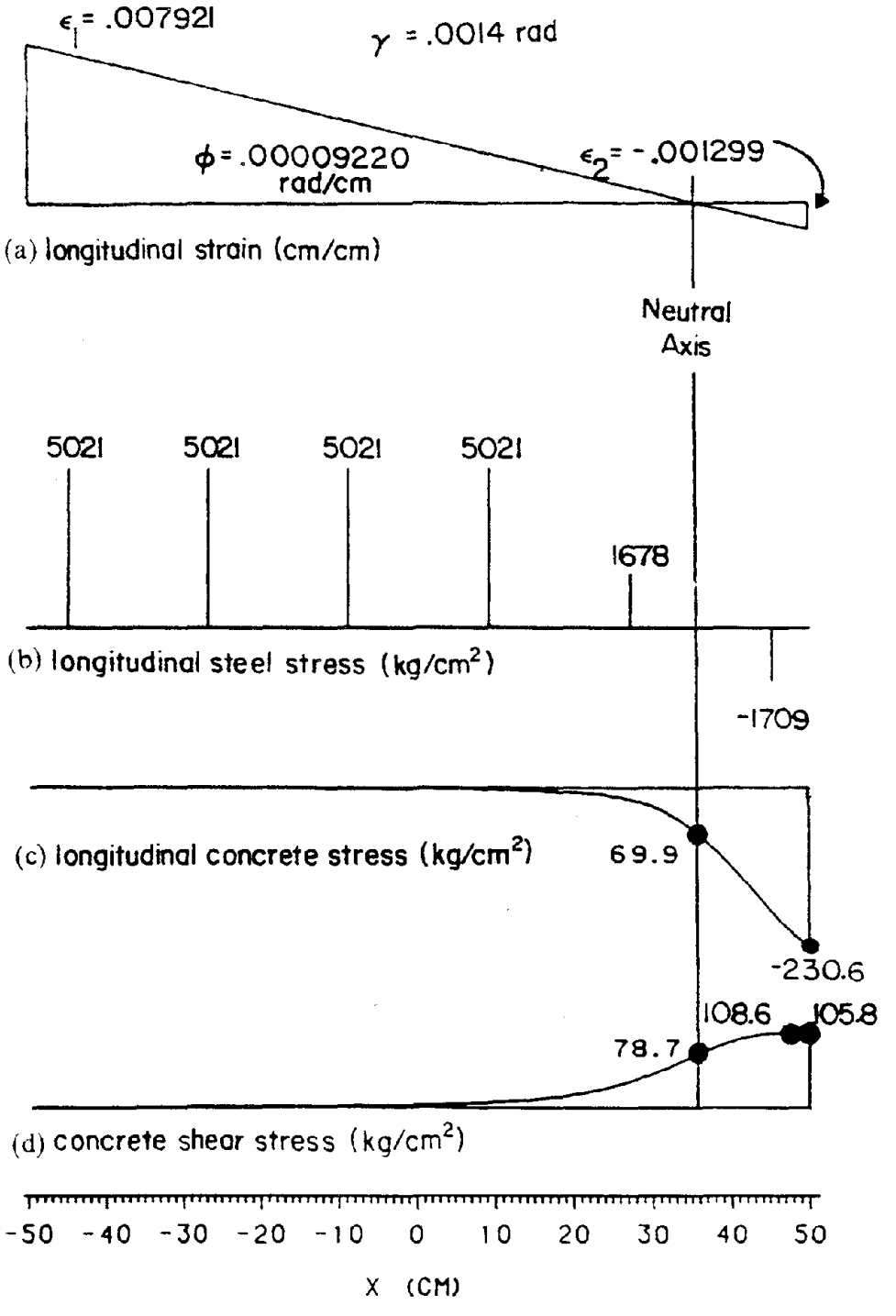

Figure 38. Stress Distribution on NCKU Wall SW6 Cross Section: (a) Longitudinal Strain Distribution, (b) Longitudinal Steel Stress, (c) Longitudinal Concrete Stress, (d) Concrete Shear Stress

stress decreases[4] faster than the principal compressive stress decreases[5], resulting in an increasing shear stress. At x = 48 cm, the shear stress has reached a maximum of $\tau_x = 108.6$ kg/cm^2. To the left of this point, the principal stress decreases faster than the angle of principal stress decreases, resulting in a decreasing shear stress.

Pure shear strain exists at the neutral axis, x = 35.915 cm. The principal strains at this point are $\varepsilon_{pc} = -.00070$, $\varepsilon_{pt} = .00070$, and the angle of principal strain is $\beta = 45°$. The shear softening term, at the neutral axis, is $\lambda = 1.503$. The principal stresses at this point are $\sigma_{pc} = 148.6$ kg/cm^2 and $\sigma_{pt} = 8.86$ kg/cm^2. Rotating the principal strains through angle β yields longitudinal and shear stresses of $\sigma_x = 69.9$ kg/cm^2 and $\tau_x = 78.7$ kg/cm^2, respectively. To the left of the neutral axis, the longitudinal strains are tensile. However, the longitudinal stresses are in compression. This is because the shear strain influences both the principal strains, and the orientation of the principal strains. Given the same longitudinal strain distribution, for lower values of shear strain, the longitudinal stress in this region would be zero, or in tension.

5. Equilibrium of Forces. For a given longitudinal strain distribution and shear strain, the forces acting on the concrete are determined by integrating the stresses across the wall's cross section. Similarly, the forces on the steel bars are determined by summing all of the individual bar forces. Thus the axial load, P, in the wall, due to the assumed strain distribution is

---

4 At constant principal stresses, as the angle of principal stress decreases from $\beta = 66.43°$ to $\beta = 45°$, the shear stress, τ_x, increases.

5 At a constant angle of principal stress, as the principal compressive stress decreases, the shear stress, τ_x, decreases.

$$P = \int_A \sigma_x \, dA + \sum_{\text{steel bars}} (f_{sx} - \sigma_x) A_s \tag{3.15}$$

Likewise the moment, M, and shear, V, acting on the wall, due to the assumed strain distribution are given by

$$M = \int_A \sigma_x \, x \, dA + \sum_{\text{steel bars}} (f_{sx} - \sigma_x) \, x \, A_s \tag{3.16}$$

$$V = \int_A \tau_x \, dA_{shear} \tag{3.17}$$

where $\int_A dA$ is the cross sectional area of the wall, including steel bars and boundary elements if applicable. For a rectangular wall, $\int_A dA$ = thickness $\int_{x_1}^{x_2} dx$. The shear area, $\int_A dA_{shear}$, includes the web, the area of square boundary columns, and a portion of the area of flanged boundary elements. A_s is the area of the steel bars at coordinate x. For the stress distribution in Figure 38, Equations 3.15 through 3.17 yield a moment of M = 1539 Ton cm, a shear of V = 23.38 Ton, and the sum of axial force is P = -0.02 kg.

Many models, including the ACI strength equations, calculate a separate shear resistance due to both concrete and steel. The proposed analytical model includes the effects of steel reinforcing bars in an indirect manner. When the concrete is subject to shear, it expands. If this expansion is restrained, the strength and stiffness of the concrete increases. As concrete expands, its reinforcing steel goes into tension, and provides a clamping force that resists expansion. For lightly reinforced shear walls, as the amount of reinforcing steel is increased, the clamping force increases, and both shear strength and stiffness also increase. Thus the reinforcing steel has a very large

influence on the shear strength of a shear wall, that is not obvious when inspecting Equation 3.17.

Low-rise shear walls are restrained against expanding horizontally by the horizontal elements at the top and bottom of the wall, and by the horizontal reinforcing steel. Thus the low-rise shear wall expands along its longitudinal axis, and the longitudinal bars provide the clamping force that resists shear. As the height to width ratio of the wall increases, the restraint against horizontal expansion due to the horizontal boundary elements decreases. Examine a typical beam, with a height to width[6] ratio of 20. For this beam, the boundary provides negligible restraint against horizontal expansion. Thus the beam expands across it's width, and the horizontal steel, (stirrups) goes into tension and provides the clamping force that restrains the concrete, increasing the shear strength and stiffness. Since horizontal expansion is not included in the proposed analytical model, the use of the model for members with a large height to width ratio and a significant amount of shear is discouraged.

The intergration of concrete stress in Equations 3.15 to 3.17 is divided into two parts, one on each side of the wall's neutral axis. Each of the two parts is then integrated numerically with Romberg integration[7].

---

6 Shear walls are typically vertical elements, and the height to width ratio is used to gauge its slenderness. A beam is typically a horizontal element, thus the span to depth ratio is used to gauge its slenderness. Both the height to width and span to depth ratios are identical. For this discussion, assume the beam is oriented vertically. Thus horizontal expansion of the beam is expansion in the direction of the beam's depth.

7 Romberg integration (11) is a numerical technique that 1) uses the trapezoidal rule to solve an integral with 1, 2, 4, 8, ... 2^n segments, and 2) uses the Richardson extrapolation process to improve each of the solutions. Convergence is determined by comparing the difference between successive solutions. An efficient algorithm reuses the results of the 2^{n-1} segment integral when evaluating the 2^n segment

Once the wall's forces have been calculated for a given strain distribution, the axial force, P (Equation 3.15), is compared to the applied axial load, $P_{applied}$[8]. If these two forces are equal, then the assumed strain distribution is accepted. If these forces differ, by a significant amount, then the strain distribution is modified, and the wall forces are recalculated. This iterative process is repeated untill $P \cong P_{applied}$.

Numerically, the strain distribution is modified by varying the tensile strain ε_1. For the first iteration, if $P > P_{applied}$, then ε_1 is decreased by the larger of $0.10\varepsilon_1$ or 0.0001. Likewise, if $P < P_{applied}$, then ε_1 is increased by the larger of $0.10\varepsilon_1$ or 0.0001. Denote the initial value of ε_1 as ε_i, and its accompanying axial force P_i. This new strain, ε_1, for the second iteration is denoted ε_j. The wall forces for the new strain ε_j are calculated, and the new axial load is denoted P_j. If the new axial force $P_j \neq P_{applied}$, another estimate of ε_1 is made

$$\varepsilon_1 = \varepsilon_i + (P_{applied} - P_i)\frac{\varepsilon_j - \varepsilon_i}{P_j - P_i} \tag{3.18}$$

The wall forces are recalculated with the new value of ε_1. If $P \cong P_{applied}$, then the strain distribution is accepted. Otherwise, set the strain and axial loads for the last two iterations equal to ε_i, P_i and ε_j, P_j. Then another estimate of ε_1 is made by Equation 3.18. This process is repeated untill $P \cong P_{applied}$.

The moment and shear on a wall is calculated at a given shear strain, γ, for various values of compressive strain, ε_2, ranging from 0 to about $2\varepsilon_o$. Each time the compressive strain, ε_2, is increased, the previous solution's tensile strain, ε_1, is used as

---

integral. This minimizes the number of times the concrete stresses, σ_x and τ_x, in Equations 3.15 to 3.17 are evaluated.

8 For most low-rise shear walls, the applied axial load in negligible. Thus for all of the walls analyzed in this chapter, $P_{applied} = 0$.

an initial estimate of the current tensile strain. As the compressive strain is increased for successive solutions, the moment in the wall increases for each solution. At some compressive strain, the moment will begin to decrease, due to crushing of the concrete. This denotes failure, and no further solutions are carried out at this shear strain. The shear strain is increased, the compressive strain is reset to zero, and another set of solutions is obtained. Values of the shear strain range from 0 to about $2\varepsilon_o$.

Recall the curvature, ϕ, is the slope of the longitudinal strain distribution as given in Equation 3.1. Thus the set of solutions for various longitudinal strain distributions and shear strains, γ, constitute the moment - shear - curvature and the moment - shear - shear strain interaction surfaces.

The moment - shear - curvature interaction surface for NCKU wall SW6 is shown in Figure 39. Examining Figure 39, point A (V = 0, M = 1723 Ton cm, ϕ = .000262 rad/cm) corresponds to the failure curvature for pure bending, point B (V = 24 Ton, M = 1560 Ton cm, ϕ = .000124 rad/cm) corresponds to the failure curvature, where the moment to shear ratio is $\frac{M}{V} = 65$ cm, and point C (V = 52.4 Ton, M = 0, ϕ = 0) corresponds to the failure curvature for pure shear. For low values of shear, the moment - curvature relationship is very ductile. As shear increases, the moment - curvature relationship becomes more brittle, failing at 1) lower values of curvature, and 2) lower values of moment. For low values of constant moment, at low values of shear, the curvature is independent of shear. At a larger value of moment, held constant, the curvature will increase with increasing shear. Thus the curvature is strongly influenced by both moment and shear.

The moment - shear - shear strain interaction surface for NCKU wall SW6 is shown in Figure 40. Point A (V = 0, M = 1723 Ton cm, γ = 0) corresponds to the shear strain at failure for pure bending, point B (V = 24 Ton, M = 1560 Ton cm, γ = .001803 rad) corresponds to the shear strain at failure for a moment to shear ratio of

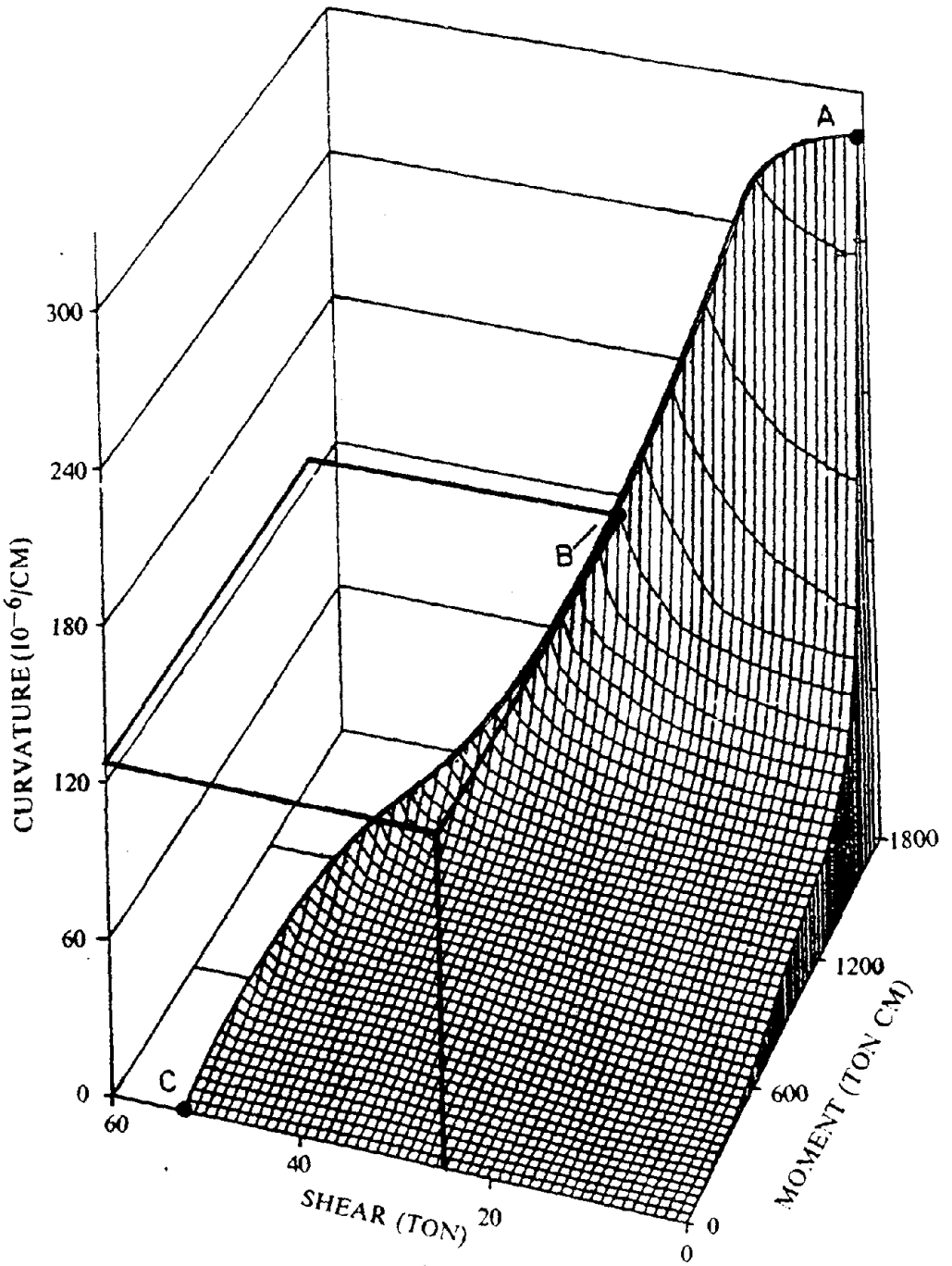

Figure 39. Moment-Shear-Curvature Interaction Surface for NCKU Wall SW6

$\frac{M}{V} = 65$ cm, and point C (V = 52.4 Ton, M = 0, $\gamma = .005000$ rad) corresponds to the shear strain at failure for pure shear. For low values of moment, the shear - shear strain relationship is very ductile. As moment increases, the shear - shear strain relationship becomes more brittle, failing at 1) lower values of shear strain, and 2) lower values of shear. For low values of constant shear, at low values of moment, the shear strain is independent of the moment. At larger values of shear, held constant, the shear strain will increase with increasing moment. Thus the shear strain is strongly influenced by both moment and shear.

6. Yield and Failure Interaction for Shear and Bending. Both the ultimate load surface and the yield surface of the moment to shear interaction surfaces are of interest and are shown in Figure 41. For NCKU wall SW6, point A (M = 1723 Ton cm, V = 0) represents the ultimate load for pure bending, point B (M = 1560 Ton cm, V = 24 Ton) represents the ultimate load for a wall with a moment to shear ratio of 65 cm, and point C (M = 0, V = 52.4 Ton) represents the ultimate load for pure shear. If the ultimate moment, at zero shear, is denoted by M_{uo} and the ultimate shear, at zero moment, is denoted by V_{uo}, then this failure surface can be described by

$$\left(\frac{V}{V_{uo}}\right)^2 + \left(\frac{M}{M_{uo}}\right)^2 = 1.0 \qquad (3.19)$$

This equation is within 3% of the calculated ultimate load for NCKU wall SW6.

The yield point of a wall is the load where the first steel bar yields. Point D (M = 1195 Ton cm, V = 0) in Figure 41 represents the yield point for pure bending, point E (M = 1112 Ton cm, V = 17.1 Ton) represents the yield point for a wall with a moment to shear ratio of 65 cm and point F (M = 0, V = 51.9 Ton) represents the yield point for pure shear. If the yield moment, at zero shear, is denoted by M_{yo} and the

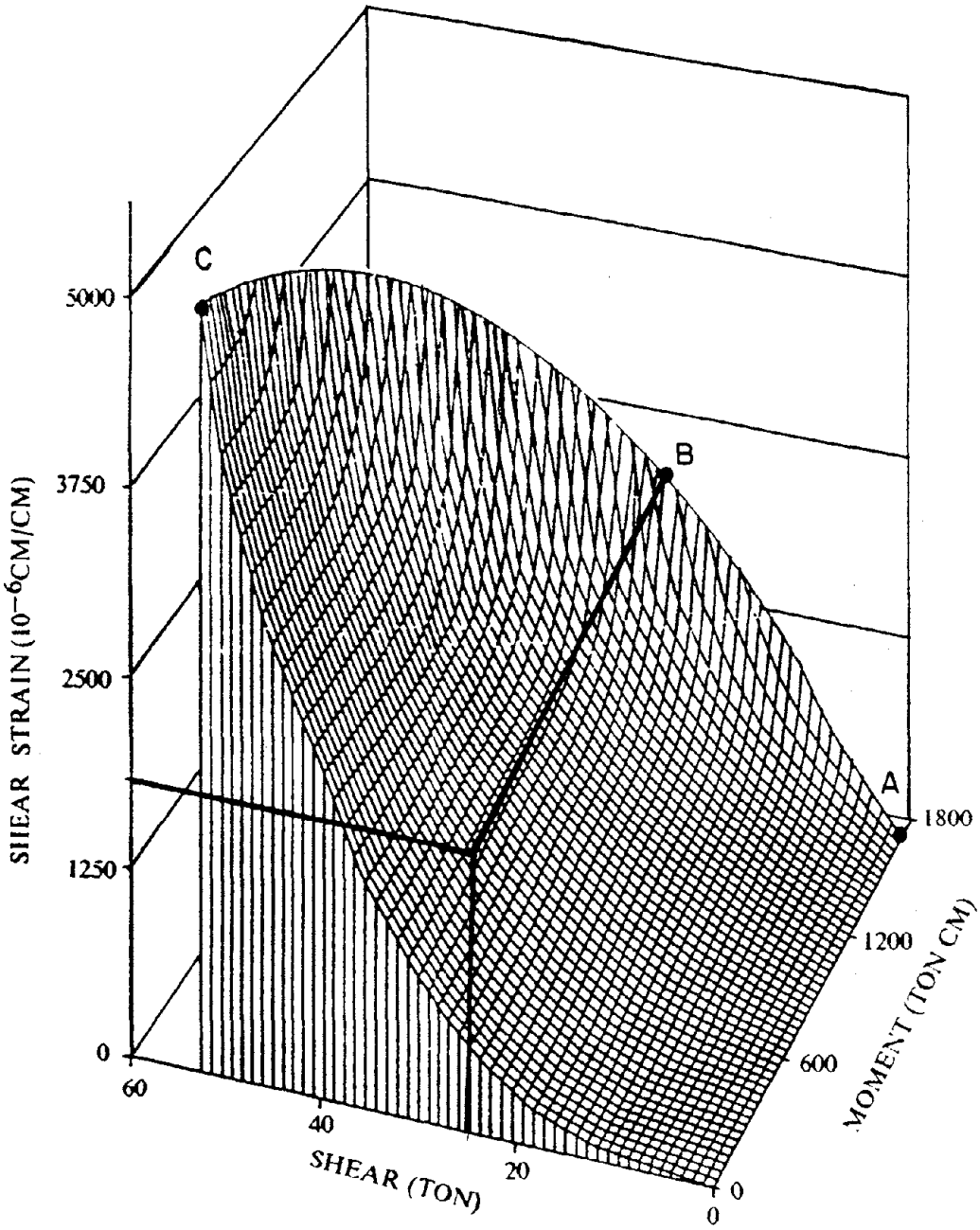

Figure 40. Moment-Shear-Shear Strain Interaction Surface for NCKU Wall SW6

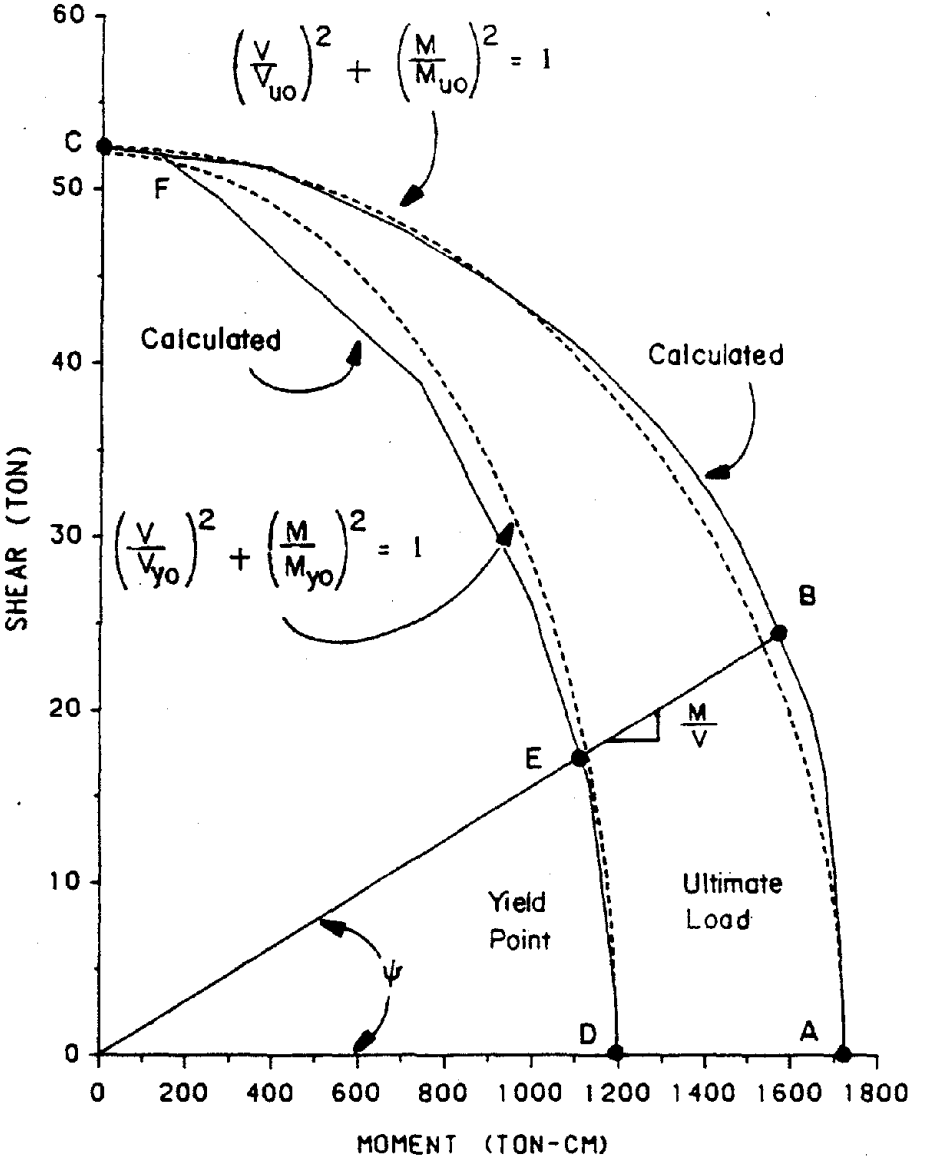

Figure 41. Moment-Shear Yield and Failure Surfaces for NCKU Wall SW6

yield shear, at zero moment, is denoted by V_{yo}, then this yield surface can be described by

$$\left(\frac{V}{V_{yo}}\right)^2 + \left(\frac{M}{M_{yo}}\right)^2 = 1.0 \tag{3.20}$$

This equation is within 9% of the calculated yield point for NCKU wall SW6.

7. Shear Bending Influence Angle, ψ. There are several ways to quantify the significance of bending and shear deformations in a given wall. One is to examine the ratio of bending deformation to total deformation, as discussed in Chapter II. This method has the advantage of being very simple. Unfortunately, as shown in Figures 15 and 16, the percentage of bending deformation often varies with the load level.

Another method to quantify the significance of bending and shear deformations in a given wall is to locate a normalized moment to shear ratio on a normalized interaction diagram. This is represented by the angle ψ in Figure 41. Let

$$\psi = \text{atan}\left[\left(\frac{V}{M}\right)\left(\frac{M_{uo}}{V_{uo}}\right)\right] \tag{3.21}$$

Point A in Figure 41 has a shear bending influence angle $\psi = 0$, which represents pure bending. For point C, $\psi = 90°$, which represents pure shear. Point B has a shear bending influence angle of

$$\psi = \text{atan}\left(\frac{1}{65\text{ cm}}\frac{1723\text{ Ton cm}}{52.4\text{ Ton}}\right) = 26.8° \tag{3.22}$$

which indicates that bending has a stronger influence than shear.

8. Base Rotation Model. At the base of the shear wall, the steel reinforcing bars have a very high tensile stress. As these bars transfer their stresses to the boundary element[9], they slip or pull out of the boundary element, with a deformation of δ_i. This deformation allows the wall to rotate as a rigid body about it's base, causing additional lateral deformation at the top of the wall.

This mechanism for deformation may be understood by examining Figure 42. For a given point on the moment - shear interaction surface, the strain distribution and force in each bar is known. Thus steel bar i, has an axial load of T_0 or an axial stress of σ_o, and an axial strain of ε_o at the base of the wall.

The actual bond stress distribution between the steel bar and the concrete in the boundary element is a function of the stress in the bar, the strain in the bar, the concrete strength, and the degree to which the concrete around the steel bar is confined. However, a simple, constant bond stress distribution between the bar and concrete may be assumed (80), because the deformation due to bond slip is a small portion of the total deformation. Thus the constant bond stress, U, is

$$U = 9.5\sqrt{\frac{f'_c}{d}} \leq 800 \text{ psi} \qquad (3.23)$$

where d is the diameter of the steel bar, in inches, and f'_c is in psi.

Summing the forces on a section of the bar that has a length z,

$$\sum F_Z = 0, \qquad T_0 = T_Z + Uz\pi d \qquad (3.24)$$

The stress in the steel bar as a function of length is determined by dividing Equation 3.24 by the area of the steel bar,

---

9 Typical boundary elements at the base of the wall are pile caps, mats, and footings.

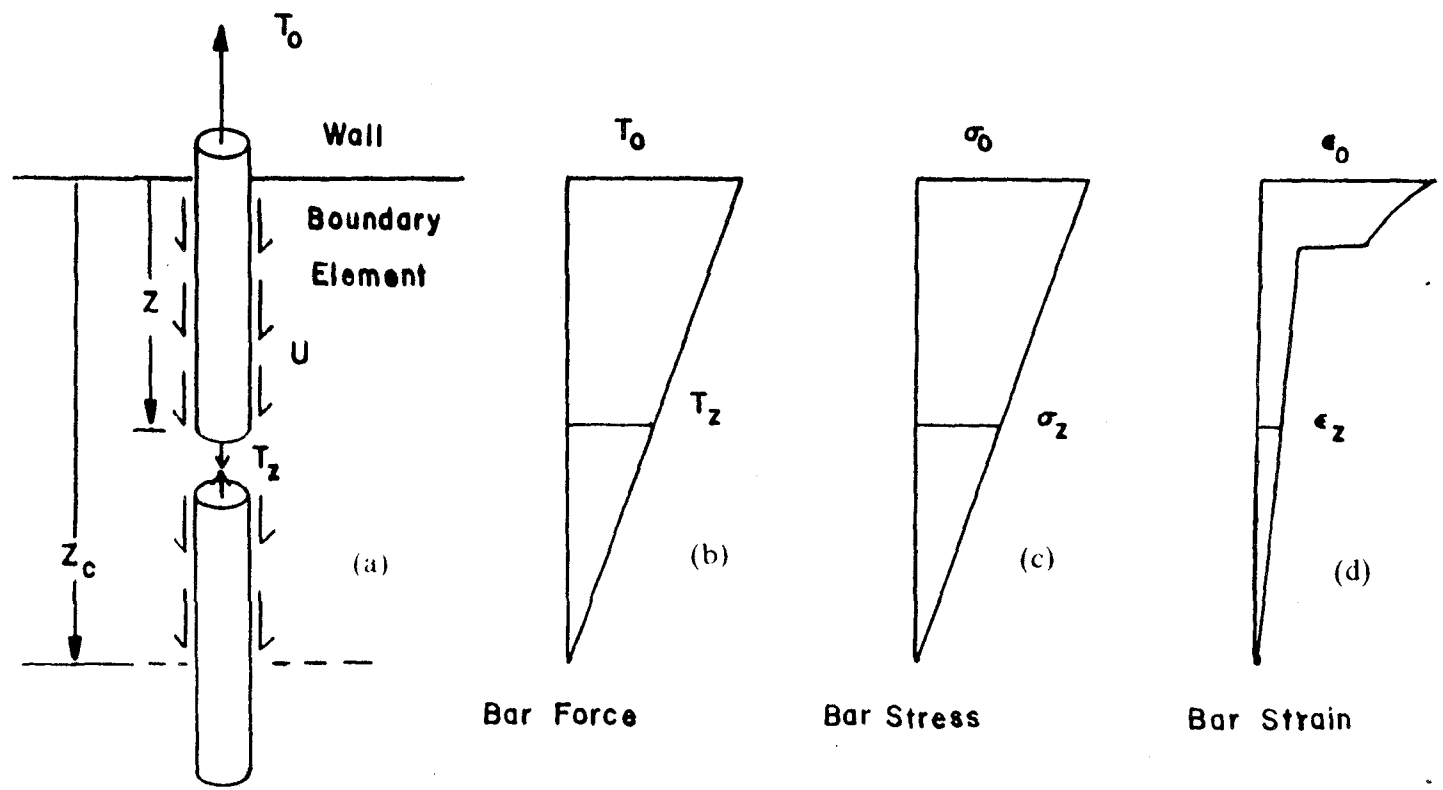

Figure 42. Bond Slip at the Base of a Shear Wall: (a) Bar Embedded in Base of a Shear Wall, (b) Bar Force, (c) Bar Stress, (d) Bar Strain

$$\sigma_z = \sigma_0 - \frac{4Uz}{d} \tag{3.25}$$

At the end of the development length, z_c, the stress in the bar, σ_z, is zero. Solving Equation 3.24 and 3.25 for the development length yields

$$z_c = \frac{T_0}{U\pi d} = \frac{\sigma_0 d}{4U} \tag{3.26}$$

Since the stress-strain curve for the steel bar is known, the steel bar's strain distribution is determined. A typical bar force distribution, bar stress distribution and bar strain distribution is shown in Figure 42. The strain distribution is integrated along the development length, to determine the pull out, δ_i, of bar i,

$$\delta_i = \int_0^{z_c} \varepsilon_z \, dz \tag{3.27}$$

where ε_z is the variation of strain along the bar's axis. The strain distribution, ε_z, consist of discrete values. Thus the integral in Equation 3.27 is evaluated numerically.

The rotation of the base of the wall due to bar i, shown in Figure 43, is given by

$$\theta_i = \frac{\delta_i}{x_{NA} - x_i} \tag{3.28}$$

where x_{NA} is the coordinate of the neutral axis. Similarly, the rotation for bars i + 1 through n are calculated. The base rotation for bars i and i + 1 may not be compatible, $\theta_i \neq \theta_{i+1}$, because the bond stress distribution has been over simplified. A rational method to resolve this incompatibilty, yet retain the simplicity of this approach, is to use a weighted average of the bond slip for each bar. Thus the base rotation of the entire wall, θ_{br}, is given by

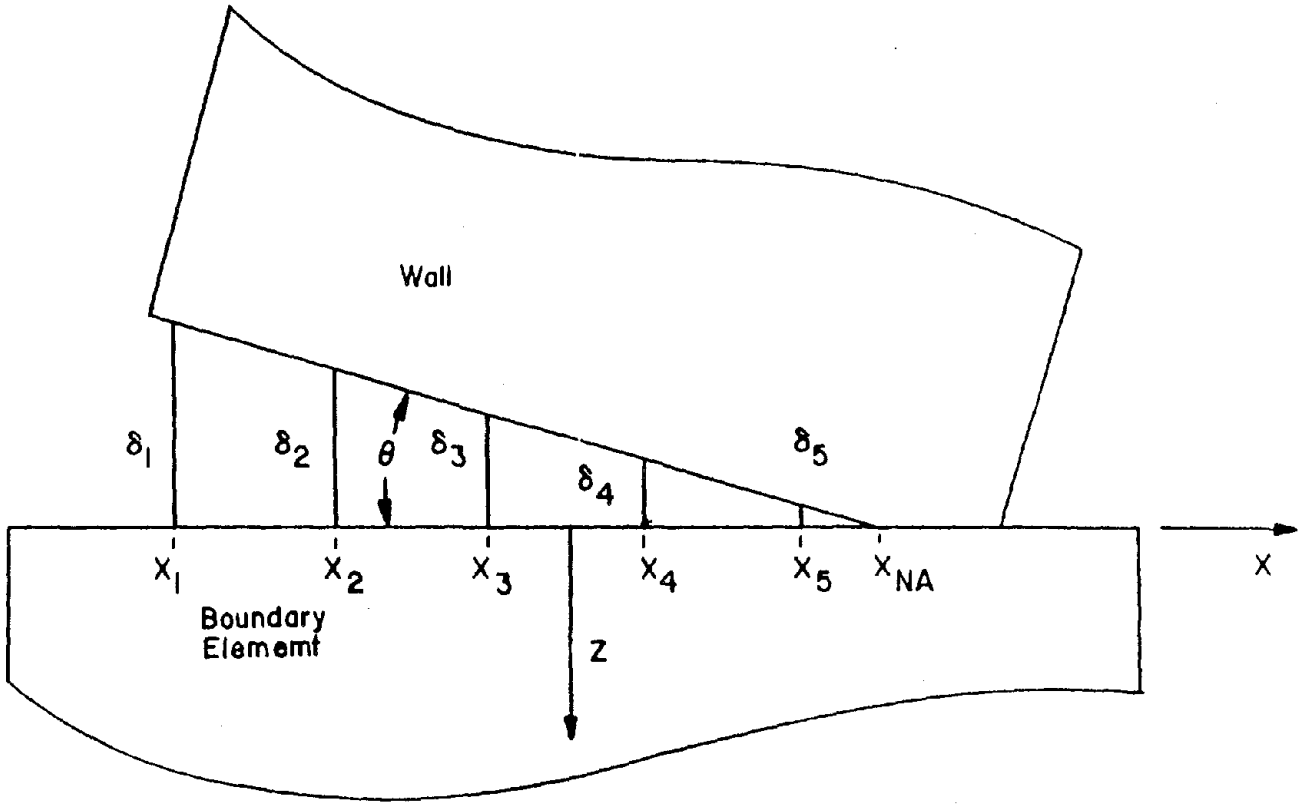

Figure 43. Base Rotation of a Shear Wall

$$\theta_{br} = \frac{\sum T_i \theta_i}{\sum T_i} \tag{3.29}$$

Recall the stress distribution example for NCKU wall SW6, Figure 38. Five bars are on the tensile side of the neutral axis. The force, bond slip and rotation angle for each bar is

Bar	$x_{na} - x_i$	T_o	δ_i	θ_i	$T_o\theta_i$
1	80.92	6477	.03506	.000433	2.806
2	62.92	6477	.03498	.000556	3.601
3	44.92	6477	.03489	.000777	5.031
4	26.92	6477	.03487	.001295	8.392
5	8.92	2164	.00389	.000436	0.944
Σ		28,072			20.78

where the units are kg, cm and each bar has a diameter of 1.27 cm and an area of 1.29 cm^2. The base rotation angle, θ_i, varies from 0.000436 rad to 0.001295 rad for two adjacent bars. The weighted average base rotation is $\theta = \frac{20.78}{28,072} = 0.00074$ rad.

Calculating the base rotation of the wall for each point on the moment - shear interaction surface, determines the moment - shear - base rotation interaction surface. This interaction surface is shown in Figure 44 for NCKU wall SW6. Point A (V = 0, M = 1723 Ton cm, θ_{br} = .001356 rad) corresponds to the base rotation at failure for pure bending, point B (V = 24 Ton, M = 1560 Ton cm, θ_{br} = .000775 rad) corresponds to the base rotation at failure for a moment to shear ratio of $\frac{M}{V} = 65$ cm, and point C (V = 52.4 Ton, M = 0, $\theta_{br} = 0$) corresponds to the base rotation at failure for pure shear. At low values of shear, the moment - base rotation relationship has a ductile behavior. As the shear increases, both the failure rotation and failure moment decrease.

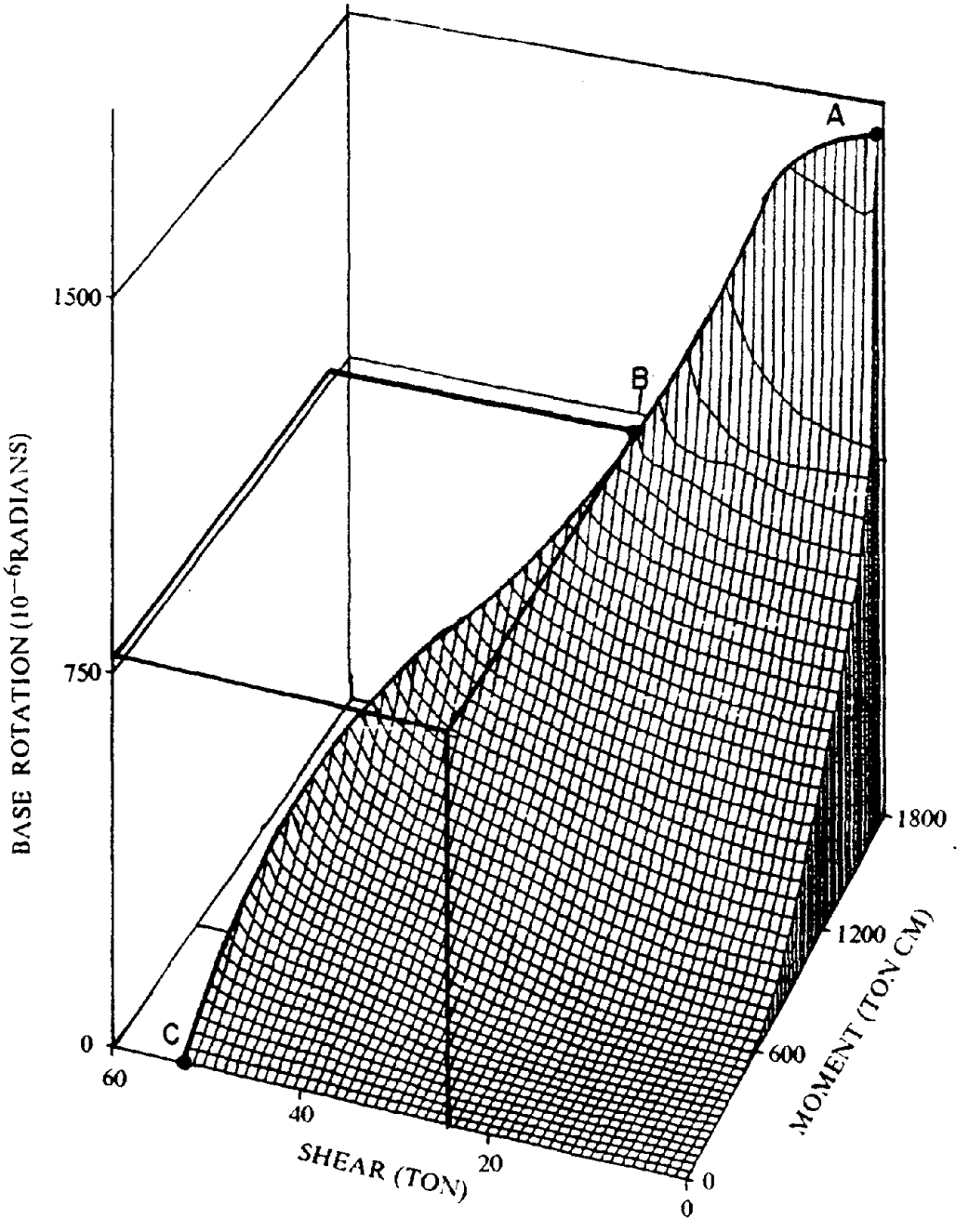

Figure 44. Moment-Shear-Base Rotation Interaction Surface for NCKU Wall SW6

B. SHEAR AND BENDING BACKBONE CURVES

Isolated shear walls subject to either static or dynamic loading have a constant moment to shear ratio. The shear walls in low-rise buildings, subject to dynamic loading, also have a fairly constant moment to shear ratio. For a fixed moment to shear ratio, the interaction curves can be decoupled, yielding separate moment - curvature, shear - shear strain and moment - base rotation relationships.

The deformation due to base rotation, and the bending deformation could not be separated during the analysis of the experimental data, Chapter II. Therefore the calculated base rotation and bending deformations will be combined 1) to be consistent with the experimental deformations, and 2) to reduce the number of hysteresis models used for cyclic loadings. The deformation of a low-rise shear wall due to base rotation, δ_{br}, is given by

$$\delta_{br} = \theta_{br}\, h \tag{3.30}$$

where h is the height of the wall.

For low-rise shear walls, the entire wall is in the hinging region. Thus the equivalent moment on the wall is constant. Likewise the curvature distribution is constant as shown in Figure 10. Treating the curvature distribution as a conjugate beam, the bending deformation of a low-rise shear wall is given by

$$\delta_{\phi} = \frac{\phi h^2}{2} \tag{3.31}$$

The combined bending and base rotation deformation is given by

$$\delta_b = (\frac{\theta_{br}}{h} + \frac{\phi}{2})h^2 = \theta_u\, h^2 \tag{3.32}$$

which hereafter is referred to as the bending deformation. The bending rotation of a unit length wall is θ_u, and θ_u h is the bending rotation of the wall. The relationship between bending moment and the bending rotation is known as the bending backbone curve.

For an isolated, low-rise shear wall, the shear in the wall, V, is equal to the applied load. Given the shear and the moment to shear ratio, then the shear strain, γ, is determined from the moment - shear - shear strain interaction surface. The relationship between the shear, V, and shear strain, γ, at a constant moment to shear ratio is the shear backbone curve. For low-rise shear walls, with a constant moment to shear ratio, the shear strain is constant over the height of the wall. Thus the shear deformation δ_s, is given by

$$\delta_s = \gamma \, h \tag{3.33}$$

For NCKU wall SW6 at point B on the interaction surfaces, Figures 39, 40, and Figures 44, the deformations are

$$\delta_{br} = 0.000775 \times 43.75 = 0.0339 \text{ cm} \tag{3.34}$$

$$\delta_\phi = \frac{0.000124}{2} \times (43.75)^2 = 0.1186 \text{ cm} \tag{3.35}$$

$$\delta_s = 0.001803 \times 43.75 = 0.0789 \text{ cm} \tag{3.36}$$

Thus the bending deformation is $\delta_b = \delta_\phi + \delta_{br} = 0.1526$ cm, and the total deformation is $\delta_t = \delta_b + \delta_s = 0.2315$ cm. For this load level, base rotation accounts for 14.6% of the total deformation, deformation due to curvature accounts for 51.3% of the total deformation, and shear accounts for 34.1% of the total deformation. Bending ($\delta_\phi + \delta_{br}$) accounts for 65.9% of the total deformation.

Experience in comparing calculated backbone curves with experimental backbone curves has demonstrated that the proposed analytical method underestimates the failure displacement. This is partially due to the unloading region of the concrete stress-strain model. The Vecchio-Collins stress-strain model has a rather steep unloading branch as shown in Figure 34, which underestimates the strength of concrete at the high strains that are associated with larger deformations. Thus the overconservative stress-strain model forces the analytical method to predict failure at lower values of strain, and the failure deformation is underestimated.

In Chapter II an average failure ductility of $\mu = 10$ is observed for the NCKU walls. This experimentally observed failure ductility is used to modify the calculated backbone curve. Thus

$$\left.\begin{aligned} \delta_b\big|_{fail} &= 10\delta_b\big|_{yield} \\ \delta_s\big|_{fail} &= 10\delta_s\big|_{yield} \end{aligned}\right\} \qquad (3.37)$$

The calculated moments and shears at failure are used with $\delta_b|_{fail}$ and $\delta_s|_{fail}$ to define the end point on the backbone curve. Recall that the average ductility of 10 is based on a lightly reinforced isolated wall with a height to width ratio of 0.50, and a moment to shear ratio of 65 cm. Caution must be used when extrapolating this failure ductility to other walls.

The modified bending and shear backbone curves for NCKU wall SW6, at five different moment to shear ratios, are shown in Figures 45 and 46. As the moment to shear ratio increases, 1) both the bending yield point and the ultimate bending load increase, 2) the bending rotation at failure increases, 3) the bending stiffness increases, 4) both the shear yield point and the ultimate shear decrease, 5) the shear strain at failure decreases, and 6) the shear stiffness decreases. For the pure shear case,

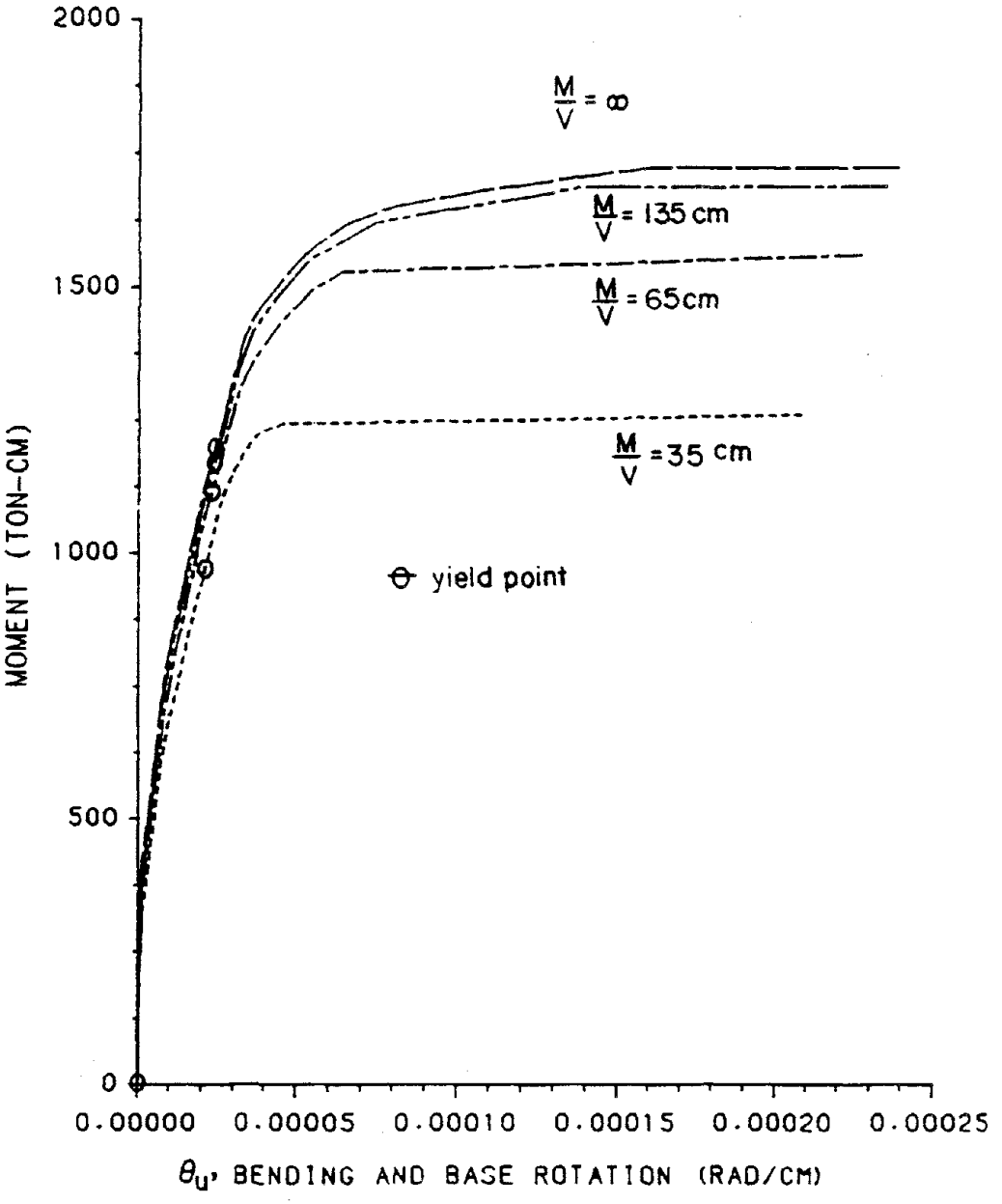

Figure 45. Moment-Curvature Relationship at Various Moment to Shear Ratios for NCKU Wall SW6

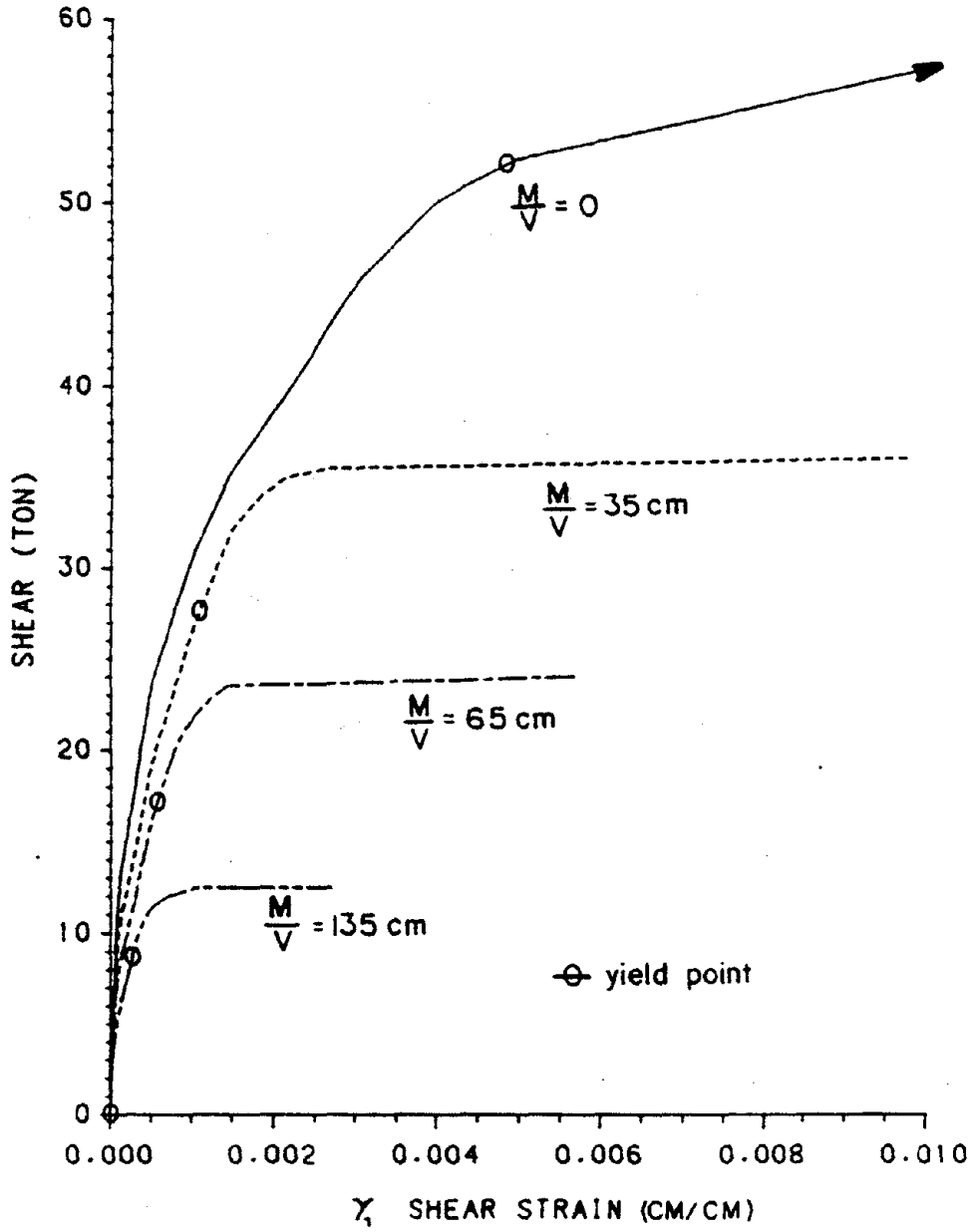

Figure 46. Shear-Shear Strain Relationship at Various Moment to Shear Ratios for NCKU Wall SW6

$\frac{M}{V} = 0$, the shear backbone curve yields at a shear strain of $\delta_{sy} = 0.004834$ rad. This is a relatively large shear strain, and it is doubtful that a failure strain of $10\delta_{sy}$ could be achieved.

C. COMPARISON OF CALCULATED AND EXPERIMENTAL STATIC MONOTONIC LOAD-DEFORMATION RESPONSE OF ISOLATED SHEAR WALLS

To evaluate the accuracy of the proposed analytical method, the calculated monotonic load deformation response of 27 R/C shear walls is compared with the experimental response. Fifteen of these walls were tested at NCKU (72). These walls are presented in Chapter II, Table I. The remaining twelve walls were tested by PCA (57, 59, 7). These walls are introduced below.

Height to width ratios for the 27 walls range from 0.50 to 2.40. Four wall cross sections are investigated: 1) rectangular walls with nearly uniform reinforcement, 2) rectangular walls with extra reinforcing steel at the edge of the wall, 3) barbell cross sections (walls with square boundary columns), and 4) walls with flanges. Web reinforcement ratios varied from 0.28% to 0.78% vertically and from 0 to 1.14% horizontally. Flange reinforcement, when used, varies from 1.47% to 6.4%. Concrete strengths range from 2760 psi to 7780 psi, and the yield point of the reinforcing steel ranges from 68 ksi to 80 ksi.

Many of the walls are subjected to cyclic loading histories. These walls are identified in Table I and in the table given later in this section. An envelope of the cyclic loadings is used for the monotonic response to make the comparisons below.

1. Static Monotonic Bending Deformation. The bending deformation is calculated by Equation 3.32 for NCKU walls SW1a, SW3 and SW4, and compared with the experimental deformations in Figure 47. Similarly, calculated bending deformation for NCKU walls SW4a, SW5 and SW6 are compared with the experimental deformations in Figure 48. The vertical axis in Figures 47 and 48 is the applied load. The displacements from 0 to 3 mm are shown. Experimentally observed failure displacements range from 2.65 mm to 5.71 mm.

The loads are applied at a point 65 cm above the base of the walls as shown in Figure 1. The equivalent moment at the base of the wall is $M = 65V$, where V is both the applied load and shear in the wall. The moment to shear ratio for these walls is 65 cm. The gauges used to measure the bending, shear, and total deformations are located at a height of $h = 43.75$ cm above the base of the wall.

All six of these walls have the same dimensions. Walls SW1a and SW3 have a vertical reinforcing ratio of 0.426%, while walls SW4, SW4a, SW5 and SW6 have a vertical reinforcing ratio of 0.774%. This accounts for the increase in strength between these two sets of walls. Wall SW4 is subject to a monotonic loading, while walls SW1a, SW3, SW4a, SW5 and SW6 are subject to cyclic loadings as shown in Figures 3, 4 and 5. The difference between the experimental backbone curves for these identical[10] walls is small. Thus the practice of using an envelope of cyclic test data to represent the monotonic response is justified.

Overall, the comparison between the calculated and experimental results is good. However, the calculated response typically overestimates the initial bending stiffness, and underestimates the lateral load at failure.

---

[10] These walls have identical dimensions and reinforcing steel. The 6.7% difference in their concrete strengths is insignificant.

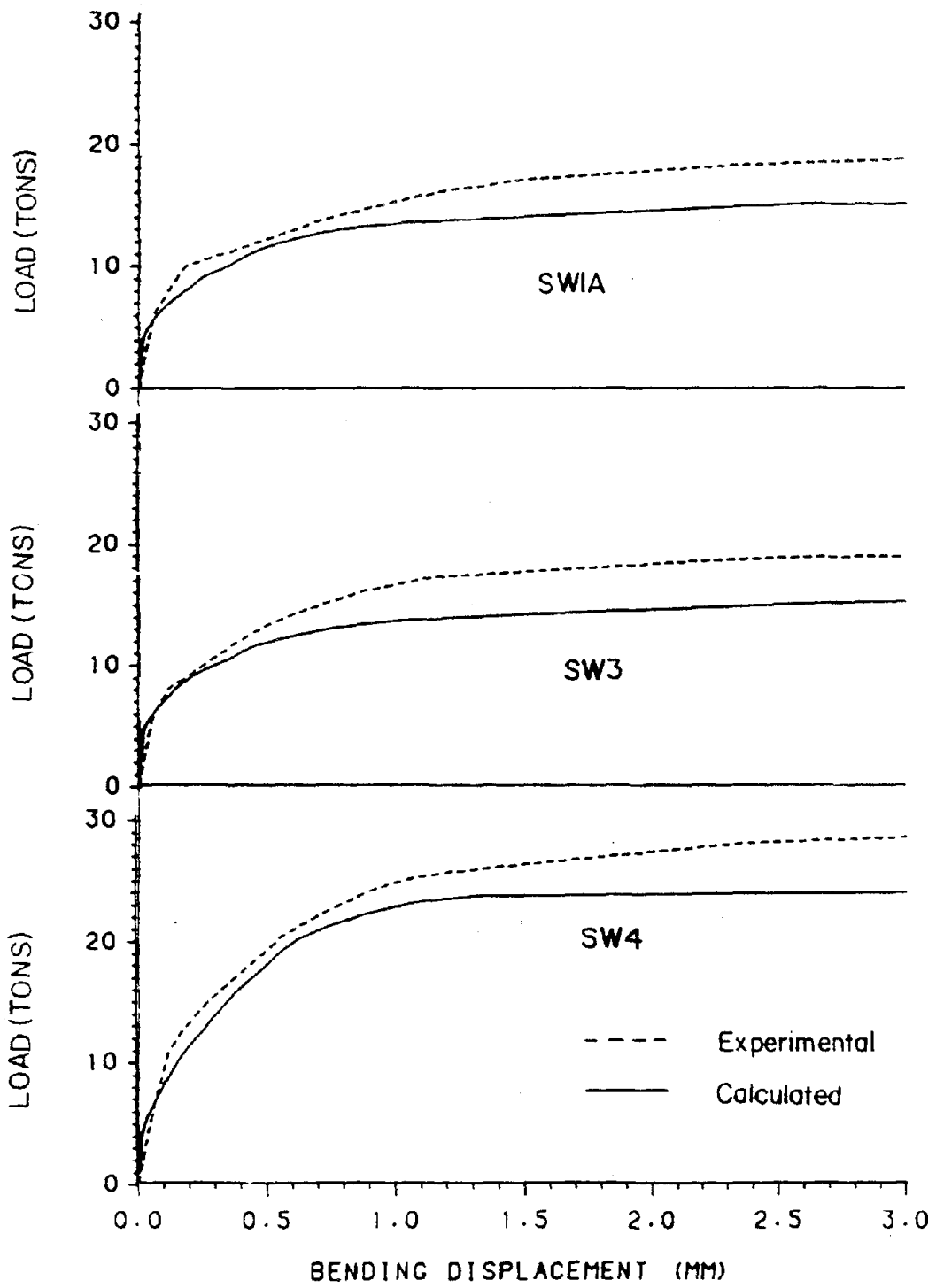

Figure 47. Calculated and Experimental Bending Backbone Curves for NCKU Walls SW1a, SW3 and SW4

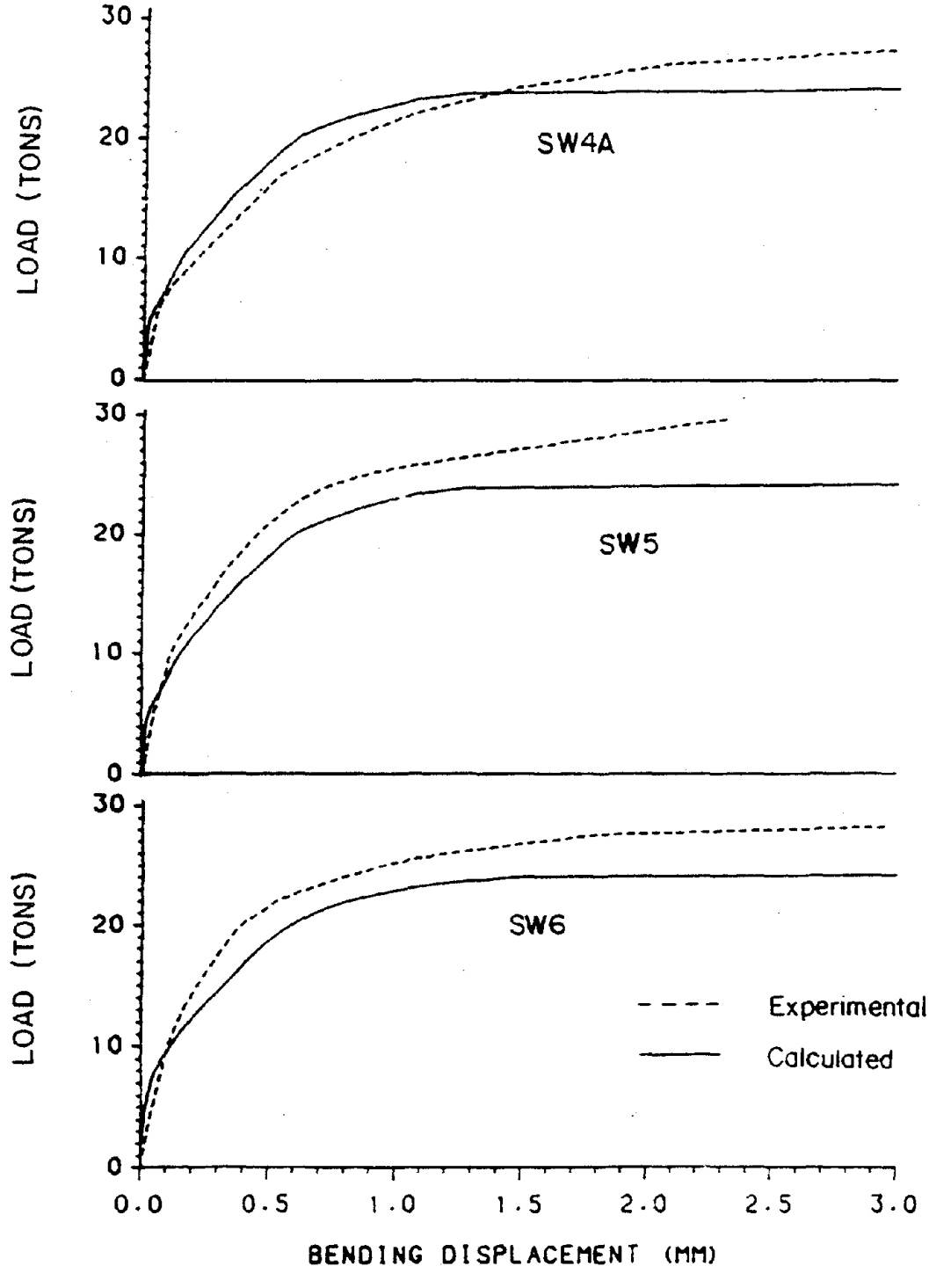

Figure 48. Calculated and Experimental Bending Backbone Curves for NCKU Walls SW4a, SW5 and SW6

2. Static Monotonic Shear Deformation. The shear deformation for NCKU walls SW1a, SW3, SW4 are calculated by Equation 3.33 and compared with the experimental deformations in Figure 49. Similarly, the calculated shear deformation for NCKU walls SW4a, SW5 and SW6 are compared with the experimental deformations in Figure 50. The range of deformations from 0 to 3 mm is emphasized in Figure 51. Experimentally observed failure deformations range from 2.51 mm to 5.77 mm.

Overall, the comparison between the calculated and experimental results is good. However, the calculated response typically overestimates the initial shear stiffness, overestimates the shear at yield, underestimates the displacement at yield, and underestimates the lateral load at failure.

3. Static Monotonic Total Deformation. The total deformation ($\delta_t = \delta_b + \delta_s$) versus applied load for NCKU walls SW1a, SW3, SW4, SW4a, SW5 and SW6 is given in Figures 51 and 52. Overall, the comparison between the calculated and experimental results for these walls is good. However, similar to the bending and shear components of deformation, the calculated response typically: 1) overestimates the initial stiffness, and 2) underestimates the lateral load at failure.

NCKU walls SW10, SW11, SW12, SW13, SW14, SW15, SW16, SW19, and SW20 are summarized in Table I. Some of these walls have different bar arrangements than the first group of NCKU walls. Walls SW10, SW11, SW12, SW13, and SW14 have the same dimensions as the first group of NCKU walls. Walls SW15, SW16, SW19 and SW20 are taller, with a moment to shear ratio of 90 cm, and their displacements are measured h = 68.75 cm from the base of the wall. The total displacements are calculated in the same manner as the first group of NCKU walls.

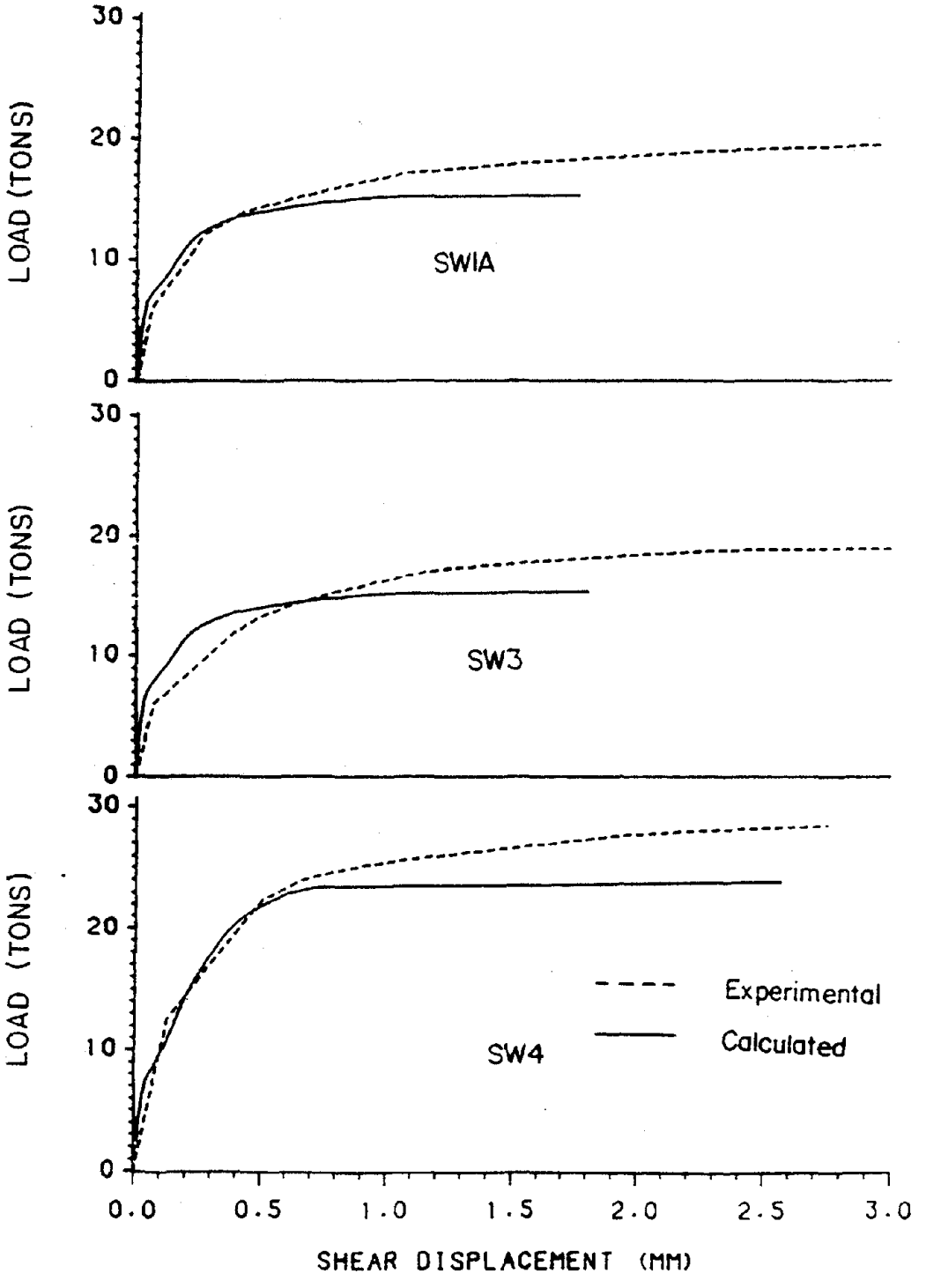

Figure 49. Calculated and Experimental Shear Backbone Curves for NCKU Walls SW1a, SW3 and SW4

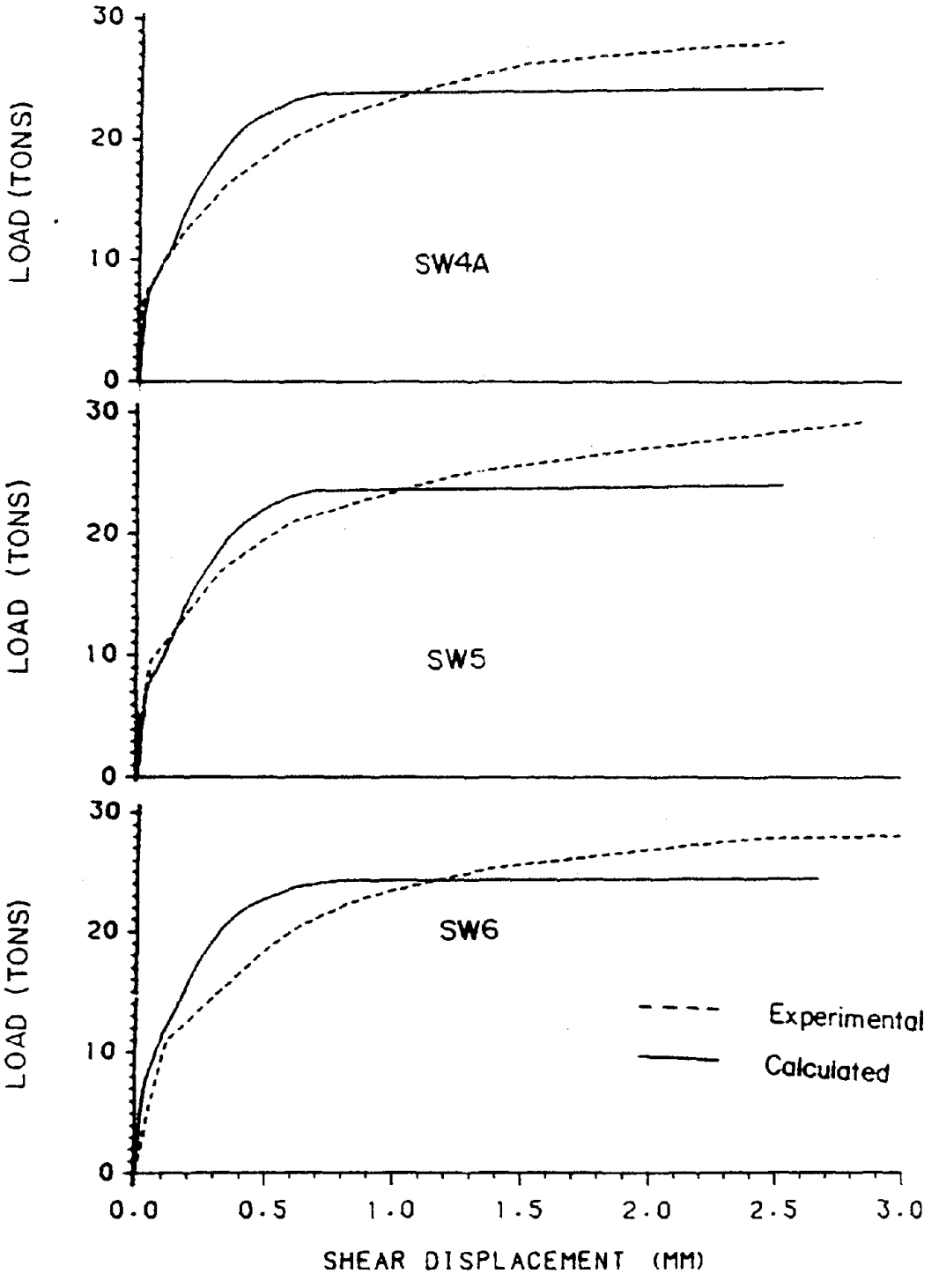

Figure 50. Calculated and Experimental Shear Backbone Curves for NCKU Walls SW4a, SW5 and SW6

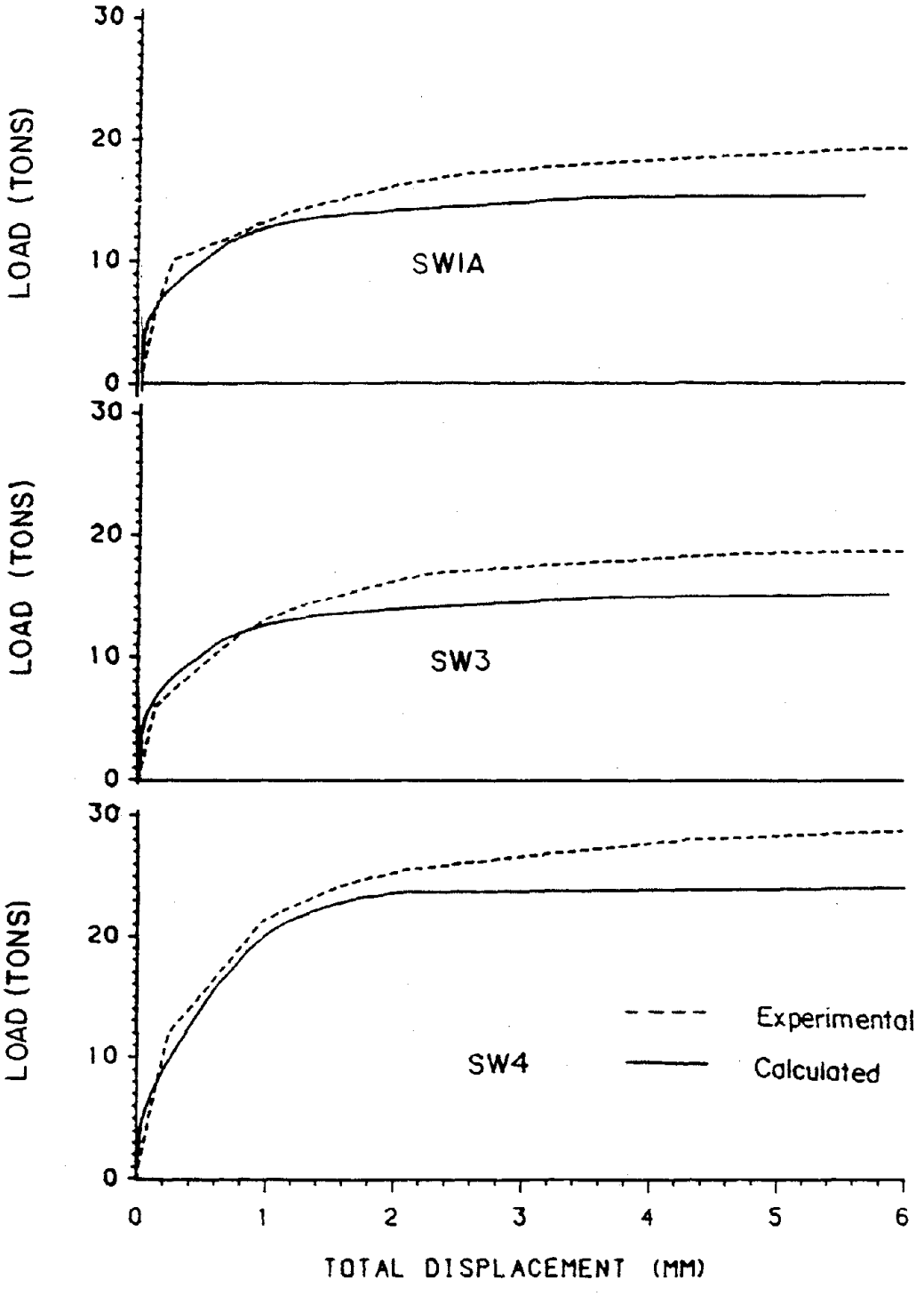

Figure 51. Calculated and Experimental Monotonic Response for NCKU Walls SW1a, SW3 and SW4

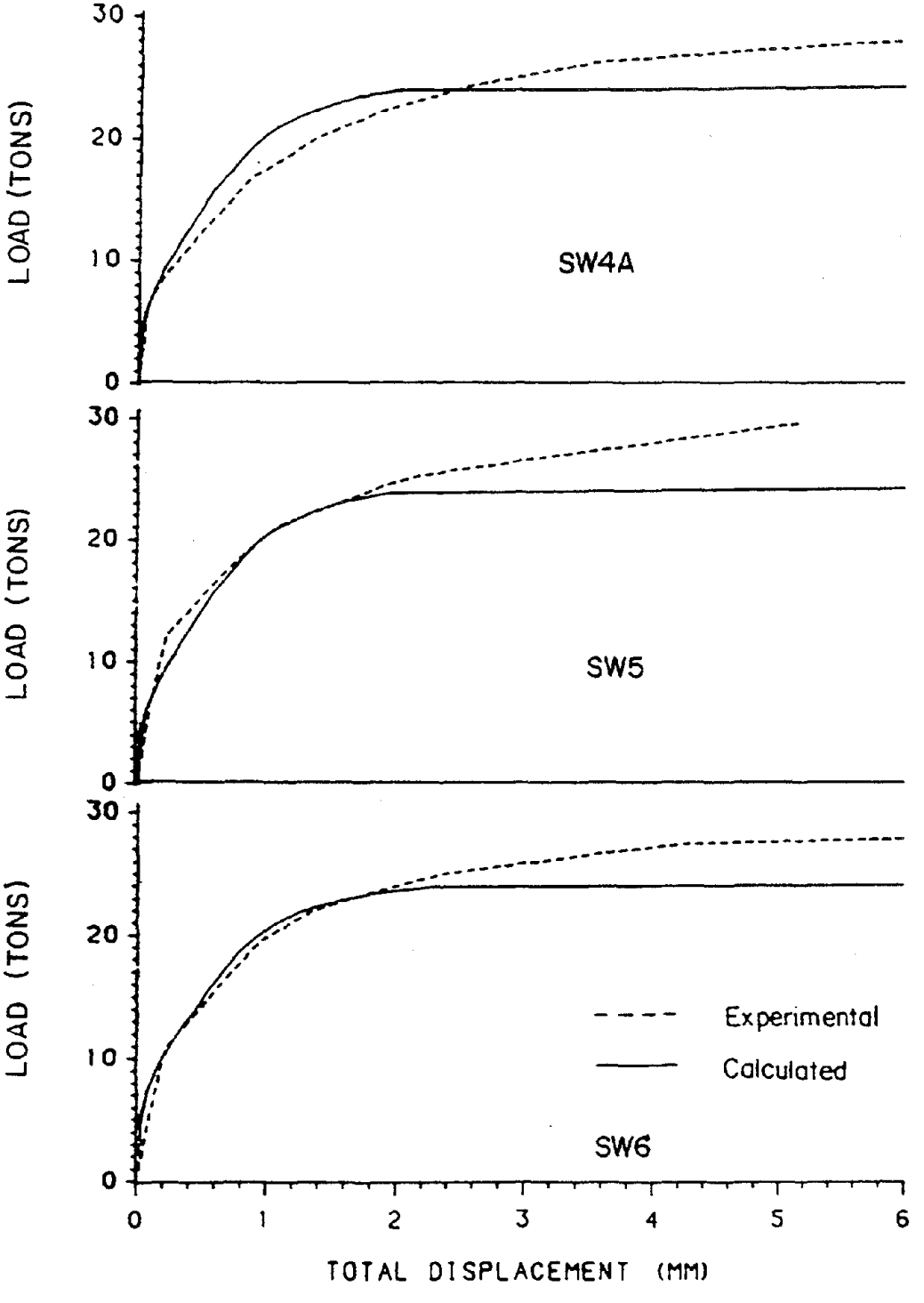

Figure 52. Calculated and Experimental Monotonic Response for NCKU Walls SW4a, SW5 and SW6

The total deformation versus applied load for NCKU walls SW10, SW11, SW12, SW13, SW14, SW15, SW16, SW19, and SW20 is given in Figures 53, 54 and 55. Overall, the comparison between the calculated and experimental results for these walls is good. However, similar to the first group of NCKU walls, the calculated response typically: 1) overestimates the initial stiffness, and 2) underestimates the lateral load at failure. Also, the shorter walls tend to overestimate the load in yielding region.

Walls SW10, SW13 and SW14 are identical except for the horizontal reinforcing steel. Wall SW14 has twice as much horizontal reinforcing steel as wall SW10. The performance of both walls is similar, however wall SW14 has an ultimate strength about 15% higher than wall SW10. Wall SW13 does not have any horizontal reinforcing steel and it's strength is about 10% less than wall SW10. Similarly, walls SW16, SW19 and SW20 are identical except that wall SW19 does not have any horizontal reinforcing steel. Wall SW19 failed at a load about 25% less than walls SW16 and SW20. Both walls SW13 and SW19 also failed at lower displacements than similar walls with horizontal steel. Thus while horizontal steel is not explicitly specified in the proposed analytical model, it is essential to the performance of the shear wall.

Walls SW15, SW16, SW19 and SW20 are taller, $\frac{M}{V} = 90$ cm, than the other NCKU shear walls, $\frac{M}{V} = 65$ cm. Since the moment to shear ratio has increased, the moment capacity and bending ductility have also increased. However, the moment arm has increased more than the moment capacity. Thus the taller walls fail at lower values of applied load. Failure deformations for the taller walls are greater than the lower walls.

PCA walls R1, R2, B1, B2, B3, B4, B5, F1, B1-1, B2-1, B3-2 and B4-3 are summarized in Table IX, and their cross sections are shown in Figure 56. These walls have different cross sections from the rectangular walls tested by NCKU. Walls R1 and R2 have extra steel bars placed at the edges of the wall. Walls B1 to B5 have

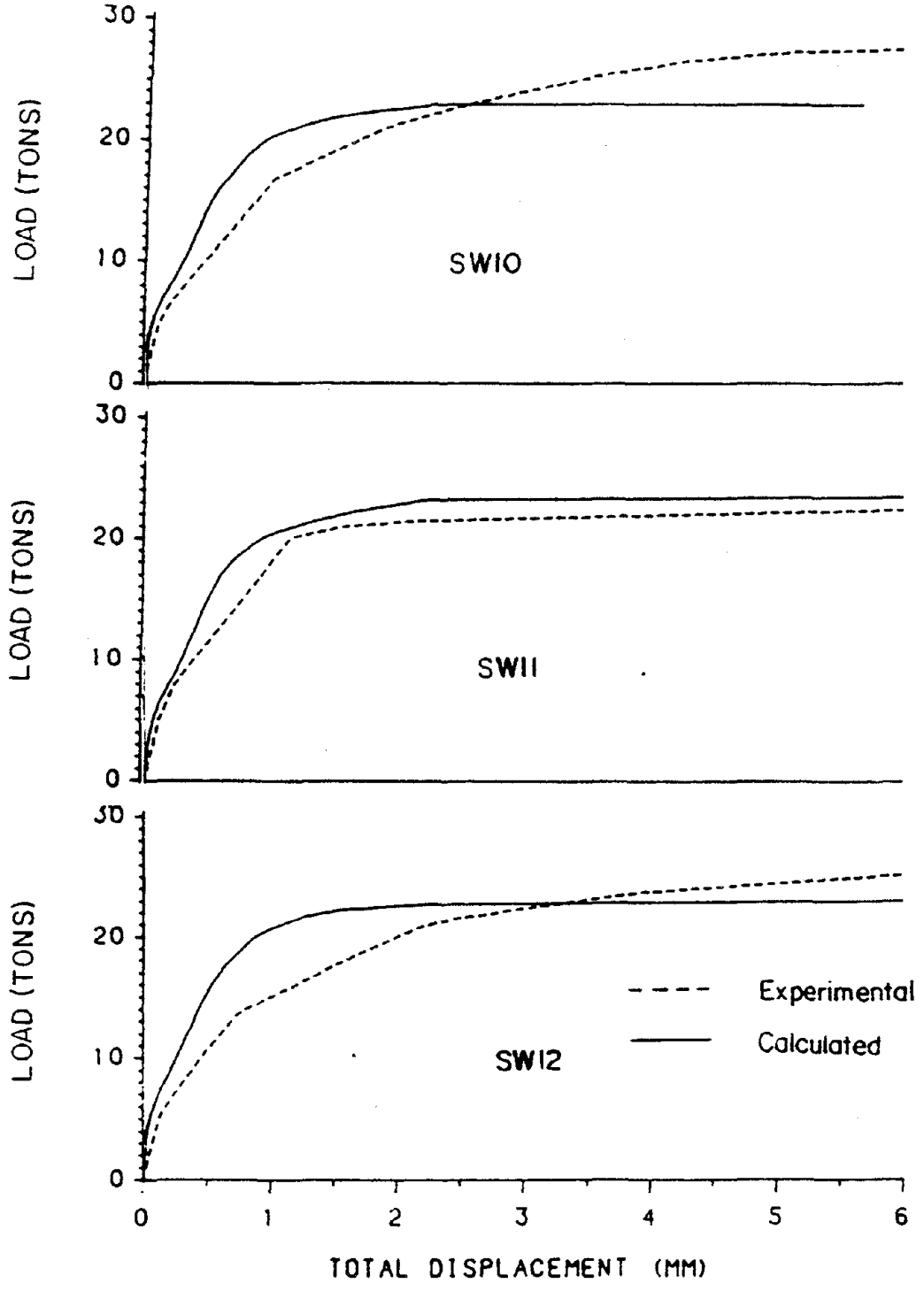

Figure 53. Calculated and Experimental Monotonic Response for NCKU Walls SW10, SW11 and SW12

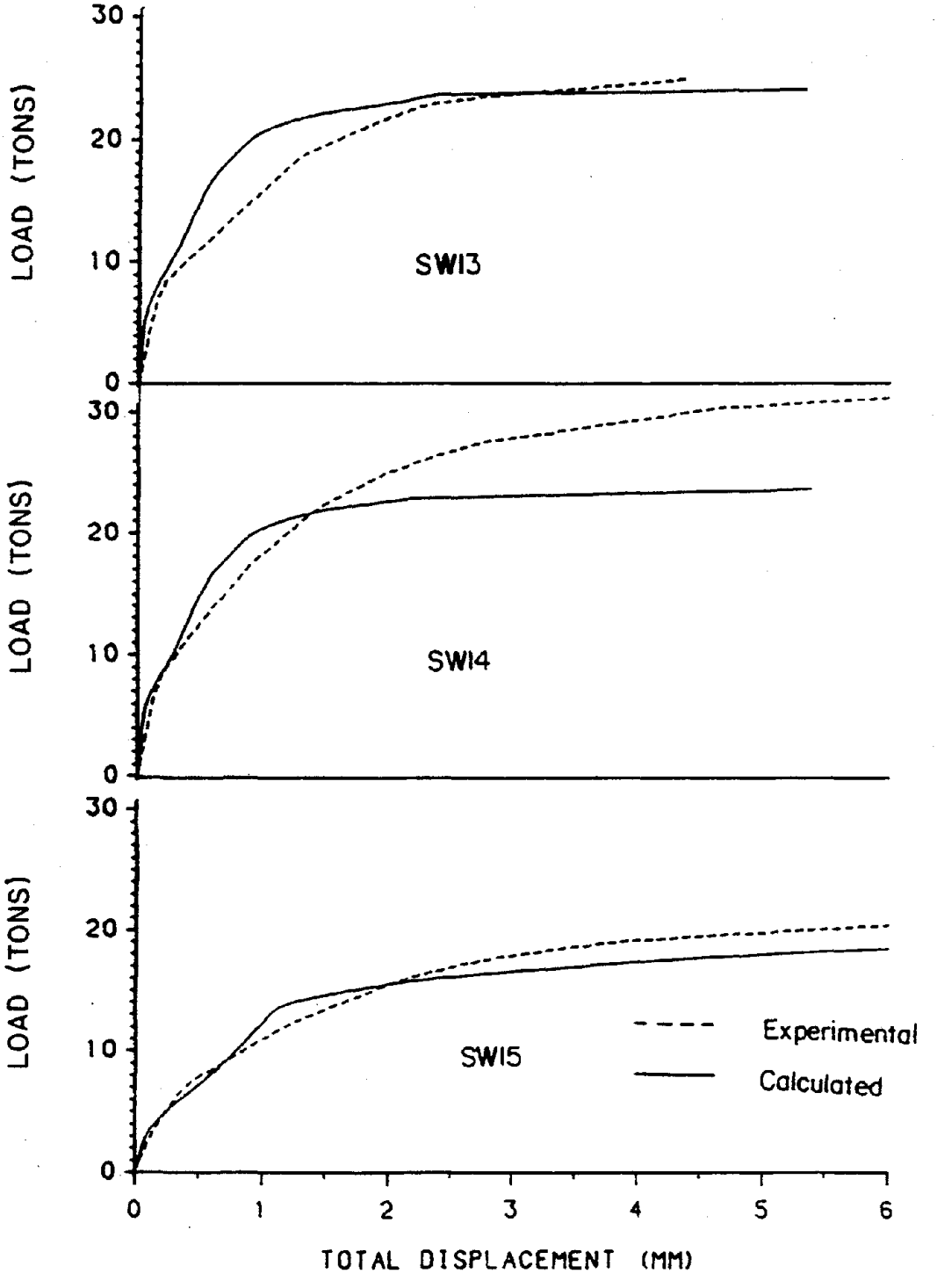

Figure 54. Calculated and Experimental Monotonic Response for NCKU Walls SW13, SW14 and SW15

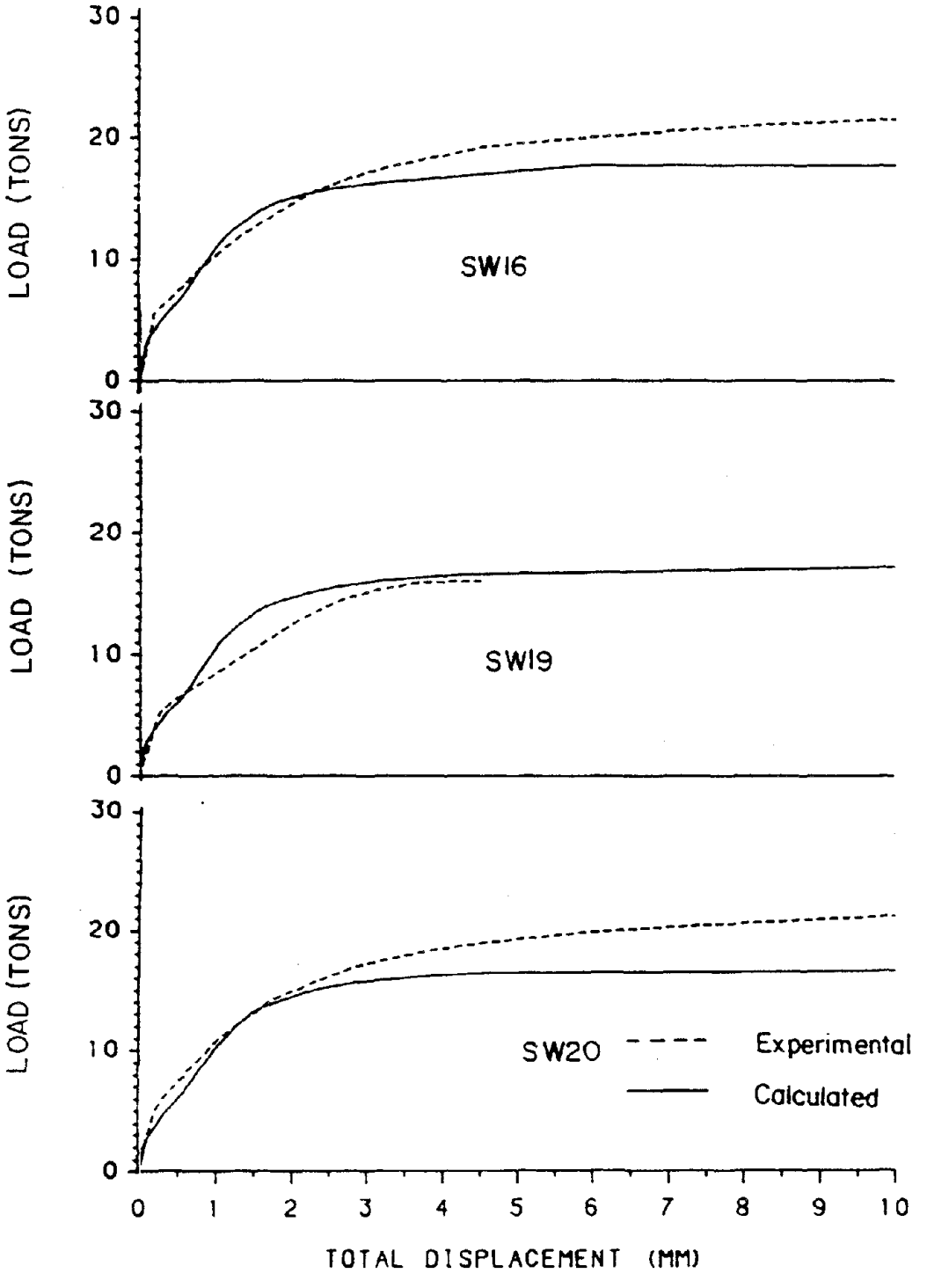

Figure 55. Calculated and Experimental Monotonic Response for NCKU Walls SW16, SW19 and SW20

boundary columns with extra longitudinal steel and transverse reinforcement to confine the concrete. Walls F1, B1-1, B2-1, B3-2, and B4-3 have a flanged cross section.

Table IX. PCA SHEAR WALLS

Wall	W x H x T	f'_c	f'_{cr}	Flange ρ %	Flange f_y	Web ρ_v %	Web ρ_w	Web f_y	$\frac{H}{W}$	Loading
R1	75x180x4 (2)	6.49	0.65	1.47	74.2	0.28	0.31	75.7	2.4	cyclic
R2	75x180x4 (2)	6.74	0.65	4.00	65.3	0.28	0.31	77.6	2.4	cyclic
B1	75x180x4 (3)	7.68	0.73	1.11	65.2	0.28	0.31	75.5	2.4	cyclic
B2	75x180x4 (3)	7.78	0.71	3.67	59.5	0.28	0.62	77.2	2.4	cyclic
B3	75x180x4 (3)	6.86	0.64	1.11	63.5	0.28	0.31	69.4	2.4	cyclic
B4	75x180x4 (3)	6.53	0.68	1.11	65.3	0.28	0.31	73.2	2.4	monotonic
B5	75x180x4 (3)	6.57	0.63	3.67	64.4	0.28	0.62	72.8	2.4	cyclic
F1	75x180x4 (4)	5.58	0.64	3.89	64.5	0.28	0.71	76.2	2.4	cyclic
B1-1	75x37.5x4 (5)	4.20	0.51	1.80	76.2	0.50	0.50	78.8	0.5	monotonic
B2-1	75x37.5x4 (5)	2.37	0.32	6.40	70.6	0.50	0.50	80.0	0.5	monotonic
B3-2	75x37.5x4 (5)	3.92	0.47	4.10	60.0	0.50	0.50	79.0	0.5	cyclic
B4-3	75x37.5x4 (5)	2.76	0.37	4.10	76.5	0.50	0.00	77.6	0.5	cyclic

Notes:
(1) All units are inch, kip.
(2) The flange steel is concentrated in a 7.5″x4.0″ region at the edges of the wall.
(3) A 12″x12″ boundary column at the edge of the wall contains the flange steel.
(4) A 36″x4″ flange at the edge of the wall contains the flange steel.
(5) A 24″x4″ flange at the edge of the wall contains the flange steel.

PCA walls R1, R2, B1, B2, B3, B4, B5, and F1 are 180″ tall and have height to width ratio of 2.4. For these walls the hinging region is assumed to equal one half of the wall's width. The equivalent moment diagram used for these walls is shown in Figure 56. Since the moment varies in the upper portion of the wall, the curvature distribution is not constant. Thus the bending deformations are calculated by the conjugate beam method

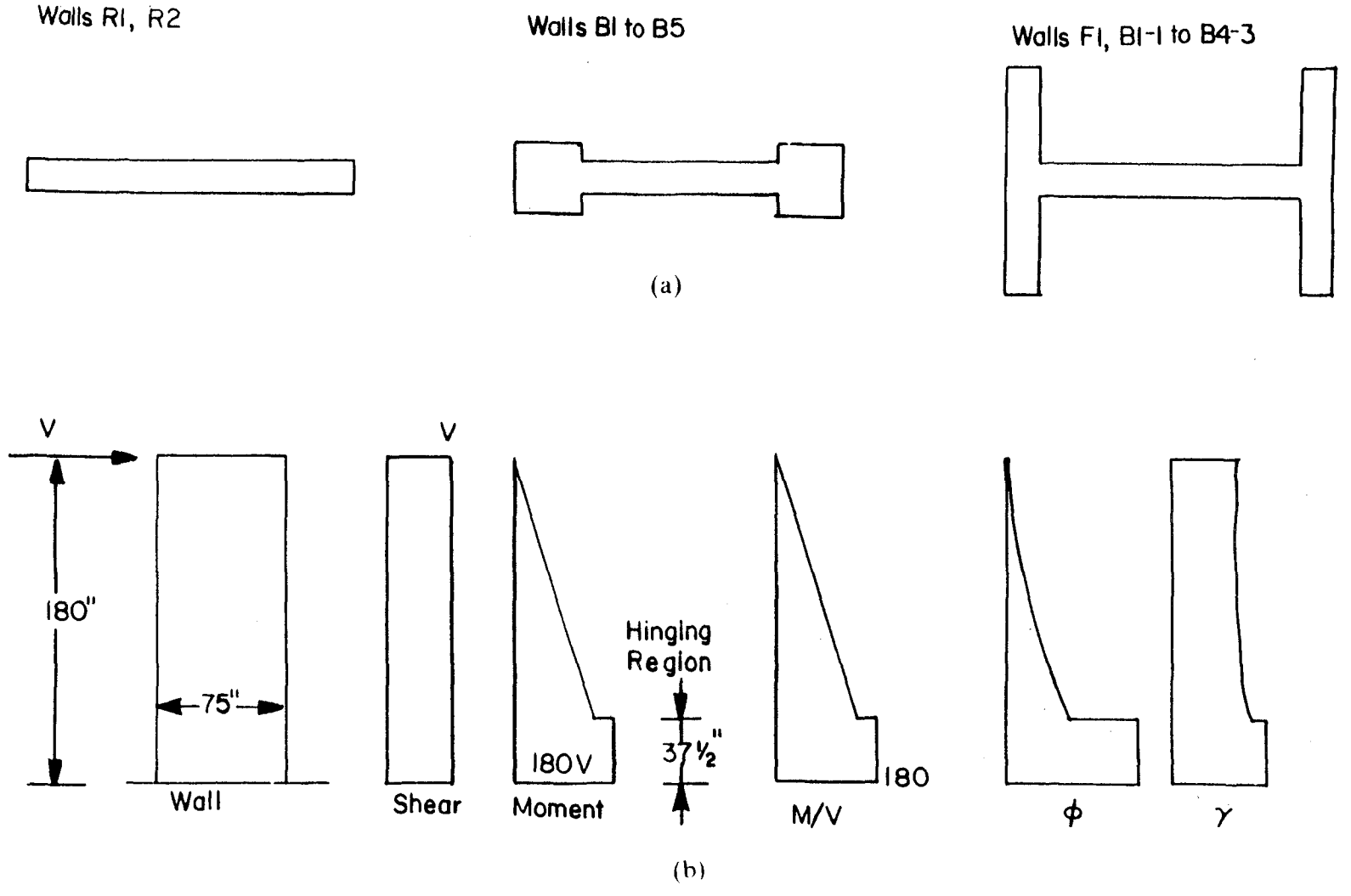

Figure 56. PCA Walls Cross Sections, Shear, Moment Diagrams, Curvature and Shear Strain Distributions: (a) PCA Walls Cross Sections, (b) Loading, Shear, Moment, M/V, ϕ and γ

$$\delta_b = \int_0^h \phi_z \, z \, dz + \theta_{br} h \tag{3.38}$$

where z is measured from the top of the wall.

The flanges in walls F1, B1-1, B2-1, B3-2 and B4-3 contribute more to the moment capacity than the shear capacity. Thus the flange area included in the shear calculation, Equation 3.17, is limited to $A_{\text{flange shear}} = 2t^2$, where t is the thickness of the flange[11].

While shear is constant, the bending moment is not constant on the upper portion of these walls. Thus the moment to shear ratio varies with height, as seen in Figure 56, and the shear strain on the wall is not constant. The shear deformation is obtained by integrating shear strains over the height of the wall

$$\delta_s = \int_0^h \gamma_z \, dz \tag{3.39}$$

The analytical backbone curves are compared to the experimental backbone curves in Figures 57 through 61. The calculated failure ductility of walls B1, B3 and B4 exceeded $10\delta_{yield}$. Thus the calculated failure point is used instead of Equation 3.37. For the lightly reinforced walls without flanges, R1, R2, B1, B3 and B4, the comparison between experimental and calculated values is very good. The deformation in these walls is dominated by bending, with minimal shear influence.

---

[11] Wall F1 has a flange shear area of $3t^2$ and wall B3-2 has a flange shear area of t^2.

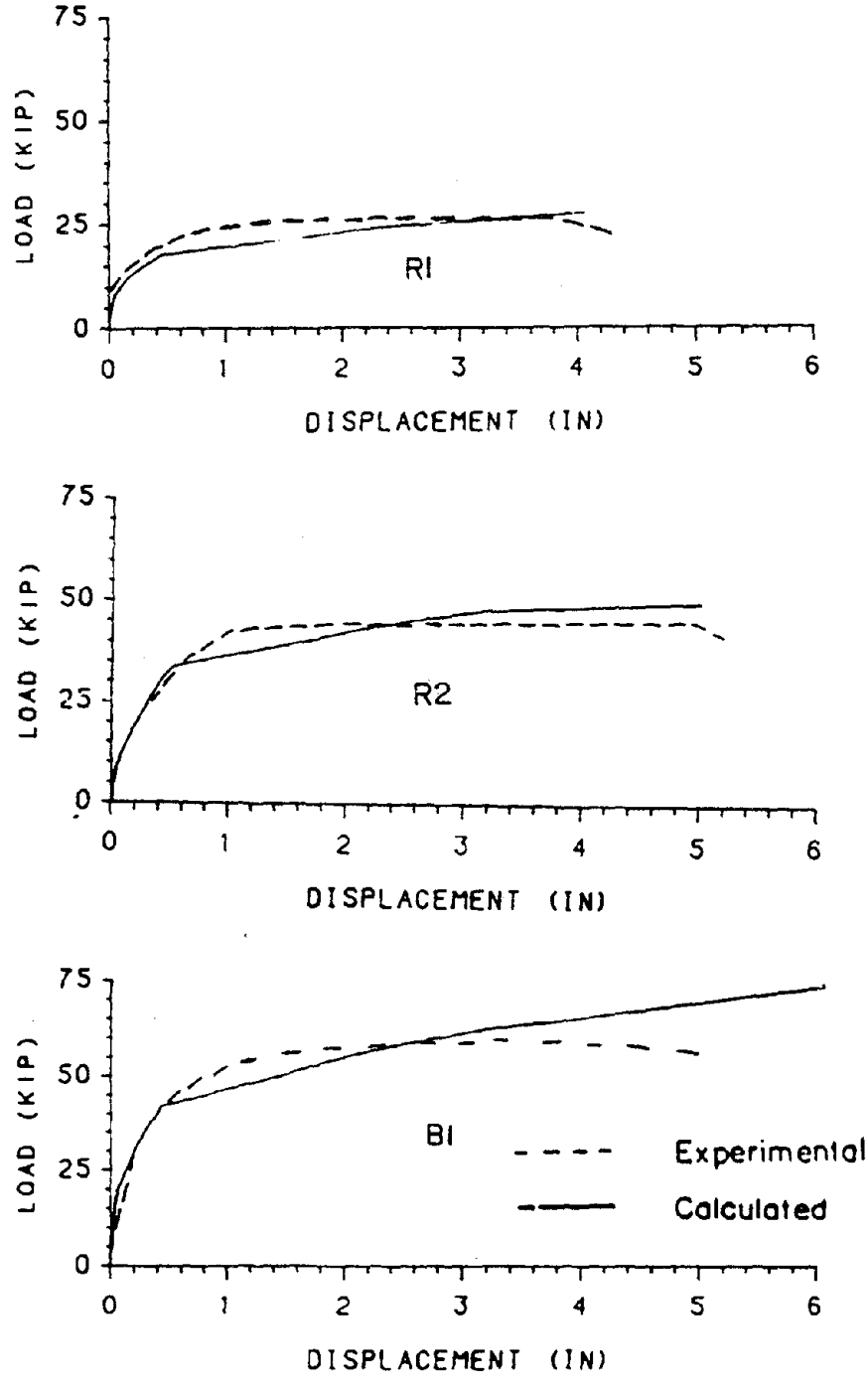

Figure 57. Calculated and Experimental Monotonic Response for PCA Walls R1, R2 and B1

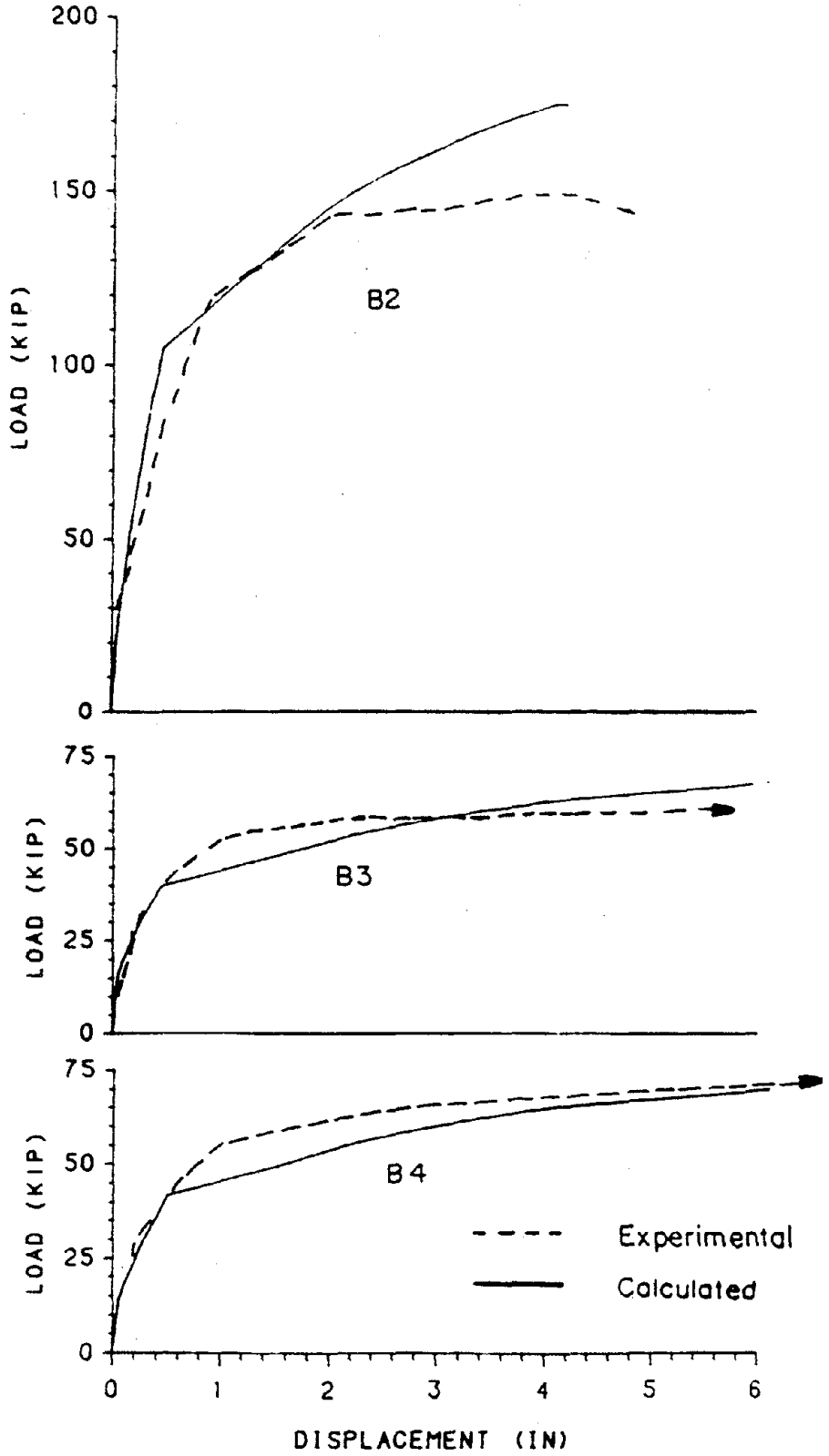

Figure 58. Calculated and Experimental Monotonic Response for PCA Walls B2, B3 and B4

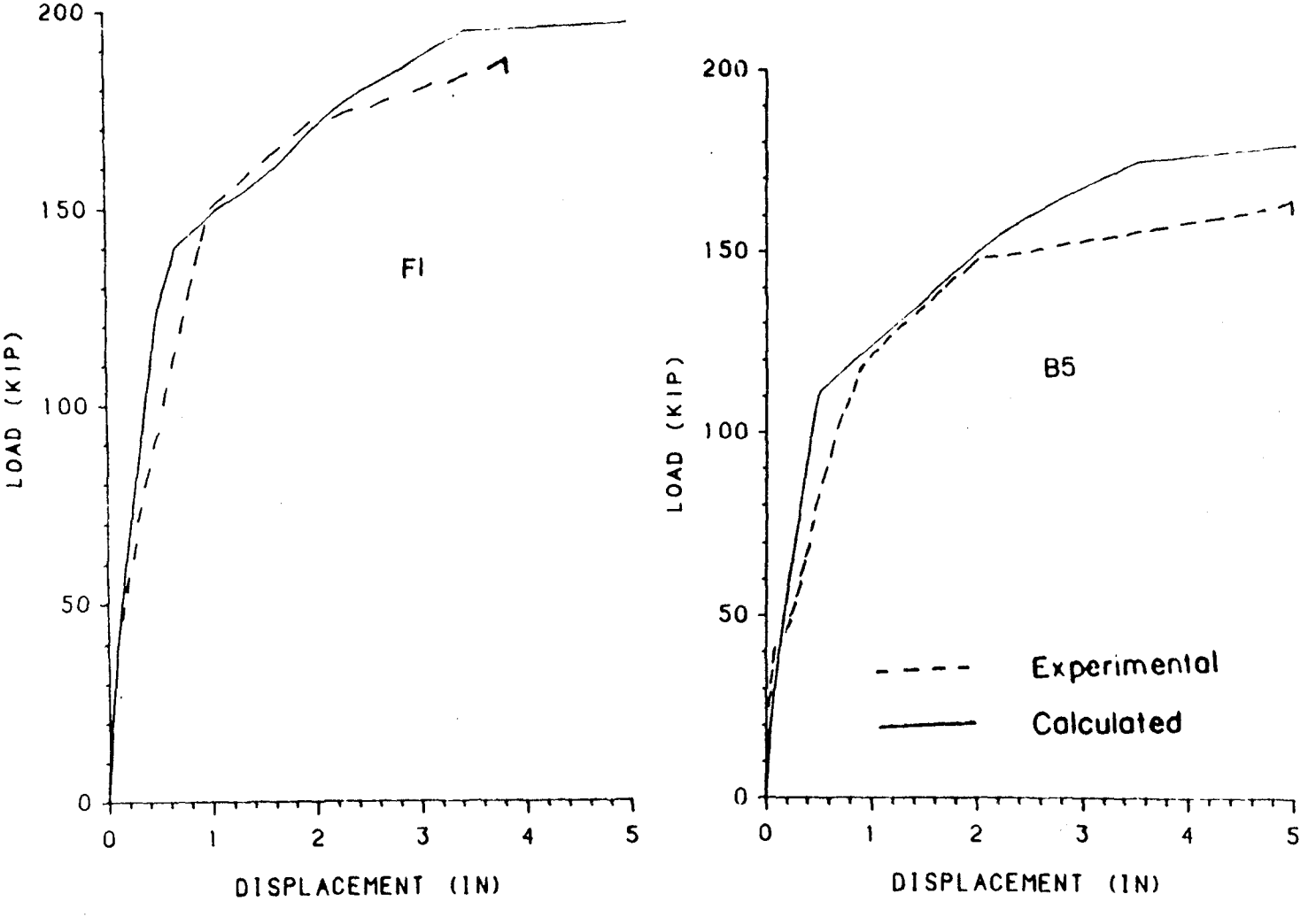

Figure 59. Calculated and Experimental Monotonic Response for PCA Walls B5 and F1

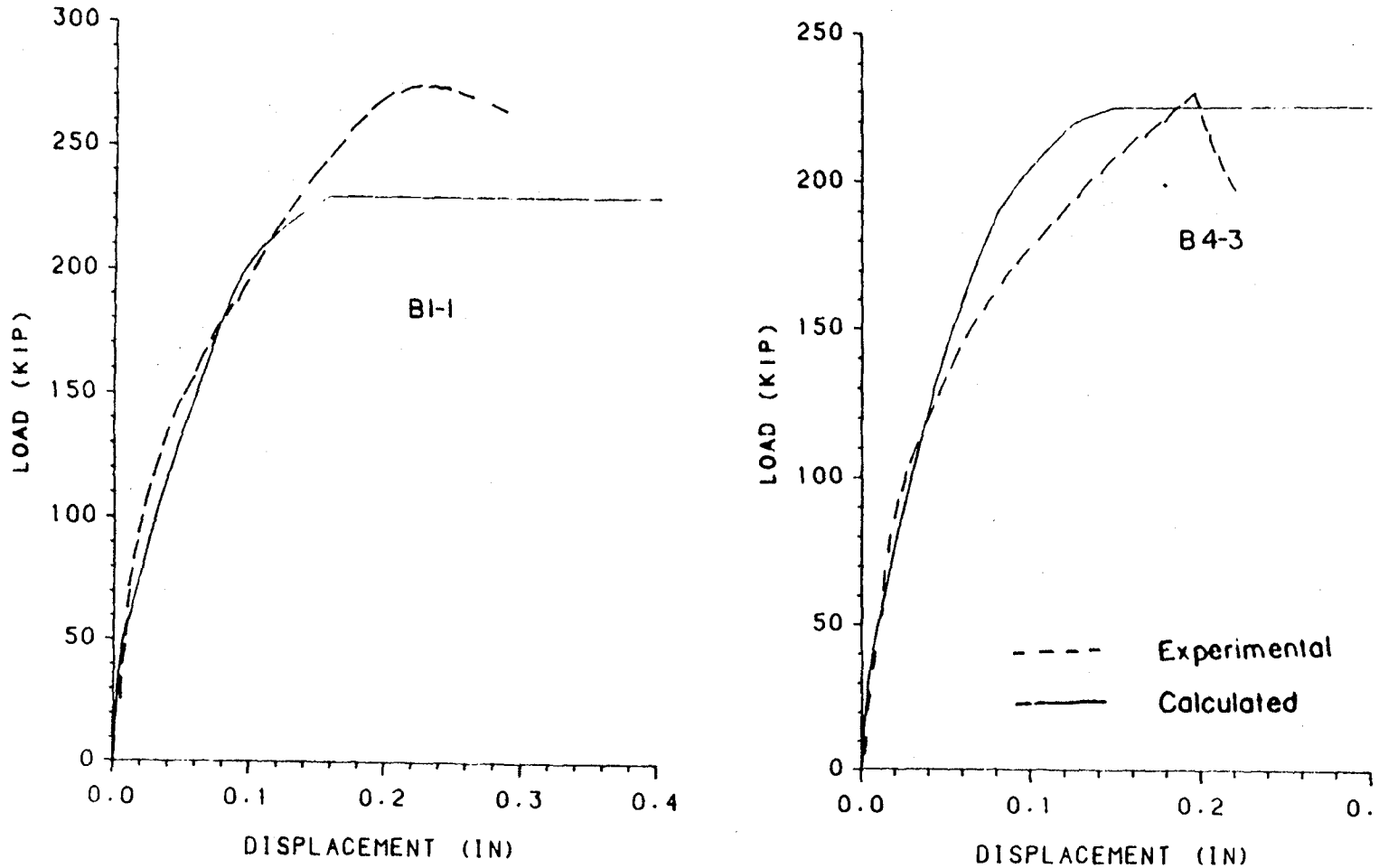

Figure 60. Calculated and Experimental Monotonic Response for PCA Walls B1-1 and B4-3

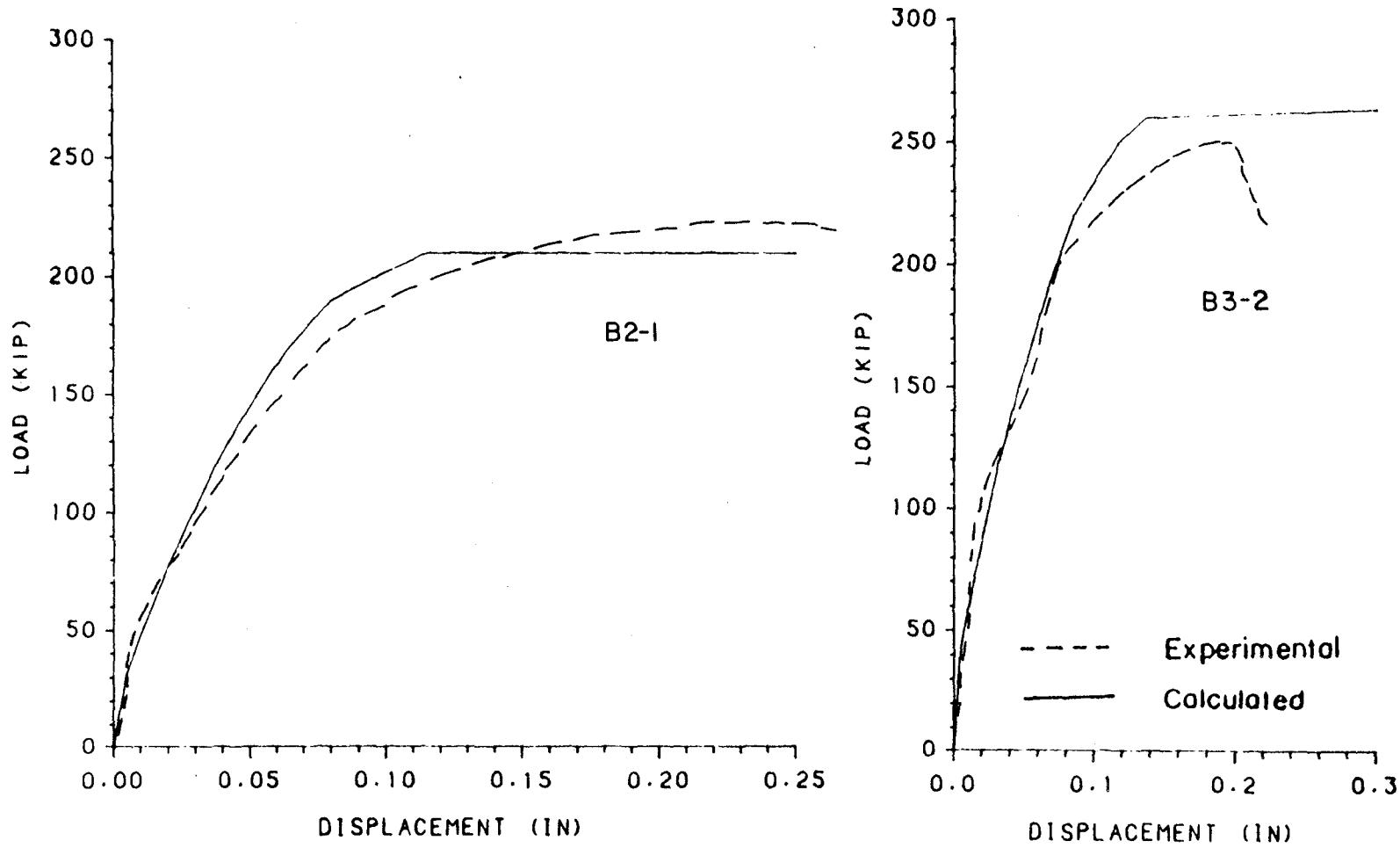

Figure 61. Calculated and Experimental Monotonic Response for PCA Walls B2-1 and B3-2

For walls B2, B5 and F1 the comparison is good except that the failure load is overestimated. These walls have higher reinforcing ratios than the other PCA walls. Thus these walls are failing at much higher load levels. Web crushing[12] (60) is the experimentally observed failure mode for walls B2, B5, and F1. This is a compressive failure of the web concrete near either a horizontal or vertical boundary element. Web crushing has only been observed on highly reinforced walls with boundary columns or flanges subject to large cyclic deformations. The proposed analytical model does predict the crushing of concrete on an inclined compressive strut.

Walls B2, B5, and F1 have a height to width ratio of 2.40. For walls in this range, the horizontal expansion begins to become important. Consider the Mohr's circle for strain in Figure 62. Case 1 is the wall without horizontal expansion, $\varepsilon_h = 0$. A longitudinal compression strain ε_x and a shear strain γ are present on the element, yielding principal compression and tensile strains ε_{pc1} and ε_{pt1}. For Case 2, the wall has a horizontal expansion $\varepsilon_h > 0$, and the same longitudinal and shear strains as Case 1. The principal compressive strain for Case 2 is less than Case 1, $|\varepsilon_{pc2}| < |\varepsilon_{pc1}|$, and the principal tensile strain for Case 2 is greater than Case 1, $\varepsilon_{pt2} > \varepsilon_{pt1}$. Since the shear softening term λ is a function of $\left|\frac{\varepsilon_{pt}}{\varepsilon_{pc}}\right|$, the shear softening term for Case 2 is greater than Case 1, $\lambda_2 > \lambda_1$. Thus the inclusion of horizontal expansion reduces the concrete's principal compression strength,

[12] Web crushing mechanism: As the wall is loaded, inclined cracks form at the base of the wall, and will extend throughout the hinging region of the wall. Between each of these cracks is an inclined compression strut. These inclined compression struts span the web. As the wall is cycled, shear resistance between the base of the wall and the compression struts degrades. Struts on the tension side of the neutral axis degrade first, transferring their load to struts on the compression side of the neutral axis. At some point, the remaining inclined web compression struts will crush, usually at the base of the wall, and the load capacity of the wall is diminished. Web crushing has been observed in the presence of large cyclic deformations.

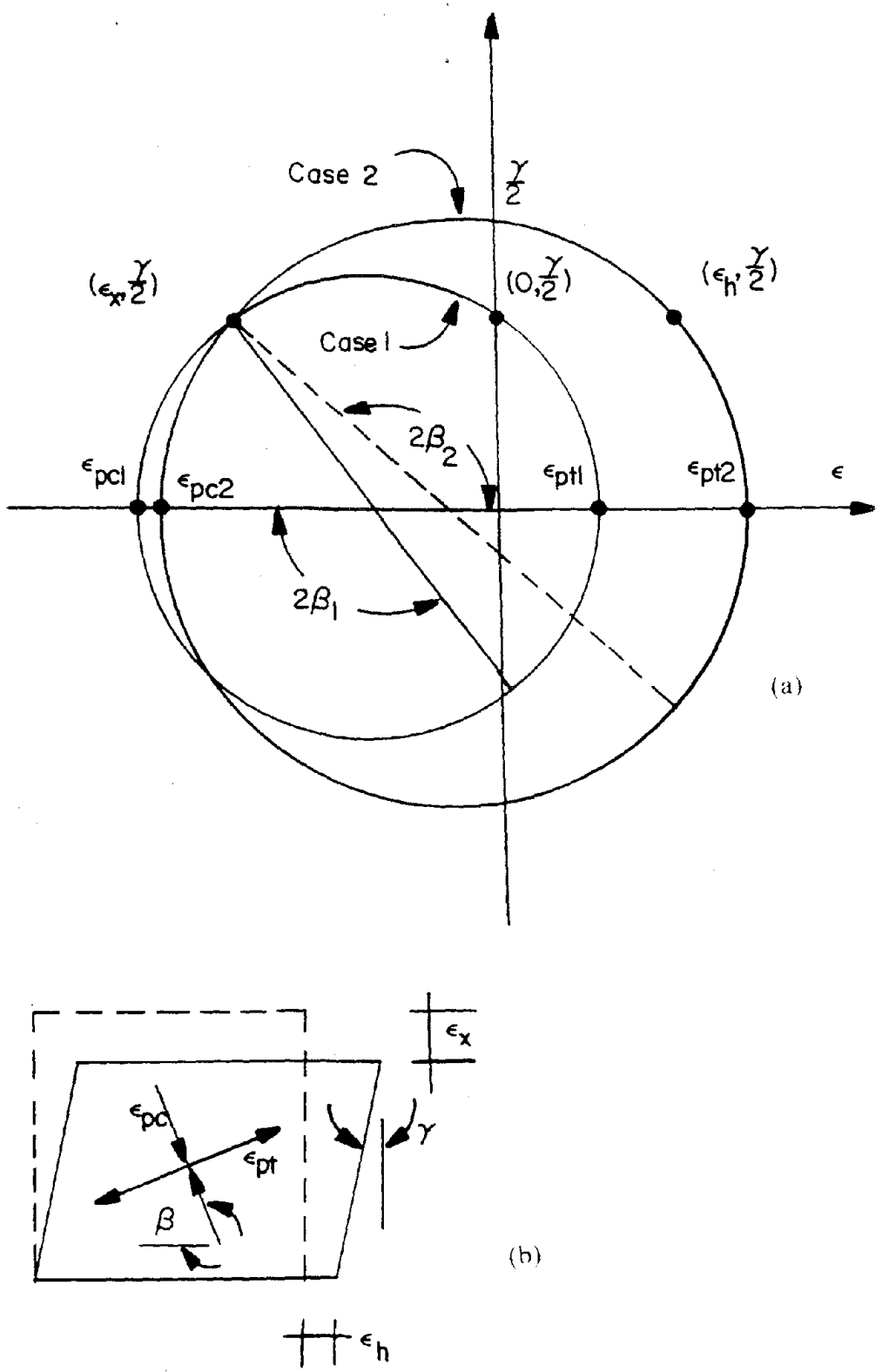

Figure 62. Mohr's Circle for Strain with Horizontal Expansion: (a) Mohr's Circle For Concrete Strain (b) Principal Strains on an Element

$\frac{f'_c}{\lambda_2} < \frac{f'_c}{\lambda_1}$, reducing the capacity of the wall. The analytical model without horizontal expansion, overestimates the strength of walls B2, B5 and F1. If the experimental model had included floors at quarter points along the wall's height, the horizontal expansion would have been restrained, the load capacity increased, and the comparison with the analytical model would be better.

Walls R1, R2, B1, B3, and B4 also have a height to width ratio of 2.4, but the shear in these walls is low. Thus the horizontal expansion is small, and these walls compared very well with the proposed analytical model.

For walls B1-1, B2-1, B3-2 and B4-3 the comparison between calculated and experimental results is good. However, the proposed analytical model underestimates the failure load of wall B1-1, overestimates the yielding region of walls B2-1, B3-2 and B4-3, and overestimates the failure ductility of walls B1-1, B3-2 and B4-3.

These low-rise walls have height to width ratios of 0.50, with heavily reinforced, flanged boundary elements. The relative influence of bending and shear can be determined by comparing the shear bending influence angle ψ for different walls, Table X. The ψ values of walls B1-1, B2-1, B3-2 and B4-3 are clearly much higher than any of the other walls examined thus far. These walls are dominated by shear. One variable that deserves further attention is the flange contribution to shear area. Another is the assumption that the strain is constant across the width of the flange (shear lag).

Hsu's pure shear model (46) also has a good comparison with walls B1-1, B2-1, B3-2 and B4-3. Hsu assumes that the longitudinal strain across the width of the wall is constant, a given amount of the flange steel is effective in resisting the vertical expansion due to shear, and that the concrete tensile stress is zero. The softened

Table X. SHEAR BENDING INFLUENCE ANGLE, Ψ

Wall	V_{uo}	M_{uo}	$\frac{M}{V}$	ψ
SW1a	1070.4	38.306	65.0	23.3°
SW3	1072.3	38.452	65.0	23.2°
SW4	1702.0	50.068	65.0	27.6°
SW4a	1704.3	50.329	65.0	27.5°
SW5	1711.5	51.106	65.0	27.3°
SW6	1722.9	52.383	65.0	26.8°
SW10	1690.0	48.019	65.0	28.4°
SW11	1970.5	46.316	65.0	33.2°
SW12	1758.5	48.952	65.0	28.9°
SW13	1771.5	54.503	65.0	26.6°
SW14	1757.4	53.367	65.0	26.9°
SW15	1969.8	46.254	90.0	25.3°
SW16	1682.2	47.399	90.0	21.5°
SW19	1651.7	44.863	90.0	22.2°
SW20	1585.1	39.486	90.0	24.0°
R1	5327.9	223.270	180.0	7.6°
R2	9508.7	338.830	180.0	8.9°
B1	13519.0	485.220	180.0	8.8°
B2	32554.0	840.120	180.0	12.1°
B3	13104.0	456.010	180.0	9.0°
B4	13331.0	459.060	180.0	9.2°
B5	33010.0	737.640	180.0	14.0°
F1	43756.0	471.060	180.0	27.3°
B1-1	20069.0	275.000	37.5	62.8°
B2-1	42069.0	214.660	37.5	79.2°
B3-2	31114.0	274.440	37.5	71.7°
B4-3	32411.0	229.780	37.5	75.1°

Notes:
(1) The units of walls SW1a to SW20 are Ton cm.
(2) The units of walls R1, R2, B1 to B5, F1, B1-1, B2-1, B3-2, and B4-3 are inch kips.

concrete stress strain model, with a modified λ, is used. This model's use is limited to walls that have negligible bending.

4. Summary of Observations. The monotonic load deformation response of reinforced concrete shear walls is influenced by many parameters. Several of these parameters are discussed below.

The monotonic load deformation response for shear walls with four different wall cross sections is calculated. These are 1) rectangular walls, 2) rectangular walls with extra reinforcing steel, 3) barbell shaped walls, and 4) flanged walls. Whenever concrete and steel are added to the edge of a wall, the bending capacity is increased. For taller walls, R1, R2, B1 to B5 and F1, the increased bending capacity is matched by a larger moment. For low-rise walls, B1-1 to B4-3, the increased bending capacity forces shear to dominate the behavior of the wall. Flanged cross sections provide the additional complicating factors of shear lag, and effective flange shear area.

Vertical web reinforcing steel ratios varied from 0.28% to 0.78%. All else being equal, as the web reinforcement increased, the walls became stronger and lost ductility. For walls without boundary columns or flanges, the strength of the wall is sensitive to the vertical web reinforcing steel ratio.

Horizontal web reinforcing steel ratios varied from 0 to 1.14%. All else being equal, as the amount of horizontal web steel increases, the strength increases. Omission of the horizontal web steel decreases the ductility. Thus while not included in the analytical model, horizontal web steel has an important role in low-rise walls.

For taller walls horizontal expansion becomes important, and the horizontal web steel acts as stirrups to resist shear. This behavior is not included in the analytical model and is partially responsible for the analytical model overestimating the strength of walls B2, B5 and F1. Walls R1, R2, B1, B3 and B4 are dominated by bending, thus the influence of horizontal expansion is not as evident.

For any given wall cross section, varying the height to width ratio can shift the wall's behavior from pure bending to pure shear. Walls with height to width ratios between 0.5 and 2.4 are in good comparison with the analytical model.

The shear bending influence angle, ψ, is used to determine the relative influence of shear and bending on a wall. Calculated values of the shear and bending influence angle ranged from 7.6° to 79.2° for the walls studied. This indicates that the proposed model is tested over a wide range of different wall behaviors. When the bending component is strong, $\psi < 30°$, the analytical model compared very well with the experimental results. When shear dominates the response, $\psi > 60°$, the analytical model has some difficulty predicting the yield load, failure load, and failure ductility. The behavior in the high shear range, $\psi > 60°$, is a recommended topic for further research.

IV. HYSTERESIS RULES FOR ISOLATED SHEAR WALLS

Hysteresis models are used to represent the cyclic behavior of materials, elements and building components. A good hysteresis model will capture the essential behavior of the element (force-deformation relationship, energy dissipation) yet remain as simple as possible to facilitate efficient numerical computation.

Many material hysteresis models have been proposed for metals, ranging from the simple, elasto-plastic model, to the complex Ramberg-Osgood model. These models have been extended to represent the element's behavior. Similarly, hysteresis models have also been developed for plain concrete (71, 50). However, because of the interaction with reinforcing steel, the plain concrete hysteresis model cannot be used to represent the behavior of reinforced concrete elements.

The cyclic behavior of a R/C beam differs from both the steel and concrete models. Takeda, et al (75) tested a series of cantilever beams and developed a hysteresis model for bending. Takeda's model has a trilinear backbone curve (crack, yield and ultimate), a one segment variable stiffness unloading curve, small amplitude hysteresis loops and large stable hysteresis loops without pinching. Many researchers have used Takeda's model, or modified versions of the model, to study the response of R/C frames (70, 62, 63, 21) and tall coupled shear walls (32, 69, 51).

The Shina model (70) is a Takeda-like model that was developed to include the pinching behavior due to bond slip in R/C beam column joints. Hiraishi (44) proposed using this model to study the pinching behavior of R/C shear walls.

Kabeyasawa, et al (49) analyzed a tall R/C shear wall with boundary columns as part the analytical studies for the full scale seven-story test structure. A hysteresis model that assumes the loading and unloading paths pass through the origin was used for both the bending and shear deformations of the wall's web. The origin orientated

hysteresis model does not dissipate energy. Boundary columns were modeled with a separate axial stiffness hysteresis model.

In this chapter, separate bending and shear hysteresis models are developed for low-rise shear walls. These hysteresis models are verified by comparison with the experimental response of five low-rise shear walls. An axial hysteresis model, developed by Kabeyasawa, et al (49), is also discussed.

A. SHEAR AND BENDING HYSTERESIS MODELS

The following semi-empirical bending and shear hysteresis models are based on NCKU shear walls SW1a, SW3, SW4a, SW5 and SW6. Walls SW1a and SW4a were subjected to one sided cyclic loading as shown in Figure 3. Walls SW3 and SW6 were subjected to an earthquake type loading as shown in Figure 4. Wall SW5 was subjected to a two sided cyclic loading as shown in Figure 5. The shear and bending deformations were separated using Equations 2.9 and 2.20. The individual components of deformation were studied. Trends were observed in the experimental data and synthesized into hysteresis rules. Each of these hysteresis rules is presented in detail and discussed below.

The bending hysteresis model is shown in Figure 63, and the shear hysteresis model is shown in Figure 64. Both hysteresis models consist of eleven rules. Several of the more prominent features of the bending and shear hysteresis models are:

- Both hysteresis models have a highly nonlinear backbone curve, without well defined break points as shown by rules B1.1 and S1.1 in Figures 63 and 64, respectively. Typically six to ten points are required to accurately describe the backbone curve. The curve is symmetric for both positive and negative loadings. An analytical method for calculating the backbone curve was presented in Chapter III.

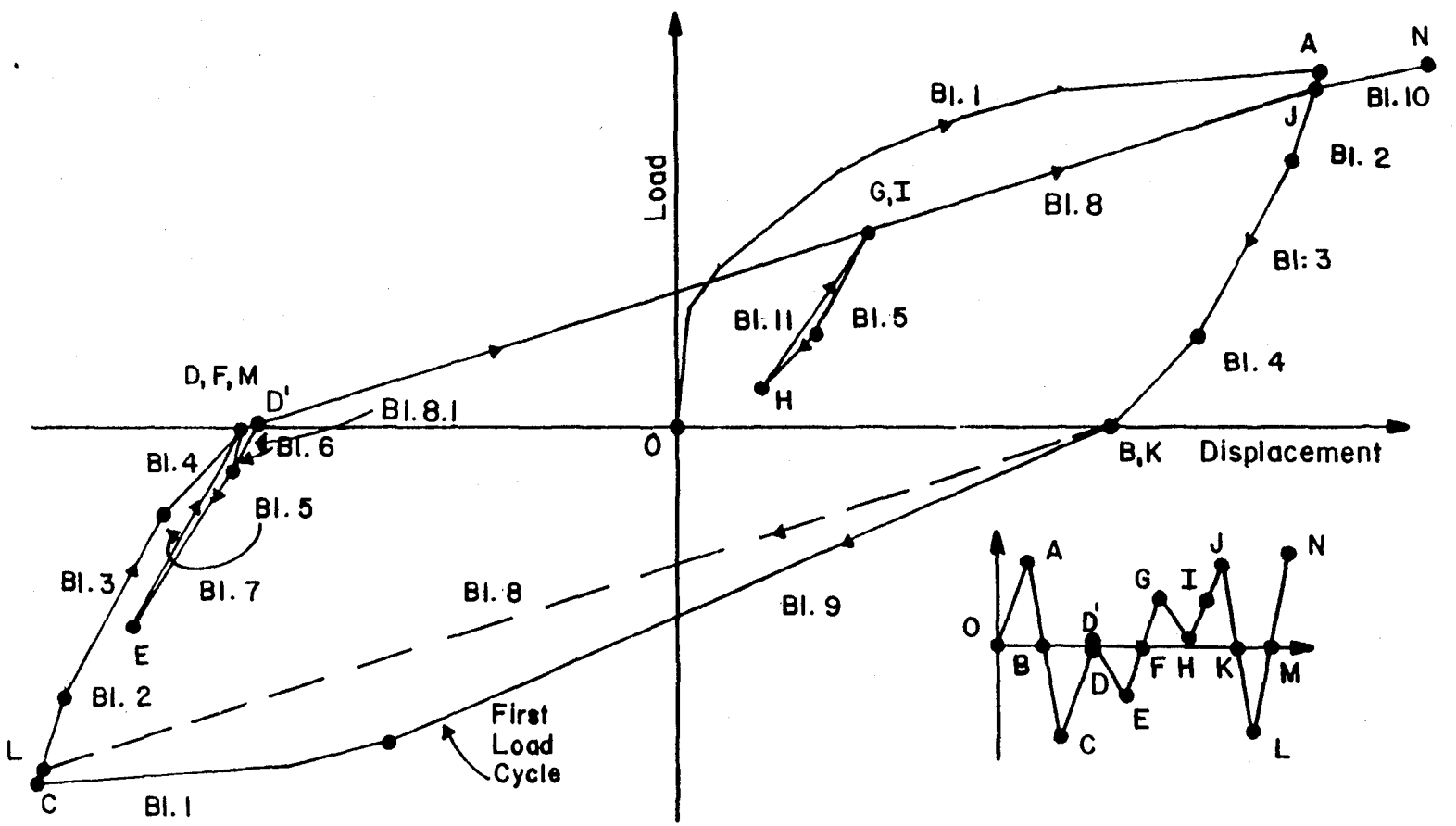

Figure 63. Bending Hysteresis Model

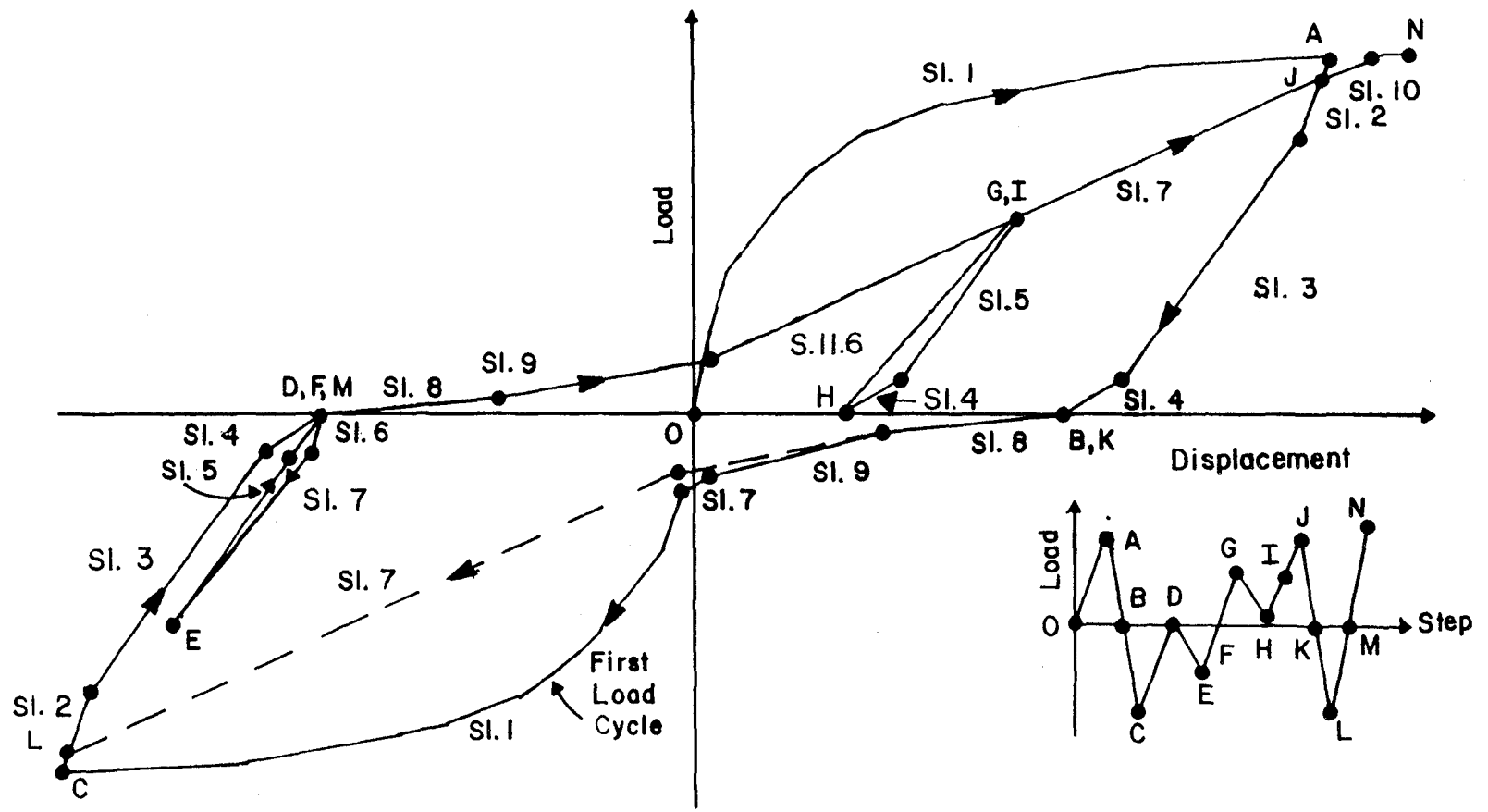

Figure 64. Shear Hysteresis Model

- The unloading branch for both hysteresis models is represented by three linear unloading segments as shown by rules B1.2, B1.3 and B1.4 in Figures 63 and rules S1.2, S1.3 and S1.4 in Figure 64. Each unloading segment has an empirical stiffness which degrades with various levels of displacement.
- When the wall is cycled at a constant load, near the maximum past load, the deformations tend to increase with each cycle. When the wall is cycled well below the maximum past load, the hysteresis loops are stable. Thus both hysteresis models reduce the reloading stiffness for loads near the maximum past load. The rate of bending stiffness reduction is cycle dependent, with less stiffness on the first cycle than on subsequent cycles. The shear stiffness reduction is cycle independent.
- The reloading curve of the shear hysteresis model is dominated by pinching. The pinch is highly nonlinear and is represented by three linear segments, as shown by rules S1.8, S1.9 and S1.7 in Figure 64. The stiffness of each segment is dependent on the maximum past displacement.
- The energy absorption increases with increasing peak displacements. This is accomplished in the hysteresis model by varying the unloading and loading stiffness. However, the energy absorption of the shear hysteresis model is less than the bending hysteresis model because of pinching.

Both the bending and shear hysteresis models are posed in terms of load and displacement, because they were derived directly from experimental load-displacement test data. However, the hysteresis models are often used in terms of moment and rotation or shear and shear strain (see Chapter V). This is possible by directly substituting moment or shear for load, and rotation or shear strain for displacement in the respective hysteresis models. All of the empirical stiffnesses are normalized with respect to the initial stiffness and cracking displacement. Thus these values are also converted to moment-rotation, or shear-shear strain form.

In both hysteresis models, loading, unloading and reversal are terms used to define the state of the applied load. Loading is defined as increasing the absolute value of the applied load as shown by load paths O-A and B-C in Figures 63 and 64. When the absolute value of the load decreases, the wall is unloading as shown by load paths A-B and C-D in Figures 63 and 64. A load reversal occurs when the load changes direction from one load step to another. For example, in Figures 63 and 64 the load path A-B is unloading from a positive load, load path B-C is loading with a negative load, and point B is the load reversal point. Load path B-C in Figures 63 and 64 is referred to as loading after unloading from the opposite direction (load path A-B). Load path D-E in Figures 63 and 64 is referred to as reloading after unloading from the same direction (load path C-D).

Both hysteresis models utilize the variable DIR, which indicates the sign of the load (positive or negative) and the status of the current load path (loading or unloading). Thus in Figures 63 and 64, DIR = 1 represents loading with a positive load, as shown by load path O-A, DIR = 2 represents unloading with a positive load, as shown by load path A-B, DIR = 3 represents loading with a negative load, as shown by load path B-C, and DIR = 4 represents unloading with a negative load, as shown by load path C-D. Another variable DIRL is the value of DIR from the previous load step.

Both hysteresis models utilize many common variables such as P, the current load, D, the current displacement, and K, the stiffness of the wall. The numerical values of these common variables are not equivalent. The bending displacement, D, used in the bending hysteresis model is quite different from the shear displacement, D, used in the shear hysteresis model. There is an implied subscript 'b' on each variable used with the bending hysteresis model.

Because the calculations for a load cycle are tedious, the hysteresis rules are intended to be used as part of a computer program. Each rule is prefaced with several logical tests. If these tests are satisfied, the rule is executed. If the logical test are not satisfied, the next rule is examined. The rules are examined in order, from Rule 0 through Rule 11. The hysteresis rules are summarized in Table XI. The stiffnesses in Table XI are defined in the hysteresis rules and are provided here for reference.

Table XI. SUMMARY OF HYSTERESIS RULES

Bending		Shear		
Rule #	Stiffness	Rule #	Stiffness	Description
B1.0	SI	S1.0	SI	Elastic Behavior
B1.1	*	S1.1	*	Loading on the Backbone Curve
B1.2	S1	S1.2	S1	Unloading
B1.3	S2	S1.3	S2	Unloading
B1.4	S3	S1.4	S3	Unloading
B1.5	*	S1.5	*	Unloading inside small amplitude loops
B1.6	SL	S1.6	S1	Reloading after unloading from the same direction
B1.7	*	S1.7	*	Reloading toward the common point
B1.8	SR	S1.8	SR1	Reloading after unloading from the opposite direction
B1.8.1	S′			Reloading after unloading from the opposite direction
B1.9	*	S1.9	SR2	Reloading after unloading from the opposite direction
B1.10	*	S1.10	*	Reloading above the common point
B1.11	SR	S1.11.1	SRL	Reloading inside small amplitude loops
		S1.11.2	SX1	Reloading inside small amplitude loops
		S1.11.3	SRL	Reloading inside small amplitude loops
		S1.11.4	SX1	Reloading inside small amplitude loops
		S1.11.5	SX2	Reloading inside small amplitude loops
		S1.11.6	SRL	Reloading inside small amplitude loops

Note:
* The stiffness is defined by an equation in the hysteresis rule.

1. Loading on the Backbone Curves. In Chapter III, the bending and shear backbone curves were developed. These curves are nonlinear, without well defined break points. In both hysteresis models the backbone curves are represented by a series of piecewise linear segments. Rules B1.1 and S1.1 address loading on the backbone curve.

When a virgin wall is loaded, the first significant change in stiffness occurs when the first crack forms in the wall. The load and displacement at this point are denoted by Pc and Dc, for cracking load and cracking displacement. Thus the first point on the backbone curve is the cracking load. When a virgin wall is loaded below the cracking load, its behavior is elastic. Rules B1.0 and S1.0 address loading and unloading in the elastic range.

a. Bending Hysteresis Model, Rules B1.0 and B1.1. The bending backbone curve is divided into a series of piecewise linear segments that join NB points, as shown in Figure 65. Define the first point as the bending cracking load, PB(1) = Pc, DB(1) = Dc, where PB and DB are arrays containing the backbone curve; P and D signify the load and displacement at the current point.

Assuming that the analysis begins with a virgin wall, the first time the hysteresis model is accessed, RULE=0. RULE is a variable that contains the previous rule number that the hysteresis model executed.

For the elastic region, rule B1.0 sets the current bending stiffness, K, to the initial bending stiffness, SI, where

$$SI = \frac{Pc}{Dc} \tag{4.1}$$

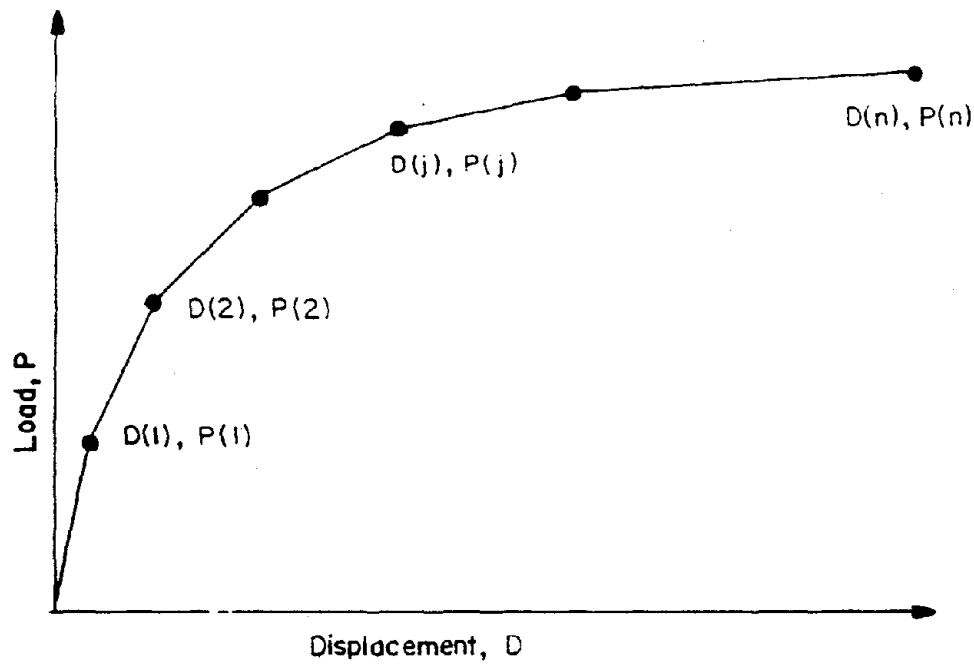

Figure 65. Multiple Segment Backbone Curve

In the elastic range, the wall can experience both loading and unloading. Once the wall has cracked, loading continues on the backbone curve.

Thus the bending hysteresis model rules B1.0 and B1.1 are

Rule B1.0 Elastic behavior

If 1) RULE = 0, and

2) $|P| < Pc$

Then

K = SI

RULE = B1.0

Rule B1.1 Loading on the backbone curve

If 1) (BACKB = true or RULE = 0), and

2) DIR = 1 or DIR = 3

Then

Determine j, such that $PB(j-1) \leq |P| \leq PB(j)$

$$K = \frac{PB(j) - P}{DB(j) - D}$$

A = PB(j)

IR = 0

BACKB = true

RULE = B1.1

BACKB is a logical variable that signifies whether the loading is on the backbone curve, or on a hysteresis loop. The variable A denotes the load where the stiffness will change, if loading continues in the same direction. The variable IR, is a counter for the number of small amplitude loops used by rules B1.5 and B1.11, which is discussed later. Setting IR = 0 signifies that there are no small amplitude loops currently active.

b. Shear Hysteresis Model, Rules S1.0 and S1.1. The shear backbone curve is also similarly divided into a series of piecewise linear segments that join NS points as shown in Figure 65. Define the first point as the shear cracking load, PS(1) = Pc, DB(1) = Dc; P and D represent the shear and shear displacement, respectively, at the current point. Similar to the bending backbone curve, RULE = 0 the first time the hysteresis model is accessed.

For the elastic region, rule S1.0 sets the current shear stiffness, K, to the initial shear stiffness, SI,

$$SI = \frac{Pc}{Dc} \tag{4.2}$$

In the elastic range, the wall can experience both loading and unloading. Once the wall has cracked, loading continues on the backbone curve.

Thus the shear hysteresis rules S1.0 and S1.1 are

Rule S1.0 Elastic behavior
If 1) RULE = 0, and
2) $|P| < Pc$
Then
K = SI
RULE = S1.0

Rule S1.1 Loading on the backbone curve

If 1) (BACKB = true or RULE = 0), and

2) DIR = 1 or DIR = 3

Then

Determine j, such that $PS(j-1) \leq |P| \leq PS(j)$

$$K = \frac{PS(j) - P}{DS(j) - D}$$

$A = PS(j)$

$IR = 0$

BACKB = true

RULE = S1.1

Similar to the bending hysteresis rules B1.0 and B1.1, BACKB is a logical variable that designates loading on the backbone curve. The variable A denotes the load where the stiffness will change if loading continues in the same direction. The variable IR is a counter for the number of small amplitude loops used by rules S1.5 and S1.11, which is discussed later.

2. Unloading in the Nonlinear Range. Typical bending and shear unloading curves for NCKU wall SW1a are shown in Figure 66. The initial unloading range has a high stiffness. As the load decreases, the stiffness also decreases resulting in a nonlinear unloading curve. As the maximum displacement increases, the unloading stiffness decreases. Insight into this nonlinear behavior is gained by examining separate bending and shear unloading mechanisms.

Examine the loaded shear wall in Figure 67 to determine the unloading mechanism for bending deformation. The wall has uniformly distributed longitudinal reinforcing steel. On the right side of the wall concrete is in compression, while steel

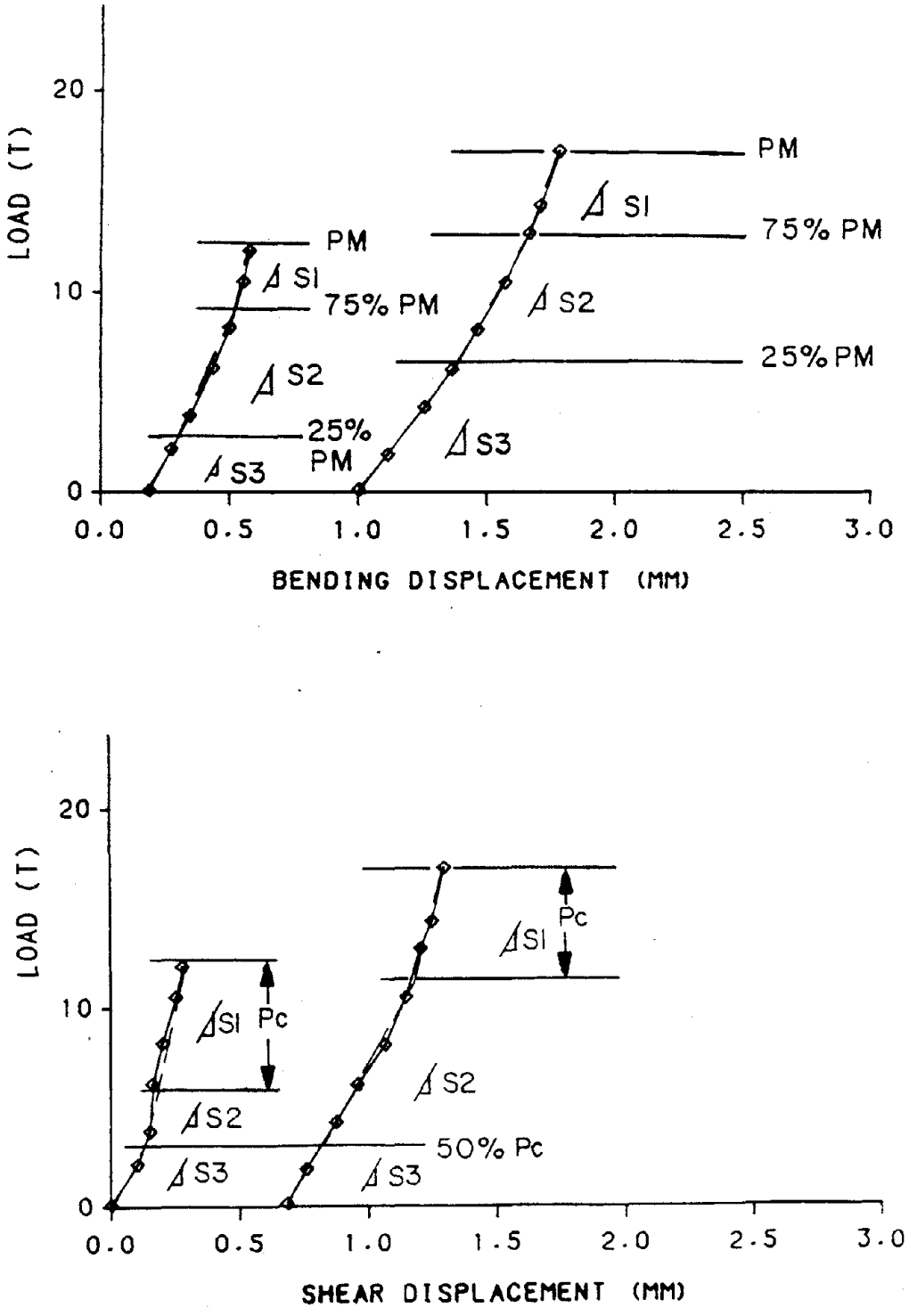

Figure 66. NCKU Wall SW1a, Typical Bending and Shear Unloading Curves

is in tension on the left side of the wall. As the load P is reduced the concrete rebounds. From Karsan and Jirsa's (50) studies on the hysteretic behavior of plain concrete as shown in Figure 68:

- The initial unloading range has a high stiffness.
- As the loading decreases, the stiffness of plain concrete also decreases.
- As the maximum strain increases, the unloading stiffness of plain concrete decreases.

The unloading curve for plain concrete has the same general shape as the unloading curve for bending deformation. Thus the nonlinear unloading curve for bending deformation is partially due to the unloading behavior of concrete.

The steel stress distribution in the loaded wall is not linear. Examine two bars, #1 and #2 in Figure 69a. Before unloading begins bar #1 is in its plastic stage, while bar #2 is elastic as shown in Figure 69b. As the wall is unloaded, bar #1 rebounds to zero stress while the wall still has a positive curvature as shown in Figure 69c. Note that bar #2 still has tensile stress and the unloading path of both bars is linear as shown in Figure 69b. The wall has tension on the left side and compression on the right, thus the moment still is greater than zero. Unloading the wall to zero moment compresses bar #1 as shown in Figure 69d, while bar #2 is in tension and the concrete on the right side is still in compression. Since the unloading path for both bars is linear, the load-deformation relationship due to the steel bars is also linear. Thus while the reinforcing steel unloading stress distribution is interesting, it is not the cause of the nonlinear unloading behavior for bending deformation.

The unloading mechanism for shear deformation is also closely related to the unloading curve for plain concrete. Figure 70 shows a shear wall with shear deformations. The major load resisting mechanism is the concrete struts, parallel to

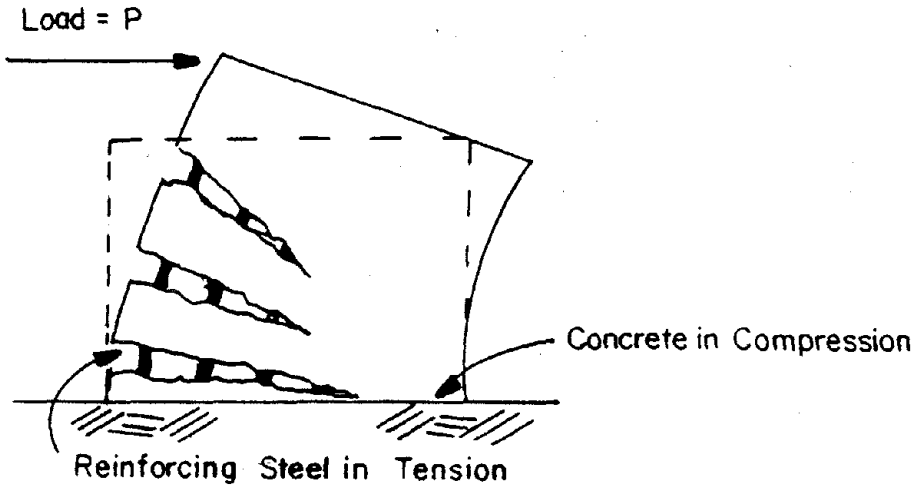

Figure 67. Deformation of a Loaded Shear Wall Due to Bending

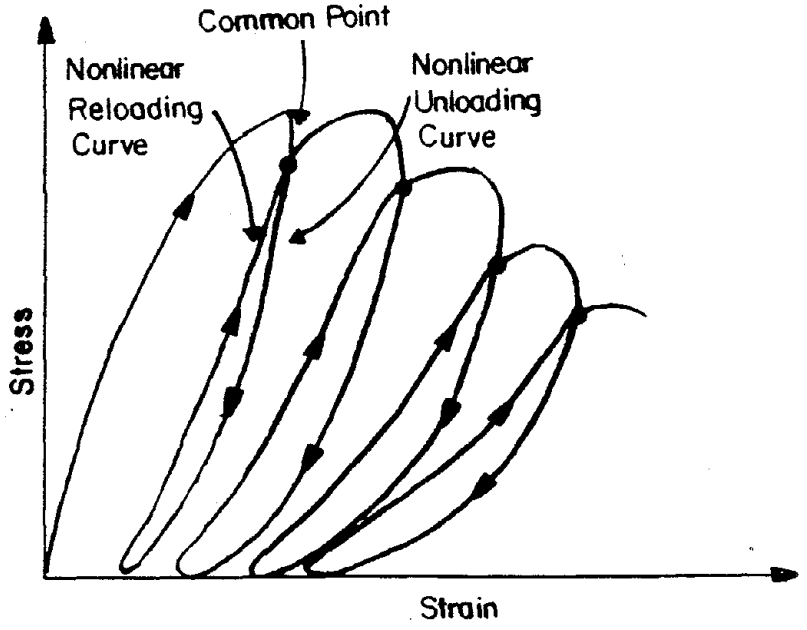

Figure 68. Hysteretic Behavior of Plain Concrete (Ref. 50)

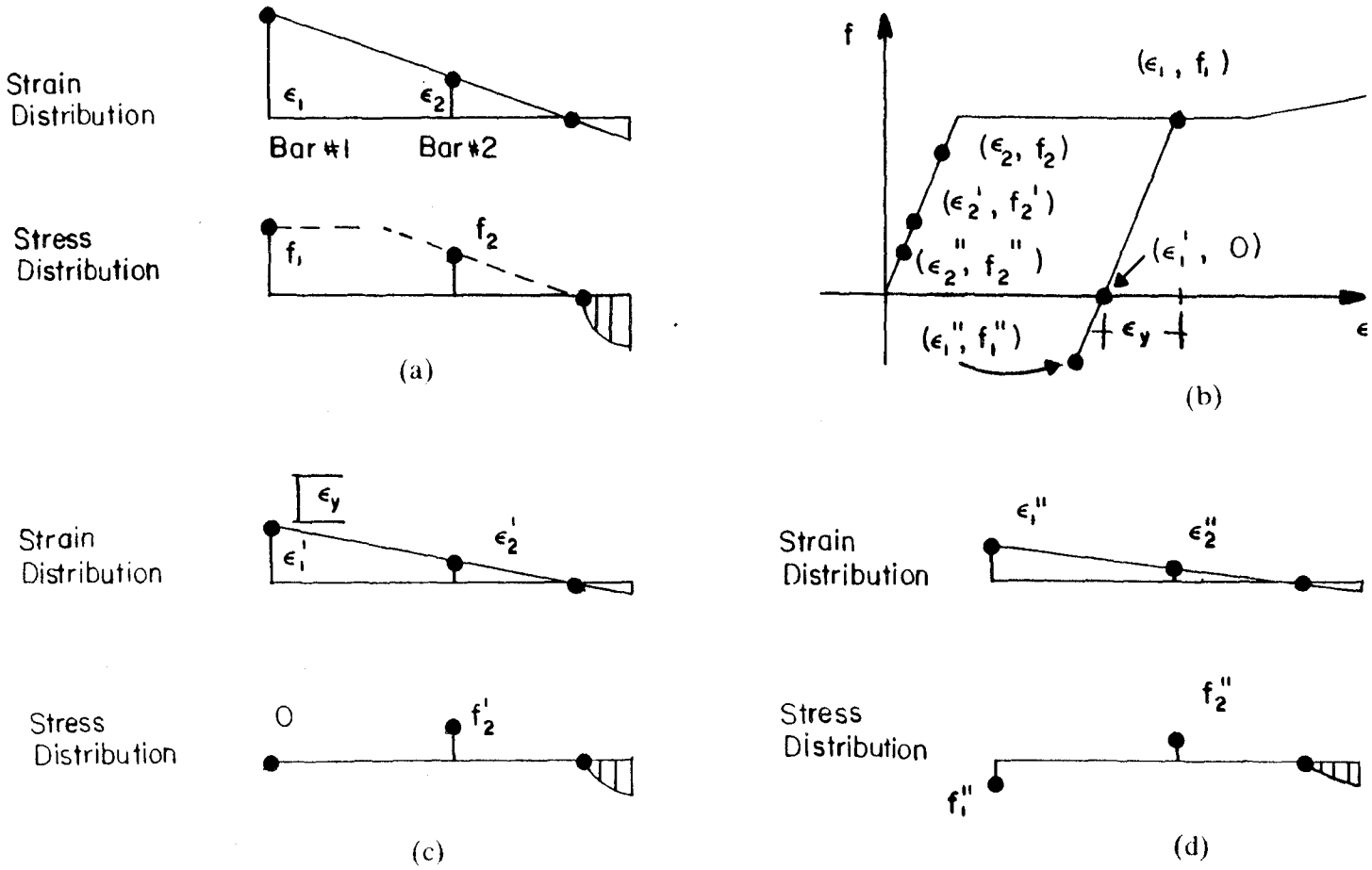

Figure 69. Wall Bending Stress Distribution for Unloading: (a) Strain and Stress Distribution before Unloading (b) Stress-Strain Diagram (c) Strain and Stress Distribution after Partial Unloading (d) Strain and Stress Distribution after Unloading

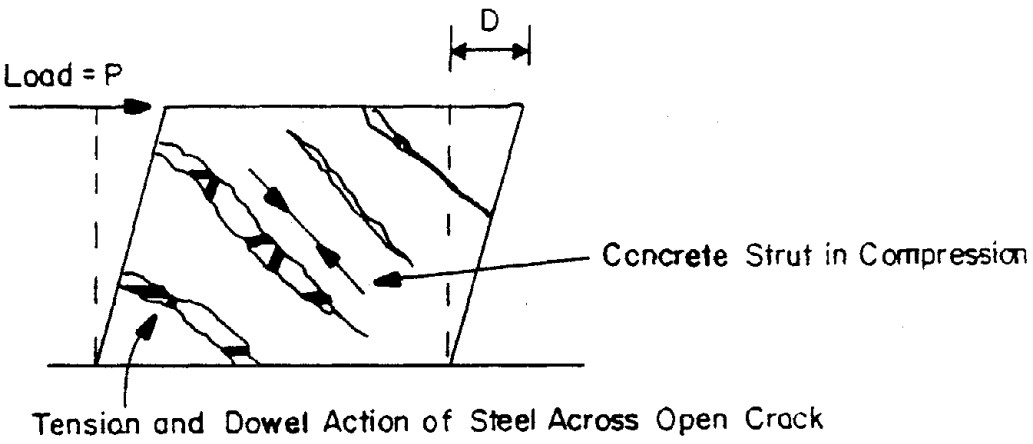

Figure 70. Deformation of a Loaded Shear Wall Due to Shear

the concrete cracks. Tensile steel at an angle to the cracks ties the struts to the base of the wall. As the lateral load is reduced:

- The concrete compression strut will rebound. Recall the unloading curve for plain concrete is nonlinear as shown in Figure 68. The unloading behavior of the wall's shear deformation is similar to the plain concrete behavior.
- The bars across the cracks will rebound. As seen previously, the rebound of all the reinforcement will be linear. Thus the walls rebound due to steel will also be linear.

Therefore, the unloading mechanism for shear deformation is primarily due to concrete rebound.

The unloading mechanism for combined shear and bending deformations is more complicated than the simple bending and shear mechanisms presented above. Two of the complicating factors are:

- The same concrete must act as both the compression strut, and as a compression element for bending. Thus the concrete is in a state of biaxial stress. Recall the plain concrete stress-strain model as shown in Figure 68 is for uniaxial stress.
- As the wall is unloaded, the cracks close. Since concrete expands under shear strains, the cracks will close at a larger tensile strain than they opened at. Thus, the stress distribution in Figure 69d will be altered.

Until reliable biaxial cyclic stress-strain models are developed, and the crack closing point can be accounted for, it is not feasible to quantitatively calculate the actual unloading curve.

Thus, an empirical unloading curve for both hysteresis models is developed with the following attributes:

- The unloading stiffness decreases with the load level. This requirement precludes the use of a single linear unloading curve.

- The amount of rebound increases with the maximum past displacement. This is because the rebounding mechanism is dependent on the strain level, which increases with the maximum past displacement.
- To provide continuity with the elastic case, the unloading stiffness near the cracking load and displacement is approximately SI.

a. Bending Hysteresis Model, Rules B1.2, B1.3, and B1.4. The semi-empirical bending unloading curve is a set of three linear segments, with stiffness S1, S2, and S3 as shown in Figure 71. The limiting case for the unloading stiffnesses is shown in Figure 72, and will be discussed later. The break points between the linear segments of 75% PM and 25% PM were chosen by inspection. Linear segments were fitted to the test data for walls SW1a, SW4a and SW5 as shown in Figure 66. Experimental stiffnesses were determined, and normalized by dividing by the initial stiffness. The shape of the unloading curves is similar for both positive and negative loadings, even when the loading pattern is non-symmetrical. Thus, the maximum absolute value of past displacement, in either direction, Dmax, is used to determine the unloading stiffnesses. Dmax is also normalized by dividing by the cracking displacement. The unloading stiffnesses, S1, S2, and S3 were obtained by curve fitting, as shown in Figures 73 through 75.

$$S1 = SI\left(\frac{Dc}{Dmax}\right)^{0.294} \tag{4.3}$$

$$S2 = SI\left(\frac{0.8344\ Dc}{Dmax} + 0.1656\right) \tag{4.4}$$

$$S3 = SI\left(\frac{0.9092\ Dc}{Dmax} + 0.0908\right) \tag{4.5}$$

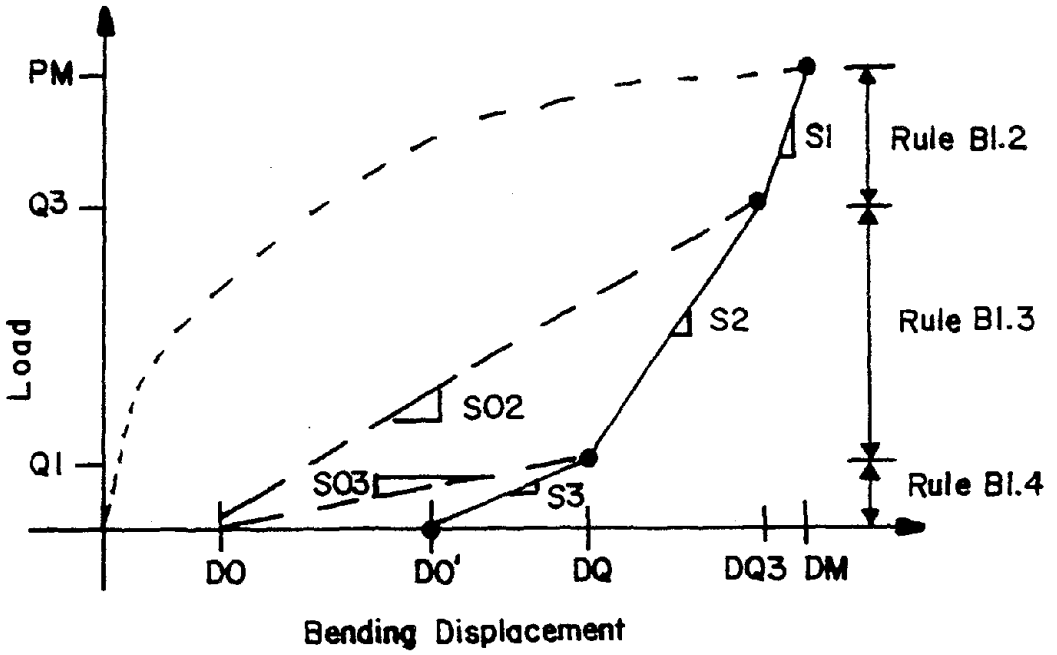

Figure 71. Bending Hysteresis Model, Rules B1.2, B1.3 and B1.4

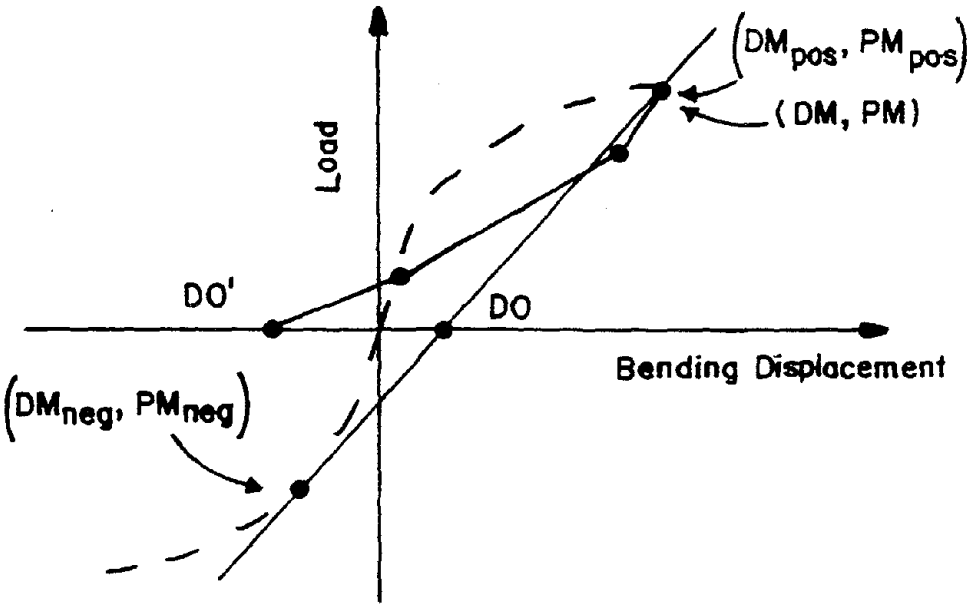

Figure 72. Bending Hysteresis Model, Special Case for Unloading

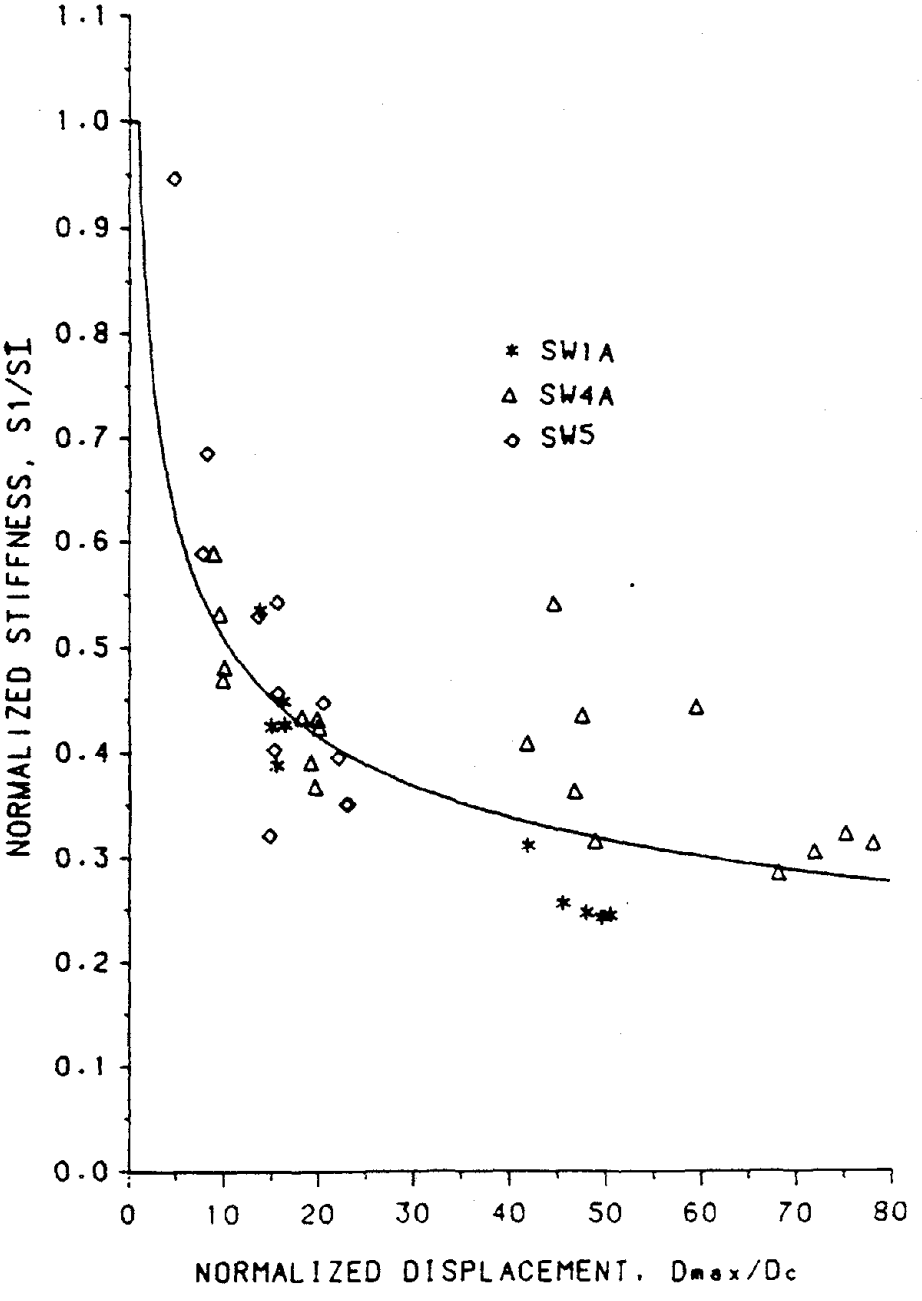

Figure 73. Bending Unloading Stiffness, S1

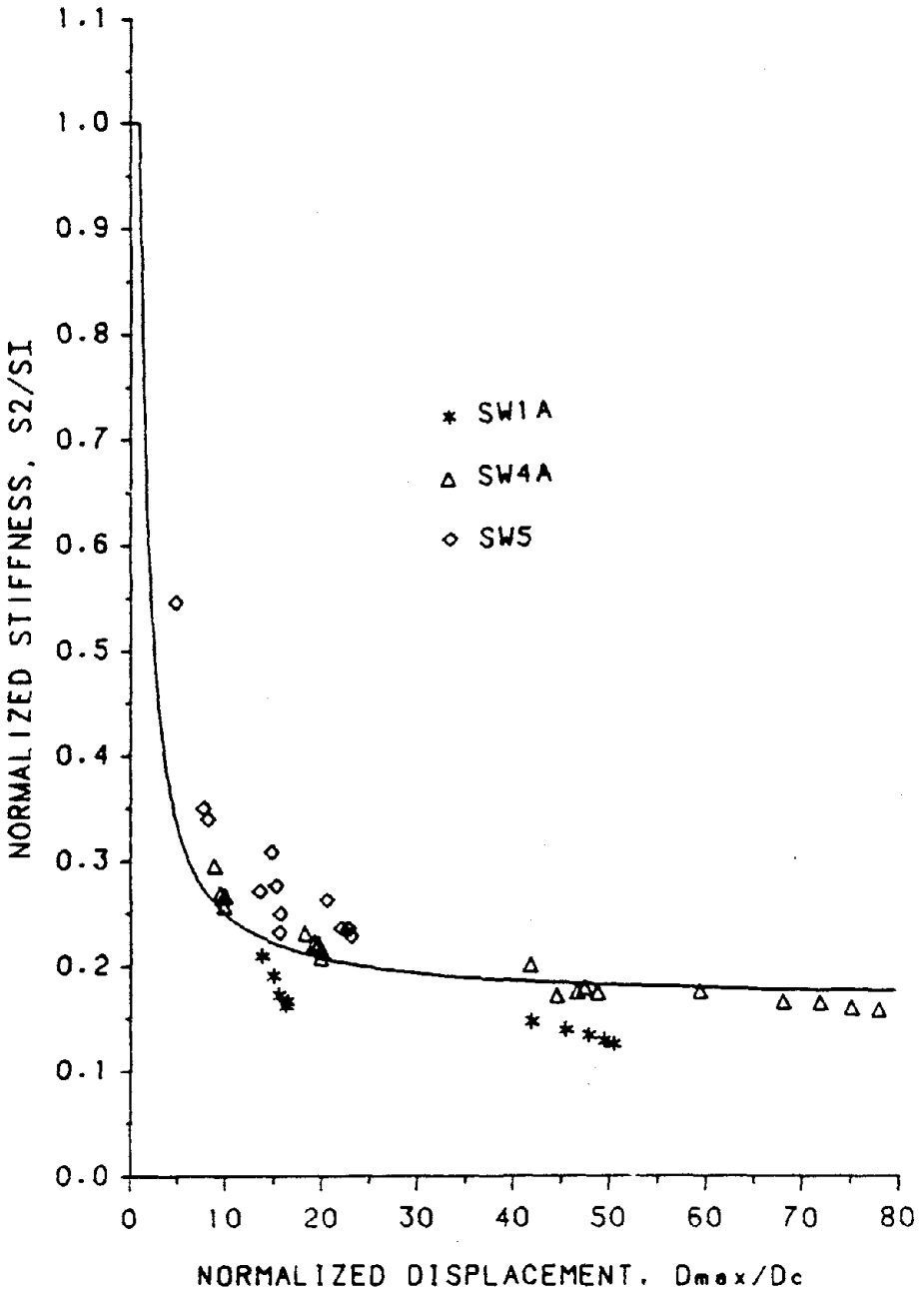

Figure 74. Bending Unloading Stiffness, S2

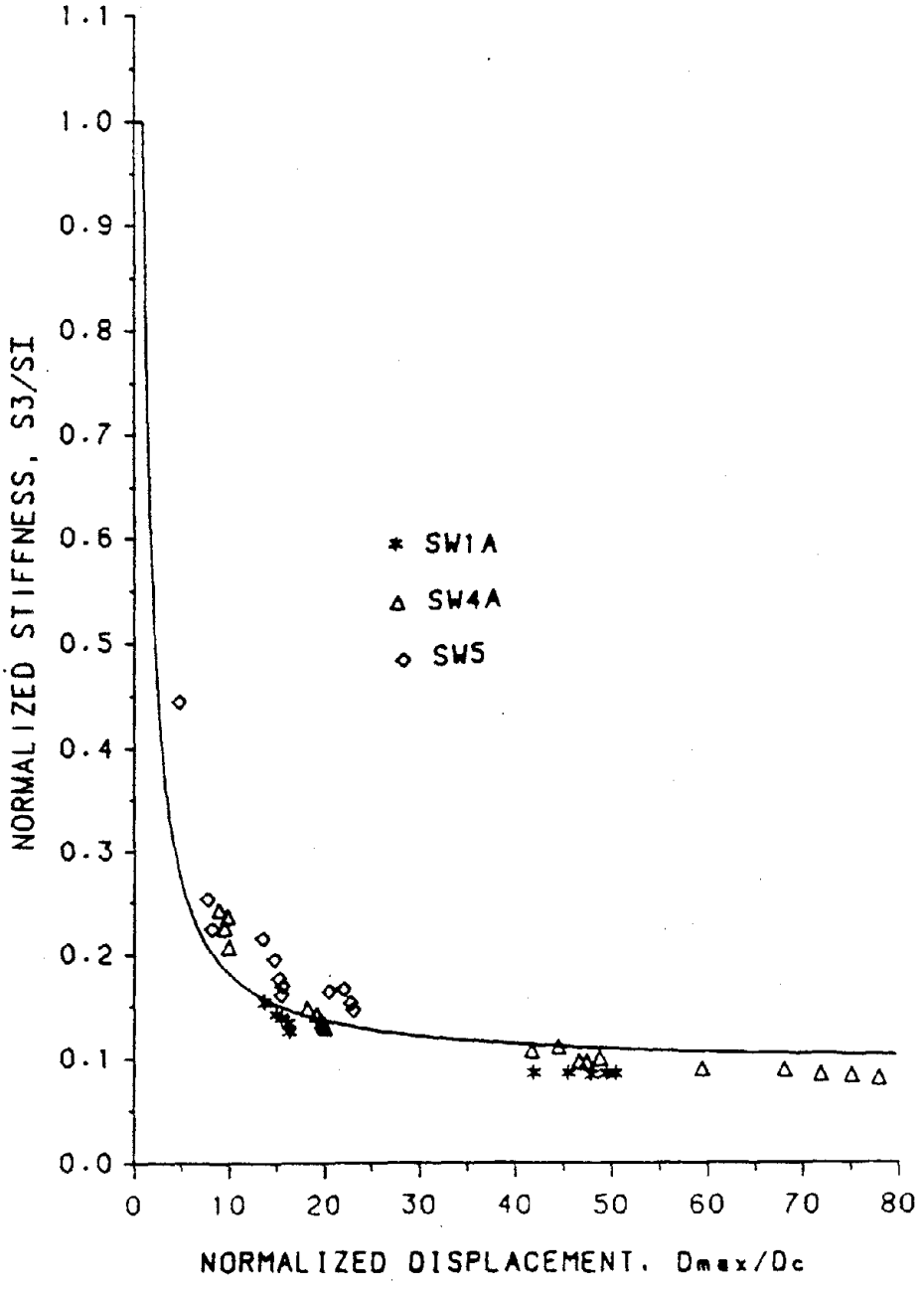

Figure 75. Bending Unloading Stiffness, S3

Note that while the test data has considerable scatter, the empirical relationships for S1, S2, and S3 capture the trends of the test data.

Define the load and displacement at 75% of the maximum past load as

$$Q3 = 75\%\ PM \qquad DQ3 = DM - \frac{25\%\ PM}{S1} \tag{4.6}$$

where PM and DM are the maximum past load and displacement in the current direction as shown in Figure 71. PM and DM may be either positive or negative. The load and displacement at 25% of the maximum past load is

$$Q1 = 25\%\ PM \qquad DQ1 = DQ3 - \frac{50\%\ PM}{S2} \tag{4.7}$$

and the displacement at zero load is

$$D0' = DQ3 - \frac{25\%\ PM}{S3} \tag{4.8}$$

The unloading stiffnesses in Equations 4.3, 4.4 and 4.5 do not guarantee that the sign of the zero load displacement, D0', is the same as the sign of the maximum past displacement, DM, as shown in Figure 72. This type of behavior was not observed in the experimental data. Thus the unloading stiffness is restricted such that $D0' \geq D0$ when unloading from positive loads, and $D0' \leq D0$ when unloading from negative loads. D0 is the displacement intercept of a line connecting the peak displacements of both the positive and negative loadings, and is given by

$$D0 = DM - PM\frac{DM_{pos} - DM_{neg}}{PM_{pos} - PM_{neg}} \tag{4.9}$$

where (DM_{pos}, PM_{pos}) are the maximum past displacement and load for positive loading, and (DM_{neg}, PM_{neg}) are the maximum past displacement and load for

negative loading. The inequalities (D0′≥D0: positive unloading, D0′≤D0: negative unloading) are satisfied by limiting the unloading stiffnesses S2 and S3. Define the limiting slope between (DQ3, Q3) and (D0, 0) as

$$S02 = \frac{Q3}{DQ3 - D0} \qquad SI \geq S02 \geq 0 \tag{4.10}$$

and the limiting slope between (DQ1, Q1) and (D0, 0) as

$$S03 = \frac{Q1}{DQ1 - D0} \qquad SI \geq S03 \geq 0 \tag{4.11}$$

Initially, set SU = 0. This is a limiting stiffness that is determined by the small amplitude rule, B1.5 and is discussed later.

Thus, rules B1.2, B1.3, and B1.4 are

Rule B1.2 Unloading above 75% PM

If 1) (DIR = 2 or DIR = 4), and

2) |P| ≥ |Q3|, and

3) IR = 0

Then

K = max(S1, SU)

A = Q3

RULE = B1.2

Rule B1.3 Unloading between 75% and 25% PM

If 1) (DIR = 2 or DIR = 4), and

2) $|Q3| \geq |P| \geq |Q1|$, and

3) IR = 0

Then

K = max(S2, S02, SU)

A = Q1

RULE = B1.3

Rule B1.4 Unloading below 25% PM

If 1) (DIR = 2 or DIR = 4), and

2) $|Q1| \geq |P|$, and

3) IR = 0

Then

K = max(S3, S03, SU)

A = 0

RULE = B1.4

b. Shear Hysteresis Model, Rules S1.2, S1.3 and S1.4. The semi-empirical shear unloading curve may be either bilinear or trilinear depending on the maximum previous loading. When the maximum past load in the current direction is between Pc and 150% Pc the unloading curve is bilinear as shown in Figure 76. The first segment is described by rule S1.2, has a stiffness of S1, and acts over the load range of Pc. The second segment is described by rule S1.4, has a stiffness of S3, and acts over the remainder of the load.

When the maximum past load is greater than 150% Pc, the unloading curve is trilinear as shown in Figure 76. The first segment is described by rule S1.2, has a

stiffness of S1, and acts over the load range of Pc. The second segment is described by rule S1.3, has a stiffness of S2, and unloads to 50% Pc. The third segment is described by rule S1.4, has a stiffness of S3, and acts over the remainder of the load. A special case of the unloading rules is shown in Figure 77 and is discussed later.

The unloading stiffness for S1, S2 and S3 are obtained by curve fitting experimental data for NCKU walls SW1a, SW3, SW4a, SW5 and SW6 as shown in Figures 78, 79, and 80. The shape of the unloading curves is similar for positive and negative loadings, even when the loading pattern is non-symmetric. Thus, the maximum absolute value of the past displacement, Dmax, in either direction, is used to determine S1, S2 and S3. The expressions for the unloading stiffnesses are

$$S1 = 1.4675\ SI\left(\frac{Dc}{Dmax}\right)^{0.343} \le SI \tag{4.12}$$

$$S2 = .7761\ SI\left(\frac{Dc}{Dmax}\right)^{0.3195} \tag{4.13}$$

$$S3 = SI\left(.0707 + \frac{1.369\ Dc}{Dmax}\right) \le SI \tag{4.14}$$

Similar to the unloading bending stiffness, the unloading shear stiffness has been normalized with respect to the initial stiffness and Dmax has been normalized with respect to the cracking displacement.

When unloading with a positive load, DIR = 2, define point 'A' between S1 and S2, and point 'B' between S2 and S3 as

$$\begin{aligned} PA &= PM - Pc & DA &= DM - \frac{Pc}{S1} \\ PB &= \min(PA, \frac{Pc}{2}) & DB &= DA - \frac{PA - PB}{S2} \end{aligned} \tag{4.15}$$

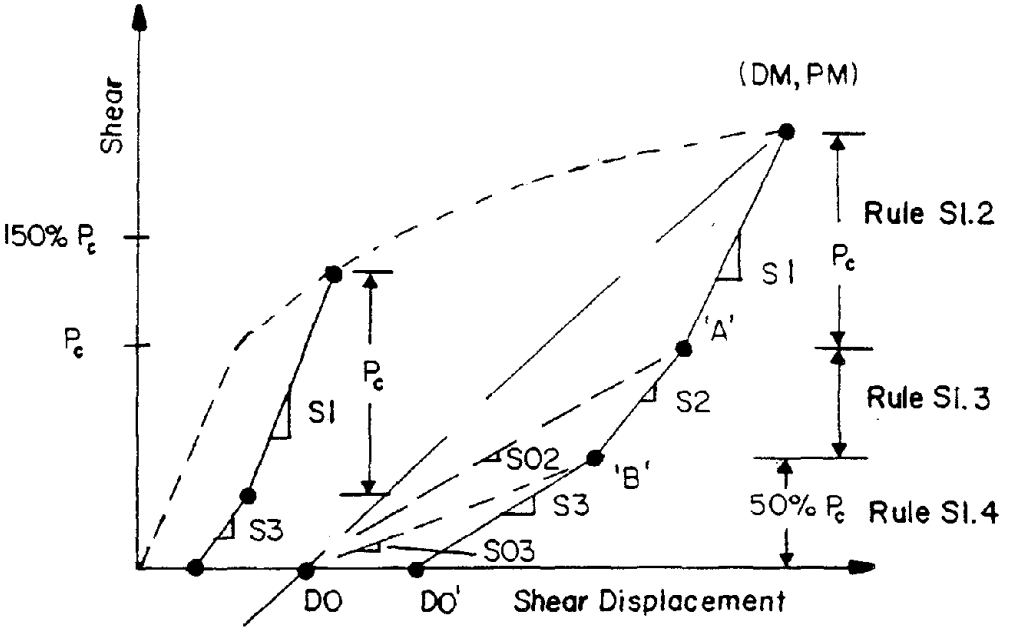

Figure 76. Shear Hysteresis Model, Rules S1.2, S1.3 and S1.4

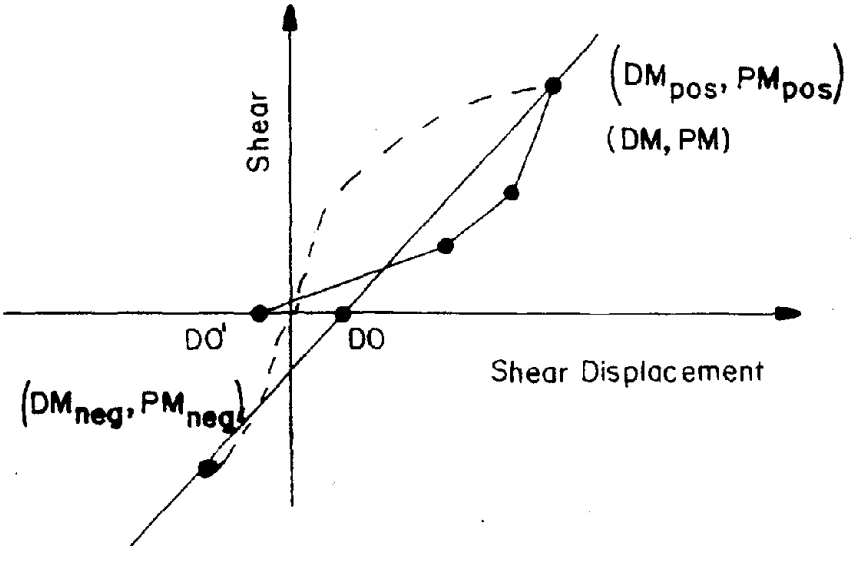

Figure 77. Shear Hysteresis Model, Special Case for Unloading

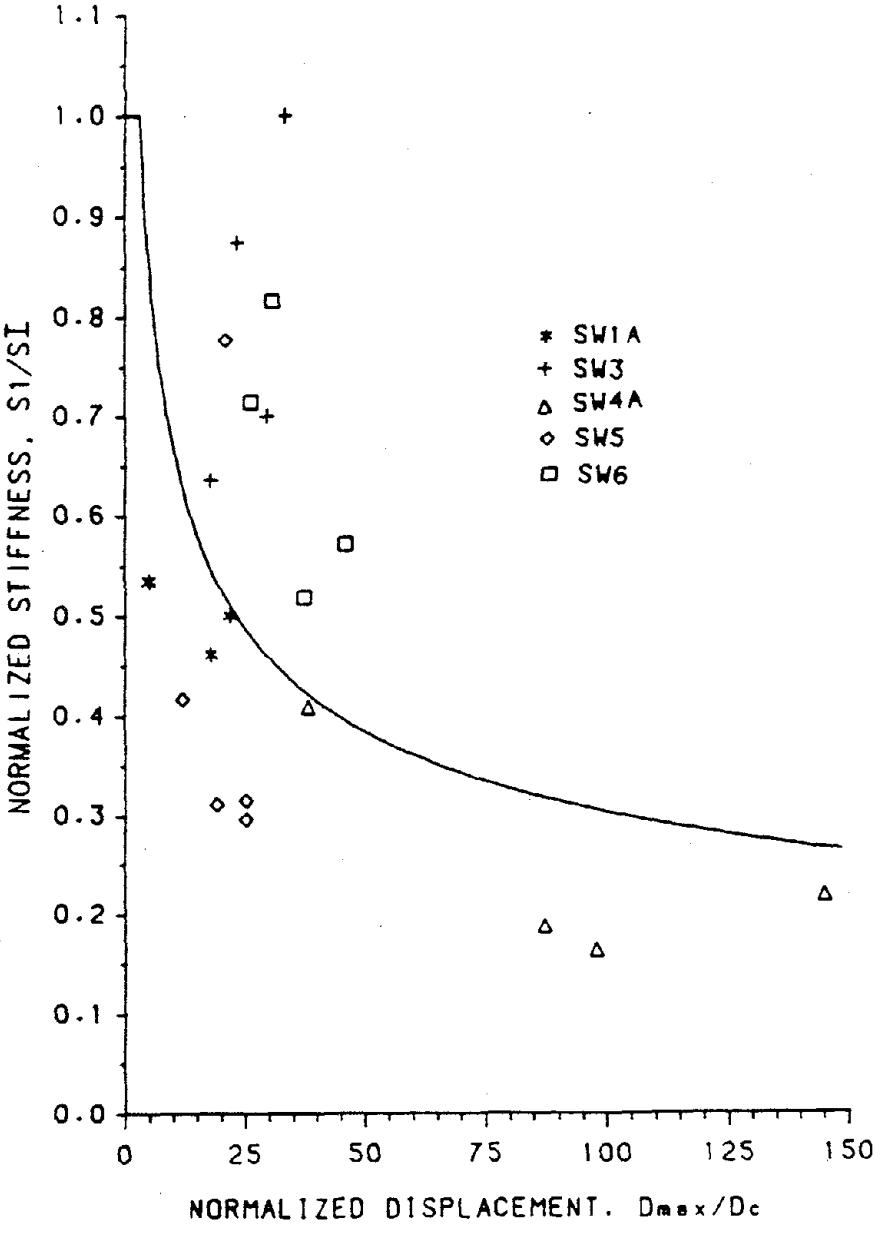

Figure 78. Shear Unloading Stiffness, S1

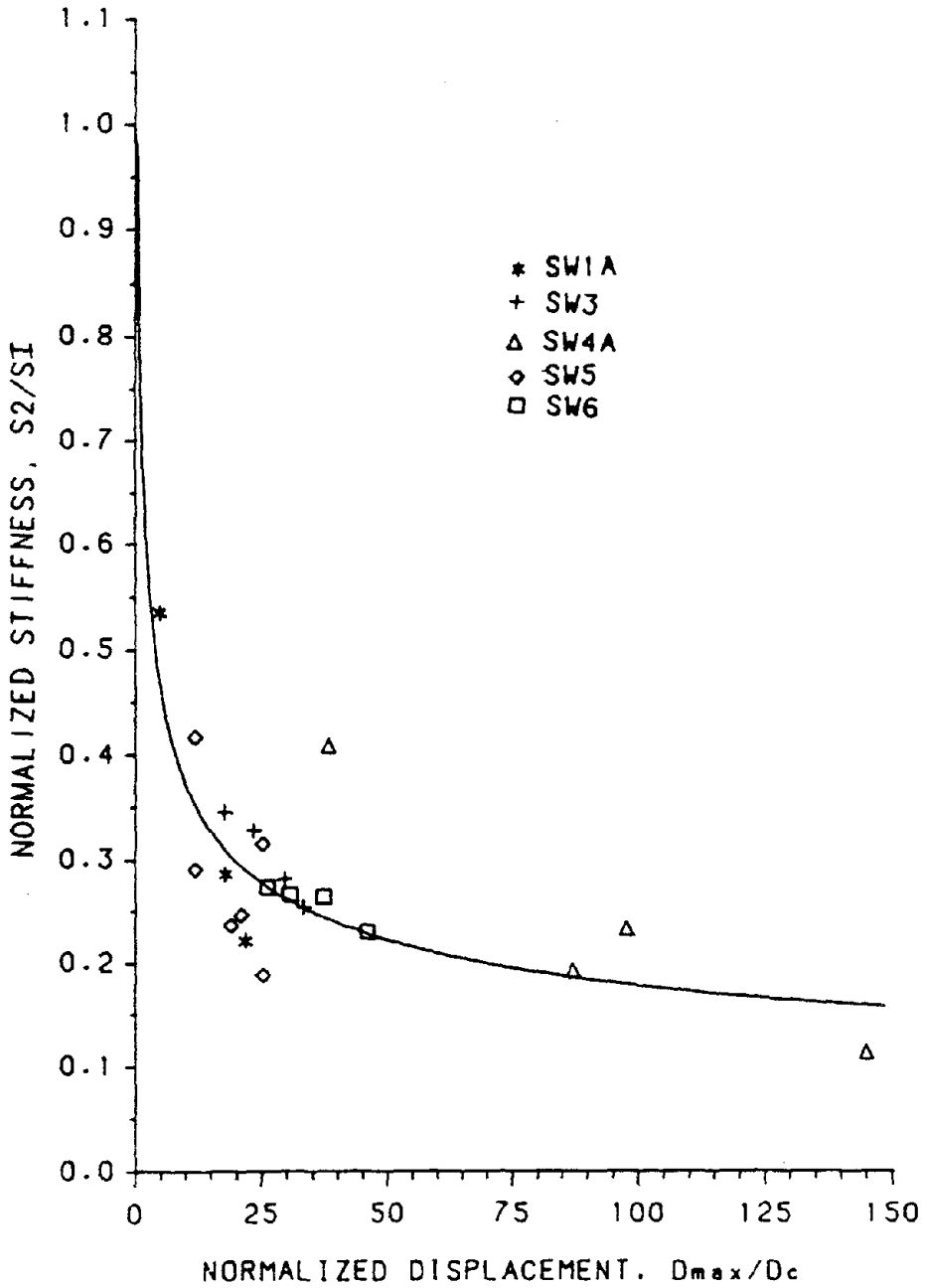

Figure 79. Shear Unloading Stiffness, S2

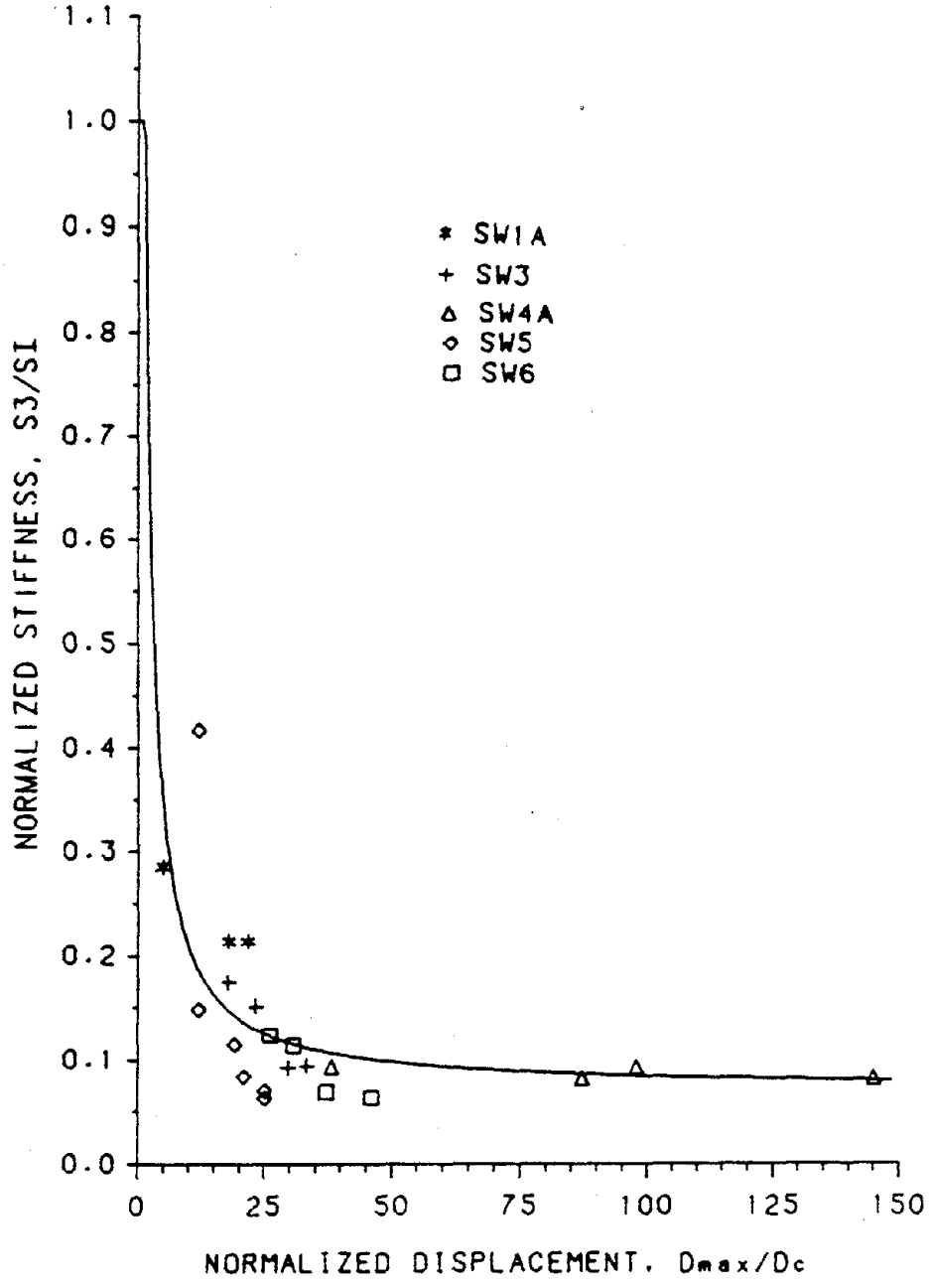

Figure 80. Shear Unloading Stiffness, S3

where points 'A' and 'B' are shown in Figure 76. When unloading with a negative load, DIR = 4, define points 'A' and 'B' as

$$PA = PM + Pc \qquad DA = DM + \frac{Pc}{S1}$$
$$PB = \max(PA, \frac{-Pc}{2}) \qquad DB = DA - \frac{PA - PB}{S2} \tag{4.16}$$

The displacement at zero load, D0' is

$$D0' = DB - \frac{PB}{S3} \tag{4.17}$$

Similar to the bending unloading rules, the unloading stiffnesses in Equations 4.12, 4.13 and 4.14 do not guarantee that the sign of the zero load displacement, D0', is the same as the sign of the maximum past displacement, DM, as shown in Figure 77. This type of behavior was not observed in the experimental data. Thus the unloading stiffness is restricted such that $D0' \geq D0$ when unloading from positive loads, and $D0' \leq D0$ when unloading from negative loads. D0 is the displacement intercept of a line containing the peak displacements of both the positive and negative loadings, and is given by

$$D0 = DM - PM\left(\frac{DM_{pos} - DM_{neg}}{PM_{pos} - PM_{neg}}\right) \tag{4.18}$$

where (DM_{pos}, PM_{pos}) are the maximum past displacement and load for positive loading, and (DM_{neg}, PM_{neg}) are the maximum past displacement and load for negative loading. The inequalities ($D0' \geq D0$: positive unloading, $D0' \leq D0$: negative unloading) are satisfied by limiting the unloading stiffnesses S2 and S3. The limiting stiffness between points 'A' and (D0,0) is

$$S02 = \frac{PA}{DA - D0}, \qquad SI \geq S02 > 0 \tag{4.19}$$

and the limiting stiffness between points 'B' and (D0,0) is

$$S03 = \frac{PB}{DB - D0}, \qquad SI \geq S03 > 0 \tag{4.20}$$

Initially, set SU = 0. SU is a limiting stiffness used by the small amplitude loops in rules S1.5 and S1.11.

Thus, the shear hysteresis rules S1.2, S1.3 and S1.4 are

Rule S1.2 Unloading between PM and PA

If 1) (DIR = 2 or DIR = 4), and
2) |P| > |PA|, and
3) IR = 0

Then
K = max(S1, SU)
A = PA
RULE = S1.2

Rule S1.3 Unloading between PA and PB

If 1) (DIR = 2 or DIR = 4), and
2) |PA| ≥ |P| > |PB|, and
3) IR = 0

Then
K = max(S2, S02, SU)
A = PB
RULE = S1.3

Rule S1.4 Unloading below PB

If 1) (DIR = 2 or DIR = 4), and

2) $|PB| \geq |P|$, and

3) IR = 0

Then

K = max (S3, S03)

A = 0

RULE = S1.4

3. Reloading after Unloading from the Same Direction. Several typical bending and shear reloading curves for NCKU wall SW4a are shown in Figure 81. Initially, these curves have a high stiffness. As the reloading progresses, the stiffness decreases. At a point near the maximum previous load, the unloading curve and the reloading curves intersect. The reloading mechanisms for both bending and shear deformations are similar to the unloading mechanisms.

Consider the bending deformation of the wall in Figure 82. After unloading and prior to reloading, the wall has 1) steel and concrete in compression at opposite edges of the wall, 2) steel in tension in the center of the wall, and 3) existing flexural cracks. As the lateral load, P, is reapplied from the zero loading position, the concrete on the compression side of the wall is reloaded. Again, refer to the concrete reloading behavior of plain concrete as shown in Figure 68. Initially, the concrete reloading branch has a high initial stiffness. As reloading progresses, the concrete stiffness decreases. At a load level near the previous maximum past load, the reloading and unloading branches intersect. This intersection is called the 'common point' (50). The behavior of the bending curve's reloading branch is similar to the reloading branch for plain concrete.

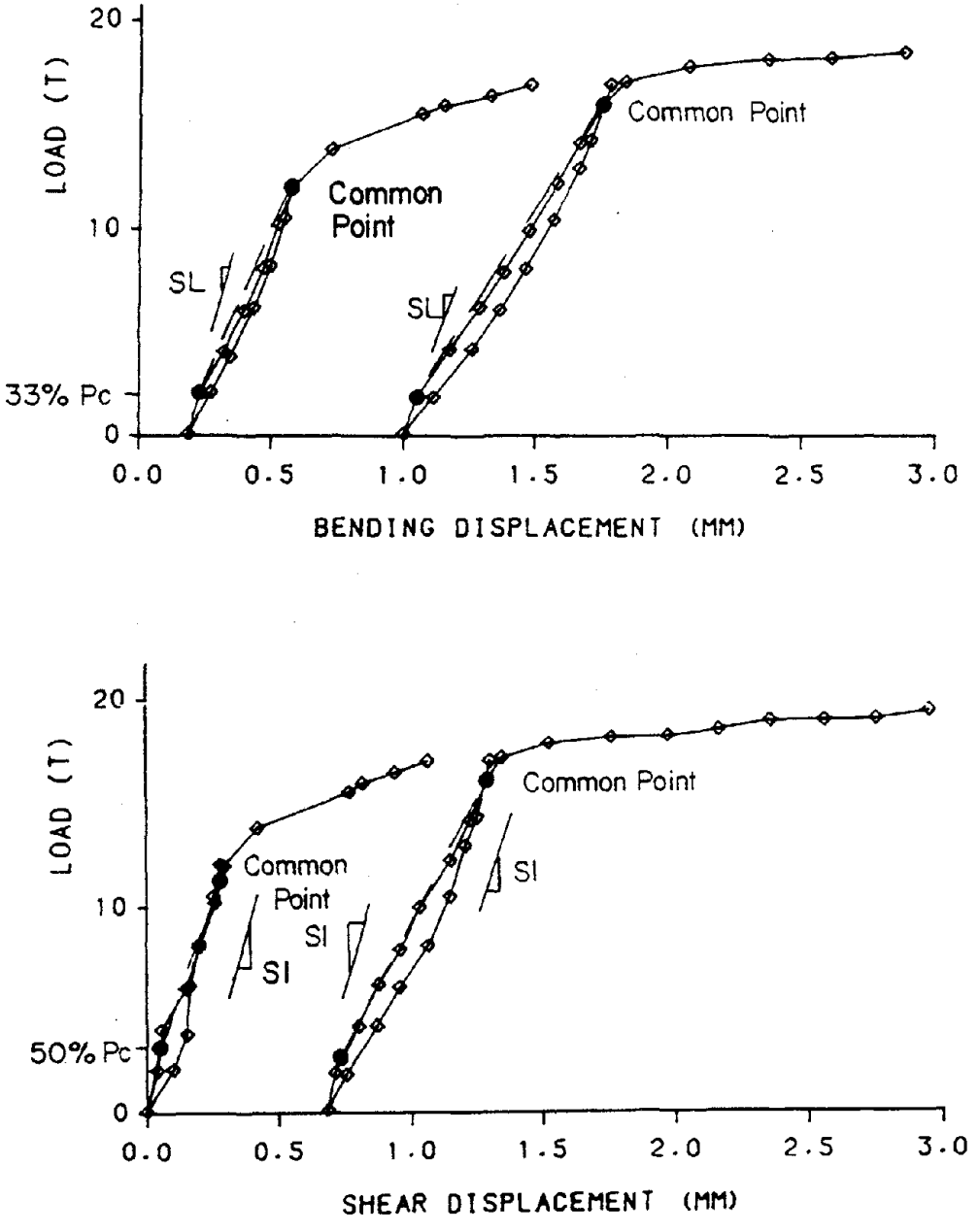

Figure 81. NCKU Wall SW1a, Typical Bending and Shear Reloading Curves

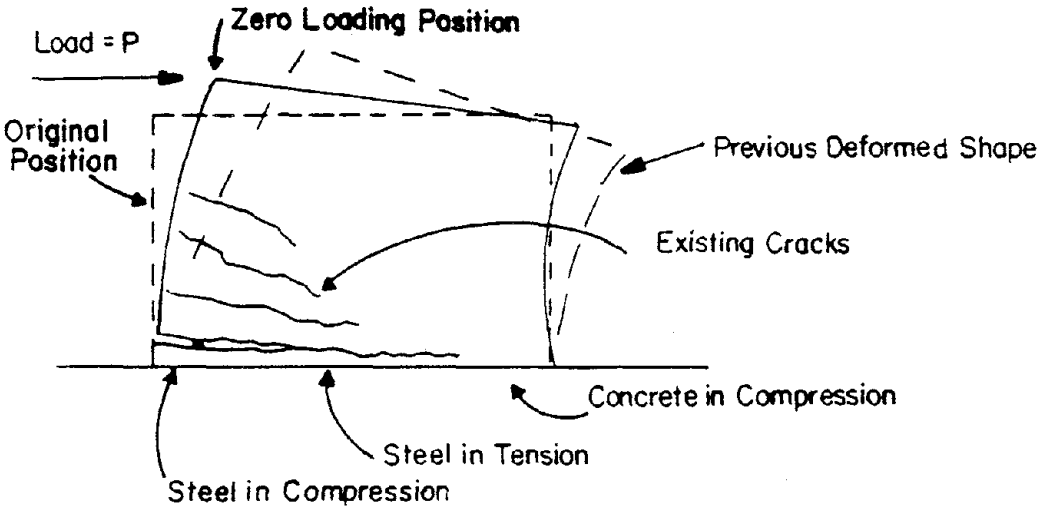

Figure 82. Deformation of an Unloaded Shear Wall Due to Bending

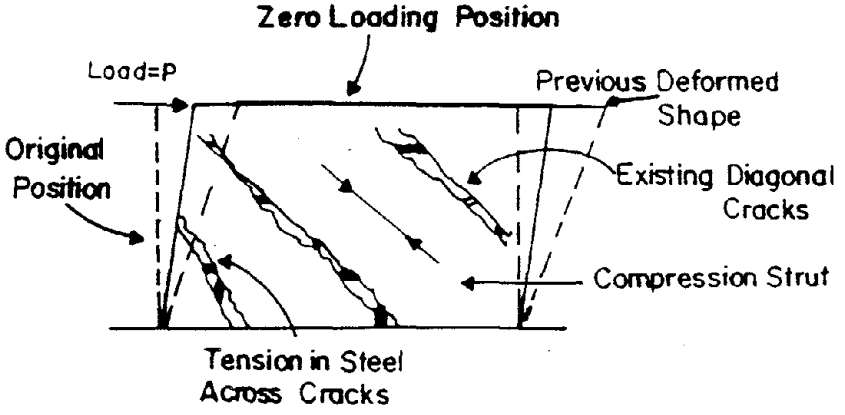

Figure 83. Deformation of an Unloaded Shear Wall Due to Shear

Likewise, consider the shear deformation of a wall subject to reloading in Figure 83. Prior to reloading, diagonal cracks exist in the wall. As the wall is reloaded, the concrete compression strut resists the applied shear. The stiffness of this strut is similar to plain concrete upon reloading, as shown in Figure 68. As previously discussed, plain concrete upon reloading has a high initial stiffness, which decreases with applied load. At the common point, the unloading and loading branches intersect. Again the behavior of the shear deformation mechanism is similar to the behavior of plain concrete.

It can be qualitatively shown that the bending and shear deformation reloading curves are nonlinear, with a high initial stiffness that decreases with reloading. However, a good quantitative model is not available due to uncertainties in material models, crack width and distribution, and the interaction between shear and bending. Thus an empirical reloading curve is used for the bending and shear hysteresis models.

a. Bending Hysteresis Model Rules B1.6 and B1.7. The reloading curve as shown in Figure 84 consists of two linear segments. The lower segment is defined in the bending hysteresis model by rule B1.6, and has a stiffness SL, that was empirically determined by examining walls SW1a and SW4a as shown in Figure 85.

$$SL = SI\left(\frac{Dc}{Dmax}\right)^{0.285} \tag{4.21}$$

Similar to S1, S2 and S3, SL is a function of the maximum past displacement in either direction and is also normalized with respect to SI and Dc. While the test data has considerable scatter, SL captures the trend of the data.

The stiffness SL terminates at 33% Pc. The coordinates of this point are (DC3, PC3). For reloading with a positive load, DIR = 1,

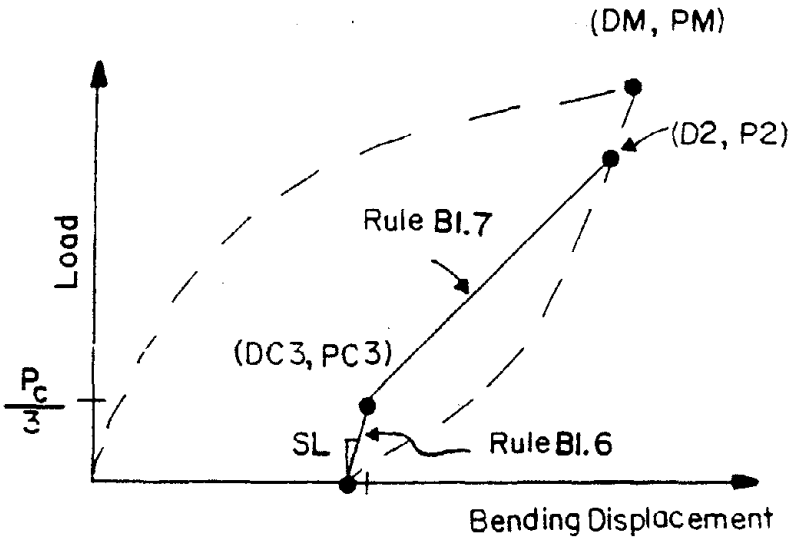

Figure 84. Bending Hysteresis Model, Rules B1.6 and B1.7

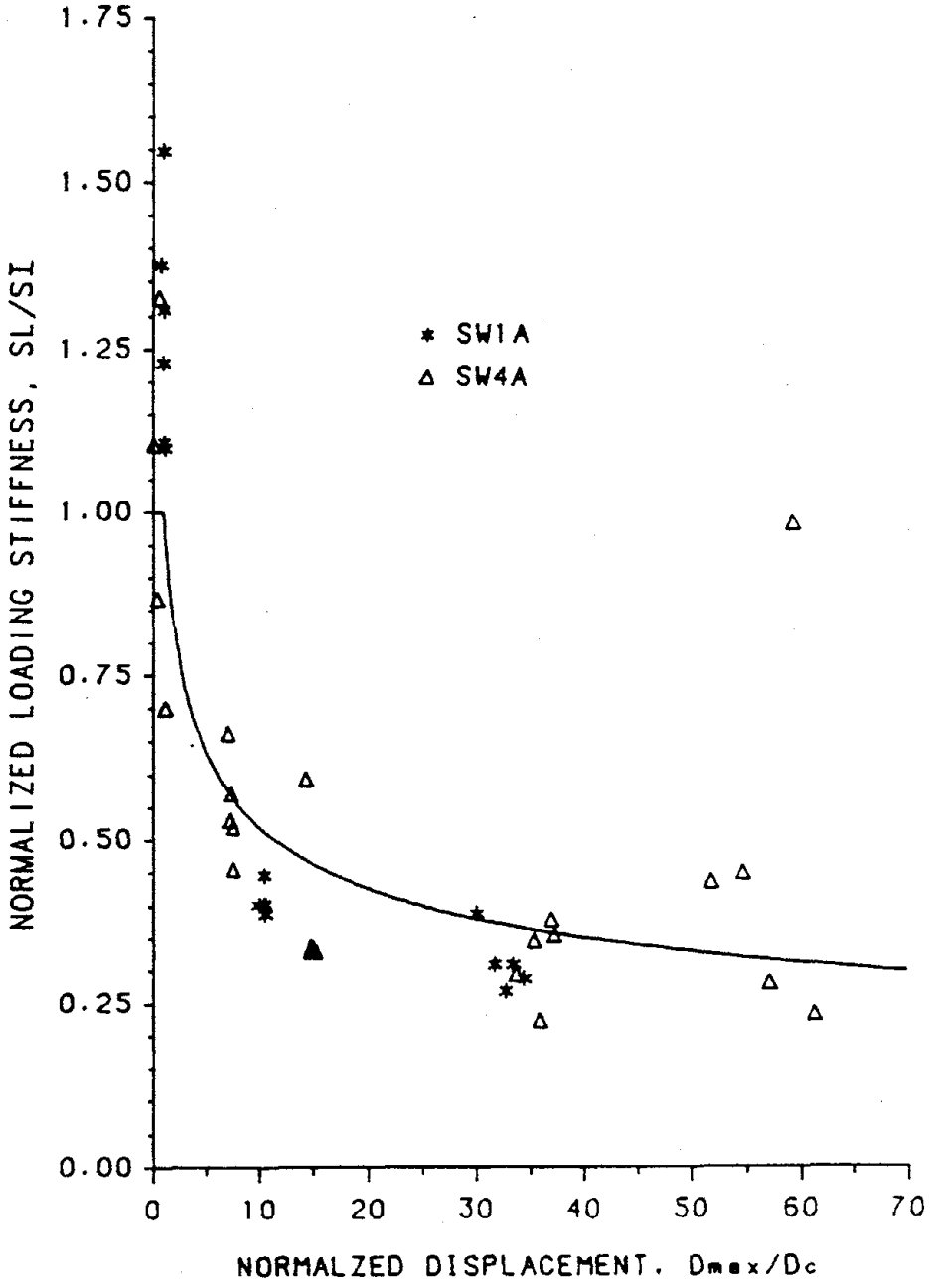

Figure 85. Bending Reloading Stiffness, SL

$$PC3 = \frac{Pc}{3} \qquad DC3 = \max(D0', D0) + \frac{PC3}{SL} \tag{4.22}$$

and for reloading with a negative load, DIR = 3,

$$PC3 = \frac{-Pc}{3} \qquad DC3 = \min(D0', D0) + \frac{PC3}{SL} \tag{4.23}$$

where D0′ and D0 were calculated by rules B1.2, B1.3 and B1.4, Equations 4.8 and 4.9.

The loading and unloading curves were observed to intersect near 95% of the previous maximum load. This 'common point' has the coordinates (D2,P2),

$$P2 = 95\%\ PM, \qquad D2 = DM - \frac{5\%\ PM}{S1} \tag{4.24}$$

where S1 is the unloading stiffness for rule B1.2, Equation 4.3. If the wall is uncracked in the current direction then the common point is equal to the crack point

$$\text{If} |DM| \le Dc \text{ then} \qquad P2 = Pc, \qquad D2 = Dc \tag{4.25}$$

The upper segment of the reloading curve connects the terminal end of the lower segment and the common point, and is defined in the bending hysteresis model by rule B1.7.

Thus the bending hysteresis model reloading rules B1.6 and B1.7 are

Rule B1.6 Reloading below Pc after unloading from the same direction

If 1) [(DIR = 1 and DIRL = 2) or (DIR = 3 and DIRL = 4)], and

2) |P| < |PC3|, and

3) IR = 0

Then

K = SL

A = PC3

RULE = B1.6

Rule B1.7 Reloading towards the common point

If 1) (DIR = 1 or DIR = 3), and

2) |PC3| ≤ |P| ≤ |P2|, and

3) IR = 0

Then

$$K = \frac{P - P2}{D - D2}$$

A = P2

RULE = B1.7

b. Shear Hysteresis Model, Rules S1.6 and S1.7. The shear reloading curve is also represented by two linear segments. Inspecting the test data reveals that the stiffness of the lower segment is similar to the unloading stiffness S1, acting over a load range of 50% Pc. This segment is represented by rule S1.6 as shown in Figure 86. The coordinates of its terminal point, for positive reloadings, are given by

$$PC2 = 50\%\ Pc \qquad DC2 = \max(D0', D0) + \frac{PC2}{S1} \tag{4.26}$$

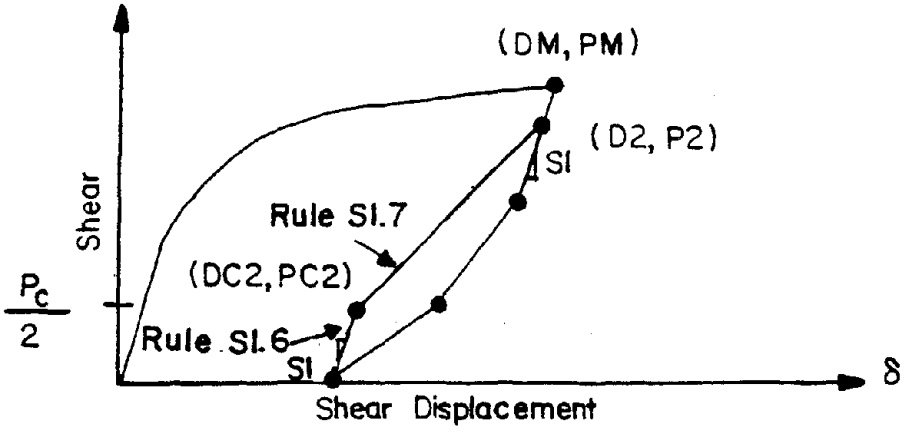

Figure 86. Shear Hysteresis Model, Rules S1.6 and S1.7

and for negative reloadings, are given by

$$PC2 = -50\%\ Pc \qquad DC2 = \min(D0', D0) + \frac{PC2}{S1} \tag{4.27}$$

where D0', D0 and S1, defined by rules S1.2, S1.3 and S1.4, were expressed in Equations 4.17, 4.18 and 4.12, respectively.

Similar to the bending hysteresis model, the common point is observed to be at 95% of the past maximum load. Let the coordinates (D2, P2) designate the common point, where

$$P2 = 95\%\ PM, \qquad D2 = DM - \frac{5\%\ PM}{S1} \tag{4.28}$$

If the wall is uncracked in the current direction, then the common point is equal to the crack point

$$\text{If } |DM| \le Dc \text{ then } \quad P2 = Pc, \quad D2 = Dc \tag{4.29}$$

The second segment, represented by rule S1.7, loads to the common point as shown in Figure 86.

Thus the shear hysteresis model rules S1.6 and S1.7 are

Rule S1.6 Reloading below 50% Pc after unloading from the same direction

If 1) [(DIR = 1 and DIRL = 2) or (DIR = 3 and DIRL = 4)], and
2) |P| < |PC2|, and
3) IR = 0

Then
K = S1
RULE = S1.6

Rule S1.7 Reloading towards the common point

If 1) (DIR = 1 or DIR = 3), and

2) [50 % Pc ≤ |P| < |95 % PM| and LAST RULE = S1.6], or

[75 % Pc ≤ |P| < |95 % PM| and LAST RULE = S1.9]

Then

$$K = \frac{P2 - P}{D2 - D}$$

A = P2

RULE = S1.7

4. Reloading after Unloading from the Opposite Direction. Typical bending and shear reloading curves for NCKU wall SW6 are shown in Figure 87. The bending deformation curve loads towards the maximum past deformation, forming large stable hysteresis loops. The hysteresis loops for the shear deformation are pinched. Examining the bending and shear reloading mechanisms may explain their different behavior.

For bending deformation, the state of the wall after unloading is shown in Figure 88; concrete is in compression at the old compression edge, steel is in tension in the middle of the wall, and at the old tension edge steel is in compression, while the cracks in the wall remain open. As the wall is loaded in the new loading direction:

- Initially the old tensile cracks are open, yielding a stiffness similar to the old unloading stiffness S3 as shown in Region A of Figure 89.
- As the cracks on the old tension side close, the stiffness increases as shown in Region B of Figure 89.
- As the new tension side cracks open and bars on the new tension side yield, the stiffness decreases as shown in Region C of Figure 89.

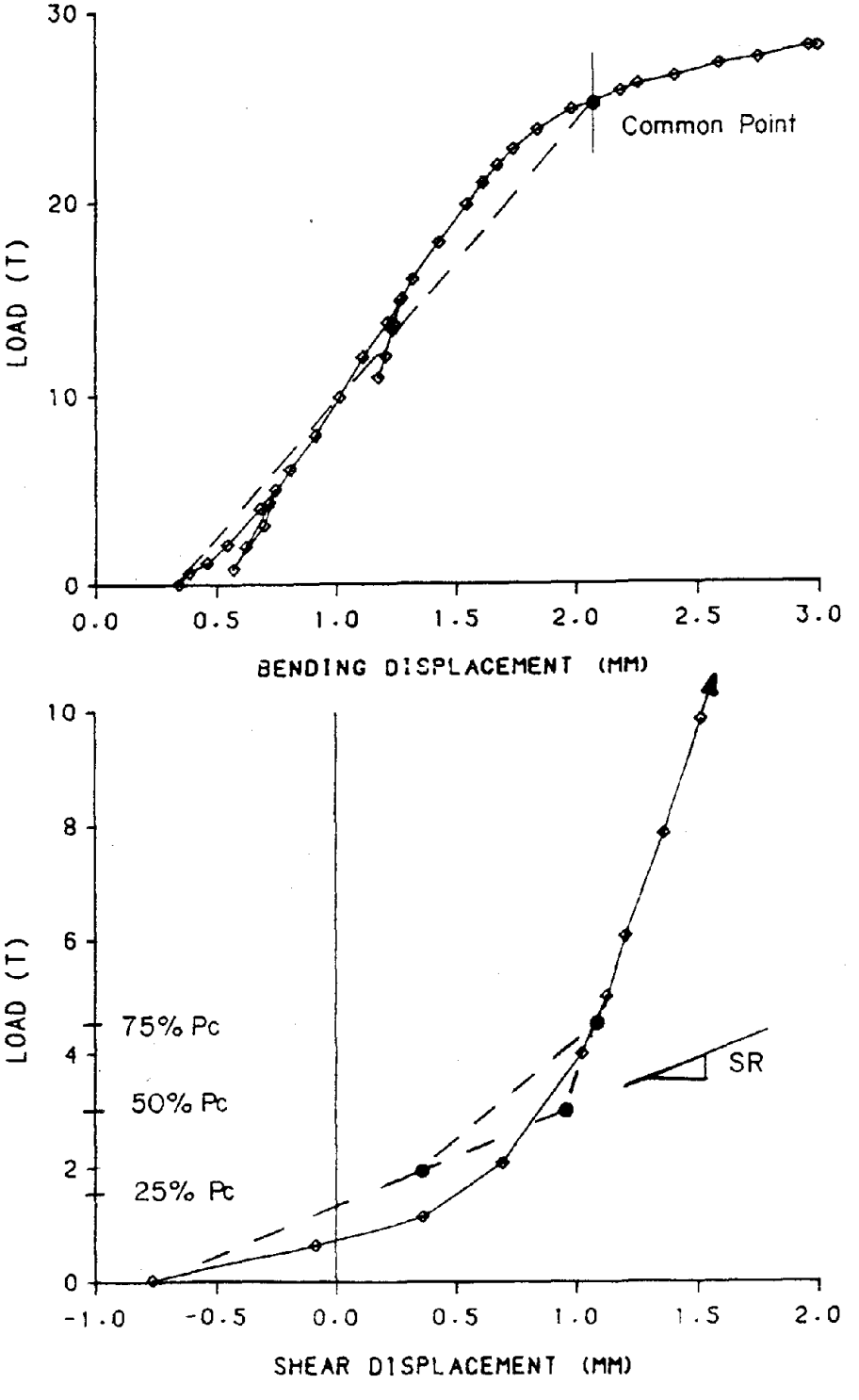

Figure 87. NCKU Wall SW6, Typical Bending and Shear Reloading With Reversal Curves

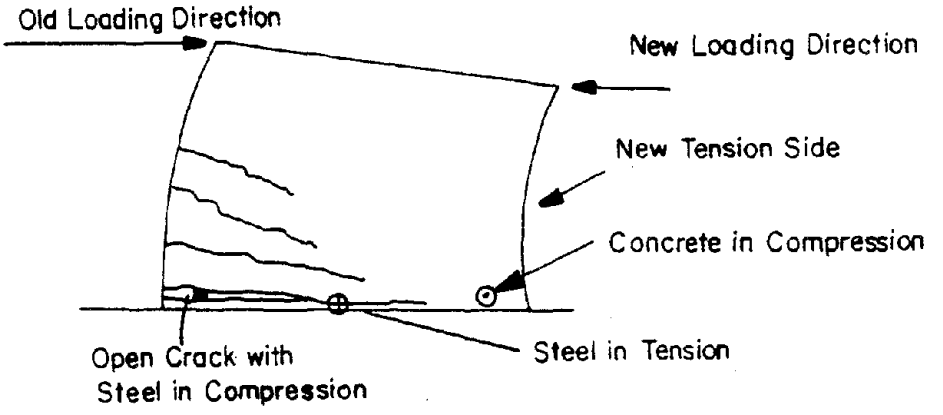

Figure 88. Deformation Before Reloading With Reversal Due to Bending

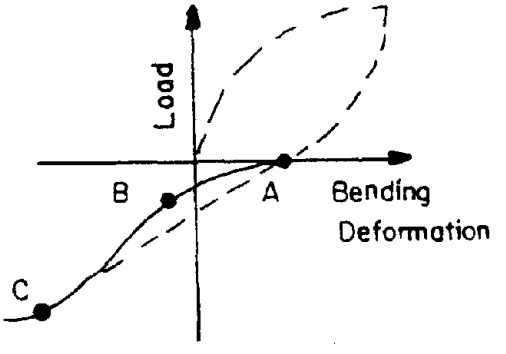

Figure 89. Bending Pinching For Reloading With Reversal

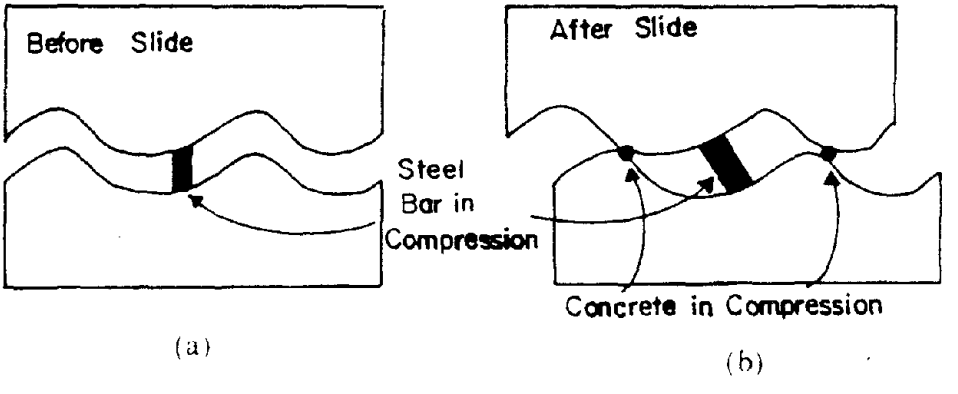

Figure 90. Influence of Shear Sliding: (a) Before Slide, (b) After Slide

Thus the bending reloading curve, A-B-C in Figure 89, has a slight pinching behavior. Park, et al. (64) calculated a similar pinching behavior for R/C beams subject to cyclic bending loads. The pinching observed in the bending deformation of NCKU walls is minor. This is due to the presence of shear. At low load levels, the wall slides as shown in Figure 90. This closes the old tension cracks on the wall at a lower load level than bending deformations alone would. Thus the wall reloads on path A-C in Figure 89. The bending reloading curve is represented by a single line connecting the reversal point and the common point.

The shear deformation behavior upon reloading after reversal is dominated by pinching at low load levels. Recall that after the wall is unloaded, the diagonal cracks are open, as shown in Figure 91. As the wall is loaded in the new loading direction:

- The steel across the open cracks goes into compression. The stiffness of the steel across the cracks is low compared to the concrete compression strut, resulting in a low initial stiffness as shown in Region A of Figure 92.
- Before the old cracks close completely, cracks parallel to the new compression strut open up. At this stage, the wall slides across the open cracks, producing a very low stiffness as shown in Region B or Figure 92.
- As the old cracks close the stiffness increases as shown in Region C of Figure 92 because 1) the sliding mechanism is inhibited, and 2) concrete rather than steel carries the majority of the compressive loads. This point is called the crack closing point.

Thus the shear deformation behavior for reloading after reversal is pinched.

The bending and shear behavior for reloading after reversal are dependent on crack width, crack location and sliding across cracked surfaces. Since these values are very difficult to calculate, it is not feasible to quantitatively predict the loading behavior of a shear wall. Thus semi-empirical models are used.

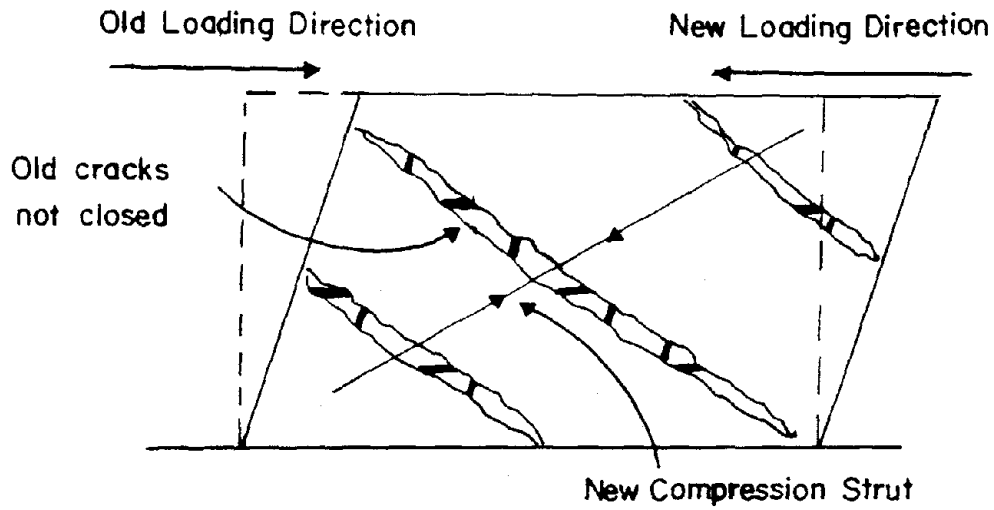

Figure 91. Deformation Before Reloading With Reversal Due to Shear

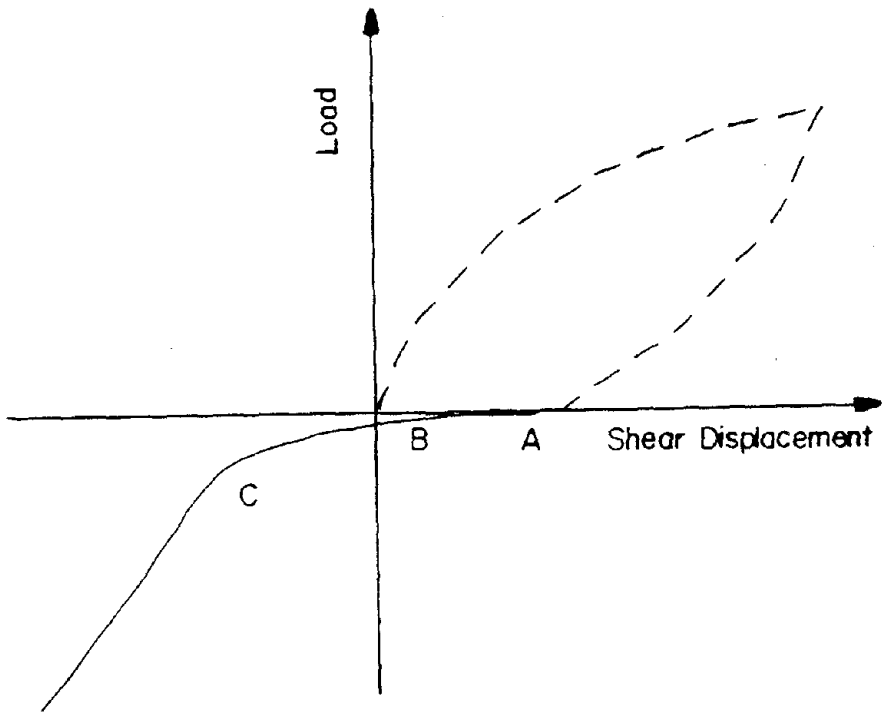

Figure 92. Shear Pinching for Reloading With Reversal

a. Bending Hysteresis Model, Rules B1.8 and B1.9. The reloading curve for the bending hysteresis models is represented by a single line connecting the reversal point and the common point as shown in Figure 93. The reloading stiffness is given by

$$SR = \frac{P2}{D2 - DR} \tag{4.30}$$

where DR is the displacement of the load reversal point and (D2,P2) are the coordinates of the common point, Equation 4.24 or 4.25. Rule B1.8 represents reloading after reversal.

Additional considerations are:

- When reloading after a very small loop in the opposite direction, the behavior should be similar to reloading after unloading from the same direction, rules B1.6 and B1.7 as shown in Figure 94. Recall that the transition point between rules B1.6 and B1.7 is (DC3,PC3), Equations 4.22 and 4.23. For very small loops in the opposite direction, reloading towards the common point (D2,P2) will generate a smaller loop than reloading with rules B1.6 and B1.7 as shown in Figure 94. To prevent this, the larger of the stiffnesses from the load reversal point, DR, to (D2,P2) or (DC3,PC3) is used for the reloading stiffness. Let

$$S' = \frac{PC3}{DC3 - DR} \tag{4.31}$$

be the stiffness from the current point to (DC3, PC3). If the stiffness from the reversal point to (DC3,PC3) is larger, rule B1.8.1 is used to load up to PC3, and rule B1.7 is used to load beyond PC3.

- When loading from a large displacement in one direction to a small displacement in the opposite direction, a pinched loop may occur in the hysteresis model as shown in Figure 95. This pinched behavior was not observed in the experimental

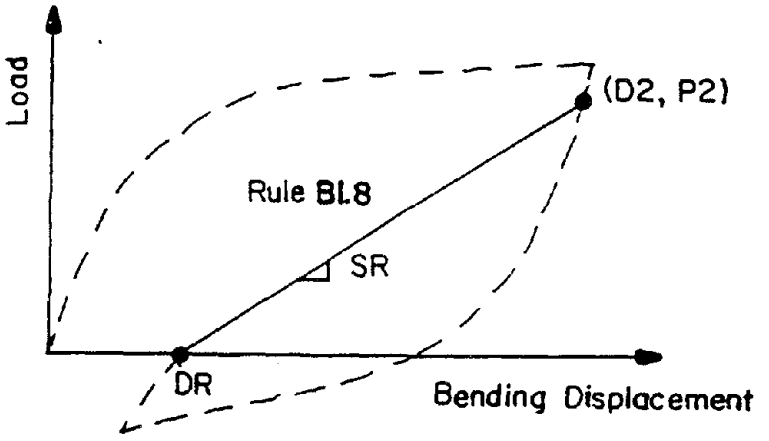

Figure 93. Bending Hysteresis Model, Rule B1.8

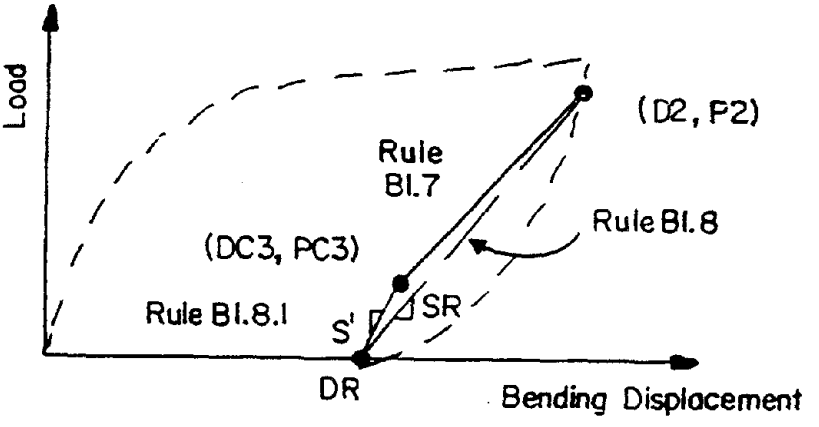

Figure 94. Bending Hysteresis Model, Rule B1.8.1

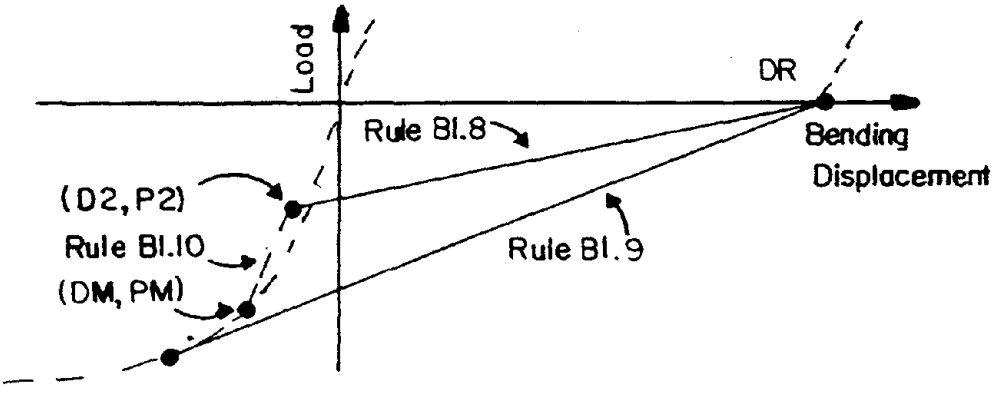

Figure 95. Bending Hysteresis Model, Rule B1.9

test data. To overcome this problem, rule B1.9 is used to load to a point tangent to the bending backbone curve, eliminating the potential pinched behavior.

Thus, the reloading after reversal rules B1.8 to B1.9 are

Rule B1.8 Reloading after reversal

If 1) [(DIR = 1 and DIRL = 4) or (DIR = 3 and DIRL = 2)], and

2) $|P| < |PC3|$, and

3) IR = 0

Then

K = SR

A = P2

RULE = B1.8

If ($S' \geq K$) and ($|P| \leq |PC3|$) Then

K = S'

A = PC3

RULE = B1.8.1

End

If (DIR = 1 and DR < 0) or (DIR = 3 and DR > 0) Then Go to Rule B1.9

Rule B1.9 Reloading from large to small displacements

Execute this rule after executing Rule 8

For all J, such that $PB(J) > |PM|$, $j \leq NB$

$$K = \max\left(\frac{PB(J)}{DB(J) - DR}, SR\right)$$

A = PB(J) or P2, whichever yields the maximum value of K.

RULE = B1.9

If A = PB(J), Then BACKB = true

b. Shear Hysteresis Model, Rules S1.8 and S1.9. An empirical relationship is used to model the pinching behavior, which consists of two linear segments, and a transition curve as shown in Figure 96. The stiffness of the first segment, SR, is based on experimental data for NCKU walls SW3, SW5 and SW6 as shown in Figure 97. When the peak displacement is large in one direction and small in the other, the reloading stiffness, SR, in both directions is similar. Thus the absolute value of the maximum displacement in either direction, Dmax, is used to determine SR. The empirical expression for SR is

$$SR = SI\left(\frac{Dc}{Dmax}\right)^{1.02} \tag{4.32}$$

While the test data has considerable scatter, the empirical relationship for SR captures the general trend of the data.

Additional considerations are:

- An upper limit on the reloading stiffness, SR, is the case without pinching. The stiffness of this upper limit, S, is the slope of the line from the load reversal point to the common point (D2,P2) as shown in Figure 96, and is given by

$$S = \frac{P2}{D2 - DR} \leq SI \tag{4.33}$$

  where DR is the displacement of the load reversal point and the common point (D2, P2) is given by Equation 4.28 or 4.29.

- When the peak displacement in the current direction (DM, PM) is large, and the peak displacement in the previous direction is small, the reloading stiffness, SR, may give an unrealistically low reloading stiffness. Recall the transition point between rules S1.6 and S1.7 is (DC2, PC2), Equations 4.26 and 4.27. Define the minimum reloading stiffness

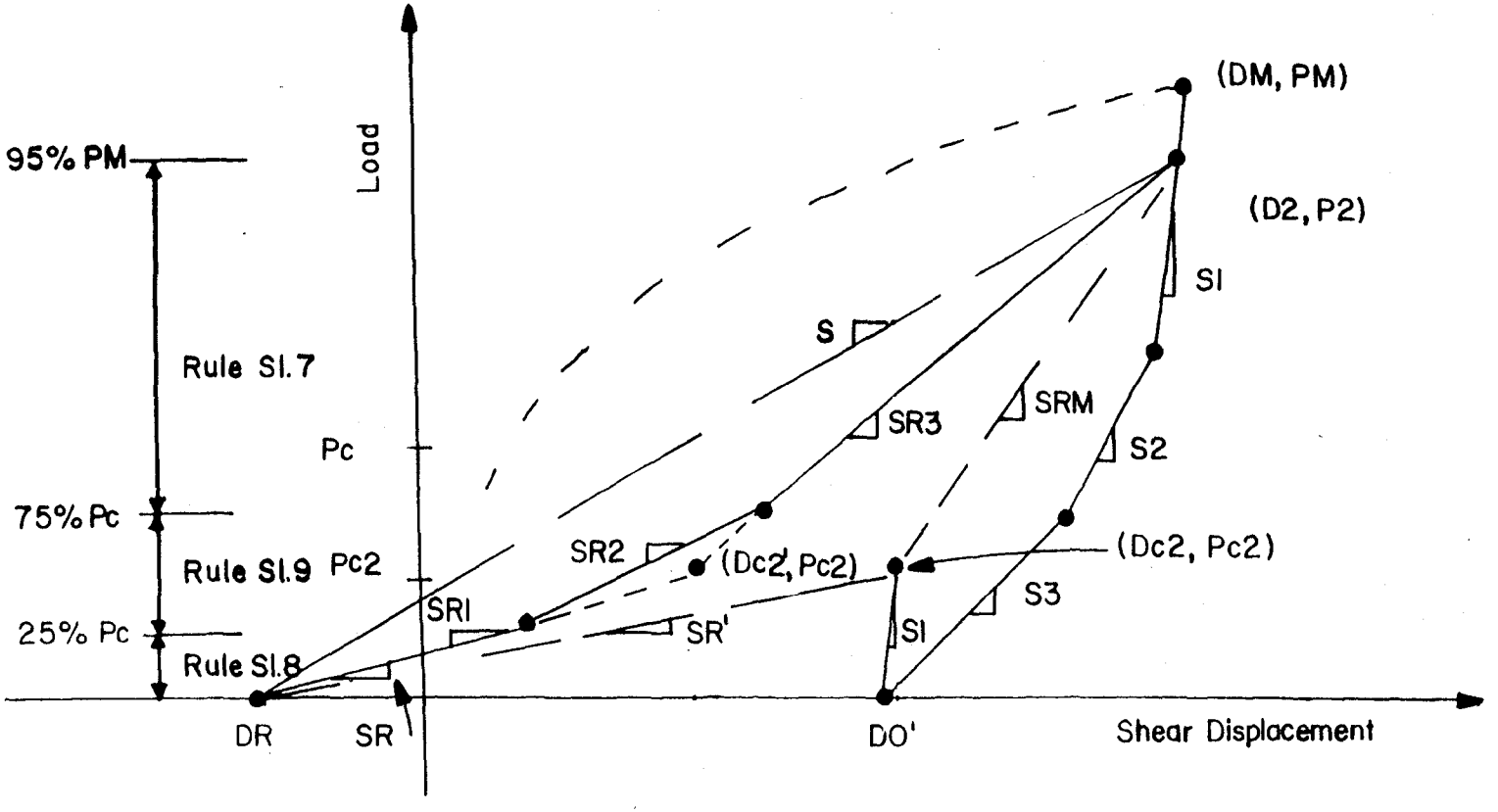

Figure 96. Shear Hysteresis Model, Rules S1.8 and S1.9

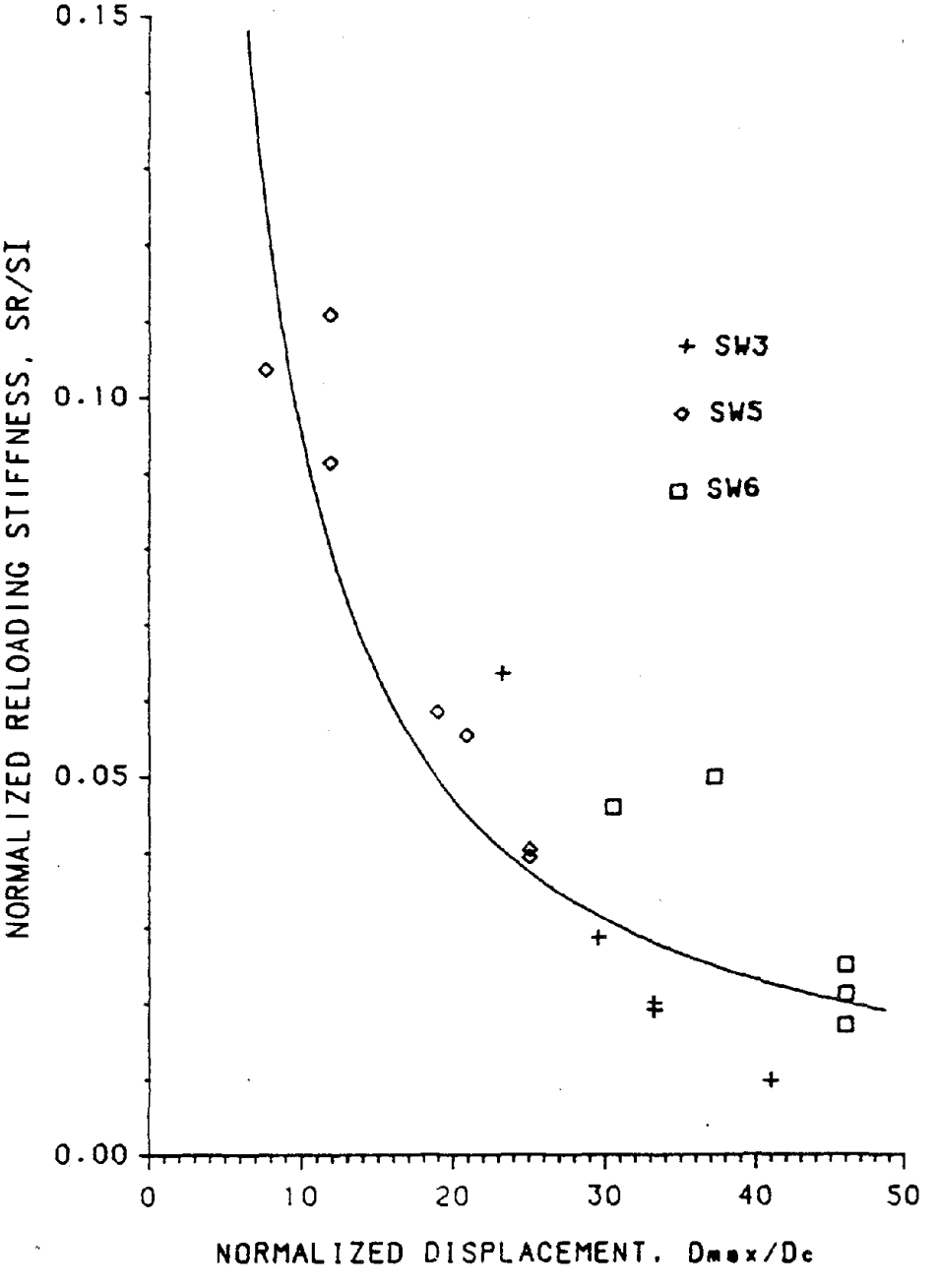

Figure 97. Shear Reloading With Reversal Stiffness, SR

$$SR' = \frac{PC2}{DC2 - DR} \tag{4.34}$$

as the slope of a line from the load reversal point to (DC2,PC2).

- When reloading after a very small loop in the opposite direction, pinching is negligible and the behavior should be similar to reloading after unloading from the same direction, rules S1.6 and S1.7. Let SRM be the slope of a line from (DC2,PC2) to (D2,P2) or

$$SRM = \frac{P2 - PC2}{D2 - DC2} \leq SI \tag{4.35}$$

If the upper limit of the reloading stiffness, S, is greater than SRM, then load to (DC2, PC2) and continue with rule S1.7. This case is similar to rule B1.8.1.

- The first reloading segment has a stiffness SR1, where

$$SR1 = \max(SR', \min(SR,S)) \tag{4.36}$$

Assume a bilinear model is used to represent the pinching and the crack closing point is chosen at PC2. The displacement at the crack closing point is

$$DC2' = DR + \frac{PC2}{SR1} \tag{4.37}$$

The abrupt change of stiffness at (DC2', PC2) may lead to overshooting problems in the nonlinear analysis. Thus, a transition curve between the two segments is used to soften the abrupt stiffness change at the crack closing point as shown in Figure 96. The first segment has a stiffness of SR1, extends from 0 to 25% PC and is modeled by Rule S1.8. The second segment has a stiffness of

$$SR3 = \frac{P2 - PC2}{D2 - DC2'} \leq SI \tag{4.38}$$

extends from 75% Pc to P2 and is modeled by rule S1.7. The transition curve has a stiffness of

$$SR2 = \frac{2}{\frac{1}{SR1} + \frac{1}{SR3}} \tag{4.39}$$

and extends from 25% Pc to 75% PC and is modeled by rule S1.9.

Thus shear hysteresis rules S1.8 and S1.9 are

Rule S1.8 Loading below 25% Pc

If 1) $|P| \leq$ 25% Pc, and

2) [(DIR = 1 and DIRL = 3) or (DIR = 4 and DIRL = 2)]

Then

K = SR1

A = 0.5 × PC2

RULE = S1.8

If S ≥ SRM Then Go to Rule S1.6, and omit the first test.

Rule S1.9 Loading between 25% Pc and 75% Pc

If 25% Pc < $|P| \leq$ 75% Pc, and

2) LAST RULE = S1.8

Then

K = SR2

A = 1.5 × PC2

RULE = S1.9

5. Degrading Under Cyclic Loading. Typical hysteresis loops from NCKU walls SW1a are shown in Figure 98. The experimental data for bending and shear deformation shows that when the walls were cycled at a constant load above the common point, the peak displacement increased for each cycle. However, when the walls were cycled at a constant load below the common point, the hysteresis loops were stable.

The mechanism for this behavior is partly explained by examining the behavior of plain concrete as shown in Figure 99.

- When the concrete is cycled below the common point, the maximum strain (displacement) does not increase.
- Once the common point has been exceeded, the next loop will be at a larger strain level.
- As the load is increased past the common point, the loading curve intersects the backbone curve.
- The common point for plain concrete tends to decrease as the number of cycles increases.

The behavior of the reinforced concrete shear wall is similar to the plain concrete. However, the load level of the common point was not observed to decrease as the number of load cycles increased. Thus the common point is assumed to have a constant load level for both the bending and shear hysteresis models.

a. Bending Hysteresis Model, Rule B1.10. Degradation above the common point is modeled by a transition curve between the common point and the backbone curve. The transition curve passes through the point (αDM,PM) as shown in Figure 100. The stiffness of the transition curve is determined by the factor α, where α is the increase in displacement from one cycle to another. NCKU walls SW1a, SW4a and SW5 were examined to determine an appropriate value of α. The average bending stiffness

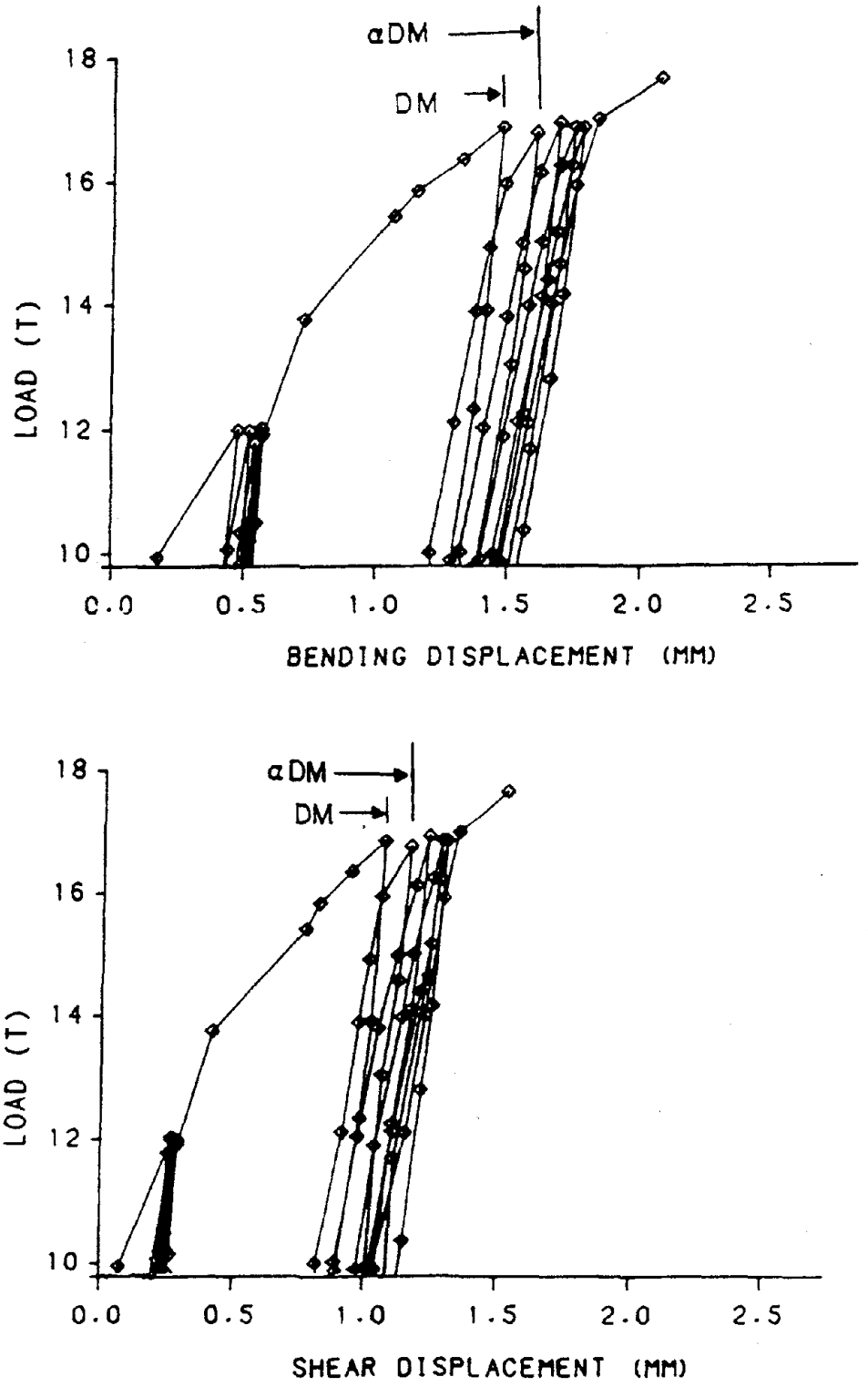

Figure 98. NCKU Wall SW1a, Typical Bending and Shear Degrading Stiffness Under Cyclic Loading Curves

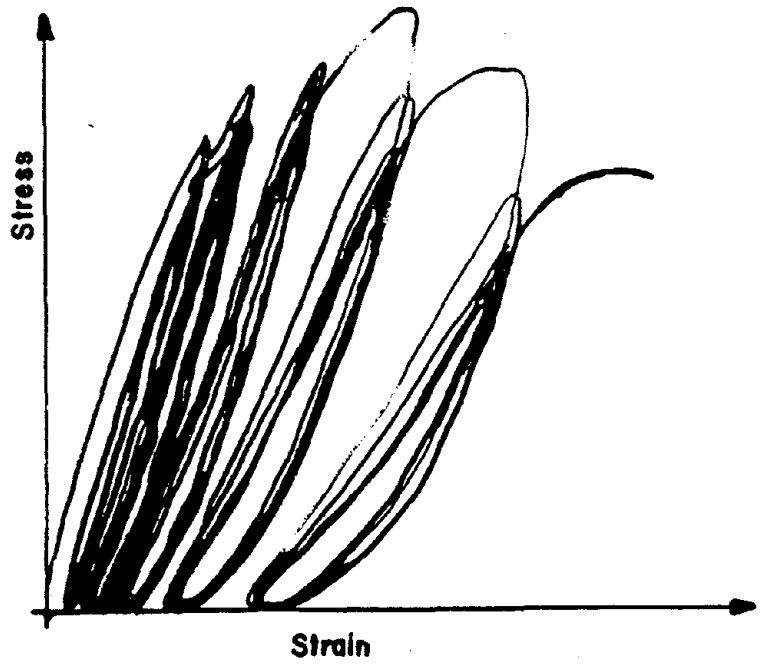

Figure 99. Degrading Stiffness Under Cyclic Loading of Plain Concrete (Ref. 50)

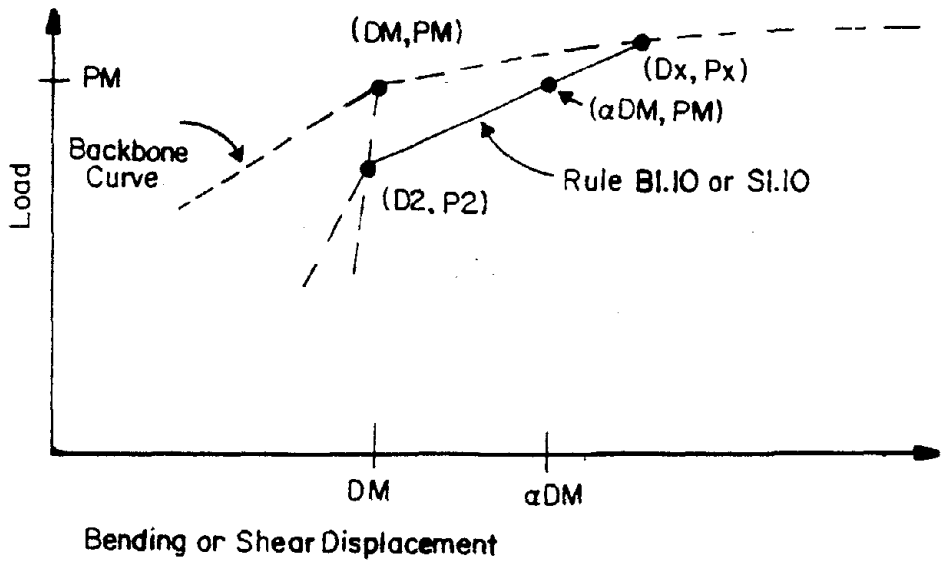

Figure 100. Bending and Shear Hysteresis Models, Rules B1.10 and S1.10

degradation is cycle dependent, with $\alpha = 1.129$ for the first cycle, and $\alpha = 1.029$ for subsequent cycles. Thus the bending hysteresis rule B1.10 is

Rule B1.10 Loading above 95% PM, not on the backbone curve

If 1) (DIR = 1 or DIR = 3), and

2) $|P| \geq P2$, and

3) NOT (BACKB)

Then

$\alpha = 1.129$- first cycle at a given load

$\alpha = 1.029$- subsequent cycles below Px

(Dx,Px) = Intersection of line through (D2,P2), with a slope of K, and the bending backbone curve

$$K = \frac{5\%\ PM}{\alpha DM - D2}$$

$A = P_X$

RULE = B1.10

IR = 0

b. Shear Hysteresis Model, Rule S1.10. Similar to the bending hysteresis model, the degradation above the common point, (D2,P2), is modeled by a transition curve. The transition curve is described by rule S1.10, and goes between the common point and the backbone curve. This transition curve passes through the point (αDM,PM) as shown in Figure 100. The stiffness of the transition curve is controlled by the factor α, where α is the increase in displacement from one cycle to another. NCKU walls SW1a, SW4a and SW5 were examined to determine an average factor $\alpha = 1.04$. For the shear hysteresis model, the stiffness degradation factor α is not strongly dependent on the cycle.

Thus the shear hysteresis model rule S1.10 is

Rule S1.10 Loading above 95% PM, not on the backbone curve

If 1) (DIR = 1 or DIR = 3), and

2) $|P| \geq P2$, and

3) NOT (BACKB)

Then

$\alpha = 1.04$

(Dx,Px) = Intersection of line through (D2,P2), with a slope of K, and the shear backbone curve

$$K = \frac{5\%\ PM}{\alpha DM - D2}$$

$A = P_X$

RULE = S1.10

IR = 0

6. Small Amplitude Loops. The following trends were observed in the NCKU shear wall test data.

- Small amplitude loops below the common point (D2,P2) have stable hysteresis loops as shown in Figures 101, 102, and 103, versus unstable hysteresis loops as shown in Figure 104.
- Small amplitude hysteresis loops form inside of small amplitude hysteresis loops as shown in Figure 101.
- Stable loops are formed with reversal, provided that the common point is not reached in either direction as shown in Figures 102, 103.
- Unloading in a small amplitude loop is parallel to the large amplitude loop unloading, except in the region near the previous reversal point as shown in Figures 101, 102, and 103. Rules B1.5 and S1.5 model the unloading by determing if the current point is in the region near the previous reversal point. If so, unloading

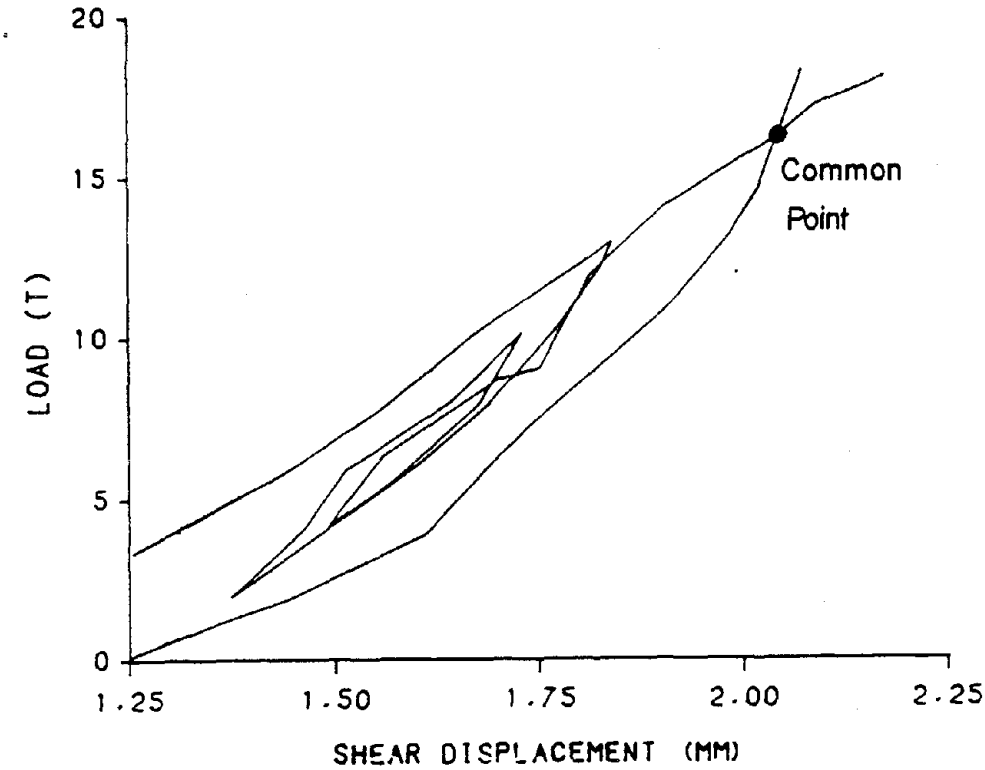

Figure 101. Shear Displacement of NCKU Wall SW3, Steps 2830 to 3330

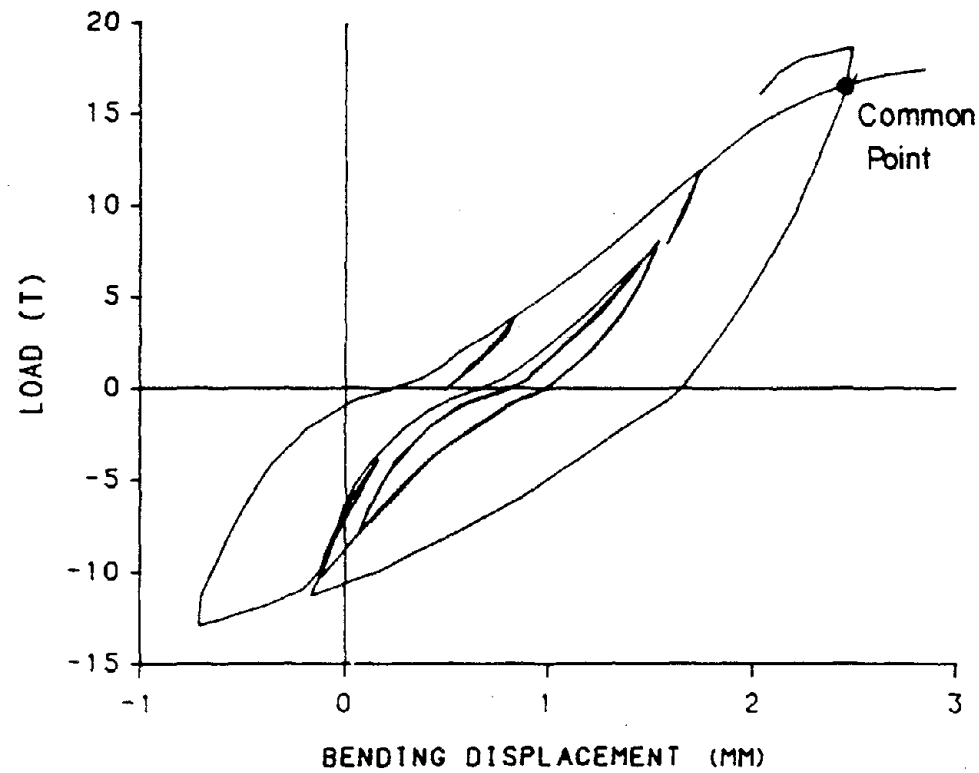

Figure 102. Bending Displacement of NCKU Wall SW3, Steps 3330 to 5050

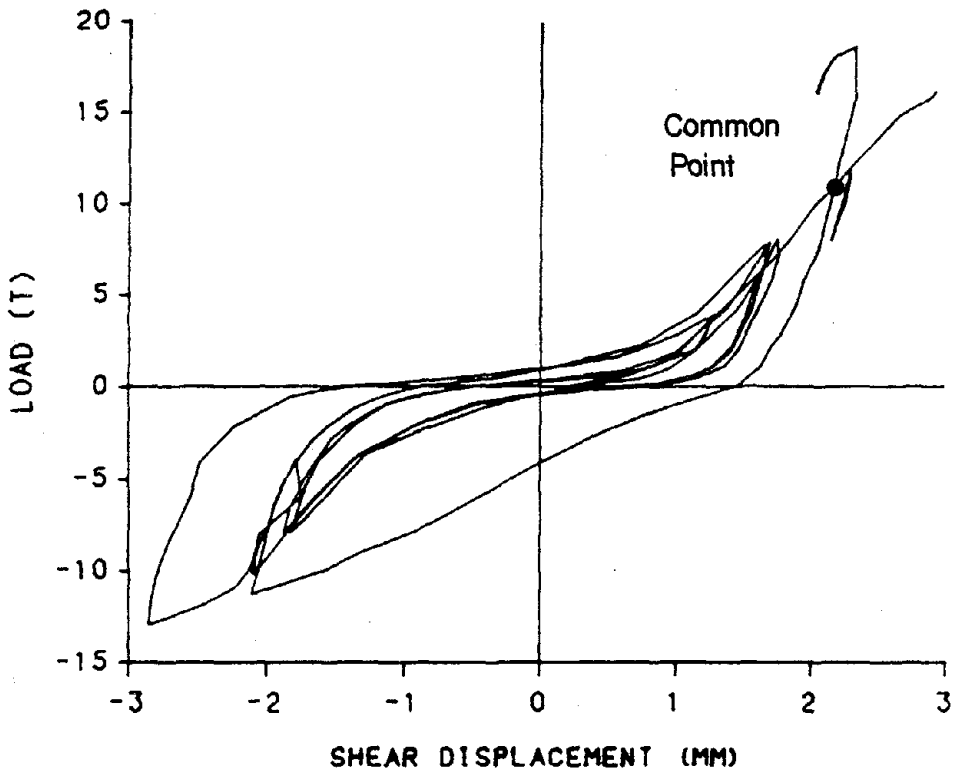

Figure 103. Shear Displacement of NCKU Wall SW3, Steps 3330 to 5050

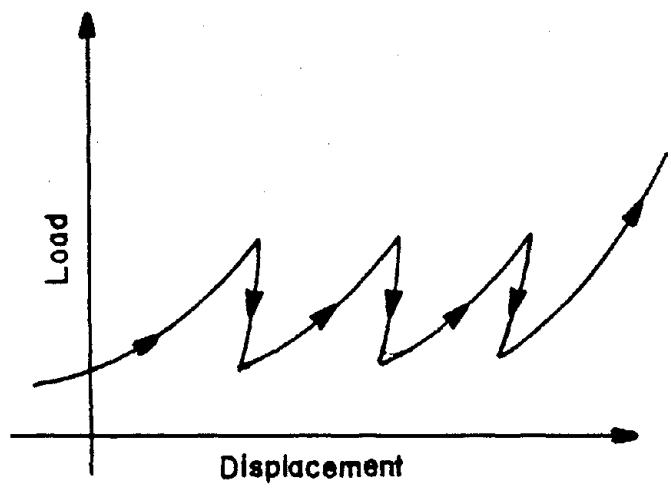

Figure 104. Unstable Small Amplitude Hysteresis Loops

progresses towards the previous reversal point. If not, unloading progresses parallel to the unloading curve generated by rules B1.2, B1.3 and B1.4 or S1.2, S1.3 and S1.4 as shown in Figure 105

- For the bending model reloading inside of small amplitude loops proceeds towards the last reversal point as shown in Figure 102.
- For the shear model the pinched behavior of the shear deformation is maintained by the small amplitude hysteresis loops. Thus, the reloading curve is a function of both the current displacement and the reversal point as shown in Figure 103.

Rules 5 and 11 for both the shear and bending hysteresis models are based on these trends.

Each time the direction changes in a small amplitude loop the reversal load, reversal displacement and a flag are stored in the arrays PR, DR, and FR. A counter IR contains the current number of reversal points stored. The flag FR contains one of two values as shown in Figure 106. When the arithmetic value of the load changes from increasing to decreasing, FR = '7'. When the arithmetic value of the load changes from decreasing to increasing, FR = 'L'.

a. Bending Hysteresis Model Rules B1.5 and B1.11. Bending hysteresis model rules B1.5 and B1.11 are

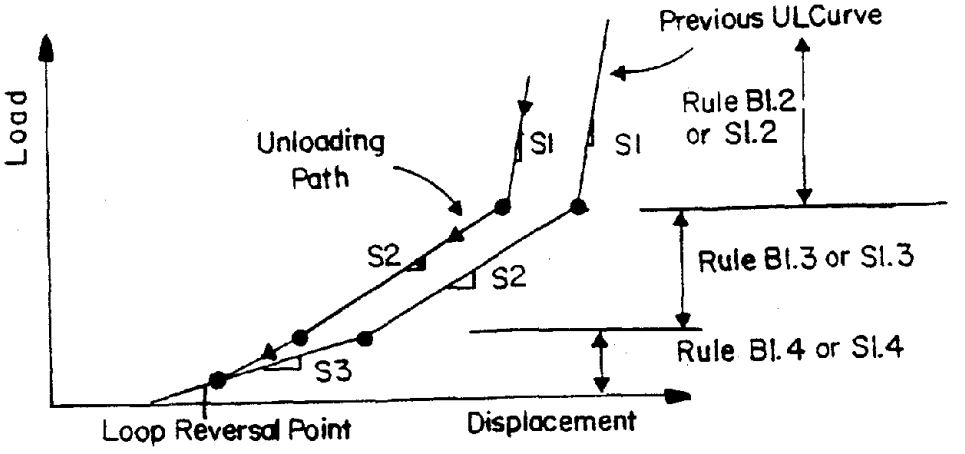

Figure 105. Bending and Shear Hysteresis Models, Unloading in Small Amplitude Hysteresis Loops

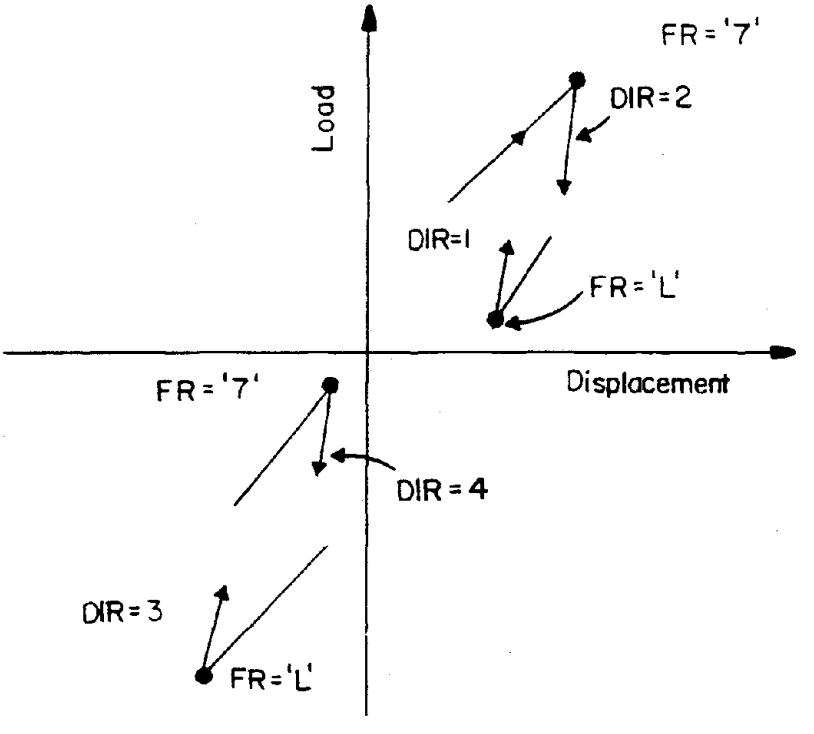

Figure 106. Reversal Point Flags for Small Amplitude Hysteresis Loops

Rule B1.5 Unloading inside small amplitude loops

If 1) (DIR = 2 or DIR = 4), and

2) IR≥1

Then

Using the last small amplitude loop reversal point (DR(I),PR(I)) with a flag FR(I) such that

[(DIR = 2 and FR(I) = L) or (DIR = 4 and FR(I) = 7)]

If (DIR = 2 and ($P > PR(I) > Q3$, or

$Q3 \geq P > PR(I) > Q1$, or

$Q1 \geq P > PR(I) > 0$)), or

(DIR = 4 and ($P < PR(I) < Q3$, or

$Q3 \leq P < PR(I) < Q1$, or

$Q1 \leq P < PR(I) < 0$))

Then

$$K = \frac{PR(I) - P}{DR(I) - D}$$

$A = PR(I)$

RULE = B1.5

If $K > SI$, or $K \leq 0$ use the next to last small amplitude loop point that satisfies the conditions above.

Once unloading continues below A, erase the reversal point I.

Thus IR = IR-1

Else

$$SU = \frac{PR(I) - P}{DR(I) - D}$$

Go to rule B1.2, B1.3, or B1.4 as applicable. Omit the test IR = 0.

Rule B1.11 Reloading inside small loops

If IR > 0

Then

Using the last small amplitude loop point (DR(I),PR(I)) with a flag FR(I) such that

[(DIR = 1 and FR(I) = 7) or (DIR = 3 and FR(I) = L)]

$$K = \frac{PR(I) - P}{DR(I) - D}$$

A = PR(I)

RULE = B1.11

If K > SI or K ≤ 0 use the next to last small amplitude loop point that satisfies the condition above.

Once unloading continues above A, erase the reversal point I.

Thus IR = IR-1

b. Shear Hysteresis Model Rules S1.5 and S1.11. Unloading inside small amplitude shear loops is similar to the bending hysteresis model. However, upon reloading inside the small amplitude loops, the shear model maintains its pinched shape. The reloading path with pinching is dependent on both the reversal point and the current point. Six different reloading paths are discussed below.

If the reversal point (DR, PR) is less than 25% Pc, the reloading is from the current point to the reversal point with the stiffness

$$SRL = \frac{PR(I) - P}{DR(I) - D} \tag{4.40}$$

where I is the last small amplitude loop point with a flag FR(I) such that (DIR = 1 and FR(I) = 7) or (DIR = 3 and FR(I) = L). This case is represented by Rule S1.11.1 and is shown in Figure 107.

If the loop reversal point is between 25% Pc and 75% Pc, there are two possible reloading paths as shown in Figure 108 and 109. The reloading stiffness is determined from Equation 4.40. If SRL $\leq$ SR2, then reload to the intersection of rules S1.8 and S1.9. Let PC25 and X1 represent this point, where

$$PC25 = \frac{PC}{2} \qquad X1 = DC2' - \frac{PC25}{SR1} \tag{4.41}$$

DC2′ and SR1 are defined in equations 4.37 and 4.36, respectively. The reloading stiffness becomes

$$SX1 = \frac{PC25 - P}{X1 - D} \tag{4.42}$$

This case is defined by rule S1.11.2 and shown in Figure 108. If SRL>SR2, then reloading proceeds with the stiffness SRL. This case is defined by rule S1.11.3 and shown in Figure 109.

If the reversal point is between 75% Pc and P2, there are three possible reloading paths as shown in Figure 110. Define the shifted reloading curve's break points as

$$PC75 = 1.5 \times PC2 \qquad X2 = DR(I) + \frac{PC75 - FR(I)}{SRM} \tag{4.43}$$

$$PC25 = 0.5 \times PC2 \qquad X1 = X2 - \frac{PC2}{SR2} \tag{4.44}$$

where I is the last small amplitude loop point with a flag FR(I) such that (DIR = 1 and FR(I) = 7) or (DIR = 3 and FR(I) = L), SRM is the stiffness given in Equation 4.35 and SR2 is the stiffness given in Equation 4.39. The reloading stiffness, SRL, is calculated

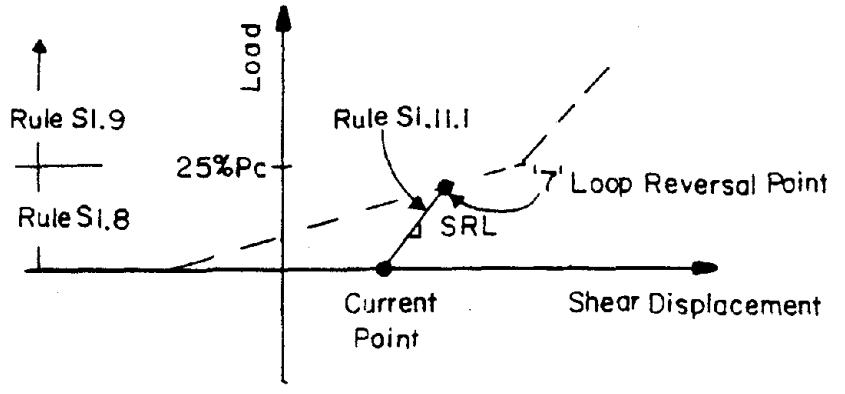

Figure 107. Shear Hysteresis Model, Rule S1.11.1

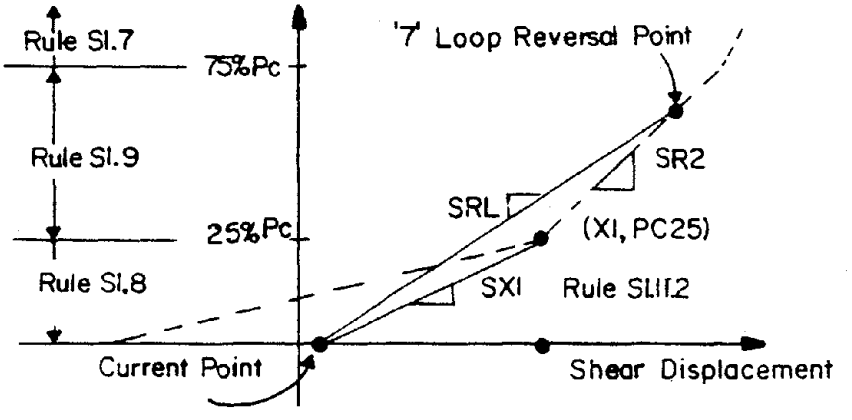

Figure 108. Shear Hysteresis Model, Rule S1.11.2

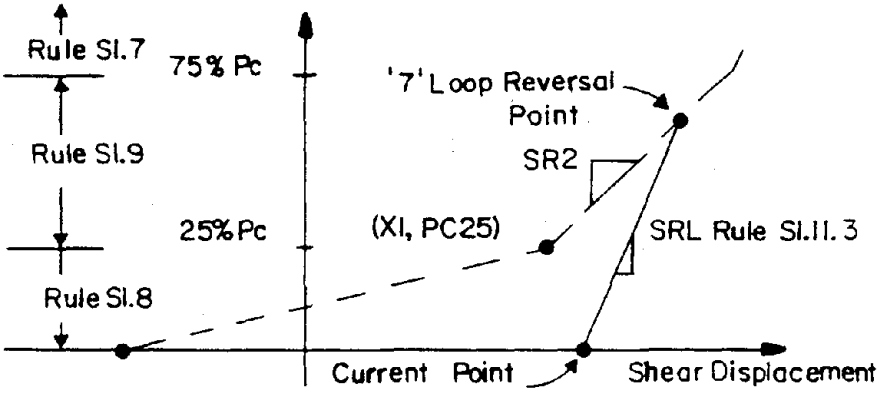

Figure 109. Shear Hysteresis Model, Rule S1.11.3

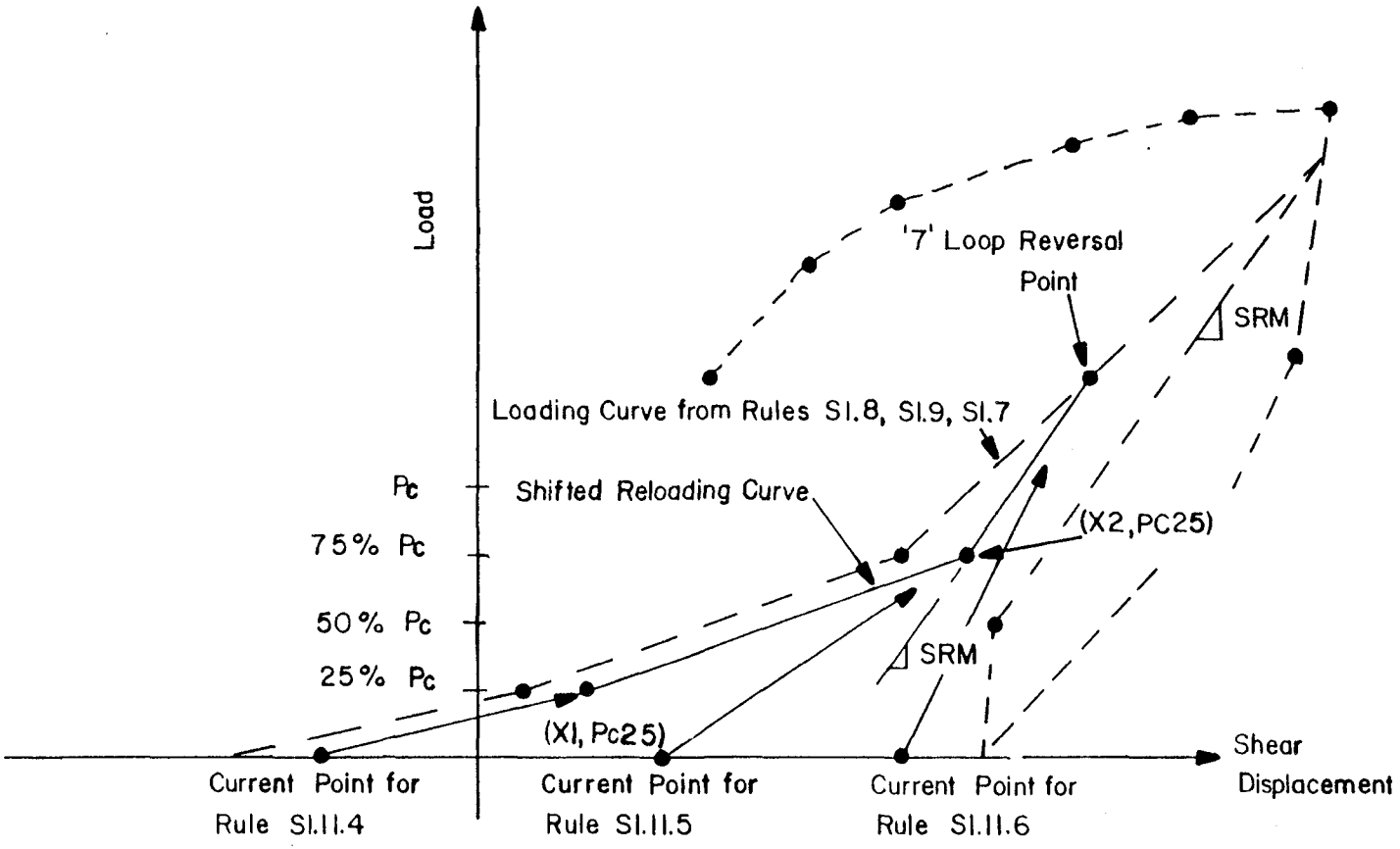

Figure 110. Shear Hysteresis Model, Rules S1.11.4, S1.11.5 and S1.11.6

from Equation 4.40. If SRL>SRM, then the loading proceeds with the stiffness SRL. This case is defined by rule S1.11.6. Define the displacement at 25% of the cracking load as

$$X = D + \frac{PC25 - P}{SR2} \tag{4.45}$$

If ($X \leq X1$ and DIR = 1) or ($X \geq X1$ and DIR = 3), then reloading proceeds to the point (X1, PC25). The stiffness from the current point to (X1, PC25) is

$$SX1 = \frac{PC25 - P}{X1 - D} \tag{4.46}$$

This case is defined by rule S1.11.4. If (X>X1 and DIR = 1) or (X<X1 and DIR = 3), then reloading proceeds to the point (X2, PC75). The stiffness from the current point to (X2, PC75) is

$$SX2 = \frac{PC75 - P}{X2 - D} \tag{4.47}$$

This case is defined by rule S1.11.5.

Thus, shear hysteresis Rules S1.5 and S1.11 are

Rule S1.5 Unloading inside small amplitude loops

If 1) (DIR = 2 or DIR = 4), and

2) IR≥1

Then

Using the last small amplitude loop reversal point (DR(I),PR(I)) with a flag FR(I) such that

[(DIR = 2 and FR(I) = L) or (DIR = 4 and FR(I) = 7)]

If (DIR = 2 and ($P > PR(I) > PA$, or

$PA \geq P > PR(I) > PB$, or

$PB \geq P > PR(I) > 0$)), or

(DIR = 4 and ($P < PR(I) < PA$, or

$PA \leq P < PR(I) < PB$, or

$PB \leq P < PR(I) < 0$))

Then

$$K = \frac{PR(I) - P}{DR(I) - D}$$

$A = PR(I)$

RULE = S1.5

If $K > SI$, or $K \leq 0$ use the next to last small amplitude loop point that satisfies the conditions above.

Once unloading continues below A, erase the reversal point I.

Thus IR = IR-1

Else

$$SU = \frac{PR(I) - P}{DR(I) - D}$$

Go to rule S1.2, S1.3, or S1.4 as applicable. Omit the test IR = 0.

Rule S1.11 Reloading inside small amplitude loops

If 1) (DIR = 1 or DIR = 3), and

2) IR > 0

Then

Using the last small amplitude reversal point (DR(I),PR(I)) with a flag FR(I) such that

[(DIR = 1 and FR(I) = 7) or (DIR = 3 and FR(I) = L)]

Case 1 If |PR(I)| ≤ 25% Pc

K = SRL

A = PR(I)

RULE = S1.11.1

Case 2 If 1) 25% Pc < |PR(I)| ≤ 75% Pc, and

2) SRL < SR2

K = SX1

A = PC25

RULE = S1.11.2

Case 3 If 1) 25% Pc < |PR(I)| ≤ 75% Pc, and

2) SRL ≥ SR2

K = SRL

A = PR(I)

RULE = S1.11.3

Case 4 If 1) SRL < SRM, and

2) [(X ≤ X1 and DIR = 1) or (X ≥ X1 and DIR = 3)]

K = SX1

A = PC25

RULE = S1.11.4

Case 5 If 1) SRL < SRM, and

2) [(X > X1 and DIR = 1) or (X < X1 and DIR = 3)]

K = SX2

A = PC75

RULE = S1.11.5

Case 6 If SRL ≥ SRM

K = SRL

A = PR(I)

RULE = S1.11.6

B. COMPARISON BETWEEN HYSTERESIS MODELS AND EXPERIMENTAL RESULTS

The experimental and calculated hysteresis loops for five NCKU walls SW1a, SW3, SW4a, SW5, and SW6 are compared below. These NCKU walls were presented in Chapter II, Table I. The experimentally observed backbone curves for these walls are used to calculate the hysteresis loops, rather than the calculated backbone curve. Comparisons between calculated and experimental backbone curves are made in Chapter III.

1. Bending Deformation. The calculated and experimental bending hysteresis loops for NCKU walls SW1a, SW3, SW4a, SW5, and SW6 are compared in Figures 111, 112, 113, 114, and 115, respectively. Overall, the comparison between calculated and experimental hysteresis loops is very good. However, several points warrant further discussion:

a. Unloading in the Nonlinear Range. For wall SW1a unloading from a small displacement shown in Curve 'A' of Figure 111, the calculated unloading stiffness is slightly larger than the experimental unloading stiffness. Unloading the same wall from a larger displacement, Curve 'B', the calculated unloading stiffness is also larger than the experimental unloading stiffness. Recall that the curve fitting used to determined these unloading stiffnesses as shown in Figures 73, 74 and 75 typically overestimated the unloading stiffness for wall SW1a.

Contrarily, for wall SW4a, unloading from both small and large displacements shown in Curves 'A' and 'B' of Figure 113 the calculated unloading stiffness is close to the experimental unloading stiffness. The empirical expression for unloading stiffness

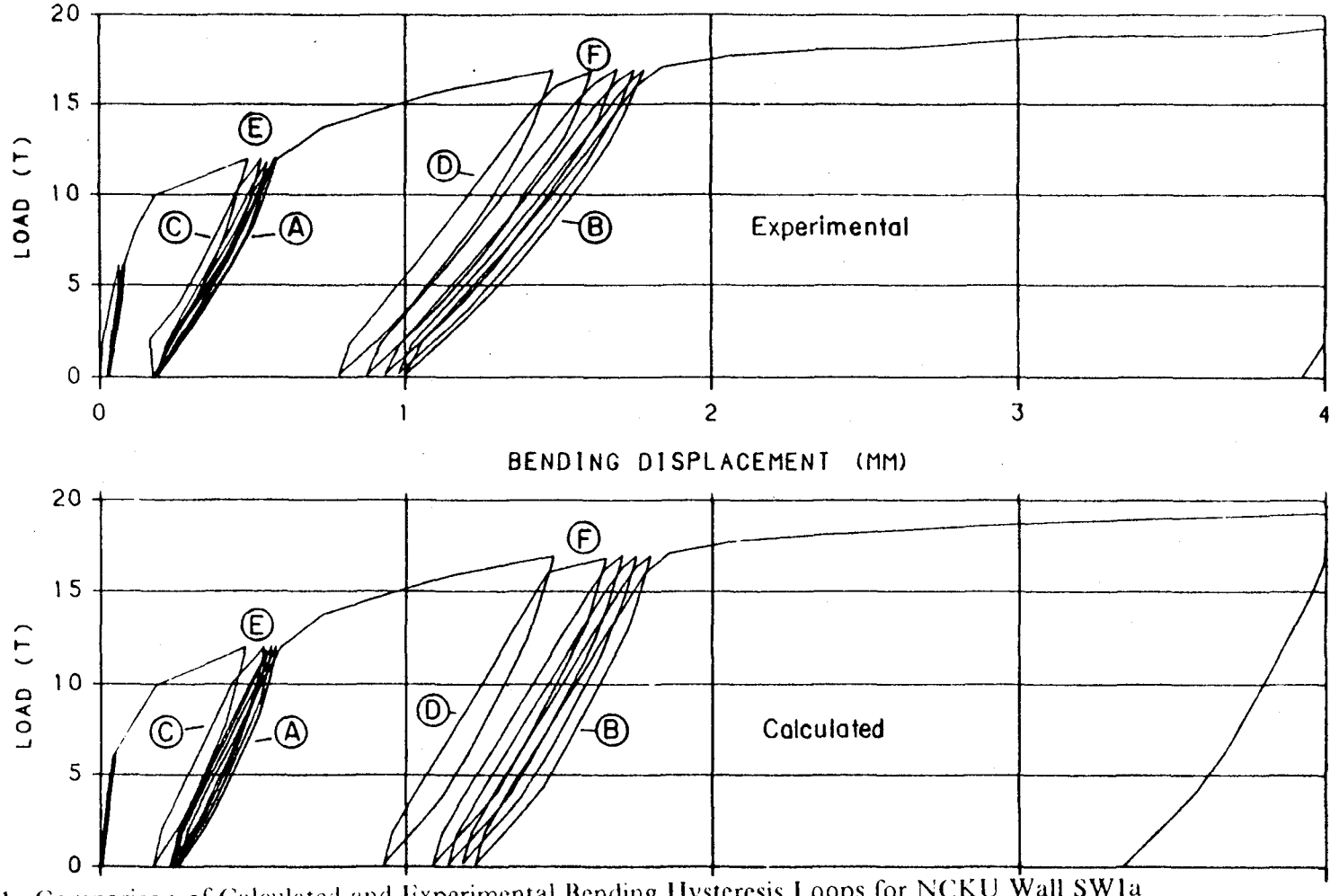

Figure 111. Comparison of Calculated and Experimental Bending Hysteresis Loops for NCKU Wall SW1a

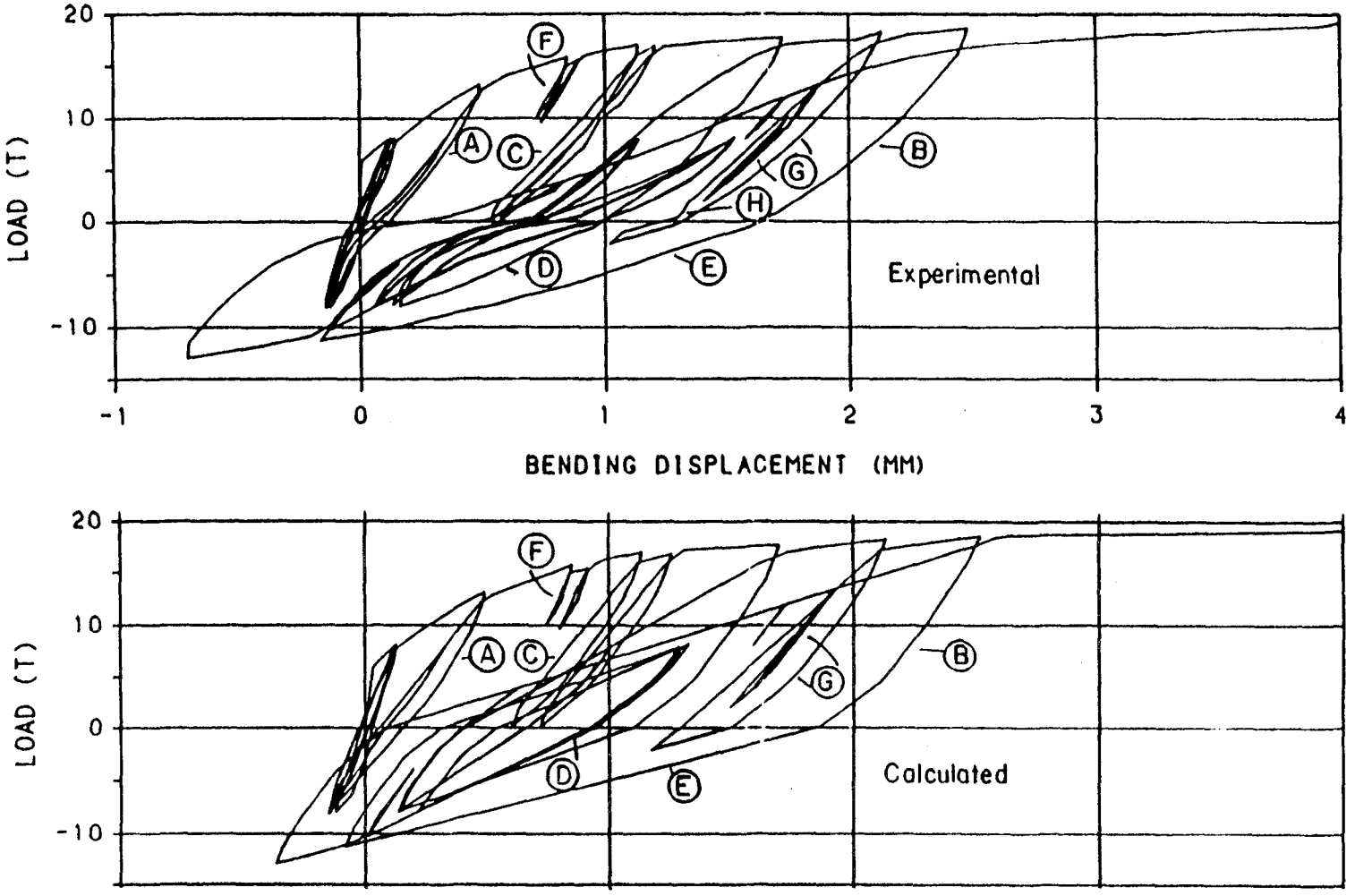

Figure 112. Comparison of Calculated and Experimental Bending Hysteresis Loops for NCKU Wall SW3

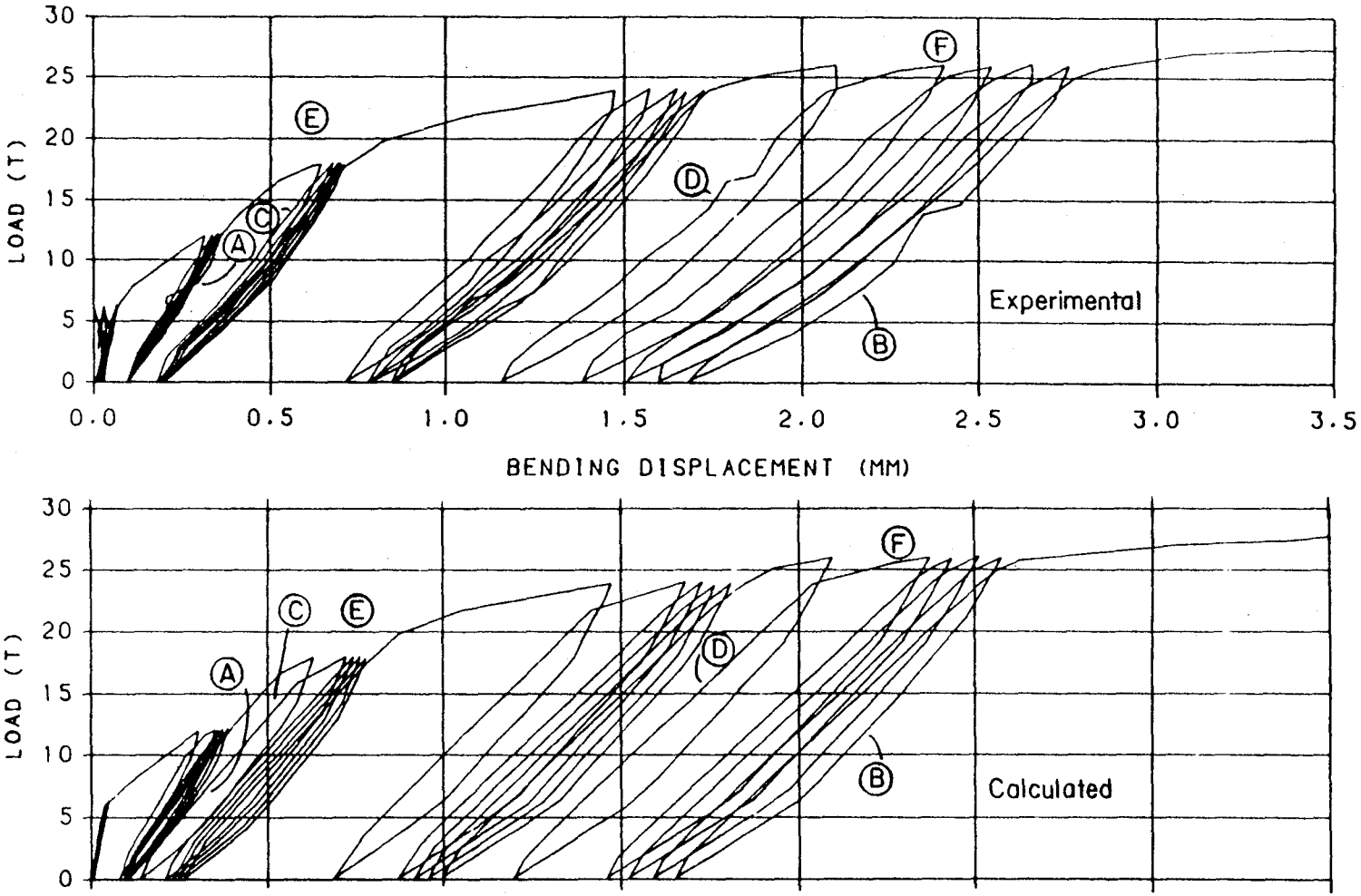

Figure 113. Comparison of Calculated and Experimental Bending Hysteresis Loops for NCKU Wall SW4a

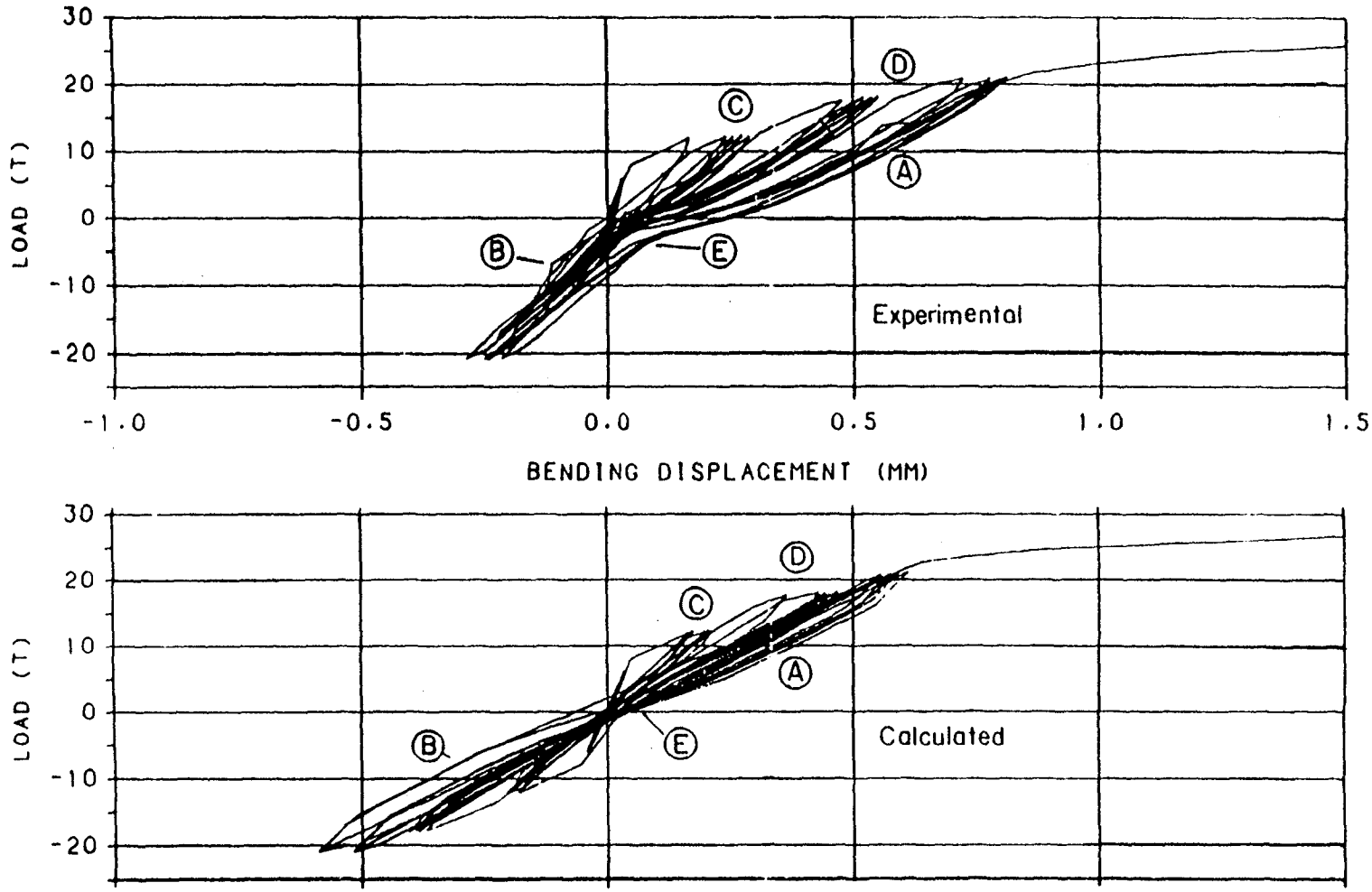

Figure 114. Comparison of Calculated and Experimental Bending Hysteresis Loops for NCKU Wall SW5

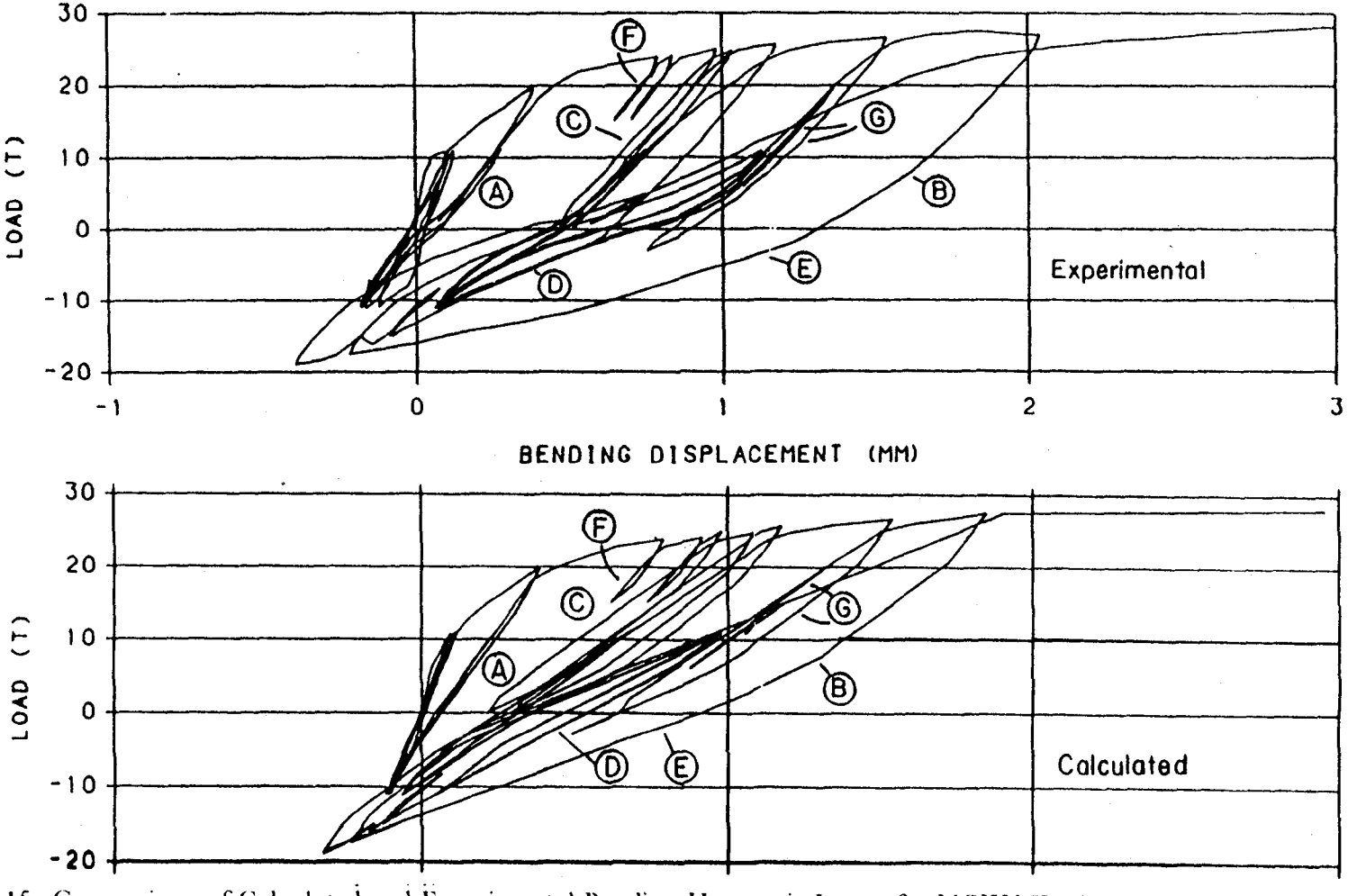

Figure 115. Comparison of Calculated and Experimental Bending Hysteresis Loops for NCKU Wall SW6

is typically close to the experimentally observed unloading stiffnesses as shown in Figures 73, 74 and 75.

The unloading stiffness for wall SW3 at small displacements shown in Curve 'A' of Figure 112 is close to the experimental unloading stiffness, while at large displacements, Curve 'B', the calculated unloading stiffness is slightly higher than experimental value.

The unloading stiffness for wall SW6 at small displacements shown in Curve 'A' of Figure 115 is close to the experimental unloading stiffness. At large displacements, Curve 'B', the calculated unloading stiffness is lower than experimental value.

The experimental bending hysteresis loops for wall SW5 are not symmetric. This may be due to the influence of sliding across diagonal cracks on the vertical displacement gauges. Unsymmetric bending hysteresis loops were not observed in other walls with symmetric loadings. Unloading from a positive load is shown in Curve 'A' of Figure 114, where the experimental unloading curve is close to the calculated unloading curve. However, unloading from a negative load, Curve 'B', the experimental unloading stiffness is greater than the calculated unloading stiffness.

b. Reloading after Unloading from the Same Direction. The reloading curves for wall SW1a at both small and large displacements are shown in Curves 'C' and 'D' of Figure 111, where the calculated results are close to the experimental work. Similar amounts of energy were dissipated for both the calculated and experimental curves.

The calculated reloading curve for wall SW4a at small displacements shown in Curve 'C' of Figure 113 is close to the experimental reloading curve, however, more energy is dissipated by the calculated reloading curve. At larger displacements, Curve

'D', the calculated reloading curve and energy dissipated are similar to the experimental values.

The reloading curve for wall SW3 shown in Curve 'C' of Figure 112 is close to the experimental reloading curve, however, more energy is dissipated by the calculated reloading curve.

The reloading curve for wall SW6 shown in Curve 'C' of Figure 115 is also close to the experimental reloading curve. Again, more energy is dissipated by the calculated reloading curve than the experimental reloading curve.

c. Reloading after Unloading from the Opposite Direction. The calculated reloading curves for wall SW3 at both small and large displacements shown in Curves 'D' and 'E' of Figure 112 are reloading towards the correct common point. Recall the calculated unloading stiffness for Curve 'B' is greater than the experimental value. Thus the calculated reloading Curve 'E', which begins at the terminal point of Curve 'B', dissipates more energy than the experimental curve.

The reloading curves for wall SW6 at both small and large displacements shown in Curves 'D' and 'E' of Figure 115 are reloading towards the correct common point. Recall the unloading stiffness for Curve 'B' was less than the experimental value. Thus the calculated reloading Curve 'E', which begins at the terminal point of Curve 'B', dissipates less energy than the experimental curve.

The reloading curves for wall SW5 as shown in Figure 114 are similar to the experimental reloading curve except the calculated reloading curves are symmetric, and the calculated reloading curves do not pinch near Point 'E'.

d. Degrading Under Cyclic Loading. The experimental degrading stiffness factor, α, for wall SW1a at both small and large displacements as shown by Points 'E' and 'F' of Figure 111 are similar to the calculated values, except that the calculated α is larger than the experimental value for the first cycle at 'F'.

The experimental degrading stiffness factor, α, for wall SW4a at small displacements as shown by Point 'E' of Figure 113 is less than the calculated values for all five cycles. The experimental degrading stiffness factor, at larger displacements, Point 'F', is similar to the calculated value for the first cycle, and slightly larger than the calculated values for subsequent cycles.

The experimental degrading stiffness factor, α, for wall SW5 at small displacements as shown by Point 'C' of Figure 114 is greater than the calculated values for all five cycles. The experimental degrading stiffness factor at larger displacements, Point 'D', is smaller than the calculated value for the first cycle, and similar to the calculated values for subsequent cycles.

e. Loading and Unloading in Small Amplitude Loops. Two small amplitude loops are at Point 'F' in Figure 112 for wall SW3. The calculated loops have the same shape and dissipate the same amount of energy as the experimental data. A calculated loop with a load reversal at Point 'G' dissipates more energy than the experimental loop, because the experimental loop has a slight pinch near Point 'H'.

Two small amplitude loops are at Point 'F' in Figure 115 for wall SW6. The calculated loops have a similar shape and dissipate a little more energy than the experimental loop. A calculated loop with a load reversal at Point 'G' has the same shape and dissipates a similar amount of energy as the experimental loop.

At any given point the calculated bending stiffness may be a little more or less than the experimental stiffness. This is due in part to 1) scatter in the experimental data, 2) the choice of variables used for curve fitting, and 3) uncertainties in the separation of bending and shear displacement. Overall, the bending hysteresis model is able to represent the general bending behavior of the wall.

2. Shear Deformation. The calculated and experimental shear hysteresis loops for NCKU walls SW1a, SW3, SW4a, SW5, and SW6 are compared in Figures 116, 117, 118, 119, and 120, respectively. Overall, the comparison between calculated and experimental hysteresis loops is good. However, several points warrant further discussion:

a. Unloading in the Nonlinear Range. For wall SW1a the calculated unloading curves from both a small and large displacement shown in Curves 'A' and 'B' in Figure 116 are similar to the experimental unloading curves.

For wall SW4a the experimental hysteresis loops are very erratic. The calculated unloading stiffnesses for both small and large displacements shown in Curves 'A' and 'B' of Figure 118 are similar to the experimental data.

The unloading stiffnesses for wall SW3 at both small and large displacements shown in Figure 117 Curves 'A' and 'B' are close to the experimental values.

The unloading stiffnesses for wall SW6 at both small and large displacements shown in Figure 120 Curves 'A' and 'B' are also close to the experimental values. However, the calculated unloading Curve 'B' is not as nonlinear as the experimental unloading curve, thus, the calculated unloading curve dissipates less energy than the experimental unloading curve.

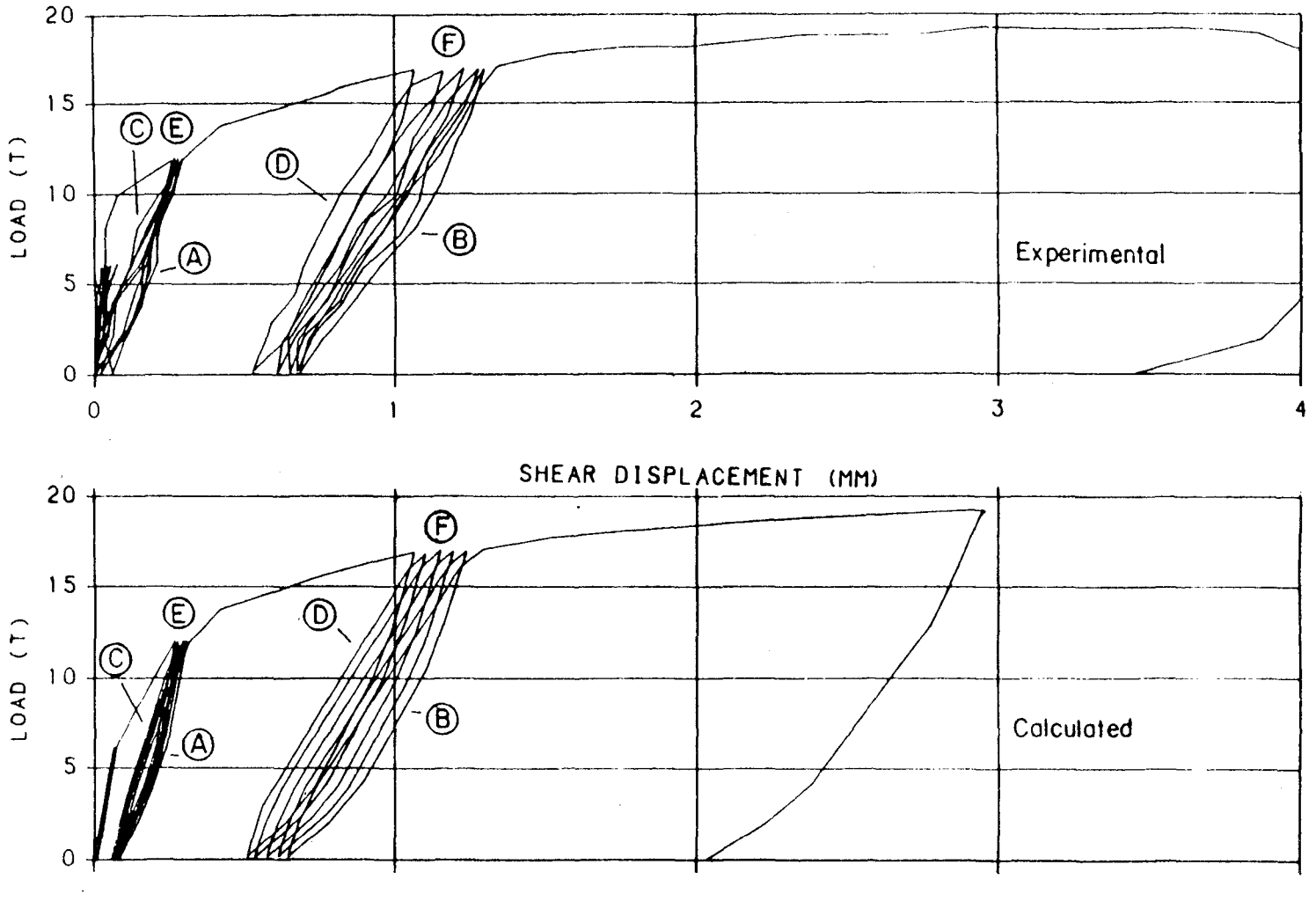

Figure 116. Comparison of Calculated and Experimental Shear Hysteresis Loops for NCKU Wall SW1a

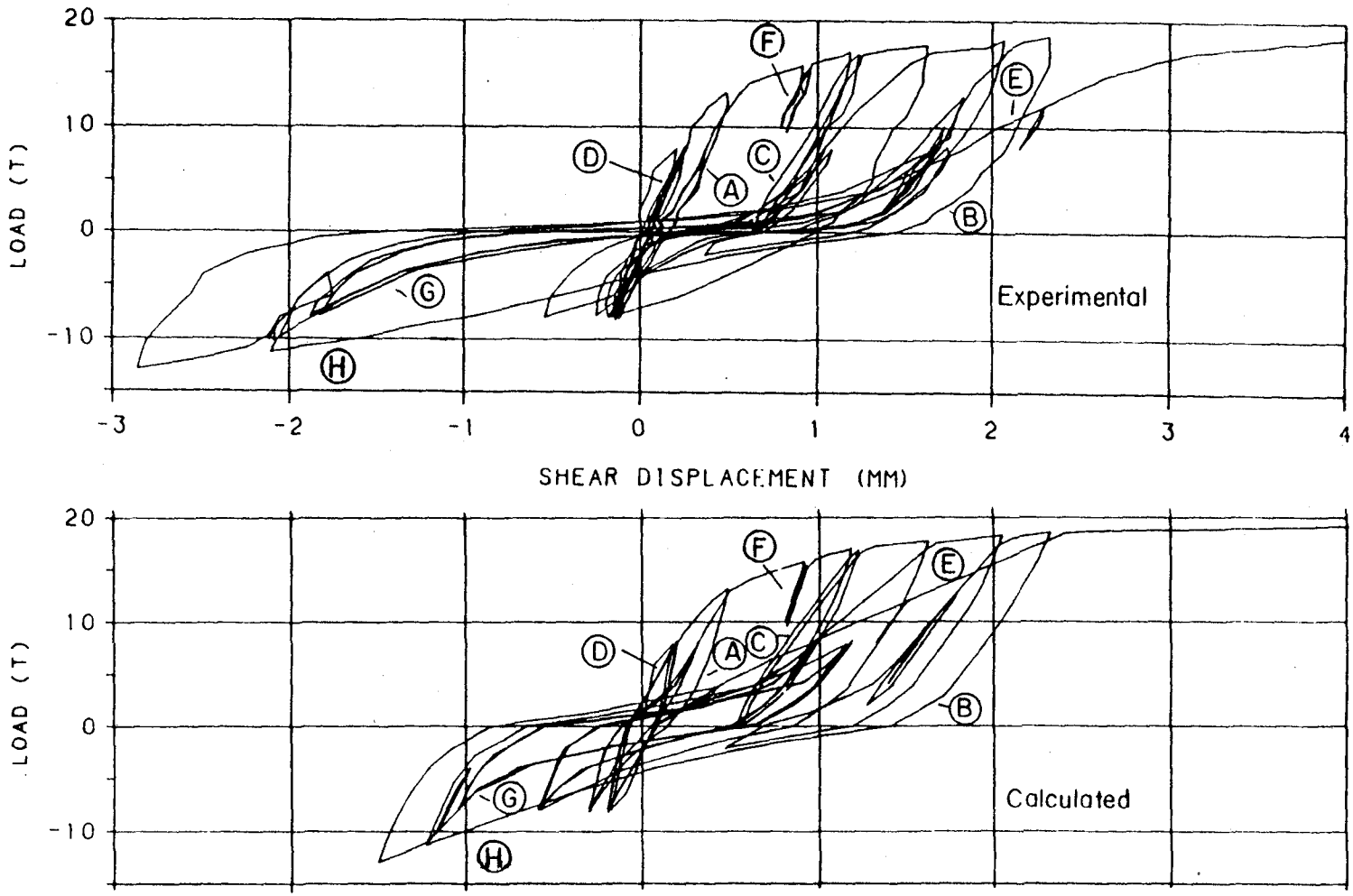

Figure 117. Comparison of Calculated and Experimental Shear Hysteresis Loops for NCKU Wall SW3

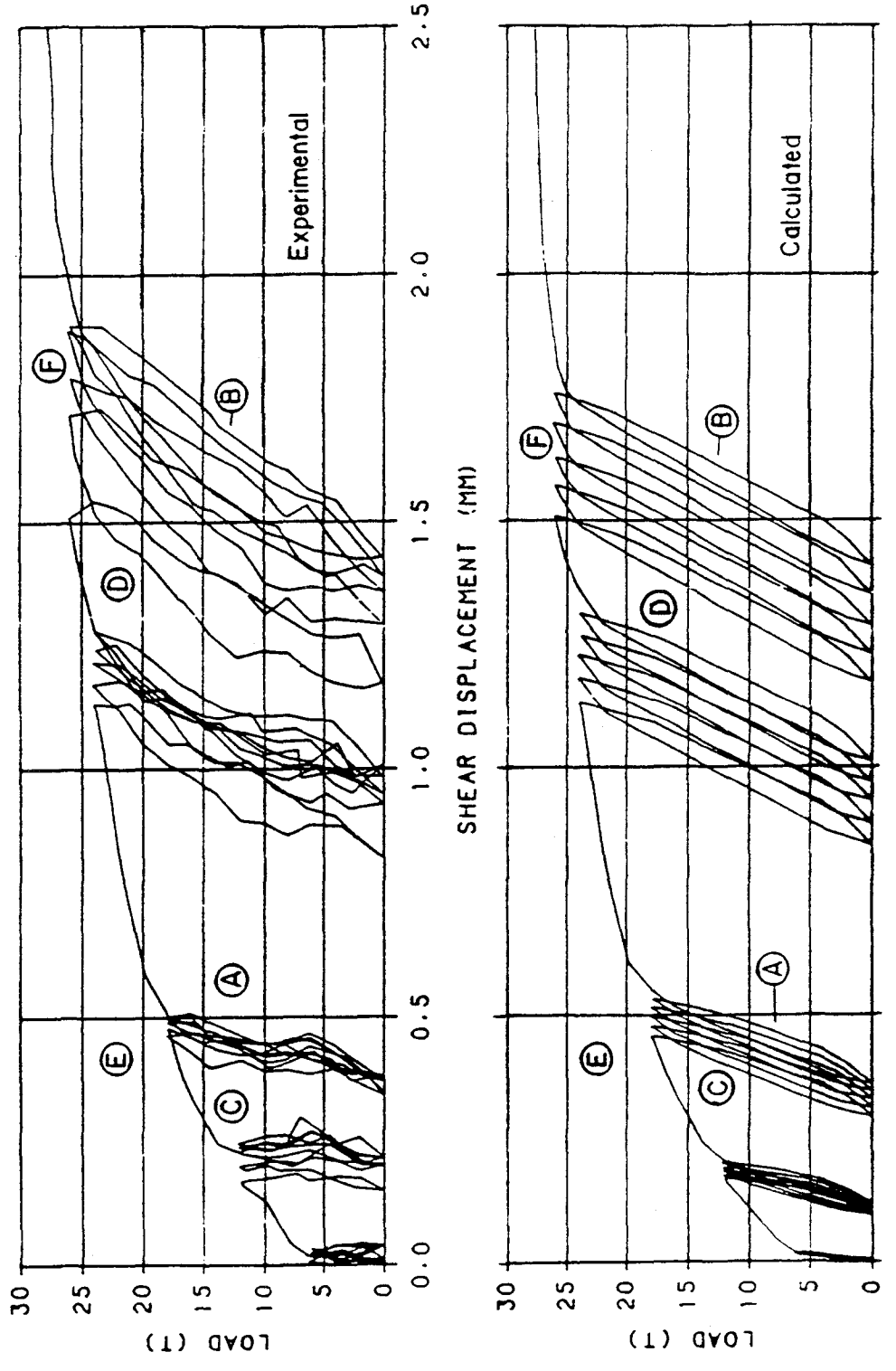

Figure 118. Comparison of Calculated and Experimental Shear Hysteresis Loops for NCKU Wall SW4a

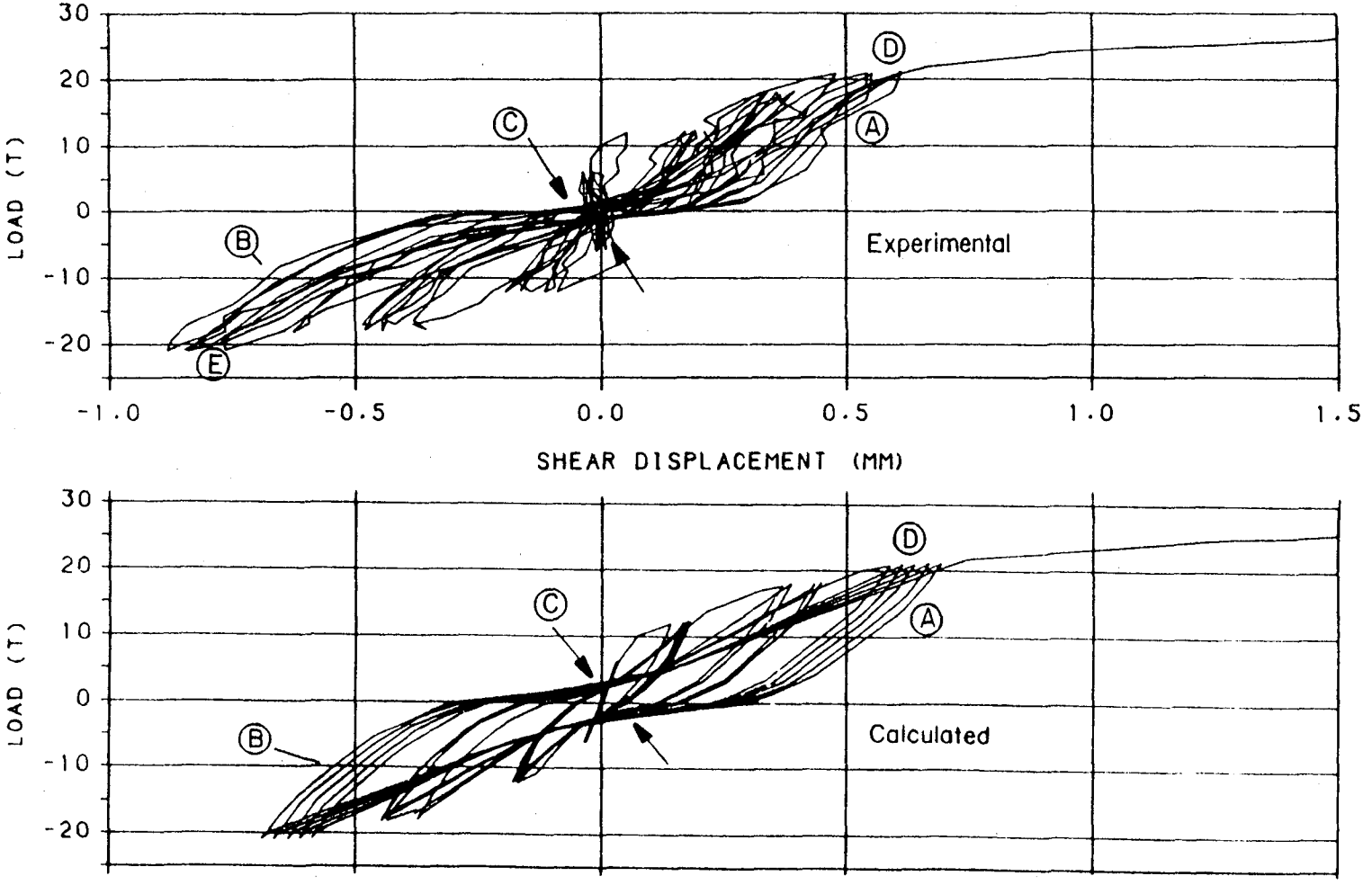

Figure 119. Comparison of Calculated and Experimental Shear Hysteresis Loops for NCKU Wall SW5

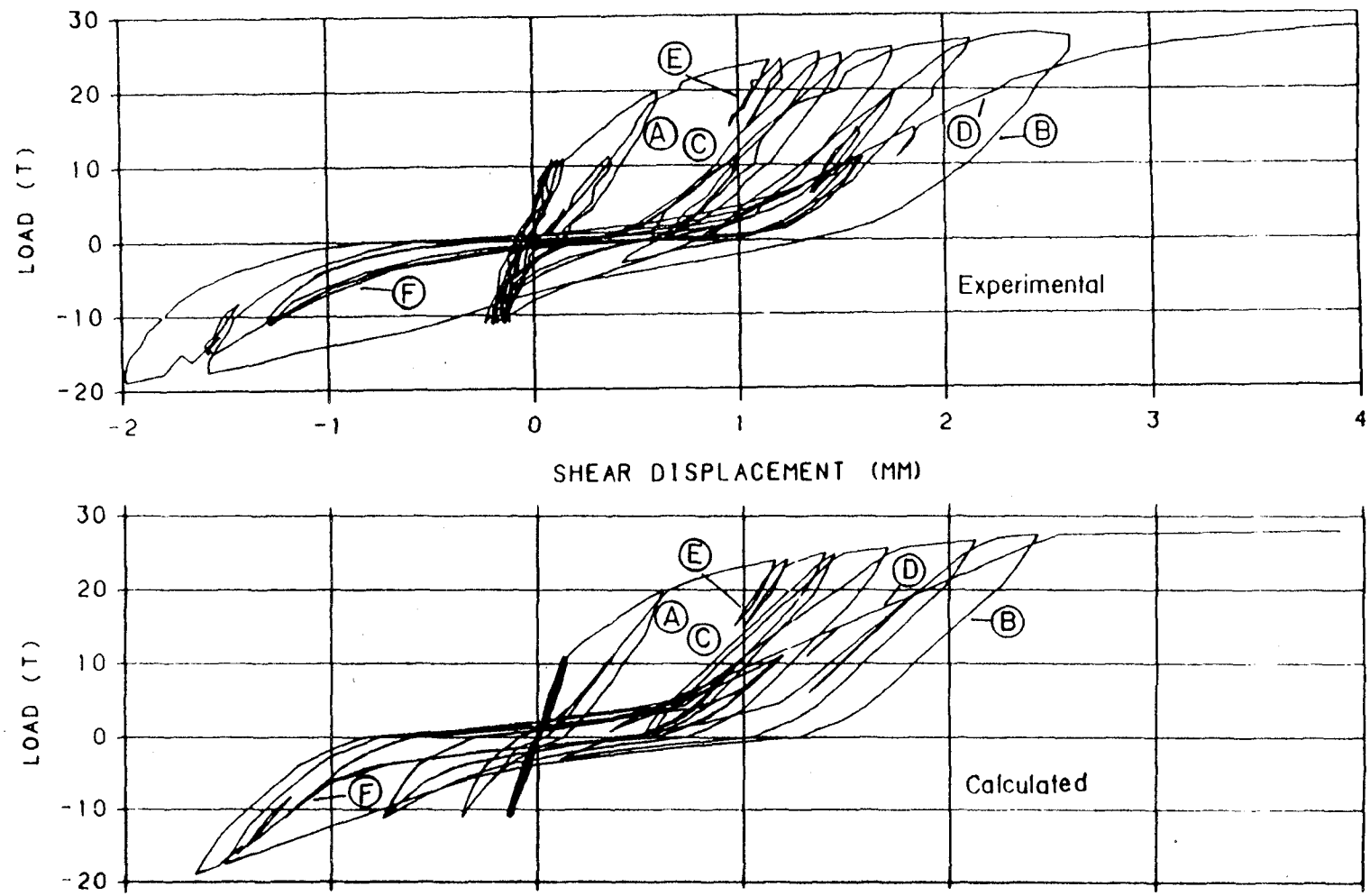

Figure 120. Comparison of Calculated and Experimental Shear Hysteresis Loops for NCKU Wall SW6

The hysteresis loops for wall SW5 are very erratic. Unloading from a positive load shown in Curve 'A' in Figure 119 the experimental unloading curve is similar to the calculated unloading curve. Recall the shear deformation is determined by subtracting the bending deformation from the total deformation. In the previous discussion it was shown that the bending deformation is unsymmetric, with larger positive displacements than negative displacements. In the next section, the total deformation of wall SW5 is shown to be nearly symmetric. Thus the unsymmetric shear displacements shown in the figure, with larger negative displacements than positive displacements, are reasonable given that the bending displacements are unsymmetric. However the lack of symmetry for the shear deformation is not as severe as the bending deformation. Thus unloading from a negative load, Curve 'B', the experimental unloading curve is also similar to the calculated unloading curve.

b. Reloading after Unloading from the Same Direction. The reloading curves for wall SW1a at both small and large displacements shown Curves 'C' and 'D' in Figure 116 are close to the experimental reloading curves. Similar amounts of energy were dissipated by both the calculated and experimental hysteresis loops.

The experimental reloading curve for wall SW4a at both small and large displacements shown Curves 'C' and 'D' in Figure 118 are very erratic. The calculated reloading curves are a reasonable approximation of the experimental data.

The reloading curve for wall SW3 shown in Curve 'C' in Figure 117 is close to the experimental reloading curve. However, the calculated hysteresis loop dissipates more energy than the experimental data.

The reloading curve for wall SW6 shown in Curve 'C' in Figure 120 is also close to the experimental reloading curve.

c. Reloading after Unloading from the Opposite Direction. The reloading curve for wall SW3 at a small displacement shown in Curve 'D' of Figure 117 is reloading towards the correct common point. At this small displacement, pinching is negligible. Reloading with a larger displacement, Curve 'E', the calculated pinching is much less than the experimental pinching. Thus the calculated hysteresis loops dissipate more energy than the experimental hysteresis loops. Reloading with a negative displacement, Curve H, the calculated reloading stiffness is greater than the experimental reloading stiffness, causing the calculated reloading curve to be smaller.

The calculated reloading curves for wall SW6 at large displacement shown in Curve 'D' of Figure 120 has less pinching than the experimental data. However the shapes of the two curves are similar.

The reloading curves for wall SW5 are very erratic. The amount of pinching in the calculated reloading curves as shown by Point 'C' of Figure 119 is larger than the amount of pinching in the experimental reloading curves. Thus the calculated hysteresis loops dissipate more energy than the experimental hysteresis loops.

d. Degrading Under Cyclic Loading. The experimental degrading stiffness factor, α, for wall SW1a at both small and large displacements shown by Points 'E' and 'F' of Figure 116 is similar to the calculated values, except for the first load cycle at 'F', where the experimental α is greater than the calculated α.

The experimental degrading stiffness factor, α, for wall SW4a at small displacements shown by Point 'E' of Figure 118 is less than the calculated values for all five cycles. The experimental degrading stiffness factor at larger displacements, Point 'F', is greater than the calculated values.

The experimental degrading stiffness factor, α, for wall SW5 at large displacements for both positive and negative loadings shown by Points 'D' and 'E' of Figure 119 is similar to the calculated values.

e. Loading and Unloading in Small Amplitude Loops. Two small amplitude loops are at Point 'F' shown in Figure 117 for wall SW3. The calculated loops have the same shape and dissipate the same amount of energy as the experimental data. A calculated loop with a load reversal, Curve 'G', is smaller than the experimental loop.

The two small amplitude loops at Point 'E' shown in Figure 120 for wall SW6 have a similar shape and dissipate a little more energy than the experimental data. A calculated loop with a load reversal, Curve 'F', has the same shape and dissipates a similar amount of energy as the experimental data.

At any given point, the calculated shear stiffness may be a little more or less than the experimental stiffness as was discussed in the bending stiffness case. Overall, the shear hysteresis model is able to represent the general behavior of the wall.

3. Total Deformation. The calculated shear and bending deformations are added together, and compared with the measured total deformations for NCKU walls SW1a, SW3, SW4a, SW5, and SW6 in Figures 121, 122, 123, 124, and 125, respectively. Overall, the comparison between calculated and experimental hysteresis loops is very good.

The total energy stored in the calculated and experimental hysteresis loops is also compared for NCKU walls SW1a, SW3, SW4a, SW5, and SW6 in Figures 126, 127, 126, 128, and 127, respectively. The total energy for step I is determined from

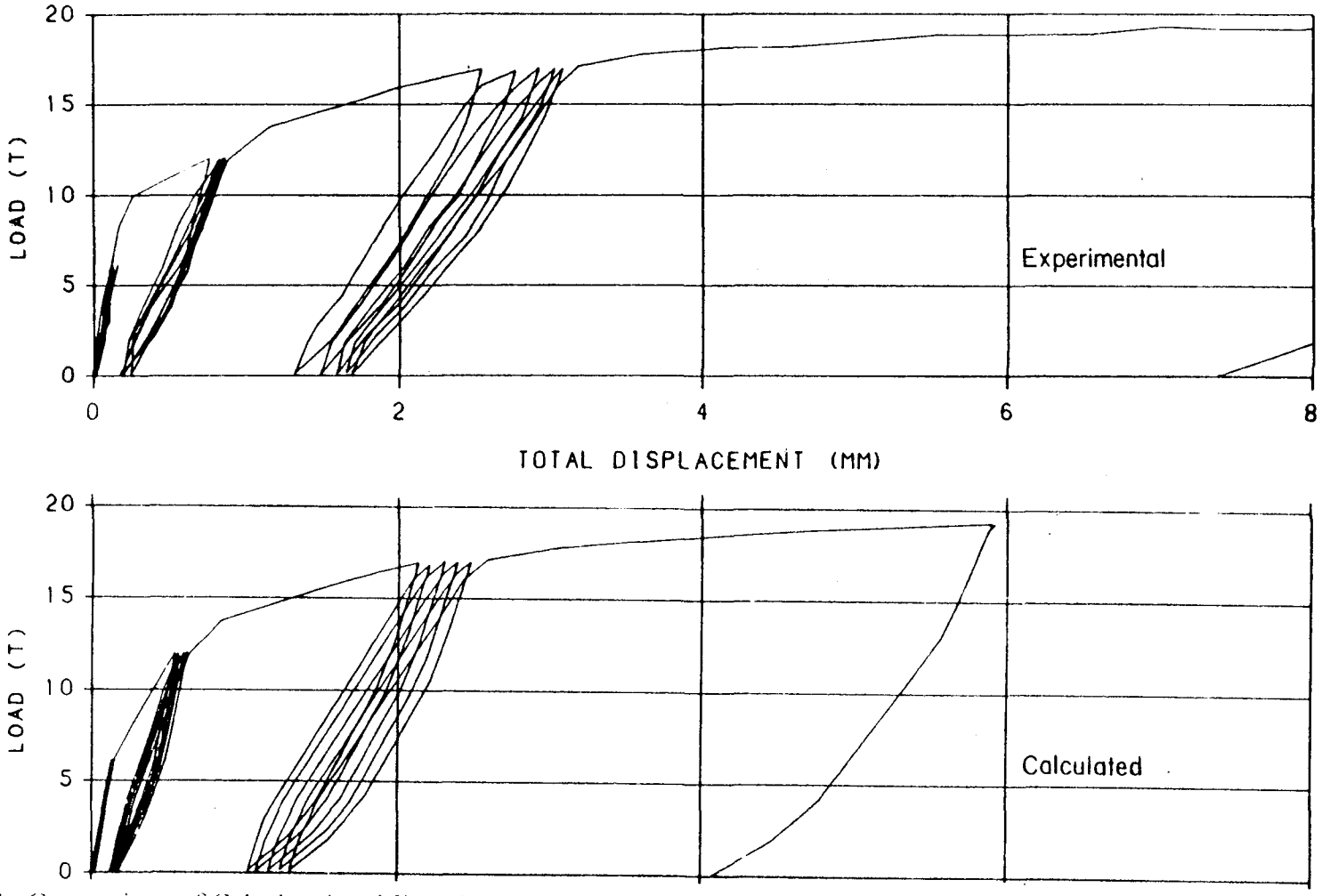

Figure 121. Comparison of Calculated and Experimental Total Deformation Hysteresis Loops for NCKU Wall SW1a

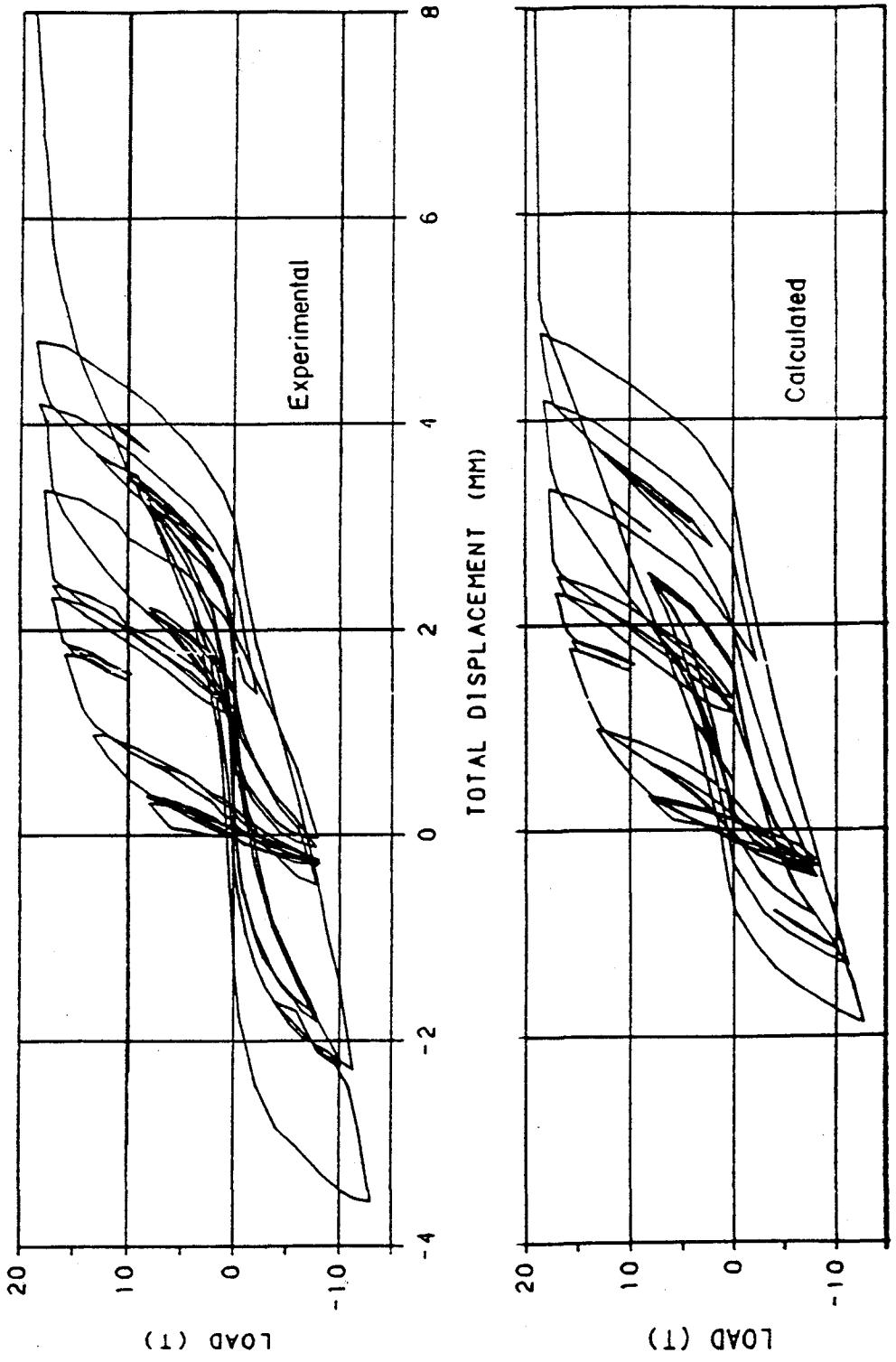

Figure 122. Comparison of Calculated and Experimental Total Deformation Hysteresis Loops for NCKU Wall SW3

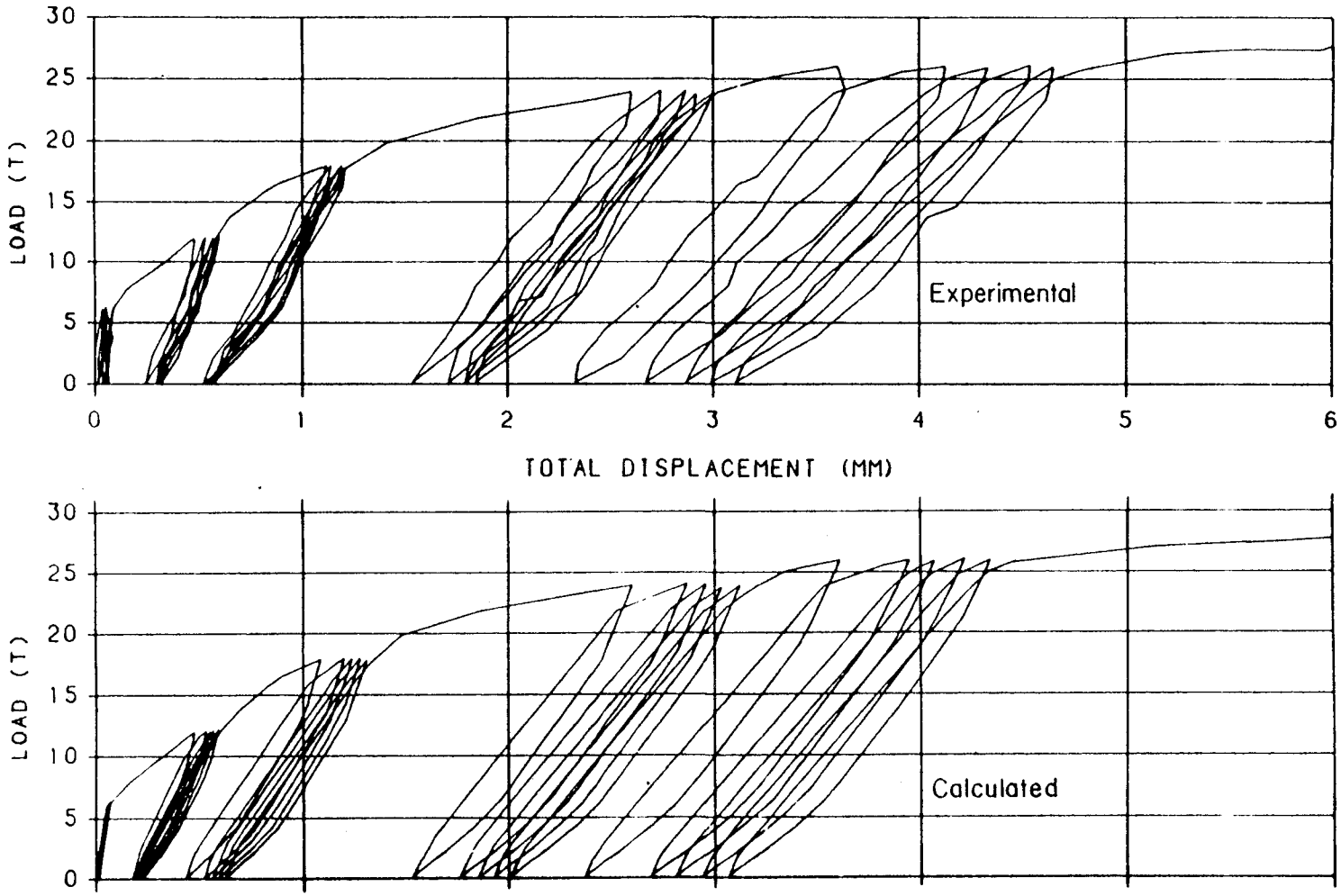

Figure 123. Comparison of Calculated and Experimental Total Deformation Hysteresis Loops for NCKU Wall SW4a

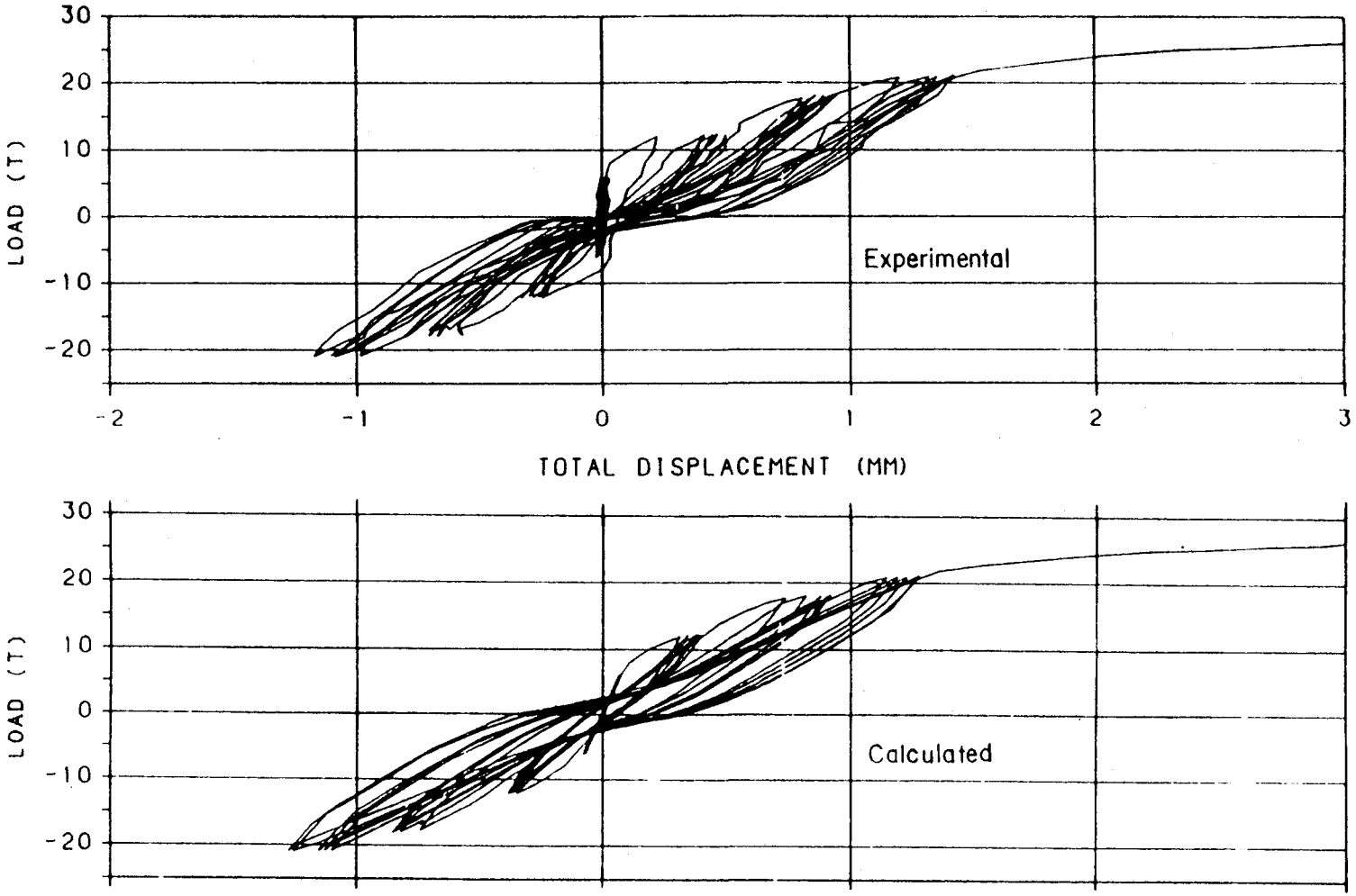

Figure 124. Comparison of Calculated and Experimental Total Deformation Hysteresis Loops for NCKU Wall SW5

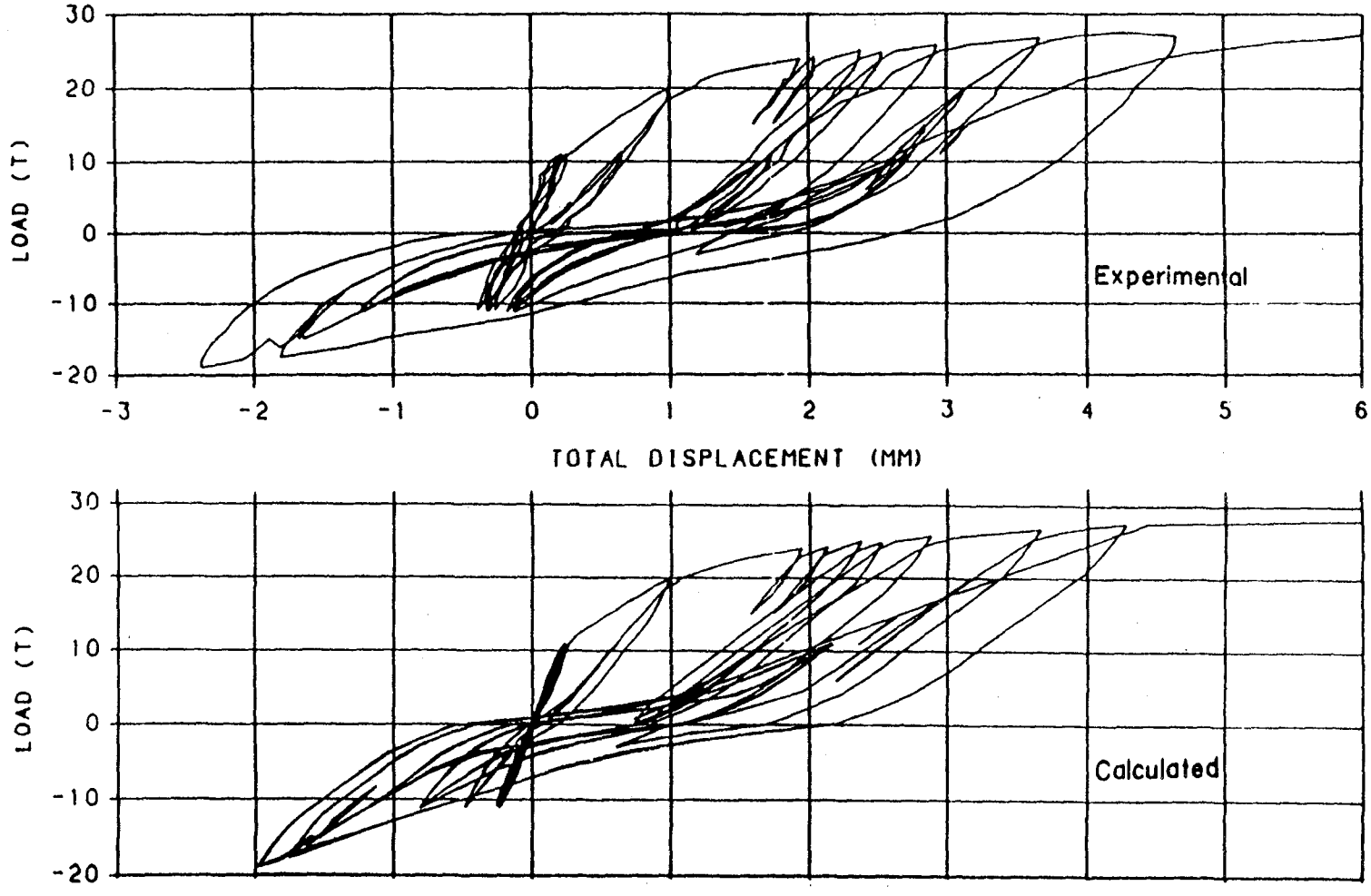

Figure 125. Comparison of Calculated and Experimental Total Deformation Hysteresis Loops for NCKU Wall SW6

$$\text{Energy}_I = \text{Energy}_{I-1} + \frac{P(I) + P(I-1)}{2}[D(I) - D(I-1)] \quad (4.48)$$

where the calculated displacement D, is used to determine the calculated energy.

The calculated hysteresis loops for wall SW1a as shown in Figure 121 are the same size and shape as the experimental hysteresis loops. The calculated hysteresis loops dissipate a little more energy than the experimental loops as shown in Figure 126. Overall, this comparison is very good.

The calculated hysteresis loops for wall SW3 as shown in Figure 122 are the same size and shape as the experimental hysteresis loops, except that 1) the calculated loops do not have as large of a displacement in the negative direction, and 2) the calculated pinching is not as severe as the experimental pinching. Thus the calculated hysteresis loops dissipate about 10% more energy than the experimental loops as shown in Figure 127. Except for the two items mentioned above, this comparison is good.

The calculated hysteresis loops for wall SW4a shown in Figure 123 are the same size and shape as the experimental hysteresis loops. At small displacements the calculated hysteresis loops dissipate a little more energy than the experimental loops as shown in Figure 126. At larger displacements the experimental loops dissipate more energy than the calculated loops. Overall, this comparison is good.

The calculated hysteresis loops for wall SW5 shown in Figure 124 do not pinch as much as the experimental loops. This causes the energy dissipated by the calculated hysteresis loops to exceed the energy dissipated by the experimental hysteresis loops by about 33% as shown in Figure 128. Aside from the pinching, the comparison between these two loops is good.

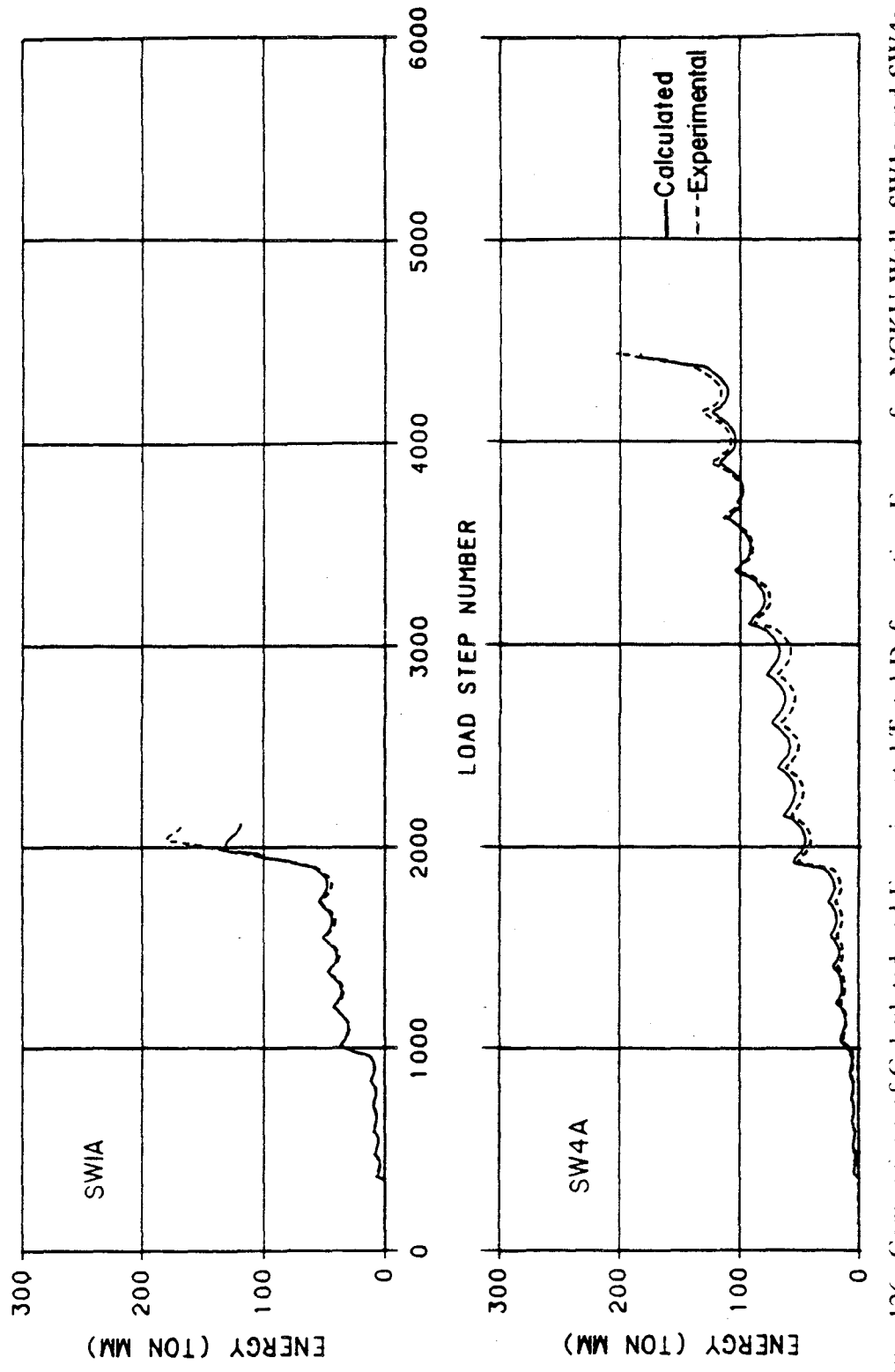

Figure 126. Comparison of Calculated and Experimental Total Deformation Energy for NCKU Walls SW1a and SW4a

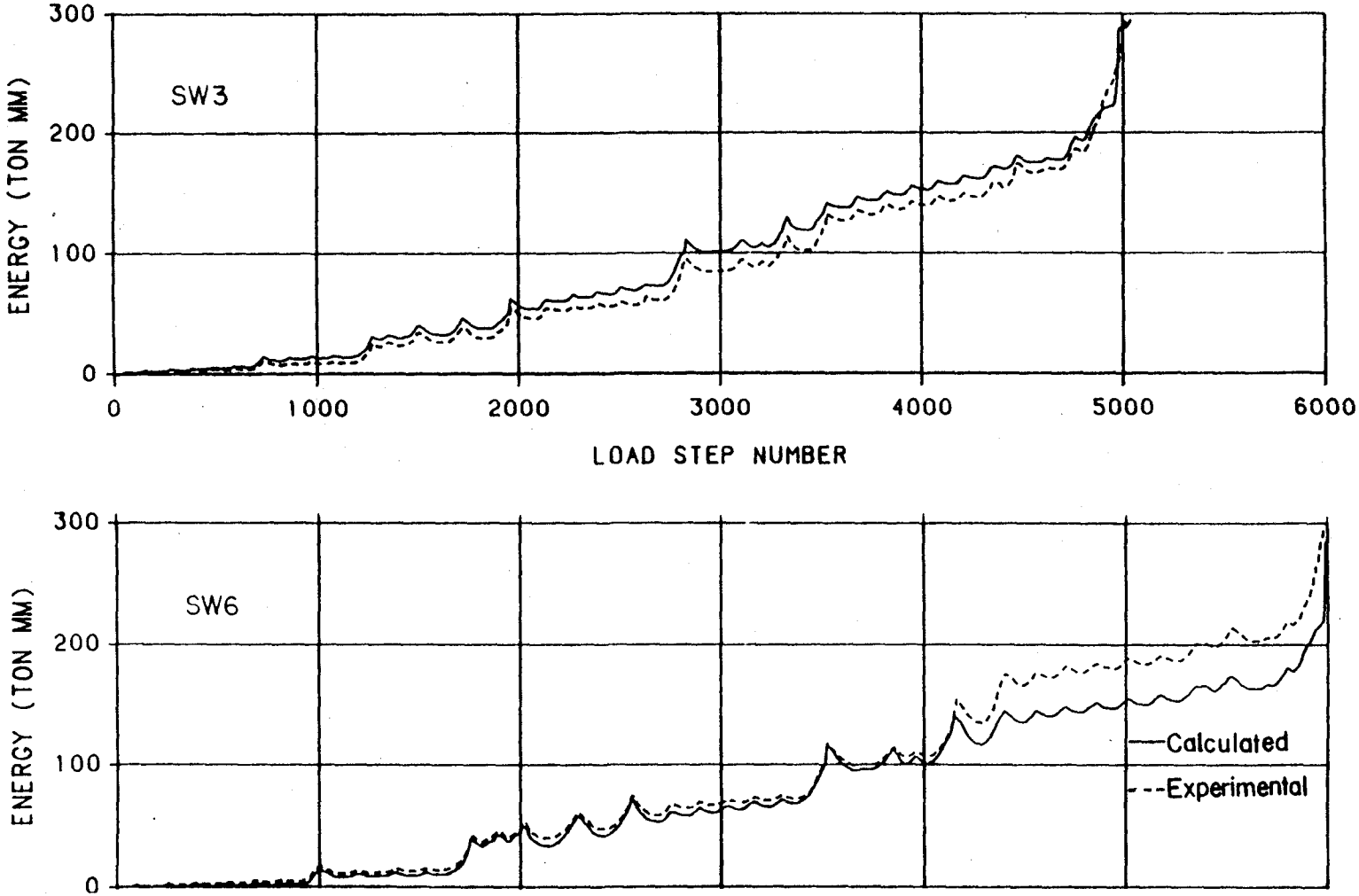

Figure 127. Comparison of Calculated and Experimental Total Deformation Energy for NCKU Walls SW3 and SW6

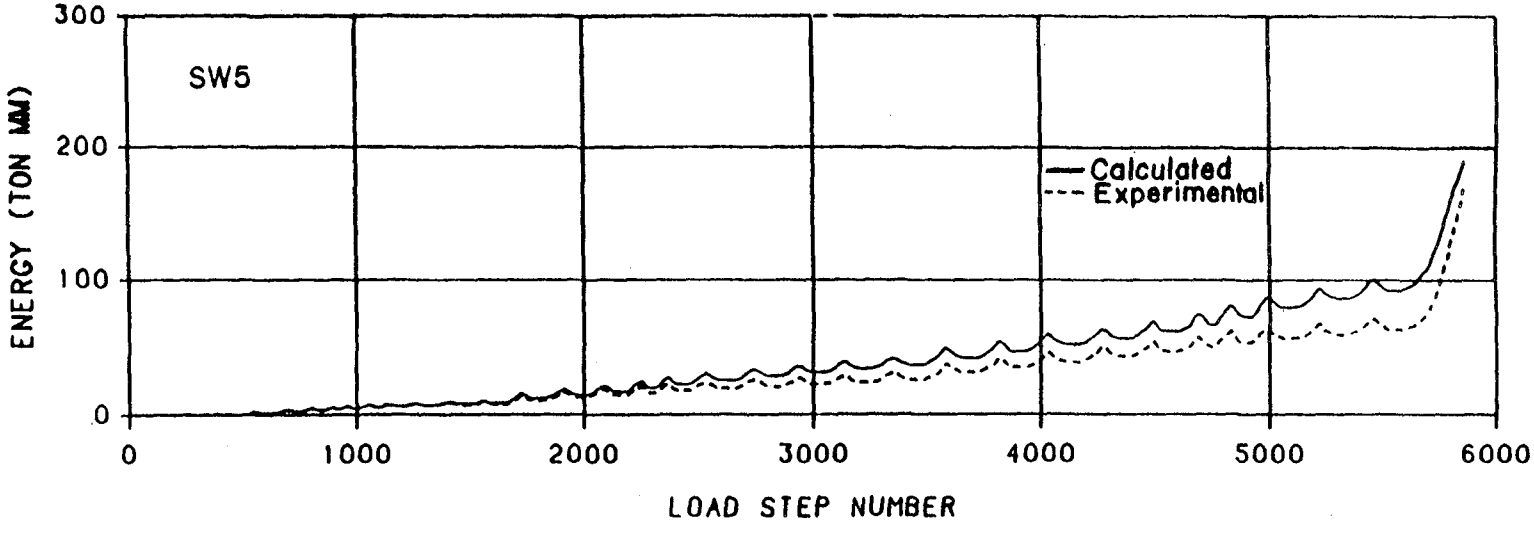

Figure 128. Comparison of Calculated and Experimental Total Deformation Energy for NCKU Wall SW5

The calculated hysteresis loops for wall SW6 shown in Figure 125 are close to the experimental hysteresis loops, with a couple of exceptions. For one loop, the experimental unloading begins at a displacement of +4.6 mm, while the calculated displacement is at +4.3 mm. As unloading progresses, the experimental hysteresis loop dissipates more energy than the calculated hysteresis loop. Also, upon reloading the experimental hysteresis loop does not pinch as much as the calculated hysteresis loop. Thus, the experimental hysteresis loop dissipates more energy than the calculated hysteresis loop as shown in Figure 127. Overall, the comparison between calculated and experimental hysteresis loops is good.

C. AXIAL HYSTERESIS MODEL

The axial hysteresis model was developed by Kabeyasawa, et al (49) for shear walls and boundary columns as part of the analytical studies for the full scale seven story test structure. This hysteresis model as shown in Figures 129 and 130 has the following attributes.

1. Tensile Backbone Curve. The tensile backbone curve is bilinear. The initial tensile stiffness is

$$Kt = 0.90\, Ec\, Ag \tag{4.49}$$

where Ec is the concrete modulus of elasticity and Ag is the gross cross sectional area of the member. The stiffness changes at the steel yield point (Dyt, Fy),

$$Fy = fy\, As, \qquad Dyt = \frac{Fy}{Kt}, \tag{4.50}$$

where fy is the yield point of the steel bars and As is the area of the reinforcing steel. The post yield stiffness is given by

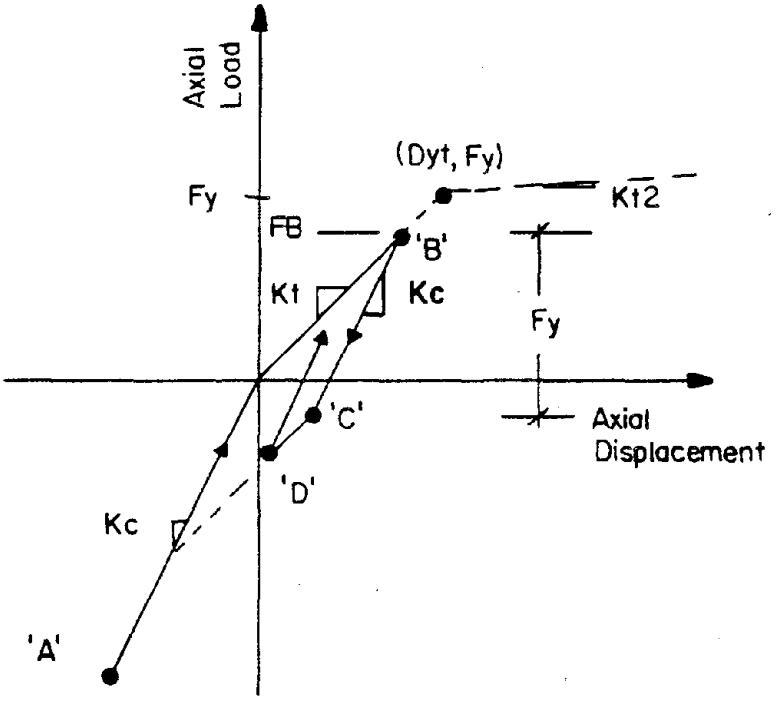

Figure 129. Axial Hysteresis Model before Tensile Yield

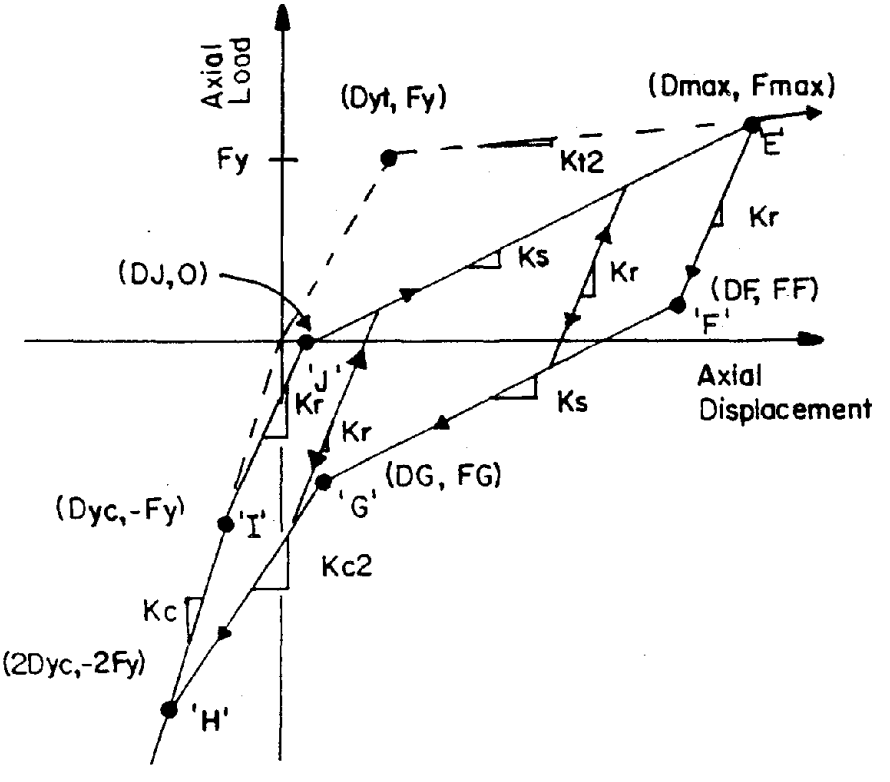

Figure 130. Axial Hysteresis Model after Tensile Yield

$$Kt2 = 0.001\ Ec\ Ag \tag{4.51}$$

2. Compression Backbone Curve. The compressive backbone curve is linear, which is a reasonable assumption for concrete, if compressive stresses remain below $0.50f'_c$. The gross compressive stress in a shear wall is usually much less than $0.50f'_c$. Thus the compressive stiffness is given by

$$Kc = Ec\ Ag \tag{4.52}$$

3. Cyclic Loadings before Yielding. For cyclic loadings before the member has yielded, a bilinear hysteresis loop is used as shown in Figure 129. Consider a member with an initial compressive load at 'A'. As that member is loaded[13], it has a stiffness of Kc. Once the member goes into tension, the loading stiffness becomes Kt. At point 'B', the load is FB. Unloading from point 'B', the stiffness is Kc, until point 'C', which has a load of FB – Fy. Further unloading continues with a stiffness of Kt to point 'D'. Reloading from point 'D' continues with a stiffness of Kc.

4. Cyclic Loadings after Yielding. For cyclic loadings after the member has yielded, a modified bilinear hysteresis loop is used as shown in Figure 130. Consider a member that has yielded in tension and is at point 'E' with a load and displacement of Fmax and Dmax. As the member is unloaded, the unloading stiffness is

---

[13] Since the axial hysteresis model behaves differently in compression than tension, the following definition of loading and unloading is used. Loading corresponds to applying a tensile load, or reducing a compressive load. Unloading corresponds to reducing a tensile load or applying a compressive load.

$$Kr = Kc\left(\frac{Dyt}{Dmax}\right)^{\alpha} \geq \left(\frac{Fmax + Fy}{Dmax - Dyc}\right) \tag{4.53}$$

where $Dyc = \frac{-Fy}{Kc}$ and $\alpha = 0.90$. Unloading continues to point 'F', which has a load and displacement of

$$FF = Fmax - Fy, \qquad DF = Dmax - \frac{Fy}{Kr} \tag{4.54}$$

Below this point, unloading continues with a stiffness of

$$Ks = \frac{FF + Fy}{DF - Dyc} \tag{4.55}$$

to point 'G', which has a displacement of

$$DG = Dyc + 0.20(DF - Dyc) \tag{4.56}$$

and a load of

$$FG = FF + Ks(DG - DF) \tag{4.57}$$

Beyond point 'G' unloading continues on a transition curve that goes from point 'G' to point 'H' on the compression backbone curve and has the stiffness

$$Kc2 = \frac{FG + 2 \times Fy}{DG - 2 \times Dyc} \tag{4.58}$$

Further unloading and loading are on the compression backbone curve, until the member is loaded beyond point 'I', which has the coordinates (Dyc, -Fy). Loading beyond point 'I' has a stiffness of Kr and continues to point 'J' which has the coordinates

$$FJ = 0 \qquad DJ = Dyc + \frac{FY}{Kr} \tag{4.59}$$

Reloading beyond point 'J' has a stiffness of Ks and continues back to point 'E'. Reloading beyond point 'E' continues on the tension backbone curve. Loading and unloading on small amplitude loops inside the region 'E-F-G-H-I-J-E' have a stiffness of Kr.

5. Summary of Axial Hysteresis Model. This model was developed primarily for reinforced boundary columns. As additional data become available from experimental studies of axial loads on R/C shear walls, this model may be updated. This topic is recommended for further research.

V. ANALYTICAL FORMULATION FOR 3-D STRUCTURAL SYSTEMS

This chapter presents the matrix formulation for analyzing 3-D structural systems subject to both static and seismic loadings. A shear wall stiffness element is developed that utilizes the bending and shear backbone curves and the hysteresis models included in Chapters III and IV, respectively. Additionally, the input, stored and dissipated energy in the structure, the damage index, and the ductility and excursion ratio are presented.

A. JOINT BASED DEGREES OF FREEDOM

The structural model consists of an assemblage of elements. The point where two or more elements connect is a called a joint. A structure is modelled by first giving the location and orientation of each joint; the elements that connect the joints and the orientations of the elements are then defined. The structure's degrees of freedom are determined by the joints, their orientation, and the joint constraints. This section discusses the location and orientation of the joints, the degrees of freedom associated with the joints, and the joint constraints.

1. Global Coordinate System. The structure is defined in the global coordinate system (GCS). The GCS is a Cartesian coordinate system with three perpendicular axes X_g, Y_g, and Z_g. The Z_g axis is defined as X_g cross Y_g (right hand rule) as shown in Figure 131. The location of the GCS's origin is arbitrary and is usually taken at the centroid of the structure's base.

2. Joint Coordinate System. The location of a joint is defined by its coordinates (X_g, Y_g, Z_g) in the GCS. At each joint, there is an individual joint coordinate system (JCS). The JCS is defined by the axes X_j, Y_j and Z_j and has its origin at the joint.

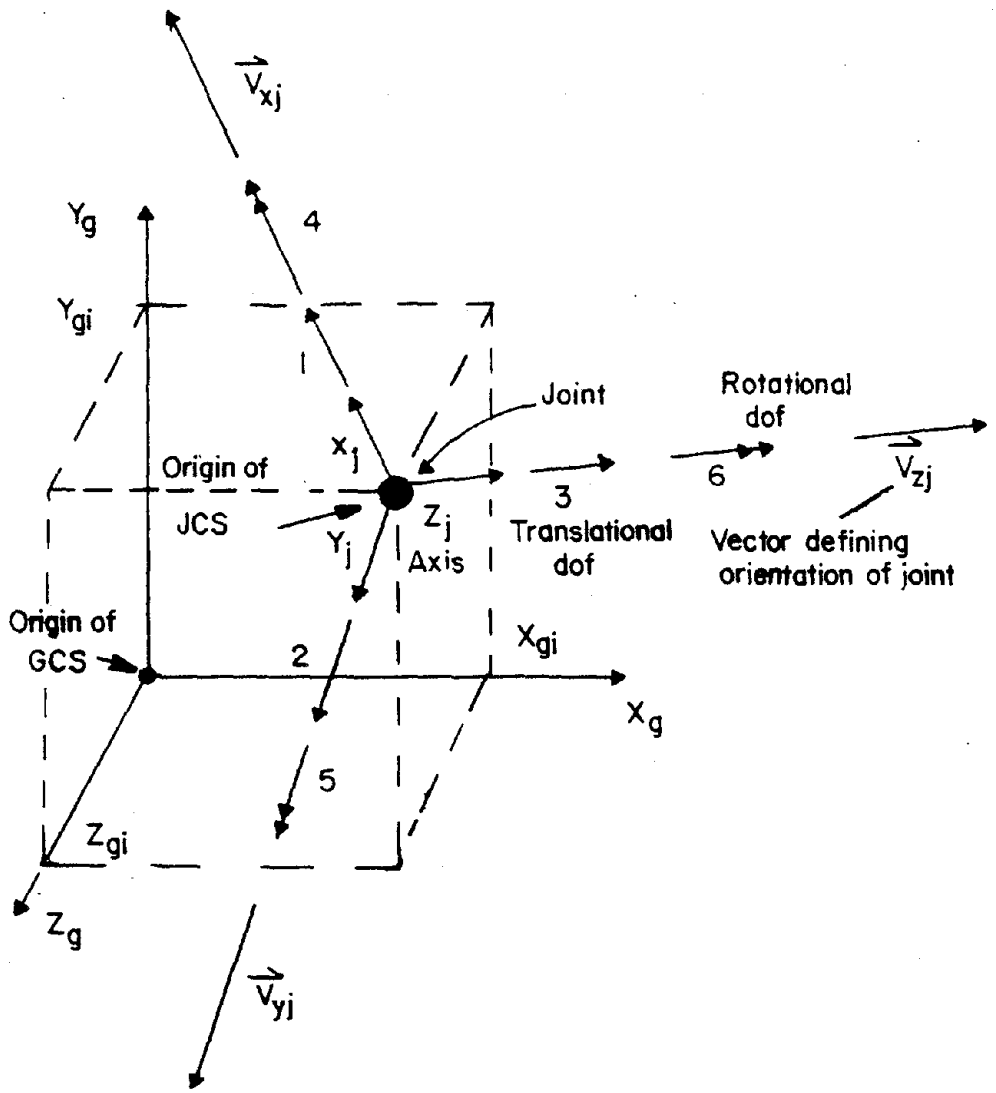

Figure 131. Global (GCS) and Joint (JCS) Coordinate System

The orientation of the JCS may not be parallel to the GCS and is defined by two perpendicular unit vectors $\vec{V}_{xj}$, and $\vec{V}_{yj}$ as shown in Figure 131. A third vector $\vec{V}_{zj}$ is defined as $\vec{V}_{zj} = \vec{V}_{xj} \times \vec{V}_{yj}$. The three vectors are written in matrix form as

$$\left[\vec{V}_j\right] = \begin{bmatrix} \vec{V}_{xj} \\ \vec{V}_{yj} \\ \vec{V}_{zj} \end{bmatrix} = \begin{bmatrix} c_{11} & c_{12} & c_{13} \\ c_{21} & c_{22} & c_{23} \\ c_{31} & c_{32} & c_{33} \end{bmatrix} \begin{bmatrix} \vec{i} \\ \vec{j} \\ \vec{k} \end{bmatrix} = \left[C_j\right] \begin{bmatrix} \vec{i} \\ \vec{j} \\ \vec{k} \end{bmatrix} \tag{5.1}$$

where $\vec{i}$, $\vec{j}$ and $\vec{k}$ are unit vectors parallel to the X_g, Y_g and Z_g axes, and c_{ij} are the direction cosines for vector i.

Each joint has three translational and three rotational degrees of freedom (dof). Degrees of freedom 1, 2 and 3 are translational corresponding to the joint's X_j, Y_j, and Z_j axes. Degrees of freedom 4, 5 and 6 are rotational about the joint's X_j, Y_j and Z_j axes as shown in Figure 131. The orientation of the JCS determines the orientation of the degrees of freedom for that joint.

3. Constraint Equations. Often the deformation of one building component is very small relative to the deformations of other components. The component with very small deformation may be idealized as a rigid body. Two joints on the rigid body are constrained, such that the deformation of one joint (the 'slave' joint) is represented by the deformation of the other joint (the 'master' joint). Thus the degrees of freedom for the 'slave' joint are transferred to the 'master' joint, and the number of degrees of freedom is reduced. The reduced set of degrees of freedom is referred to as the global

degrees of freedom (Gdof)[14]. Transformations for a 3-D constraint and a planar constraint are developed below.

Let joint m be the 'master' joint and joint s be the 'slave' joint. Also, let the orientation of both joints be identical, $\left[\vec{V}_j\right]_m = \left[\vec{V}_j\right]_s$. Assume that the two joints are connected by a rigid body. Thus the forces at the 'slave' joint are transferred to the 'master' joint, and the displacements of the 'slave' joint are expressed in terms of the 'master' joint.

Examining Figure 132, for the typical notation, F_{jmX} represents the force at the master joint in the JCS X direction and M_{jmZ} represents the moment at the master joint about the JCS Z axis. Likewise F_{jsX} represents the force at the slave joint in the JCS X direction and M_{jsZ} represents the moment at the slave joint about the JCS Z axis. Summing the forces acting on the slave joint about the master joint, in three dimensions, yields the force transformation for a 3-D rigid body (84).

$$\begin{bmatrix} F_{jmX} \\ F_{jmY} \\ F_{jmZ} \\ M_{jmX} \\ M_{jmY} \\ M_{jmZ} \end{bmatrix} = \begin{bmatrix} 1 & 0 & 0 & 0 & 0 & 0 \\ 0 & 1 & 0 & 0 & 0 & 0 \\ 0 & 0 & 1 & 0 & 0 & 0 \\ 0 & -Z_{ms} & Y_{ms} & 1 & 0 & 0 \\ Z_{ms} & 0 & -X_{ms} & 0 & 1 & 0 \\ -Y_{ms} & X_{ms} & 0 & 0 & 0 & 1 \end{bmatrix} \begin{bmatrix} F_{jsX} \\ F_{jsY} \\ F_{jsZ} \\ M_{jsX} \\ M_{jsY} \\ M_{jsZ} \end{bmatrix} \tag{5.2}$$

or

---

[14] Gdof are degrees of freedom in the JCS at 'master' and unconstrained joints. These degrees of freedom are global in the sense that they describe the structural motion, not that they are parallel to the GCS.

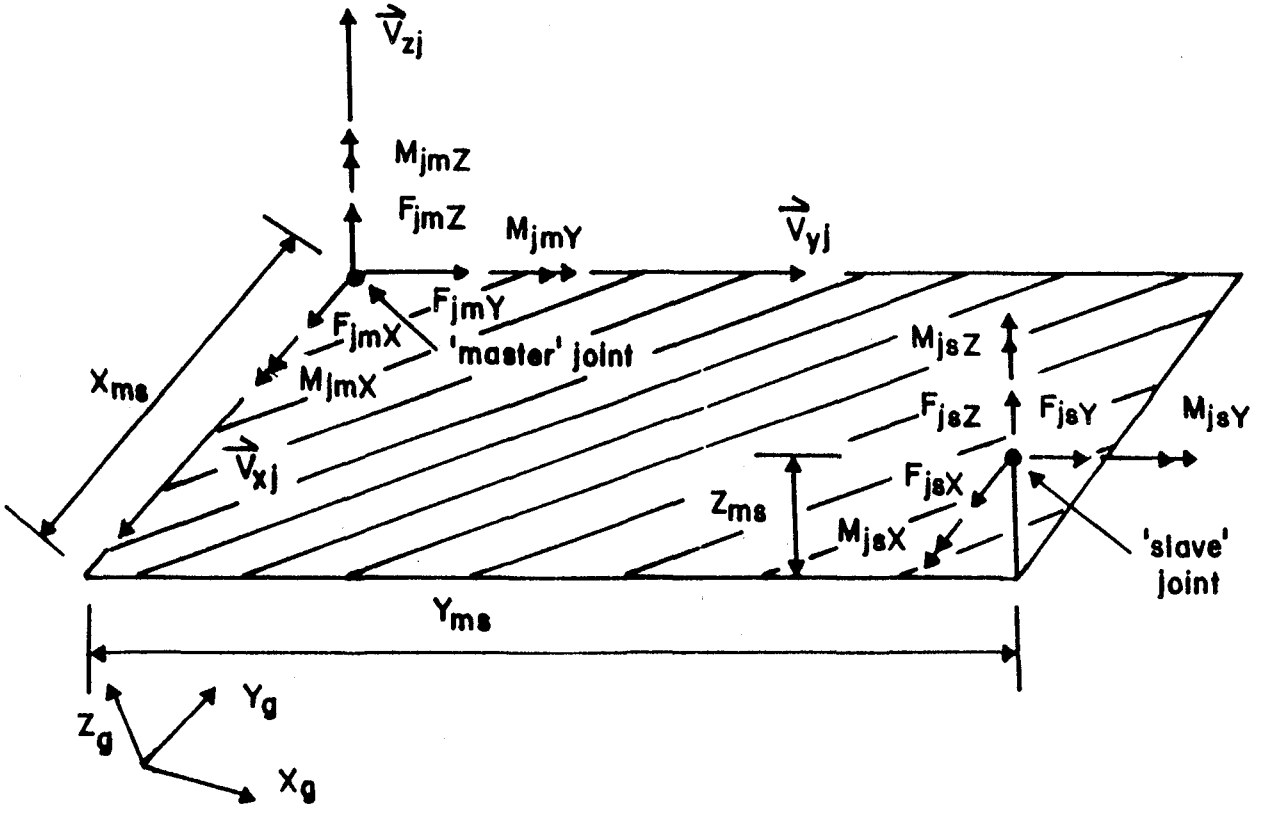

Figure 132. Rigid Body Constraint

$$[F_{jm}] = [T_{ms}][F_{js}] \tag{5.3}$$

where $[F_{jm}]$ represents the forces acting on the master joint, and $[F_{js}]$ represents the forces acting on the slave joint. A similar transformation for displacements can be derived

$$[\delta_{js}] = [T_{ms}]^T[\delta_{jm}] \tag{5.4}$$

where $[\delta_{jm}]$ represents the displacements of the master joint, and $[\delta_{js}]$ represents the displacements of the slave joint.

The distances X_{ms}, Y_{ms} and Z_{ms} are in the master joint's JCS. Recall the joint's coordinates are defined in the GCS. Transferring the coordinates of both joints from the GCS into the JCS and subtracting yield

$$\begin{bmatrix} X_{ms} \\ Y_{ms} \\ Z_{ms} \end{bmatrix} = [C_j] \begin{bmatrix} X_{gs} \\ Y_{gs} \\ Z_{gs} \end{bmatrix} - [C_j] \begin{bmatrix} X_{gm} \\ Y_{gm} \\ Z_{gm} \end{bmatrix} \tag{5.5}$$

where the typical notation X_{gm} represents the global X coordinate of the 'master' joint m, and Z_{gs} represents the global Z coordinate of the 'slave' joint s.

Since the displacement of the 'slave' joint is dependent on the displacement of the 'master' joint, the slave joint cannot be restrained. However, if the 'master' joint is restrained, the 'slave' joint will also be restrained.

A rigid floor slab in a building is very stiff in the plane of the floor, yet it is flexible out of plane. Thus a planar constraint is used to treat the rigid floor slab's diaphragm stiffness as a rigid body. The rigid floor slab is in the joint's X_j, Y_j plane as shown in Figure 133. The moments about the X_j and Y_j axes and the force in the Z_j axis can

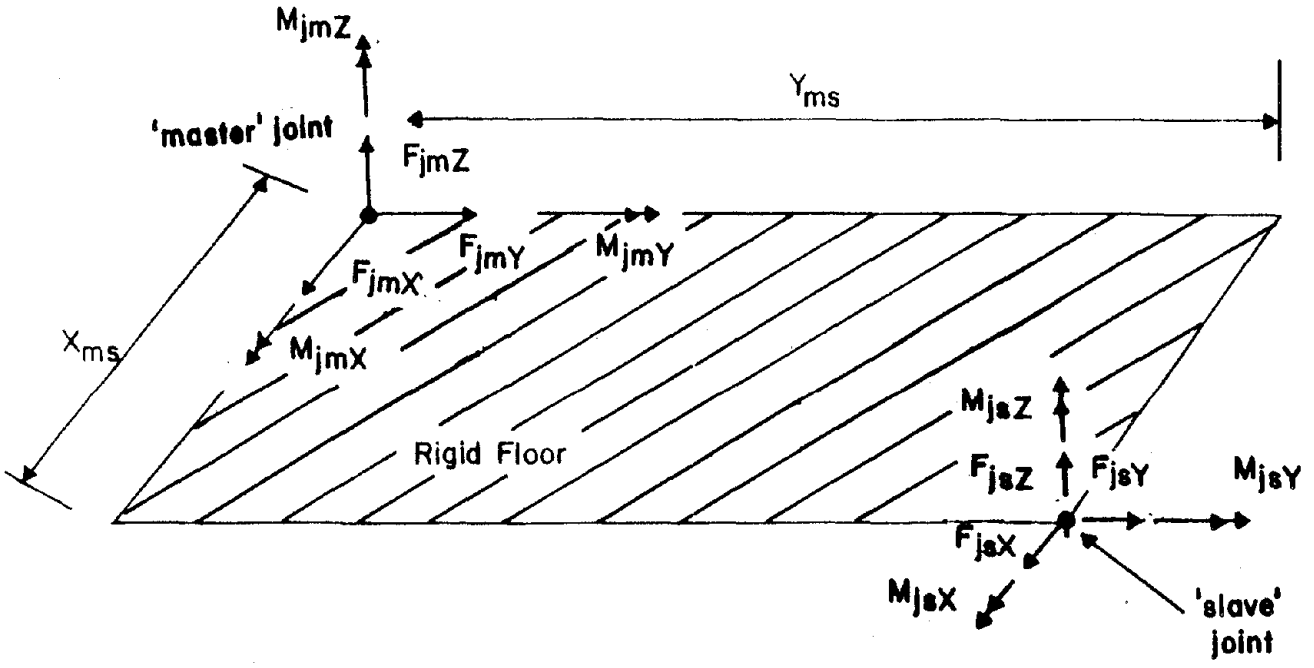

Figure 133. X-Y Planar Constraint

not be transferred from the slave to the master joint because the floor is flexible out of plane. Thus, the force transformation is

$$\begin{bmatrix} F_{jmX} \\ F_{jmY} \\ F_{jsZ} \\ M_{jsX} \\ M_{jsY} \\ M_{jmZ} \end{bmatrix} = \begin{bmatrix} 1 & 0 & 0 & 0 & 0 & 0 \\ 0 & 1 & 0 & 0 & 0 & 0 \\ 0 & 0 & 1 & 0 & 0 & 0 \\ 0 & 0 & 0 & 1 & 0 & 0 \\ 0 & 0 & 0 & 0 & 1 & 0 \\ -Y_{ms} & X_{ms} & 0 & 0 & 0 & 1 \end{bmatrix} \begin{bmatrix} F_{jsX} \\ F_{jsY} \\ F_{jsZ} \\ M_{jsX} \\ M_{jsY} \\ M_{jsZ} \end{bmatrix} \tag{5.6}$$

Translation in the X_j, Y_j axes and rotation about the Z_j axis are transferred to the 'master' joint. Translation in the Z_j axis and rotation about the X_j and Y_j axes remain at the 'slave' joint.

4. Global Degrees of Freedom. The global degrees of freedom (Gdof) are in the JCS, which are unconstrained degrees of freedom at 'master' and unconstrained joints. These degrees of freedom describe the structure's motion. Once the joints have been defined and the constraints have been identified, the global degrees of freedom are numbered. The following items should be considered when numbering the degrees of freedom:

- The Gdof numbers determine the location of the terms in the mass and stiffness matrices. Thus the Gdof numbering system determines the bandwidth of the stiffness matrix. For a structure with two different Gdof numbering schemes, the scheme with the smaller bandwidth will require less numerical calculations than the scheme with the larger bandwidth. Thus the Gdof numbers influence the efficiency of the numerical calculations.
- During the static and dynamic analysis the stiffness matrix is partitioned between condensed, free and restrained degrees of freedom. Identifying which degrees of

freedom are condensed, free or restrained before the degree of freedom numbers are chosen, prevents the unnecessary shuffling of the stiffness matrices rows and columns.

The analyst determines the joint numbers, and the Gdof numbers are assigned in the following order:

1) Degrees of freedom to be condensed out

   From the lowest joint number to the highest joint number.

   From joint dof 1 to joint dof 6, omitting constrained dof.

2) Free degrees of freedom

   From the lowest joint number to the highest joint number.

   From joint dof 1 to joint dof 6, omitting constrained dof.

3) Restrained degrees of freedom (KEY = 1)[15]

   From the lowest joint number to the highest joint number.

   From joint dof 1 to joint dof 6, omitting constrained dof.

4) Restrained degrees of freedom (KEY = 2)[15]

   From the lowest joint number to the highest joint number.

   From joint dof 1 to joint dof 6, omitting constrained dof.

An example of the Gdof numbering system is presented in Section A of Chapter VII. Generally, if the difference between joint numbers on each element is minimized, the structure's bandwidth is also minimized. The global degree of freedom numbers for each joint are stored in the array $\{Lm_j\}$.

---

[15] The restrained degrees are divided into two cases: KEY = 1 are the degrees of freedom that actually have reactions, and KEY = 2 are restrained dummy degrees of freedom. Typical restrained dummy degrees of freedom are all of the out of plane dof in a planar frame, or rotational dof for a truss structure. The restrained dummy degrees of freedom are not used in the analysis.

B. SHEAR WALL ELEMENT

The reinforced concrete shear wall element consists of a panel linking four joints, Figure 134. Nonlinear bending and shear deformations in the plane of the wall are considered, along with nonlinear axial deformation. The bending, shear and axial deformations are lumped into three nonlinear springs. A rigid body connects the joints at the top of the wall with the springs, while a second rigid body connects the joints at the bottom of the wall with the springs. Bending and shear stiffness perpendicular to the plane of the wall are neglected. A lumped parameter formulation of the geometric stiffness considers both in-plane and out of plane P-Δ effects.

1. Element Coordinate System and Degrees of Freedom. The four joints at the corners of the element are denoted J1 through J4 as shown in Figure 135. The global coordinates of each joint are X_{g1}, Y_{g1}, Z_{g1}, through X_{g4}, Y_{g4}, Z_{g4}. The vectors $\vec{V}_{xt}$ and $\vec{V}_{xb}$ are defined at the top and bottom of the wall.

$$\vec{V}_{xt} = (X_{g1}-X_{g2})\vec{i} + (Y_{g1}-Y_{g2})\vec{j} + (Z_{g1}-Z_{g2})\vec{k} \tag{5.7}$$

$$\vec{V}_{xb} = (X_{g4}-X_{g3})\vec{i} + (Y_{g4}-Y_{g3})\vec{j} + (Z_{g4}-Z_{g5})\vec{k} \tag{5.8}$$

Define a vector $\vec{V}_{y'}$ along with the average longitudinal axis of the wall.

$$\vec{V}_{y'} = \left[\frac{X_{g1}+X_{g2}}{2} - \frac{X_{g3}+X_{g4}}{2}\right]\vec{i} + \left[\frac{Y_{g1}+Y_{g2}}{2} - \frac{Y_{g3}+Y_{g4}}{2}\right]\vec{j} + \left[\frac{Z_{g1}+Z_{g2}}{2} - \frac{Z_{g3}+Z_{g4}}{2}\right]\vec{k} \tag{5.9}$$

The height of the wall, h, is given by

$$h = |\vec{V}_{y'}| \tag{5.10}$$

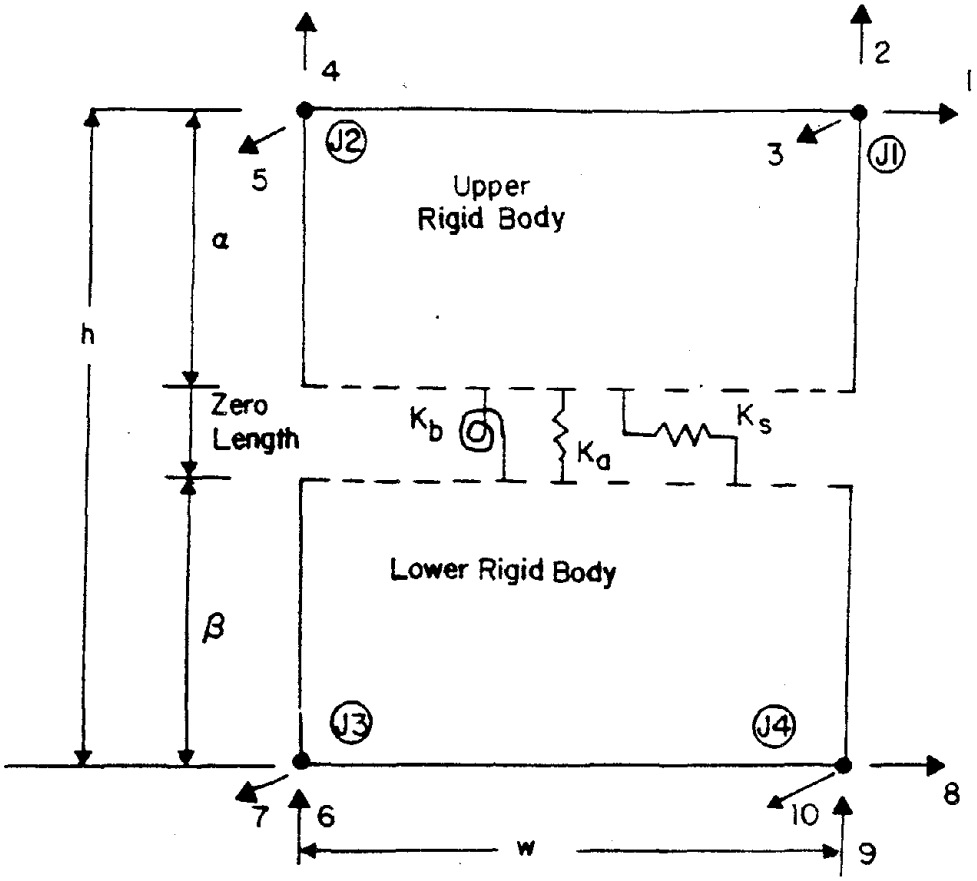

Figure 134. Shear Wall Element

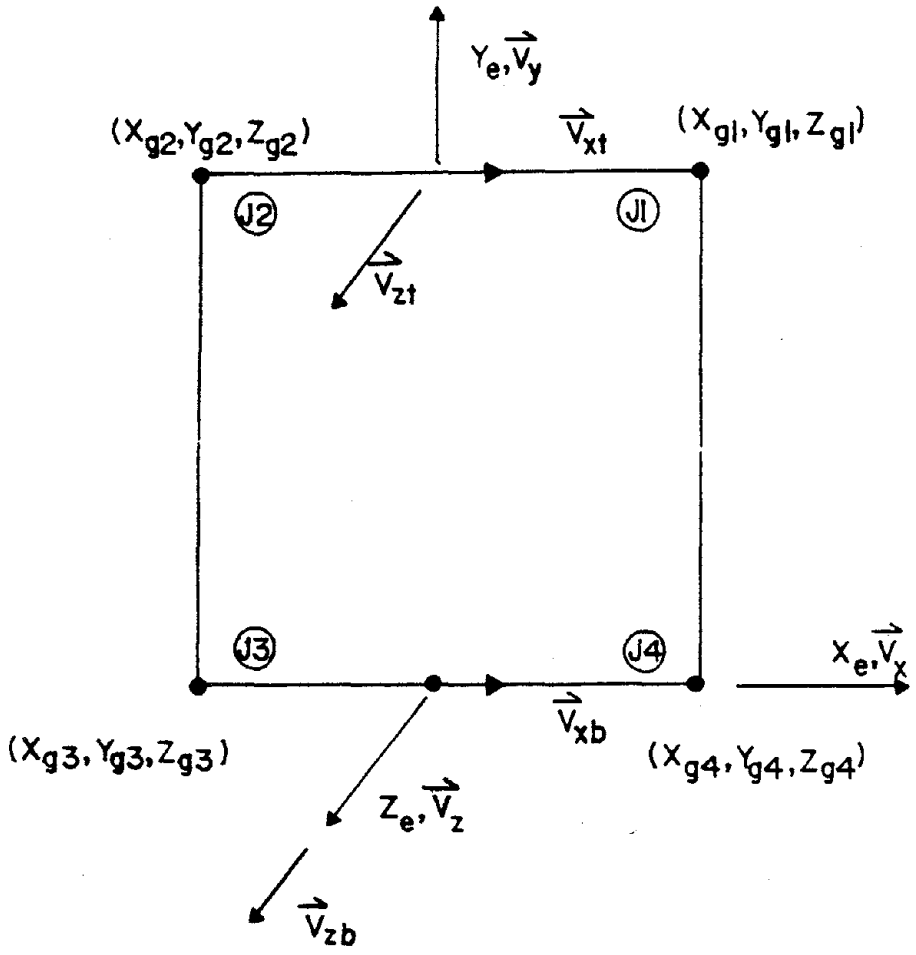

Figure 135. Shear Wall Coordinate System

Let α be the distance from the top of the wall to the springs and β the distance from the bottom of the wall to the springs, then

$$\beta = h - \alpha \tag{5.11}$$

Normalizing $V_{y'}$ yields

$$\vec{V}_y = \frac{\vec{V}_{y'}}{h} \tag{5.12}$$

The average width of the wall, w, perpendicular to $\vec{V}_y$ is given by

$$w = \frac{|\vec{V}_y \times \vec{V}_{xt} \times \vec{V}_y| + |\vec{V}_y \times \vec{V}_{xb} \times \vec{V}_y|}{2} \tag{5.13}$$

Define the vectors $\vec{V}_{zb}$ and $\vec{V}_{zt}$, which are perpendicular to the wall as

$$\vec{V}_{zb} = \vec{V}_{xb} \times \vec{V}_y, \qquad \vec{V}_{zt} = \vec{V}_{xt} \times \vec{V}_y \tag{5.14}$$

If the wall is planar, $\vec{V}_{zb}$ and $\vec{V}_{zt}$ are parallel, or

$$\vec{V}_{zb} \bullet \vec{V}_{zt} \cong 0 \tag{5.15}$$

Equation 5.15 is used as a check, to insure that joints J1-J4 are coplanar. Since the wall is planar, a single unit vector perpendicular to the plane of the wall can be defined as

$$\vec{V}_z = \frac{\vec{V}_{zb}}{|\vec{V}_{zb}|} \tag{5.16}$$

and the vector $\vec{V}_x$, perpendicular to the length in the plane of the wall, as

$$\vec{V}_x = \vec{V}_y \times \vec{V}_z \tag{5.17}$$

The three unit vectors $\vec{V}_x$, $\vec{V}_y$, and $\vec{V}_z$ define the element's coordinate system (ECS), denoted X_e, Y_e, Z_e, with the origin midway between joints J3 and J4. The three unit vectors that define the orientation of the ECS are written in matrix form as

$$[\vec{V}_e] = \begin{bmatrix} \vec{V}_x \\ \vec{V}_y \\ \vec{V}_z \end{bmatrix} = \begin{bmatrix} c_{11} & c_{12} & c_{13} \\ c_{21} & c_{22} & c_{23} \\ c_{31} & c_{32} & c_{33} \end{bmatrix} \begin{bmatrix} \vec{i} \\ \vec{j} \\ \vec{k} \end{bmatrix} = [C_e] \begin{bmatrix} \vec{i} \\ \vec{j} \\ \vec{k} \end{bmatrix} \tag{5.18}$$

where $[C_e]$ is the direction cosine matrix for the ECS.

The element has ten translational degrees of freedom as shown in Figure 134. Degrees of freedom 1 and 8 are used to represent in-plane shear and bending deformations, along with the in-plane geometric stiffness. Degrees of freedom 2, 4, 6, and 9 represent axial deformation and bending rotations while degrees of freedom 3, 5, 7, and 10 are used to represent the out-of-plane geometric stiffness. In matrix form, these local forces and displacements in the ECS are

$$\begin{aligned} [F_e] &= [F_1\ F_2\ F_3\ F_4\ F_5\ F_6\ F_7\ F_8\ F_9\ F_{10}]^T \\ [\delta_e] &= [\delta_1\ \delta_2\ \delta_3\ \delta_4\ \delta_5\ \delta_6\ \delta_7\ \delta_8\ \delta_9\ \delta_{10}]^T \end{aligned} \tag{5.19}$$

2. Element Stiffness Matrix in the Element Coordinate System. Let K_b, K_s and K_a represent the bending, shear and axial stiffnesses of a unit height wall. The bending backbone curve and hysteresis model that determine the bending stiffness, are derived in terms of moment and unit height rotation, Equation 3.32. Similarly, the shear

backbone curve and hysteresis model that determine the shear stiffness are derived in terms of shear and shear strain; and the axial hysteresis model is in terms of axial load and strain. Examining Figure 136, the force deformation relationship for each of the springs is given by

$$M_a = K_b\theta_u = \frac{K_b}{h}(\theta_a - \theta_b) = -M_b \tag{5.20}$$

$$V_a = K_s v_u = \frac{K_s}{h}(v_a - v_b) = -V_b \tag{5.21}$$

and

$$P_a = K_a u_u = \frac{K_a}{h}(u_a - u_b) = -P_b \tag{5.22}$$

where K_b is the bending stiffness of a unit height wall, given by the bending hysteresis model in Chapter IV,

K_s is the shear stiffness of a unit height wall, given by the shear hysteresis model in Chapter IV,

K_a is the axial stiffness of a unit height wall, given by the axial hysteresis model in Chapter IV,

θ_a, θ_b are the rotations at the top and bottom of the bending spring,

v_a, v_b are the shear deformations at the top and bottom of the shear spring,

u_a, u_b are the axial deformations at the top and bottom of the axial spring,

M_a, M_b are the moments at the top and bottom of the bending spring,

V_a, V_b are the shears at the top and bottom of the shear spring,

P_a, P_b are the axial forces at the top and bottom of the axial spring,

θ_u is the relative unit rotation for bending,

v_u is the relative unit shear deformation, and

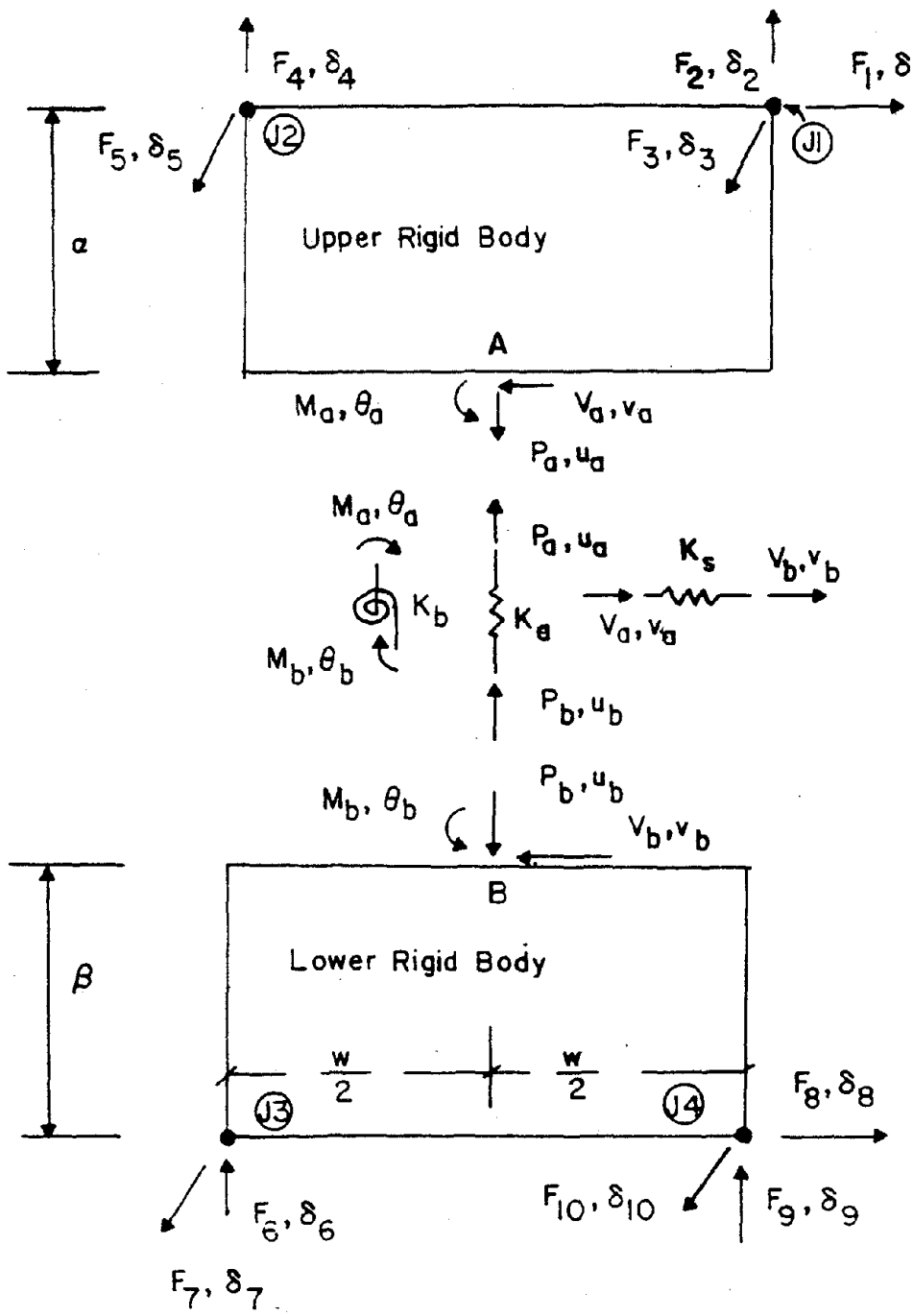

Figure 136. Shear Wall Forces and Deformations

u_u is the relative unit axial deformation.

Fixing the bottom of the shear wall and applying a positive load to degree of freedom 1, the sign convention yields a positive moment and shear at end 'A' of the springs. Fixing the bottom of the shear wall and applying a positive load to degrees of freedom 2 and 4, yield a positive axial load at end 'A' of the spring. Rewriting Equations 5.20 through 5.22 in matrix form yields

$$\begin{bmatrix} M_a \\ M_b \\ V_a \\ V_b \\ P_a \\ P_b \end{bmatrix} = \begin{bmatrix} 1 & 0 & 0 \\ -1 & 0 & 0 \\ 0 & 1 & 0 \\ 0 & -1 & 0 \\ 0 & 0 & 1 \\ 0 & 0 & -1 \end{bmatrix} \begin{bmatrix} M_a \\ V_a \\ P_a \end{bmatrix} = [A_1] \begin{bmatrix} M_a \\ V_a \\ P_a \end{bmatrix} \tag{5.23}$$

and

$$\begin{bmatrix} M_a \\ V_a \\ P_a \end{bmatrix} = [SI] \begin{bmatrix} \theta_u \\ v_u \\ u_u \end{bmatrix} = [SI][A_1]^T \begin{bmatrix} \theta_a \\ \theta_b \\ v_a \\ v_b \\ u_a \\ u_b \end{bmatrix} \tag{5.24}$$

where $[SI]$ is the unit length spring stiffness matrix

$$[SI] = \frac{1}{h} \begin{bmatrix} K_b & 0 & 0 \\ 0 & K_s & 0 \\ 0 & 0 & K_a \end{bmatrix} \tag{5.25}$$

From summation of forces and moments in Figure 136 the relation between the spring and element forces are determined.

$$\sum F_{x\ top} = 0 = F_1 - V_a, \qquad F_1 = V_a \tag{5.26}$$

$$\sum M_{j1} = 0 = M_a - wF_4 + P_a\frac{w}{2} - \alpha V_a, \qquad F_4 = \frac{M_a}{w} + \frac{P_a}{2} - \frac{\alpha}{w}V_a \tag{5.27}$$

$$\sum M_{j2} = 0 = M_a + wF_2 - P_a\frac{w}{2} - \alpha V_a, \qquad F_2 = \frac{-M_a}{w} + \frac{P_a}{2} + \frac{\alpha}{w}V_a \tag{5.28}$$

$$\sum F_{x\ bot} = 0 = F_8 - V_b, \qquad F_8 = v_b \tag{5.29}$$

$$\sum M_{j4} = 0 = M_b - wF_6 + \frac{w}{2}P_b + \beta V_b, \qquad F_6 = \frac{M_b}{w} + \frac{P_b}{2} + \frac{\beta}{w}V_b \tag{5.30}$$

$$\sum M_{j3} = 0 = M_b + wF_9 - \frac{w}{2}P_b + \beta V_b, \qquad F_9 = \frac{-M_b}{w} + \frac{P_b}{2} - \frac{\beta}{w}V_b \tag{5.31}$$

Rewriting Equations 5.26 to 5.31 in matrix form

$$[F_e] = \begin{bmatrix} F_1 \\ F_2 \\ F_3 \\ F_4 \\ F_5 \\ F_6 \\ F_7 \\ F_8 \\ F_9 \\ F_{10} \end{bmatrix} = \frac{1}{2w} \begin{bmatrix} 0 & 0 & 2w & 0 & 0 & 0 \\ -2 & 0 & 2\alpha & 0 & w & 0 \\ 0 & 0 & 0 & 0 & 0 & 0 \\ 2 & 0 & -2\alpha & 0 & w & 0 \\ 0 & 0 & 0 & 0 & 0 & 0 \\ 0 & 2 & 0 & 2\beta & 0 & w \\ 0 & 0 & 0 & 0 & 0 & 0 \\ 0 & 0 & 0 & 2w & 0 & 0 \\ 0 & -2 & 0 & -2\beta & 0 & w \\ 0 & 0 & 0 & 0 & 0 & 0 \end{bmatrix} \begin{bmatrix} M_a \\ M_b \\ V_a \\ V_b \\ P_a \\ P_b \end{bmatrix} = [A_2] \begin{bmatrix} M_a \\ M_b \\ V_a \\ V_b \\ P_a \\ P_b \end{bmatrix} \tag{5.32}$$

Substituting Equation 5.32 in Equation 5.23

$$[F_e] = [A_2][A_1] \begin{bmatrix} M_a \\ V_a \\ P_a \end{bmatrix} \tag{5.33}$$

The shear wall's stiffness in the ECS is given by

$$[K_e] = [A_2][A_1][S_1]\left[[A_2][A_1]\right]^T \tag{5.34}$$

Recall that bending and shear stiffness perpendicular to the wall are neglected. Thus the stiffness terms associated with degrees of freedom 3, 5, 9 and 10 are zero. To prevent a singular stiffness matrix, the out of plane dof must be restrained when analyzing a planar frame.

3. Element Stiffness Matrix in Global Degrees of Freedom. The transformation of degrees of freedom from the ECS to Gdof consists of two steps. First, the degrees of freedom at each of the four joints are rotated from the ECS to each of the JCS, at joints J1 through J4. Second, the constraint transformation moves degrees of freedom from each of the 'slave' joints to the 'master' joints. The degrees of freedom at the master joints are the Gdof.

Recall the transformation between the global forces and forces in a rotated coordinated system is given by

$$[F_{rotated}] = [C][F_{global}] \tag{5.35}$$

where $[F_{rotated}]$ is the force in the rotated coordinated system, $[C]$ is the direction cosine matrix of the rotated coordinated system, and $[F_{global}]$ is the force in the global coordinate system. The rotated coordinate system may be the JCS, the ECS or some other coordinate system that is not parallel to the GCS. Solving for the global forces yields[16]

$$[F_{global}] = [C]^{-1}[F_{rotated}] = [C]^{T}[F_{rotated}] \tag{5.36}$$

Thus rotating the element forces at a joint i, $[F_{ei}]$, to global forces at joint i, $[F_{gi}]$, is achieved by

$$[F_{gi}] = [C_e]^{T}[F_{ei}] \tag{5.37}$$

and rotating the global forces at joint i, $[F_{gi}]$, to joint forces, $[F_{ji}]$, at joint i is achieved by

---

[16] The transformation matrix $[C]$ is orthogonal. Inverting an orthogonal matrix is equivalent to the transpose.

$$[F_{ji}] = [C_i][F_{gi}] = [C_i][C_e]^T[F_{ei}] = [C_i C_e^T][F_{ei}] \tag{5.38}$$

where $[C_i]$ is the direction cosine of the JCS for joint i. At joints J2 and J3, the wall does not have translational degrees of freedom parallel to the ECS X axis (F_{J2X}, F_{J2X}), thus a transformation matrix, A3, is used to create dummy degrees of freedom at these joints.

$$\begin{bmatrix} F_{e1} \\ F_{e2} \\ F_{e3} \\ F_{e4} \end{bmatrix} = \begin{bmatrix} F_{J1X} \\ F_{J1Y} \\ F_{J1Z} \\ F_{J2X} \\ F_{J2Y} \\ F_{J2Z} \\ F_{J3X} \\ F_{J3Y} \\ F_{J3Z} \\ F_{J4X} \\ F_{J4Y} \\ F_{J4Z} \end{bmatrix} = \begin{bmatrix} 1 & 0 & 0 & 0 & 0 & 0 & 0 & 0 & 0 & 0 \\ 0 & 1 & 0 & 0 & 0 & 0 & 0 & 0 & 0 & 0 \\ 0 & 0 & 1 & 0 & 0 & 0 & 0 & 0 & 0 & 0 \\ 0 & 0 & 0 & 0 & 0 & 0 & 0 & 0 & 0 & 0 \\ 0 & 0 & 0 & 1 & 0 & 0 & 0 & 0 & 0 & 0 \\ 0 & 0 & 0 & 0 & 1 & 0 & 0 & 0 & 0 & 0 \\ 0 & 0 & 0 & 0 & 0 & 0 & 0 & 0 & 0 & 0 \\ 0 & 0 & 0 & 0 & 0 & 1 & 0 & 0 & 0 & 0 \\ 0 & 0 & 0 & 0 & 0 & 0 & 1 & 0 & 0 & 0 \\ 0 & 0 & 0 & 0 & 0 & 0 & 0 & 1 & 0 & 0 \\ 0 & 0 & 0 & 0 & 0 & 0 & 0 & 0 & 1 & 0 \\ 0 & 0 & 0 & 0 & 0 & 0 & 0 & 0 & 0 & 1 \end{bmatrix} \begin{bmatrix} F_1 \\ F_2 \\ F_3 \\ F_4 \\ F_5 \\ F_6 \\ F_7 \\ F_8 \\ F_9 \\ F_{10} \end{bmatrix} = [A_3][F_e] \tag{5.39}$$

where the typical notation $[F_{e1}] = [F_{J1X} \;\; F_{J1Y} \;\; F_{J1Z}]^T$ represents the forces on joint J1 in the ECS. Rotating the forces at each of the walls four joints from the ECS to the JCS yields

$$\begin{bmatrix} F_{J1} \\ F_{J2} \\ F_{J3} \\ F_{J4} \end{bmatrix} = \begin{bmatrix} \left[C_{J1}C_e^T\right] & 0 & 0 & 0 \\ 0 & \left[C_{J2}C_e^T\right] & 0 & 0 \\ 0 & 0 & \left[C_{J3}C_e^T\right] & 0 \\ 0 & 0 & 0 & \left[C_{J4}C_e^T\right] \end{bmatrix} \begin{bmatrix} F_{e1} \\ F_{e2} \\ F_{e3} \\ F_{e4} \end{bmatrix} = [A_4] \begin{bmatrix} F_{e1} \\ F_{e2} \\ F_{e3} \\ F_{e4} \end{bmatrix} \tag{5.40}$$

where $[F_{J1}]$ represents the X, Y, and Z forces acting on joint J1 in the JCS.

Recall the constraint transformation equation $[T_{ms}]_i$ for an individual slave joint i Equation 5.2 or 5.6 has the form

$$[T_{ms}]_i = \begin{bmatrix} [I] & [0] \\ [XYZ]_i & [I] \end{bmatrix} \tag{5.41}$$

The second column of $[T_{ms}]$ pertains to rotational degrees of freedom at the slave joint. Since $[F_{ji}]$ for the wall element only contains translational degrees of freedom, the second column is omitted. Thus for shear walls the constraint equations become

$$[T'_{ms}]_i = \begin{bmatrix} [I] \\ [XYZ]_i \end{bmatrix} \tag{5.42}$$

The modified constraint $[T'_{ms}]$ generates rotational degrees of freedom at the master joints. For unconstrained joints, a dummy constraint transformation with a zero $[XYZ]_i$ is used. Combining the transformation for all four joints yields

$$\begin{bmatrix} F_{J1m} \\ F_{J2m} \\ F_{J3m} \\ F_{J4m} \end{bmatrix} = \begin{bmatrix} [T'_{ms}]_1 & 0 & 0 & 0 \\ 0 & [T'_{ms}]_2 & 0 & 0 \\ 0 & 0 & [T'_{ms}]_3 & 0 \\ 0 & 0 & 0 & [T'_{ms}]_4 \end{bmatrix} \begin{bmatrix} F_{J1} \\ F_{J2} \\ F_{J3} \\ F_{J4} \end{bmatrix} = [A_5] \begin{bmatrix} F_{J1} \\ F_{J2} \\ F_{J3} \\ F_{J4} \end{bmatrix} \tag{5.43}$$

where $[F_{jm}] = [F_{jmX}\ F_{jmY}\ F_{jmZ}\ M_{jmX}\ M_{jmY}\ M_{jmZ}]^T$ at master joint j. Substituting Equation 5.39 into 5.40, and Equation 5.40 into 5.43 yields

$$\begin{bmatrix} F_{J1m} \\ F_{J2m} \\ F_{J3m} \\ F_{J4m} \end{bmatrix} = [A_5][A_4][A_3][F_e] \tag{5.44}$$

Substituting Equation 5.33 for $[F_e]$ yields the transformation from internal wall forces $[M_a\ V_a\ P_a]^T$ to forces acting on 'master' joints at global degrees of freedom

$$\begin{bmatrix} F_{J1m} \\ F_{J2m} \\ F_{J3m} \\ F_{J4m} \end{bmatrix} = [A] \begin{bmatrix} M_a \\ V_a \\ P_a \end{bmatrix} \tag{5.45}$$

where $[A] = [A_5][A_4][A_3][A_2][A_1]$. Similarly, the transformation for the deformations of the springs is given by

$$\begin{bmatrix} \theta_a \\ v_a \\ u_a \end{bmatrix} = [A]^T \begin{bmatrix} \delta_{J1m} \\ \delta_{J2m} \\ \delta_{J3m} \\ \delta_{J4m} \end{bmatrix} \tag{5.46}$$

where $[\delta_{jm}] = [\delta_{jmX}\ \delta_{jmY}\ \delta_{jmZ}\ \theta_{jmX}\ \theta_{jmY}\ \theta_{jmZ}]^T$ for 'master' joint j.

Recall $\{Lm_j\}$ is a vector containing the degree of freedom numbers for joint j. For element e, the vector $\{Lm_e\}$ that contains the global degrees of freedom is

$$\{Lm_e\} = \begin{bmatrix} \{Lm_{J1}\} \\ \{Lm_{J2}\} \\ \{Lm_{J3}\} \\ \{Lm_{J4}\} \end{bmatrix} \tag{5.47}$$

The vector of Gdof numbers is used later in the assembly of the global stiffness matrix.

The stiffness matrix is transformed from the spring stiffnesses Equation 5.25 to the global degrees of freedom by

$$[K_{eg}] = [A][SI][A]^T \tag{5.48}$$

If any two degrees of freedom, from opposite ends of the wall (top vs. bottom) are constrained to the same degrees of freedom, then those two degrees of freedom are eliminated.

4. Geometric Stiffness Matrix. The P-Δ forces are modeled by a lumped parameter geometric stiffness matrix. In the plane of the wall, the wall is idealized as a rigid bar joining degrees of freedom 1 and 8 with an axial load N as shown in Figure 137. The axial load, N, is positive when the wall is in compression. Perpendicular to the plane of the wall, the wall is idealized as two rigid bars as shown in Figure 137. The first rigid bar joins degrees of freedom 3 and 10 with $\frac{N}{2}$ axial load. The second joins degrees of freedom 5 and 7 with $\frac{N}{2}$ axial load. Thus the element geometric stiffness matrix is

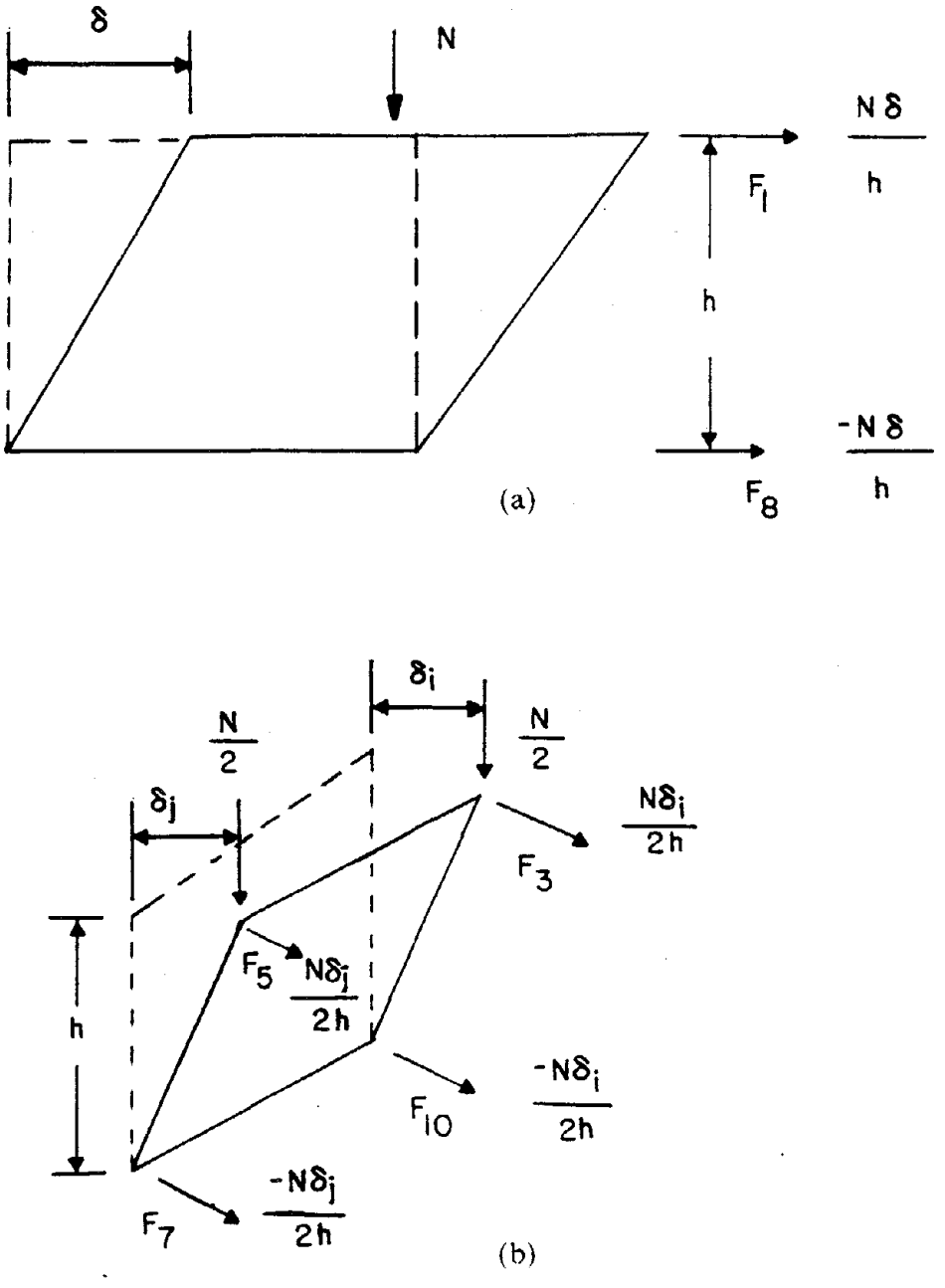

Figure 137. P-Δ Forces for the Shear Wall Element: (a) In Plane Deformation, (b) Out of Plane Deformation

$$[G_e] = \frac{N}{2h}\begin{bmatrix} 2 & 0 & 0 & 0 & 0 & 0 & 0 & -2 & 0 & 0 \\ 0 & 0 & 0 & 0 & 0 & 0 & 0 & 0 & 0 & 0 \\ 0 & 0 & 1 & 0 & 0 & 0 & 0 & 0 & 0 & -1 \\ 0 & 0 & 0 & 0 & 0 & 0 & 0 & 0 & 0 & 0 \\ 0 & 0 & 0 & 0 & 1 & 0 & -1 & 0 & 0 & 0 \\ 0 & 0 & 0 & 0 & 0 & 0 & 0 & 0 & 0 & 0 \\ 0 & 0 & 0 & 0 & -1 & 0 & 1 & 0 & 0 & 0 \\ -2 & 0 & 0 & 0 & 0 & 0 & 0 & 2 & 0 & 0 \\ 0 & 0 & 0 & 0 & 0 & 0 & 0 & 0 & 0 & 0 \\ 0 & 0 & -1 & 0 & 0 & 0 & 0 & 0 & 0 & 1 \end{bmatrix} \tag{5.49}$$

The geometric stiffness is transferred from element to global degrees of freedom by the transformation

$$[G_{eg}] = [A_5][A_4][A_3][G_e]\left[[A_5][A_4][A_3]\right]^T \tag{5.50}$$

C. UNBALANCED ELEMENT FORCES

The incremental displacements of the unit length springs for the shear wall element are given by

$$\begin{bmatrix} \Delta\theta_u \\ \Delta v_u \\ \Delta u_u \end{bmatrix} = \frac{1}{h}[A]^T \begin{bmatrix} \Delta\delta_{J1m} \\ \Delta\delta_{J2m} \\ \Delta\delta_{J3m} \\ \Delta\delta_{J4m} \end{bmatrix} \tag{5.51}$$

and the incremental spring forces are given by

$$\begin{bmatrix} \Delta M_a \\ \Delta V_a \\ \Delta P_a \end{bmatrix} = \begin{bmatrix} K_b & 0 & 0 \\ 0 & K_s & 0 \\ 0 & 0 & K_a \end{bmatrix} \begin{bmatrix} \Delta\theta_u \\ \Delta v_u \\ \Delta u_u \end{bmatrix} \tag{5.52}$$

where K_b, K_s, and K_a represent the stiffness tangent to the hysteresis model at the beginning of the load step. For the bending hysteresis model in Figure 138 with the load step beginning at Point A, K_{b1} is the stiffness tangent to the hysteresis model at the beginning of the load step. Let the forces and displacements at the beginning of the load step be

$$\begin{bmatrix} M_a \\ V_a \\ P_a \end{bmatrix}_0 \quad \text{and} \quad \begin{bmatrix} \theta_u \\ v_u \\ u_u \end{bmatrix}_0 \tag{5.53}$$

Thus the forces and displacements at the end of the step are

$$\begin{bmatrix} M_a \\ V_a \\ P_a \end{bmatrix}_1 = \begin{bmatrix} M_a \\ V_a \\ P_a \end{bmatrix}_0 + \begin{bmatrix} \Delta M_a \\ \Delta V_a \\ \Delta P_a \end{bmatrix} \quad \text{and} \begin{bmatrix} \theta_u \\ v_u \\ u_u \end{bmatrix}_1 = \begin{bmatrix} \theta_u \\ v_u \\ u_u \end{bmatrix}_0 + \begin{bmatrix} \Delta\theta_u \\ \Delta v_u \\ \Delta u_u \end{bmatrix} \tag{5.54}$$

Consider a one degree of freedom structure with bending displacement only. Examining the bending hysteresis model, Figure 138, assume that Point A is on the loading curve and has a unit displacement and moment of θ_{u0} and M_{a0}. An incremental moment of $\Delta M = M_{a1} - M_{a0}$ is applied to the structure. The tangent stiffness at Point A, K_{b1}, is used to determine that the structure displaces to Point B', which has a unit displacement and moment of θ'_{u1} and M_{a1}. However, the stiffness changed during the load step, and the structure should have displaced to Point B. Point B has a unit displacement and moment of θ_{u1} and M_{a1}. During the second

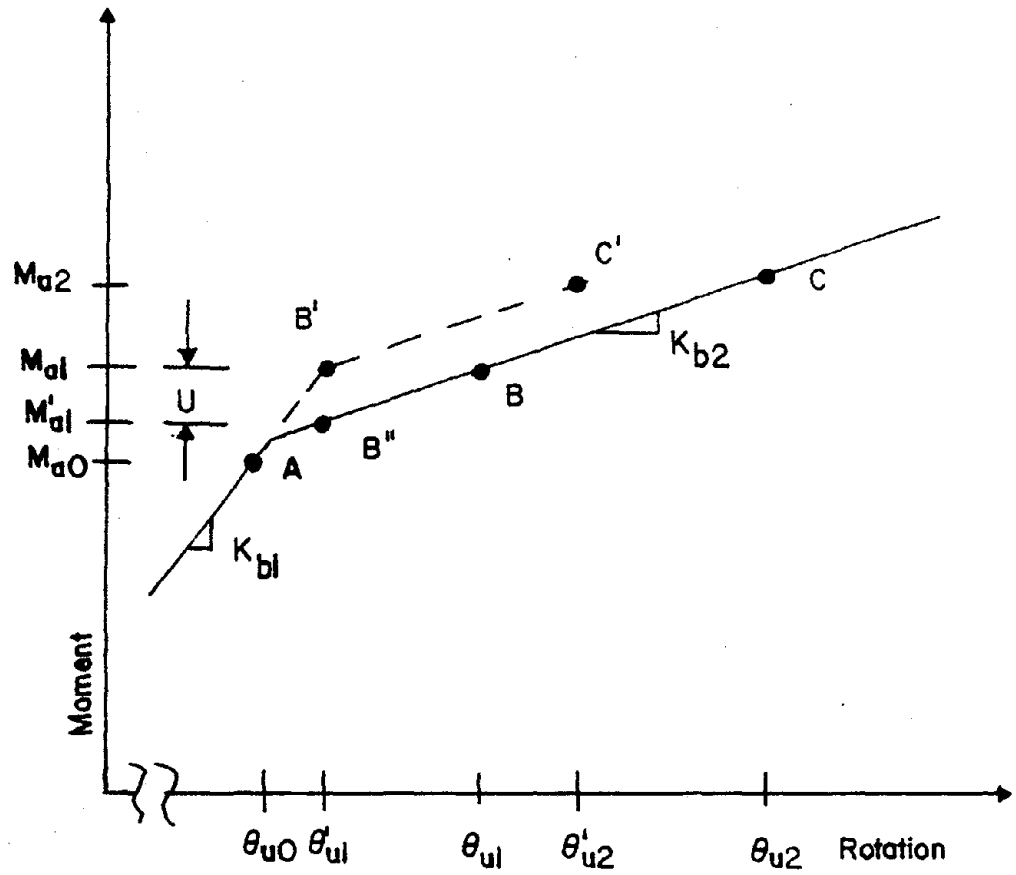

Figure 138. Unbalanced Force

load step, an incremental moment of $\Delta M = M_{a2} - M_{a1}$ is applied to the structure. The tangent stiffness at Point B′, K_{b2}, is used to determine that the structure displaces to Point C′, which has a unit displacement and moment of θ'_{u2} and M_{a2}. Loading from Point B, with the same stiffness, would displace the structure to Point C, which has a unit displacement and moment of θ_{u2} and M_{a2}. The calculated solution A-B′-C′ is diverging from the true solution A-B-C because the calculated solution overshot the loading curve in the first step.

There are several techniques to correct for overshooting. The simplest is to reduce the size of the load step. However, experience has shown that very small load steps are required for convergence, leading to excessive solution times. Another technique to correct for overshooting is to locate the points where the stiffness changes, and reanalyze the structure with different load steps. For large structures, several elements may change stiffness in a single load step, leading to excessive solution times. A third technique is to determine the unbalance force which is applied as a load in the next load step (62, 21).

Returning to the example in Figure 138, from the hysteresis model, the moment at a displacement of θ'_{u1} should have been M'_{a1}. Let this moment be the internal moment on the structure, and label this point B″. At a displacement of θ'_{u1} the external force acting on the structure is M_{a1}, which exceeds the internal force M'_{a1}. The unbalanced force is $U = M_{a1} - M'_{a1}$. An incremental load of $\Delta M = M_{a2} - M_{a1} + U = M_{a2} - M'_{a1}$ is applied to the structure, yielding an incremental displacement of $\theta_{u2} - \theta'_{u1}$. From the hysteresis model, with the current internal moment and displacement of M'_{a1} and θ'_{u1}, and an incremental displacement of $\theta_{u2} - \theta'_{u1}$, the incremental internal moment is $M_{a2} - M'_{a1} = \Delta M$. Thus the new internal moment and displacement are M_{a2} and θ_{u2}, and the internal moment has loaded from B″ to C. The external force has a load increment of

$\Delta M - U = M_{a2} - M_{a1}$ and loads from B′ to C. Thus the calculated and true solutions converge.

For the shear wall element, the unbalanced forces are determined for bending, shear and axial springs and are applied to the global degrees of freedom by

$$\begin{bmatrix} U_{J1me} \\ U_{J2me} \\ U_{J3me} \\ U_{J4me} \end{bmatrix} = [A]\left[\begin{bmatrix} M_a \\ V_a \\ P_a \end{bmatrix}_1 - \begin{bmatrix} M'_a \\ V'_a \\ P'_a \end{bmatrix}\right] \tag{5.55}$$

where U_{J1me} is the unbalanced force from element e, acting on the master joint J1; M'_a, V'_a and P'_a are the internal forces from the hysteresis models at displacements θ_{u1}, v_{u1} and u_{u1} (the displacements are determined from Equation 5.54); and M_a, V_a and P_a are the external forces acting on the element as given in Equation 5.52. The global unbalanced joint force vector, {U}, is assembled by

$$\left.\begin{aligned} U(li) = U(li) + U_{jm}(i)_e, \quad & \text{for } i = 1 \text{ to } 6 \\ & j = J1 \text{ to } J4 \\ & e = 1 \text{ to NELEM} \\ & li = Lm_j(i) \end{aligned}\right\} \tag{5.56}$$

where e is the element number, and NELEM is the total number of elements in the structure.

D. ASSEMBLY OF THE GLOBAL STRUCTURAL AND GEOMETRIC STIFFNESS

The structural stiffness matrix is assembled by the direct element method, where the element's stiffness is mapped into the global degrees of freedom. Recall $\{Lm_e\}$ is

a vector that contains the global degrees of freedom for element e, and $[K_{eg}]$ is the global stiffness of element e. The structural stiffness $[K]$ is given by

$$\left.\begin{aligned} K(li,lj) = K(li,lj) + K_{eg}(i,j), \quad & \text{for } i = 1 \text{ to NELDOF} \\ & j = 1 \text{ to NELDOF} \\ & e = 1 \text{ to NELEM} \\ & li = Lm_e(i) \\ & lj = Lm_e(j) \end{aligned}\right\} \tag{5.57}$$

where NELDOF is the number of degrees of freedom for element e, and NELEM is the total number of elements in the structure.

The axial load N, used to formulate the geometric stiffness for element e, can be estimated by the analyst. Recall that the axial load, N, is positive when the element is in compression, and is assumed to be due to gravity loading only (21). The load is factored by $F_{\ddot{Z}}$ to reflect the vertical ground acceleration

$$F_{\ddot{Z}} = 1 + \frac{A_{gZ}(t)}{g} \tag{5.58}$$

where $A_{gZ}(t)$ is the vertical ground acceleration of the ground at time t, and g is the acceleration of gravity.

The geometric stiffness matrix can be formed by subtracting the geometric stiffness from the structural stiffness and storing in the structural stiffness matrix.

$$\left.\begin{aligned} K(li,lj) = K(li,lj) + K_{eg}(i,j) - F_{\ddot{Z}}G_{eg}(i,j), \quad & \text{for } i = 1 \text{ to NELDOF} \\ & j = 1 \text{ to NELDOF} \\ & e = 1 \text{ to NELEM} \\ & li = Lm_e(i) \\ & lj = Lm_e(j) \end{aligned}\right\} \tag{5.59}$$

where $[G_{eg}]$ is the geometric stiffness of element e, having degrees of freedom $\{Lm_e\}$. This technique uses the minimum storage. However, if either the structural stiffness or geometric stiffness is updated, both must be reformed.

An alternate method is to form a separate geometric stiffness, $F_{\ddot{Z}}[G]$, where

$$\left.\begin{aligned} F_{\ddot{Z}}G(li,lj) = F_{\ddot{Z}}G(li,lj) + F_{\ddot{Z}}G_{eg}(i,j), \quad & \text{for } i = 1 \text{ to NELDOF} \\ & j = 1 \text{ to NELDOF} \\ & e = 1 \text{ to NELEM} \\ & li = Lm_e(i) \\ & lj = Lm_e(j) \end{aligned}\right\} \quad (5.60)$$

This technique uses more storage than the previous method, because both the structural stiffness and the geometric stiffness matrices are stored separately. For structures where the geometric stiffness is only formed once, this technique has less calculations and yields faster solutions.

For the numerical examples in Chapters VI and VII, the axial load is estimated by the analyst, and vertical ground acceleration is neglected. For static loadings, the geometric stiffness is subtracted from the elements stiffness (Equation 5.59). For the dynamic analysis, a separate geometric stiffness matrix (Equation 5.60) is used to avoid recalculating the geometric stiffness each time the structural stiffness is updated.

E. STATIC ANALYSIS OF 3-D STRUCTURAL SYSTEMS

The nonlinear static response of a 3-D structure subject to either monotonic or cyclic loadings is determined in this section. Loadings may consist of joint loads (force control), imposed displacements (displacement control) or combination of joint loads

and imposed displacements[17]. The loading is divided into increments, and applied to the structure in steps. At the beginning of each load step, the tangent stiffness of the structure is determined, and the structure is assumed to behave linearly for the duration of the time step. Unbalanced forces, when they exist, are calculated at the end of each load step, and added to the incremental loads for the next step. The structural stiffness is updated each step if necessary. Depending on the assumed axial loading, the geometric stiffness may be constant throughout the analysis, or updated for each load step. At the end of each load step, total forces and displacements are determined by summing the values for the previous step and the incremental values.

Either concentrated forces or moments may be applied as joint loads. In incremental form, the forces at joint i are

$$[\Delta F_{js}] = [\Delta F_{jsX}\ \ \Delta F_{jsY}\ \ \Delta F_{jsZ}\ \ \Delta M_{jsX}\ \ \Delta M_{jsY}\ \ \Delta M_{jsZ}]^T \tag{5.61}$$

If joint j is a constrained 'slave' joint, the joint loads are transferred from the 'slave' to 'master' joints by

$$[\Delta F_{km}] = [T_{ms}][\Delta F_{js}] \tag{5.62}$$

where $[\Delta F_{km}]$ are the forces acting on 'master' joint k. If joint j is a master joint then rename $[\Delta F_{js}]$ as $[\Delta F_{km}]$. The incremental global joint force, $\{\Delta F\}$, is given by

$$\left.\begin{aligned} \Delta F(li) = \Delta F(li) + \Delta F_{km}(i), \quad & \text{for } i = 1 \text{ to } 6 \\ & li = Lm_k(i) \\ & k = 1 \text{ to NJOINTS} \end{aligned}\right\} \tag{5.63}$$

---

[17] A joint load and an imposed displacement can not exist at the same degree of freedom. However, different degrees of freedom may have joint loads and imposed displacements for the same load step.

The stiffness matrix is formed for both free and restrained degrees of freedom. Recall the equation of equilibrium $[K]\{\Delta\delta\} = \{\Delta F\} + \{U\}$. Partitioning the stiffness[18] $[K]$, displacements $\{\Delta\delta\}$, load $\{\Delta F\}$ and the unbalanced force $\{U\}$ matrices between free, (f), and restrained, (r), degrees of freedom, yields

$$\begin{bmatrix} [K_{ff}] & [K_{fr}] \\ [K_{rf}] & [K_{rr}] \end{bmatrix} \begin{Bmatrix} [\Delta\delta_f] \\ [\Delta\delta_r] \end{Bmatrix} = \begin{Bmatrix} \{\Delta F_f\} + \{U_f\} \\ \{\Delta R\} + \{U_r\} \end{Bmatrix} \tag{5.64}$$

where $\{\Delta\delta_r\}$ represent the support settlements or imposed displacements and $\{\Delta R\}$ represent the reactions. Expanding Equation 5.64

$$[K_{ff}][\Delta\delta_f] + [K_{fr}][\Delta\delta_r] = \{\Delta F_f\} + \{U_f\} \tag{5.65a}$$

$$[K_{rf}][\Delta\delta_f] + [K_{rr}][\Delta\delta_r] = \{\Delta R\} + \{U_r\} \tag{5.65b}$$

Rewriting Equation 5.65a yields

$$[K_{ff}][\Delta\delta_f] = \{\Delta F_f\} + \{U_f\} - [K_{fr}][\Delta\delta_r] \tag{5.66}$$

which is solved for the free global degrees of freedom $[\Delta\delta_f]$ by Gaussian elimination. The displacements for 'master' joint k, are extracted from the free and restrained incremental displacements by

$$\left.\begin{aligned} \Delta\delta_{km}(i) = \Delta\delta(li), \quad & \text{for } i = 1 \text{ to } 6 \\ & li = Lm_k(i) \end{aligned}\right\} \tag{5.67}$$

yielding $\{\Delta\delta_{km}\}$. The displacements of constrained 'slave' joint j, is determined from

---

[18] The structural stiffness has been softened to account for the geometric stiffness, Equation 5.59.

$$\{\Delta\delta_{js}\} = [T_{ms}]^T\{\Delta\delta_{km}\} \tag{5.68}$$

Rewriting Equation 5.65b yields the reactions

$$\{\Delta R\} = [K_{rf}][\Delta\delta_f] + [K_{rr}][\Delta\delta_r] - \{U_r\} \tag{5.69}$$

The reactions[19] at joint j, are extracted from the incremental reactions by

$$\left.\begin{array}{l} \Delta R_j(i) = \Delta R(li) \quad \text{when li is a restrained dof} \\ \Delta R_j(i) = 0 \qquad \text{when li is a free dof,} \\ \qquad\qquad \text{for } i = 1 \text{ to } 6 \\ \qquad\qquad li = Lm_k(i) \end{array}\right\} \tag{5.70}$$

yielding $\{\Delta R_j\}$, which can be rotated from the JCS to the GCS by

$$\{\Delta R_{jG}\} = \begin{bmatrix} [C_j]^T & 0 \\ 0 & [C_j]^T \end{bmatrix}\{\Delta R_j\} \tag{5.71}$$

Transferring the reactions from the joint to the origin of the global coordinate system yields

---

[19] If the joint's dof are not restrained, their reaction is set to zero.

$$\{\Delta R_{jGO}\} = \begin{bmatrix} 1. & 0 & 0 & 0 & 0 & 0 \\ 0 & 1 & 0 & 0 & 0 & 0 \\ 0 & 0 & 1 & 0 & 0 & 0 \\ 0 & -Z_g & Y_g & 1 & 0 & 0 \\ Z_g & 0 & -X_g & 0 & 1 & 0 \\ -Y_g & X_g & 0 & 0 & 0 & 1 \end{bmatrix} \{\Delta R_{jG}\} \tag{5.72}$$

where $\{\Delta R_{jGO}\}$ are the incremental reactions at the global origin for joint j, and the transformation is identical to the rigid body constraint in Equation 5.2. Summing reactions for all restrained joints in the GCS about the global origin yields

$$\{\Delta R_{GO}\} = \sum \{\Delta R_{jGOi}\} \tag{5.73}$$

The summation of reactions is used by the analyst to check input loadings, determine the overturning of a structure, and to calculate the energy balance.

Total forces, displacements, reactions and sums of reactions for step t are determined from

$$\{\delta\}_t = \{\delta\}_{t-1} + \{\Delta\delta\} \tag{5.74}$$

$$\{F\}_t = \{F\}_{t-1} + \{\Delta F\} \tag{5.75}$$

$$\{R\}_t = \{R\}_{t-1} + \{\Delta R\} \tag{5.76}$$

$$\{R_{GO}\}_t = \{R_{GO}\}_{t-1} + \{\Delta R_{GO}\} \tag{5.77}$$

F. DYNAMIC ANALYSIS OF 3-D STRUCTURAL SYSTEMS

The nonlinear dynamic response of a 3-D structure subject to multi-component ground motions is determined in this section. The ground motions may consist of one, two or three translational components orientated on an arbitrary axis. The structure's mass is assumed to be lumped at the joints. Combined mass and stiffness proportional damping is used. At the beginning of each time step the tangent stiffness is determined, and the structure is assumed to behave linearly for the duration of the time step. Unbalanced forces, when they exist, are calculated at the end of each time step, and added to the dynamic loading for the next time step. Non-dynamic degrees of freedom are condensed out by Guyan reduction. The resulting reduced dynamic equations of motion are solved by the linear acceleration method. The displacements, velocities and accelerations at condensed degrees of freedom are determined. At the end of each time step, the total acceleration, velocity and displacement are calculated by summing the values from the previous step and the incremental values.

1. Mass Matrix. The structure is idealized as a set of joints, connected by elements, and the structure's mass is assumed to be concentrated at these joints. The mass matrix of an individual joint, in the JCS is

$$[M_j] = \begin{bmatrix} M_X & 0 & 0 & 0 & 0 & 0 \\ 0 & M_Y & 0 & 0 & 0 & 0 \\ 0 & 0 & M_Z & 0 & 0 & 0 \\ 0 & 0 & 0 & I_{XX} & -I_{YX} & -I_{ZX} \\ 0 & 0 & 0 & -I_{YX} & I_{YY} & -I_{ZY} \\ 0 & 0 & 0 & -I_{ZX} & -I_{ZY} & I_{ZZ} \end{bmatrix} \tag{5.78}$$

where M_X is the joint's X_j axis translational mass,

M_Y is the joint's Y_j axis translational mass,

M_Z is the joint's Z_j axis translational mass,

I_{XX} is the mass moment of inertia about the joint's X_j axis,

I_{YY} is the mass moment of inertia about the joint's Y_j axis,

I_{ZZ} is the mass moment of inertia about the joint's Z_j axis,

I_{YX} is the mass product of inertia about the joint's X_j and Y_j axes,

I_{ZX} is the mass product of inertia about the joint's X_j and Z_j axes, and

I_{ZY} is the mass product of inertia about the joint's Y_j and Z_j axes.

If the joint is constrained, its mass matrix is transferred to the 'master' joint by

$$[M_j]_{master} = [T_{ms}][M_j]_{slave}[T_{ms}]^T \tag{5.79}$$

where $[T_{ms}]$ is the constraint transformation, Equation 5.2 or 5.6. The total structural mass matrix $[M]$ is formed by the direct element method.

$$\left.\begin{aligned} M(li,lk) = M(li,lk) + M_j(i,k), \quad & \text{for } i = 1 \text{ to } 6 \\ & k = 1 \text{ to } 6 \\ & j = 1 \text{ to NJOINTS} \\ & li = Lm_j(i) \\ & lk = Lm_j(k) \end{aligned}\right\} \tag{5.80}$$

where NJOINTS is the number of joints in the structure. Note that the mass is transferred from the 'slave' to the 'master' joint, and then added to the 'master' joint's mass. Thus the mass at a 'master' joint may have both translational and rotation terms.

2. Proportional Damping Matrix. Both mass and stiffness proportional damping is used to represent the damping matrix

$$[C] = \alpha[M] + \beta[K] - \beta F_{\ddot{Z}}[G] \tag{5.81}$$

where α and β are damping constants.

Consider the simple structure shown in Figure 139, with mass and stiffness matrices

$$[M] = \begin{bmatrix} M_1 & 0 & 0 \\ 0 & M_2 & 0 \\ 0 & 0 & 0 \end{bmatrix}, \qquad [K] = \begin{bmatrix} K_1 & -K_1 & 0 \\ -K_1 & K_1 + K_2 & -K_2 \\ 0 & -K_2 & K_2 \end{bmatrix} \tag{5.82}$$

where dof 1 corresponds to the roof, dof 2 corresponds to the floor, and dof 3 is restrained. The mass proportional damping force, $\{F_{DM}\}$, is based on the velocity of the floor, relative to the ground. Or,

$$\{F_{DM}\} = [C]\{\dot{\delta}\} = \alpha[M]\{\dot{\delta}\} = \alpha \begin{Bmatrix} M_1\dot{\delta}_1 \\ M_2\dot{\delta}_2 \\ 0 \end{Bmatrix} \tag{5.83}$$

And the mass proportional damping model has a total reaction

$$\{\Sigma R_{DM}\} = -\{1\}^T\{F_{DM}\} = -\alpha\{1\}^T[M]\{\dot{\delta}\} \tag{5.84}$$

at the base of the structure, where $\{1\}$ is a unit vector with the same number of rows as $\{\dot{\delta}\}$. The mass proportional damping reaction acts on the ground, not at a specific joint. Thus reactions of mass proportional damping forces cannot be calculated in a manner similar to reactions due to element forces. The simple structure in Figure 139 has parallel JCS and GCS. For the general case, the mass proportional damping forces are rotated from the JCS to the GCS before the summation in Equation 5.84 is preformed.

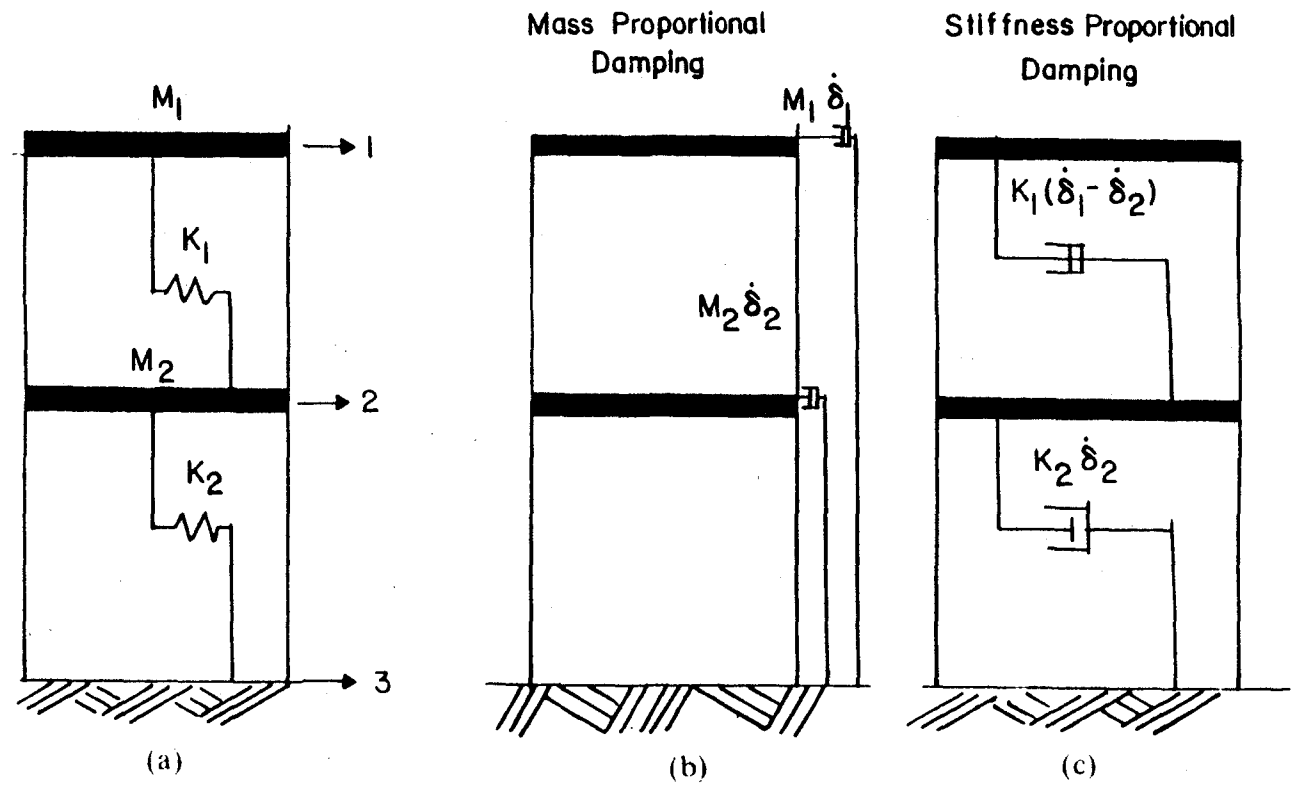

Figure 139. Proportional Damping Models: (a) Structural Model, (b) Mass Proportional Damping Model, (c) Stiffness Proportional Damping Model

Consider the same structure with stiffness proportional damping. The stiffness proportional damping force is dependent on the relative velocity between floors. Both the reactions of the dampers at the base of the structure and the summation of reactions $\{\Sigma R_{DK}\}$ are calculated in a manner similar to the reactions due to element forces, Equations 5.69 to 5.73.

For an elastic structure, the multiple degree of freedom system can be decoupled by the orthogonality relationship yielding the damping term for mode i

$$2\rho_i\omega_i = \alpha + \beta\omega_i^2 \tag{5.85}$$

where ρ_i is the damping ratio for mode i and ω_i is the natural frequency for mode i. One method of determining the constants α and β is by estimating the damping ratio and natural frequency of two modes i and j, then solving

$$\begin{bmatrix} 2\rho_i\omega_i \\ 2\rho_j\omega_j \end{bmatrix} = \begin{bmatrix} 1 & \omega_i^2 \\ 1 & \omega_j^2 \end{bmatrix} \begin{bmatrix} \alpha \\ \beta \end{bmatrix} \tag{5.86}$$

for α and β. Thus

$$\alpha = \frac{2\omega_i\omega_j(\rho_i\omega_j - \rho_j\omega_i)}{\omega_j^2 - \omega_i^2}, \qquad \beta = \frac{2(\rho_j\omega_j - \rho_i\omega_i)}{\omega_j^2 - \omega_i^2} \tag{5.87}$$

When $\rho_i = \rho_j = \rho$, Equation 5.87 simplifies to

$$\beta = \frac{2\rho}{\omega_j + \omega_i}, \qquad \alpha = \omega_i\omega_j\beta \tag{5.88}$$

3. Dynamic Loading. The dynamic loading consists of three input ground accelerations $A_1(t)$, $A_2(t)$ and $A_3(t)$ as shown in Figure 140. The orientation of the

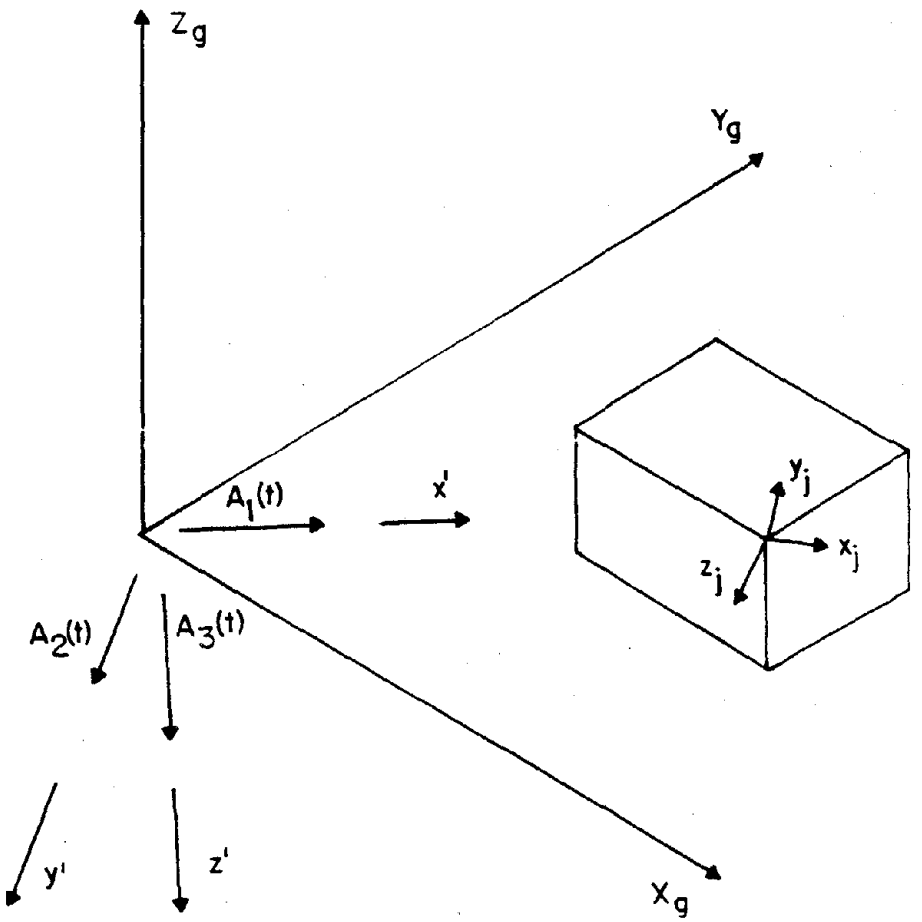

Figure 140. Orientation of Ground Acceleration

ground accelerations coincides with a rotated X', Y', Z' coordinate system. The ground accelerations are rotated to the global X_g, Y_g, Z_g coordinate system. The ground accelerations in the global coordinate system X_g, Y_g, Z_g are then rotated to the joint coordinate system X_j, Y_j, Z_j. The resulting accelerations, in the same coordinate system as the degrees of freedom, are premultiplied by the mass matrix to generate dynamic loads.

Let $\vec{V}_1$ and $\vec{V}_2$ be two perpendicular unit vectors defining the direction of the accelerations $A_1(t)$ and $A_2(t)$, and vector $\vec{V}_3 = \vec{V}_1 \times \vec{V}_2$ defines the orientation of $A_3(t)$, then the three vectors may be expressed in matrix form as

$$\begin{bmatrix} \vec{V}_1 \\ \vec{V}_2 \\ \vec{V}_3 \end{bmatrix} = [C_{123}] \begin{bmatrix} \vec{i} \\ \vec{j} \\ \vec{k} \end{bmatrix} \tag{5.89}$$

where $[C_{123}]$ is the direction cosine matrix of the input ground motion. The incremental accelerations in the global coordinate system are

$$\begin{Bmatrix} \Delta A_{gx} \\ \Delta A_{gy} \\ \Delta A_{gz} \end{Bmatrix} = [C_{123}]^T \begin{Bmatrix} \Delta A_1 \\ \Delta A_2 \\ \Delta A_3 \end{Bmatrix} \tag{5.90}$$

where the typical notation, $\Delta A_1 = A_1(t1) - A_1(t0)$, represents the incremental ground acceleration in the X' axis. The times t0 and t1 are at the beginning and end of the time step, respectively.

The direction cosine matrix for joint j's three translational degrees of freedom is $[C_j]$. The incremental translational ground accelerations in the JCS of joint j are

$$\{\Delta\ddot{\delta}_j\} = \begin{Bmatrix} \Delta A_{jx} \\ \Delta A_{jy} \\ \Delta A_{jz} \end{Bmatrix} = [C_j] \begin{Bmatrix} \Delta A_{gx} \\ \Delta A_{gy} \\ \Delta A_{gz} \end{Bmatrix} \tag{5.91}$$

Since the input ground acceleration only consists of translational components, the rotational ground acceleration is always zero. The incremental Gdof acceleration vector $\{\Delta\ddot{\delta}\}$ is assembled from

$$\left.\begin{aligned} \Delta\ddot{\delta}_{(li)} &= \Delta\ddot{\delta}_j(i), \quad \text{for } i = 1 \text{ to } 3 \text{ (translational dof)} \\ \Delta\ddot{\delta}_{(li)} &= 0, \quad \text{for } i = 4 \text{ to } 6 \text{ (rotational dof)} \\ & \quad j = 1 \text{ to NJOINTS} \\ & \quad li = Lm_j(i) \end{aligned}\right\} \tag{5.92}$$

Note that for constrained joints $\{\Delta\ddot{\delta}_j\}$ is the same for both the 'master' and 'slave' degrees of freedom. Only the 'master' joint is used in the above assemblage.

The incremental dynamic load is the product of mass and incremental acceleration, and is given by

$$\{\Delta F\} = -[M]\{\Delta\ddot{\delta}\} \tag{5.93}$$

For computational efficiency, the incremental accelerations in Equation 5.90 are replaced by an identity matrix. The resulting unit joint translational accelerations are

$$[\hat{A}_j] = [C_j][C_{123}]^T[I] \tag{5.94}$$

These are assembled into a Gdof unit acceleration matrix $[\hat{\Lambda}]$ by

$$\left.\begin{aligned} &\hat{A}(li,k) = \hat{A}_j(i,k), \quad \text{for } i = 1 \text{ to } 3 \text{ (translational dof)} \\ &\hat{A}(li,k) = 0, \quad \text{for } i = 4 \text{ to } 6 \text{ (rotational dof)} \\ &\qquad k = 1 \text{ to } 3 \\ &\qquad j = 1 \text{ to NJOINTS} \\ &\qquad li = Lm_j(i) \end{aligned}\right\} \tag{5.95}$$

and the incremental dynamic loads are obtained by

$$\{\Delta F\} = [\text{Mcos}] \begin{Bmatrix} \Delta A_1 \\ \Delta A_2 \\ \Delta A_3 \end{Bmatrix} \tag{5.96}$$

where

$$[\text{Mcos}] = \left[-[M][\hat{A}] \right] \tag{5.97}$$

Note that [Mcos] is independent of the input acceleration's value, and is only calculated once.

The ground acceleration in the global coordinate system at time t is

$$\{A_g(t1)\} = \{A_g(t0)\} + \{\Delta A_g\} \tag{5.98}$$

The response of the ground, in the global coordinate system, is calculated by assuming the acceleration varies linearly over the time step Δt, integrating the ground acceleration to yield the ground velocity

$$\{V_g(t1)\} = \{V_g(t0)\} + \frac{\Delta t}{2}\left(\{A_g(t0)\} + \{A_g(t1)\}\right) \tag{5.99}$$

and by integrating the ground velocity to yield ground displacement

$$\{D_g(t1)\} = \{D_g(t0)\} + \Delta t\{V_g(t0)\} + \frac{\Delta t^2}{6}\left(2\{A_g(t0)\} + \{A_g(t1)\}\right) \tag{5.100}$$

where $\{V_g\}$ and $\{D_g\}$ are the ground velocity and displacement, and $\Delta t = t1 - t0$ is the time step.

4. Condensation. Often the number of degrees of freedom required to represent the dynamic behavior of a structure is less than the total number of degrees of freedom.

The stiffness matrix is partitioned between condensed, c, free, f, and restrained, r, degrees of freedom. Omitting the restrained degrees of freedom, the partitioned stiffness matrix for constrained and free degrees of freedom is

$$[K] = \begin{bmatrix} [K_{cc}] & [K_{cf}] \\ [K_{fc}] & [K_{ff}] \end{bmatrix} \tag{5.101}$$

Expanding $[K]\{\Delta\delta\} = 0$ yields,

$$[K_{cc}]\{\Delta\delta_c\} + [K_{cf}]\{\Delta\delta_f\} = 0 \tag{5.102a}$$

$$[K_{fc}]\{\Delta\delta_c\} + [K_{ff}]\{\Delta\delta_f\} = 0 \tag{5.102b}$$

Solving Equation 5.102a for $\{\Delta\delta_c\}$ yields

$$\{\Delta\delta_c\} = -[K_{cc}]^{-1}[K_{cf}]\{\Delta\delta_f\} \tag{5.103}$$

or,

$$\begin{Bmatrix} \{\Delta\delta_c\} \\ \{\Delta\delta_f\} \end{Bmatrix} = \begin{bmatrix} -[K_{cc}]^{-1}[K_{cf}] \\ [I]_{f\times f} \end{bmatrix} \{\Delta\delta_f\} = [\Gamma]\{\Delta\delta_f\} \tag{5.104}$$

where $[I]_{f\times f}$ is an identity matrix. Equation 5.104 relates the condensed degrees of freedom to the free degrees of freedom. Taking the derivative of Equation 5.104 with respect to time yields the velocity and acceleration relationships.

$$\begin{Bmatrix} \{\Delta\dot{\delta}_c\} \\ \{\Delta\dot{\delta}_f\} \end{Bmatrix} = [\Gamma]\{\Delta\dot{\delta}_f\} \tag{5.105}$$

$$\begin{Bmatrix} \{\Delta\ddot{\delta}_c\} \\ \{\Delta\ddot{\delta}_f\} \end{Bmatrix} = [\Gamma]\{\Delta\ddot{\delta}_f\} \tag{5.106}$$

5. Equation of Motion. Recall that the incremental equation of motion for a structure subject to ground motion is

$$[M]\{\Delta\ddot{\delta}\} + [C]\{\Delta\dot{\delta}\} + [K]\{\Delta\delta\} - F_{\ddot{z}}[G]\{\Delta\delta\} = \{\Delta F\} + \{U\} \tag{5.107}$$

The equation of motion is partitioned between condensed, c, free, f, and restrained, r, degrees of freedom. Set the support displacements, velocities and accelerations equal to zero, $\{\Delta\delta_r\} = \{0\}$, $\{\Delta\dot{\delta}_r\} = \{0\}$ and $\{\Delta\ddot{\delta}_r\} = \{0\}$. Thus the global incremental displacement, velocity and acceleration vectors become

$$\{\Delta\delta\} = \begin{Bmatrix} \{\Delta\delta_c\} \\ \{\Delta\delta_f\} \\ \{0\} \end{Bmatrix} \qquad \{\dot{\delta}\} = \begin{Bmatrix} \{\Delta\dot{\delta}_c\} \\ \{\Delta\dot{\delta}_f\} \\ \{0\} \end{Bmatrix} \qquad \{\ddot{\delta}\} = \begin{Bmatrix} \{\Delta\ddot{\delta}_c\} \\ \{\Delta\ddot{\delta}_f\} \\ \{0\} \end{Bmatrix} \tag{5.108}$$

Expanding Equation 5.107 by 1) substituting in Equation 5.108 for the displacement, velocity and acceleration, and 2) partitioning the mass, damping and stiffness matrices yields two independent equations.

$$\begin{bmatrix}[M_{cc}][M_{cf}]\\ [M_{fc}][M_{ff}]\end{bmatrix}\begin{Bmatrix}\{\Delta\ddot{\delta}_c\}\\ \{\Delta\ddot{\delta}_f\}\end{Bmatrix}+\begin{bmatrix}[C_{cc}][C_{cf}]\\ [C_{fc}][C_{ff}]\end{bmatrix}\begin{Bmatrix}\{\Delta\dot{\delta}_c\}\\ \{\Delta\dot{\delta}_f\}\end{Bmatrix}+\begin{bmatrix}[K_{cc}][K_{cf}]\\ [K_{fc}][K_{ff}]\end{bmatrix}\begin{Bmatrix}\{\Delta\delta_c\}\\ \{\Delta\delta_f\}\end{Bmatrix}$$

$$-F_{\ddot{z}}\begin{bmatrix}[G_{cc}][G_{cf}]\\ [G_{fc}][G_{ff}]\end{bmatrix}\begin{Bmatrix}\{\Delta\delta_c\}\\ \{\Delta\delta_f\}\end{Bmatrix}=\begin{Bmatrix}\{F_c\}\\ \{F_f\}\end{Bmatrix}+\begin{Bmatrix}\{U_c\}\\ \{U_f\}\end{Bmatrix} \tag{5.109}$$

$$\left[[M_{rc}][M_{rf}]\right]\begin{Bmatrix}\{\Delta\ddot{\delta}_c\}\\ \{\Delta\ddot{\delta}_f\}\end{Bmatrix}+\left[[C_{rc}][C_{rf}]\right]\begin{Bmatrix}\{\Delta\dot{\delta}_c\}\\ \{\Delta\dot{\delta}_f\}\end{Bmatrix}+\left[[K_{rc}][K_{rf}]\right]\begin{Bmatrix}\{\Delta\delta_c\}\\ \{\Delta\delta_f\}\end{Bmatrix}$$

$$-F_{\ddot{z}}\left[[G_{rc}][G_{rf}]\right]\begin{Bmatrix}\{\Delta\delta_c\}\\ \{\Delta\delta_f\}\end{Bmatrix}=\{\Delta R\}+\{U_r\} \tag{5.110}$$

where $\{\Delta R\}$ are the incremental reactions at the restrained joints. Equation 5.109 represents the vibration of the structure, while Equation 5.110 represents the reactions at the restrained dof. Substituting Equations 5.104 to 5.106 into Equation 5.109 and premultipling by $[\Gamma]^T$ yields

$$[M^*_{ff}]\{\Delta\ddot{\delta}_f\}+[C^*_{ff}]\{\Delta\dot{\delta}_f\}+[K^*_{ff}]\{\Delta\delta_f\}-F_{\ddot{z}}[G^*_{ff}]\{\Delta\delta_f\}=\{\Delta F^*_f\} \tag{5.111}$$

where

$$[M^*_{ff}]=[\Gamma]^T\begin{bmatrix}[M_{cc}][M_{cf}]\\ [M_{fc}][M_{ff}]\end{bmatrix}[\Gamma] \tag{5.112}$$

$$[C^*_{ff}]=[\Gamma]^T\begin{bmatrix}[C_{cc}][C_{cf}]\\ [C_{fc}][C_{ff}]\end{bmatrix}[\Gamma] \tag{5.113}$$

$$[K^*_{ff}]=[\Gamma]^T\begin{bmatrix}[K_{cc}][K_{cf}]\\ [K_{fc}][K_{ff}]\end{bmatrix}[\Gamma] \tag{5.114}$$

$$[G_{ff}^{*}] = [\Gamma]^{T}\begin{bmatrix}[G_{cc}][G_{cf}]\\ [G_{fc}][G_{ff}]\end{bmatrix}[\Gamma] \tag{5.115}$$

$$\{\Delta F_{f}^{*}\} = [\Gamma]^{T}\left(\begin{Bmatrix}\{\Delta F_{c}\}\\ \{\Delta F_{f}\}\end{Bmatrix} + \begin{Bmatrix}\{U_{c}\}\\ \{U_{f}\}\end{Bmatrix}\right) \tag{5.116}$$

The unbalanced force is combined with the dynamic load to reduce the number of transformations. Hereafter, $\{\Delta F_{f}^{*}\}$ contains both dynamic loads and unbalanced forces. For proportional damping, the damping term

$$[C_{ff}^{*}] = \alpha[M_{ff}^{*}] + \beta\left([K_{ff}^{*}] - F_{\ddot{z}}[G_{ff}^{*}]\right) \tag{5.117}$$

is used in lieu of Equation 5.113.

Numerically the matrices in Equations 5.112 through 5.116 are condensed one row at a time. For the stiffness matrix, this is equivalent to Gaussian elimination. Thus the inversion, $[K_{cc}]^{-1}$, to determine the transformation $[\Gamma]$ in Equation 5.104 has an order of one. This is computationally more efficient than inverting a $c \times c$ matrix and performing the multiplication required above for each transformation. However, the Gaussian elimination scheme has one drawback. The geometric stiffness and mass matrices cannot be condensed independently. If only the geometric stiffness matrix is updated, both the geometric and structural stiffness matrices must be reformed and condensed together.

a. Linear Acceleration Method. The linear acceleration method was originally developed by Newmark (56). Since then the linear acceleration method has been presented in many different forms with numerous variations (86 ,21).

Assume that the acceleration of the structure varies linearly over the time step Δt. Let the time at the end of the time step be $t = \Delta t$, and the time at the beginning of the time step is $t0 = t - \Delta t = 0$. Thus a linear equation for accelerations between times t0 and t is

$$\{\ddot{\delta}_f(t)\} = 6\{A\}t + 2\{B\} \tag{5.118}$$

Integrating Equation 5.118 with respect to time yields the velocity

$$\{\dot{\delta}_f(t)\} = 3\{A\}t^2 + 2\{B\}t + \{C\} \tag{5.119}$$

And integrating Equation 5.119 with respect to time yields the displacement

$$\{\delta_f(t)\} = \{A\}t^3 + \{B\}t^2 + \{C\}t + \{D\} \tag{5.120}$$

From the initial conditions at time $t = t0 = 0$

$$\left.\begin{aligned} \{\ddot{\delta}_f(t0)\} &= 2\{B\}, \qquad \text{or } \{B\} = \frac{\{\ddot{\delta}_f(t0)\}}{2} \\ \{\dot{\delta}_f(t0)\} &= \{C\} \\ \{\delta_f(t0)\} &= \{D\} \end{aligned}\right\} \tag{5.121}$$

and from the final condition at time $t = \Delta t$

$$\{\ddot{\delta}_f(t)\} = 6\{A\}\Delta t + \{\ddot{\delta}_f(t0)\}, \quad \text{or } \{A\} = \frac{\{\ddot{\delta}_f(t)\} - \{\ddot{\delta}_f(t0)\}}{6\Delta t} = \frac{\Delta\ddot{\delta}_f}{6\Delta t} \tag{5.122}$$

Substituting the constants A, B, C and D into Equation 5.120 and solving for the incremental displacements, $\{\Delta\delta_f\}$, yields

$$\left.\begin{aligned} \{\Delta\delta_f\} &= \{\delta_f(t)\} - \{\delta_f(t0)\} \\ &= \{\Delta\ddot{\delta}_f\}\frac{\Delta t^2}{6} + \{\ddot{\delta}_f(t0)\}\frac{\Delta t^2}{2} + \{\dot{\delta}_f(t0)\}\Delta t \end{aligned}\right\} \tag{5.123}$$

Solving for the incremental acceleration, $\{\Delta\ddot{\delta}_f\}$, yields

$$\left.\begin{aligned}\{\Delta\ddot{\delta}_f\} &= \frac{6}{\Delta t^2}\{\Delta\delta_f\} - \left(3\{\ddot{\delta}_f(t0)\} + \frac{6}{\Delta t}\{\dot{\delta}_f(t0)\}\right) \\ &= \frac{6}{\Delta t^2}\{\Delta\delta_f\} - \{A_n\}\end{aligned}\right\} \tag{5.124}$$

Substituting the constants A, B, and C into Equation 5.119 and solving for the incremental velocities yields

$$\left.\begin{aligned}\{\Delta\dot{\delta}_f\} &= \{\dot{\delta}_f(t)\} - \{\dot{\delta}_f(t0)\} \\ &= \frac{\Delta t}{2}\{\Delta\ddot{\delta}_f\} + \{\ddot{\delta}_f(t0)\}\Delta t\end{aligned}\right\} \tag{5.125}$$

Substituting in Equation 5.124 for $\{\Delta\ddot{\delta}_f\}$ yields

$$\left.\begin{aligned}\{\Delta\dot{\delta}_f\} &= \frac{3}{\Delta t}\{\Delta\delta_f\} - \left(\frac{\Delta t}{2}\{\ddot{\delta}_f(t0)\} + 3\{\dot{\delta}_f(t0)\}\right) \\ &= \frac{3}{\Delta t}\{\Delta\delta_f\} - \{B_n\}\end{aligned}\right\} \tag{5.126}$$

Substituting $\{\Delta\dot{\delta}_f\}$ and $\{\Delta\ddot{\delta}_f\}$ into the incremental equation of motion, Equation 5.111, and substituting in Equation 5.117 for proportional damping yields

$$[M_{ff}^*]\left(\frac{6}{\Delta t^2}\{\Delta\delta_f\} - \{A_n\}\right) + \left[\alpha[M_{ff}^*] + \beta[K_{ff}^*] - \beta F_{\ddot{z}}[G_{ff}^*]\right]\left(\frac{3}{\Delta t}\{\Delta\delta_f\} - \{B_n\}\right)$$

$$+ \left[[K_{ff}^*] - F_{\ddot{z}}[G_{ff}^*]\right]\{\Delta\delta_f\} = \{\Delta F_f^*\} \tag{5.127}$$

Combining terms

$$\left(1+\frac{3\beta}{\Delta t}\right)\left[[K_{ff}^{*}]-F_{\dot{z}}[G_{ff}^{*}]\right]\{\Delta\delta_f\}+\left(\frac{3\alpha}{\Delta t}+\frac{6}{\Delta t^2}\right)[M_{ff}^{*}]\{\Delta\delta_f\}$$

$$-\beta\left[[K_{ff}^{*}]-F_{\dot{z}}[G_{ff}^{*}]\right]\{B_n\}=\{\Delta F_f^{*}\}+[M_{ff}^{*}]\{\{A_n\}+\alpha\{B_n\}\} \tag{5.128}$$

Let $c_0=\frac{3\alpha}{\Delta t}+\frac{6}{\Delta t^2}$

$$c_1=\frac{1}{1+\frac{3\beta}{\Delta t}} \tag{5.129}$$

$c_2=c_0c_1$

$c_3=\alpha-c_2\beta$

Substituting c_0 through c_3 into Equation 5.128 and subtracting $c_2\beta[M_{ff}^{*}]\{B_n\}$ for both sides of the equation yields

$$\left[[K_{ff}^{*}]-F_{\dot{z}}[G_{ff}^{*}]\right]\frac{\{\Delta\delta_f\}}{c_1}+c_2[M_{ff}^{*}]\frac{\{\Delta\delta_f\}}{c_1}-\beta\left[[K_{ff}^{*}]-F_{\dot{z}}[G_{ff}^{*}]\right]\{B_n\}$$

$$-c_2\beta[M_{ff}^{*}]\{B_n\}=\{\Delta F_f^{*}\}+[M_{ff}^{*}]\{\{A_n\}+\alpha\{B_n\}\}-c_2\beta[M_{ff}^{*}]\{B_n\} \tag{5.130}$$

Combining terms

$$\left[[K_{ff}^{*}]-F_{\dot{z}}[G_{ff}^{*}]+c_2[M_{ff}^{*}]\right]\left(\frac{\{\Delta\delta_f\}}{c_1}-\beta\{B_n\}\right)$$

$$=\{\Delta F_f^{*}\}+[M_{ff}^{*}]\{\{A_n\}+c_3\{B_n\}\} \tag{5.131}$$

or

$$[\overline{K}]\{\overline{\Delta\delta}\}=\{\overline{\Delta P}\} \tag{5.132}$$

where

$$[\overline{K}]=[K_{ff}^{*}]-F_{\dot{z}}[G_{ff}^{*}]+c_2[M_{ff}^{*}] \tag{5.133}$$

$$\{\overline{\Delta\delta}\} = \frac{\{\Delta\delta_f\}}{c_1} - \beta\{B_n\} \tag{5.134}$$

$$\{\overline{\Delta P}\} = \{\Delta F_f^*\} + [M_{ff}^*]\{\{A_n\} + c_3\{B_n\}\} \tag{5.135}$$

If neither the structural stiffness nor the geometric stiffness vary from step to step, Equation 5.133 is only calculated once. Equation 5.132 is solved for $\{\overline{\Delta\delta}\}$ by Gaussian elimination. The incremental free displacements are obtained by

$$\{\Delta\delta_f\} = c_1\{\overline{\Delta\delta}\} + c_1\beta\{B_n\} \tag{5.136}$$

The incremental displacements are substituted into Equations 5.126 and 5.124 to yield the incremental velocities and accelerations.

The displacements, velocities and accelerations of condensed degrees of freedom are calculated by Equations 5.104 to 5.106. Numerically, the displacements, velocities and accelerations are found by back substitution with the condensed stiffness matrix. This provides a more efficient solution than performing the multiplications in Equations 5.104 to 5.106.

b. Reactions. Two formulations for reactions are used. The first is the reactions of the element forces on restrained degrees of freedom

$$[\Delta R] = \left[[K_{rc}][K_{rf}]\right]\begin{Bmatrix}\{\Delta\delta_c\}\\ \{\Delta\delta_f\}\end{Bmatrix} - \{U_r\} \tag{5.137}$$

This is equivalent to Equation 5.69 for the case $\{\Delta\delta_r\} = 0$. The summation of incremental reactions $\{\Delta\Sigma R_{GO}\}$ is determined by Equations 5.69 through 5.73.

The second formulation for reactions is based on Equation 5.110, and is used for the energy balance. Solving Equation 5.110 for $\{\Delta R\}$, with proportional damping

$$\{\Delta R\} = \left[[M_{rc}][M_{rf}]\right]\begin{Bmatrix}\{\Delta\ddot{\delta}_c\}\\ \{\Delta\ddot{\delta}_f\}\end{Bmatrix}$$
$$+\left(\alpha\left[[M_{rc}][M_{rf}]\right]+\beta\left[[K_{rc}][K_{rf}]\right]-\beta F_{\ddot{z}}\left[[G_{rc}][G_{rf}]\right]\right)\begin{Bmatrix}\{\Delta\dot{\delta}_c\}\\ \{\Delta\dot{\delta}_f\}\end{Bmatrix}$$
$$+\left(\left[[K_{rc}][K_{rf}]\right]-F_{\ddot{z}}\left[[G_{rc}][G_{rf}]\right]\right)\begin{Bmatrix}\{\Delta\delta_c\}\\ \{\Delta\delta_f\}\end{Bmatrix}-\{U_r\} \qquad (5.138)$$

The first term is the reaction due to inertial forces. If a consistent mass formulation were used to determine the mass matrix, $[M_{rc}]$ and $[M_{rf}]$ would be nonzero, and reactions due to inertial forces would exist. For a lumped mass model, $[M_{rc}]$ and $[M_{rf}]$ are zero. Thus the inertial forces are not transferred to the ground. Since the lumped mass matrix is used in this study, the first term is dropped.

The second term consists of the reaction due to proportional damping. As previously discussed, the reactions due to lumped mass proportional damping at specific dof are undefined. However, the summation of the incremental mass proportional damping $\Sigma\Delta R_{DM}$ is determined by Equation 5.84. The sum of the incremental stiffness proportional damping, $\Sigma\Delta R_{DK}$, is calculated in a manner similar to the reactions due to element forces. $\{\Sigma\Delta R_{GO}\}$.

The third term consists of reactions due to 1) stiffness, 2) geometric stiffness and 3) unbalanced forces. The geometric stiffness is actually a load occasioned on the structure by the so called P-Δ forces and is omitted. The sum of incremental reactions due to stiffness and unbalanced forces $\{\Sigma\Delta R_{GO}\}$ was determined in Equations 5.69 through 5.73.

c. Total Displacements, Velocities, Accelerations and Reactions. The total displacements, velocities accelerations and reactions are determined from

$$\{\delta(t)\} = \{\delta(t0)\} + \{\Delta\delta\} \tag{5.139}$$

$$\{\dot{\delta}(t)\} = \{\dot{\delta}(t0)\} + \{\Delta\dot{\delta}\} \tag{5.140}$$

$$\{\ddot{\delta}(t)\} = \{\ddot{\delta}(t0)\} + \{\Delta\ddot{\delta}\} \tag{5.141}$$

$$\{R(t)\} = \{R(t0)\} + \{\Delta R\} \tag{5.142}$$

The initial conditions $\{\delta(0)\}$, $\{\dot{\delta}(0)\}$, $\{\ddot{\delta}(0)\}$ and $\{R(0)\}$ are zero for a structure subjected to an earthquake.

G. ENERGY FORMULATION

Two purposes are served by examining the energy in a structure. First, conservation of energy, or an energy balance, is used to check the accuracy of the numerical solution. Second, the behavior of a structure can be studied by examining the amount of energy stored in, and dissipated by the structure (26, 21).

From the conservation of energy

$$E_i = E_s + E_d \tag{5.143}$$

where E_i = The energy input into the structure.

E_s = The energy stored in the structure, which consist of kinetic energy, KE, and elastic strain energy, ESE; $E_s = KE + ESE$

E_d = The energy dissipated by the structure, which consist of plastic strain energy, PSE, and energy dissipated by damping, DE; $E_d = PSE + DE$

Thus Equation 5.143 becomes

$$E_i = KE + ESE + PSE + DE \tag{5.144}$$

Equation 5.144 is used to check the accuracy of the numerical solution. The relative error of the solution in percent, is expressed by

$$Re = \frac{E_i - (KE + ESE + PSE + DE)}{E_i} 100 \tag{5.145}$$

1. Input Energy. Energy is transmitted into the structure by 1) the reactions moving through a ground displacement, and 2) the geometric stiffness forces moving through an absolute displacement. For ground motions consisting of three translational components, the total energy input at time t is given by

$$E_i = \int_0^t \{\Sigma R(t)\}^T d\{D_g\} + \int_0^t \{F_{Gf}(t)\}^T d\{\delta_f + \delta_{gf}\} \tag{5.146}$$

where $\{D_g\}$ represents the three components of ground translation, and $\{\delta_{gf}\}$ is a vector of the ground translations in the Gdof. The summation of reactions at time t, $\{\Sigma R(t)\}$, consists of

1) Reactions due to lumped mass proportional damping $\{\Sigma R_{DM}(t)\}$,

2) Reactions due to stiffness proportional damping $\{\Sigma R_{DK}(t)\}$,

3) Reactions due to member forces $\{\Sigma R_{GO}(t)\}$.

The geometric stiffness forces for free degrees of freedom at time t, $\{F_{Gf}(t)\}$, are determined by

$$\{F_{Gf}(t)\} = \{F_{Gf}(t0)\} + F_{\dot{z}} [G^*_{ff}] \{\Delta\delta_f\} \tag{5.147}$$

In incremental form Equation 5.146 becomes

$$E_i(t) = E_i(t0) + \left\{\overline{\{R_{DM}\}} + \overline{\{R_{Dk}\}} + \overline{\{R_{GO}\}}\right\}^T \{\Delta\delta_g\} + \overline{\{F_{Gf}\}}\{\Delta\delta_f + \Delta\delta_{gf}\} \qquad (5.148)$$

where $\overline{\{\ \}}$ are the average summation of reactions or geometric stiffness forces over the time step Δt. Neither the summation of reactions, nor the geometric stiffness forces are linear over time Δt. Thus Equation 5.148 is an approximation of the input energy.

2. Kinetic Energy. The total kinetic energy of the structure at time t is given by

$$KE(t) = \frac{1}{2}\{\dot{\delta}_f(t) + \dot{\delta}_{gf}(t)\}^T [M^*_{ff}]\{\dot{\delta}_f(t) + \dot{\delta}_{gf}(t)\} \qquad (5.149)$$

3. Strain Energy. The strain energy is calculated for each individual element. The total strain energy of the structure is the sum of all the individual element's strain energy. The strain energy for a given element is a function of both the element type and the type of hysteresis model used to represent the elements inelastic behavior. For the general force - deformation relationship, shown in Figure 141, the total strain energy is the area bounded by OAB. The total strain energy, SE, is composed of two parts: 1) the elastic or stored strain energy, ESE, represented by the area bounded by ABC, and 2) the inelastic or dissipated strain energy, PSE, represented by the area bounded by OAC. Thus

$$SE = ESE + PSE \qquad (5.150)$$

The total strain energy per unit height, for each of the shear wall's components of deformation is given by

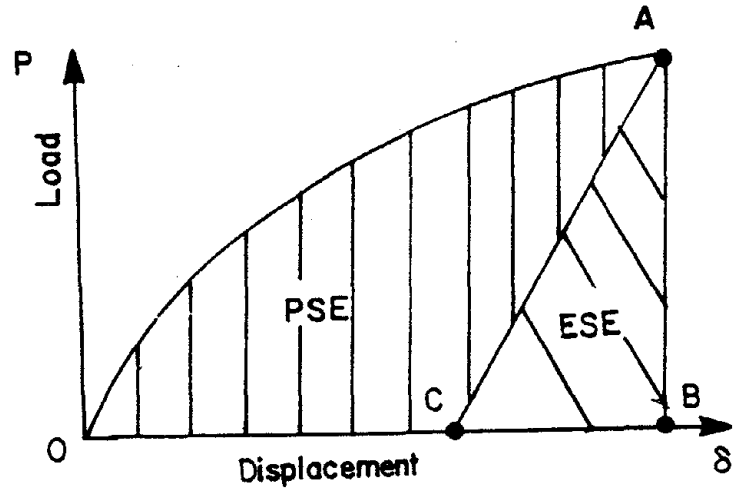

Figure 141. Strain Energy

$$\left.\begin{aligned} SE_{bending}(t) &= SE_{bending}(t0) + 0.5[M_a(t) + M_a(t0)][\theta_u(t) - \theta_u(t0)] \\ SE_{shear}(t) &= SE_{shear}(t0) + 0.5[V_a(t) + V_a(t0)][v_u(t) - v_u(t0)] \\ SE_{axial}(t) &= SE_{axial}(t0) + 0.5[P_a(t) + P_a(t0)][u_u(t) - u_u(t0)] \end{aligned}\right\} \quad (5.151)$$

The plastic strain energy for each component of deformation is based on each component's equivalent unloading stiffness, K_{eu}, and is given by

$$\left.\begin{aligned} PSE_{bending}(t) &= \frac{M_a^2(t)}{2K_{b\,eu}} \\ PSE_{shear}(t) &= \frac{V_a^2(t)}{2K_{s\,eu}} \\ PSE_{axial}(t) &= \frac{P_a^2(t)}{2K_{a\,eu}} \end{aligned}\right\} \quad (5.152)$$

where the equivalent unloading stiffness is chosen such that the area under the actual unloading curve, area ABDEF, is equivalent to area ABC in Figure 142.

For the bending hysteresis model, the area ABDEF is

$$Area = 0.875PM(DM - DQ3) + 0.5PM(DQ3 - DQ1) + 0.125PM(DQ1 - D0') \quad (5.153)$$

where PM, DM, DQ3, DQ1 and D0′ are defined in Section A.2.a of Chapter IV.

The equivalent bending unloading stiffness is

$$K_{b\,eq} = \frac{PM^2}{2Area} \quad (5.154)$$

For the shear hysteresis model, the area ABDEF is

$$Area = \frac{(PM + PA)(DM - DA)}{2} + \frac{(PA + PB)(DA - DB)}{2} + \frac{PB(DB - D0')}{2} \quad (5.155)$$

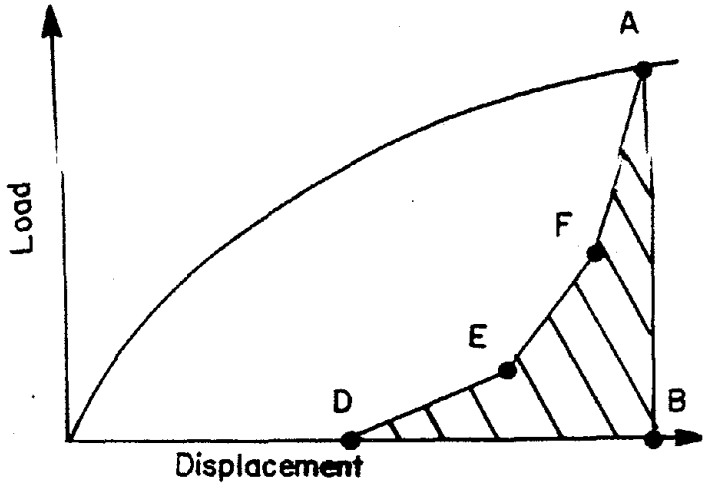

(a)

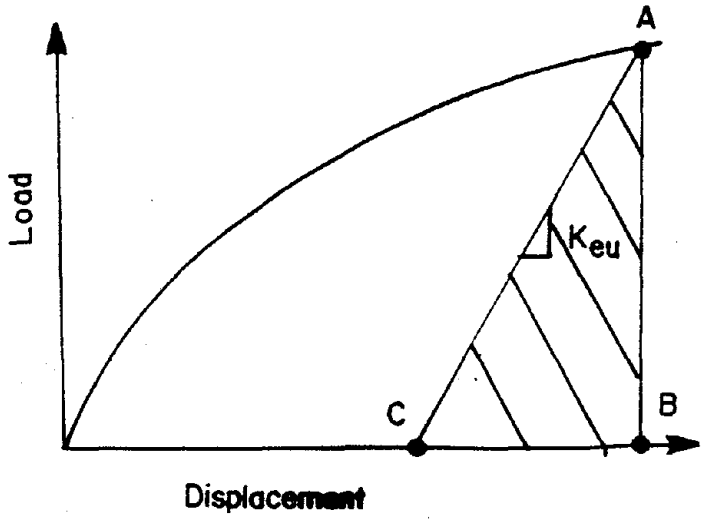

(b)

Figure 142. Equivalent Unloading Stiffness: (a) Actual Unloading Stiffness, (b) Equivalent Unloading Stiffness

where PM, DM, PA, DA, PB, DB and D0′ are defined in Section A.2.b of Chapter IV. The equivalent shear unloading stiffness is

$$K_{s\ eq} = \frac{PM^2}{2Area} \tag{5.156}$$

For the axial hysteresis model, the unloading stiffness is used for the equivalent unloading stiffness. The axial unloading stiffness is given in Section C.3 and C.4 of Chapter IV.

The strain energy and plastic strain energy, for each component of deformation given in Equations 5.151 and 5.152 are multiplied by the wall's height, h, to determine the total energy in the element.

4. Energy Dissipated by Damping. The energy dissipated by damping is the integral of damping force times the incremental relative displacement. Substituting $\Delta t\{\dot{\delta}_f\}$ for the incremental displacement, the energy dissipated by damping becomes

$$DE = \int_0^t \Delta t\{F_D(t)\}^T d\{\dot{\delta}_f\} \tag{5.157}$$

This integral is approximated by an incremental expression for DE. The incremental damping force in a time step for proportional damping is given by

$$\{\Delta F_D\} = \alpha[M_{ff}^*]\{\Delta\dot{\delta}_f\} + \beta[K_{ff}^*]\{\Delta\dot{\delta}_f\} - \beta F_{\ddot{z}}[G_{ff}^*]\{\Delta\dot{\delta}_f\} \tag{5.158}$$

The total energy dissipated by damping is

$$DE(t) = DE(t0) + \Delta t\left[F_D(t0) + \frac{\Delta F_D}{2}\right]\{\Delta\dot{\delta}_f\} \tag{5.159}$$

H. DUCTILITY AND EXCURSION RATIO

Three definitions of ductility are considered in this study. The first and most common definition is the displacement definition as shown in Figure 143. Let the displacement ductility be defined as

$$\mu_d = \frac{|\delta_{max}|}{\delta_y} \tag{5.160}$$

when δ_{max} represents the maximum displacement, rotation or strain in the structure or element, and δ_y is the yield displacement, rotation or strain.

Cheng, et al, (26, 21) have proposed several energy based ductility definitions. Both the variable strain energy and the constant strain energy formulations are used in this study. The variable strain energy definition of the ductility is shown in Figure 144 and defined as

$$\mu_{vse} = 1 + \frac{PSE}{ESE} \tag{5.161}$$

where PSE corresponds to the plastic strain energy for the current half cycle. The constant strain energy definition of the ductility is shown in Figure 145 and defined as

$$\mu_{cse} = 1 + \frac{PSE}{CSE} \tag{5.162}$$

where CSE is the constant strain energy corresponding to displacement at yield.

For each ductility ratio, a corresponding excursion ratio exist, where the excursion ratio is given by

$$\varepsilon = \sum(\mu - 1) \tag{5.163}$$

and the summation is carried out for each half cycle.

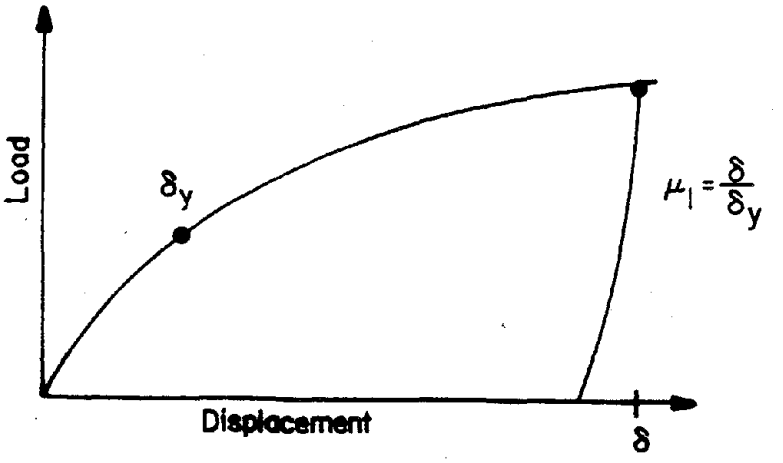

Figure 143. Displacement Definition of Ductility

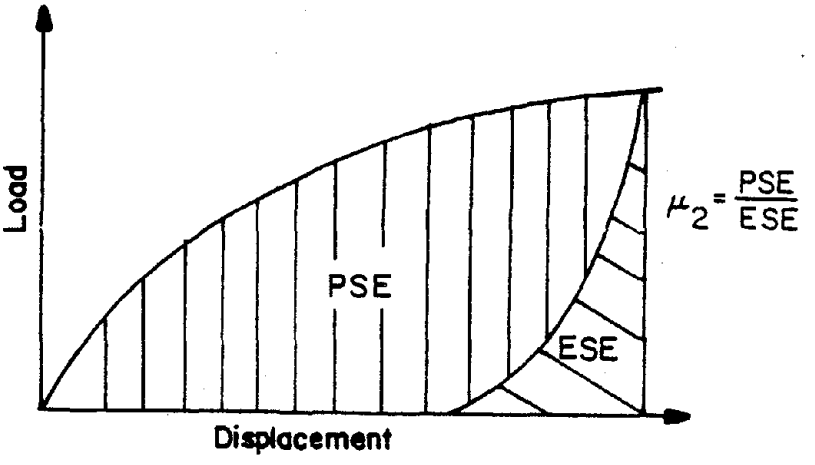

Figure 144. Variable Strain Energy Definition of Ductility

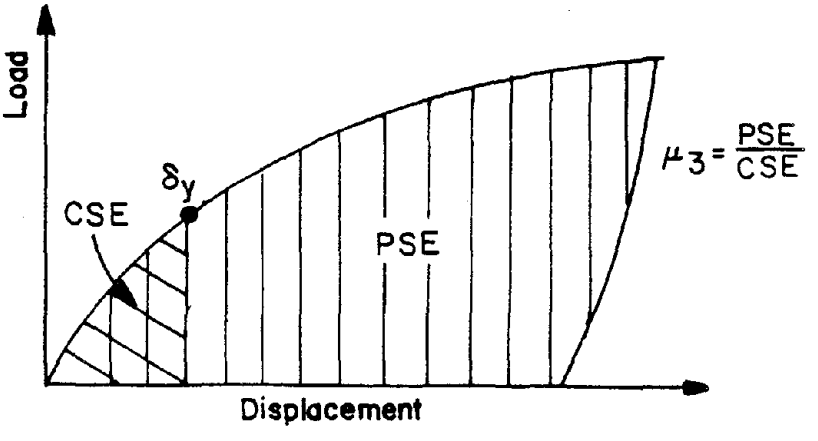

Figure 145. Constant Strain Energy Definition of Ductility

I. DAMAGE INDEX

The damage index is a parameter developed by Ang, et al, to assess the damage in a structure (65, 66, 5). A damage index greater than 1.0 indicates total damage or collapse. The damage index is defined as

$$DI = \frac{\delta_{max}}{\delta_{ult}} + \frac{\beta}{Fy\,\delta_{ult}} \int_0^t d(PSE) \tag{5.164}$$

where δ_{max} is the maximum displacement, δ_{ult} is the failure displacement under monotonic loading, Fy is the yield force, and β is a hysteretic energy coefficient. For R/C shear walls, Sheu (72) determined $\beta = 0.20$, based on NCKU walls SW1a through SW6.

In this study, the damage index is calculated independently for the bending, shear and axial components of deformation in a shear wall. The damage index for the entire structure is then calculated by taking a weighted average of each individual component's damage index, where the strain energy, SE_i, given in Equation5.151 is used as the weighting factor. Thus

$$DI = \frac{\sum SE_i\, DI_i}{\sum SE_i} \tag{5.165}$$

where the summation is carried out for all the members. A sample calculation of the damage index is included in Section B.1 of Chapter VI.

VI. RESPONSE STUDIES OF LOW-RISE BUILDINGS WITH ISOLATED SHEAR WALLS

Low-rise R/C buildings commonly rely on isolated shear walls to resist lateral loads. These walls are chosen because of their strength and rigidity. The response of a reinforced concrete shear wall building to earthquake ground motions is influenced by several parameters: 1) the amount of structural damage, 2) the symmetry of the building system, 3) the type of earthquake ground motion, and 4) the number of components of the earthquake ground motion. Numerical studies are performed to investigate the effects of these parameters. These studies consist of two buildings (symmetric and nonsymmetric) subject to various earthquake ground motions (El Centro, Taft and Mexico) using both one and two components of ground motion. Additionally the input angle of the two-component El Centro ground motion is rotated 26° in an attempt to calculate the maximum response for various ground motion input angles (17). The responses of elastic (undamaged) and nonlinear (damaged) buildings are examined. The nonlinear response is calculated at three different intensities of ground motion to determine the response at various damage levels.

A. STATIC RESPONSE OF SYMMETRIC AND UNSYMMETRIC BUILDINGS

1. Symmetric Building. The symmetric building used in this study is shown in Figure 146. This two-story square building has four 30' wide shear walls, symmetrically placed on the building's perimeter. All of the lateral loads are resisted by the shear walls. Most of the gravity loads in the building are carried by a separate vertical load resisting system, with the shear walls carrying the remainder of the gravity loads. The symmetric building's gravity loads are summarized in Table XII. The center of mass and the center of rigidity of a symmetric building coincide. However, to account for

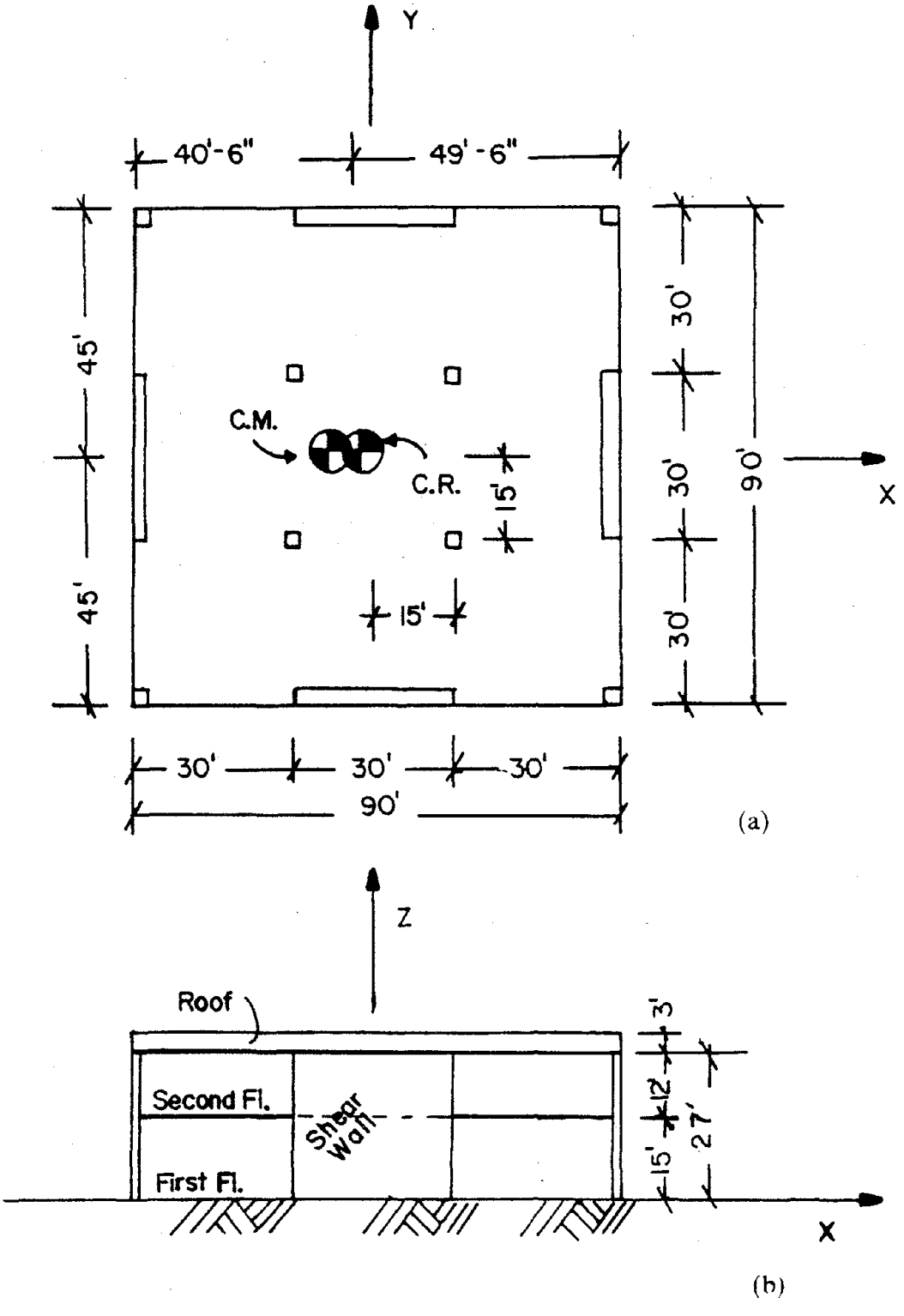

Figure 146. Two-Story Symmetric Building: (a) Plan, (b) Elevation

the uncertainties in the location of the gravity loads, the mass center is offset 5% of the building's width.

Table XII. GRAVITY LOADINGS OF THE SYMMETRIC BUILDING

Dead load				
Roof	Structure	15 psf x 90′ x 90′	121.5 k	
	HVAC	15 k + 5 psf x 90′ x 90′	55.5 k	
	Brick Curtain Wall	40 psf x 9′ x 360′	129.5 k	
	Shear Wall	120 psf x 6′ x 120′	86.4 k	
Total Roof Dead Load				392.2 k
Second Floor	Structure	50 psf x 90′ x 90′	405.0 k	
	HVAC	5 psf x 90′ x 90′	40.5 k	
	Brick Curtain Wall	40 psf x 13.5′ x 360′	194.4 k	
	Shear Wall	120 psf x 13.5′ x 120′	194.4 k	
Total Second Floor Dead Load				834.3 k
Total Building Dead Load				1226.5 k
Live load				
Roof	Snow	25 psf x 90′ x 90′	202.5 k	
Second Floor	Occupancy	50 psf x 90′ x 90′	405.0 k	
Total Building Live Load				607.5 k

The 30′ wide shear walls are shown in Figure 147. The height to width ratios of the first and second floor walls is 0.50 and 0.40, respectively. These walls are 8″ thick and are made of 4000 psi (f'_c) concrete. The walls are reinforced with 2 #3 @11″ each way for vertical and horizontal reinforcement ratios of $\rho = 0.25\%$. The reinforcement steel has a yield point of 60 ksi. The shear wall has an axial working stress of about $2.5\% f'_c$ under full dead plus full live loading. This axial stress is small enough to be neglected when calculating the backbone curves.

The moment to shear ratio for the shear wall is determined by applying the UBC design base shear to the building and then examining the bending moment and shear

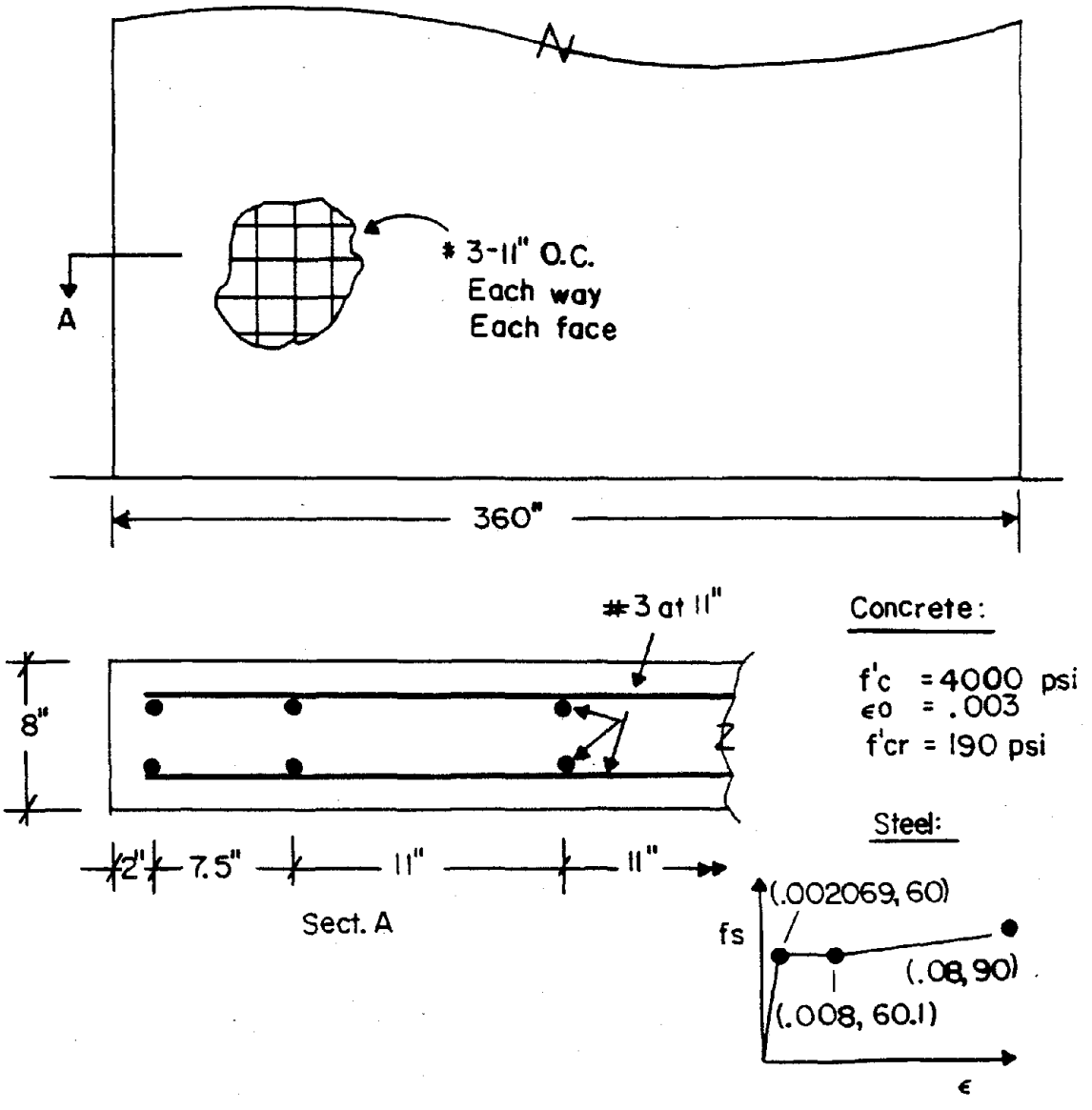

Figure 147. 30 ft Wide Shear Wall

forces in the shear wall. The 1988 Uniform Building Code (77) section 2312(e) provides a design base shear of

$$V = \frac{Z\,I\,C}{R_W} W, \quad \text{for} \quad C = \frac{1.25\,S}{T^{2/3}} \leq 2.75 \tag{6.1}$$

where $Z = 0.40$, UBC zone 4,

$I = 1.0$, normal occupancy,

$R_W = 6$, load bearing concrete shear wall system,

$S = 1.0$ to 2.0, depending on soil type,

T = the period of the structure, and

W = the total seismic dead load of the structure.

Assume that the building's period, T, is less than 0.30 seconds, which yields the peak value of $C = 2.75$ regardless of the soil type factor, S. Thus the UBC base shear is

$$V = \frac{0.40\,(1.0)\,2.75}{6} 1226.5 = 225 \text{ k} \tag{6.2}$$

Distributing the base shear to the roof's mass center yields

$$F_2 = \frac{W_2\,h_2\,V}{\sum W_i\,h_i} = \frac{392.2 \times 27 \times V}{392.2 \times 27 + 834.3 \times 15} = 103.1 \text{ k} \tag{6.3}$$

Distributing the base shear to the floor's mass center yields

$$F_1 = \frac{834.3 \times 15 \times V}{392.2 \times 27 + 834.3 \times 15} = 121.9 \text{ k} \tag{6.4}$$

These forces at the mass center are distributed to the individual walls by statics. The forces on the shear wall closest to the mass center are shown in Figure 148. The load at the roof is 56.7 k and the load at the second floor is 67.0 k. The shear and moment on the second and first floor walls is $V = 56.7$ k, $M = 8{,}165$ in-k and $V = 123.7$ k, $M = 30{,}431$ in-k, respectively. Thus the moment to shear ratio is $M/V = 144''$ for the

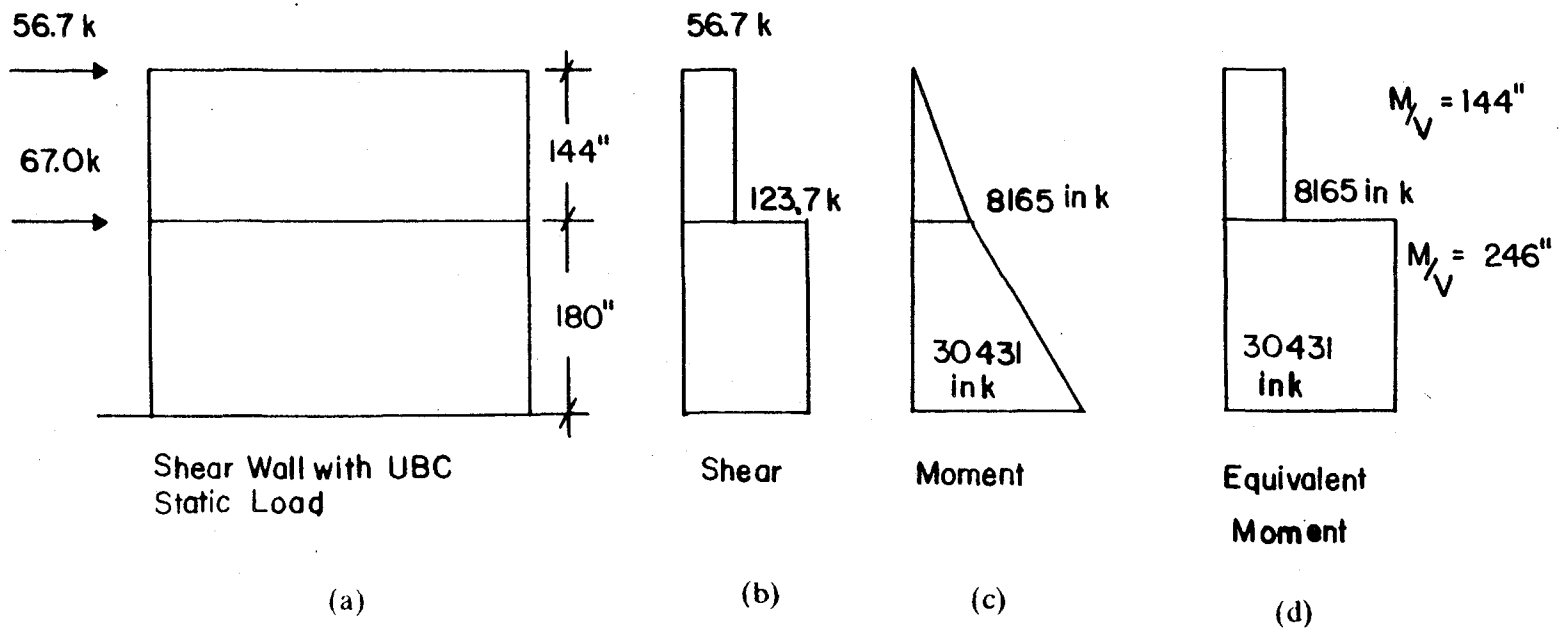

Figure 148. UBC Static Shear Wall Loading: (a) Shear Wall with UBC Static Load, (b) Shear, (c) Moment, (d) Equivalent Moment

second floor shear wall, and M/V = 246" for the first floor shear wall. Both the moment diagram from statics and the equivalent moment diagram used in the analysis are shown in Figure 148.

The backbone curves for the first and second floor walls are determined by the method presented in Chapter III, using the moment to shear ratios determined above. The bending and shear backbone curves are shown in Figures 149 and 150, respectively. Yield occurs in the second and first floor walls at shears of 364 k and 231 k, respectively. Failure occurs in the second and first floor walls at shears of 509 k and 315 k, respectively. Using the distribution of shears between the second and first floor walls in Figure 148, the first floor wall will fail at a shear of 315 k, while the second floor wall has a shear of 144 k. Thus the second floor wall never yields. The backbone curves have been modified to provide a failure ductility of 10, as discussed in Chapter III.

The shear bending influence angles, ψ, Equation 3.21, for these low-rise shear walls are $\psi_2 = 33.6°$ and $\psi_1 = 21.5°$ for the second and first floor, respectively. The relatively low shear bending influence angle for the first floor wall indicates that bending will be the predominant component of deformation.

The JCS for each of the joints used to define the symmetric building coincide with the GCS. The symmetric building is modeled with 8 shear wall elements as shown in Figure 151. Both the second floor and the roof are considered to be rigid diaphragms. Thus the planar constraint, Equation 5.6, is used to transfer the horizontal translational degrees of freedom (F_X, F_Y) and the rotational degrees of freedom (M_Z) to the diaphragm's mass center. Vertical translational degrees of freedom exist at the intersection of each wall's edge and the floor or roof slab. The model has a total of 22, non-restrained, global degrees of freedom as shown in Figure 151. Vertical degrees of freedom, Gdof 1 through 16, are condensed out, and the remaining four translational

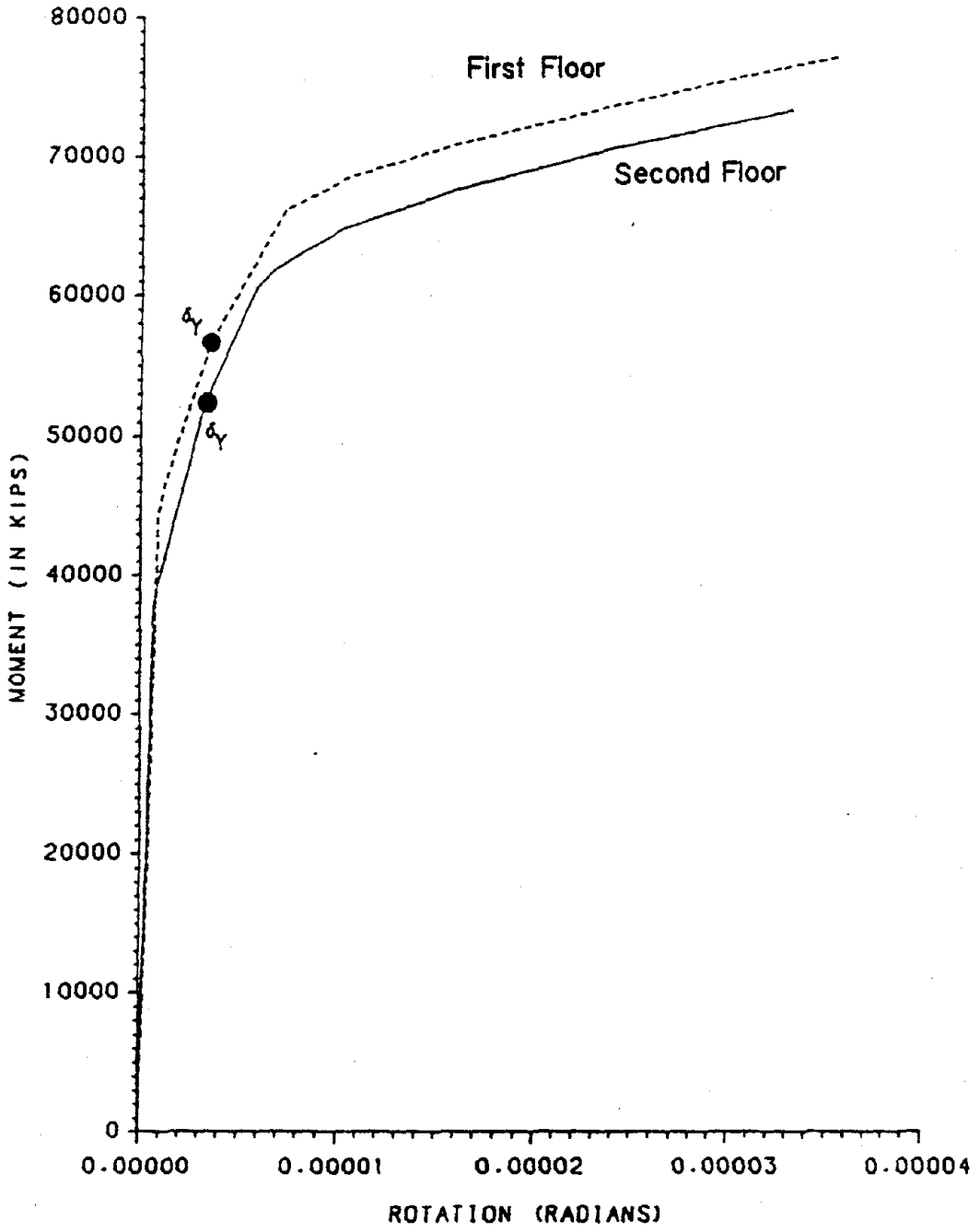

Figure 149. Bending Backbone Curve for the 30 ft Wide Shear Wall

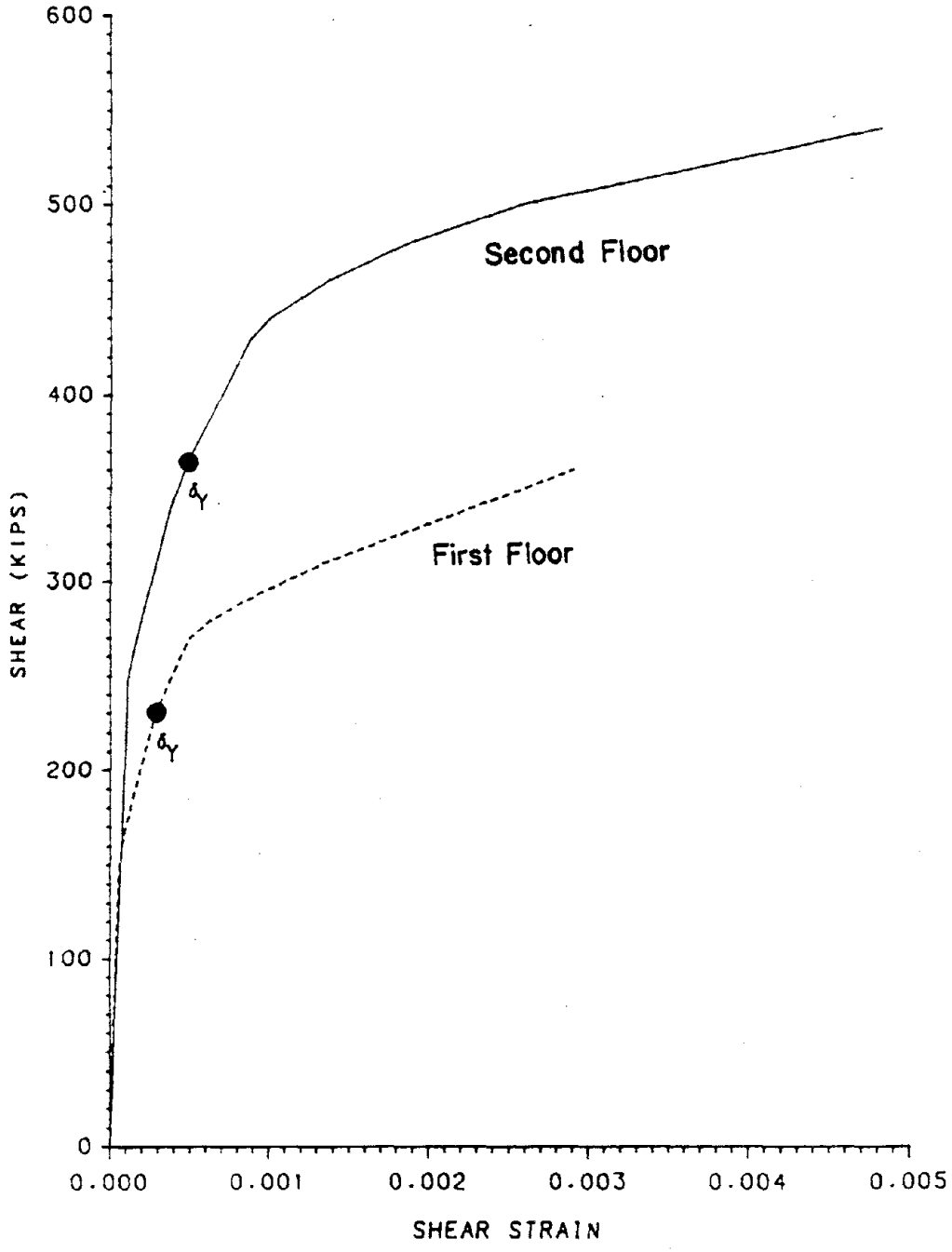

Figure 150. Shear Backbone Curve for the 30 ft Wide Shear Wall

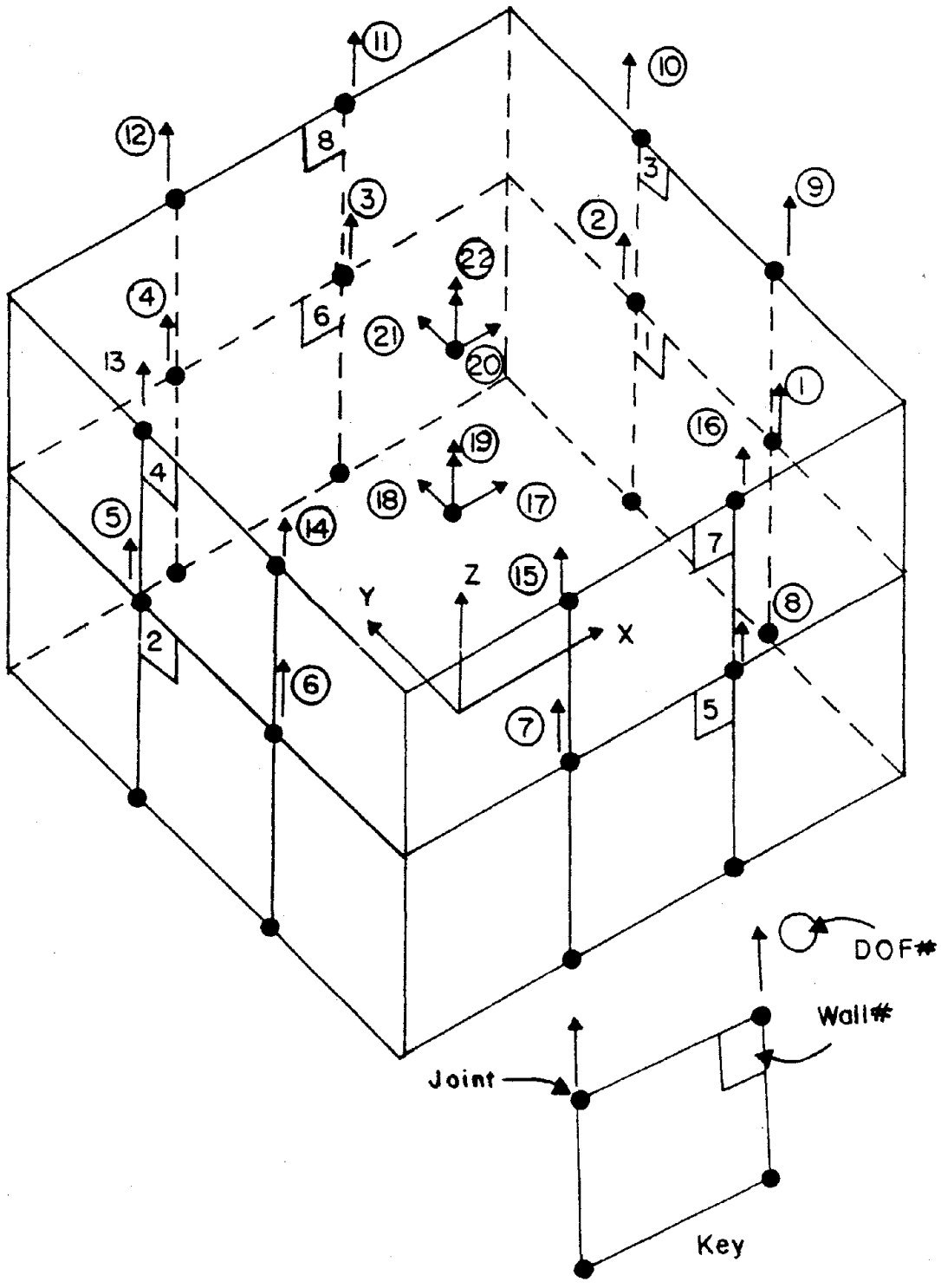

Figure 151. Two Story Symmetric Building Degrees of Freedom

and two rotational degree of freedom, Gdof 17 through 22, are used in the dynamic analysis. The separate vertical load resisting system is not included in the model.

The full dead plus full live load case is used to generate the axial load, N, for the geometric stiffness. Even though the shear walls do not carry all of the vertical loads, they do stabilize the vertical load resisting system. Thus all of the gravity loads in the building are distributed to the shear walls for the purpose of calculating the geometric stiffness.

The elastic natural frequency of a structure is determined by solving the eigenproblem

$$\left|[K - G] - \omega^2[M]\right| = 0 \tag{6.5}$$

where K is the initial stiffness, G is the geometric stiffness, ω is the frequency, and M is the mass matrix. The fundamental period of the symmetric building is 0.155 seconds. Thus the assumption used to calculate the UBC static forces, that the period is less than 0.30 seconds, is valid.

A static load, based on the UBC design base shear shown in Equations 6.1 to 6.4, is applied monotonically to the mass center of the second floor and roof parallel to the building's global Y axis. This load is increased until failure. The displacements of the mass center at the second floor and roof are shown in Figure 152.

The structure has a gradual yielding behavior. Wall #2, the first floor wall next to the mass center yields first at a base shear of 460 k, with the displacement of the roof and second floor at 0.253" and 0.156", respectively. The yield drift ratios of the second and first floor are $\frac{1}{1500}$ and $\frac{1}{1150}$, respectively.

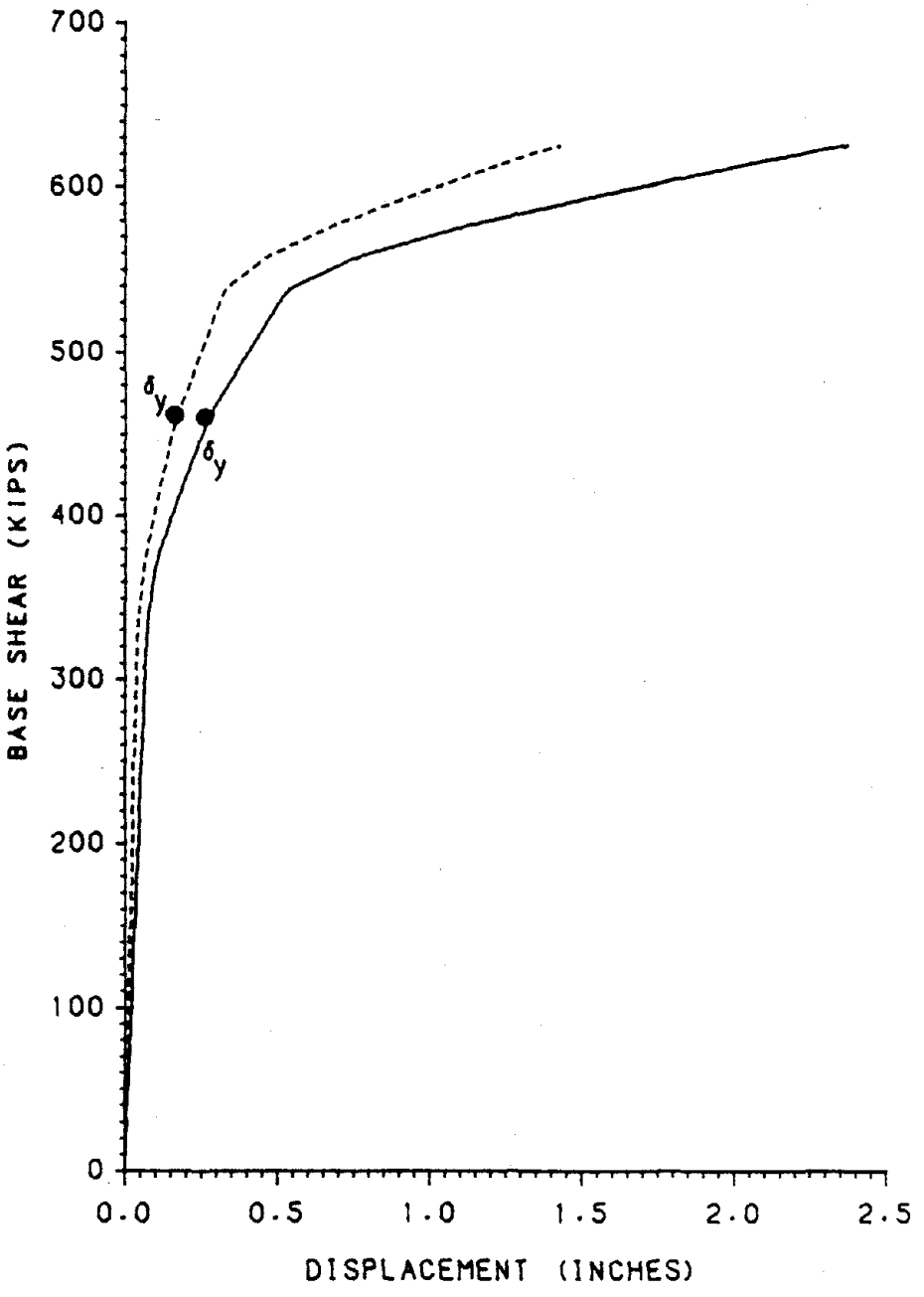

Figure 152. Monotonic Static Response of the Symmetric Building

Failure occurs at a base shear of 627 k or 2.79 times the UBC static base shear. The displacement of the roof and second floor at the ultimate load are 2.37" and 1.43", respectively. The failure drift ratios of the second and first floor are $\frac{1}{153}$ and $\frac{1}{125}$, respectively.

2. Unsymmetric Building. The unsymmetric building used in this study is shown in Figure 153. This 'L' shaped, two-story building has four 30' wide shear walls. All of the lateral loads are resisted by the shear walls. Some of the gravity loads in the building are carried by a separate vertical load resisting system, with the shear walls carrying the remainder of the gravity loads. The unsymmetric building's gravity loads are summarized in Table XIII.

Table XIII. GRAVITY LOADINGS OF THE UNSYMMETRIC BUILDING

Dead load				
Roof	Structure	15 psf x 4500 sq ft	67.5 k	
	HVAC	10 k + 5 psf x 4500 sq ft	32.5 k	
	Brick Curtain Wall	40 psf x 9' x 360'	129.5 k	
	Shear Wall	120 psf x 6' x 120'	86.4 k	
Total Roof Dead Load				315.9 k
Second Floor	Structure	50 psf x 4500 sq ft	225.0 k	
	HVAC	5 psf x 4500 sq ft	22.5 k	
	Partition	20 psf x 4500 sq ft	90.0 k	
	Brick Curtain Wall	40 psf x 13.5' x 360'	194.4 k	
	Shear Wall	120 psf x 13.5' x 120'	194.4 k	
Total Second Floor Dead Load				726.3 k
Total Building Dead Load				1042.2 k
Live load				
Roof	Snow	25 psf x 4500 sqft	112.5 k	
Second Floor	Occupancy	50 psf x 4500 sq ft	225.0 k	
Total Building Live Load				337.5 k

Area / Floor = 5 (30' x 30') = 4500 sq ft

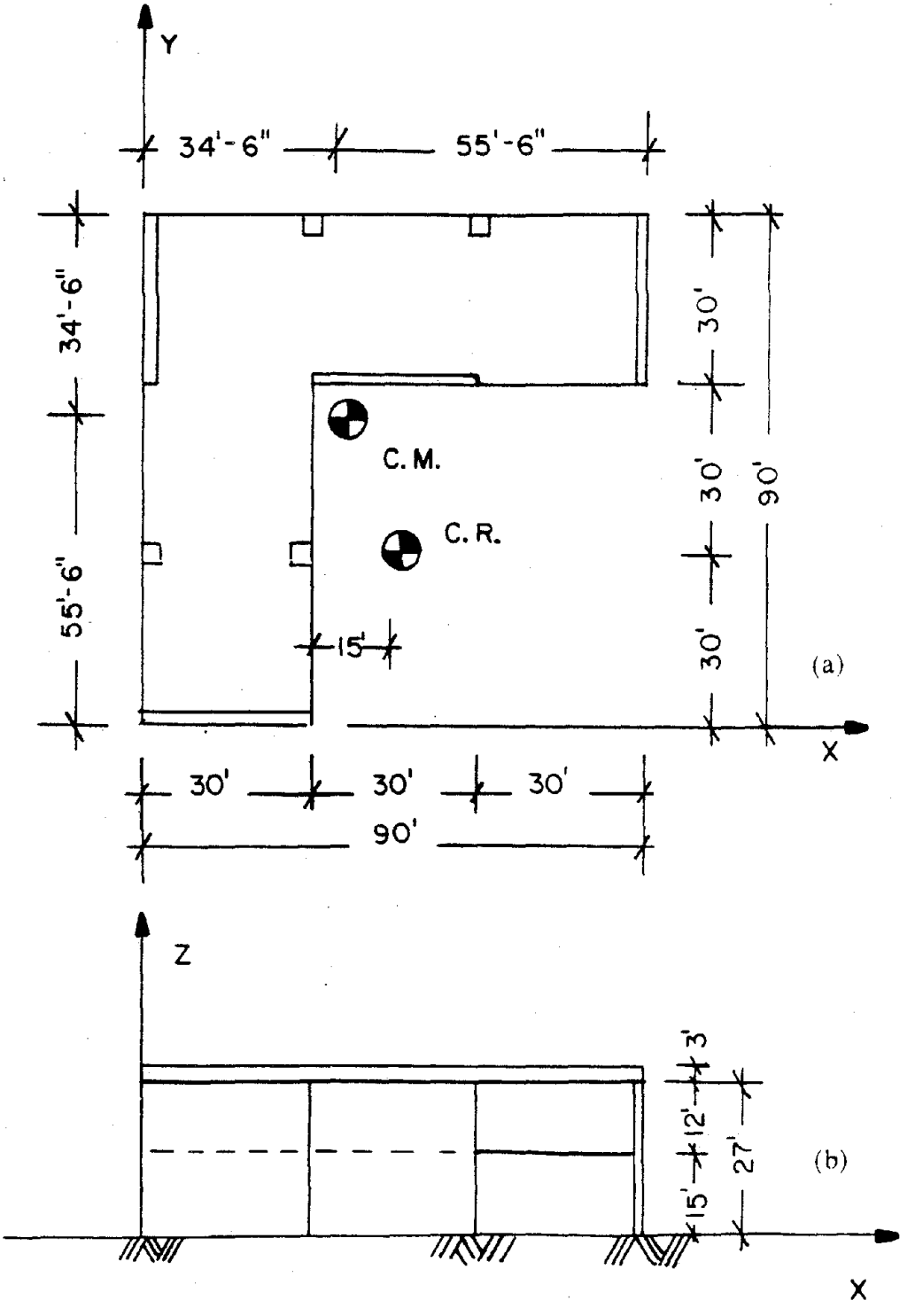

Figure 153. Two Story Unsymmetric building: (a) Plan, (b) Elevation

The mass center and the center of rigidity for an unsymmetric building do not coincide as shown in Figure 153. The largest eccentricity is parallel to the global Y axis and is about 28% of the buildings width. The eccentricity parallel to the global X axis is about 12% of the buildings width.

Similar to the symmetric building, the moment to shear ratio in the walls is determined by applying the UBC static seismic forces[20] to the building and examining the bending moment and shear forces in the shear wall. This procedure yields moment to shear ratios of M/V = 144 for the second floor shear wall, and M/V = 243 for the first floor shear wall. These values are very close to the moment to shear ratios determined for the symmetric building. Thus for the same 30′ walls shown in Figure 147, the backbone curves in Figures 149 and 150 are used in both the symmetric and unsymmetric buildings.

The model used for the unsymmetric building is similar to the symmetric building's model. The unsymmetric building also has 8 shear wall elements, 16 vertical degrees of freedom, 2 translational degrees of freedom at each level and one rotational degree of freedom at each level as shown in Figure 154. All 16 of the vertical degrees of freedom are condensed out, leaving the 2 translational and one rotational degrees of freedom at each level, Gdof 17 through 22, for the dynamic analysis. The separate vertical load resisting system is not included in the model. The geometric stiffness of the unsymmetric building also reflects all of the gravity loads on the structure. The fundamental period of the unsymmetric building is 0.188 seconds.

---

[20] Section 2312(d) 8, Item B (iii), UBC (77) allows the static lateral force procedure to be used for irregular structures less than 5 stories or 65′ tall.

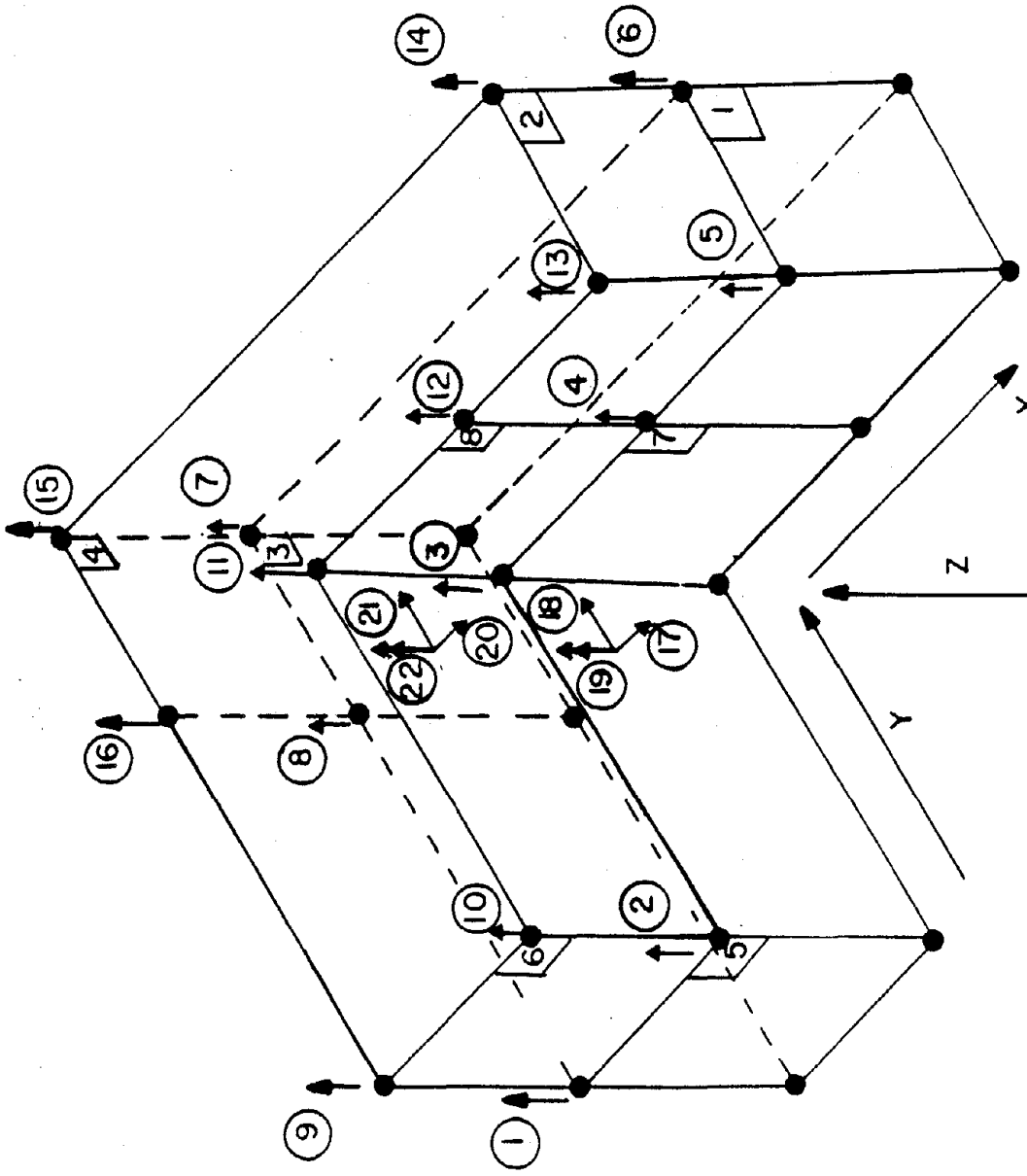

Figure 154. Two Story Unsymmetric Building Degrees of Freedom

A static load, based on the UBC base shear, is applied monotonically to the mass center of the second floor and roof in the buildings X axis, and this load is increased until failure. The displacements of the mass center at the second floor and roof are shown in Figure 155.

Wall #7, the first floor wall next to the mass center, yields at a base shear of 428 k, with the displacement at the roof and second floor mass center of 0.262″ and 0.156″, respectively. The yield drift ratios of the second and first floors are $\frac{1}{1360}$ and $\frac{1}{1160}$, respectively.

Failure occurs at a base shear of 586 k or 3.13 times the UBC static base shear. The displacements of the roof and second floor at the ultimate load are 2.37″ and 1.39″, respectively. The failure drift ratios of the second and first floors are $\frac{1}{147}$ and $\frac{1}{129}$, respectively. Similar to the symmetric building, the second floor shear walls do not yield.

B. DYNAMIC RESPONSE OF SYMMETRIC AND UNSYMMETRIC BUILDINGS

Elastic and nonlinear analyses of both buildings subjected to a series of seven different ground motions, at three different load levels are performed. The seven different ground motions used in this study are given in Table XIV. The first 10 seconds of the 1940 El Centro ground motion and the first 15 seconds of the 1952 Taft ground motion are used. The ground accelerations at the Secretaria de Comunicaciones y Transportes were used as the basis for the Mexico ground motion. This ground motion was recorded during the September 19, 1985 earthquake, and is 180 seconds long. A 10 second strong motion segment of this earthquake is used in this study, which corresponds approximately to the 55 to 65 second range of the original ground motion. The Mexico ground motion is included to study the behavior

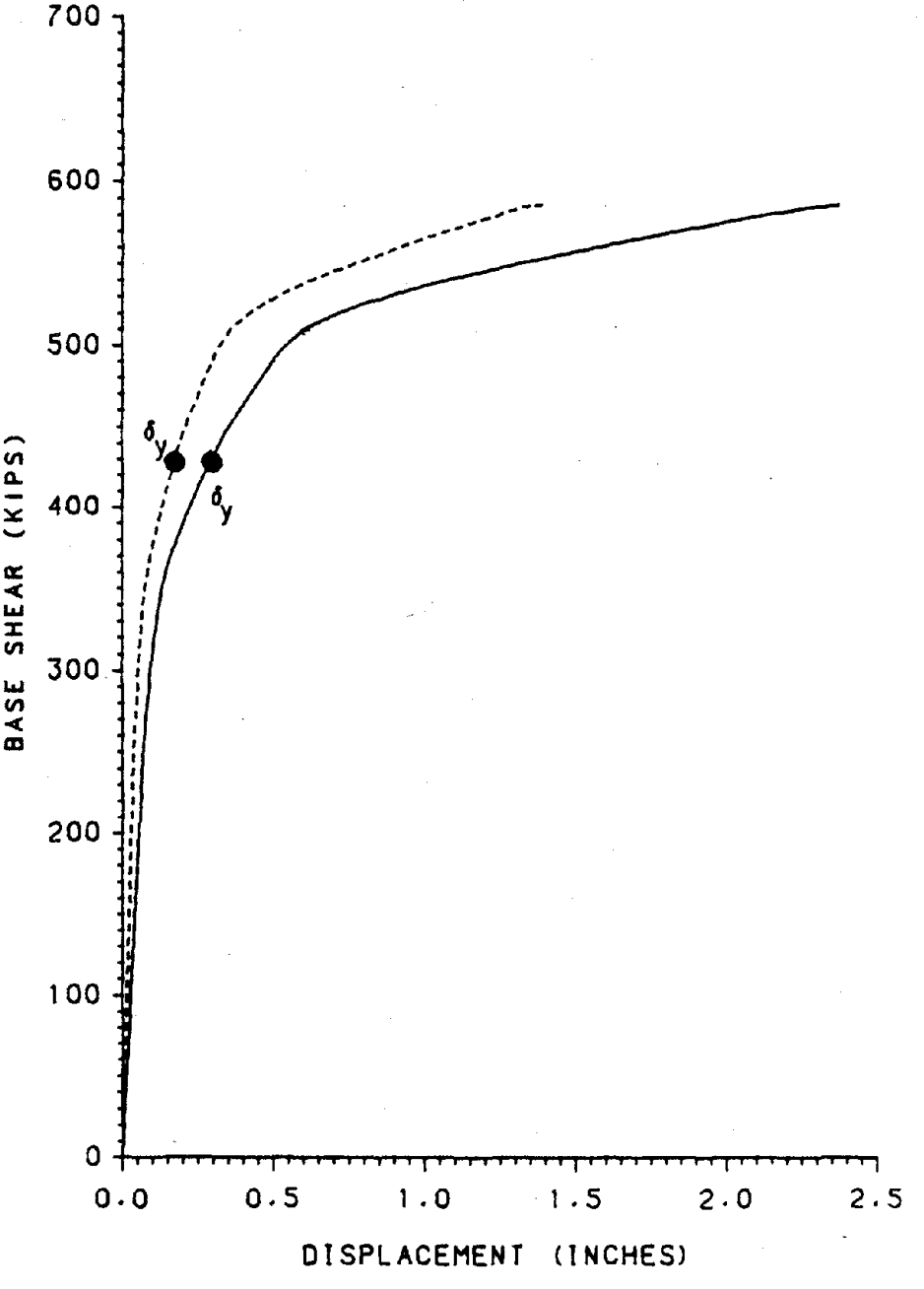

Figure 155. Monotonic Static Response of the Unsymmetric Building

of shear walls subject to ground motions having longer periods. No attempt is made to correlate the peak displacements resulting from the entire 180 second record, and the 10 second segment.

Table XIV. GROUND ACCELERATION RECORDS

Case	Ground Motion	Symmetric Building Global Axis	Unsymmetric Building Global Axis
A	1940 El Centro NS	Y	X
B	1940 El Centro NS	Y	X
	1940 El Centro EW	X	Y
C	1940 El Centro NS, rotated 26°	Y	X
	1940 El Centro EW, rotated 26°	X	Y
D	1952 Taft N69W	Y	X
E	1952 Taft N69W	Y	X
	1952 Taft S21W	X	Y
F	1985 Mexico S00E	Y	X
G	1985 Mexico S00E	Y	X
	1985 Mexico N90W	X	Y

Penzien, et al (68) and later Cheng, et al (17) have recognized that a 3-D building's response to a multicomponent ground motion may not be a maximum if the ground motions are applied to the buildings principal axes. Thus the two-component El Centro ground motion is rotated 26° with respect to the buildings principal axes in an attempt to determine the maximum response.

Also shown in Table XIV is the building global axis corresponding to each particular earthquake component. The symmetric building typically has the stronger of the two-components applied parallel to its global Y axis, while the unsymmetric

building typically has the stronger of the two-components applied parallel to its global X axis.

The three different loading levels are accomplished by scaling the amplitude of each ground motion. The peak ground accelerations for these three loading levels are given in Table XV, along with the actual peak ground acceleration for the earthquake.

Table XV. PEAK GROUND ACCELERATION FOR VARIOUS LOADING LEVELS

Load	El Centro		Taft		Mexico	
Level	NS	EW	N69W	S21W	S00E	N90W
1	0.3143g	0.1614g	0.3114g	0.3114g	0.3425g	0.1943g
2	0.4715g	0.2421g	0.4449g	0.4449g	0.4281g	0.2429g
3	0.5500g	0.2824g	0.5335g	0.5335g	0.4709g	0.2671g
*	0.3143g	0.1614g	0.1778g	0.1778g	0.1712g	0.0972g

* Unfactored ground accelerations

The initial stiffness of the building is used for the elastic analysis. Each building is analyzed once for each of the seven different ground motions at load level 3. The response at load levels 2 and 1 is obtained by scaling the response at load level 3. For the elastic case, damping is neglected.

For the nonlinear analysis, each building is analyzed once for each of the seven different ground motions, at each of the three different load levels. Thus a total of 21 nonlinear analyses per building were performed. A mass and stiffness proportional damping of 5% critical is used for both structures.

The time step used to solve the equation of motion varied from 0.005 seconds for an elastic analysis to 0.00025 seconds for a nonlinear analysis. The energy balance is used to verify the accuracy of the solution. The gross relative error varied from 3.5% (unsymmetric building, ground acceleration D, load level 1) to 0.28% (symmetric building, ground acceleration A, load level 3) for the nonlinear analysis. The maximum gross relative error is less than 0.25% for all of the elastic analysis.

1. Displacements, Energies, Member Forces and Deformations of the Unsymmetric Building Subject to Two-Component Seismic Input. The nonlinear response of the unsymmetric building subjected to the two-component El Centro ground motion (B) with a peak ground acceleration of 0.5500 g (load level 3) is discussed in this section. The displacement of the unsymmetric building's roof mass center in the X direction is given in Figure 156. The displacements are larger in the positive X direction than in the negative X direction. Between 6 seconds and 9 seconds the displacements have a permanent set in the positive X direction. This permanent set is typical of nonlinear behavior. The peak displacement in the building's X direction is 1.56" versus 0.963" in the Y direction.

The base shear for this building is given in Figure 157. Recall that the ultimate base shear for the unsymmetric building is 586 k. The peak base shear for this loading is -507 k, or about 87% of the buildings ultimate load capacity.

The energy balance used to verify the accuracy of the nonlinear dynamic solution is given in Figure 158. The input energy is approximately equal to the total energy throughout the time history. The gross relative error of this solution is 0.62%, indicating that the solution is acceptable.

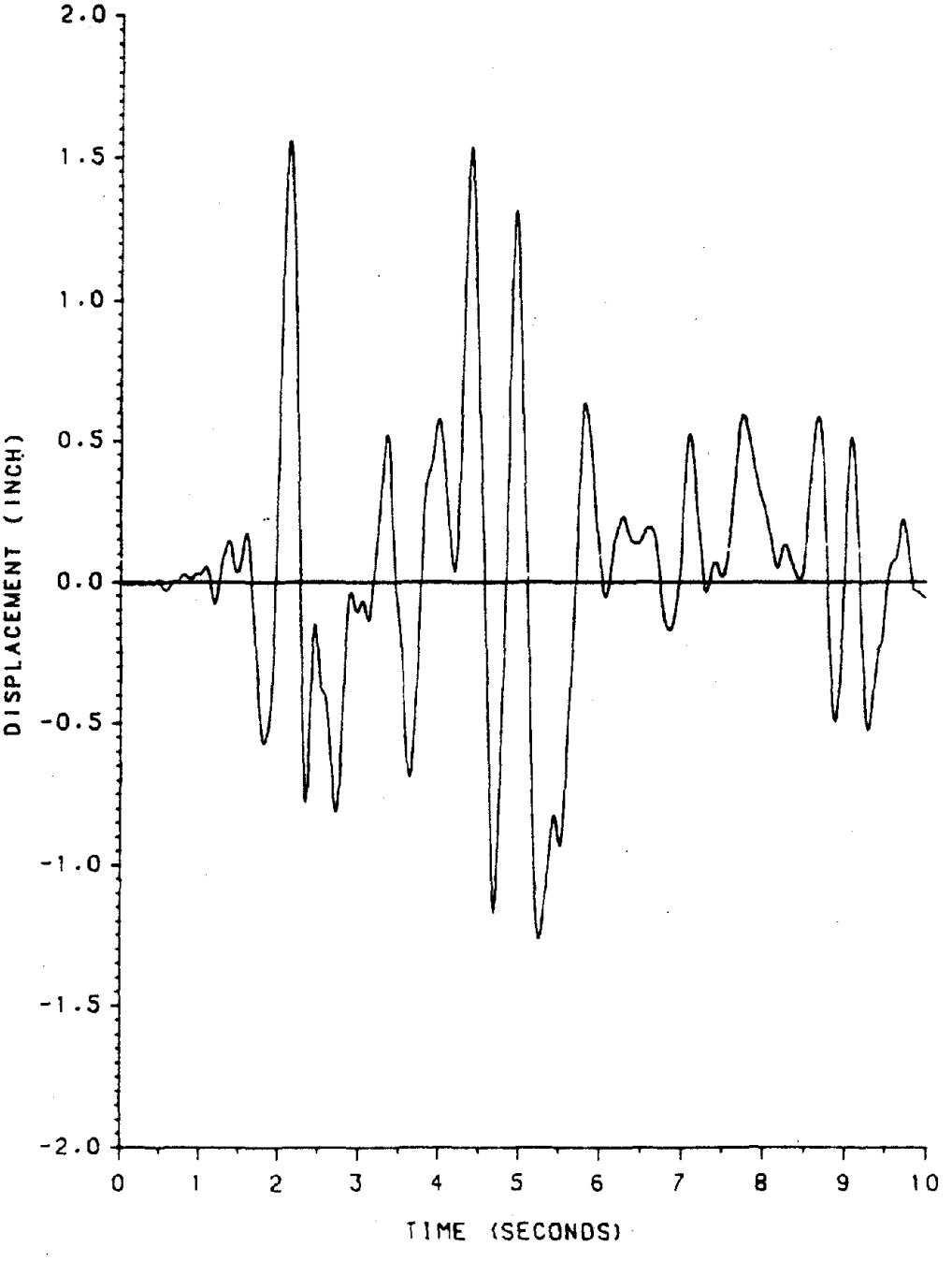

Figure 156. Roof Displacement of the Unsymmetric Building at the Mass Center (Ground Motion:B, Load Level:3)

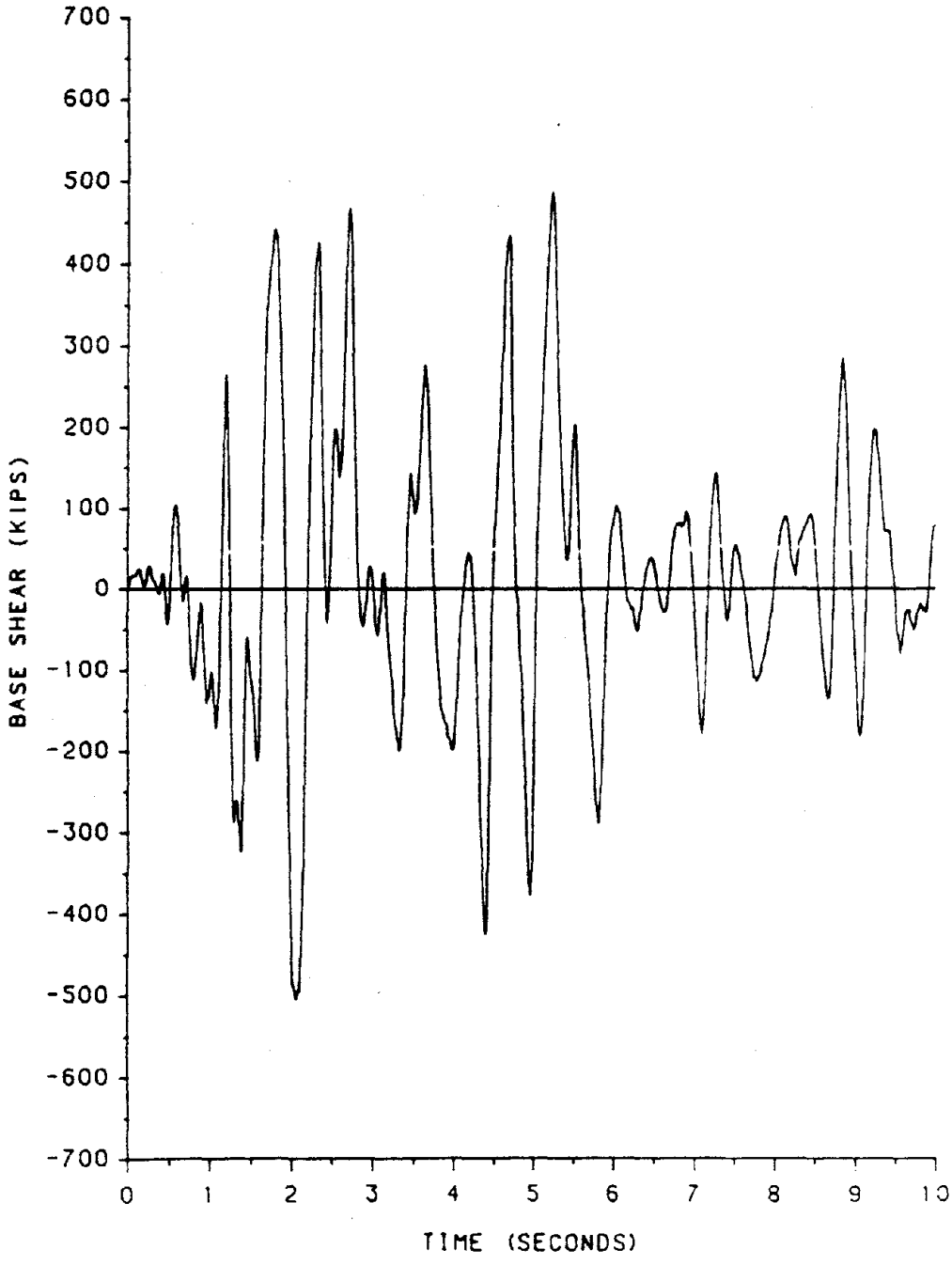

Figure 157. Base Shear of the Unsymmetric Building (Ground Motion:B, Load Level:3)

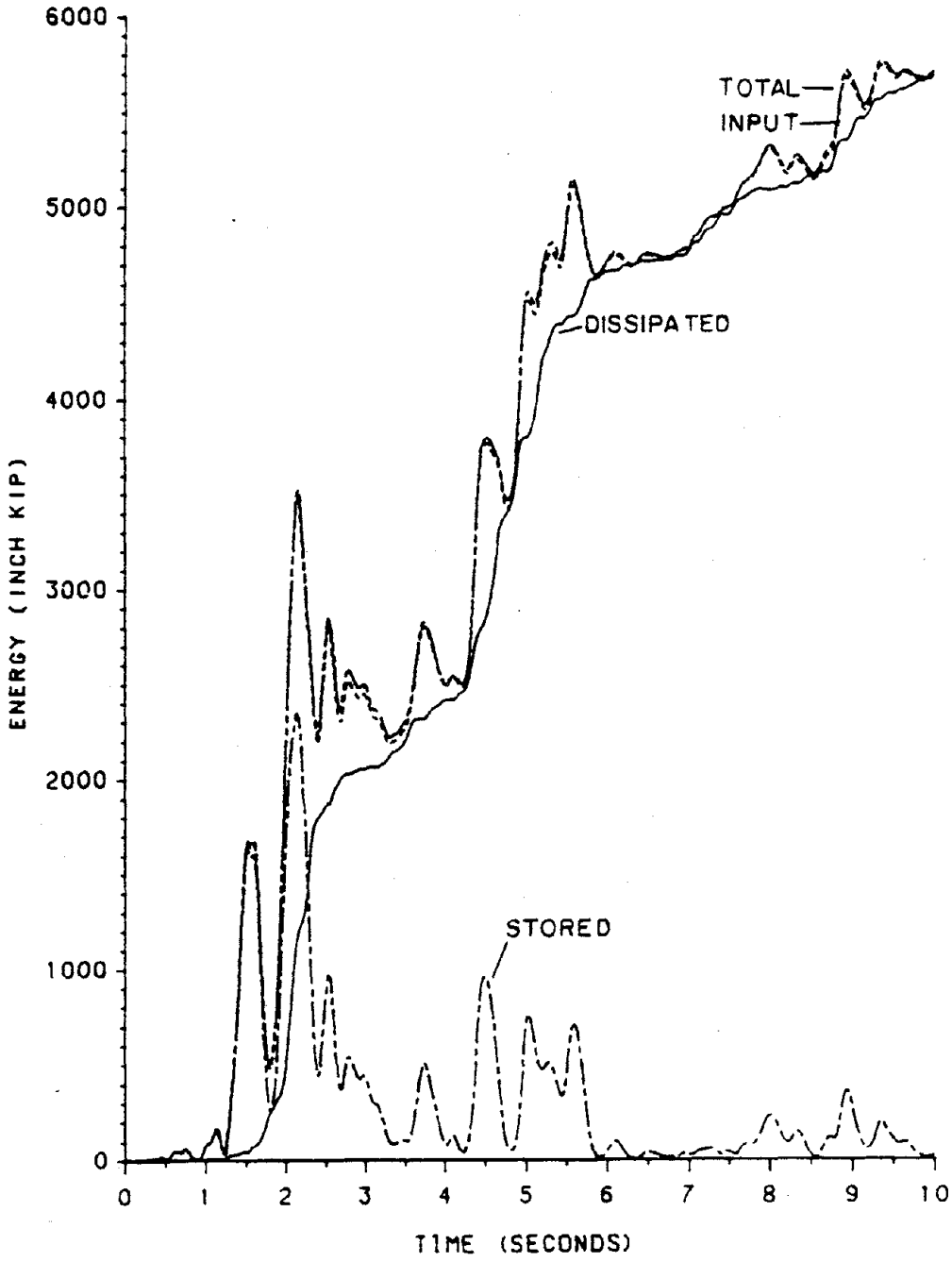

Figure 158. Energy Balance of the Unsymmetric Building (Ground Motion:B, Load Level:3)

Typical bending and shear hysteresis loops are given in Figures 159 and 160 for wall #7. Wall #7 is the first floor wall, next to the mass center, as shown in Figure 154. This wall suffered the most damage during the ground motion, while the walls on the second floor remained elastic. The bending and shear hysteresis loops for wall #7 have several large amplitude hysteresis loops and many small amplitude hysteresis loops. Thus the small amplitude hysteresis loops in the bending and shear hysteresis models are important.

The peak bending displacement for wall #7 is 0.835", while the peak shear displacement is 0.099". Thus at the peak displacement, bending deformation accounted for about 90% of the total deformation.

The bending displacement ductility for wall #7 is 7.24, and the shear displacement ductility is 1.90. Bending and shear excursion ratios are 48.8 and 5.7, respectively. Both the bending and shear ductility ratios are below the failure limit of 10.

The strain energy for wall #7 is shown in Figure 161. Note that the bending energy is about 15 times larger than the shear energy, which indicates that the energy absorption of this wall is predominated by bending. This is influenced by two factors: 1) the bending deformation of the wall is much larger than the shear deformation, and 2) pinching causes the shear hysteresis model to dissipate less energy than the bending hysteresis model.

The bending moment and shear are plotted against each other in Figure 162. Recall that an assumed moment to shear ratio of $M/V = 246$ is used to establish the bending and shear backbone curves. Comparing the assumed and actual moment to shear ratio demonstrates that 1) the assumption that the moment to shear ratio would remain fairly constant throughout the loading history is justified, 2) the assumed

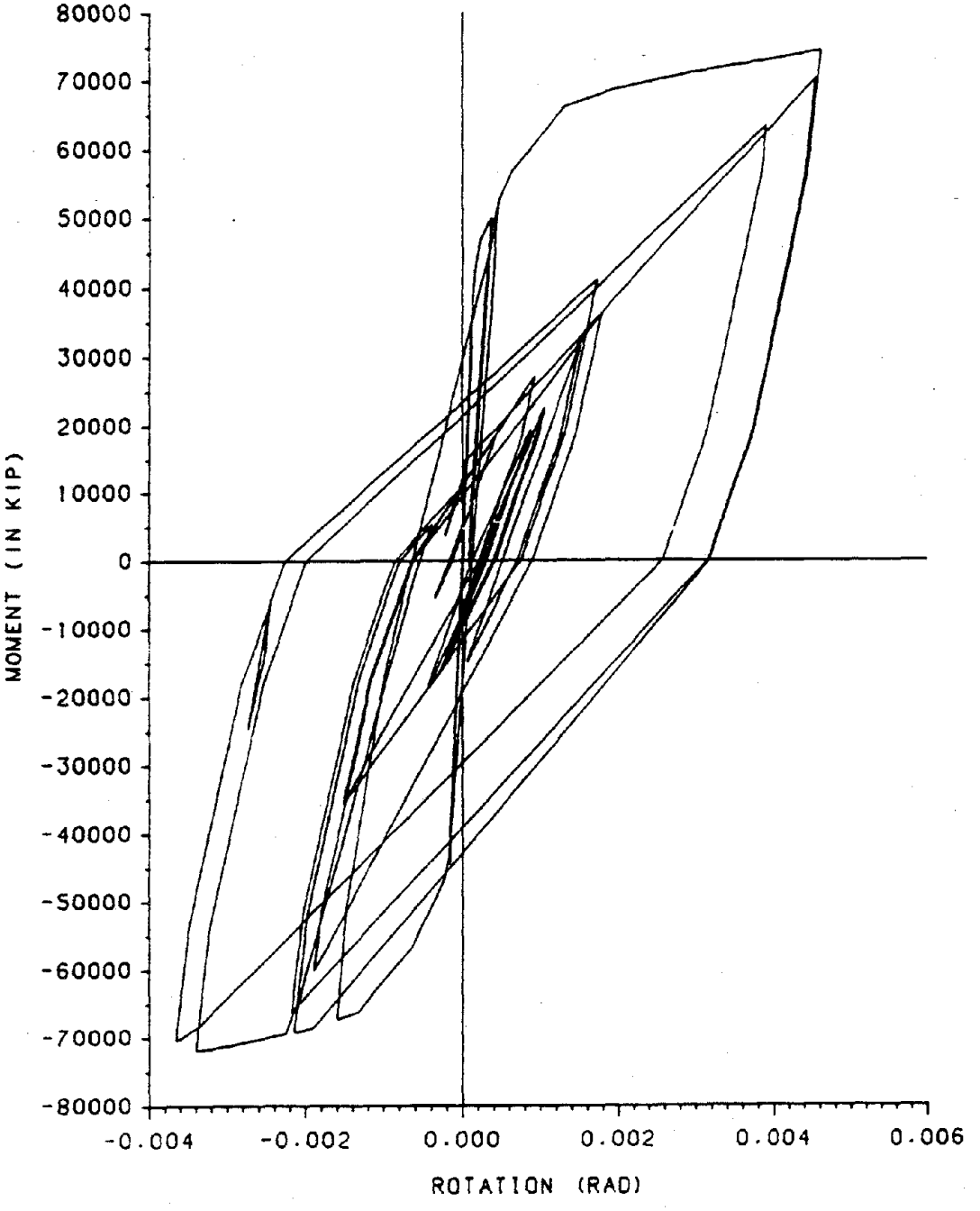

Figure 159. Bending Hysteresis Loops for Wall #7 of the Unsymmetric Building (Ground Motion:B, Load Level:3)

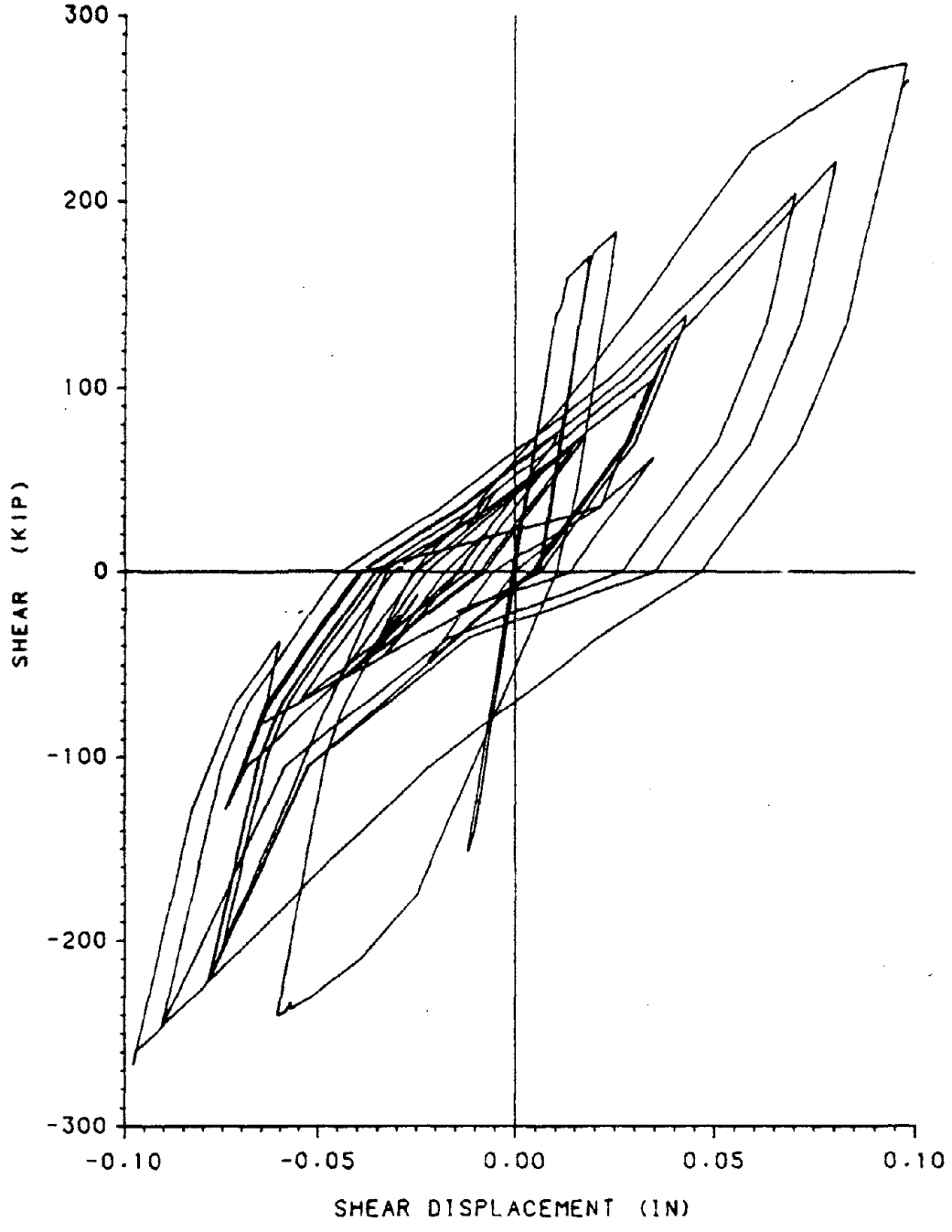

Figure 160. Shear Hysteresis Loops for Wall #7 of the Unsymmetric Building (Ground Motion:B, Load Level:3)

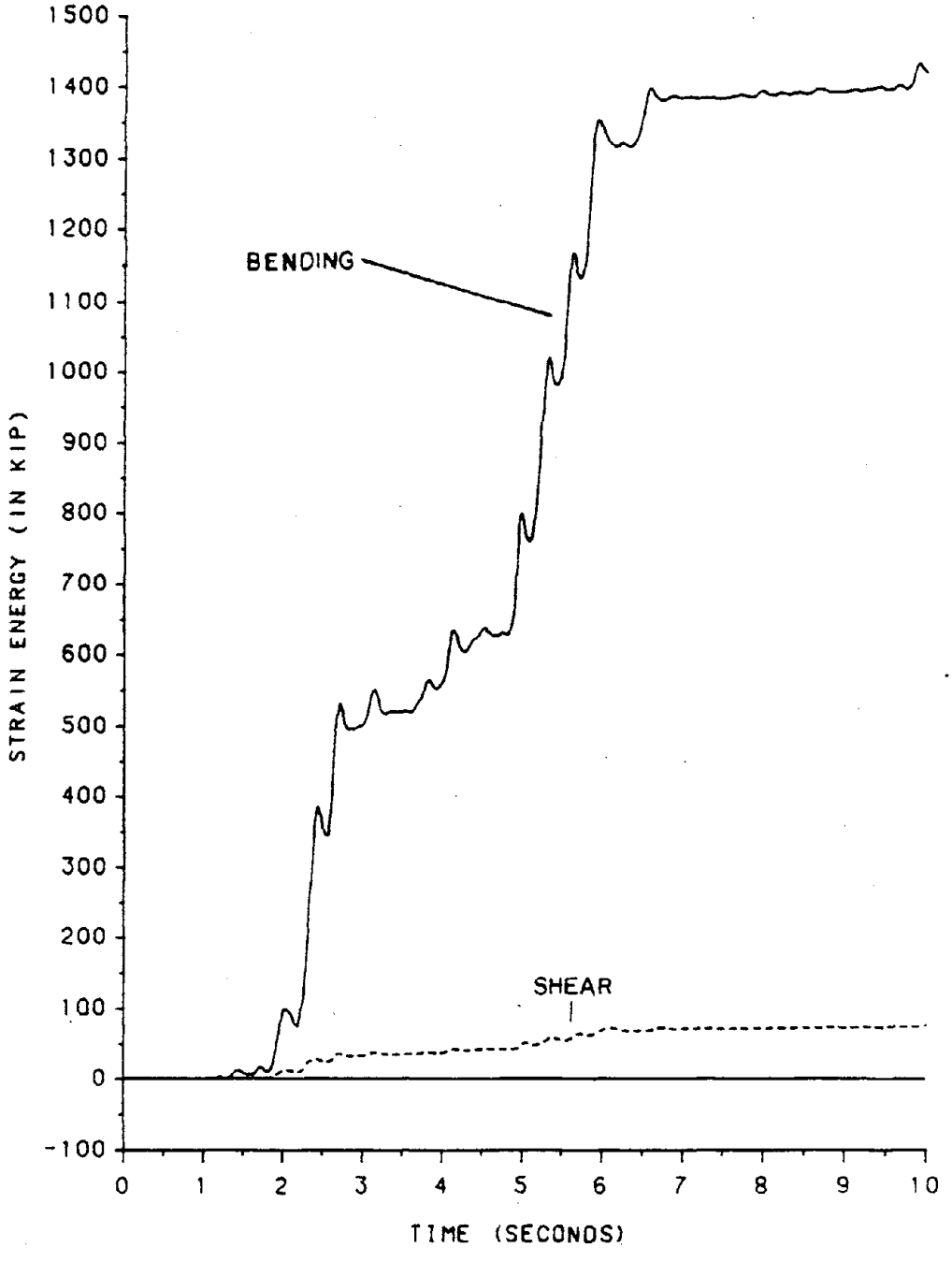

Figure 161. Bending and Shear Strain Energy for Wall #7 of the Unsymmetric Building (Ground Motion:B, Load Level:3)

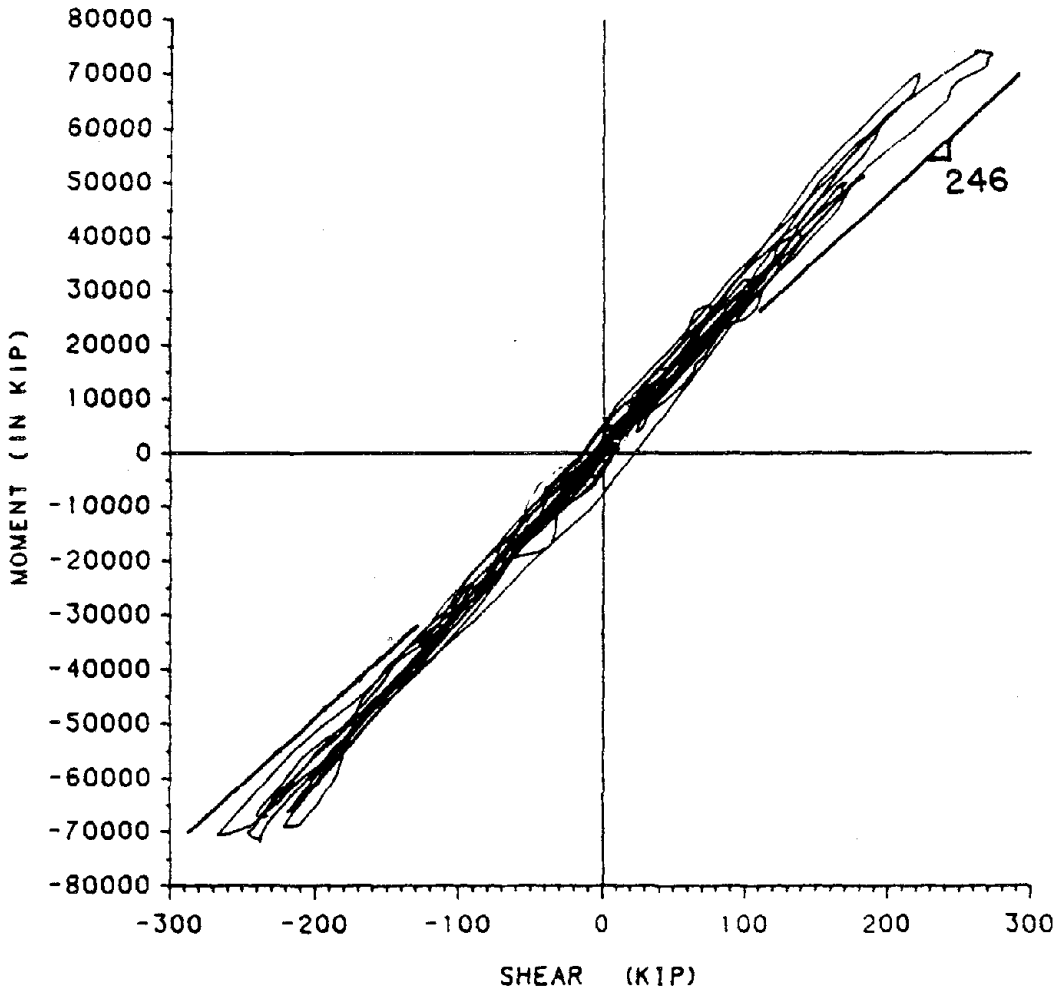

Figure 162. Moment vs. Shear for Wall #7 of the Unsymmetric Building (Ground Motion:B, Load Level:3)

moment to shear ratio of 246 is close to the actual moment to shear ratio, and 3) the method used to estimate the moment to shear ratio is reasonable.

Parallel to the buildings global Y axis, wall #3 also has heavy damage. The bending ductility and excursion ratios are 7.2 and 46.5, respectively. The shear ductility and excursion ratios are 1.56 and 1.77, respectively. Wall #3 resists torsional forces and lateral loads in the global Y direction. Wall #7 resists torsional forces and lateral loads in the global X direction. While the forces in the X direction are larger than the forces in the Y direction ($\ddot{\delta}_{gx} > \ddot{\delta}_{gy}$), wall #3 resists more torsion than wall #7, because wall #3 is farther from the center of rigidity. Thus walls #3 and #7 have similar forces. For ground motions with the same magnitude of ground acceleration in both directions, (i.e. Taft) the forces in wall #7 are larger than the forces in wall #3.

The damage index for the bending component of wall #7 is calculated by Equation 5.164

$$DI = \frac{\delta_{max}}{\delta_{ult}} + \frac{\beta}{Fy\,\delta_{ult}} \int_0^t d(PSE)$$

or

$$DI = \frac{2.577 \times 10^{-5}}{3.559 \times 10^{-5}} + \frac{0.20}{(56644)3.559 \times 10^{-5}}(8.1435) = 1.532 \qquad (6.6)$$

where $\delta_{ult} = 3.559 \times 10^{-5}$ rad, and Fy = 56644 in-k are the ultimate rotation and yield moment from the bending backbone curve for a unit height wall, Figure 149. The maximum unit length displacement $\delta_{max} = 2.577 \times 10^{-5}$ rad and unit length dissipated plastic strain energy $\int_0^t d(PSE) = 8.1435$ in-k are determined from the analysis. The damage index and energies for all of the walls are summarized in Table XVI. The damage index for the building is given by Equation 5.165

Table XVI. WALL DAMAGE INDICES OF THE UNSYMMETRIC BUILDING (GROUND MOTION:B, LOAD LEVEL:3)

Wall	DI	PSE	SE	SE DI
Bending Component				
1	0.7627	3.4906	3.4936	2.6646
2	0.0152	0.0000	0.0000	0.0000
3	1.3021	5.8674	5.8833	7.6606
4	0.0159	0.0000	0.0004	0.0000
5	0.8110	3.7702	3.7825	3.0676
6	0.0167	0.0000	0.0003	0.0000
7	1.5323	8.1435	8.1447	12.4801
8	0.0170	0.0000	0.0000	0.0000
Shear Component				
1	0.2379	0.3653	0.3659	0.0870
2	0.0184	0.0000	0.0000	0.0000
3	0.2566	0.3383	0.3399	0.0872
4	0.0191	0.0000	0.0005	0.0000
5	0.2211	0.2955	0.2970	0.0657
6	0.0202	0.0000	0.0004	0.0000
7	0.3314	0.4733	0.4735	0.1569
8	0.0205	0.0000	0.0000	0.0000
Sum			22.7820	26.2697

Note: The damage indices for the axial component of deformation are zero.

$$DI = \frac{\sum SE_i \, DI_i}{\sum SE_i}$$

or

$$DI = \frac{26.2697}{22.7820} = 1.1531 \qquad (6.7)$$

A damage index greater than 1 usually indicates collapse. However, before the building can collapse, both walls parallel to the global X axis must fail. Wall #7 is the most

heavily loaded of these walls. As stated above, there is some concern as to whether wall #7 failed or not. Wall #5 is the other first floor wall parallel to the global X axis. Its ductility and excursion ratios are well below the failure limits. Even if wall #7 does fail, it is unlikely that wall #5 will also fail. Thus it is not likely that the building will collapse. However, at a drift ratio of $\frac{1}{200}$ the building has significant structural and architectural damage.

2. Displacements, Base Shears, Ductilities, Excursion Ratios and Damage Indices of Symmetric and Unsymmetric Buildings Subject to Different Earthquakes.

a. Maximum Base Shears and Mass Center Displacements. While the time history response of a dynamic system is important, often key parameters such as the maximum base shear and displacement are sufficient to describe how a building behaves. For the symmetric building, the base shears and mass center displacements are selected in the building's Y direction. For the unsymmetric building, the base shears and mass center displacements are selected in the building's X direction. The symmetric building is denoted B1, and the unsymmetric building is denoted B2. The base shears and displacements for each given ground motion, denoted A through G (refer to Table XIV) are plotted against the peak ground acceleration (refer to Table XV) in Figures 163 through 166.

For the symmetric building, the one-component ground motion response is approximately equal to the two-component ground motion response. This can be seen by comparing both the displacements and base shear of B1-A with B1-B, B1-D with B1-E, and B1-G with B1-F for both the elastic and nonlinear cases. Vibration about the symmetric building's X and Y axis are essentially uncoupled, due to the small amount of eccentricity between the mass center and the center of rigidity. Thus the addition of a second ground motion on the symmetric building's X axis doesn't

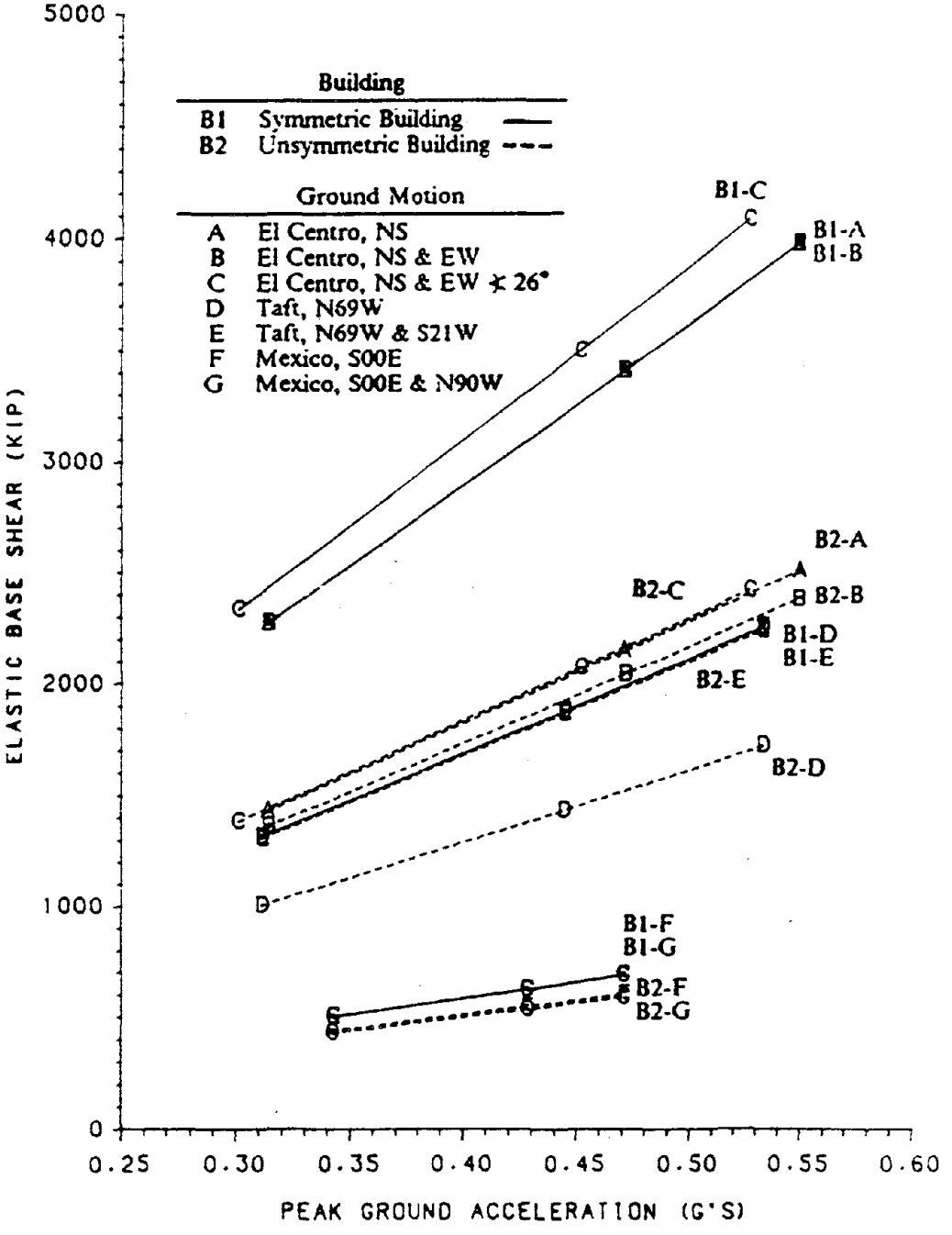

Figure 163. Elastic Base Shear vs. Peak Ground Acceleration

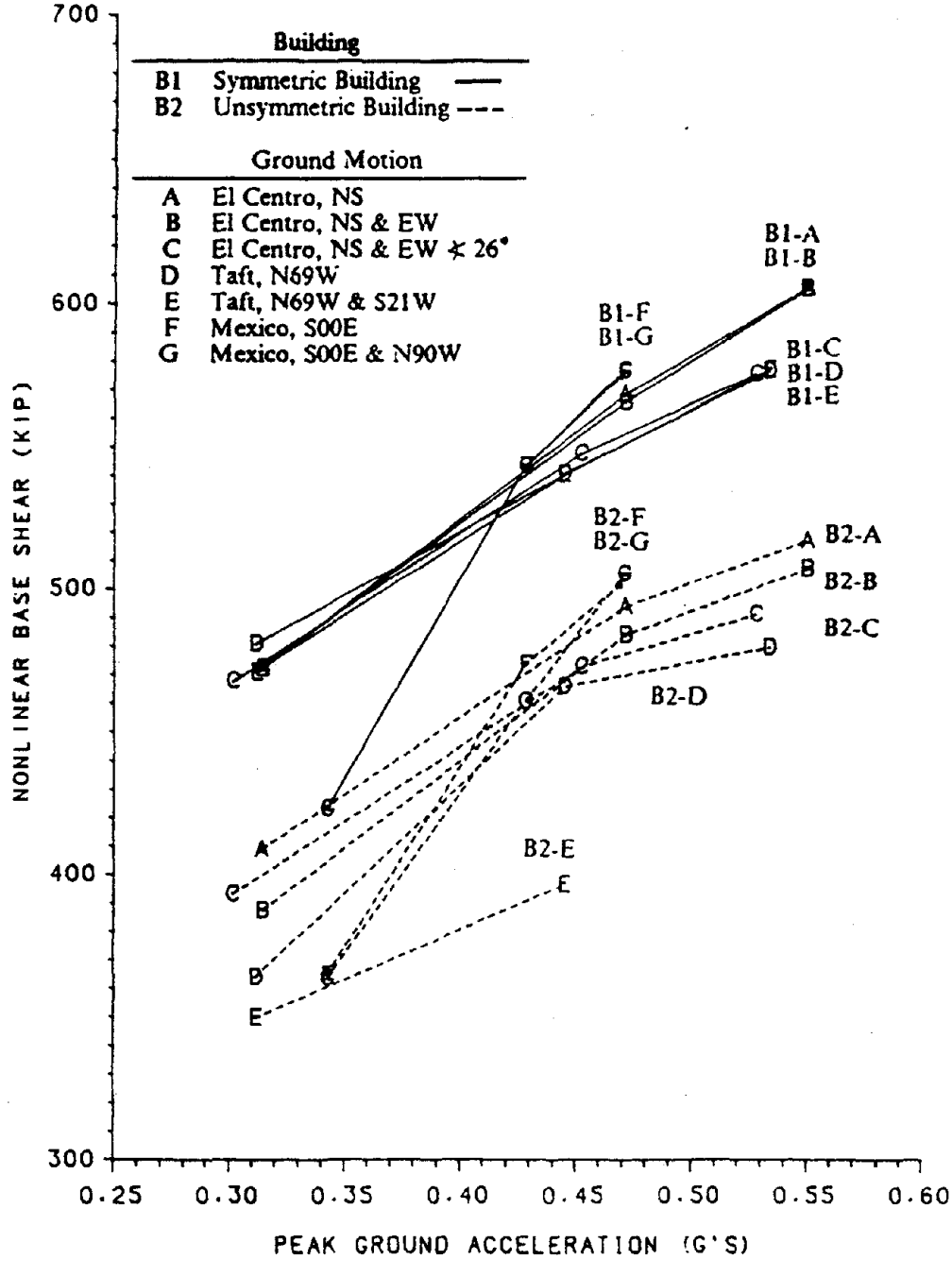

Figure 164. Nonlinear Base Shear vs. Peak Ground Acceleration

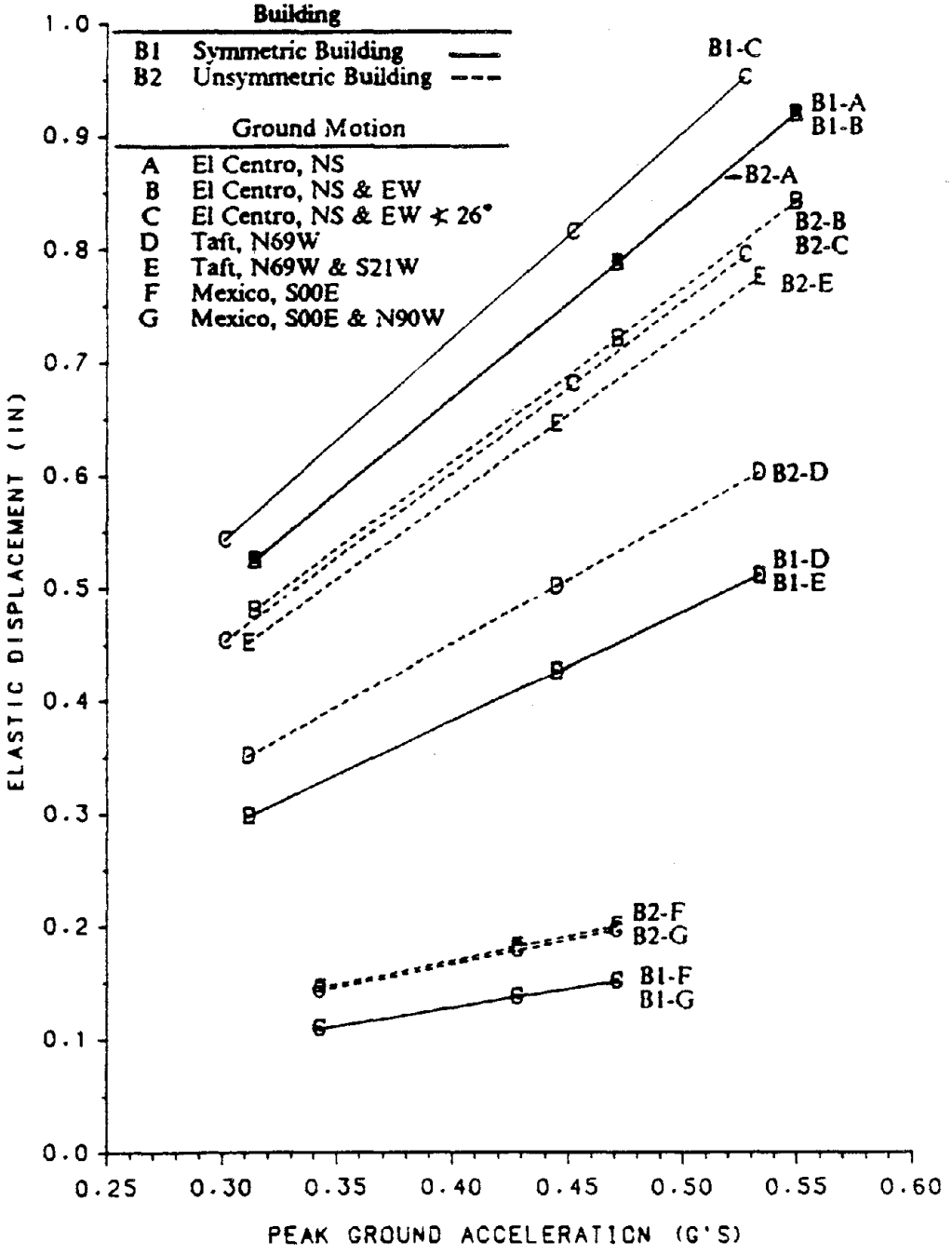

Figure 165. Elastic Mass Center Roof Displacements vs. Peak Ground Acceleration

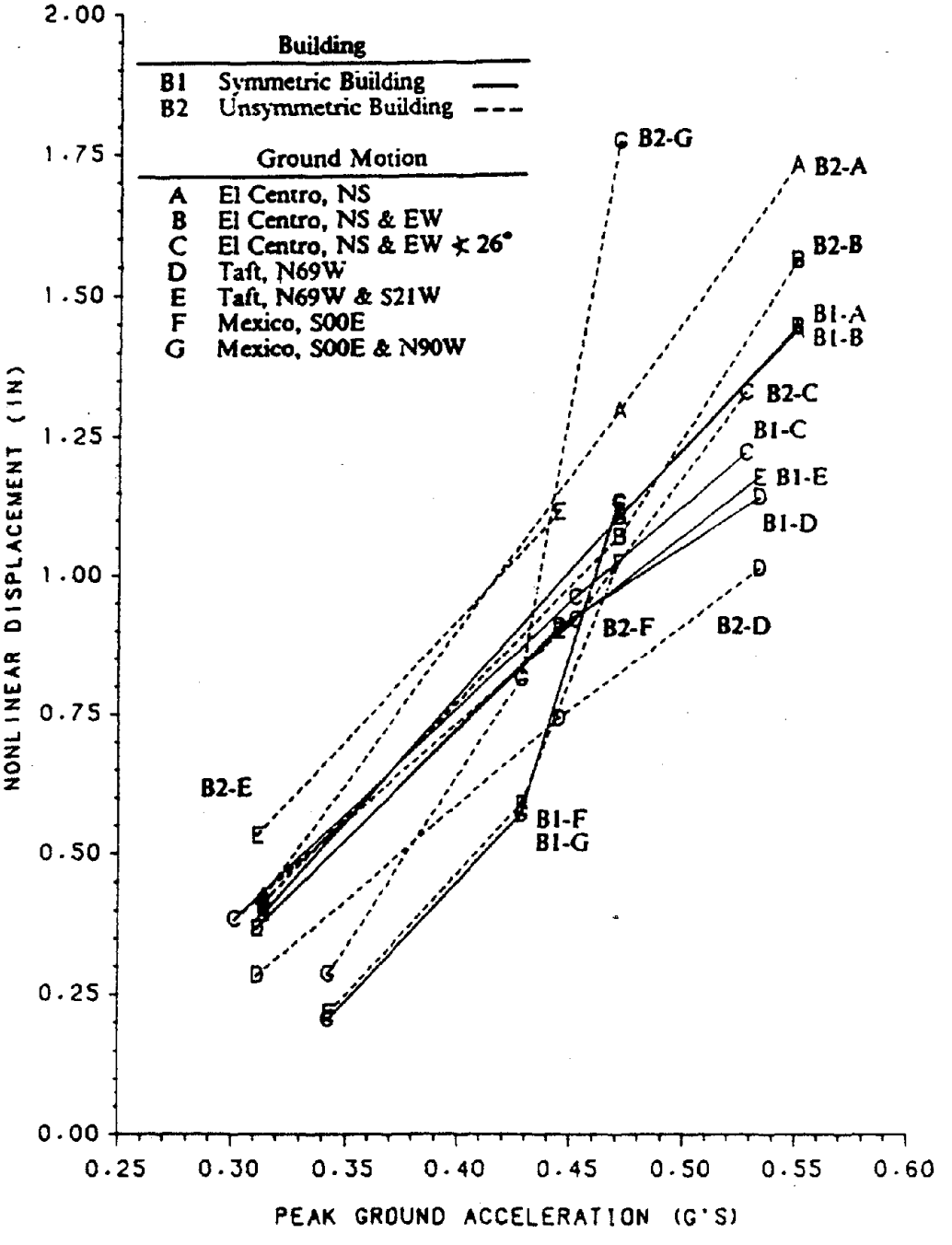

Figure 166. Nonlinear Mass Center Roof Displacements vs. Peak Ground Acceleration

significantly affect the response on the symmetric building's Y axis. The unsymmetric building has a much larger eccentricity between the mass center and the center of rigidity, which causes coupling between the X and Y axis. This coupling is responsible for the difference in response between the one and two component ground motions for the unsymmetric building.

For the Mexico ground motion, the elastic response of the unsymmetric building to a one-component ground motion, B2-F, is slightly larger than the response to a two-component ground motion, B2-G, as shown in Figures 163 and 165. This is because the second component of the Mexico ground motion is applied such that it counteracts the torsion caused by the first component, resulting in a slight decrease in the two-component response compared to the one-component response. If the orientation of the ground motion with respect to the building's axes is varied, then an orientation may be found where the second component of ground motion increases the torsion caused by the first component, and the response to the two-component ground motion will be larger than the response to the one-component ground motion.

Either the one or two component ground motion may yield the maximum response for the unsymmetric building. Whether the one or two component ground motion yields the maximum response depends on how the components of that specific ground motion interact with the building. For the elastic base shear and displacements, the one-component El Centro ground motion, B2-A in Figures 163 and 165, has a larger response than the two-component ground motion B2-B. Contrarily, the two-component Taft ground motion B2-E has a larger response than the one-component Taft B2-D. It is believed that the two-component ground motion provides a more accurate representation of the building's actual response, since one-component ground motions do not occur in nature.

Recall that the two-component El Centro ground motion was rotated 26° to maximize the response. For the elastic analysis of the symmetric building, the response to the rotated ground motion, B1-C, is greater than the responses with the ground motion parallel to the buildings axes, B1-B, as shown in Figures 163 and 165. For the elastic analysis of the unsymmetric building, the rotated response has a larger base shear, B2-C > B2-B as shown in Figure 163, while the rotated response has smaller displacements, B2-C < B2-B as shown in Figure 165. For the nonlinear analysis, the response to the rotated ground motion at loading level 3 is less than the response with the ground motion parallel to the buildings axes, as can be seen by comparing B1-C with B1-B and B2-C with B2-B in Figures 164 and 166. Additional research on the maximum response related to seismic input direction may be found in References 17 and 18.

For these two elastic buildings, the El Centro and Taft earthquakes have a larger response than the Mexico earthquake. Recall that the elastic natural period of the symmetric and unsymmetric building is 0.155 and 0.188 seconds, respectively. The majority of the El Centro and Taft earthquake's energies lie in the range between 0.2 second and 1.0 seconds. The majority of the Mexico earthquake's energy is between 1 second and 3 seconds. Since the building's natural periods are closer to the El Centro and Taft earthquake's, these earthquakes yield a larger response than the Mexico earthquake.

For nonlinear structures the displacement due to the Mexico earthquake is on the same order of magnitude as those due to the El Centro and Taft earthquakes. As a building deforms nonlinearly, the stiffness decreases, causing an increase in the building's period. For the Mexico earthquake the natural period shifts toward the region where the earthquake's energy is the strongest. For the El Centro and Taft earthquakes, the natural period is shifting through and out of the ranges where those

earthquake's energies are strongest. Thus as the loading level is increased, the displacement due to the Mexico ground motion will increase more rapidly than those due to the El Centro or Taft ground motions. This can be seen by comparing the slope of B1-F with B1-A or B1-D in Figure 166.

For nonlinear structures at higher load levels, the base shear for a given building approaches a common value, regardless of the ground motion. This is because once the walls have yielded, the base shear only increases a small amount for a correspondingly large increase in displacement. The limiting base shear for each building is its static ultimate base shear.

The energy balance diverged for the nonlinear analysis of the unsymmetric building subject to the two-components of the Taft ground motion B2-E at load level 3. This is because the ductility demand on the ground floor walls is greater than the maximum allowable ductility, $\mu = 10$. When this ductility demand is exceeded, the wall is assumed to have failed, and its stiffness is set to zero. As successive walls failed, the structural stiffness approached zero, and the energy balance failed. This corresponds to total collapse of the building. Thus the results for this case are omitted.

The base shear of the nonlinear unsymmetric building subject to the two-components of the Taft ground motion B2-E for load levels 1 and 2 appears to be much lower than for the one-component of the Taft ground motion B2-D as shown in Figure 164. Contrarily, the displacement for the two-component ground motion B2-E is greater than for the one-component ground motion B2-D as shown in Figure 166. The distribution of the peak shears in the ground level walls for these two ground motions is given in Figure 167. For the one-component case, the shears in the two walls (walls #5 and #7) parallel to the direction of loading are similar. This is because the walls (walls #1 and #3) perpendicular to the direction of loading resist most of the torsion forcing walls #5 and #7 to displace similar amounts. For the two-component

case, walls #1 and #3 must resist forces from the Y direction ground acceleration in addition to the torsional forces. These walls are more heavily loaded than under the one-component ground motion, and consequently have a lower stiffness, resulting in a building that has a larger torsional flexibility. The maximum torsional rotation for the roof is 0.00172 radians for the two-component ground motion, versus 0.00058 radians for the one-component ground motion at load level 2. As torsional rotation increases, walls #5 and #7 displace different amounts resulting in the shear distribution shown in Figure 167. Thus the two-component ground motion's base shear in the X direction is less than the one-component ground motion's base shear, even though the actual shear in wall #7 for the two-component ground motion is larger. The largest shear for the two-component case is in wall #3, which is parallel to the building's Y axis. Also note that the walls closest to the mass center, walls #3 and #7, are the most heavily loaded. For the nonsymmetric building, the one-component ground motion yields an unrealistic distribution of shears in the walls. The nonlinear dynamic response of any unsymmetric structure subject to a one component ground motion should be used with extreme caution.

b. Ductilities and Excursion Ratios. The ductility of the building can be calculated several different ways. First consider the displacement ductility for the entire building. Let δ_y be the yield displacement of the building's roof mass center, determined from the static analysis as shown in Figures 152 or 155; also, let δ_m be the peak displacement of the building's roof mass center; then the ductility of the entire building may be defined as

$$\mu_1 \text{ building} = \frac{\delta_m}{\delta_y} \tag{6.8}$$

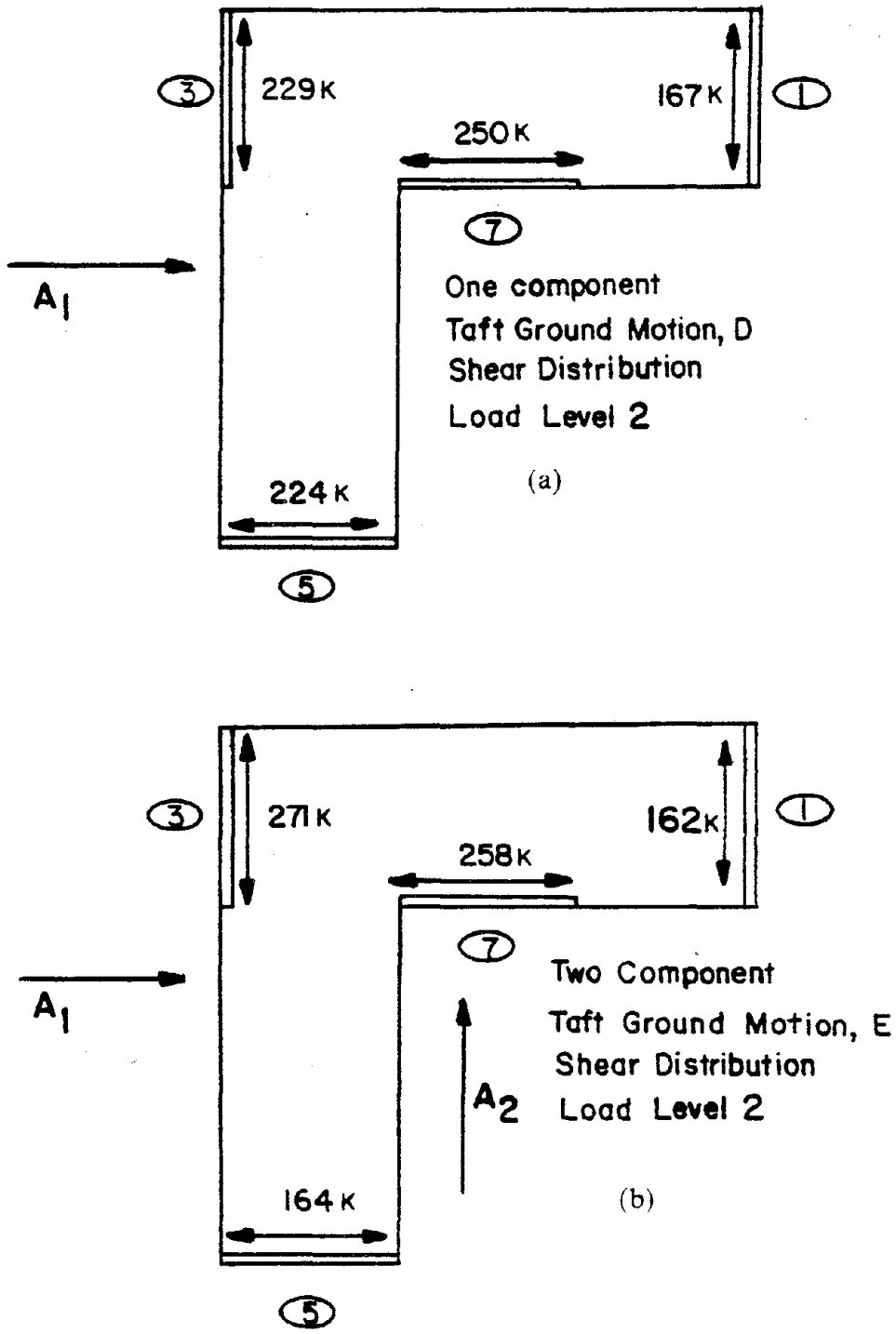

Figure 167. Unsymmetric Building Base Shear Distribution: (a) One Component Ground Motion, (b) Two Component Ground Motion

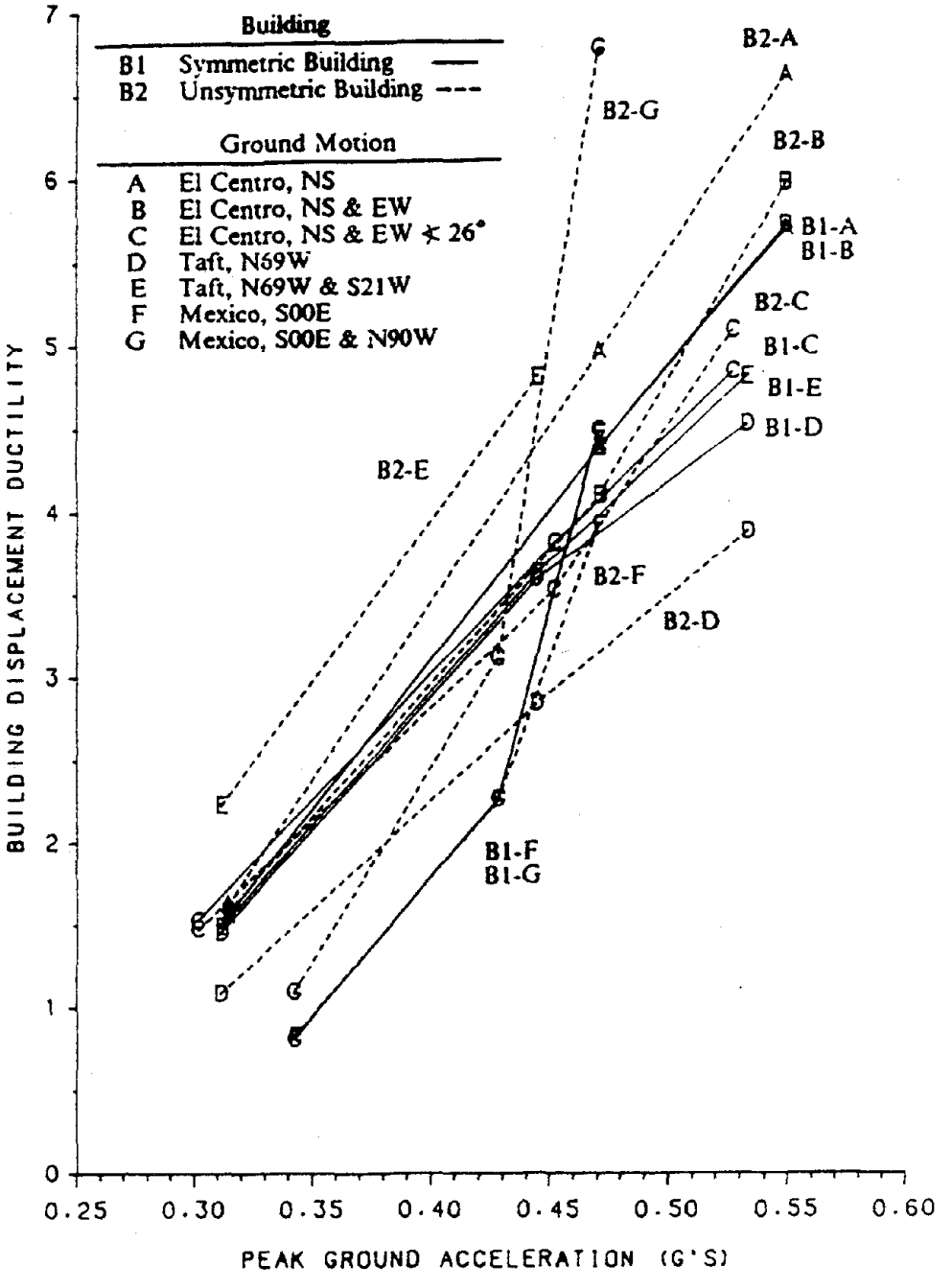

Figure 168. Building Displacement Ductility Definition vs. Peak Ground Acceleration

This ductility, given in Figure 168, is for various levels of peak ground acceleration. Most of the ductilities range from 0.8 to 1.6 for the lowest load level 1. At the highest load level 3, the majority of the ductilities range from 4 to 6.

Generally, the unsymmetric building has higher ductilities than the symmetric building. For similar ground motions, the unsymmetric building has more torsion than the symmetric building. This puts additional loads on the shear walls, increasing their displacement and yielding larger ductilities in the unsymmetric building. Thus the torsion in the unsymmetric building is partially responsible for the higher ductilities.

The ductilities are based on the maximum displacement divided by the yield displacement. Since the yield displacement of the symmetric and unsymmetric buildings is similar, there is a very strong similarity between the nonlinear displacements in Figure 166 and the building ductilities in Figure 168. Thus the influence of the parameters discussed previously on the ductilities is similar to their influence on the nonlinear displacements.

Ductilities are reported herein with inclusion of the values less than 1. For the classic elasto-plastic system, any deformation less than the yield deformation is elastic, and the ductility is therefore undefined. For reinforced concrete shear walls, the elastic range ends at cracking, which is always less than the yield deformation. Thus ductilities less than 1 convey the information that the wall deformation is less than yield and that the wall behavior may be nonlinear.

Another method of calculating the ductility is to consider the displacement of an isolated shear wall. Let δ_{by} be the bending yield displacement, δ_{sy} be the shear yield displacement, δ_{bm} be the maximum bending displacement, and δ_{sm} be the maximum shear displacement of a shear wall. Define the ductility of a shear wall as

$$\mu_{1\ \text{wall}} = \frac{\delta_{bm} + \delta_{sm}}{\delta_{yb} + \delta_{ys}} \tag{6.9}$$

The wall displacement ductility is shown in Figure 169. These ductilities have values similar to those based on the building ductility definition.

Plotting the wall displacement ductility versus the building displacement ductility in Figure 170, we observe that the building displacement ductilities are only slightly larger than the wall displacement ductilities. Thus the ductilities of the wall with the most damage, and the building's ductility are approximately equal.

One exception is the unsymmetric building subject to the two component Taft earthquake, B2-E. For this case the maximum wall ductility occurs in wall #3, which is perpendicular to the direction that the building's ductility is calculated. Because of the torsion, the displacements of wall #3 are greater than the displacements at the mass center. Thus the ductility of the wall is larger than the ductility of the building.

The displacement ductility can also be calculated separately for the bending and shear components of deformation in a shear wall. Define the bending ductility as

$$\mu_{1\ \text{bending}} = \frac{\delta_{bm}}{\delta_{yb}} \tag{6.10}$$

and the shear ductility as

$$\mu_{1\ \text{shear}} = \frac{\delta_{sm}}{\delta_{ys}} \tag{6.11}$$

The bending ductility is given in Figure 171. The majority of the bending ductilities at the lowest load level 1 range from 1 to 2, while at the highest load level the bending ductilities range from about 4.5 to 8. This is larger than the structure and wall

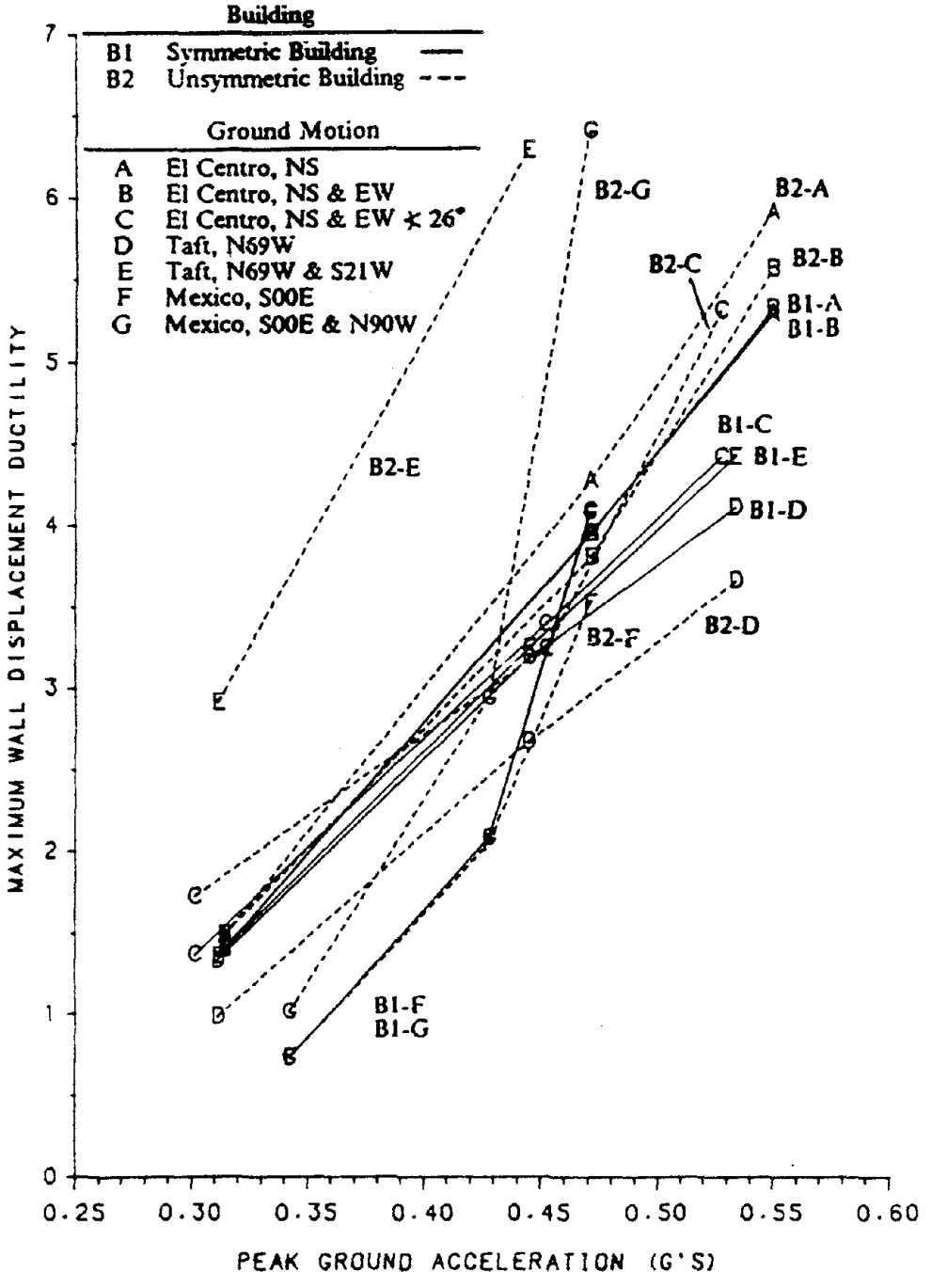

Figure 169. Shear Wall Displacement Ductility Definition vs. Peak Ground Acceleration

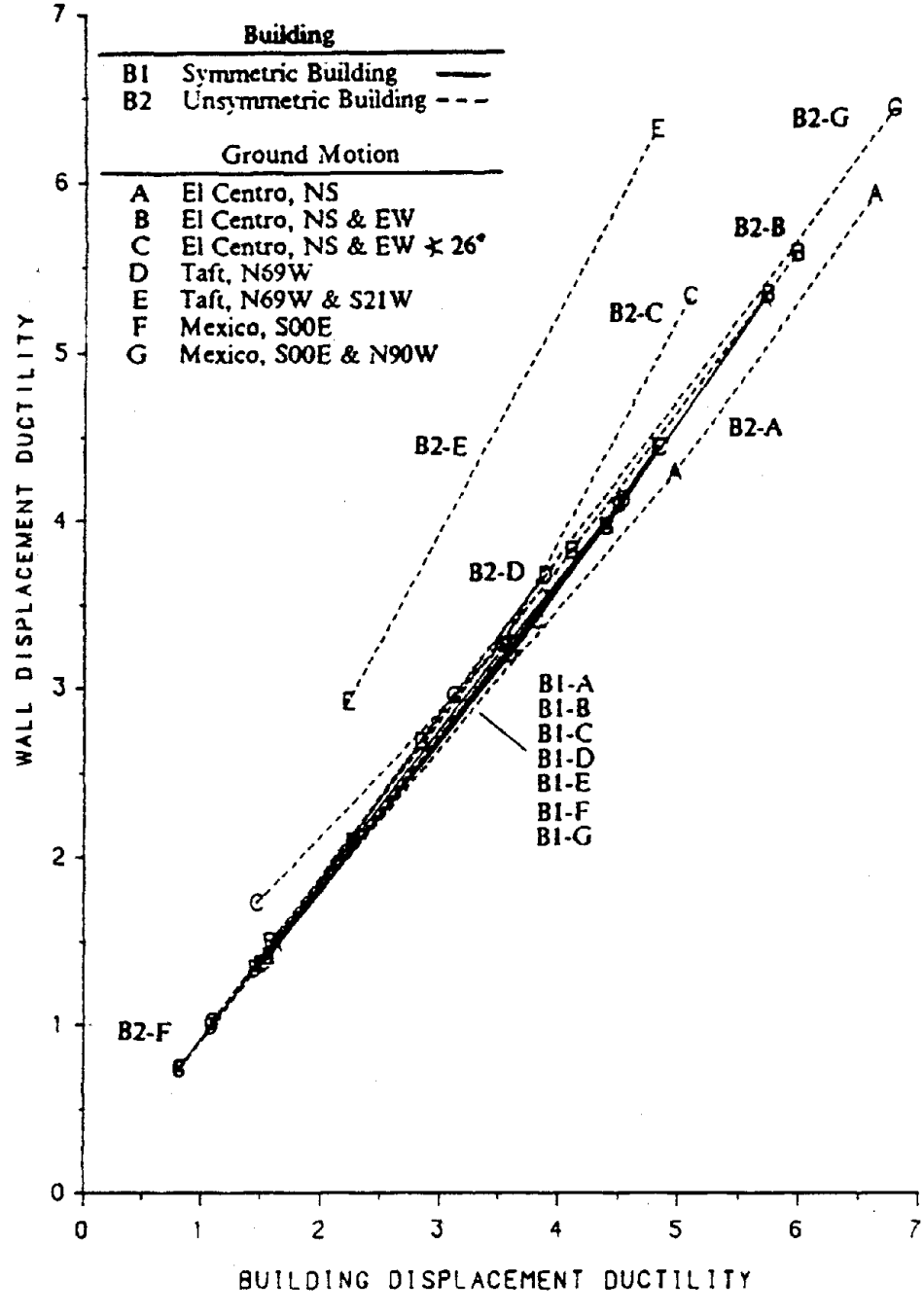

Figure 170. Shear Wall Displacement Ductility vs. Building Displacement Ductility

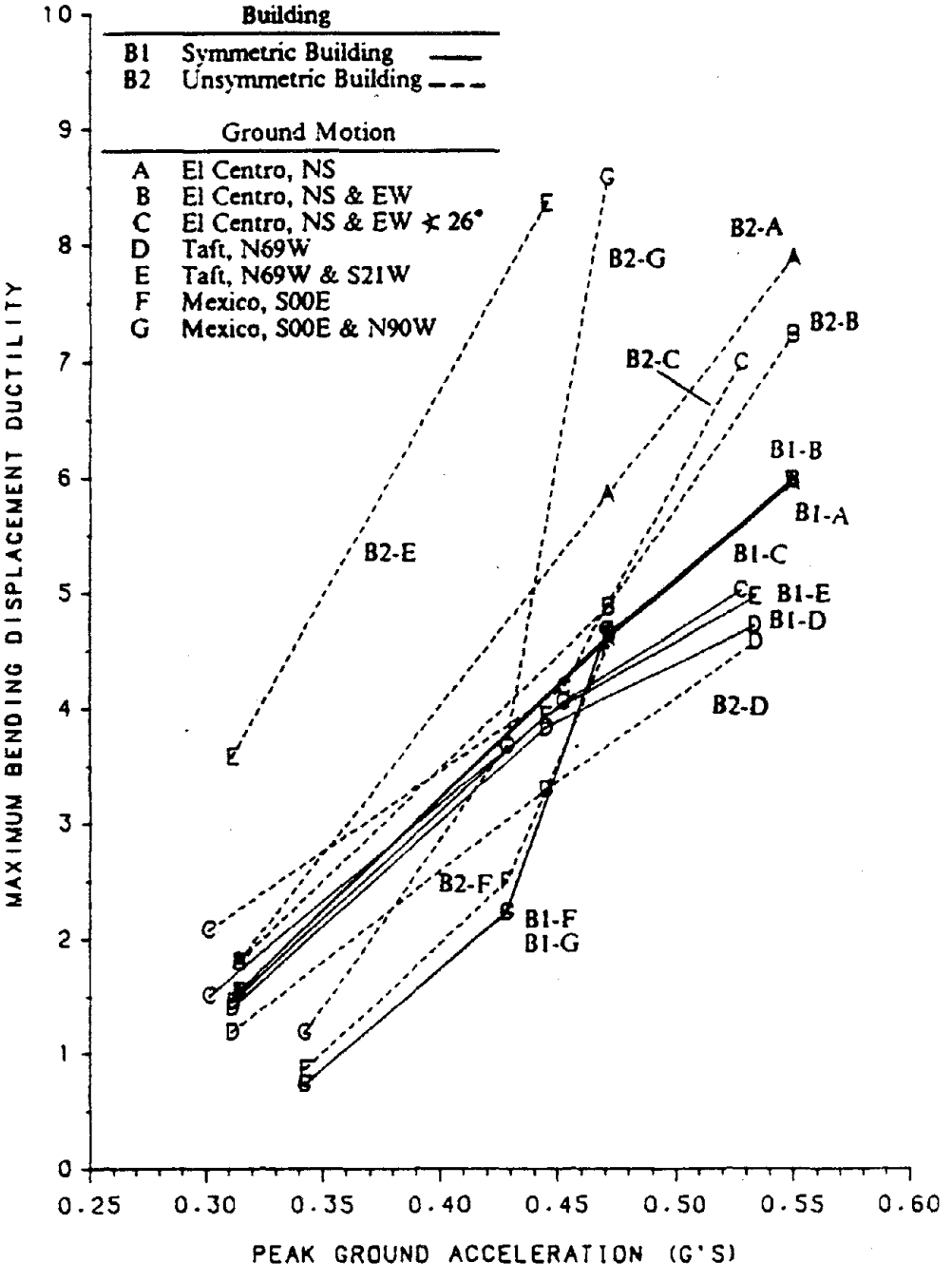

Figure 171. Shear Wall Bending Displacement Ductility vs. Peak Ground Acceleration

ductilities, which, as previously discussed, have a majority of ductilities ranging from 4 to 6 at the highest load level.

The shear ductility is given in Figure 172. The shear ductilities at the lowest load level 1 range from 0.5 to 1.5, while at the highest load level the shear ductilities range from 1 to 4. The shear ductility is less than the bending, wall and structure ductility.

The excursion ratios based on the shear and bending displacement ductilities are given in Figures 173 and 174. The majority of the bending excursion ratios range from 20 to 50 for load case 3, while the shear excursion ratios are much lower. If the total duration of the ground acceleration record is used instead of a 10 or 15 second segment, these excursion ratios would be larger.

The ductilities and excursion ratios are also calculated by the variable strain energy definitions and the constant strain energy definitions, Equations 5.161 and 5.162. On the average, for bending the constant strain energy ductilities are about 35% larger than the displacement ductilities, and the variable strain energy ductilities are about 16% larger than the displacement ductilities. The bending excursion ratios by the three different definitions yield similar results. For the shear ductilities, on the average, the variable strain energy ductilities are about 120% larger than the displacement ductilities, and the constant strain energy ductilities are about 40% larger than the displacement ductilities. The shear excursion ratios have considerable variation, due to the difference in ductilities.

c. Damage Indices. The damage indices are calculated for each of the buildings and are presented in Figure 175 for various levels of ground acceleration.

Generally, the unsymmetric building has more damage than the symmetric building for similar ground motions. This is consistent with the observed ductilitites.

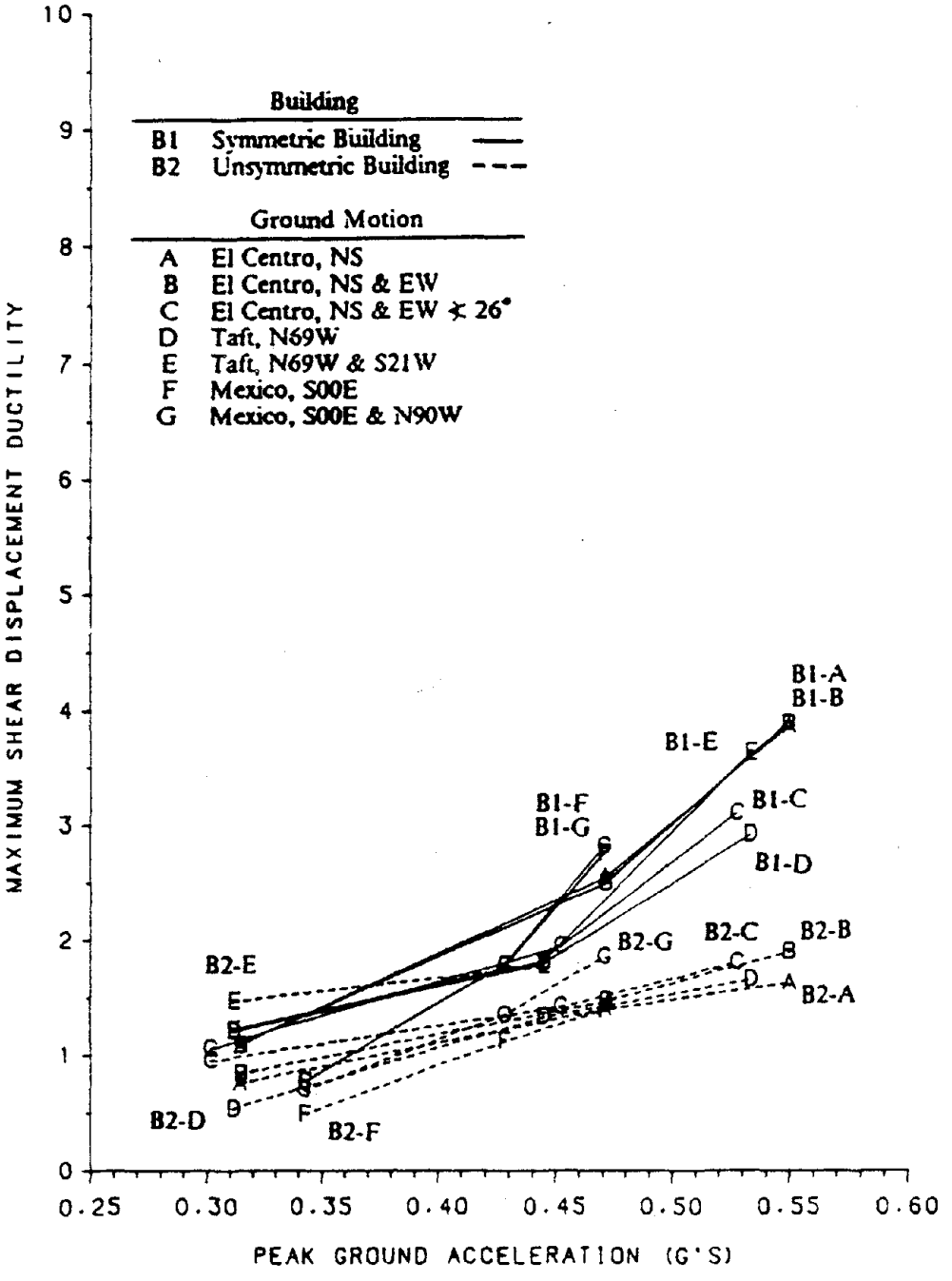

Figure 172. Shear Wall Shear Displacement Ductility vs. Peak Ground Acceleration

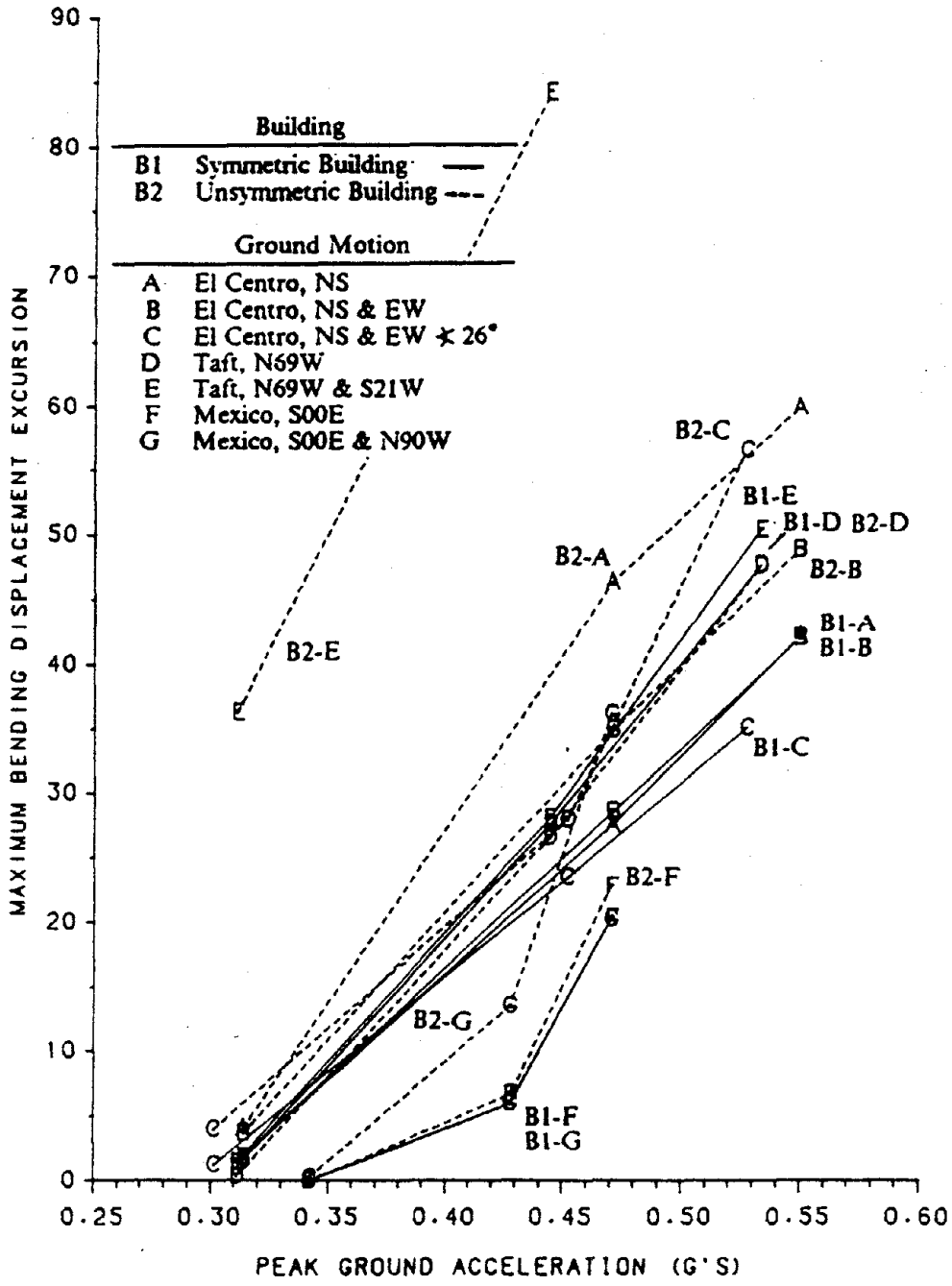

Figure 173. Shear Wall Bending Displacement Excursion Ratio vs. Peak Ground Acceleration

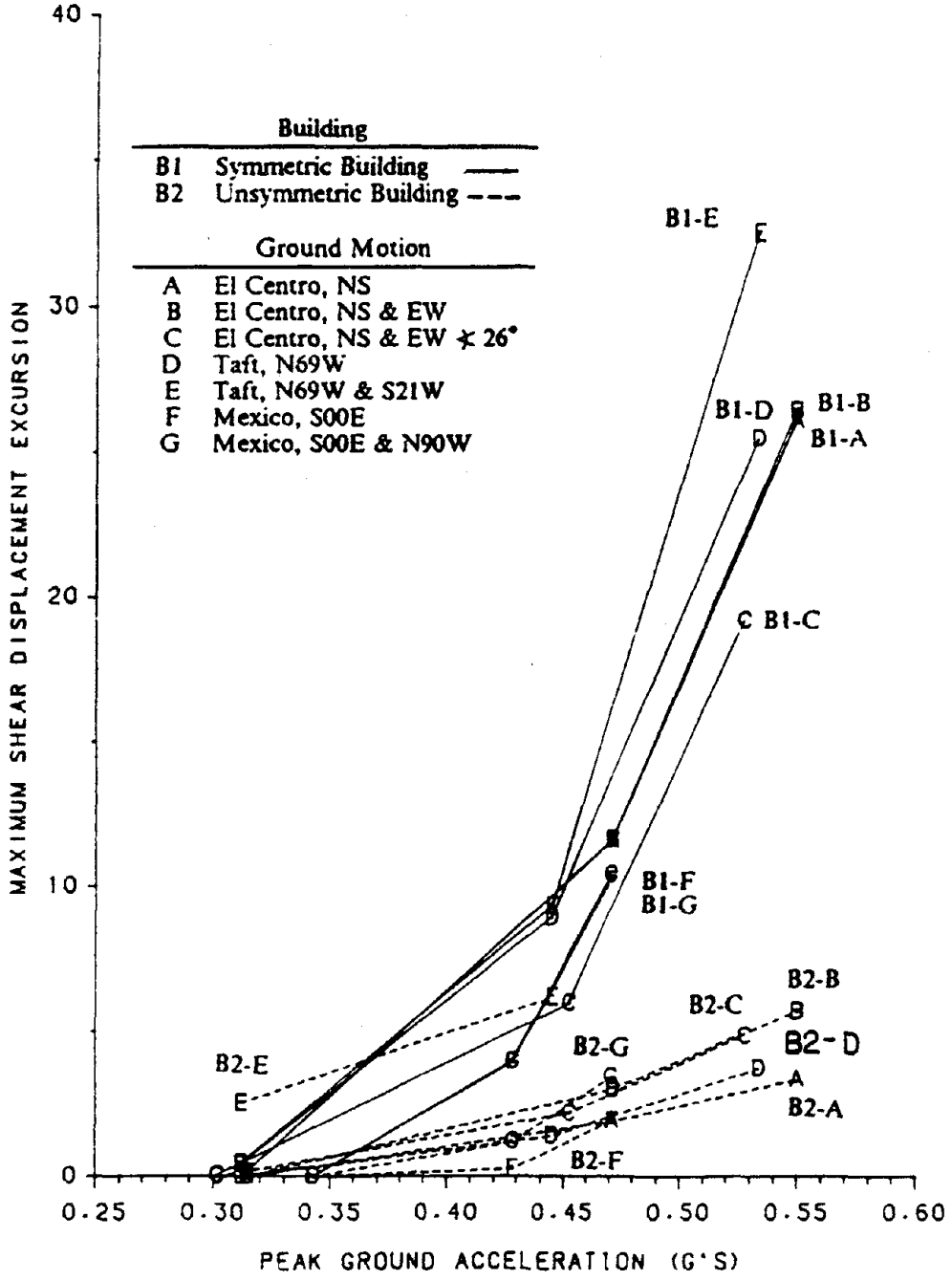

Figure 174. Shear Wall Shear Displacement Excursion Ratio vs. Peak Ground Acceleration

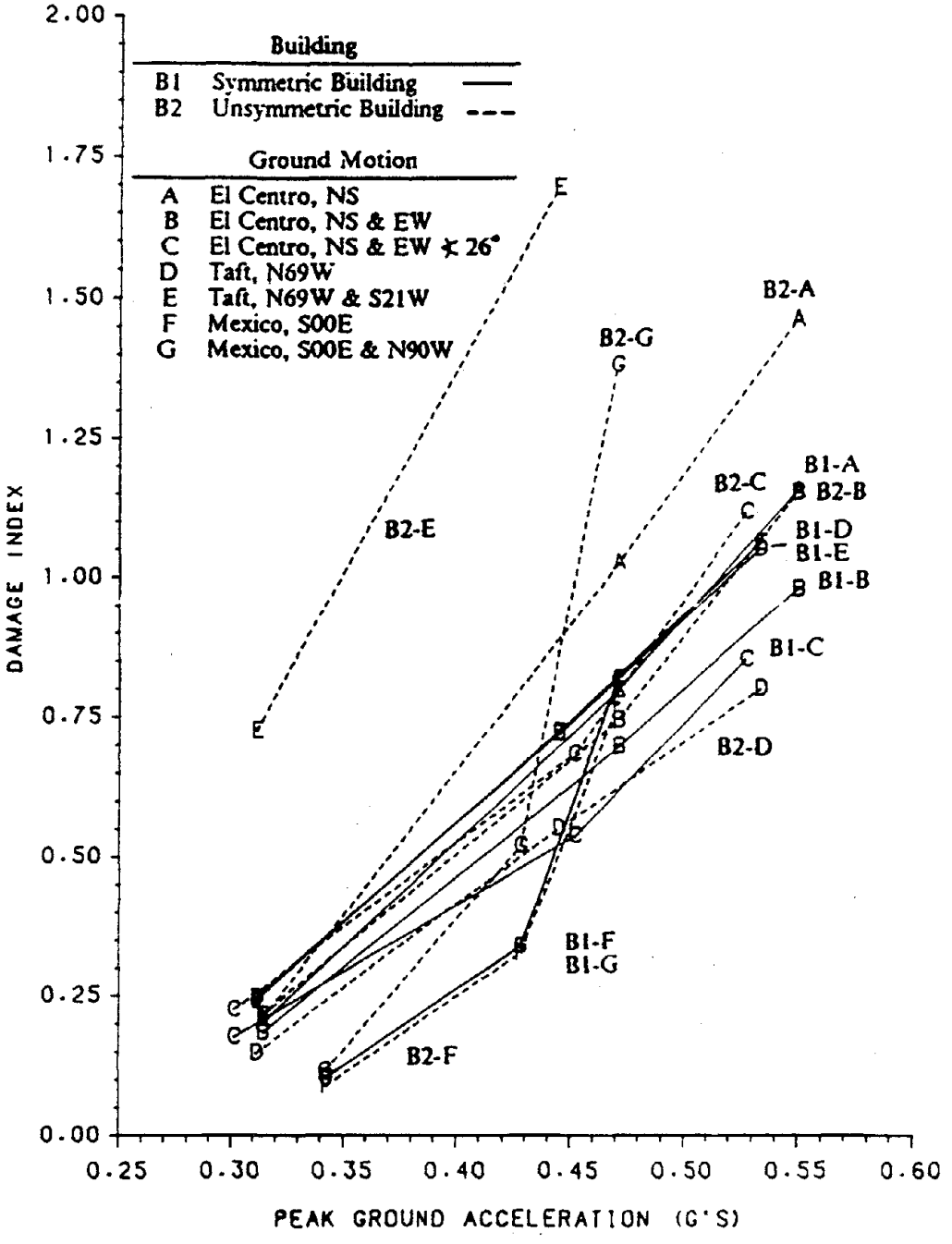

Figure 175. Damage Index vs. Peak Ground Acceleration

The unsymmetric building is subjected to torsional forces in addition to the lateral forces that the symmetric building experiences. Thus it is reasonable that the unsymmetric building would experience more damage.

The symmetric building's damage index for a one-component ground motion is higher than the damage index for a two-component ground motion, compare B1-A and B1-B. Recall that a weighted average of the elements damage indices is taken to get the building's damage index, where the weighting factor is strain energy in the element, Equation 5.165. For the two-component ground motion, the sum of energy in all the walls is much larger than the one-component ground motion, while the sum of damage index times energy is only slightly larger than the one-component case. Thus the two-component ground motion has a lower damage index than the one-component ground motion due to the weighting method. Recall that the maximum displacement of the symmetric building for both the one and two component ground motions is about equal. Thus the building has similar amounts of damage due to the one and two component ground motions, and the damage indices should be approximately equal. It is important to note that the two-component ground motion yields more realistic damage indices, because one-component ground motions do not occur naturally.

The rate at which the damage index increases with the ground acceleration is much higher for the Mexico ground motions than the Taft or El Centro ground motions. Recall that the displacement for the Mexico ground motion also increased rapidly with an increase in ground acceleration.

d. Failure Criteria. Two different failure criteria have been discussed and are evaluated in this section.

• Maximum Displacement Ductility. This failure criteria is based on the average observed failure ductilities in NCKU walls which ranged from 5.6 to 17.5. An average

ductility of 10 is used as the failure limit. The peak ductilities for both of the buildings are less than the failure limit.

• Damage Index. The damage index is based on a weighted average of the buildings ductility, and the strain energy dissipated during the loading history. The strain energy dissipated during the loading history is similar to the constant strain energy excursion ratio. Thus the damage index is actually a combination of the ductility failure criteria and the excursion ratio. Because the damage index is based on strain energy, it is sensitive to the length of the ground motion record. The damage index for several of the cases exceeds the failure limit of 1.0 at loading level 3. If the entire ground motion record is used instead of a 10 or 15 second segment, the damage indices would be larger. Thus one might conclude that the cases corresponding to load level 3 have exceeded the failure limit.

The hysteretic energy coefficient β used in determining the damage index is based on 8 shear walls (72). For reinforced concrete beams and columns, Park and Ang (65) examined the results of 261 tests and determined expressions for β that have a coefficient of variation of 55% when compared to experimental results. This indicates considerable scatter in the experimental data. As more shear wall data becomes available, and the β value for shear walls becomes more refined, similar scatter can be expected. Thus the damage index of 1 should not be rigidly interperted as indicating collapse.

C. SENSITIVITY OF R AND C_D TO EL CENTRO, TAFT AND MEXICO EARTHQUAKES

An elastic response to an earthquake ground motion requires large forces, as seen by the elastic base shears in Figure 163. Experience has shown that ductile structures can survive an earthquake with much lower base shears, as seen by the nonlinear base

shears in Figure 164. The structural analyses recommended in the design codes, such as UBC, are based on an elastic response spectrum. This elastic response spectrum is then modified to reflect the actual nonlinear behavior of the structure by the response modification factor, R. Common design practice considers the elastic response due to loadings that have been modified to account for nonlinear behavior. Thus the response modification factor, R, is a very important code parameter.

The load-deformation response of a structure may be represented by Figure 176. Curve O-A-B-C-D represents the actual nonlinear behavior of a structure under a specific ground motion. Point A represents the working load, point B represents the first significant yield[21] of the structure, point C represents the maximum nonlinear load and displacement that the structure achieved during the ground motion and point D represents the ultimate capacity of the building. The curve O-A-B-E represents the elastic response of the building to the same ground motion. Point E represents the maximum response of an elastic structure. The NEHRP Recommended Provisions for the Development of Seismic Regulations for New Buildings (55) defines the response modification factor, R, as the ratio of the maximum elastic force (Point E) to the yield force (Point B), or

$$R = \frac{P_E}{P_B} \tag{6.12}$$

A second parameter C_d is defined as the ratio of the maximum nonlinear displacement (Point C) to the yield displacement (Point B), or

---

[21] The first significant yield corresponds to the formulation of a plastic hinge in one of the structure's critical elements. This occurs at a higher load than the yield point, which corresponds to the yielding of the first reinforcing bar in a concrete structure.

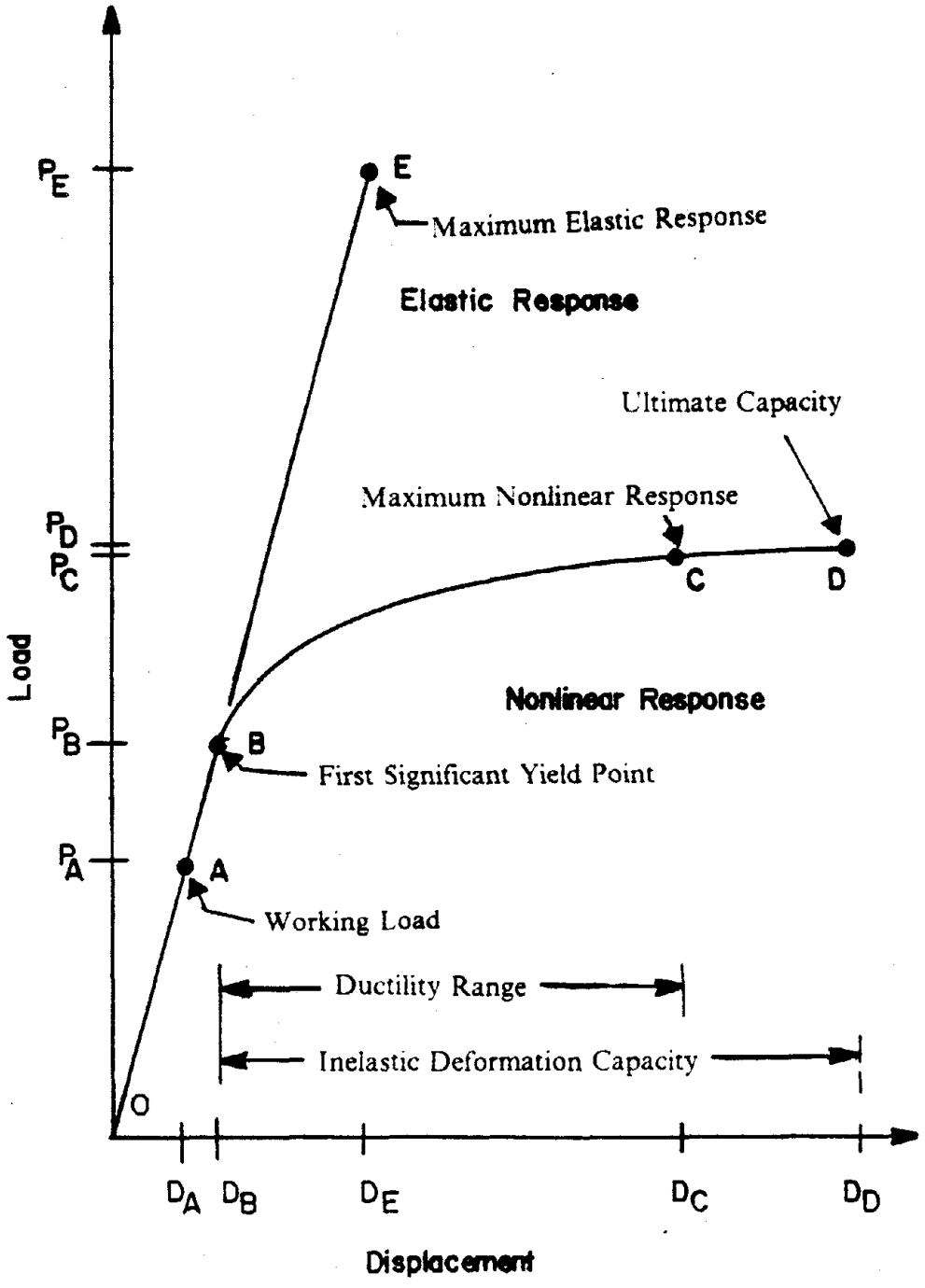

Figure 176. Load-Deformation Response

$$C_d = \frac{D_C}{D_B} \tag{6.13}$$

Since the first significant yield is greater than the structures yield point, then C_d is greater than the buildings displacement ductility. The NEHRP recommends the values of $R = 4.5$ and $C_d = 4$ for R/C shear walls. Similarly, the Uniform Building Code (77) defines the response modification factor R_w as the ratio of the maximum elastic force (Point E) to the working stress force (Point A).

$$R = \frac{P_E}{P_A} \tag{6.14}$$

The UBC recommends the value of $R = 6$ for R/C shear walls. The elastic response spectrum is reduced by R_w in Equation 6.1 to calculate the equivalent static lateral load in the UBC code. This static load corresponds to the working load. Buildings designed to resist this lateral load will behave nonlinearly if the design earthquake is experienced.

1. Response Modification Factor, R. The response modification factor, R, from Equation 6.12 is presented as a function of damage index in Figure 177. The point of the first significant yield, P_B, for the symmetric building is near 540 kips as shown in Figure 152 and near 510 kips for the unsymmetric building as shown in Figure 156 for one-component static loadings. The elastic base shear, P_E, is given in Figure 163, and the damage indices are given in Figure 175.

The El Centro ground motion has a much higher response modification factor than the Mexico ground motion. Recall that the Mexico ground motion has a period

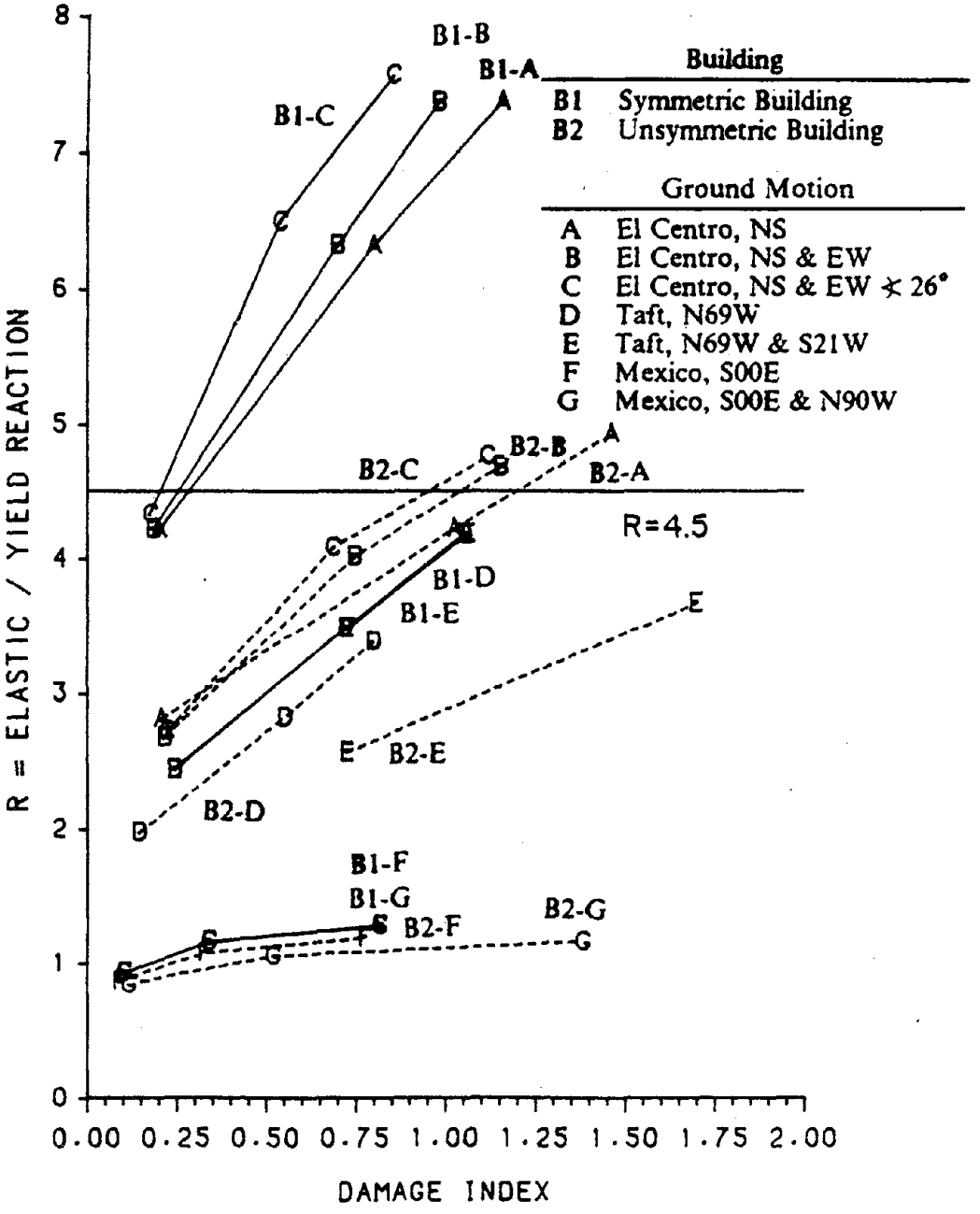

Figure 177. R vs. Damage Index

that is significantly longer than the elastic fundamental period. Thus the elastic response is relatively small, compared to El Centro and Taft. As the building deforms nonlinearly due to the Mexico ground motion, the fundamental period of the building increases and shifts towards the period of the ground motion. The closer the building's period is to the ground motion's period, the larger the response. Note that the nonlinear response to the Mexico ground motion is on the same order of magnitude as the El Centro and Taft ground motions. Thus the response modification factor is a function of both the buildings period, and the period of the ground motion. This implies that the response modification factor is site dependant.

The angle of the earthquake input direction on the structure also influenced the response modification factor, as shown by comparing B1-B with B1-C, and B2-B with B2-C in the figure. Thus for a given earthquake and building there exist a range of response modification factors depending on the orientations of the seismic input. The lower bound of this range will determine the maximum base shear.

An actual earthquake has two horizontal components of ground motion. For unsymmetric buildings which are sensitive to multicomponent ground motions, it is unrealistic to use the one-component ground motion to determine the response modification factor. Symmetric buildings may or may not be sensitive to multicomponent ground motions, that depends on the relative distance between and the relative locations of the mass center and the rigidity center. For this case the response modification factor for one and two component ground motions is similar. However, the damage index for symmetric buildings is component sensitive.

As the level of damage in the building increases, the response modification factor also increases. This is because both the elastic base shear and the damage index

increase with increasing magnitudes of ground motion. Thus Figure 177 can be used to choose a response modification factor based on an acceptable level of damage.

The symmetric building at failure (DI ~ 1.0) has a higher response modification factor than the unsymmetric building. One cause of this difference is that the elastic base shear for the symmetric building is typically larger than the unsymmetric building as shown by Figure 163. The differences in elastic response are due to different fundamental periods and the unsymmetric building's coupling of response in the X and Y axes. Another cause is that the unsymmetric building typically has more damage than the symmetric building. The increased damage is also due to the unsymmetric building's coupling of response in the X and Y axes. Thus the response modification factor is a function of the building type.

Additional studies are required before the response modification factor for reinforced concrete shear walls can be determined. These should include buildings with a wider range of geometries, natural frequencies and shear wall height to width ratios. A family of earthquakes records that are based on the code response spectrum should be used. The two-component ground motions are preferred over one-component ground motion. Additionally, the angle of the ground motion to the building should be varied to determine the range of response modification factors for each combination of building and ground motion.

Based on the limited study of two buildings, the response modification factor recommended by the NEHRP, R=4.5, seems reasonable for the El Centro and Taft ground motions. The response modification factor for the longer period ground motion of the Mexico earthquake is close to 1.

2. Deflection Amplification Factor, C_d. The NEHRP definition of the deflection amplification factor C_d, from Equation 6.13, is presented as a function of damage

index in Figure 178. The point of the first significant yield is determined from the static monotonic response which is shown in Figures 152 and 155. The nonlinear displacement, D_C, is given in Figure 166, and the damage indices are given in Figure 175.

The displacement amplification factor increases with damage index. Recall that the damage index consists of 1) maximum displacement divided by ultimate displacement and 2) a term containing the plastic strain energy. Since the deflection amplification factor, C_d, consists of the maximum displacement divided by the yield displacement, the deflection amplification factor and the damage index are closely related. The deflection amplification factor C_d varies from 2 to 3 at failure (DI $\sim$ 1). This is slightly lower than the NEHRP suggested value of 4.

The point of the first significant yield is determined from Figures 152 and 155. The displacement at this point is about twice of the first yield displacement. Shear walls have a gradual yielding behavior. Thus the exact location of the yield point is based on judgment. Modifying the location of the significant yield point will have a larger impact on the displacements than on the load. Thus the deflection amplification factor is more sensitive to the location of the yield point than the response modification factor.

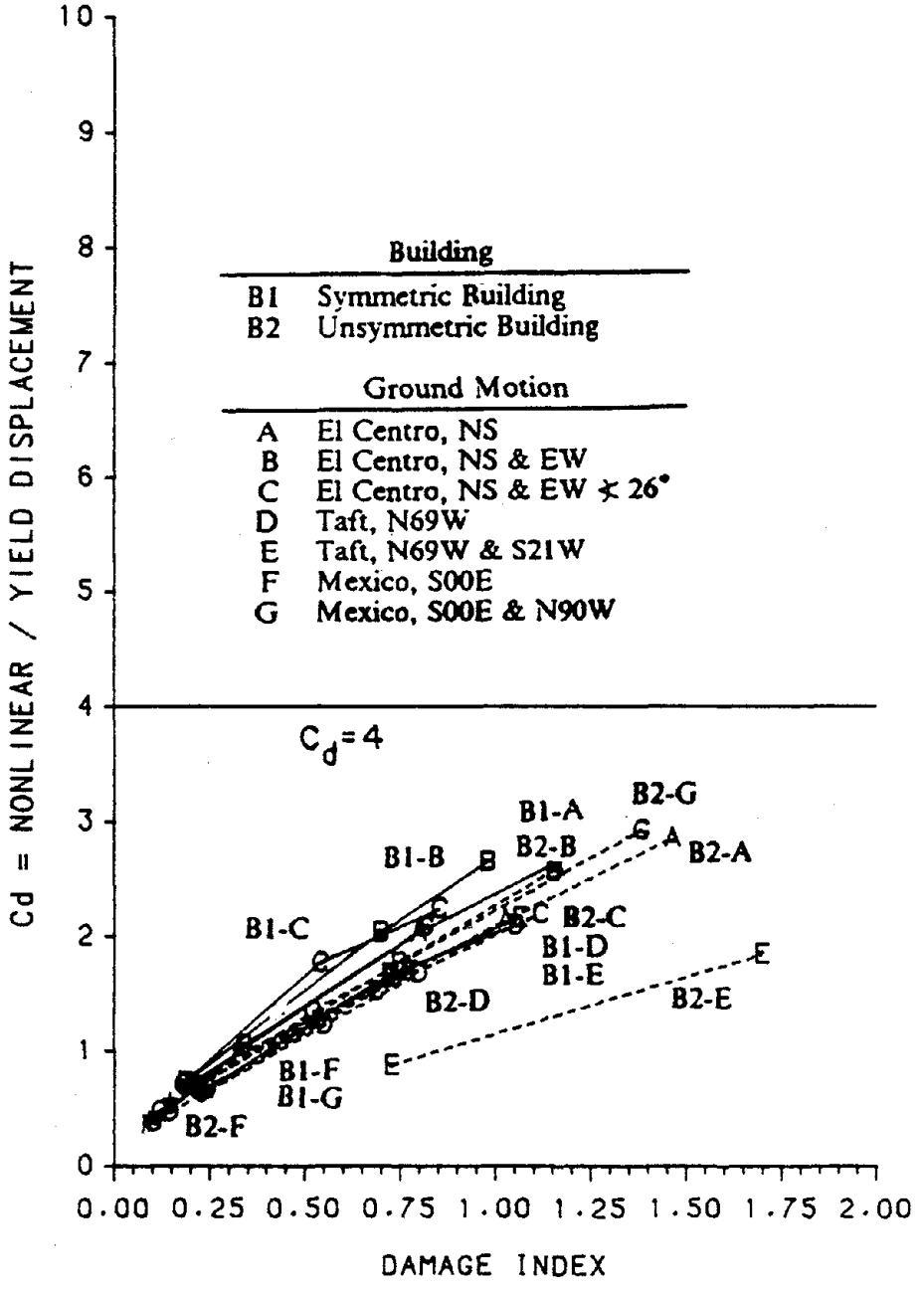

Figure 178. C_d vs. Damage Index

VII. RESPONSE STUDIES OF LOW-RISE BOX TYPE BUILDINGS

In buildings with isolated R/C shear walls, each wall resists lateral loads by bending and shear. Since the floor is considered to be flexible in its plane, the vertical displacements of the different walls in the building are incompatible, and the axial loads in the walls are only due to gravity loadings. The building's lateral stiffness is the sum of the individual wall's bending and shear stiffnesses.

In box type R/C buildings, the shear walls are connected along their vertical edges. Thus the vertical displacement of adjacent walls is compatible. External bending moments are resisted by bending in the plane of the shear wall and by axial loads in shear walls on both sides of the center of rigidity. The box type building's lateral stiffness is 1) the sum of the individual wall's bending and shear stiffnesses and 2) the sum of the individual wall's axial stiffness times the square of the distance to the center of rigidity. The influence of the wall's axial stiffness on the building's lateral stiffness causes the behavior of box type R/C buildings to be different from the behavior of R/C buildings with isolated shear walls.

A. STATIC ANALYSIS

Box section UT-B6 was tested with a cyclic static loading by Umemura, et al (78, 79) at the University of Tokyo. This box is 83 cm wide, 80 cm tall and has 8 cm thick walls, as shown in Figure 179. Reinforcing consists of 2 D6 bars[22] 13.2 cm on center, each way, for a reforcing ratio of 0.6%. The steel stress-strain curve and the concrete properties are also given in the figure.

---

[22] A D6 reinforcing bar is approximately equal to a #3 reinforcing bar.

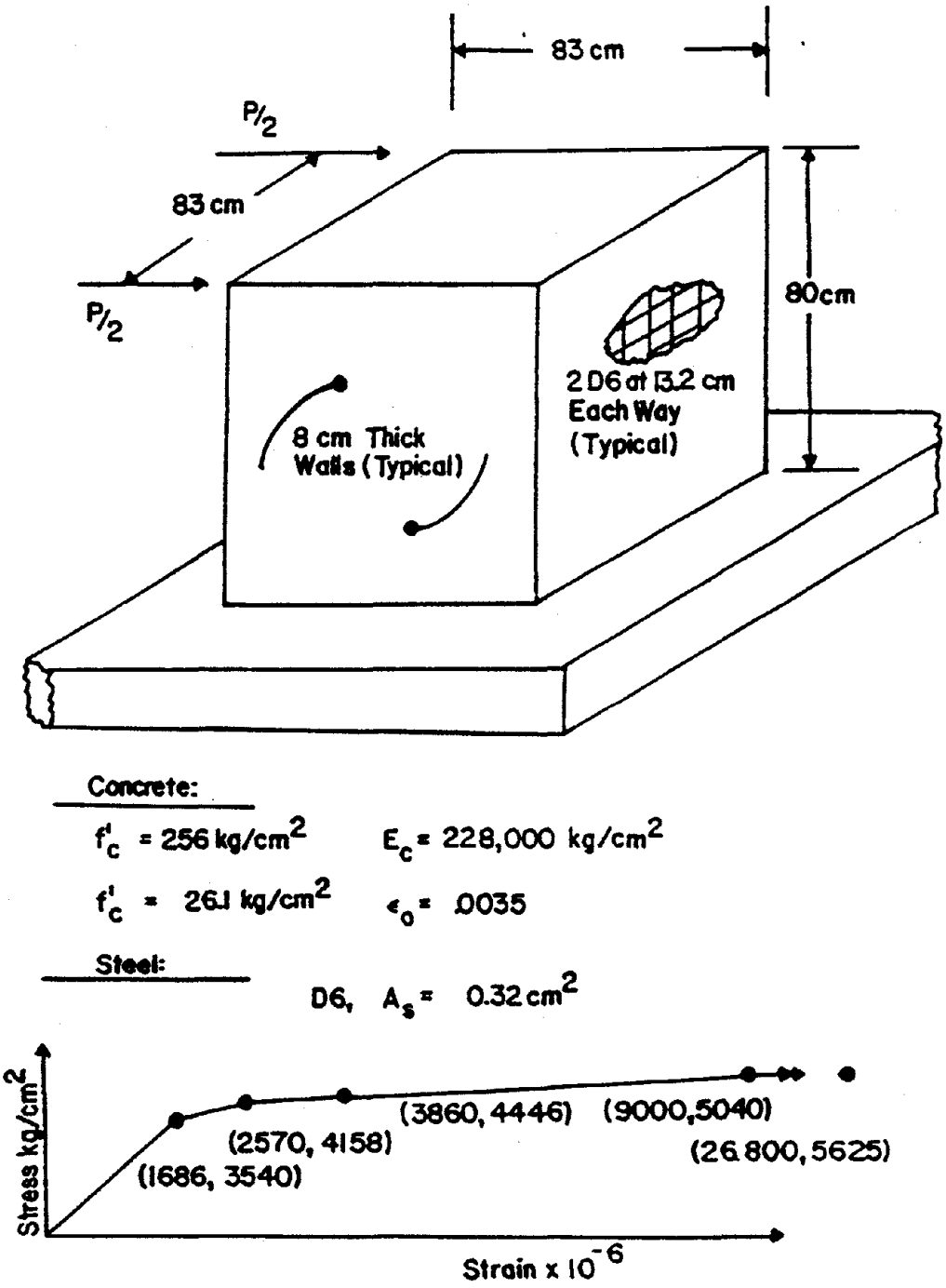

Figure 179. University of Tokyo Box Section B6

Nine joints are used to define the three dimensional structural model as shown in Figure 180. At the base, joints 1 through 4 define the corners of the box. Joints 11 through 14 define the corners of the box at the roof. Joint 10 is at the mass center of the roof. The JCS for all of the joints is parallel to the GCS. The three dimensional structural model consists of four shear wall elements, numbered 1 through 4. The wall's center line dimensions are used for the structural model, thus each of the shear wall elements is 75 cm wide and 80 cm tall.

As discussed in Chapter V, each joint has 6 degrees of freedom. At the base of the box, joint 1 through 4, all six degrees of freedom are restrained. The slab at the top of the box is assumed to be a rigid diaphragm. A planar constraint is used to transfer the translations in the X and Y axes and the rotation about the Z axis from joints 11 through 14, at the corners of the box, to joint 10, at the mass center. The planar constraint at the roof reduces the number of degrees of freedom at joints 11 through 14, leaving rotational dof about the X and Y axes which are restrained and translational dof in the Z axis which is free to displace. None of the elements are connected to joint 10. Thus joint 10 does not have any stiffness before joints 11 through 14 are constrained to it. As a 'master' joint, joint 10 has translational stiffness in the X and Y axes, and rotational stiffness about the Z axis. Loading consist of imposed displacements of joint 10 in the X direction. Thus the X translational dof of joint 10 is restrained. The Z translational dof and the rotations about the X and Y axes are also restrained, because these dof do not have any stiffness. The Y translational dof and the Z rotational dof of joint 10 are free to displace. The dof are numbered in accordance with the Gdof numbering scheme presented in Section A.4 of Chapter V, as shown in Table XVII. None of the dof are condensed out since this is a static analysis. All of the rotations about the X and Y axes are restrained with the restraint option KEY = 2, which was discussed in Section A of Chapter V.

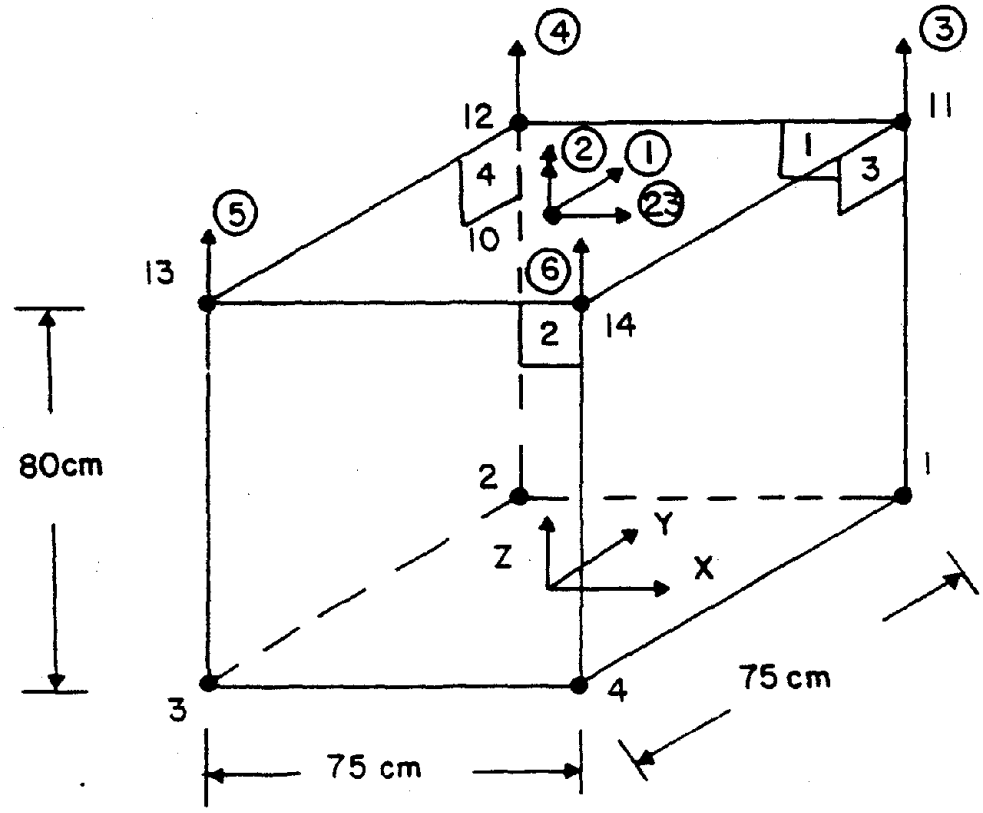

Figure 180. UT Box B6 Degrees of Freedom

Table XVII. DEGREES OF FREEDOM FOR UT BOX B6

Joint	Condensed DOF						Free DOF						Restrained DOF *						Restrained DOF **					
#	TX	TY	TZ	RX	RY	RZ	TX	TY	TZ	RX	RY	RZ	TX	TY	TZ	RX	RY	RZ	TX	TY	TZ	RX	RY	RZ
1													7	8	9			10					25	26
2													11	12	13			14					27	28
3													15	16	17			18					29	30
4													19	20	21			22					31	32
10								1				2	23					24					33	34
11								1c	3			2c	23c										35	36
12								1c	4			2c	23c										37	38
13								1c	5			2c	23c										39	40
14								1c	6			2c	23c										41	42

Notes:

1) TX, TY and TZ signify translation in the joints X, Y and Z axes respectively.
2) RX, RY and RZ signify rotation about the joints X, Y and Z axes respectively.
3) The constrained dof of 'slave' joints are represented by #c, where # is the dof number of the 'master' joint.

* Restraint code KEY = 1, as discussed in Section A of Chapter V.

** Restraint code KEY = 2, as discussed in Section A of Chapter V.

In the experimental study, the load is applied 80 cm above the base of the box section. Displacements at each of the four corners are measured and averaged. For analysis the load and displacements are assumed to be acting at the mass center of the box, which corresponds to joint 10. Loading consists of imposed displacements of the mass center in the global X direction (Gdof 23). P-Δ effects are neglected since the only axial loads are the self weight of the box.

Bending moments about the global Y axis are resisted by walls #1 and #2 in bending and by walls #3 and #4 with axial loads. Thus the portion of bending resisted by a single wall is dependent on the walls stiffness relative to the stiffness of the whole box section. One method to estimate the percentage of bending which a single wall resists is to take a ratio of the wall's moment of inertia to the moment of inertia for the whole box section. Let Ig be the gross moment of inertia for the whole box section,

$$Ig = \frac{83^4 - 67^4}{12} = 12\,275\,600 \text{ cm}^4 \tag{7.1}$$

and Iw be the moment of inertia for a single wall, say wall #1,

$$Iw = \frac{8 \times 83^3}{12} = 281\,250 \text{ cm}^4 \tag{7.2}$$

then wall #1 will resist $\frac{Iw}{Ig} = 0.124$ of the total moment. If the applied moment is 80P, then wall #1 resists a moment of approximately 10P.

For loading in the global X axis, walls #1 and #2 each resists an equal portion of the shear, while walls #3 and #4 do not resist any shear. For an applied load of P, the shear in wall #1 is 0.5P. Thus wall #1 has a moment to shear ratio of $\frac{10P}{0.5P} = 20$ cm.

The bending and shear backbone curves for walls #1 and #2 are determined by the method presented in Chapter III. If the load were applied in the global Y direction, a similar analysis would yield the same backbone curves for walls #3 and #4. Thus the same backbone curves are used for all four walls. Axial stiffness is determined in accordance with the axial hysteresis model presented in Chapter IV.

The calculated response is compared with the experimental response as shown in Figure 181. The calculated backbone curve is very close to experimental curve for a displacement less than or equal to 1 cm as shown by Curve A in the figure. For displacements larger than 1 cm the calculated backbone curve has slightly larger loads than the experimental curve. The calculated unloading stiffness of Curve B in the figure is less than the experimental unloading stiffness. Thus the calculated hysteresis loops dissipate less energy than the experimental hysteresis loops.

The low unloading stiffness is primarily due to the unloading branch of the axial hysteresis model. The axial hysteresis loops for wall #4 are shown in Figure 182. Recall that the unloading stiffness of the axial hysteresis model, Equation 4.53, is

$$Kr = Kc\left(\frac{Dyt}{Dmax}\right)^{\alpha} \geq \left(\frac{Fmax + Fy}{Dmax - Dyc}\right)$$

where $\alpha = 0.90$. For the walls in box UT B6 this unloading stiffness is too low. The axial unloading stiffness in Equation 4.53 is increased by setting $\alpha = 0.40$.

The calculated response with $\alpha = 0.40$ is compared with the experimental response in Figure 183. Overall the comparison between the calculated and experimental response is good. The comparison between calculated and experimental backbone, Curves A, is identical to the previous analysis. The unloading stiffness, Curve B in the figure, is very close to the experimental unloading stiffness. This improvement over the previous analysis is due to the modification of the axial hysteresis model.

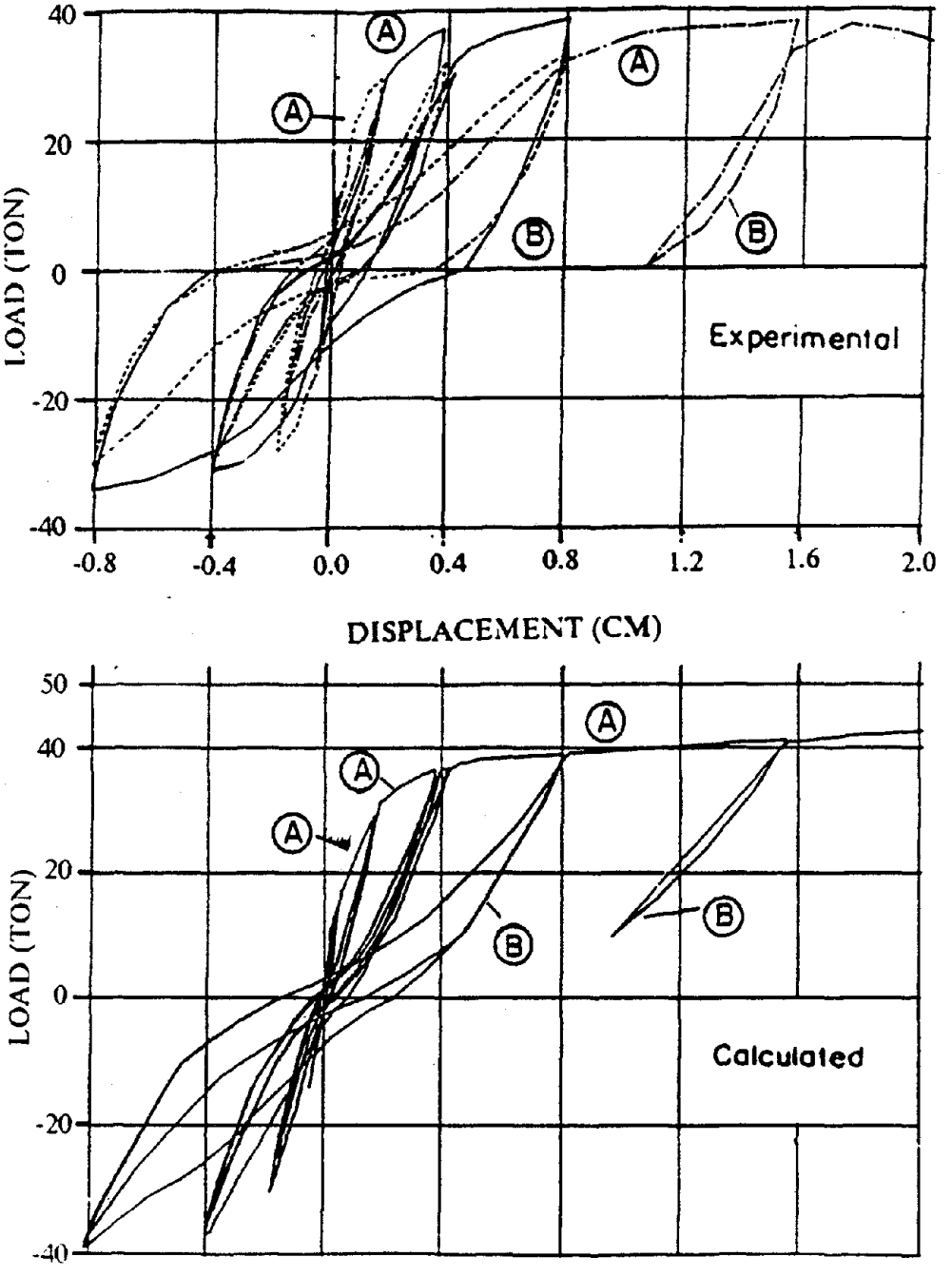

Figure 181. UT Box B6 Comparison of Calculated and Experimental Response (Experimental Response, Ref. 78)

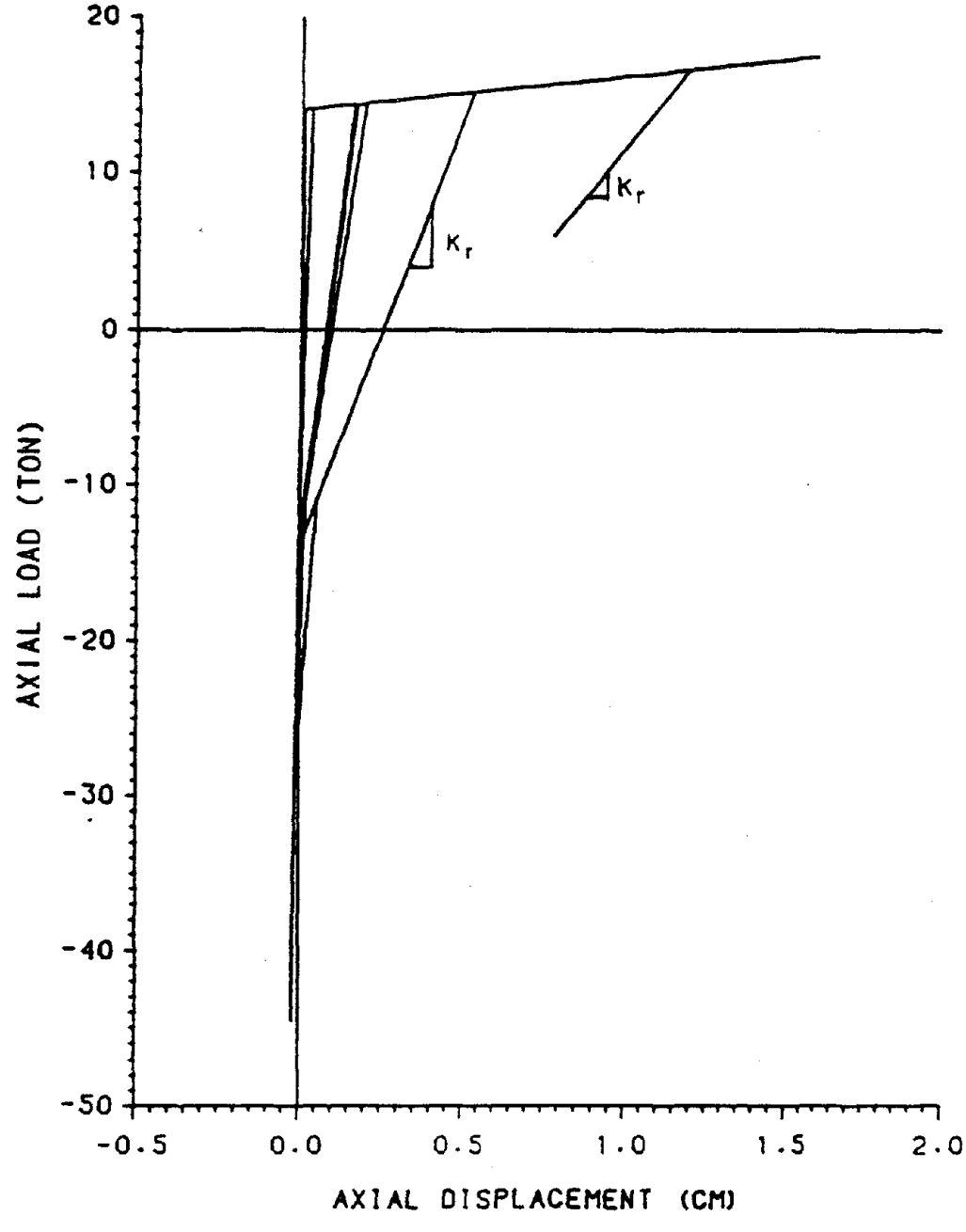

Figure 182. UT Box B6 Axial Hysteresis Loops for Wall #4

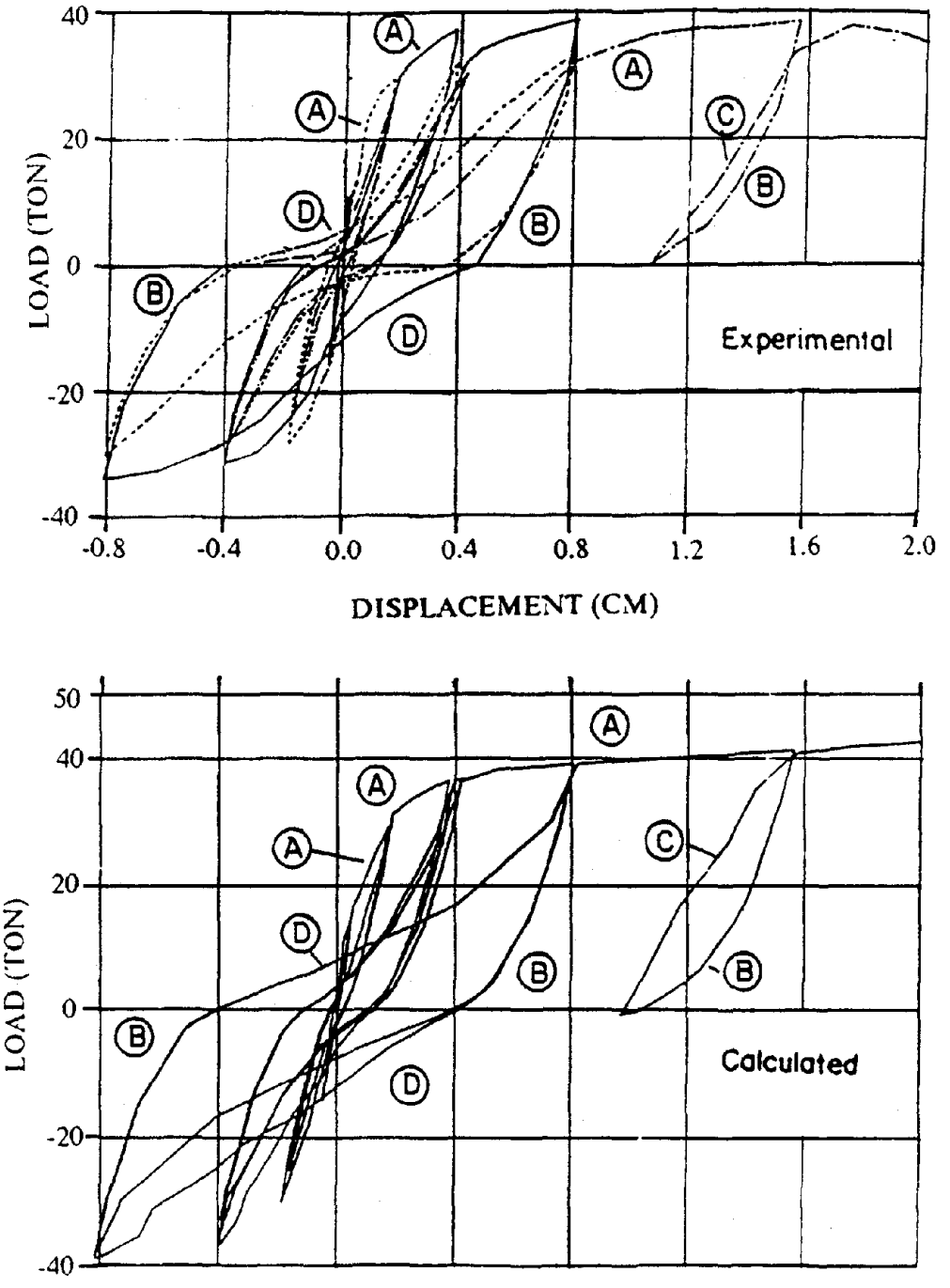

Figure 183. UT Box B6 Comparison of Calculated and Experimental Response, $\alpha = 0.40$ (Experimental Response, Ref. 78)

The calculated reloading loops, after unloading from the same direction as shown in Curve C of Figure 183, are larger than the experimental loops. Similar to the unloading in Curve B of the figure, the reloading curve is strongly influenced by the axial hysteresis model. Curve C in Figure 184 is the axial hysteresis loop for wall #4 that coincides with the calculated reloading loop in Curve C of Figure 183. This axial hysteresis loop is very large. Reducing the reloading stiffness would reduce the size of this axial hysteresis loop and improve the correlation between the calculated and experimental response in Figure 183.

The calculated reloading loops, after unloading from the opposite direction as shown in Curve D of Figure 183, do not pinch as much as the experimental loops. This is partially due to the shear hysteresis model, which has a tendency to underestimate pinching (Chapter IV). However the pinching in the shear hysteresis loops for walls #1 and #2, as shown in Figure 185, appears to be fairly severe. Another cause is the axial hysteresis model's stiffness for reloading after reversal, in Curve D in Figure 184; softening this reloading curve would increase pinching and improve the correlation between the calculated and experimental response.

The bending hysteresis loops for walls #1 and #2 are shown in Figure 186. Note that the bending hysteresis model has large stable loops while the shear hysteresis model has pinched loops. As the axial and bending stiffnesses change, the portion of bending resisted by the wall changes. Thus the moment to shear ratio for walls #1 and #2 is not constant as shown in Figure 187. However, the assumed moment to shear ratio of $M/V = 20$ is a reasonable approximation.

The axial hysteresis loops for walls #1 and #2 are shown in Figure 188. Note that the wall yielded axially, implying that all of the steel in the wall has also yielded. Recall that the axial load was neglected when the moment-shear interaction surface was calculated. If the interaction between axial tension, moment and shear were

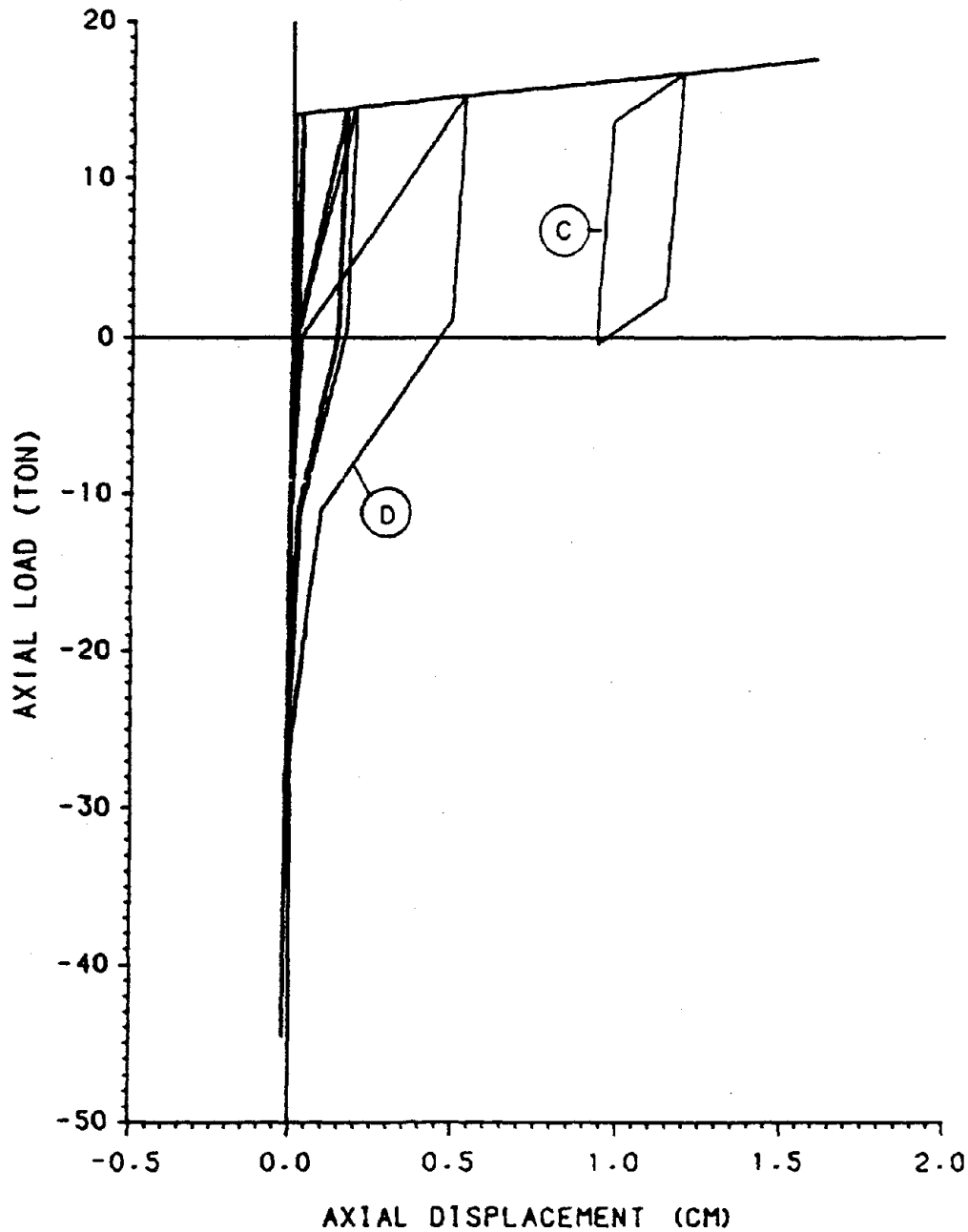

Figure 184. UT Box B6 Axial Hysteresis Loops for Wall #4, $\alpha = 0.40$

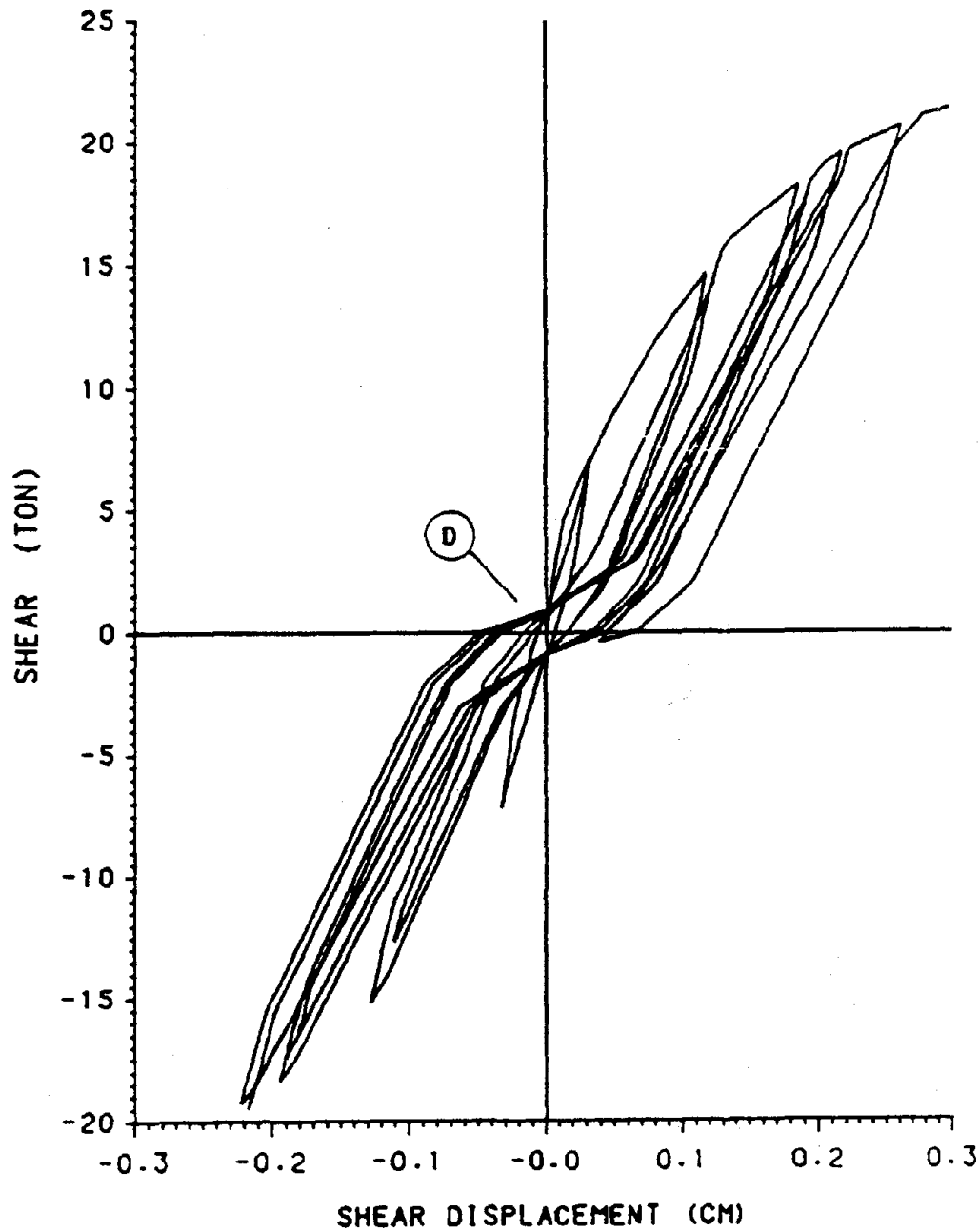

Figure 185. UT Box B6 Shear Hysteresis Loops for Wall #1, $\alpha = 0.40$

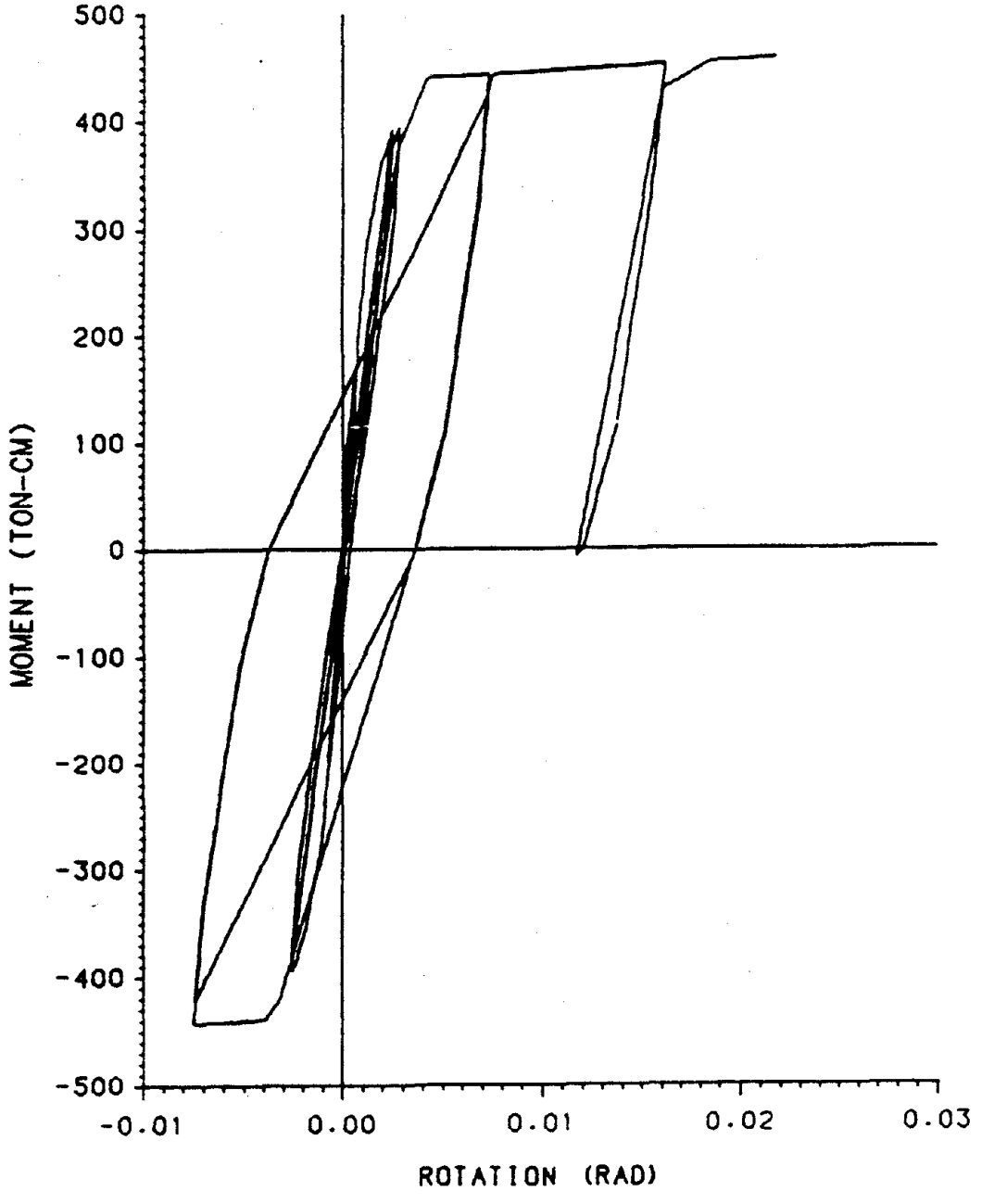

Figure 186. UT Box B6 Bending Hysteresis Loops for Wall #1, $\alpha = 0.40$

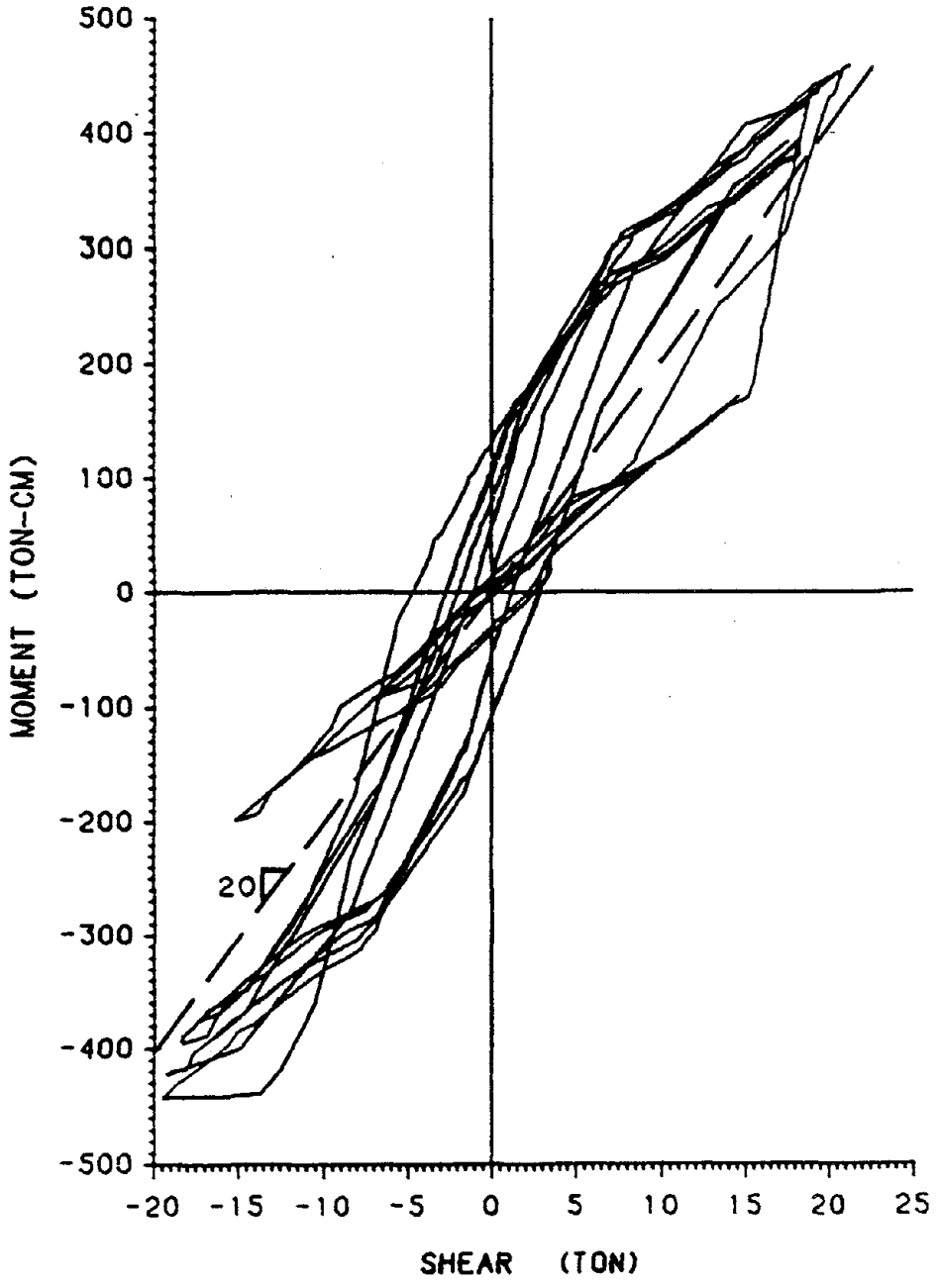

Figure 187. UT Box B6 Moment vs Shear for Wall #1, $\alpha = 0.40$

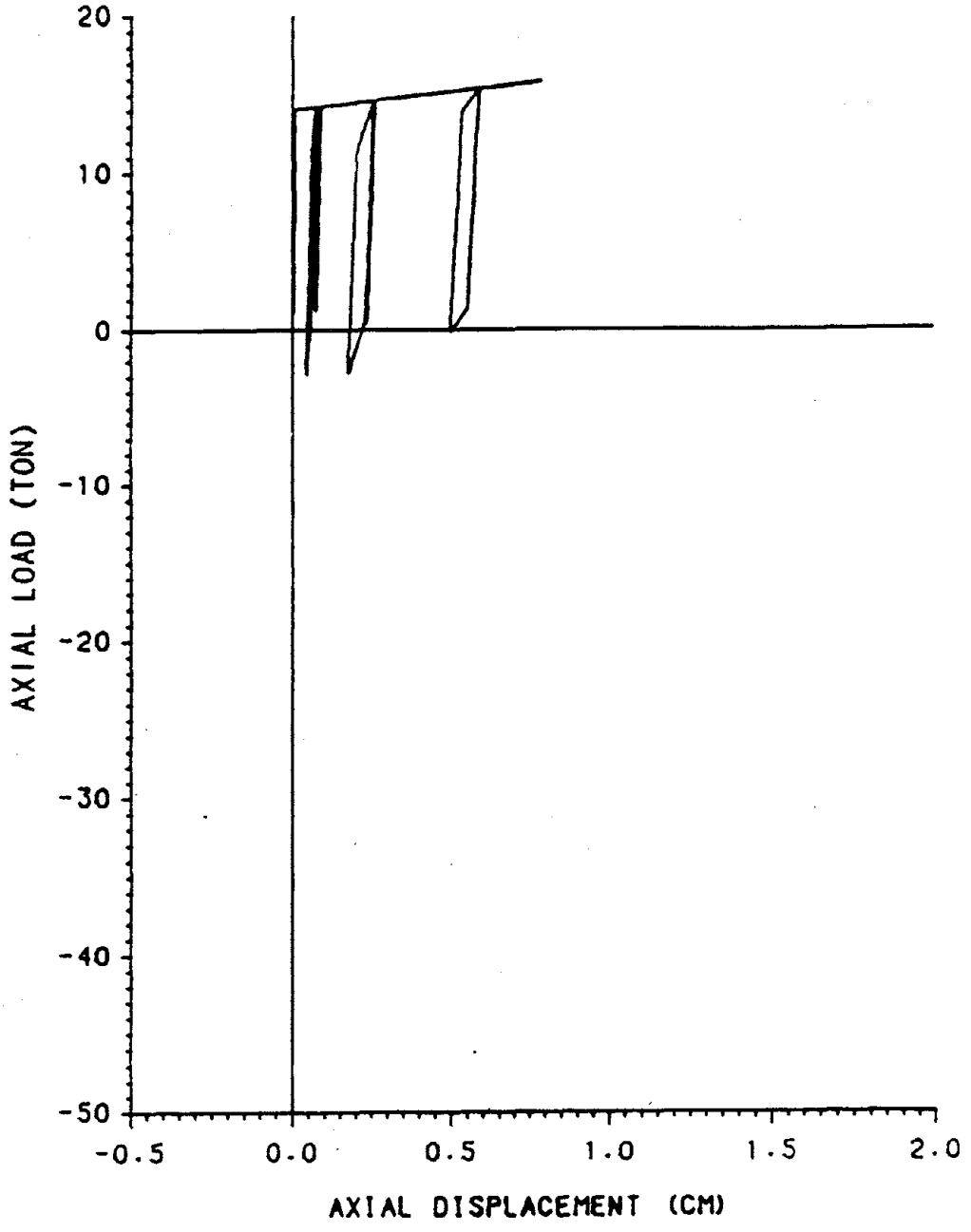

Figure 188. UT Box B6 Axial Hysteresis Loops for Wall #1, $\alpha = 0.40$

considered, the bending and shear stiffnesses would be reduced. For box type buildings, it is apparent that the interaction between axial, moment and shear forces is very important. This topic is recommended for further research.

The axial hysteresis loop for walls #3 is shown in Figure 189. Similar to wall #4, wall #3 has yielded. However since walls #3 and #4 are on opposite sides of the center of rigidity, wall #3 is in compression while wall #4 is in tension.

In summary, the comparison between the experimental response and the calculated response is good. However, deficiencies in several of the axial hysteresis model's rules have been identified. Recall that the axial hysteresis model was developed for boundary columns. Thus a different axial hysteresis model for shear walls needs to be developed. Additionally, the interaction between axial force, bending and shear should be considered.

B. DYNAMIC ANALYSIS

The two-story model box structure, 3D11, was dynamically tested on a shaking table by Bennett, Anderson, Endebrock, et al (3, 30, 31, 33, 34, 35) of the Los Alamos National Laboratory. This box structure was previously introduced in Chapter II, Figure 18. Two layers of 0.5" hail screen are used for the reinforcement with a reinforcing ratio of 0.54%. The hail screen consists of 0.042"ϕ wires 0.5" on center, each way, with a yield point of 42.7 ksi at $\varepsilon = 0.001668$ in/in, and an ultimate stress of 53.1 ksi at $\varepsilon = 0.04$ in/in. The box structure is made of micro concrete, with an ultimate stress of 2.89 ksi at $\varepsilon_0 = 0.0033$in/in, an initial modulus of 2750 ksi, and a tensile strength of 0.42 ksi.

The box structure is attached to a uniaxial shaking table. The direction of motion coincides with the structure's global Y axis as shown in Figure 190. The experimental

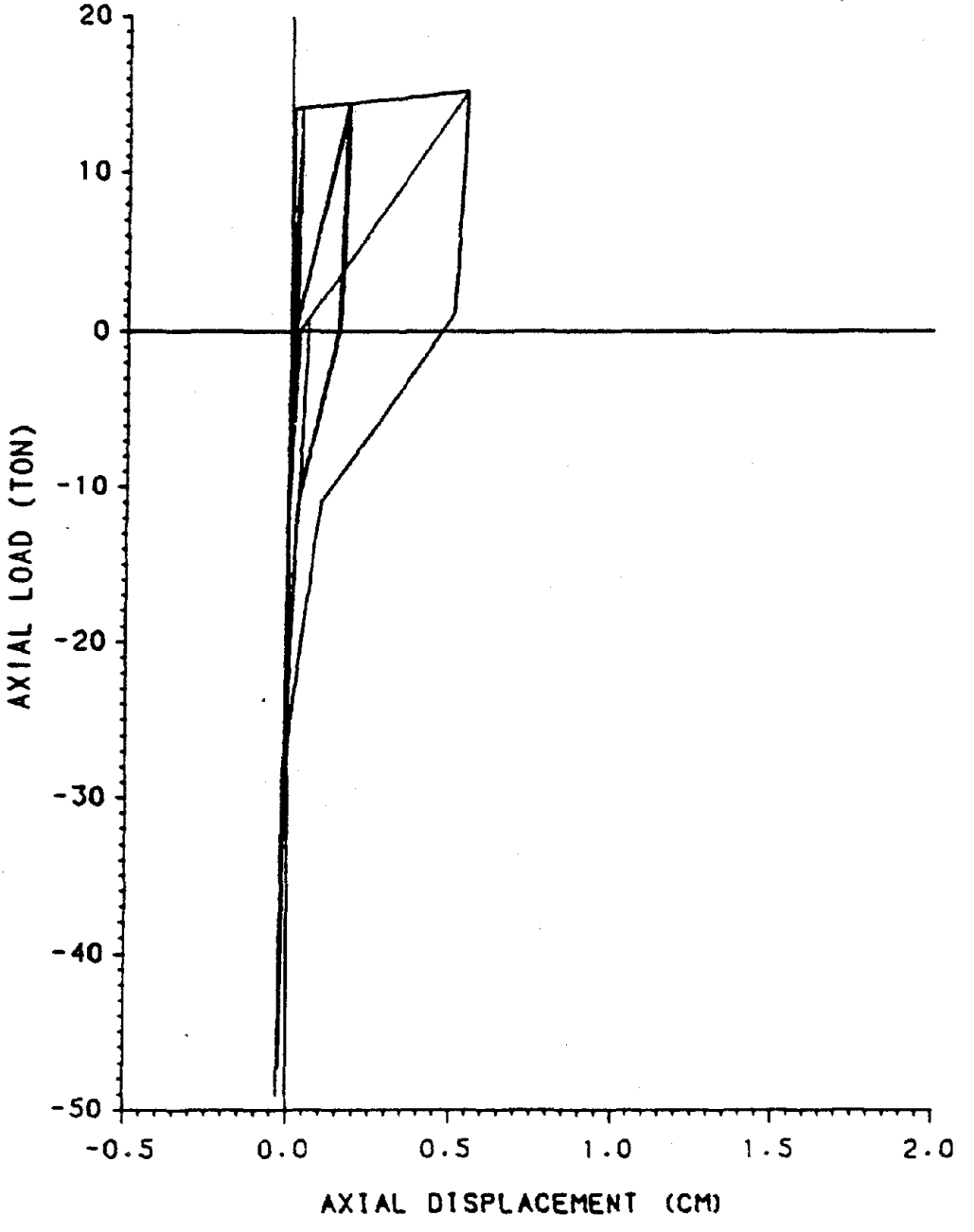

Figure 189. UT Box B6 Axial Hysteresis Loops for Wall #3, $\alpha = 0.40$

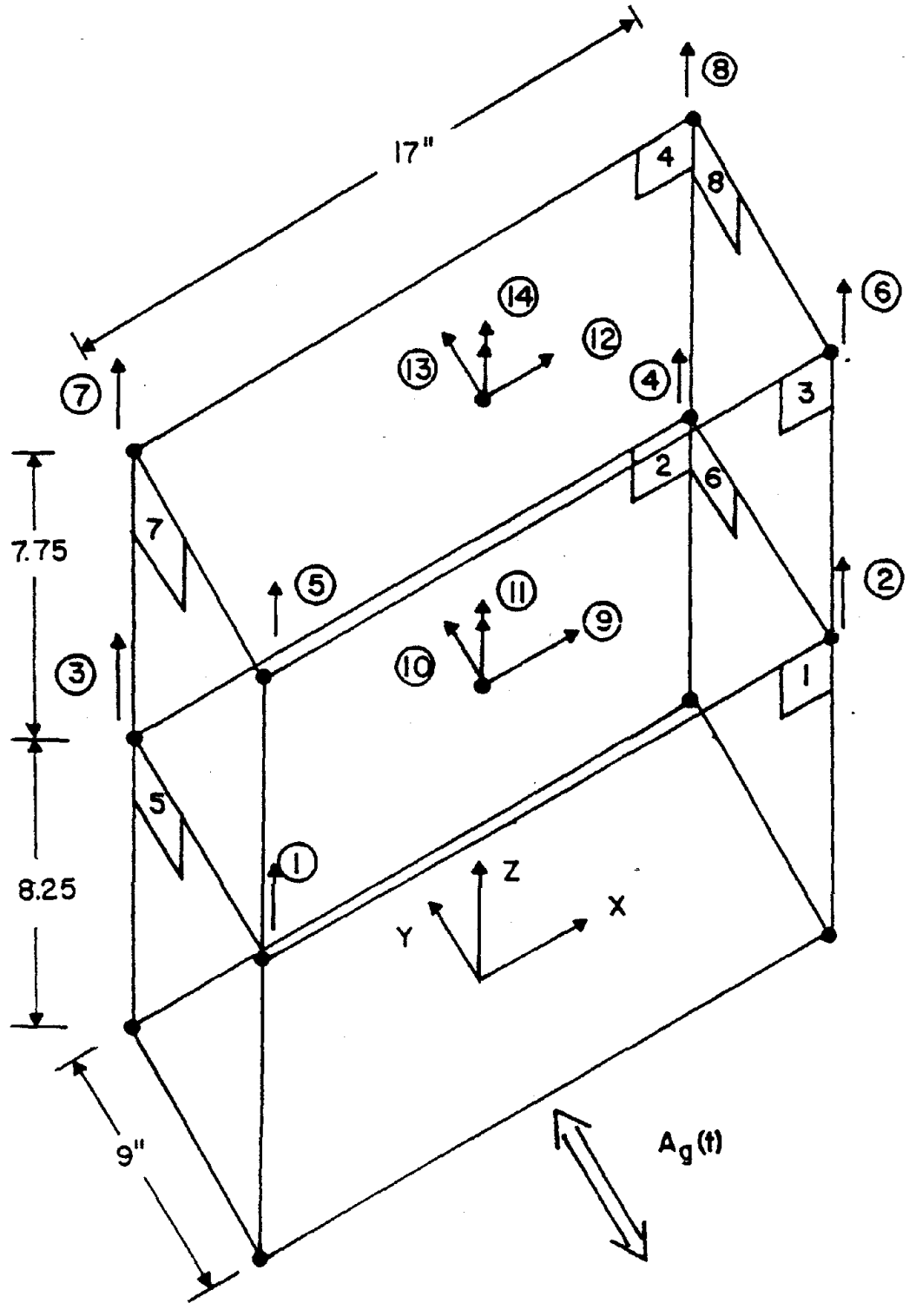

Figure 190. LANL Box 3D11, Degrees of Freedom

response was determined in Section B of Chapter II. The 3D structural model consists of eight shear wall elements. The wall and floor center line dimensions are used for the structural model. Thus the walls are 9″ or 17″ wide, and 7.75″ or 8.25″ tall, depending on their location. The mass center and center of gravity of the structure coincide. The second floor and roof slabs are assumed to be rigid diaphragms. Planar constraints are used at each level to transfer the joint degrees of freedom from the corners to the mass center. An additional weight of 0.23 k is added to both the roof and second floor. These weights are included with the weight of the box structure in the axial loads for the P-Δ forces.

Bending moments about the structure's X axis are resisted by walls #5 to #8 in bending and by walls #1 to #4 in axial tension or compression. Similar to UT box B6, the moment to shear ratios for the walls are estimated by taking ratios of the moments of inertia. Bending and shear backbone curves are generated by the method presented in Chapter II.

Walls #1 and #2 have a height to width ratio of $\frac{h}{w} = \frac{7.75}{17} = 0.43$. For walls with this height to width ratio, the axial strain will not be constant over the width of the wall due to shear lag. Gupta (43) developed an elastic stiffness reduction factor $r_f = \frac{2h}{3w} \leq 1$ for the flanges of box structures. Thus for wall #1, the effective axial stiffness for a unit length member is

$$Ka = \frac{E_c\, w\, t}{l}\left(\frac{2h}{3w}\right) = \frac{2750x17x1}{l}\left(\frac{2x7.75}{3x17}\right) = 13\ 290\ \text{k/in} \qquad (7.3)$$

The stiffness reduction factor was derived for elastic structures, and its direct application to nonlinear structures is inappropriate. Another method to determine the effective axial stiffness is to loosely interpret the effective overhanging flange width criterion for a R/C T-beam with the slab on one side, ACI 8.10.3 (1). This effective width criterion is calibrated to calculate the ultimate strength of T-beams. Thus the

applicability of the criterion for nonlinear analysis is established. The effective overhanging flange width, w_{eo}, is the minimum of 1) one-twelfth of the span length, 2) six times the flange thickness, or 3) one-half the clear distance between beams (1). For wall #1, w_{eo} is the smallest of 1) $\frac{16}{12} = 1.33$ in, where 16 in. is the total height of both stories, 2) $6 \times 1 = 6$ in, or 3) $\frac{14}{2} = 7$ in. Adding 0.5 in. for the width of the web, and multipling by two for both sides as shown in Figure 191, yields

$$w_e = 2(0.5 + w_{eo}) = 2(0.5 + 1.33) = 3.67 \text{ in} \tag{7.4}$$

Thus the effective axial stiffness per unit length of the wall is

$$Ka = \frac{E_c w_e t}{1} = \frac{2750 \times 3.67 \times 1}{1} = 10\,092 \text{ k/in} \tag{7.5}$$

The tensile stiffness and yield point are similarly calculated with an effective width of 3.67 in.

Note that Gupta's effective stiffness is about 30% higher than the ACI criterion. Assuming that wall #1 yields, it is more rational to use the criterion based on ultimate strength (ACI) than the criterion based on elastic behavior (Gupta). Thus the axial stiffness of wall #1 is 10092 k/in. For box 3D11 the effective width criterion is applied to all of the walls.

Recall that the full axial stiffness was used for box UT-B6, which had a height to width ratio of about 1. It is not known whether the shear lag is negligible in box UT-B6 or not. The shear lag problem for walls is very complicated and deserves further study.

The experimentally measured base excitation is used as the input ground motion for the dynamic analysis and is shown in Figure 27. The analysis is performed with a

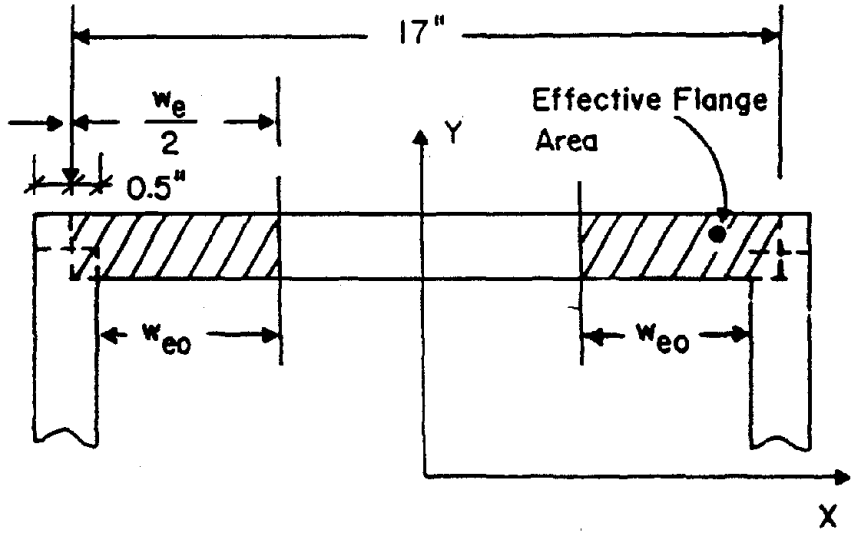

Figure 191. Effective Width for a Box Section Flange

time step of $\Delta t = 0.00001$ second, and a duration of 0.20 seconds. Five percent mass and stiffness proportional damping is assumed. Since the tests are performed on a structural model, the magnitude and duration of the exciting motion have been scaled in accordance with similitude studies.

The calculated and experimental displacements for the roof are compared in Figure 192. Overall the comparison between calculated and experimental displacements is good. The peak calculated and experimental displacements are 0.00173" and 0.00143", respectively. The calculated period is close the the experimental period. Beyond time 0.16 seconds, the calculated amplitude is much greater than experimental amplitude.

The calculated and experimental accelerations are compared in Figure 193. Overall the comparison between the calculated and experimental accelerations is good. The peak calculated and experimental accelerations are $-1.84g$ and $-1.77g$, respectively. Both the calculated and experimental results yield a similar frequency spectrum as shown in Figure 194. A strong 83 hz acceleration signal is observed in both spectra. However, the calculated acceleration is higher at 83 hz than the experimental acceleration, which corresponds to the difference in peak displacements. Between 200 and 300 hz the calculated response is much larger than the experimental response.

The calculated and experimental displacements for the second floor are compared in Figure 195. Overall the comparison between calculated and experimental displacements is fair. From the displacements it can be seen that experimental response has a larger high frequency content than the calculated values.

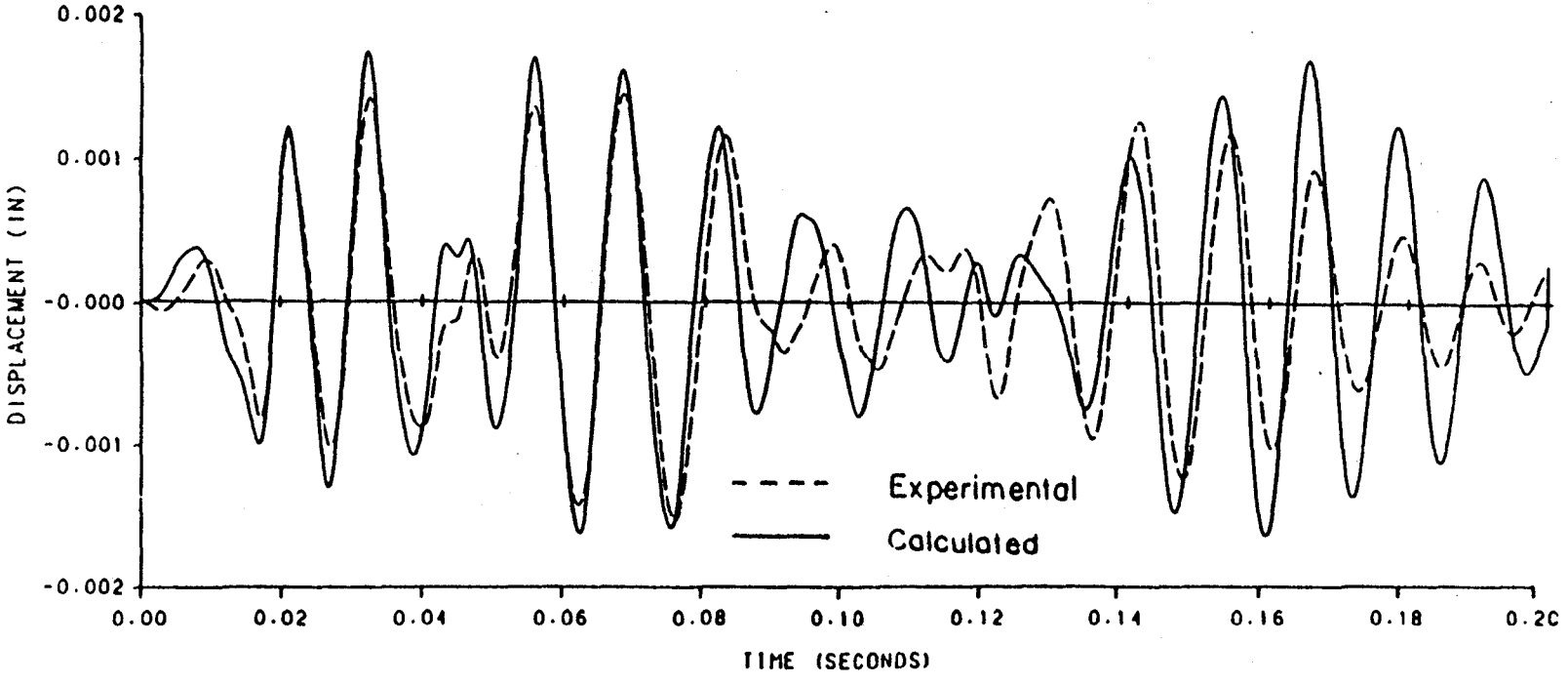

Figure 192. LANL Box 3D11, Comparison of Calculated and Experimental Roof Displacements

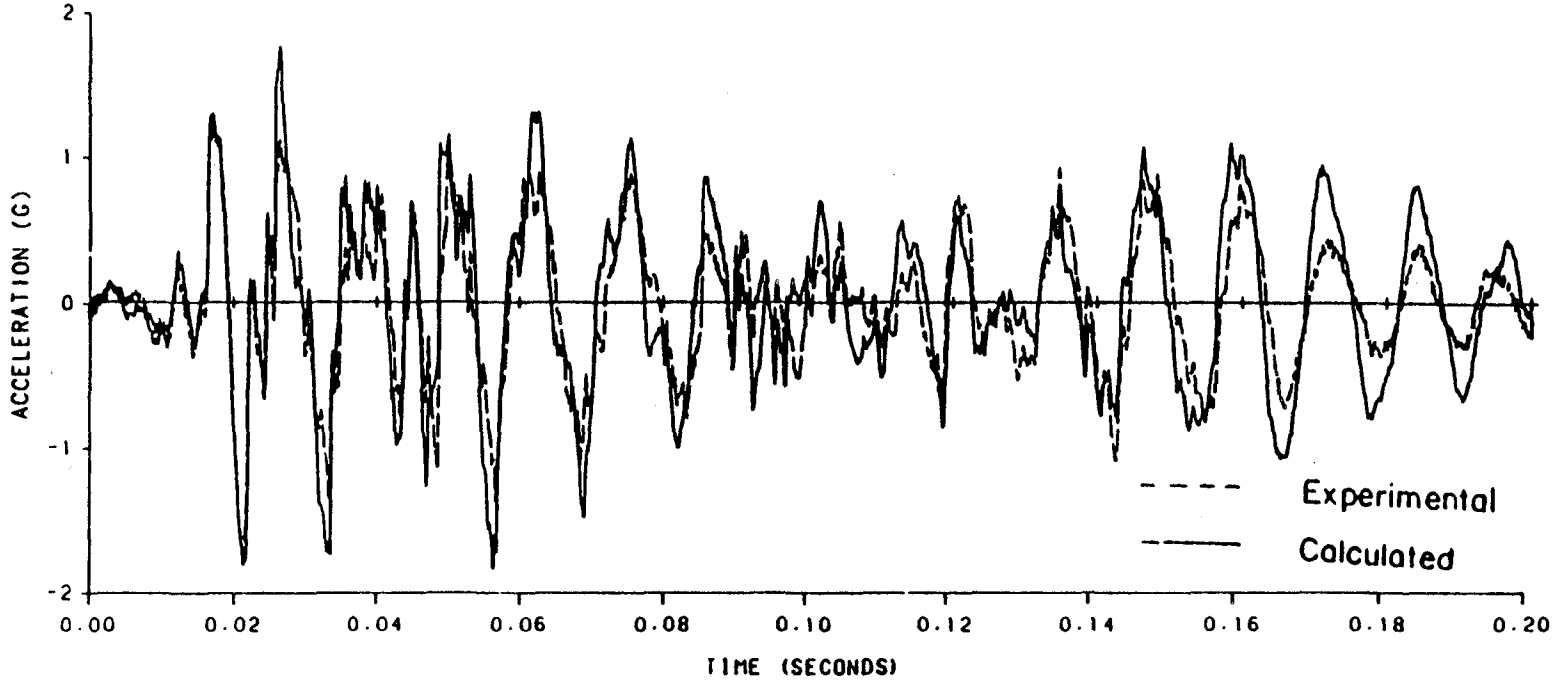

Figure 193. LANL Box 3D11, Comparison of Calculated and Experimental Roof Accelerations

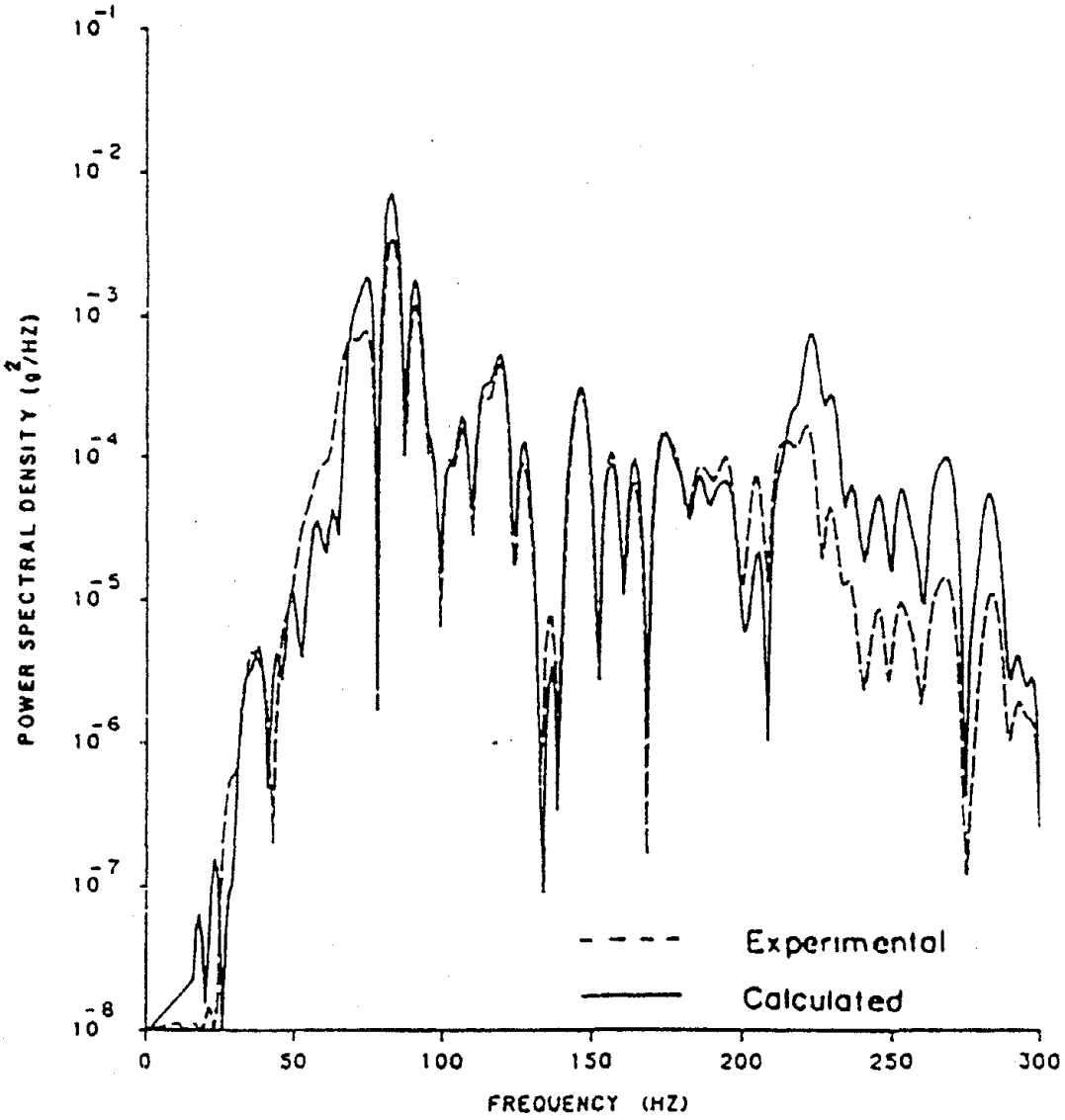

Figure 194. LANL Box 3D11, Comparison of Calculated and Experimental Roof Acceleration PSD

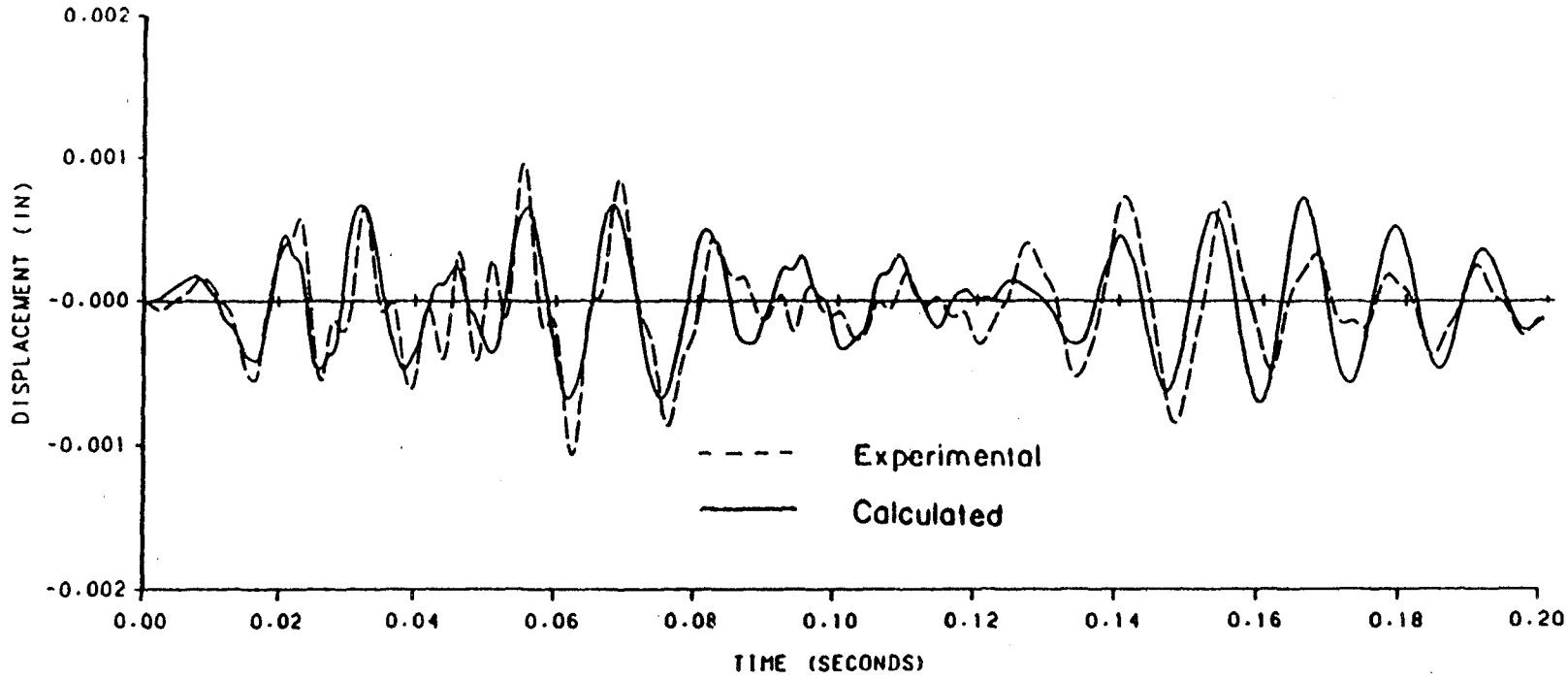

Figure 195. LANL Box 3D11, Comparison of Calculated and Experimental Second Floor Displacements

The calculated and experimental frequency response functions[23] for the roof are compared in Figure 196. The calculated and experimental first mode are at 73 hz and 65 hz, respectively. The calculated and experimental FRF for the second floor are compared in Figure 197. Again the first mode of the calculated and experimental response is at 73 hz and 65 hz, respectively. The calculated second mode is at 280 hz, while the experimental second mode is at 210 hz.

The maximum bending moment in walls #5 and #6 is 0.65 in-k, which is less than the cracking moment of 4.5 in-k. The maximum shear in walls #5 and #6 is 0.175 k, which is less than the cracking shear of 1.8 k. The peak axial loads in walls #1 and #2 is 0.39 k, which is less than the yield force of 0.89 k. Thus the response of LANL box 3D11 is elastic.

The moment to shear ratio for walls #5 and #6 is shown in Figure 198. The average moment to shear ratio appears to be about 3.6″. A moment to shear ratio of 2″ was used to develop the bending and shear backbone curves, based on the width of walls #1 and #2 being fully effective. The analysis is based on the width of walls #1 and #2 being partially effective. The bending and shear stiffness of NCKU Wall SW6 is insensitive to the moment to shear ratio when the loading is below the cracking load as shown in Section B of Chapter III, Figures 45 and 46. Similarly, the shear walls in this structure are also insensitive to the moment to shear ratios when the loading is below the cracking load. Thus the assumed moment to shear ratios for the backbone curves are not revised. If this structure is subjected to larger lateral loadings and the walls behave nonlinearly, then the moment to shear ratio and the backbone curves must be modified.

---

[23] The frequency response function (FRF) is the ratio of a structure's response to its base acceleration in the frequency domain and is calculated by Equation A.38 of Appendix A.

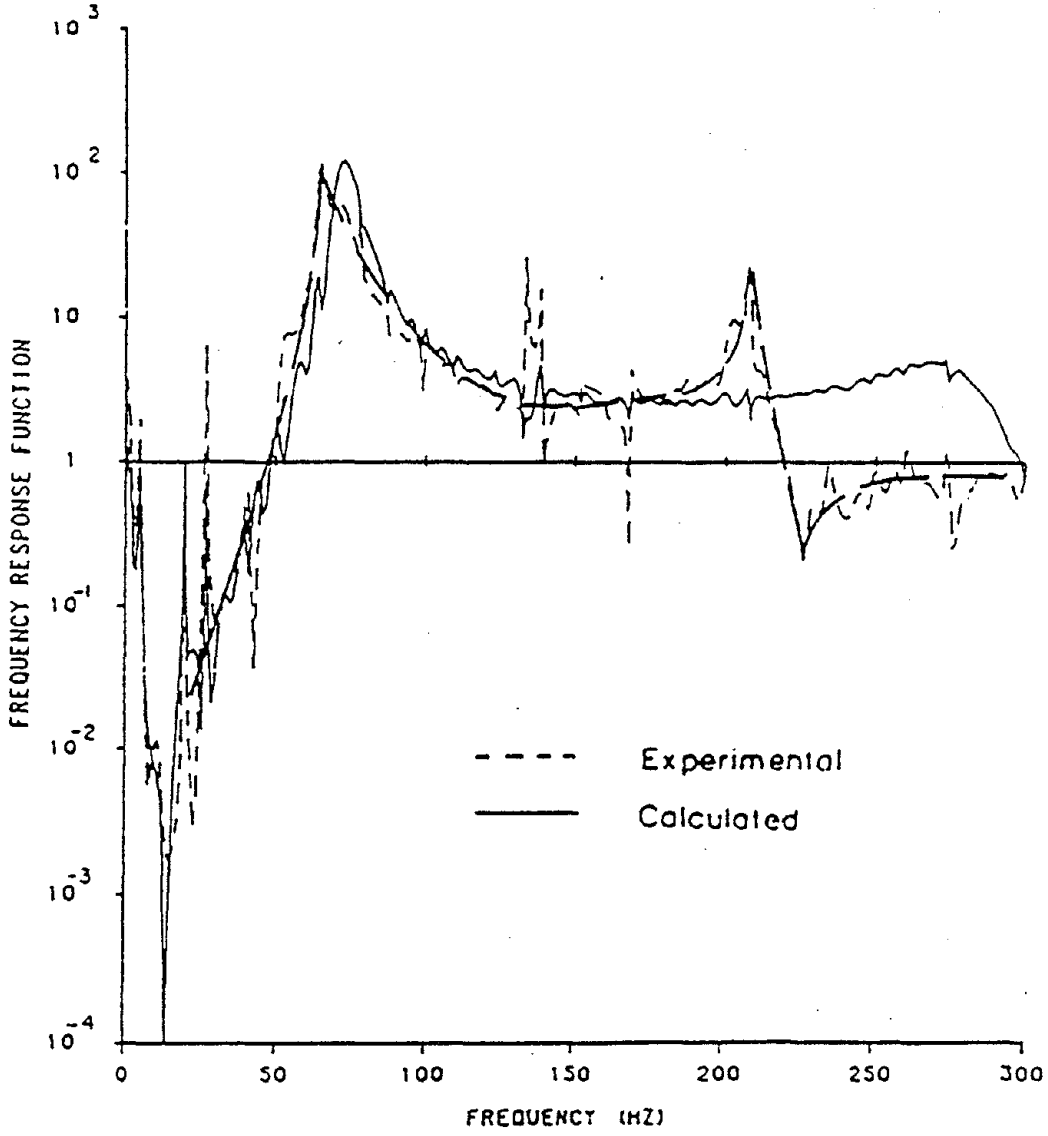

Figure 196. LANL Box 3D11, Comparison of Calculated and Experimental Roof Acceleration FRF

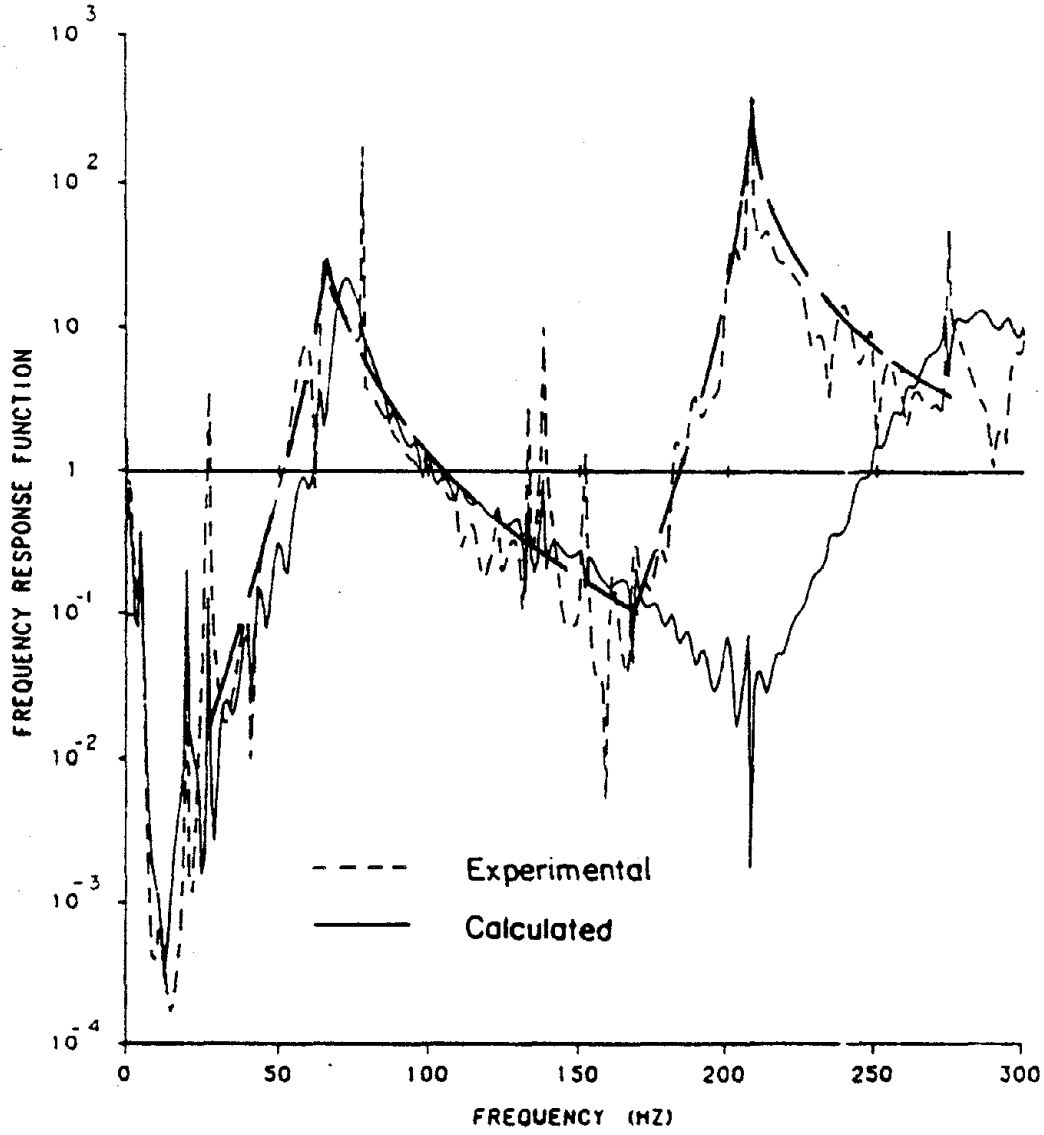

Figure 197. LANL Box 3D11, Comparison of Calculated and Experimental Second Floor Acceleration FRF

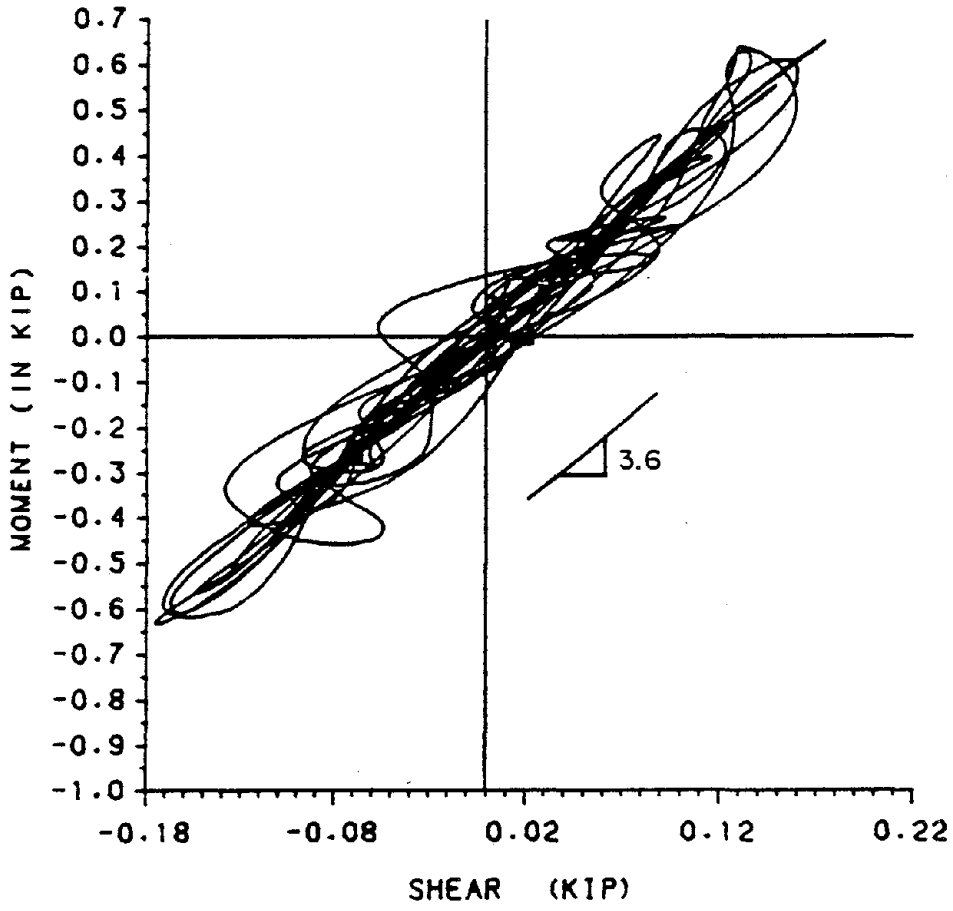

Figure 198. LANL Box 3D11, Calculated Moment vs. Shear for Walls #5 and #6

VIII. SUMMARIES AND CONCLUSIONS

The objectives of this study are to develop nonlinear hysteresis models of low-rise R/C shear walls for system analysis and to study the static and seismic response behavior of typical low-rise buildings with isolated shear walls as well as the box type structures. The behavior parameters studied include the separation of bending and shear deformations, ductility factors, excursion ratios, response reduction factors, and damage indices. The effects of multicomponent seismic input on the behavior parameters are also investigated. This chapter consists of the summaries of the work along with pertinent observations and conclusions.

A. NONLINEAR SHEAR WALL ELEMENT

1. Monotonic Load-Deformation Behavior. An analytical method for calculating the monotonic load-deformation response of isolated shear walls is developed in Chapter III. This method considers the coupling behavior between bending and shear by combining the bending and shear strains on a differential element in the wall. The bending strain is assumed to vary linearly across the width of the wall and the shear strain is assumed to be constant over the entire wall. The horizontal expansion of the NCKU walls having a height to width of 0.50 is found to be from 0.1 to 0.5 times the vertical expansion. Thus horizontal expansion of the walls is neglected. Principal strains are determined from the longitudinal and shear strains on the wall. The angle of the principal tensile strain is from 30° to 60° above the horizontal. This corresponds to the observed angle of cracking in the walls.

Principal stress-strain models are used to determine the concrete stresses on a rotated plane. The Vecchio-Collins stress-strain model is used for compressive

concrete stresses and a graded tensile model is used for tensile concrete stresses. The longitudinal and shear stresses are determined from the principal stresses.

Bending and shear stresses on the wall for an assumed strain distribution are summed to yield the moment and shear on the wall. An iterative procedure modifies the strain distribution until the axial load on the wall equals the applied loadings. The moment and shear on the wall, for different strain distributions, form the moment-shear interaction surface. From these interaction surfaces one can observe that shear reduces the bending capacity, ductility, and stiffness. Similarly, bending reduces the shear capacity, ductility, and stiffness. A nondimensional parameter ψ is developed to measure the relative influence of bending and shear for a given wall with a moment to shear ratio. For the walls studied, ψ varies from $\psi = 7.6°$ to $79.2°$, where $\psi = 0°$ indicates pure bending and $\psi = 90°$ indicates pure shear.

The experimental curvature distributions on the NCKU walls are observed to be irregular or inverted in some walls due to the interaction between bending and shear in the hinging region of the wall. Thus an equivalent moment diagram that reflects the average curvature over the hinging region is used with the analytical moment-shear interaction surface to determine the bending, shear and total deformation of an isolated wall subject to monotonic loading.

The experimental displacements of the NCKU walls are analyzed to separate bending and shear deformations from the total deformations. For the NCKU walls with a height to width ratios ranging from 0.50 to 0.75, the bending deformation typically ranges from 40% to 60% of the total deformation.

The monotonic load-deformation curves of bending and shear are typically linear up to the cracking load. After the cracking load, the stiffness gradually decreases. A gradual yielding behavior is observed. Average observed bending and shear ductilities

are 10.39 and 11.0, respectively, and the average observed bending and shear excursion ratios are 19.2 and 25.0, respectively, for five of the NCKU walls.

The calculated monotonic load-deformation curves are verified by comparison with the experimental results of 27 shear walls. Height to width ratios for the walls[24] range from 0.50 to 2.40. Four wall cross sections are investigated: 1) rectangular walls with nearly uniform reinforcement, 2) rectangular walls with extra reinforcing steel at the edge of the wall, 3) barbell cross sections (walls with square boundary columns), and 4) walls with flanges. Web reinforcement ratios vary from 0.28% to 0.78% vertically, and from 0 to 1.14% horizontally. Flange reinforcement, when used, varies from 1.47% to 6.4%. Concrete strengths range from 2760 psi to 7780 psi, and the yield stresses of the reinforcing steel range from 68 ksi to 80 ksi. Overall the comparison of the calculated and experimental response is good.

The influences of several parameters on the walls' monotonic load-deformation behavior are:

- Boundary elements increase the bending capacity more than the shear capacity. Thus low-rise walls with boundary elements are often dominated by shear deformation.
- As the vertical web reinforcement ratio is increased, the walls gained strength and lost ductility.
- The horizontal web steel reduces the horizontal expansion in the wall. Omission of the horizontal web steel reduces the ductility.
- Reducing the height to width ratio of a wall can significantly reduce the effect of bending deformation on the wall's behavior.

---

[24] NCKU and the PCA walls. The height to width ratio of the NCKU walls range from 0.50 to 0.75, while the height to width ratio of the PCA walls range from 0.50 to 2.40.

2. Cyclic and Earthquake-Type Load-Deformation Behavior. The semi-empirical bending and shear hysteresis models are developed in Chapter IV. The cyclic and earthquake-type load-deformation behaviors of five NCKU walls are studied to determine characteristics of bending and shear hysteresis loops. Several of the more prominent features of the bending and shear hysteresis loops are:

- Both the bending and shear hysteresis loops have highly nonlinear backbone curves without well defined break points.
- The unloading branch for both bending and shear hysteresis loops is highly nonlinear, and the unloading stiffnesses decrease with increasing levels of peak displacements.
- When the wall is cycled at a constant load, near the maximum past load, the deformations tend to increase with each cycle. When the wall is cycled well below the maximum past load, the deformations do not increase with each load cycle.
- The reloading curves for the shear hysteresis loops are dominated by pinching. The degree of pinching increases for larger values of peak displacements.
- The reloading curves for the bending hysteresis loops do not pinch.
- The energy absorption increases with increasing peak displacements. The energy absorption of the shear hysteresis loops is less than the bending hysteresis loops because of pinching.

These observations have been synthesized into semi-empirical bending and shear hysteresis models. The monotonic load-deformation relationships are also utilized in developing these models.

The hysteresis rules are used to determine the bending and shear stiffnesses under cyclic and earthquake type loadings. The calculated load-deformation responses and strain energies compare favorably with the experimental results

3. Shear Wall Stiffness Element and System Formulation. The formulation of the shear wall stiffness element based on hysteresis models and the system formulation are given in Chapter V.

The shear wall stiffness element has bending, shear and axial deformations. The bending and shear deformations are in the plane of the wall. The bending stiffness out of the plane of the wall is neglected. The wall's geometric stiffness, however, includes both in plane and out of plane deformations, which is used mainly for 3D structural systems.

The system formulation has the following attributes: 1) joint based degrees of freedom, 2) rigid body and planar constraints, 3) incremental nonlinear static solution, 4) unbalanced load correction for overshooting, 5) incremental nonlinear dynamic solution, 6) mass and stiffness proportional damping, 7) condensation to reduce the size of a dynamic problem, 8) energy balance, 9) damage index, and 10) ductility and excursion ratio for various definitions of displacement, constant strain energy, and variable strain energy.

B. RESPONSE STUDIES OF LOW-RISE BUILDINGS WITH ISOLATED SHEAR WALLS

Typical symmetric and unsymmetric two-story isolated shear wall structures are studied in Chapter VI. Both buildings are made of 30′ shear walls that have a height to width ratio of 0.5 and 0.4 on the first and second floors, respectively. The shear bending influence angle is $\psi = 33.6^\circ$ and $\psi = 21.5^\circ$ for the second and first floor walls, respectively. Thus bending is the predominant component of deformation in these buildings. The fundamental periods for the symmetric and unsymmetric buildings are 0.155 second and 0.188 second, respectively.

A total of 14 elastic and 42 nonlinear dynamic analyses are performed with different earthquake ground motions, numbers of horizontal ground motion components, and intensities of ground motions.

During a typical nonlinear seismic analysis, a shear wall experiences several large amplitude load cycles, and the remainder of the loading is on small amplitude loops. Thus the small amplitude hysteresis loops are important.

The peak base shear, displacement, ductility and excursion ratio of the symmetric building are not affected by the inclusion of the second horizontal component of ground motion, because the response in the two directions is weakly coupled. Contrarily, the unsymmetric building's peak displacement, base shear, ductility and excursion ratio are significantly influenced by the addition of the second component of ground motion because the response in the two directions is strongly coupled. This is observed for both the elastic and nonlinear responses. Whether the one-component or two-component ground motion produces the maximum response in the symmetric and unsymmetric buildings, depends on the interaction of the ground motions and the relative distance between and the relative location of the mass center and the rigidity center at each floor of the structure.

The nonlinear analysis of a one-component ground motion on the unsymmetric building yields an unrealistic distribution of shears in the walls. Thus the nonlinear dynamic response of an unsymmetric structure subject to a one-component ground motion should be used with extreme caution. Since one-component ground motions do not occur in nature, analyses with two-component ground motions are preferred.

The elastic response to the 1940 El Centro and 1952 Taft earthquakes is greater than the response to the 1985 Mexico earthquake. However, the peak nonlinear response at higher levels of damage is similar for all three earthquakes.

For the symmetric building, the damage index decreases with the inclusion of the second ground motion because of the method used to average the damage indices in individual walls. The total damage of the structure with two-components of ground motion is equal to or greater than the structure's damage with one-component of ground motion. Typically the unsymmetric building suffers more damage than the symmetric building as evident by ductilities and damage indices.

The studies of code parameters R and C_d indicate that the response modification factor, R, is dependent on the building type, earthquake ground motion, orientation of ground motion, number of components, and level of damage in the building. For the two buildings studied, the R value of 4.5 recommended by the NEHRP (55) is consistent with the calculated values for the 1940 El Centro and 1952 Taft earthquakes. The calculated R value for the 1985 Mexico earthquake is close to 1. The deflection amplitude factor, C_d, increases with damage index. The C_d value of 4 recommend by the NEHRP is slightly larger than the calculated values.

Additional studies are required before the response modification factor for reinforced concrete shear walls can be determined. These should include buildings with a wider range of geometries, natural frequencies, and shear wall height to width ratios. A family of earthquakes records that are based on the code response spectra should be used. The two-component ground motions are preferred over one-component ground motion. Additionally, the angle of the ground motion to the building should be varied to determine the range of response modification factors for each combination of building and ground motion.

C. RESPONSE STUDIES OF LOW-RISE BOX TYPE BUILDINGS

A favorable comparison between the calculated and experimental response of a one-story box-type structure subjected to static cyclic loading is given in Chapter VII.

The axial hysteresis model is shown to have a very strong effect on the structure's response. This is because the overturning moment of a box-type structure is resisted by both bending in the plane of the shear wall, and axial forces in walls on opposite sides of the building's center of rigidity. The axial hysteresis model is based on the 7-story full scale testing structure with boundary columns; several modifications to the model are proposed for box-type structures.

A favorable comparison between the calculated and experimental seismic response of a two-story box-type structure subject to a scaled earthquake ground motion is also presented in Chapter VII. This box-type structure is dynamically tested on a unaxial shaking table at LANL, and the accelerations at the base and each floor were measured by accelerometers. The analytical studies include the removal of errors from the experimentally measured accelerations, and the integration of the accelerations to yield displacements. The calculated and experimental results of the first mode are 73 hz and 65 hz, respectively; while the calculated and experimental results for the second mode are 280 hz and 210 hz, respectively.

BIBLIOGRAPHY

1. ACI Committee 318, Building Code Requirements for Reinforced Concrete (ACI 318-83) (Revised 1986), American Concrete Institute, Detroit, 1986.

2. Aktan, A. E., and Bertero, V. V., "RC Structural Walls: Seismic Design for Shear," Journal of the Structural Division, ASCE, Vol. 111, No. 8, August, 1985.

3. Anderson, C. A., Bennett, J. G. and Dove, R. C., "Seismic Category-I Structures Program: Current Status and Program Plan for FY84-FY85," Appendix A, Los Alamos National Laboratory.

4. Anderson, F. E., Hansen, R. J., Murphy, H.L., Newmark, N. M., and Merit, P. W., Design of Structures to Resist Nuclear Weapons Effects, American Society of Civil Engineers, 1964.

5. Ang, A. H-S., and Park, Y. J., "Reliability and Damage Analysis Under Extreme Natural Hazards," Proceedings of the CCNAA-AIT Joint Seminar on Research for Multiple Hazards Mitigation, NCKU, Taiwan, 1984, pp. 150-163.

6. Antebi, J., Utku, S., and Hansen J. R., "The Response of Shear Walls to Dynamic Loads," MIT Department of Civil and Sanitary Engineering, Cambridge, Mass., August 1960.

7. Barda, F., Hanson, J. M., and Corley, W. G., "Shear Strength of Low-Rise Walls with Boundary Elements," PCA Research and Development Bulletin RD043D, Portland Cement Association, Skokie Ill., 1976, 19 pages.

8. Barda, F., Hanson, J. M., and Corley, W. G., "An Investigation of the Design and Repair of Low-Rise Shear Walls," PCA Research and Development Bulletin RD035D, Portland Cement Association, Skokie Ill., 1976, 5 pages.

9. Benjamin, J. R., and Williams, H. A., "The Behavior of One-Story Reinforced Concrete Shear Walls," Journal of the Structural Division, ASCE, Vol. 83, No. ST3, May 1957, pp. 1254-1 to 1254-49.

10. Berg, G. V., and Housner, G. W., "Integrated Velocity and Displacement of Strong Earthquake Ground Motion," Bulletin of the Seismological Society of America, Vol. 51, No. 2, April, 1961, pp. 175-189.

11. Burden, R. L., Faires, D. J., and Reynolds, A. C., Numerical Analysis, Second Edition, Prindle, Webber & Schmidt, 1981.

12. Cardenas, A. E., and Magura, D. M., "Strength of High-Rise Shear Walls - Rectangular Cross Sections," Response of Multistory Concrete Structures to Lateral Forces, SP 36-7, American Concrete Institute, Detroit, 1973, pp. 119-150.

13. Cardenas, A. E., Hanson, J. M., Corley, W. G., and Hognestad, E., "Design Provisions for Shear Walls," PCA Research and Development Bulletin RD02801.D, Portland Cement Association, Skokie Ill., 1975, 11 pages.

14. Cardenas, A. E., Russell, H. G., and Corley, W. G., "Strength of Low-Rise Structural Walls," Reinforced Concrete Structures Subject to Wind and Earthquake Forces, SP 63-10, American Concrete Institute, Detroit, 1980, pp. 221-241.

15. Cheng, F. Y., "Dynamic Response of Nonlinear Space Frames by Finite Element Methods," Symposium on International Association for Shell Structures, Tokyo and Kyoto, Japan, pp 817-826, 1972.

16. Cheng, F. Y., "Inelastic Analysis of 3-D Mixed Steel and Reinforced Concrete Seismic Building Structures," Journal of Computers and Structures, Vol 13, pp 189-196, 1981.

17. Cheng, F. Y. and Ger, J. F., "Maximum Response of Buildings to Multi-Seismic Input," Dynamics of Structures, ASCE, pp 397-410, 1987.

18. Cheng, F. Y. and Ger, J. F., "Translational-Torsional Spectral Method and Maximum Response for Six-Component Seismic Input," Proceedings of the Korea-Japan Joint Seminar on Engineering Technologies in Structural Engineering and Mechanics, pp 334-345, 1988.

19. Cheng, F. Y. and Juang, D. S., "Assessment of Various Code Provisions Based on Optimum Design of Steel Structures," International Journal of Earthquake Engineering and Structural Dynamics, Vol. 16, pp 45-61, 1988.

20. Cheng, F. Y., and Kitipitayangkul, P., "Multicomponent Earthquake Analysis of Mixed Structural Systems," U.S.A.-Japan Seminar on Composite Structures and Mixed Structural Systems; Developments in Composite and Mixed Construction (Ed. Ben Kayto and Le-Wu Lu) Gihodo Shuppan Co., Ltd., Tokyo, pp 337-347, 1980.

21. Cheng, F. Y., and Kitipitayangkul, P., "Investigation of the Effect of 3-D Parametric Earthquake Motions on the Stability of Elastic and Inelastic Building Systems," Technical Report prepared for the National Science Foundation. Available at the U.S. Department of Commerce, National Technical Information Service, Springfield, VA 22151, PB80-176936 (392 pages) 1977.

22. Cheng, F. Y., and Mertz, G. E., "Recent Studies of Nuclear Power Plant Auxiliary Buildings Subjected to Seismic Excitations," Proceedings of the CCNAA-AIT Joint Seminar on Research and Application for Multiple Hazard Mitigation, Taipei, Taiwan, April 1988.

23. Cheng, F. Y., and Mertz, G. E., "Hysteresis Models of Low-Rise Shear Walls with Coupled Bending and Shear Deformations," Proceedings of 10th International Conference on Structural Mechanics in Reactor Technology, August 1989.

24. Cheng, F. Y., and Oster, K. B., "Ultimate Instability of Earthquake Structures," Journal of the Structural Division, ASCE, Vol. 102, pp 961-972, 1976.

25. Cheng, F. Y., and Oster, K. B., "Effect of Coupling Earthquake Motions on Inelastic Structural Models," International Symposium on Earthquake Structural Engineering, Proceedings, Vol 1, pp 107-126, 1976.

26. Cheng, F. Y., and Oster, K. B., "Dynamic Instability and Ultimate Capacity of Inelastic Systems Parametrically Excitated by Earthquakes-- Part II," Technical Report prepared for the National Science Foundation. Available at the U.S. Department of Commerce, National Technical Information Service, Springfield, VA 22151, PB261097/AS (313 pages) 1976.

27. Cheng, F. Y. and Truman, K. Z., Optimum Design of Reinforced Concrete and Steel 3-D Static and Seismic Building Systems with Assessment of ATC-03,Final Report Series 85-20 for the National Science Foundation. Available at the U.S. Department of Commerce, National Technical Information Service, Springfield, VA 22151, PB87-168564/AS (414 pages) 1985.

28. Converse, A. M., Brady, A. G., and Joyner, W. B., "Improvmemts in Strong-Motion Data Processing Procedures", Proceedings of the Eight World Conference on Earthquake Engineering, Vol. II, 1984, pp. 143-148.

29. Cooley, J. W., Lewis, P. A. W., and Welch, P. D., IEEE Transactions and Education, Vol. E-12, No. 1, 1969, pp. 27-34.

30. Dove, R.C., Bennett, J.G., "Scale Modeling of Reinforced Concrete Category I Structures Subjected to Seismic Loads," Los Alamos National Laboratory Report, NUREG/CR-4474, 1986. ASCE, Vol. 112, No. 7, July, 1986.

31. Dove, R.C., Endebrock, E.G., Dunwoody, W.E., and Bennett, J.G., "Seismic Test on Models of Reinforced Concrete Category I Buildings," Proceedings of 8th International Conference on Structural Mechanics in Reactor Technology, Brussels, 1985.

32. Emori, K., and Schnobrich, W. C., "Inelastic Behavior of Concrete Frame-Wall Structures," Journal of the Structural Division, ASCE, Vol. 107, No. ST1, January, 1981.

33. Endebrock, E. G., Dove, R. C., and Anderson, C. A., "Seismic Category I Structures Program," Proceedings of the Twelfth Water Reactor Safety Research Information Meeting, National Bureau of Standards, Bethesda, Maryland, 1984.

34. Endebrock, E. G., Dove, R. C., and Anderson, C. A., "NRC Experimental / Analytical Program for Investigating Margins to Failure of Category I Reinforced Concrete Structures," Nuclear Engineering and Design, Vol. 69, 1982, pp. 169-178.

35. Endebrock, E. G., and Dove, R. C., "Nonlinear Seismic Response of Small-Scale Reinforced Concrete Shear Wall Structures," Proceedings of 7th International Conference on Structural Mechanics in Reactor Technology, Vol. K(a), 1983, pp. 259-266.,

36. Fintel, M., et al, Handbook of Concrete Engineering, Van Norstrand Reinhold, Second Edition, 1985.

37. Fiorato, A. E., Oesterle, R. G., and Carpenter, J. E., "Reversing Load Test on Five Isolated Structural Walls," International Symposium on Earthquake Structural Engineering, St. Louis Mo., Aug 1976, pp. 437-453.

38. Fiorato, A. E., Oesterle, R. G., and Corley, W. G., "Behavior of Earthquake Resistant Structural Walls Before and After Repair," ACI Journal, 80-39, Septermber-October 1983, pp. 403-413.

39. Galletly, G. D., "Behavior of Reinforced Concrete Shear Walls Under Static Load," MIT Department of Civil and Sanitary Engineering, Cambridge, Mass., August 1952.

40. Ghosh, S. K., and Fintel, M., "Effects of Sectional Shape on the Strength and Ductility of Slender Structural Walls in Earthquake-Resistant Multistory Buildings," International Symposium on Earthquake Structural Engineering, St. Louis Mo., Aug 1976, pp. 1181-1193.

41. Gilbert, R. I., and Warner, R. F., "Tensile Stiffening in Reinforced Concrete Slabs," Journal of the Structural Division, ASCE, Vol. 104, No. ST12, December, 1978, pp. 1885-1990.

42. Gulkan, P., "Response and Energy-Dissipation of Reinforced Concrete Frames Subject to Strong Base Motions," Structural Research Series No. 377, University of Illinois, 1971.

43. Gupta, A. K., "Modeling of Shear Wall Buildings," Nuclear Engineering and Design, Vol. 79, 1984, pp. 69-80.

44. Hiraishi, H., "Analytical Study on Load versus Deformation Relationship of Flexural Type Shear Walls," Report to the Joint Technical Coordinating Committee, U.S.-Japan Cooperative Research Program, 1982.

45. Hiraishi, H., "Evaluation of Shear and Flexural Deformations of Flexural Type Shear Walls," Proceedings of the Eighth World Conference on Earthquake Engineering, San Francisco, Ca., July 1984, Vol. V, pp. 677-684.

46. Hsu, T. T. C., and Mo, Y. L., "Softening of Concrete in Low-Rise Shear Walls," University of Houston, Civil Engineering Department Research Report UHCE 84-8, Nov 1984, 49 pages.

47. Hsu, T. T. C., and Mau, S. T., "Shear Design and Analysis of Low-Rise Structural Walls," ACI Journal, 83-33, March-April, 1986.

48. Iliya, R., and Bertero, V. V., "Effects of Amount and Arrangement of Wall-Panel Reinforcement on Hysteretic Behavior of Reinforced Concrete Walls," Report No. EERC-80/04, Earthquake Engineering Research Center, University of California, Berkley, Feb 1980. 156 pages.

49. Kabeyasawa, T., Shiohara, H., Otani, S., and Aoyama, H., "Analysis of the Full-Scale Seven-Story Reinforced Concrete Test Structure," Journal of the Faculty of Engineering, The University of Tokyo, Vol. XXXVII, No 2, 1983, pp. 431-478.

50. Karsan, I. D., and Jirsa, J. O., "Behavior of Concrete Under Compressive Loadings" Journal of the Structural Division, ASCE, Vol. 95, No. ST12, Dec 1969, pp. 2543-2563.

51. Keshavarzian, M., and Schnobrich, W. C., "Inelastic Analysis of R/C Coupled Shear Walls," Earthquake Engineering and Structural Dynamics, Vol. 13, 1985, pp. 247-448.

52. Liao, W. M., "Studies on R.C. Shear Walls amd Framed Masonary Shear Walls," Tokyo University publication, 1964.

53. Lybas, J. M., "Effect of Beam Strength and Stiffness on Dynamic Behavior of Reinforced Concrete Coupled Walls," Structural Research Series No. 444, Univ. of Illinois, 1977.

54. Ma, S. M., Popov, E. P., and Bertero, V. V., "Experimental and Analytical Studies on the Hysteretic Behavior of Reinforced Concrete Rectangular and T-Beams," Report No. EERC-76/2, Earthquake Engineering Research Center, University of California, Berkley, 1976.

55. National Earthquake Hazards Reduction Program Recommended Provisions for the Development of Seismic Regulations for New Buildings, Building Seismic Safety Council, 1985.

56. Newmark, N. M., "A Method of Computation for Structural Dynamics" Transactions, ASCE, Vol. 127, Part I, 1962, pp. 1406-1435.

57. Oesterle, R. G., Fiorato, A. E., Jahal, L. S., Carpenter, J. E., Russell, H. G., and Corley, W. G., "Earthquake Resistant Structural Walls - Test of Isolated Walls," Report to NSF by the PCA, 1976, 321 pages, (NTIS PB-271 467).

58. Oesterle, R. G., Fiorato, A. E., and Corley, W. G., "Free Vibration Test of Structural Walls," Proceedings of the Sixth World Conference on Earthquake Engineering, 1977, pp. 3239-3240.

59. Oesterle, R. G., Fiorato, A. E., Aristizabal-Ochoa, J. D., and Corley, W. G., "Hysteretic Response of Reinforced Concrete Structural Walls," Reinforced Concrete Structures Subject to Wind and Earthquake Forces, SP 63-11, American Concrete Institute, Detroit, 1980, pp. 243-273.

60. Oesterle, R. G., Aristizabal-Ochoa, J. D., Shiu, K. N., and Corley, W. G., "Web Crushing of Reinforced Concrete Structural Walls," ACI Journal, 81-22, May-June 1984, pp. 231-241.

61. Omote, Y. and Takeda, T., "Non-Linear Earthquake Response Study on the Reinforced Concrete Chimney, Part I Model Test and Analysis," Transactions, Architectural Institute of Japan, No. 215, pp 21-32, 1974 (in Japanese).

62. Otani, S., "SAKE - A Computer Program for Inelastic Response of R/C Frames Subject to Earthquakes," Civil Engineering Studies, Structural Research Series No. 413, University of Ill., Urbana, Nov 1974, 145 pages.

63. Otani, S., "Inelastic Analysis of R/C Framed Structures," Journal of the Structural Division, ASCE, Vol. 100, No. ST7, July, 1974.

64. Park, R., Kent, D. C., and Sampson, R. A., "Reinforced Concrete Members with Cyclic Loading," Journal of the Structural Division, ASCE, Vol. 98, No. ST7, July 1972, pp. 1341-1360.

65. Park, Y., and Ang, A. H-S., "Mechanistic Seismic Damage Model for Reinforced Concrete," Journal of the Structural Division, ASCE, Vol. 111, No. 4, April, 1985, pp. 722-739.

66. Park, Y., and Ang, A. H-S., "Seismic Damage Analysis of Reinforced Concrete Buildings," Journal of the Structural Division, ASCE, Vol. 111, No. 4, April, 1985, pp. 740-757.

67. Paulay, T., Priestley, M. J. N., and Synge, A. J., "Ductility in Earthquake Resisting Squat Shearwalls," ACI Journal, 79-26, July-August 1982, pp. 257-269.

68. Penzien, J., and Watabe, M., "Characteristics of 3-Dimensional Earthquake Ground Motions," Earthquake Engineering and Structural Dynamics, Vol.3, 1975, pp. 365-373.

69. Saatcioglu, M., Derecho, A. T., Corley, W. G., "Modeling Hysteretic Behavior of Coupled Walls for Dynamic Analysis," Earthquake Engineering and Structural Dynamics, Vol. 111, 1983, pp. 711-726.

70. Saiidi, M., and Sozen, M., "Simple and Complex Models for Nonlinear Seismic Response of Reinforced Concrete Structures," Civil Engineering Studies, Structural Research Series No. 465, University of Ill., Urbana, Aug 1979, 188 pages.

71. Sinha, B. P., Gerstle, K. H., and Tulin, L. G., "Stress-Strain Relations for Concrete Under Cyclic Loading," Journal of the American Concrete Institute, 61-12, February, 1984, pp. 195-211.

72. Sheu, M. S., "Behavior of Low Rise R.C. Shear Walls Subjected to Reversed Cyclic Loading," Technical Report to the National Science Council, Architectural Engineering Department, National Cheng Kung University, July, 1988 (in Chinese).

73. Synge A. J., "Ductility of Squat Shear Walls," Masters of Engineering Thesis, University of Canterbury, Christchurch, New Zealand, February 1980, 125 pages.

74. Takayanagi, T. and Schnobrich, W. C., "Computed Behavior of Reinforced Concrete Coupled Shear Walls," Structural Research Series No. 434, University of Illinois, Urbana, Illinois 1976.

75. Takeda, T., Sozen, M. A., and Nielsen N. N., "Reinforced Concrete Response to Simulated Earthquakes," Journal of the Structural Division, ASCE, Vol. 96, No. ST12, Dec 1970, pp. 2557-2573.

76. Thomson, W. T., Theory of Vibrations with Applications, Prentice-Hall, 1981, 493 pages.

77. Uniform Building Code, International Conference of Building Officials, 1988.

78. Umemura, H., Aoyama, H., Ito, M., and Hosokawa, Y., "Aseismic Characteristics of RC Box and Cylinder Walls," Proceedings of the Sixth World Conference on Earthquake Engineering, 1977, pp. 3144-3149

79. Umemura, H., Aoyama, H., Ito, M., Hosokawa, Y., and Lee, "Experimental Study of the Characteristics of Reinforced Concrete Shear Walls Under Cyclic Loading," Department of Architecture, University of Tokyo, Umemura Lab. 1975 (in Japanese).

80. Vallenas, J. M., Bertero, V. V., and Popov, E. P., "Hysteretic Behavior of Reinforced Concrete Structural Walls," Report No. EERC-79/20, Earthquake Engineering Research Center, University of California, Berkley, Aug 1979, 235 pages.

81. Vecchio, F., and Collins, M. P., "Stress-Strain Characteristics of Reinforced Concrete in Pure Shear," IABSE Colloquium Advanced Mechanics of Reinforced Concrete, Delft 1981, pp. 233-247.

82. Vecchio, F., and Collins, M. P., "The Response of Reinforced Concrete to In-Plane Shear and Normal Stresses," Department of Civil Engineering, University of Toronto, Publication No 82-03, March 1982, 332 pages.

83. Wang, T. Y., Bertero, V. V., and Popov, E. P., "Hysteretic Behavior of Reinforced Concrete Framed Walls," Report No. EERC-75/23, Earthquake Engineering Research Center, University of California, Berkley, Dec 1975.

84. Weaver, Jr., W., and Johnston, P. R., Structural Dynamics by Finite Elements, Prentice-Hall, 1987, 591 pages.

85. Wiegel, M., et al, Earthquake Engineering, Prentice-Hall, 1970.

86. Wilson, E. L., Farhoomand, I., and Bathe, K. J., "Nonlinear Dynamic Analysis of Complex Structures," Earthquake Engineering and Structural Dynamics, Vol. 1, 1973, pp. 241-252.

APPENDICES

APPENDIX A

SPECTRAL ANALYSIS

Fourier Transform. A periodic signal[25], with a period of τ can be represented by the infinite Fourier series

$$x(t) = \frac{a_0}{2} + a_1 \cos \omega_1 t + a_2 \cos \omega_2 t + a_3 \cos \omega_3 t + \cdots + b_1 \sin \omega_1 t + b_2 \sin \omega_2 t + b_3 \sin \omega_3 t + \cdots \quad (A.1)$$

where $\omega_n = n\frac{2\pi}{\tau}$. For a signal of duration T, the signal is assumed to be repeated every T seconds as shown in Figure 199.

The infinite series in Equation A.1 consists of the summation of periodic functions at different frequencies. The coefficients a_n and b_n are the amplitude of the periodic function at frequency ω_n. The amplitude of a_n is 90° out of phase with the amplitude of b_n. The resolution is the interval between frequencies ω_n and ω_{n+1}, or $\Delta\omega = \frac{2\pi}{\tau}$. Note that functions with larger periods have a finer resolution. The signal in Figure 199 has a fixed length T, yielding a resolution of $\Delta\omega = \frac{2\pi}{T}$. However, the resolution of the signal can be improved by assuming the record is longer, say T′, and the signal is zero between T and T′, as shown in Figure 200. The coefficients a_n and b_n for the signals in Figures 199 and 200 are not equal.

To determine the coefficient a_n in Equation A.1, multiply both sides of the equation by $\cos \omega_n t$ and integrate over the period.

---

[25] For structural analysis, the signal may be an earthquake ground acceleration, measured experimental acceleration, velocity or displacement.

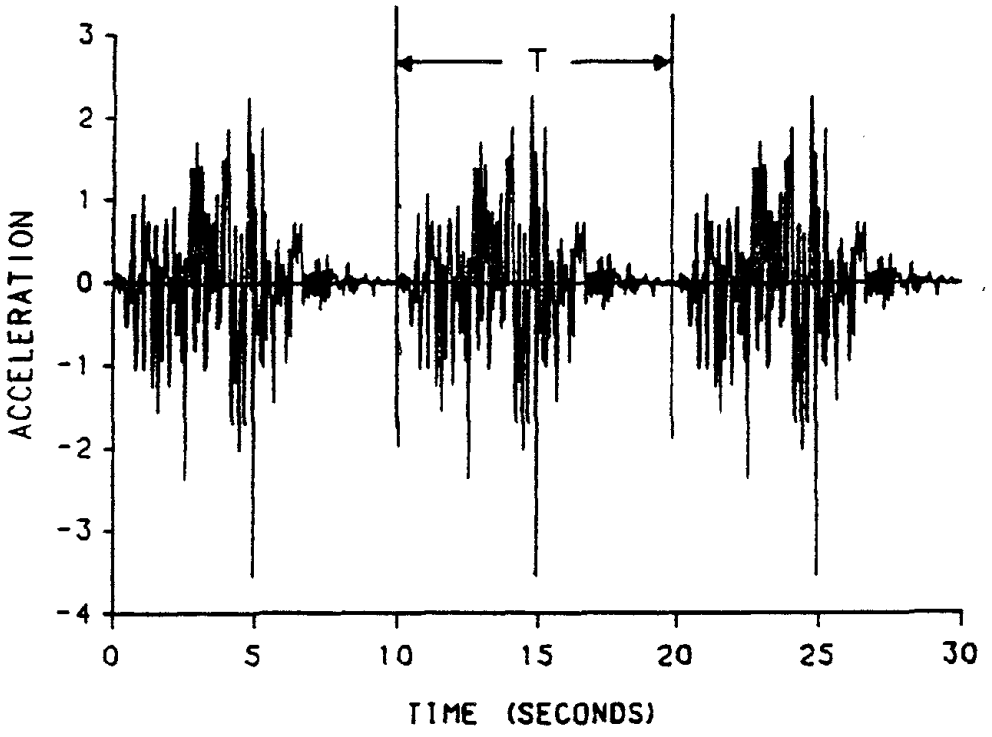

Figure 199. Periodic Earthquake Signal

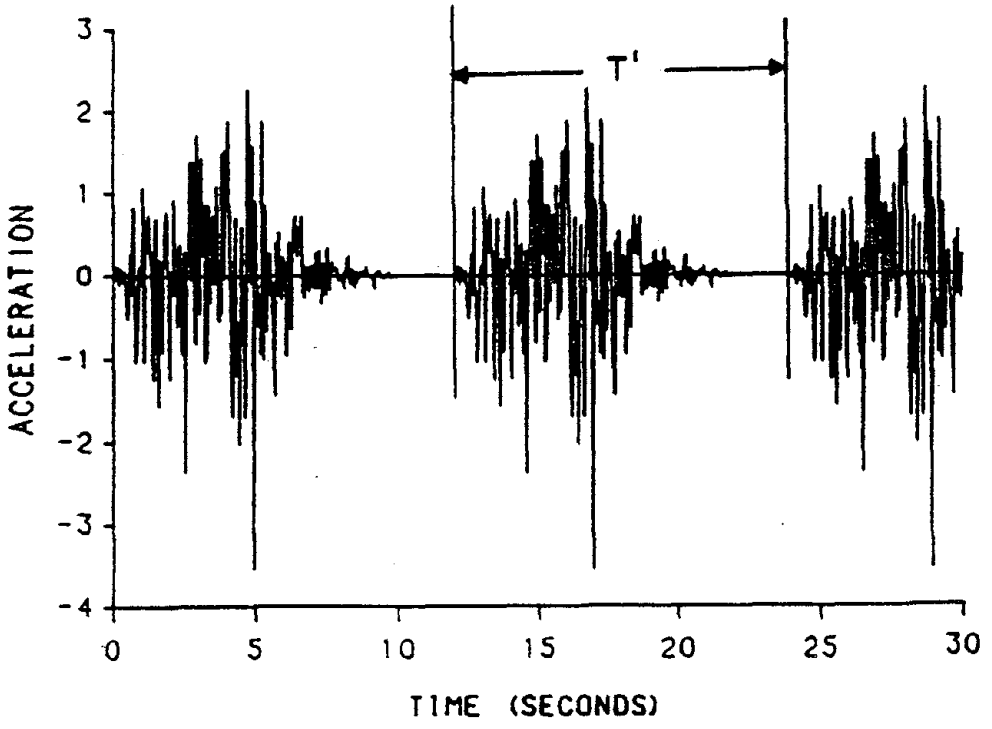

Figure 200. Earthquake Signal with Modified Period

$$\int_0^\tau x(t)\cos(\omega_n t)\,dt = \int_0^\tau \frac{a_0}{2}\cos(\omega_n t)\,dt$$

$$+ \int_0^\tau (a_1 \cos\omega_1 t + a_2 \cos\omega_2 t + a_3 \cos\omega_3 t + \cdots)\cos(\omega_n t)\,dt$$

$$+ \int_0^\tau (b_1 \sin\omega_1 t + b_2 \sin\omega_2 t + b_3 \sin\omega_3 t + \cdots)\cos(\omega_n t)\,dt \qquad (A.2)$$

When $n=0$, $\omega_n = 0$, $\cos\omega_n t = 1$ and Equation A.2 reduces to

$$\int_0^\tau x(t)(1)dt = \int_0^\tau \frac{a_0}{2}(1)dt$$

$$+ \int_0^\tau (a_1 \cos\omega_1 t + a_2 \cos\omega_2 t + a_3 \cos\omega_3 t + \cdots)(1)dt$$

$$+ \int_0^\tau (b_1 \sin\omega_1 t + b_2 \sin\omega_2 t + b_3 \sin\omega_3 t + \cdots)(1)dt \qquad (A.3)$$

Integrating the first term yields

$$\int_0^\tau \frac{a_0}{2}(1)dt = \frac{a_0}{2}(\tau - 0) = \frac{a_0\tau}{2} \qquad (A.4)$$

Integrating the m^{th} element of the second term yields

$$\int_0^\tau a_m \cos(\omega_m t)\,dt = \frac{a_m}{\omega_m}[\sin(m2\pi) - \sin(0)] = 0 \qquad (A.5)$$

And integrating the m^{th} element of the third term yields

$$\int_0^\tau a_m \sin(\omega_m t)\,dt = \frac{-a_m}{\omega_m}[\cos(m2\pi) - \cos(0)] = 0 \qquad (A.6)$$

Substituting Equations A.4, A.5, and A.6 into Equation A.3 and solving for a_0 yields

$$a_0 = \frac{2}{\tau}\int_0^{\tau} x(t)dt \tag{A.7}$$

Note that a_0 is twice the average of the record x(t). When $n \neq 0$, integrating the first term of Equation A.2 yields

$$\int_0^{\tau} \frac{a_0}{2}\cos(\omega_n t)\,dt = \frac{a_0}{2\omega_n}[\,\sin(n2\pi) - \sin(0)\,] = 0 \tag{A.8}$$

Integrating the m^{th} element of the second term yields

$$\int_0^{\tau} a_m \cos(\omega_m t)\cos(\omega_n t)\,dt$$

$$= a_n\left(\frac{\tau - 0}{2} + \frac{1}{4\omega_n}(\,\sin 4n\pi - \sin 0)\right) = a_n\frac{\tau}{2}, \quad \text{for } n = m \tag{A.9}$$

$$= \int_0^{\pi} a_m\frac{\tau}{\pi}\cos(2nz)\cos(2mz)dz = 0, \quad \text{for } n \neq m$$

And integrating the m^{th} element of the third term yields

$$\int_0^{\tau} b_m \sin(\omega_m t)\cos(\omega_n t)\,dt = \int_0^{\tau}\frac{b_m}{2}\left[\,\sin\left((n+m)\frac{2\pi t}{\tau}\right) + \sin\left((m-n)\frac{2\pi t}{\tau}\right)\right]\,dt$$

$$= \frac{-b_m}{2}\left(\frac{\cos(n+m)2\pi - \cos(0)}{(n+m)\frac{2\pi}{\tau}} + \frac{\cos(m-n)2\pi - \cos(0)}{(m-n)\frac{2\pi}{\tau}}\right) = 0 \tag{A.10}$$

Substituting Equations A.8, A.9, and A.10 into Equation A.3 and solving for a_n yields

$$a_n = \frac{2}{\tau}\int_0^{\tau} x(t)\cos(\omega_n t)\,dt \tag{A.11}$$

To determine the coefficient b_n multiply both sides of Equation A.2 by $\sin \omega_n t$ and integrate over the period. Performing the integrations, similar to the procedure for a_n, yields

$$b_n = \frac{2}{\tau}\int_0^{\tau} x(t) \sin(\omega_n t)\, dt \tag{A.12}$$

The Fourier transform is given by Equation A.1 where the constants are defined by Equations A.7, A.11 and A.12.

It is often convenient to express the Fourier transform in exponential form. Recall the Euler identities

$$\left.\begin{aligned} \cos \omega_n t &= \frac{1}{2}\left(e^{i\omega_n t} + e^{-i\omega_n t}\right) \\ \sin \omega_n t &= \frac{-i}{2}\left(e^{i\omega_n t} - e^{-i\omega_n t}\right) \end{aligned}\right\} \tag{A.13}$$

Substituting the Euler identities into Equation A.1 yields

$$x(t) = \frac{a_0}{2} + \sum_{n=1}^{\infty}\left[\frac{1}{2}(a_n - ib_n)e^{i\omega_n t} + \frac{1}{2}(a_n + ib_n)e^{-i\omega_n t}\right] \tag{A.14}$$

Let $C_n = \frac{1}{2}(a_n - ib_n)$ and $C_0 = \frac{a_0}{2}$ then Equation A.14 becomes

$$x(t) = \sum_{n=0}^{\infty} C_n e^{i\omega_n t} + \sum_{n=1}^{\infty} C_n^* e^{-i\omega_n t} \tag{A.15}$$

where C_n^* is the complex conjugate of C_n. Examine the following coefficients when n is negative

$$e^{-i\omega(-n)t} = e^{i\omega nt}$$

$$\left.\begin{aligned} a_{-n} &= \int x(t)\cos(-n\omega t)dt = a_n \\ b_{-n} &= \int x(t)\sin(-n\omega t)dt = -b_n \end{aligned}\right\} \qquad (A.16)$$

Substituting the negative coefficients into the second term of Equation A.14 yields

$$\sum_{n=1}^{\infty}\frac{1}{2}(a_n + ib_n)e^{-i\omega_n t} = \sum_{n=-1}^{-\infty}\frac{1}{2}(a_n - ib_n)e^{i\omega_n t} = \sum_{n=-1}^{-\infty} C_n e^{i\omega_n t} \qquad (A.17)$$

Thus Equation A.15 becomes

$$x(t) = \sum_{n=-\infty}^{\infty} C_n e^{i\omega_n t} \qquad (A.18)$$

where the coefficients C_n are defined by

$$C_n = \frac{1}{2}(a_n - ib_n) = \frac{1}{\tau}\int_0^{\tau} x(t)\left(\cos(\omega_n t) - i\,\sin(\omega_n t)\right)dt = \frac{1}{\tau}\int_0^{\tau} x(t)e^{-i\omega_n t}dt \qquad (A.19)$$

Thus a complex definition of the Fourier transform is defined by Equations A.18 and A.19. Note that the summation in Equation A.18 is from -∞ to ∞.

In Equation A.15 let the complex vector Z_n be equal to $C_n e^{i\omega_n t}$ and the conjugate of Z_n, be $Z_n^* = C_n^* e^{-i\omega_n t}$. Thus Equation A.15 is

$$x(t) = C_0 + \sum_{n=1}^{\infty}\left(Z_n + Z_n^*\right) \qquad (A.20)$$

The sum of a complex vector and its conjugate are twice the magnitude of the real component. Thus the Fourier transform is represented by

$$x(t) = C_0 + \sum_{n=1}^{\infty} 2\,Re\dot{Z}_n = C_0 + \sum_{n=1}^{\infty} 2\,Re\left(C_n e^{i\omega_n t}\right) \tag{A.21}$$

where ReZ_n represents the real component of the complex vector Z_n. Let $2C_n = D_n$, then the Fourier transform is represented by

$$x(t) = \frac{D_0}{2} + \sum_{n=1}^{\infty} ReD_n e^{i\omega_n t} \tag{A.22}$$

where

$$D_n = 2C_n = \frac{2}{\tau}\int_0^{\tau} x(t)e^{-i\omega_n t}dt \tag{A.23}$$

A second complex definition of the Fourier transform is given by Equations A.22 and A.23. Note that the summation in Equation A.22 is from 1 to ∞.

The Fourier transforms presented above are for continuous functions. Signals are digitized to facilitate numerical computation. These signals consist of N data points with a constant time increment of Δt and a period ranging from $t = 0$ to $t = (N-1)\Delta t$. The discrete Fourier transform that corresponds to Equations A.1, A.7, A.11 and A.12 is

$$x(t) = \sum_{n=1}^{n2-1} \left(a_n \cos \omega_n t + b_n \sin \omega_n t\right) + \frac{a_0 + a_{n2} \cos \omega_{n2} t}{2} \tag{A.24}$$

where

$$\left.\begin{aligned} a_n &= \frac{2}{\tau}\sum_{m=0}^{N-1} x(t_m)\cos(\omega_n t_m)\Delta t \\ b_n &= \frac{2}{\tau}\sum_{m=0}^{N-1} x(t_m)\sin(\omega_n t_m)\Delta t \end{aligned}\right\} \qquad (A.25)$$

and $n2 = \frac{N}{2}$. The discrete Fourier transform that corresponds to Equations A.18 and A.19 is

$$x(t) = \sum_{n=0}^{N-1} C_n e^{i\omega_n t} \qquad (A.26)$$

where

$$C_n = \frac{1}{\tau}\sum_{m=0}^{N-1} x(t_m)e^{(-i\omega_n t_m)}\,\Delta t \qquad (A.27)$$

The Fourier transform that corresponds to Equations A.22 to A.23 is

$$x(t) = \sum_{n=1}^{n2-1} \mathrm{Re}\left(D_n e^{i\omega_n t}\right) + \mathrm{Re}\left(\frac{D_0 + D_{n2}e^{i\omega_{n2} t}}{2}\right) \qquad (A.28)$$

where

$$D_n = \frac{2}{\tau}\sum_{m=0}^{N-1} x(t_m)e^{(-i\omega_n t_m)}\,\Delta t \qquad (A.29)$$

Numerically the calculations are carried out using a fast Fourier transform (FFT). The FFT is an algorithm developed by Cooley, et al (29) that can calculate the Fourier transform very efficiently when the number of time increments is a power of 2, ie $N = 2^M$. Thus the signal is commonly digitized with $2^{10} = 1024$, $2^{11} = 2048$ or $2^{12} = 4096$ points.

For the Fourier coefficients in Equations A.24 to A.28 only the first n2 coefficients are unique. Coefficients above n2 are the complex conjugate of the coefficients below n2. The frequency at n2 is $\omega_{n2} = \frac{N\pi}{\tau}$ radians/second or $f_{n2} = \frac{N}{2\tau}$ hertz is the Nyquist frequency. This is the highest frequency that the Fourier transform can detect. Frequencies above the Nyquist frequency are reflected as low frequency signals. This can be demonstrated by the sine wave in Figure 201(a). The sine wave has a period of 2π seconds and a frequency of 1 radian/second. Suppose the sine wave is sampled (digitized) with a time step of 1.5π. The Nyquist frequency is $\frac{2\pi}{2 \times 1.5\pi} = 0.67$ radians/second, which is less than the frequency of the sine wave. The resulting signal is shown in Figure 201(b), and appears to have a period of 6π seconds, and a frequency of $\frac{1}{3}$ radian/second. Thus the 1 radian/second sine wave is reflected as a $\frac{1}{3}$ radian/second sine wave. This is known as ailsing. To correctly sample the sine wave, the minimum number of points is

$$\omega_{n2} = \frac{N\pi}{\tau}, \qquad 1 = \frac{N\pi}{2\pi}, \qquad N = 2 \tag{A.30}$$

or two points, A and B in Figure 201(a), are required in the period of 2π. A signal with two points per period is also shown in Figure 201(c). Note that the Nyquist criteria is the lower limit of the number of point needed to describe the signal. To accurately describe the sine wave, more points are required. When the number of points used to sample a signal is fixed, low pass filters are used to remove the signal's frequency content above the Nyquist frequency. Filtering the sine wave in Figure 201 with a .67 rad/sec low pass filter will remove the 1 rad/sec sine wave. Sampling this filtered sine wave with a time step of 1.5π yields a null signal. Thus the low pass filter prevents the high frequency signal from being reflected as a low frequency signal, but it modifies the original signal.

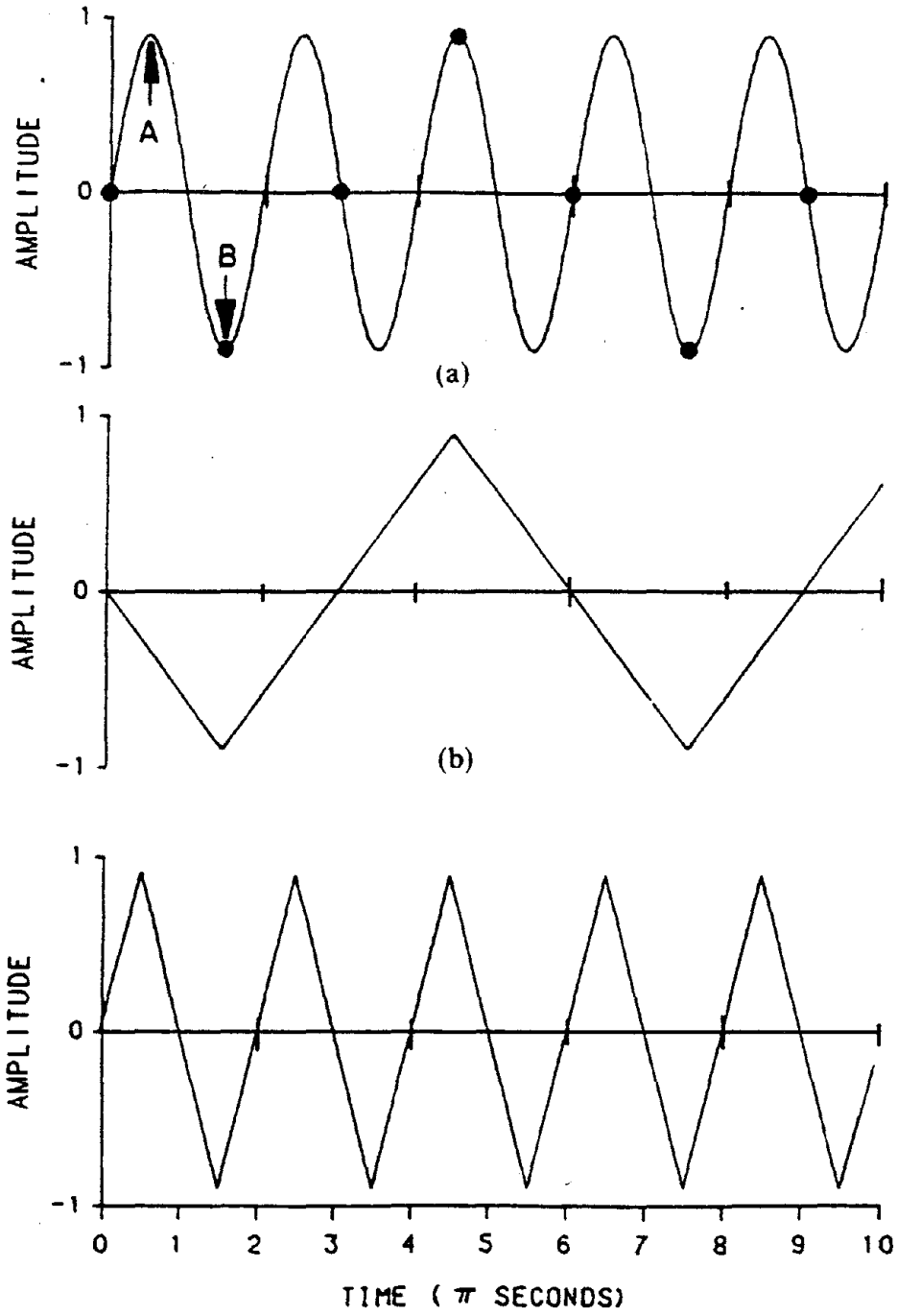

Figure 201. Sine Wave With Ailsing: (a) Sine Wave, (b) Sine Wave Sampled at $\Delta t = 1.5\pi$, (c) Sine Wave Sampled at $\Delta t = \pi$

Power Spectral Density. The frequency content of a signal may be examined by the power spectral density (PSD). The power spectrum is the magnitude of energy in a given frequency interval. The power spectrum is divided by the frequency interval to yield the PSD. Define the power spectrum for a frequency, f_n as

$$G(f_n) = \frac{1}{2} D_n D_n^* \tag{A.31}$$

where D_n is given in Equation A.23 or A.29, andD_n^* is the complex conjugate of D_n. The power spectral density is the power spectrum divided by the frequency increment, or

$$S(f_n) = \frac{G(f_n)}{\Delta f} = \frac{D_n D_n^*}{2\Delta f} = \frac{2C_n C_n^*}{\Delta f} = \frac{a_n^2 + b_n^2}{2\Delta f} \tag{A.32}$$

where the Fourier coefficient C_n is given in Equation A.19 or A.27, C_n^* is the complex conjugate of C_n, and a_n and b_n are given in Equations A.11, A.12, or A.25. The PSD is used to examine the frequency content of accelerations in Section B of Chapter II, and in Section B of Chapter VII.

Frequency Response Function. For a single degree of freedom structure subject to a cyclic forcing function, the equation of motion has the form

$$m\ddot{x} + c\dot{x} + kx = C_n e^{i\omega_n t} \tag{A.33}$$

where C_n is the magnitude of the cyclic forcing function. The steady state solution has the form

$$x(t) = H(\omega_n) C_n e^{i\omega_n t} \tag{A.34}$$

where the frequency response function (FRF), $H(\omega_n)$ is given by

$$H(\omega_n) = \frac{1}{k - m\omega_n^2 + ic\omega_n} \tag{A.35}$$

Superimposing N cyclic forcing functions, the steady state response becomes

$$x(t) = \sum H(\omega_n) C_n e^{i\omega_n t} \tag{A.36}$$

Taking the Fourier transform (Equation A.18) of Equation A.36 yields

$$\sum C'_n e^{i\omega_n t} = \sum H(\omega_n) C_n e^{i\omega_n t} \tag{A.37}$$

where C'_n are the Fourier coefficients of the response and C_n are the Fourier coefficients of the forcing function. The magnitude of the FRF at frequency n is given by

$$H(\omega_n) = \frac{C'_n}{C_n} \tag{A.38}$$

Equation A.38 is used to calculate the FRF for elastic systems in Section B of Chapter VII. The forcing function consists of the ground acceleration times the mass and the response consists of the relative floor acceleration. If the mass is omitted from the forcing function, then the FRF is multiplied by the mass. The FRF can be examined to determine the natural frequency and damping of the structure. The FRF for multiple degree of freedom structures is also obtained by Equation A.38. However, the shape of multiple degree of freedom FRF is more complex than the single degree of freedom FRF in Equation A.35.

APPENDIX B

PARABOLIC BASE LINE CORRECTION

Given an acceleration record A(t), consisting of N data points with an incremental time of Δt and having a period of τ, the parabolic function

$$f(t) = C_1 + C_2 t + C_3 t^2 \tag{B.1}$$

is subtracted from the acceleration record yielding

$$A'(t) = A(t) - f(t) = A(t) - C_1 - C_2 t - C_3 t^2 \tag{B.2}$$

Integrating Equation B.2 yields the velocity

$$V'(t) = \int (A(t) - f(t))dt = V(t) - \left(C_0 + C_1 t + \frac{C_2}{2} t^2 + \frac{C_3}{3} t^3 \right) \tag{B.3}$$

The constants C_1, C_2 and C_3 are chosen such that the sum of the velocity squared, $(V')^2$, is a minimum. Define the function U as the sum of the velocity squared,

$$U = \sum_{t=0}^{N\Delta t} [V'(t)]^2 = \sum_{t=0}^{N\Delta t} \left[V(t) - \left(C_0 + at + bt^2 + ct^3 \right) \right]^2 \tag{B.4}$$

where $a = C_1$, $b = \frac{C_2}{2}$, $c = \frac{C_3}{3}$. Set $C_0 = 0$, since the term C_0 does not appear in the acceleration $A'(t)$. Taking the partial of U with respect to a and setting equal to zero yields

$$\frac{\partial U}{\partial a} = 0 = 2 \sum_{t=0}^{N\Delta t} \left[V(t) - \left(at + bt^2 + ct^3 \right) \right] (-t) \tag{B.5}$$

Rearranging terms yields

$$\sum tV(t) = a\sum t^2 + b\sum t^3 + c\sum t^4 \tag{B.6}$$

where the summation is carried out for N points, from 0 to NΔ. Taking the partial of U with respect to b and setting equal to zero yields

$$\frac{\partial U}{\partial b} = 0 = 2\sum_{t=0}^{N\Delta t}\left[V(t) - \left(at + bt^2 + ct^3\right)\right](-t^2) \tag{B.7}$$

Rearranging terms yields

$$\sum t^2V(t) = a\sum t^3 + b\sum t^4 + c\sum t^5 \tag{B.8}$$

Taking the partial of U with respect to c and setting equal to zero yields

$$\frac{\partial U}{\partial c} = 0 = 2\sum_{t=0}^{N\Delta t}\left[V(t) - \left(at + bt^2 + ct^3\right)\right](-t^3) \tag{B.9}$$

Rearranging terms yields

$$\sum t^3V(t) = a\sum t^4 + b\sum t^5 + c\sum t^6 \tag{B.10}$$

Rewriting Equations B.6, B.8 and B.10 in matrix form

$$\begin{bmatrix} Vt1 \\ Vt2 \\ Vt3 \end{bmatrix} = \begin{bmatrix} t2 & t3 & t4 \\ t3 & t4 & t5 \\ t4 & t5 & t6 \end{bmatrix}\begin{bmatrix} a \\ b \\ c \end{bmatrix} \tag{B.11}$$

where $t2 = \sum t^2$

$t3 = \sum t^3$

$t4 = \sum t^4$

$$t5 = \sum t^5$$

$$t6 = \sum t^6$$

$$Vt1 = \sum V(t)t$$

$$Vt2 = \sum V(t)t^2$$

$$Vt3 = \sum V(t)t^3$$

Equation B.11 is solved for a, b and c, and the corrected accelerations are given by

$$A'(t) = A(t) - a - 2bt - 3ct^2 \qquad (B.12)$$

The parabolic base line correction is used to correct experimental accelerations in Section B of Chapter II.